

H24/3143

MONASH UNIVERSITY  
THESIS ACCEPTED IN SATISFACTION OF THE  
REQUIREMENTS FOR THE DEGREE OF  
DOCTOR OF PHILOSOPHY

ON..... 7 December 2001 .....

*for* Sec. Research Graduate School Committee

Under the copyright Act 1968, this thesis must be used only under the normal conditions of scholarly fair dealing for the purposes of research, criticism or review. In particular no results or conclusions should be extracted from it, nor should it be copied or closely paraphrased in whole or in part without the written consent of the author. Proper written acknowledgement should be made for any assistance obtained from this thesis.

## ADDENDUM

The following amendments were identified by reviewers during the review process and shall be made to the appropriate sections of the thesis text:

p 7 para 3, line 5: delete "Zhi-He and Yiu-Wing" and read "Jin and Mai"

p 44 para 1, line 1: delete "150mm" and read "50mm"

p 46 para 1, line 1: delete "plain" and read "plane"

p 52: Add at end of para 3:

"It should be noted that one of the implicit assumptions when using the weight function approach is that the stress distribution in a component is not relaxed with crack growth. In cases where stress relaxation does occur, this assumption can be conservative."

p 52 para 4, line 2: delete "plain" and read "plane"

p 57 para 2, line 5: delete "Zhi-He and Yui-Wing" and read "Jin and Mai"

p 121 para 3, line 8: delete "Zhi-He and Yiu-Wing" and read "Jin and Mai"

p 166 para 4, line 4: delete "plain" and read "plane"

Reference Section, final page, line 3: delete "Zhi-He J. and Yiu-Wing M." and read "Jin Z.-H. and Mai Y.-M."

The following amendments were identified by the author subsequent to the printing of the thesis and shall be made to the appropriate sections of the thesis text:

p 52: delete equation [3.12] and replace with:

$$\sigma(x) = -\alpha T(x)E + \frac{1}{2(w/2)} \int_{-\frac{w}{2}}^{\frac{w}{2}} \alpha T(x)E \cdot dx + \frac{3x}{2(w/2)^3} \int_{-\frac{w}{2}}^{\frac{w}{2}} \alpha T(x)E \cdot dx$$

p 141 para 1, line 3: delete "plain" and read "plane"

p 179 para 3, line 4: delete "smaller" and read "larger"

p 194 para 1, line 6: delete "on the next page" and read "below"

**MONASH UNIVERSITY**  
**DEPARTMENT OF MECHANICAL ENGINEERING**

**FACTORS AFFECTING CRACK GROWTH IN CARBON  
STEEL DUE TO REPEATED THERMAL SHOCK FROM  
TEMPERATURES BELOW THE CREEP RANGE**

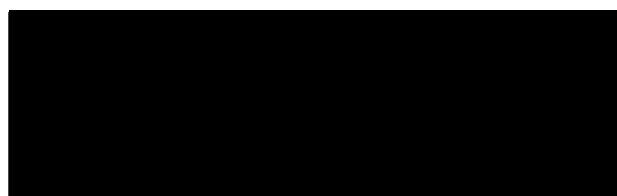
by

**BRIAN KEREZSI (B.Eng.)**

**A thesis submitted in fulfillment of the requirements for the  
degree of Doctor of Philosophy**

**July 2001**

I hereby declare that this submission is my own work and that, to the best of my knowledge and belief, it contains no material previously published or written by another person, nor material, which to a substantial extent, has been accepted for the award of any other degree or diploma of a university or other institute of higher learning, except where due acknowledgement is made in the text.



B.B. Kerezsi

July 2001



## Summary

In this thesis, an investigation into the major factors contributing to crack growth in elevated temperature carbon steel subjected to repeated thermal shock has been conducted. Experimental, numerical and theoretical techniques have all been applied to analyse the effects of mechanical loading, environment, transients and geometry on crack initiation and growth. The accurate modeling of such cracking is of particular interest in the thermal power generation industry where process variations and transients often lead to the rapid thermal shock loading of pressure piping components such as headers and tubes.

A distinction is made between the term thermal fatigue and repeated thermal shock (RTS). Thermal fatigue is defined as the broader category involving cyclic stresses resulting from the constraint of expansions and contractions of a component exposed to a change in temperature. Thermal shock on the other hand is a sub-set of thermal fatigue, defined as the particular case of exposing a component to a transient, highly non-linear temperature distribution brought on by a rapid change in operating condition.

A novel test rig, capable of applying large-scale thermal shocks to heated, flat-plate carbon steel specimens via water quenching, has been specifically developed for the investigation. The test-rig also has the ability to apply primary steady state loads and to control the cooling environment. These variables allow the simulation of operational conditions in thermal power plant.

Results from the test rig have allowed conclusions to be drawn on the effects of primary load and environment on small crack initiation and long crack growth. Comparisons of experimental results with predictions from current design and analysis codes and standards have also been made.

Specific contributions of this work include:

1. Development of a stress analysis approach, suitable for determining times to crack initiation in an RTS situation using traditional  $S-N$  techniques.
2. Suggestions of appropriate crack growth equations for use during RTS in carbon steels based on test data. These growth equations are defined by:
  - a) a high strain fatigue region where growth accelerates,
  - b) an elastic growth region affected by environmental factors where growth decelerates, and
  - c) identification of the cross over crack depth between these two regions.
3. Initial efforts towards quantifying the parameters of the above growth relations with consideration of the effects of primary load, dissolved oxygen and thermal shock levels.
4. The development of a number of charts to assist in quantifying the severity of thermal shocks on flat plates
5. Theoretical and numerical investigations of geometry effects on the thermal shock process. Specific situations investigated include:
  - a) thermal shocks inside a long cylinder with a long crack, and
  - b) thermal shock at the industrially important cases of internal (radiused) and external (sharp) corners.
6. Suggested modifications to the relevant fitness for purpose standards to help reduce high levels of conservatism.

Finally, from the work outlined, general conclusions are made. These conclusions will help make decisions on which combinations of variables can lead to accelerated thermal shock crack growth and which combinations can lead to crack arrest at relatively harmless depths.

## Acknowledgements

The author is deeply indebted and grateful to Associate Professor J.W.H. Price for his enthusiastic and attentive supervision, his invaluable guidance and his generous support. The author is also highly grateful for the technical support and assistance received from Dr R.N. Ibrahim and Dr. A. Kotousov throughout the candidature.

Particular thanks go to Mr. W Eadon, Mr. I. Little and Mr. J. Morris for assistance and support in the development and maintenance of the testing equipment and preparation of specimen samples. Thanks also to Mrs. A. Maltezos for all her administration assistance and for always knowing who to call.

Thanks to the Monash Research Graduate School and the Department of Mechanical Engineering for organising generous financial support during the candidature. Such support greatly eased the burden brought on by full time study.

The author would also like to thank the individual industrial sponsors for the project. Namely these are Pacific Power, Western Power, Optima, HRL Technology and EPRI. Particular thanks to HRL Technology for supply and machining of test specimen materials, and to Mr W. Mika and Dr. H. Moss for their valuable guidance in the early stages of the project.

Special thanks go to Miss C. Stathopoulos and Miss M. Newman for the kind sacrifices of their own time, providing proofreading services. Thanks also to all my friends (they know who they are) who have kept me laughing over the last three years, for that I am grateful

Final thanks go to my parents Mrs R. Eszes and Mr. G. Eszes, without whose unconditional love and support, I would never have been able to attempt this work.

## Table of Contents

Title	Page
Summary	i
Acknowledgments	iii
List of Tables	x
List of Figures	xi
Nomenclature	xix
Chapter 1 Introduction – Crack Growth due to Repeated Thermal Shock	1
Chapter 2 Thermal Shock Theory & Literature Review	5
2.1 Introduction	5
2.2 Repeated Thermal Shock (RTS) vs. Thermal Fatigue	5
2.3 Basic Thermal Shock Stress Theory	6
2.4 Thermal Stress Fatigue Analysis – A Brief History	8
2.4.1 Early Years	8
2.4.2 Linear Elastic Fracture Mechanics (LEFM)	9
2.4.3 Effects of Plasticity	11
2.4.4 Limits of LEFM	13
2.4.5 Differences Between Crack Initiation and Crack Growth	14
2.5 Factors Affecting RTS Crack Growth	16
2.5.1 Superimposed Mechanical Loading	16
2.5.1.1 Effect of mean loads during pure mechanical fatigue	16
2.5.1.2 Effect of mean loads on thermal fatigue	21
2.5.2 Environment	22
2.5.2.1 Crack initiation	23

2.5.2.2	Crack growth – superposition and competition models	24
2.5.2.3	Crack propagation mechanisms	27
2.5.2.4	Transient nature of environmentally assisted crack growth	30
2.5.2.5	Other environmentally assisted crack growth models	32
2.5.3	Temperature	33
2.4.3.1	Effect of temperature on fatigue crack growth	33
2.4.3.2	Low temperature creep	33
2.6	Summary	34
Chapter 3	Test Method – Experimental Analysis of RTS Crack Growth	35
3.1	Introduction	35
3.2	Review of Experimental Design	35
3.3	Test Rig Description	38
3.3.1	Furnace	39
3.3.2	Quenching Rig	41
3.3.3	Steady State Load Application	42
3.3.4	Specimen	42
3.4	Experimental Analysis Techniques	45
3.4.1	Notch Root Stresses	45
3.4.1.1	Stress profile linearisation	46
3.4.1.2	Sharp notch approximation	47
3.4.1.3	Notch sensitivity analysis	48
3.4.1.4	Neuber notch pseudostress analysis	49
3.4.1.5	Selection of preferred method	51
3.4.2	Determining Time (Cycles) to Crack Initiation	51
3.4.3	Crack Tip Stress Intensity Factors ( $K_I$ )	52
3.4.4	Limitations of LEFM Analysis	54
3.4.4.1	Notch effect	54
3.4.4.2	Plastic zone size	55
3.4.5	Temperature Analysis	56

Chapter 4	Experimental Results and Analysis – Crack Growth in a Flat Plate Specimen	61
4.1	Introduction	61
4.2	Description of Test Conditions	61
4.2.1	Verification Test (Test #1)	62
4.2.2	Controlled Testing (Tests #2 - #4)	63
4.3	Test Results Summary	65
4.3.1	Test #2; Specimens #2 & #3	65
4.3.2	Test #3; Specimens #4 & #5	65
4.3.3	Test #4; Specimens #6 & #7	67
4.4	Test Data	69
4.4.1	Temperature Data	69
4.4.2	Stress Analysis	70
4.4.3	Stress Intensity Factor Analysis	70
4.4.4	Notch Root Stress Amplitude	72
4.5	Analysis of Raw Test Data	74
4.5.1	Temperature Data	74
4.5.2	Stress Data	75
4.5.3	Stress Intensity Factor Data	75
4.5.3.1	General observations	75
4.5.3.2	<i>R</i> -ratio	76
4.5.3.3	History effects	78
4.6	Interpretation of Test Results	80
4.6.1	Crack Initiation	80
4.6.1.1	General observations – notched specimens	80
4.6.1.2	The use of <i>S-N</i> curves for predicting crack initiation	81
4.6.1.3	Placing limits on $k_f$ and the “worst case notch” approach	85
4.6.1.4	Effect of welds on crack initiation	86
4.6.2	Crack Growth	88
4.6.2.1	Short crack growth	89
4.6.2.2	Long crack growth	93

4.6.2.3	Predicting crack growth rates at different shock severities	96
4.6.3	Modelling Crack Growth in the Elastic Region	97
4.6.3.1	Torronen and Cullen (1982)	97
4.6.3.2	Gabetta et al (1990)	99
4.6.3.3	Discussion	102
4.6.4	Fractography	103
4.6.4.1	Crack mouth	103
4.6.4.2	Crack length	104
4.6.4.3	Justification of assumptions	113
4.7	Conclusions	114
4.7.1	Crack Initiation	114
4.7.2	Crack Growth	115
4.7.2.1	High strain fatigue region	115
4.7.2.2	Elastic crack growth region	116
4.7.2.3	Combined growth law	117
4.7.2.4	Crack growth mechanisms	118
Chapter 5	Transient and Geometry Effects	119
5.1	Introduction	119
5.2	Effect of Quench Duration on Crack Growth	119
5.2.1	Flat Plate Exposed to a One-Dimensional Thermal Shock	119
5.2.1.1	Stress intensity factor solutions	121
5.2.1.2	Discussion of stress intensity factor profile charts	123
5.2.1.3	The use of transient stress intensity factor charts to predict crack arrest	126
5.2.1.4	Limitations	127
5.2.1.5	Application to experimental results	128
5.2.2	Application to Hollow Cylindrical Geometry	131
5.3	Cracking at Corners Exposed to Thermal Shocks	137
5.3.1	Vertex Angles Greater than 180° (Internal Corners)	138
5.3.1.1	Introduction	138
5.3.1.2	Asymptotic stress field	140
5.3.1.3	Analytical solutions for generalised stress intensity factor $K_I$	142

5.3.1.4	Corner tip radius effect	144
5.3.1.5	Numerical simulations	146
5.3.1.6	Discussion	153
5.3.2	Vertex Angles of Less than 180° (External Corners)	155
5.3.2.1	Stress theory	155
5.3.2.2	Finite element analysis	157
5.3.2.3	Discussion	168
5.4	Conclusions	169
Chapter 6	RTS Crack Growth Prediction Using Design & Analysis Codes	171
6.1	Introduction	171
6.2	ASME Boiler and Pressure Vessel Code, Section XI (1998)	172
6.2.1	Introduction	172
6.2.2	Crack Growth Analysis	173
6.3	BS 7910 (1999)	177
6.3.1	Introduction	177
6.3.2	Crack Growth Analysis	177
6.3.2.1	Generation of stress intensity factor profiles	177
6.3.2.2	Crack growth reference curves	178
6.3.2.3	Comparison with experimental data	181
6.3.2.4	A modified approach	182
6.4	Combining ASME and BS 7910 Approaches	184
6.5	Comparisons of Alternative Analysis Techniques	186
6.6	Conclusions	188
Chapter 7	Conclusions	190
7.1	Introduction	190
7.2	Review of Literature	190
7.3	Test Method	191
7.4	Test Results	192
7.4.1	Crack Initiation	194



7.4.2	Crack Growth	196
7.4.2.1	High strain fatigue region	197
7.4.2.2	Elastic crack growth region	199
7.4.2.3	A combined growth law	203
7.4.2.4	Crack growth mechanisms	203
7.5	Transient and Geometry Effects	204
7.6	Code Analysis	208
7.6.1	ASME Boiler and Pressure Vessel Code, Section XI (1998)	208
7.6.2	BS 7910 (1999)	209
7.6.3	Combined Technique	209
7.7	Recommendations for Further Work	210
	References	211
Appendix A	Test Rig and Specimen Drawings	
Appendix B	Results of Elevated Temperature Mechanical Tests to Carbon Steel Specimens	
Appendix C	Experimental Test Result Data	
Appendix D	Authors Relevant Publications	

## List of Tables

<b>Table</b>	<b>Title</b>	<b>Page</b>
Table 4.1	Experimental testing matrix.	62
Table 4.2	Chemical composition specification(%), steel grade AS 1548-7-430R.	62
Table 4.3	Summary of experimental results for test #2, specimens #2 & #3.	66
Table 4.4	Summary of experimental results for test #3, specimens #4 & #5.	67
Table 4.5	Summary of experimental results for test #4, specimens #6 & #7.	68
Table 4.6	Notch root stresses developed during 7s thermal shock from a central specimen temperature of 330°C.	73
Table 4.7	Notch root stresses developed during repeated thermal shocks and number of cycles to crack initiation.	80
Table 4.8	Comparison of predicted and actual crack growth rates for specimen exposed to 5s thermal shocks from a set temperature of 330°C.	96
Table 5.1	Experimental data for use in crack "arrest" prediction.	130
Table 6.1	Predicted number of cycles for a crack to grow from 4.8mm to 23mm in the experimental specimen when exposed to repeated 7s thermal shocks from 370°C combined with a 90MPa steady state primary load.	187

## List of Figures

Figure	Title	Page
Figure 2.1	Temperature and stress versus distance for a heated plate with single edge down-shock.	8
Figure 2.2	Change in stress intensity factor experienced at the tip of a crack in a heated plate subjected to a single edge down-shock, plotted as a function of crack length.	10
Figure 2.3	Effect of crack closure and $R$ -ratio on effective stress intensity factor $K_{eff}$ .	20
Figure 2.4	Crack growth rate as a function of $\Delta K$ for various forms of corrosion fatigue (Austen and Walker, 1977).	26
Figure 2.5	Model for absorption of Hydrogen into crack tip (taken from Torronen and Cullen, 1982).	29
Figure 3.1	Photo of testing rig layout.	40
Figure 3.2	Schematic of testing rig layout.	41
Figure 3.3	Specimen design.	43
Figure 3.4	Stress intensity factor ratio for multiple cracks separated by 50mm and a single crack.	44
Figure 3.5	Example of linearisation of a thermal shock stress in a flat plate with notch.	46
Figure 3.6	Temperature profiles developed during one-dimensional thermal shock of flat plate specimen from 370°C. Heavy points show experimental data. Light lines represent numerical results using a surface heat transfer coefficient of 3,000W/m <sup>2</sup> at time of 1-10s.	58
Figure 3.7	Temperature profiles developed during one-dimensional thermal shock of flat plate specimen from 370°C. Heavy points show experimental data. Light lines represent numerical results using a surface heat transfer coefficient of 10,400W/m <sup>2</sup> at time of 1-10s.	58

Figure 3.8	Temperature profiles developed during one-dimensional thermal shock of flat plate specimen from 370°C. Heavy points show experimental data. Light lines represent numerical results using an infinite surface heat transfer coefficient at times of 1-10s.	59
Figure 3.9	Curve fits of experimental quench data for times of up to 10s. Specimen temperature prior to down-shock is 370°C. Heat transfer coefficient varies with time.	59
Figure 4.1	Replication of verification specimen surface.	63
Figure 4.2	Typical temperature profiles for thermal shocks of 4s, 5s, 7s and 10s at crack position 1 from central specimen set temperature of 330°C.	69
Figure 4.3	Typical elastic stress profiles for thermal shocks of 4s, 5s, 7s and 10s at crack position 1 from central specimen set temperature of 330°C.	70
Figure 4.4	Cyclic change in stress intensity factor ( $\Delta K_I$ ) as a function of crack depth for thermal shocks of 4s, 5s, 7s and 10s at crack position 1 from a central specimen set temperature of 330°C. No primary mechanical load.	71
Figure 4.5	Cyclic change in stress intensity factor ( $\Delta K_I$ ) as a function of crack depth for thermal shocks of 4s, 5s, 7s and 10s at crack position 1 from a central specimen set temperature of 330°C. 90MPa primary mechanical load included.	71
Figure 4.6	Stress intensity factor profiles for 7s thermal shock at notch position 1 from central specimen temperature of 330°C showing effects of 90MPa mechanical load.	77
Figure 4.7	$R$ -ratio as a function of crack length for a 7s quench with 90MPa mechanical load, at notch position 1 from a central specimen temperature of 330°C.	77
Figure 4.8	Rate of change of stress intensity factor ( $C$ ) for the range of test cases.	79
Figure 4.9	Number of cycles to crack initiation versus elastic notch stress amplitude ( $S_o^2$ ) for a sharp notch approximation with notch sensitivity analysis.	82

Figure 4.10	Number of cycles to crack initiation versus elastic notch stress amplitude ( $S_a^3$ ) for a sharp notch approximation with notch sensitivity analysis, $k_f$ limited to 5.0.	82
Figure 4.11	Number of cycles to crack initiation versus Neuber notch pseudostress amplitude ( $S_a'^1$ ) for an elastic sharp notch approximation with notch sensitivity analysis.	83
Figure 4.12	Number of cycles to crack initiation versus Neuber notch pseudostress amplitude ( $S_a'^2$ ) for a sharp notch approximation with notch sensitivity, $k_f$ limited to 5.0.	83
Figure 4.13	Crack initiation data using a Neuber notch pseudostress approach and assuming a uniform notch fatigue factor ( $k_f$ ) of 5.0 for all cases.	86
Figure 4.14	Crack initiation at the weld crown / base metal interface for specimen #2.	87
Figure 4.15	Raw crack length data.	88
Figure 4.16	Crack growth versus crack length (includes notch depth) for a number of cracks grown by RTS.	90
Figure 4.17	Crack growth as a function of crack length showing linear prediction curve for high strain fatigue (HSF) region.	91
Figure 4.18	Change in stress intensity factor versus crack growth rate for RTS.	94
Figure 4.19	Crack growth as a function of stress intensity factor $\Delta K$ , smoothed data.	95
Figure 4.20	Smoothed experimental crack growth data plotted against a Torronen and Cullen (1982) model prediction, allowing for the effects of environment and primary load. Experimental data for D.O. = 8ppm plotted.	98
Figure 4.21	Smoothed experimental crack growth data plotted against a Torronen and Cullen (1982) model prediction, allowing for the effects of environment and primary load. Experimental data for D.O. = 2ppm plotted.	99
Figure 4.22	Smoothed experimental crack growth data plotted against a Gabetta et al (1990) model prediction, allowing for the effects of environment and primary load. Experimental data for D.O. = 8ppm plotted.	101

Figure 4.23	Smoothed experimental crack growth data plotted against a Gabetta et al (1990) model prediction, allowing for the effects of environment and primary load. Experimental data for D.O. = 2ppm plotted.	102
Figure 4.24	Crack mouth appearance after full specimen width initiation.	104
Figure 4.25	Final crack growth, specimen #2, notch position 1.	106
Figure 4.26	Final crack growth, specimen #3, notch position 1.	107
Figure 4.27	Final crack growth, specimen #4, notch position 1.	108
Figure 4.28	Final crack growth, specimen #4, notch position 2.	109
Figure 4.29	Final crack growth, specimen #4, notch position 3.	110
Figure 4.30	Final crack growth, specimen #5, notch position 2.	110
Figure 4.31	Final crack growth, specimen #5, notch position 1.	111
Figure 4.32	Fracture surface, specimen #2, notch position 1.	112
Figure 4.33	Fracture surface, specimen #3, notch position 1.	112
Figure 4.34	Transgranular growth of sharp tipped crack.	113
Figure 5.1	Flat plate geometry with edge crack exposed to 1-d thermal shock.	120
Figure 5.2	Effect of shock duration on theoretical stress intensity factor distributions for a flat plate of depth " $W$ " with crack depth " $a$ " exposed to a one-sided thermal shock with infinite heat transfer coefficient.	122
Figure 5.3	Effect of shock duration on theoretical stress intensity factor distributions for a flat plate of depth " $W$ " with crack depth " $a$ " exposed to a one-sided thermal shock with heat transfer coefficient $10,400 \text{ W/m}^2$ .	122
Figure 5.4	Effect of shock duration on theoretical stress intensity factor distributions for a flat plate of depth " $W$ " with crack depth " $a$ " exposed to a one-sided thermal shock with heat transfer coefficient $3,000 \text{ W/m}^2$ .	123

Figure 5.5	Non-dimensional time ( $t'$ ) for development of maximum stress intensity factors during 1-d thermal shock of an edge cracked plate.	125
Figure 5.6	Example of using non-dimensional transient thermal shock stress charts to predict crack arrest depth for a shock of non-dimensional time $(\kappa t/W^2) = 0.0256$ .	127
Figure 5.7	Semi-elliptical (thumbnail) crack in a flat plate.	128
Figure 5.8	Comparison of analytical solutions with experimental results for non-dimensional time of 0.021.	131
Figure 5.9	Geometry definitions for hollow cylinder.	133
Figure 5.10	Stress intensity factors for an internal axial crack in a hollow cylinder exposed to internal thermal down-shock for different non-dimensional times.	134
Figure 5.11	Stress intensity factors for an internal circumferential crack in a hollow cylinder exposed to internal thermal down-shock for different non-dimensional times.	134
Figure 5.12	Effect of geometry on stresses developed during thermal shock. Hollow cylinder and flat plate geometries, for thermal shocks of 2s and 20s.	135
Figure 5.13	Corner cracking at an internal corner, eg. feed-water heater box.	137
Figure 5.14	Corner cracking at an external corner, eg. tube penetration into a thick walled header.	137
Figure 5.15	Corner with vertex angle ( $2\gamma$ ) greater than $180^\circ$ and coordinate system.	139
Figure 5.16	Relationship between the real part of the minimum eigenvalue $\lambda$ and vertex angle $2\gamma$ from equation [5.11].	141
Figure 5.17	Non-dimensional generalised stress intensity factor ( $\bar{K}_I$ ) as a function of vertex angle ( $2\gamma$ ).	144
Figure 5.18	Finite element mesh for analysis of $270^\circ$ corner with radius exposed to a symmetrical thermal shock.	148

Figure 5.19	Typical temperature contours for a 270° corner with radius exposed to symmetrical 100°C thermal down-shock.	149
Figure 5.20	Stress contours for a 270° corner with radius exposed to a symmetrical 100°C thermal down-shock.	150
Figure 5.21	Close-up view of stress contours at the corner radius of a 270° corner exposed to a symmetrical 100°C thermal down-shock.	151
Figure 5.22	Maximum non-dimensional stress ( $\bar{\sigma}_{\max}$ ) produced at a corner with vertex angle $2\gamma = 270^\circ$ and corner radius $r$ , exposed to thermal shock of time $t$ .	152
Figure 5.23	Corner with vertex angle ( $2\gamma$ ) less than 180° and coordinate system.	155
Figure 5.24	Cracking around the inside surface of an economiser inlet header at a tube connection	156
Figure 5.25	A 3-d finite element model for 90° corner exposed to symmetrical thermal shock.	158
Figure 5.26	Temperature contours for 90° corner exposed to symmetrical 100°C down-shock.	159
Figure 5.27	$z$ -direction stress contours for 90° corner exposed to symmetrical 100°C down-shock.	160
Figure 5.28	Close-up view of $z$ -direction stress contours at the 90° corner for a symmetrical 100°C down-shock.	161
Figure 5.29	Axisymmetric model for 90° corner symmetric thermal shock.	162
Figure 5.30	Temperature contours for axisymmetric corner model exposed to symmetric thermal down-shock of 100°C.	163
Figure 5.31	$z$ -direction stress contours for axisymmetric 90° corner exposed to symmetric thermal down-shock of 100°C.	164
Figure 5.32	Close-up view of $z$ -direction stress contours at the 90° axisymmetric corner for a symmetrical 100°C down-shock.	165
Figure 5.33	$z$ -direction stresses developed along the free surface of a 3-d corner as a function of distance ( $d$ ) from the corner for fixed time $t$ .	167



Figure 5.34	Stresses developed along the free surfaces of an axisymmetric corner as a function of distance ( $d$ ) from the corner for a fixed time $t$ .	167
Figure 6.1	Comparison of experimental crack growth data with prediction curves of ASME Boiler and Pressure Vessel Code, Section XI (1998), Appendix A.	174
Figure 6.2	Crack length vs. number of cycles. Comparison of actual data with ASME XI (1998) predictions for a 7s thermal shock from 370°C.	176
Figure 6.3	Crack length vs. number of cycles. Comparison of actual data with ASME XI (1998) predictions for a 7s thermal shock from 350°C.	176
Figure 6.4	Stress linearisation for fatigue analysis in BS 7910 (1999) for crack length ' $a$ ' in plate of width ' $W$ '.	178
Figure 6.5	Comparison of experimental crack growth data with dry environment prediction curves of BS 7910 (1999).	180
Figure 6.6	Comparison of experimental crack growth data with marine environment prediction curves of BS 7910 (1999) (no cathodic protection).	180
Figure 6.7	Crack length vs. number of cycles. Comparison of actual data with BS 7910 (1999) predictions for a 7s thermal shock from 370°C.	181
Figure 6.8	Crack length vs. number of cycles. Comparison of actual data with BS 7910 (1999) predictions for a 7s thermal shock from 350°C.	182
Figure 6.9	Modified stress linearisation for fatigue analysis in BS 7910 (1999) for crack length ' $a$ ' in a plate of width ' $W$ '.	183
Figure 6.10	Crack length vs. number of cycles. Comparison of actual data with modified BS 7910 (1999) predictions for a 7s thermal shock from 370°C.	183
Figure 6.11	Crack length vs. number of cycles. Comparison of actual data with modified BS 7910 (1999) predictions for a 7s thermal shock from 350°C.	184
Figure 6.12	Crack length vs. number of cycles. Comparison of actual data with combined ASME XI (1998) and BS 7910 (1999) approach for a 7s thermal shock from 370°C.	185

Figure 6.13 Crack length vs. number of cycles. Comparison of actual data with combined ASME XI (1998) and BS 7910 (1999) approach for a 7s thermal shock from 350°C.

185

## Nomenclature

$a$	-	crack length
$a_{allow}$	-	allowable crack length
$ASCR$	-	active surface creation rate
$c$	-	specific heat
$C$	-	Parameter for estimating loading history effects during a LEFM crack growth analysis
$d$	-	distance from corner measured along the free surface
$D$	-	notch depth
$\frac{da}{dN}$	-	crack growth per load cycle
$\frac{da}{dN_E}$	-	total environmentally assisted crack growth rate
$\frac{da}{dN_V}$	-	crack growth rate in a vacuum environment
$\frac{da}{dN_{CF}}$	-	additional crack growth due to corrosion effects
$\frac{da}{dN_{TCF}}$	-	true corrosion fatigue crack growth rate
$\frac{da}{dN_{SCF}}$	-	stress corrosion fatigue crack growth rate
$\frac{da}{dt}$	-	crack growth per unit time
$E$	-	Young's Modulus
$e_n$	-	nominal cyclic strain amplitude
$G_i$	-	free surface correction factors
$H$	-	non-dimensional shape factor
$h$	-	heat transfer coefficient
$K$	-	stress intensity factor
$K_{cl}$	-	stress intensity factor at crack closure

$K_I$	-	1st mode stress intensity factor
$\overline{K}_I$	-	non-dimensional 1st mode stress intensity factor
$K_{ISCC}$	-	stress corrosion cracking limit
$K_{ISCF}$	-	stress corrosion fatigue cracking limit
$K_{max}$	-	maximum stress intensity factor in a cycle
$K_{min}$	-	minimum stress intensity factor in a cycle
$\Delta K$	-	change in stress intensity factor
$\Delta K_c$	-	threshold for onset of stress corrosion fatigue
$\Delta K_{eff}$	-	effective change in stress intensity factor
$\Delta K_{Ia}$	-	critical stress intensity factor range
$\Delta K_{max}$	-	maximum change in stress intensity factor
$\Delta K_o$	-	normalising value for non-dimensional thermal shock stress intensity factor
$k$	-	thermal conductivity
$k_f$	-	fatigue notch factor
$k_t$	-	theoretical stress concentration factor
$k_{tb}$	-	theoretical bending stress concentration factor
$k_{tm}$	-	theoretical membrane stress concentration factor
$k_s$	-	stress concentration factor
$k_e$	-	strain concentration factor
$l$	-	crack width
$\Delta L$	-	smallest element size in finite element analysis
$N$	-	number of cycles
$N_i$	-	number of cycles to crack initiation
$N_{lifetime}$	-	number of thermal shock cycles in a components design life
$P$	-	primary load
$p$	-	pressure
$Q$	-	flaw shape parameter
$q_y$	-	plastic zone correction factor
$R$	-	cyclic load ratio
$R_i$	-	inside radius of a hollow cylinder

$R_o$	-	outside radius of a hollow cylinder
$r$	-	corner / notch radius
$r_y$	-	yield zone radius
$S_a$	-	local cyclic elastic stress amplitude
$S'_a$	-	Neuber notch pseudostress cyclic amplitude
$S_a''$	-	cyclic stress amplitude adjusted to account for mean stress effects
$S_n$	-	nominal cyclic elastic stress amplitude
$T$	-	temperature
$T_{av}$	-	volume mean temperature
$T_c$	-	temperature at point 'c' in a material exposed to a thermal shock transient
$\Delta T$	-	change in temperature
$t$	-	time
$t'$	-	estimate of the non-dimensional thermal shock duration require for development of maximum crack growth rates
$W$	-	component thickness
$Y'$	-	flow stress
$\alpha$	-	coefficient of thermal expansion
$\alpha_{ASCR}$	-	constant relating rate of change of crack mouth opening distance to ASCR
$\beta$	-	work hardening exponent
$\gamma$	-	half corner/vertex angle
$\epsilon_a$	-	local cyclic strain amplitude
$\epsilon_p$	-	plastic strain
$\Delta \epsilon_p$	-	cyclic plastic strain
$\kappa$	-	thermal diffusivity
$\lambda$	-	eigenvalue measure of corner singularity
$\nu$	-	Poisson's ratio
$\rho$	-	material density
$\rho_n$	-	Neuber constant
$\sigma$	-	stress
$\sigma_a$	-	local cyclic stress amplitude

$\sigma_b$	-	bending stress
$\sigma_c$	-	stress at point 'c' in a material exposed to a thermal shock transient
$\sigma_m$	-	membrane stress
$\bar{\sigma}_{\max}$	-	non-dimensional maximum stress in a corner with radius
$\sigma_r$	-	stress in the radial direction
$\sigma_u$	-	material ultimate stress
$\sigma_x$	-	stress in the x-direction
$\sigma_y$	-	stress in the y-direction
$\sigma_{ys}$	-	material yield stress
$\sigma_z$	-	stress in the z-direction
$\sigma_\varphi$	-	stress in the circumferential direction
$\Delta\sigma$	-	cyclic change in stress
$\Delta\sigma_b$	-	cyclic change in bending stress
$\Delta\sigma_m$	-	cyclic change in membrane stress
$\tau$	-	rise time of cyclic loading
$\tau_{r\varphi}$	-	shear stress in polar co-ordinates

## **Chapter 1:**

### **Introduction – Crack Growth due to Repeated Thermal Shock**

At its most basic level, the initiation and growth of cracks due to repeated thermal shock (RTS) is caused by the restraint of thermal expansions and contractions of a material as it is exposed to rapid changes in temperature. This restraint (either external or internal in nature) results in strains and associated stresses in the material. If the changes in temperature are severe (especially in the presence of stress concentration factors such as abrupt changes in geometry), and the resulting strains large enough, local plastic deformation of the component will occur. Repeated application of this loading leads to rapid crack initiation as per low-cycle mechanical fatigue. Further application of the loading leads to small crack and then large crack growth. In some cases, this crack growth can finally lead to component failure.

In this thesis, thermal shock stress will be distinguished from the broader category of thermal expansion stress. Thermal shock stresses are transient in nature and decrease rapidly away from the shocked surface. Alternatively, thermal expansion stresses can be developed over long periods of time and will not necessarily decrease rapidly across the section. It is the analysis of repeated development of thermal shock stresses that forms the focus for this investigation.

Currently, RTS crack growth is a poorly understood phenomenon. Although the visual characteristics of such cracking in post-service equipment are readily identifiable, the mechanism responsible for the actual crack growth behavior is unclear and confused by the interaction of many outside factors. The key factors include any mechanical loading superimposed on the thermal shock, the shape of the component, the temperatures involved and the environment in which the component is immersed. A key feature of RTS is that in some cases, it can lead to crack arrest at harmless depths and in other cases it leads to

component failure. An important requirement of this thesis is to identify the reasons for these differences.

Cracking due to RTS is a particular problem in thermal power station plant equipment. Thermal shocks in boiler equipment are an inevitable side effect of normal operation, with start-up and shut-down procedures thought to be especially damaging. Cyclic operation of traditionally base-loaded units only increases the severity of the problem. The recently identified boiler tube damage mechanism of waterside-initiated cracking in carbon steel economiser headers is related to this practice (Dooley, 1997). A typical shutdown due to such a failure can (depending on the market price of electricity at the time) cost a utility over A\$1,000,000 for replacement power. Of slightly lesser concern (though still important) is the cost associated with replacement of equipment with signs of RTS cracks designated unfit for continued operation by "fitness for service" codes such as the British Standard BS 7910 (1999).

Thermal power station pressure equipment will form the focus for the bulk of this investigation. In particular, this thesis analyses the effects of RTS on carbon steel components operating at temperatures below 400°C. This approach has been selected to avoid analysis of the complicated time dependent material interactions such as creep that occur at higher temperatures. These mechanisms have already been adequately addressed in such texts as the ASME Boiler and Pressure Vessel Code (1998).

The current methods for predicting RTS crack initiation lifetime and crack growth rates in thermal power station pressure equipment rely on standards and codes of practice such as the ASME Boiler and Pressure Vessel Code (1998), BS 7910 (1999) and API 579 (1999). All of these documents use models based on isothermal fatigue tests and simplified stress profiles. The conservatism of these codes when analysing RTS cracks is of concern. This is particularly the case when attempting to predict crack growth rates after crack initiation has been observed. An over-estimation of this growth rate can lead to premature replacement of components that otherwise may have been left in service. A particular reference to the conservatism of the ASME code can be found in work by Czuck et al



(1985) where growth at the tip of a crack exposed to cyclic thermal shock loading was found to be an order of magnitude less than that predicted by using the code. As mentioned previously, mechanical loading and environmental conditions are very important considerations when analysing RTS. Existing codes deal with these two issues only in a simplified manner.

In the case of thermal power station components, steady state mechanical loads (designated "primary loads" in ASME Boiler and Pressure Vessel Code terminology) can be a direct result of internal pressure loading. The effects of primary loads include the opening of any cracks, exposing them to the environment. The environment is aqueous in nature, which in turn means corrosion plays a significant role in the fatigue process. It is clear from just these simple considerations that both effects are connected and need to be allowed for in an effective analysis of the RTS situation.

The objective of this work is to analyse the initiation and growth of cracks in carbon steel specimens due to RTS. Particular application will be made to use the results for lifetime assessment in thermal power station pressure equipment. Chapter 2 consists of a brief explanation of the theory of thermal shock and a review of literature devoted to the analysis of thermal fatigue crack initiation and growth. A basic understanding of the thermal shock theory is necessary for a full appreciation of the work completed in the chapters that follow. The literature review will assist in determining the state of current research in the field. In turn, the remaining chapters deal with:

Chapter 3: An explanation of the test method development for the experimental stream of the work.

Chapter 4: Results and discussions from the testing phase of the research. Analyses concentrate on determining times to crack initiation and crack growth rates for flat plate carbon steel specimens exposed to RTS. Determination of the effects of primary mechanical loads and environmental variables figure heavily in these analyses.

Chapter 5: Theoretical and numerical investigations of more complicated thermal shock scenarios such as thermal shock at corners.

Chapter 6: A critique of methods developed for handling RTS in current industry accepted codes and standards.

Chapter 7: Conclusions and recommendations for further research.

## **Chapter 2:**

### **Thermal Shock Theory & Literature Review**

#### ***2.1 Introduction***

This chapter provides the framework on which the remainder of the thesis rests. A brief introduction to the theory of thermal shock stress is first provided to allow a more thorough understanding of the following literature review. The review itself serves the function of reporting the current state of knowledge in the area of repeated thermal shock crack initiation and growth. It also allows the focus of the research to be justified through identifying where the gaps in current knowledge exist. The format of the review is as follows. First a survey into the history of thermal fatigue research is completed, followed by sections concentrating on identifying and discussing the external factors that most significantly affect the initiation and growth of cracks due to repeated thermal shock.

#### ***2.2 Repeated Thermal Shock (RTS) vs. Thermal Fatigue***

As mentioned in the introduction, a major distinction will be made in this work between the terms of "thermal fatigue" and "repeated thermal shock" (hereafter referred to as RTS). Thermal fatigue will be defined as the broader category involving cyclic stressing resulting from the temperature cycling of a component. RTS is a sub-set of thermal fatigue, defined as the particular case of exposing a component to a transient, highly non-linear temperature distribution brought on by a rapid change in operating condition. RTS is the topic of investigation in this thesis, but its analysis requires review of previous works concentrating on the broader topic of thermal fatigue.

## 2.3 Basic Thermal Shock Stress Theory

In his introductory paper to the 1976 ASTM publication "Thermal fatigue of materials and components", Spera (1976) posed the question "What is thermal fatigue?". His answer took the form of a description of suggested definitions for use in thermal fatigue analysis. After defining thermal fatigue as a sub-section of the larger research area of strain controlled fatigue, Spera suggested that it be divided into two sections. These were thermal-mechanical fatigue and thermal-stress fatigue.

The major distinction between the two areas proposed by Spera lies the form of constraint. Thermal-mechanical fatigue relies on constraint external to the component to produce stresses while thermal-stress fatigue relies on internal constraint. Analysing the stresses developed in each of the cases is quite separate.

For the thermal-mechanical fatigue case, the external constraint can be due to structural supports or other large/stiff members connected to the component. In this case, temperatures and hence elastic stresses (ignoring geometry effects) are uniform across the component. The elastic stresses are quite easy to calculate and follow from:

$$\sigma_x = \sigma_y = E\alpha(\Delta T) \quad \text{for uniaxial conditions} \quad [2.1]$$

$$\sigma_x = \sigma_y = \frac{E\alpha(\Delta T)}{1-\nu} \quad \text{for equi-biaxial conditions} \quad [2.2]$$

Where  $E$ ,  $\alpha$  and  $\nu$  are the Young's Modulus, coefficient of thermal expansion and Poisson's ratio of the material respectively and  $\Delta T$  is the temperature change the component goes through.

For the thermal-stress fatigue case, the internal constraint occurs when adjacent elements of the component are at a different temperature or are made of a different material. This is the

situation during a thermal shock condition, where a component is heated non-uniformly and a steep temperature gradient is developed across it. Surrounding cool regions prevent the expansion of those that are heated, resulting in a self-equilibrating stress distribution across the component. The same can be achieved when a heated specimen is cooled locally (e.g. by quenching), with the bulk of the hot material preventing cooler areas from contracting.

Manson (1966) defines the stress at a point 'c' in a flat plate in a condition of plane strain subject to a one-dimensional, symmetric thermal shock (generated by submersing the plate in a medium of lower temperature) as being calculated from the following formula:

$$\sigma_c = \frac{E\alpha(T_{av} - T_c)}{1 - \nu} \quad [2.3]$$

Where  $T_{av}$  is the volume mean temperature of the plate, and  $T_c$  is the temperature at the point of which the stress is being calculated.

Stresses generated by a non-symmetric thermal shock (e.g. a single edge quench of a flat plate) are not described by equation [2.3]. Figure 2.1 shows the temperature and elastic stress distribution developed in a 100mm flat steel plate uniformly heated to 300°C and subject to a thermal down-shock of 200°C at one edge. The results have been obtained from a numerical solution by Zhi-He and Yiu-Wing (1995) and are plotted at a time of 20s after the thermal shock has begun.

Skelton (1983) examined this issue experimentally and theoretically. More recently, numerical methods have been used.

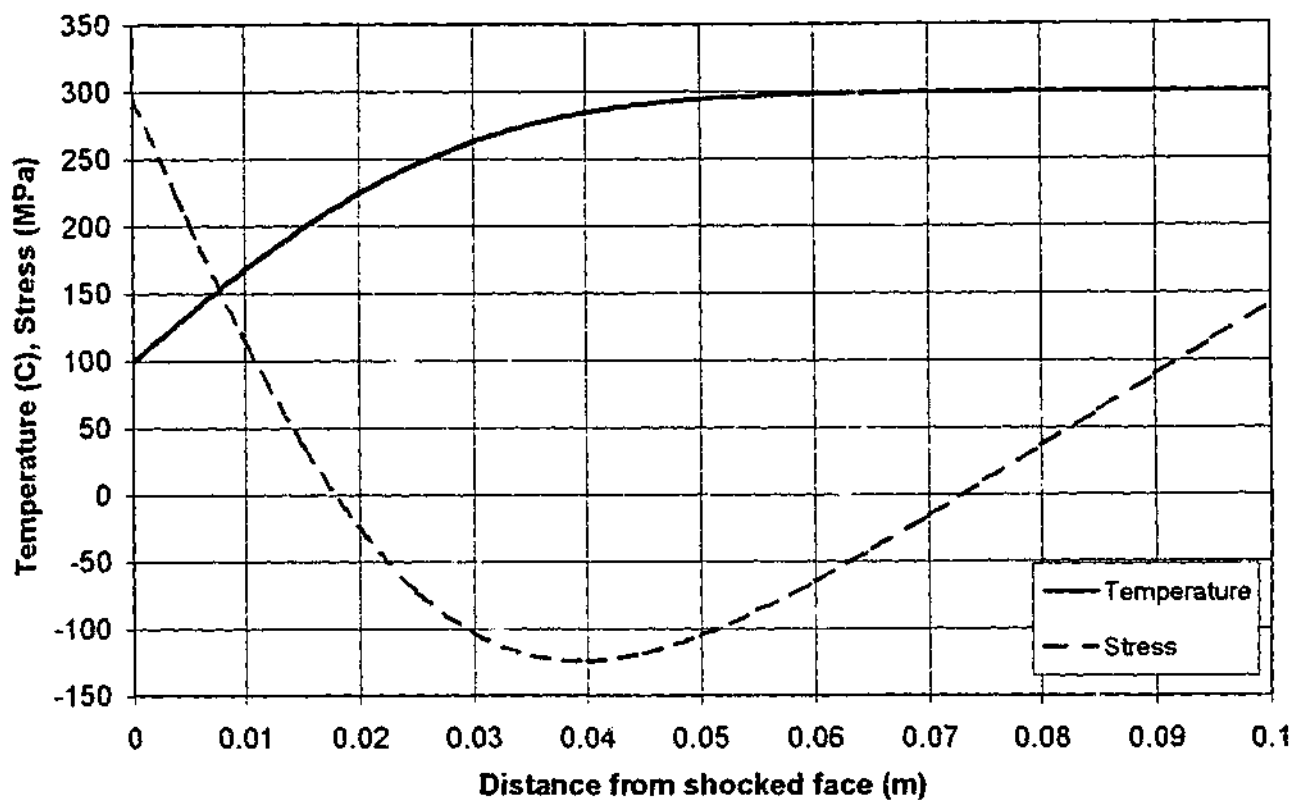


Figure 2.1: Temperature and stress versus distance for a heated plate with single edge down-shock.

## 2.4 Thermal Stress Fatigue Analysis – A Brief History

### 2.4.1 Early Years

Although the theory and industrial implications of thermal stresses in metals is an old and well established subject in engineering, it was not until the 1950's that thermal fatigue was recognised as a field in its own right. Manson (1953) and Coffin (1954) were the first to complete thorough investigations into thermal fatigue loading, producing what are now referred to as the seminal studies in the area. Between the mid 1950's and the early 1970's, these studies provided the theoretical and experimental platform upon which thermal fatigue research rested. During this time, most work concentrated on determining the effect of elevated temperatures on low cycle (or strain controlled) fatigue strength of materials and production of the appropriate  $\epsilon-N$  or fatigue-life curves.

Initially, the majority of this research was experimentally based and was completed using both high temperature isothermal and thermal-mechanical fatigue testing facilities such as

that described by Coffin and Wesley (1954) utilising servo-hydraulic test machines (Udoguchi and Wada, 1971, Lindholm and Davidson, 1973). In addition, some thermal stress fatigue work was completed using tapered disc type specimens and the fluidised bed technique, where disks at room temperature were plunged into a heated, solid fluidised media (Howes, 1973). Irrespective of the test method and the technique for generating the thermal stresses (i.e. thermal-mechanical or thermal-stress), the concentration at this time was on identifying crack initiation lifetimes for use in life prediction, rather than monitoring the crack growth for use in possible life extension analysis. White (1971) provides a more comprehensive review of investigations at this time, concentrating on British contributions.

#### **2.4.2 Linear Elastic Fracture Mechanics (LEFM)**

During the mid 1970's, Linear Elastic Fracture Mechanics (LEFM) and the use of the stress intensity factor " $K$ " for the description of stress profiles around a crack tip were popularly introduced to the analysis of fracture events. This led to a fresh batch of testing in thermal fatigue, concentrating more on identifying crack growth relationships instead of component fatigue lifetime correlations. In particular, much work was completed attempting to apply the model developed by Paris and Erdogan (1960) (also Paris et al, 1961, now commonly referred to as the Paris Law) for predicting crack growth rates in mechanical testing using stress intensity factor correlations. The standard form of the Paris Law is given below as equation [2.4]:

$$\frac{da}{dN} = C \cdot \Delta K^m \quad [2.4]$$

Here,  $da/dN$  is the slope of the crack growth versus number of cycles curve,  $\Delta K$  is the change in stress intensity factor at the tip of the crack per cycle (defined as  $K_{max} - K_{min}$ , the maximum and minimum cyclic stress intensity factors respectively) and  $C$  and  $m$  are supposed material constants, determined through the fitting of material test data.

As an illustrative example of the use of LEFM, the thermal shock case described in the previous section and figure 2.1 will be used. The change in stress intensity factor generated

at the tip of a crack resulting from the stress produced during the down-shock is shown as figure 2.2.

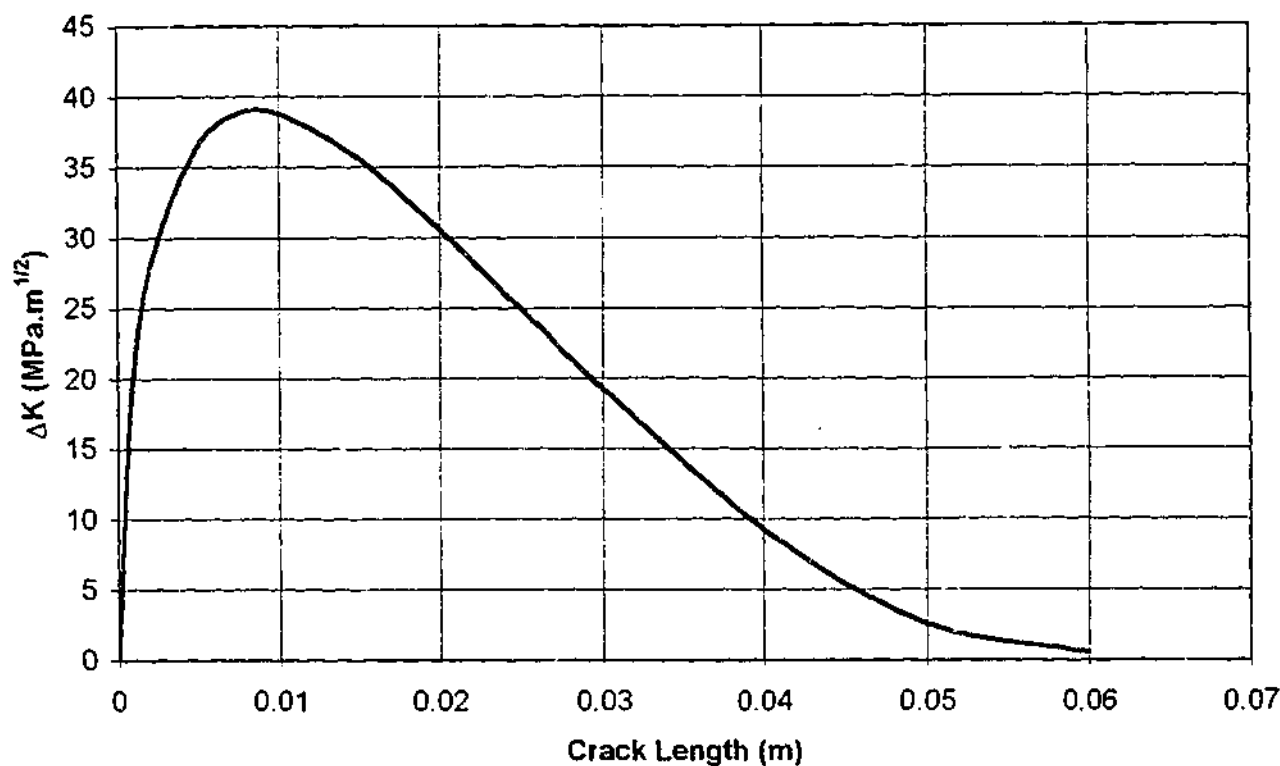


Figure 2.2: Change in stress intensity factor experienced at the tip of a crack in a heated plate subjected to a single edge down-shock, plotted as a function of crack length.

Using figure 2.2 and a Paris type crack growth law, this simple LEFM analysis would predict an acceleration in crack growth after initiation, followed by a period of rapid growth, followed by deceleration and “arrest” at around mid thickness. Although this analysis roughly describes the actual behavior of some cracks under RTS loading, it ignores many complicating factors that will be the focus of section 2.5 of this chapter.

LEFM was successfully combined with thermal fatigue analysis by Rau et al (1973) to study the effects of thermal mechanical loading on turbine blade steels. The effect of minimum and maximum temperature, strain range, mean strain and cycle shape were included in the investigation with the conclusion that the change in stress intensity factor ( $\Delta K$ ) during a thermal cycle was an acceptable parameter for modelling of the crack growth for small plastic strain values. Gamble and Paris (1976) also completed similar work for turbine blade steels (although in this case, the testing was simple elevated-temperature mechanical-fatigue). Mowbray et al (1973) completed an investigation using the fluidised



bed technique and tapered disk specimens also for turbine blade materials as did Gemma et al (1976) during strain controlled tests of a Nickel-base super alloy. These tests all provided useful results, basically showing that LEFM and the Paris Law were a valid technique for describing crack growth under certain combinations of thermal-mechanical and thermal stress fatigue.

#### **2.4.3 Effects of Plasticity**

It is now commonly known that for conditions of large plastic strain, LEFM techniques become invalid and the stress intensity factor no longer adequately describes the stresses developed around a crack tip. In these cases, it is necessary to replace the stress intensity factor with an equivalent parameter that takes into account plastic effects. Path (or contour) independent integrals were found to be an acceptable tool for this application. Initially applied to the theory of elasticity by Eshelby (1951), while determining the force acting on a singularity and extended to crack extension by Sanders (1961), the contour independent integral has the basic property of equalling zero for any contour not containing a singularity. Extending on the work of Eshelby and Sanders, Rice (1968) developed an elastic-plastic path-independent integral solution for use in mechanical loading crack extension popularly known as the  $J$ -Integral.

Unfortunately the  $J$ -Integral is not path independent in thermal stress situations and hence is not applicable for thermal shock analysis. In an attempt to remedy this, Blackburn (1977) proposed a modification to the  $J$ -Integral (now termed Blackburn's Integral or  $J^*$ ), compensating for the path dependence and allowing extension to thermal stress problems. The limitations of  $\Delta J$  and similar parameters for use in predicting mechanical loading crack growth are yet to be determined. The use of  $\Delta J^*$  (the change in Blackburn's integral per loading cycle) as a parameter for crack growth in thermal fatigue loading was investigated with some success in 1981 by Hellen et al (1981) and more recently, by Kim and Van Stone (1997).

The most comprehensive work to date in the region of crack initiation and growth due to thermal cycling of power generation components is that conducted by Skelton (1983).

Although this work is over 17 years old, it still represents the most concerted effort in the field. The format is primarily as a review of previous efforts in the area, with particular reference to his investigations. Emphasis is placed on modelling of crack growth using Paris Law type equations, and the prediction of crack arrest using LEFM generated  $\Delta K$  profiles. The  $\Delta K$  profiles are developed from the "equivalent stress profiles" generated from the specimen temperature distribution. The weight function method developed by Bueckner (1970) and Rice (1972) is then used to estimate the actual  $\Delta K$  values.

Skelton (1983) also dedicates a section in his work to the analysis of short cracks in the HSF (High Strain Fatigue) regions where large plastic strains are present. As mentioned previously, LEFM is not applicable in this region. Research of crack growth rates in this area have shown however that crack growth rate can be related to crack depth directly by the following equation:

$$\frac{da}{dN} = B.a \quad [2.5]$$

Where  $B$  is a constant and  $a$  is the crack length.

An investigation into the crack growth during thermal shock of type 301 and 316 stainless steels by Marsh (1981) successfully applied equation [2.5] in the high strain region and used LEFM for long crack growth. The following equation was applied to determine  $B$  in equation [2.5]:

$$B = \frac{\pi^2}{8} \left( \frac{\sigma}{2Y'} \right)^2 \frac{\Delta \epsilon_p}{1 + 2\beta} \quad [2.6]$$

Where  $\sigma$  is the maximum tensile stress in the cycle,  $Y'$  and  $\beta$  are the flow stress and work hardening exponent for the material respectively and  $\Delta \epsilon_p$  is the cyclic plastic strain.

Skelton also reports on attempts to determine a single parameter to model crack growth in both the HSF and LEFM regions. The  $J$ -Integral and its modifications are included as possible alternatives for achieving this. Previous studies are also listed for which the strain intensity factor ( $\Delta K_\epsilon$ , which in the LEFM region is simply  $\Delta K/E$ ) has been shown to be successful in correlating crack growth in both the HSF and LEFM ranges. Using this knowledge, an equivalent stress intensity factor  $K_{eq}$  defined in equation [2.8] was developed that is identical to the stress intensity factor but includes a plastic strain term. This was shown to compare favourably with the  $J$ -Integral and hence provided an easier (yet still as questionable) method for modelling crack growth in the HSF region.

$$\Delta K_{eq} = (E \cdot \Delta \epsilon_p + \Delta \sigma) \sqrt{\pi a} \quad [2.7]$$

where  $\Delta \epsilon_p$  and  $\Delta \sigma$  are the plastic strain and elastic stress ranges developed during the thermal shock respectively.

Notwithstanding the work of Skelton (1983), Heilen et al (1981), Kim and Van Stone (1997) and others, the accepted method for analysing thermal fatigue crack growth in most cases is still LEFM. This assumes perfectly linear material behavior and uses the stress intensity factor  $K$  to describe the stress distribution around the crack tip. This approach is due primarily to the relative simplicity of the stress intensity factor approach, with expensive and time consuming finite element work almost always required for the use of  $J$  type integral techniques (for example, see the work of Yagawa et al, 1989 and Reimers, 1993).

#### **2.4.4 Limits of LEFM**

Despite the wide acceptance in industry for use in predicting crack growth rates, stress intensity factor formulations based on the Paris Law have several important limitations. A recent paper by Paris lists numerous cases and circumstances in which the equation has been misused (Paris, 1998). These misuses include the neglect of the effects of loading history. According to Anderson (1995), a variable amplitude loading history violates the similitude assumption upon which the Paris Law was developed. No longer does the stress

intensity factor alone uniquely characterise the stress distribution at the crack tip as plastic deformation from prior load cycles also needs to be considered. Consequently, the Paris Law really only applies if  $\Delta K$  is constant during the crack growth. This is not the case with thermal shock loading where the stress distributions in components are highly non-linear (see figure 2.1), which leads to changes in the value of  $\Delta K$  as a crack grows (figure 2.2). The loading history is particularly important in a decreasing  $\Delta K$  field where the plastic zone due to former load cycles interferes with the next. However, if the change in  $\Delta K$  is relatively small during crack growth, this effect is minimal and can be ignored. The ASTM standard for measurements of fatigue crack growth rates "ASTM E 647-95a" (1995) recommends that the following equation be satisfied to ignore history effects during testing:

$$C = \frac{1}{\Delta K} \frac{d\Delta K}{da} > -0.08mm^{-1} \quad [2.8]$$

The ASTM reports this value only as a guide for the setting up of standard test conditions using carbon and low alloy steels. It is not an absolute limit and may also change for each material-environment-loading combination.

#### **2.4.5 Differences Between Crack Initiation and Crack Growth**

At this point in the review, it is appropriate to discuss the difference between using an analysis for identifying crack initiation and for determining the resulting crack growth behavior. The term "crack initiation" itself does not have a universal definition. Depending upon the approach (laboratory assessment, field assessment etc), the size at which a crack may be termed to have "initiated" will range from microscopic (in the order of a single grain size) to several millimeters in length. So if experimental results that report times to crack initiation are to be of any use, it is vitally important when completing the study that the size at which the crack is to have initiated is quoted.

It can be seen from the preceding description that there is no exact point at which crack initiation can be thought to occur. Indeed, it is the vision of some researchers today that the term crack initiation refers only to the early stages of crack propagation (Miller, 2000). In

this view, it is assumed that all structures constructed from polycrystalline materials subjected to fluctuating loads initiate surface cracks of  $10\mu\text{m}$  or longer very early in life. Hence "initiation lifetime" becomes only the time (cycles) for the crack to grow from this initial flaw to the size at which initiation is said to have occurred.

However, despite the drawbacks, a crack initiation study provides a simple manner (through the use of  $S-N$  or  $\epsilon-N$  curves) in which to classify (or rank) a materials resistance to the appearance of small cracks in any manner of environments or combination of external variants. Consequently, in cases where the presence of cracks of any size is to be avoided (e.g. turbine blades) this method remains applicable.

Alternatively, in cases where small flaws can be tolerated (as is sometimes the case with the equipment for which this study is aimed), the performance of a crack initiation analysis has less importance. However, it is still of interest to perform such a study, as it allows comparison of results with the current industry accepted procedures (e.g. ASME Boiler and Pressure Vessel Code Section VIII, Division 2, 1998) for designing against and analysing cracks in pressure equipment. This in turn gives a chance to identify areas of conservatism and non-conservatism.

## **2.5 Factors Affecting RTS Crack Growth**

As mentioned in the introduction, there are a number of external factors that can produce large changes in the amount of crack growth produced during repeated thermal shock loading. These factors include any superimposed mechanical loading, the environment, operating temperature and other transient effects (cycle frequency, time of shock etc). Individually, all of these mechanisms can significantly affect the crack growth rate. However together, they can have effects of well over an order of magnitude. A review of current understanding of the effects these factors have on fatigue crack growth follows.

### **2.5.1 Superimposed Mechanical Loading**

The effect of adding a superimposed steady state mechanical load (primary load) to repeated thermal shock testing simulates the effect of an internal pressure load in operating equipment. The exact effect of this loading on crack growth is very complex and is linked to other variables such as the environment. In order to better understand the effect that introduction of a primary load has on a complicated loading situation such as RTS, it is worthwhile to first review what its effects are when applied during pure mechanical loading.

#### **2.5.1.1 Effect of mean loads during pure mechanical fatigue**

##### *a) Mean stresses or mean strains*

The effects of mean stresses and strains on mechanical fatigue are not necessarily equivalent. When the bulk of the material of a test specimen behaves elastically, then mean stresses and strains are essentially the same. If however, the material response is elastic-plastic, quite different responses are produced. During strain controlled testing, repeated yielding results in a mean stress relaxation, resulting in little or no effect on crack initiation and growth. Stress controlled cycling on the other hand can lead to cyclic creep. The accumulation of strain associated with this creep is known as ratchetting. The effects of ratchetting and the design rules developed to avoid its occurrence are discussed briefly in section 2.5.1.2(c).

*b) Crack initiation behaviour*

For the purposes of analysis, it will be useful to individually assess the affects of mean loads on crack initiation and crack growth. As discussed in section 2.4.5 however, a clear distinction between crack initiation and growth is not possible. Using the conventions of codes such as the ASME Boiler and Pressure Vessel Code will help in this regard.

The fatigue lifetime curves presented in the ASME Boiler and Pressure Vessel Code, Section VIII, Division 2 (1998) are used for design against crack initiation in industrial components. These curves are generated from the strain life of small polished specimens. As the majority of strain life in these specimens is spent producing crack initiation, "strain-life" can be thought of as being equivalent to "initiation life" (Bannantine, 1990).

Looking then at how mean stress effects are allowed for in strain life relations will give some idea of how they affect initiation times. The ASME curves, generated from test data with no mean stress effects, have contained in them a modified form of the Goodman equation (Chopra and Shack, 1999):

$$S_a'' = S_a \left( \frac{\sigma_u - \sigma_y}{\sigma_u - S_a} \right) \quad \text{for} \quad S_a < \sigma_y \quad [2.9]$$

and

$$S_a'' = S_a \quad \text{for} \quad S_a > \sigma_y \quad [2.10]$$

Where  $S_a''$  is the adjusted value of stress amplitude  $S_a$ , and  $\sigma_u$  &  $\sigma_y$  are the material ultimate and yield stresses respectively.

These equations assume the maximum possible mean stress and have been shown to give a conservative adjustment. In general terms, equations [2.9] and [2.10] show

that mean stresses result in a reduction in strain life when the stress amplitude is less than yield and result in no reduction when the stress amplitude is above yield.

A more general approach to the effect of mean loads is taken by the British Standard BS 7608 (1993). This standard, concerned with the fatigue design and assessment of steel structures, reports no significant effect of mean stress on fatigue life in welded components. However, this result may be due to the high residual stresses remaining from the welding procedure. The effect of mean stresses on non-welded components is not reported in the code. For simplicity though, the code treats non-welded components in the same manner as if they were welded.

In a review of British contributions to the research of cyclic loading at high temperatures, White (1971) reports that mean strains have little or no effect on specimen endurance (fatigue lifetime) unless the mean strain is a significant proportion of the fracture strain. Combining this observation with the approaches of ASME and the British Standard would seem to suggest that mean loads below yield display little or no contribution to crack initiation lifetimes. A possible explanation for this observation can be developed when the effect of mean loads on crack growth is investigated.

#### *c) Crack growth behaviour*

It is an established fact that during mechanical fatigue the presence of a mean load affects both the crack growth and arrest behaviour. Mean loads are accounted for in LEFM fatigue analysis through the use of the load ratio ( $R$ ), defined as the minimum stress intensity factor ( $K_{min}$ ) divided by the maximum stress intensity factor ( $K_{max}$ ) in a single cycle. Experiments have shown that an increase in the  $R$  ratio results in an associated increase in crack growth rate for specimens cycled at the same stress intensity factor range  $\Delta K$  ( $K_{max} - K_{min}$ ).

Papers by McEvily and Ritchie (1998) and Kardomateas and Carlson (1998) provide a good review of the existing body of research in the area. In summary of



these works, the reason for the relation between crack growth and load ratio has been attributed to crack closure effects. Proposed first by Elber (Elber, 1970), crack closure involves the premature closing of a crack tip during the unloading portion of the fatigue cycle. This closure is considered to be due to plastic effects that leave a band of stretched material in the crack wake. Other effects have also been attributed to premature crack closure; these include oxide build-up on the crack face (Marshall, 1983), excess crack surface roughness and effects of viscous fluids (Suresh and Ritchie, 1984).

The effect of crack closure is to cause an increase in the minimum effective stress intensity factor during the cycle. In turn this reduces the stress intensity factor range  $\Delta K$ . If the stress intensity factor at which crack closure occurs is termed  $K_{cl}$ , then the effective stress intensity factor of the cycle ( $\Delta K_{eff}$ ) becomes:

$$\Delta K_{eff} = K_{max} - K_{cl} \quad [2.11]$$

The introduction of a mean load increases the minimum stress intensity factor in a cycle, which in turn reduces any crack closure effects. Crack closure also leads to premature arrest of cracks when  $K_{max}$  approaches  $K_{cl}$ . Once again, the application of a mean stress increases  $K_{max}$  and hence delays crack arrest.

Figure 2.3 shows a typical fatigue cycle, showing the effect of crack closure on cyclic stress intensity factor.

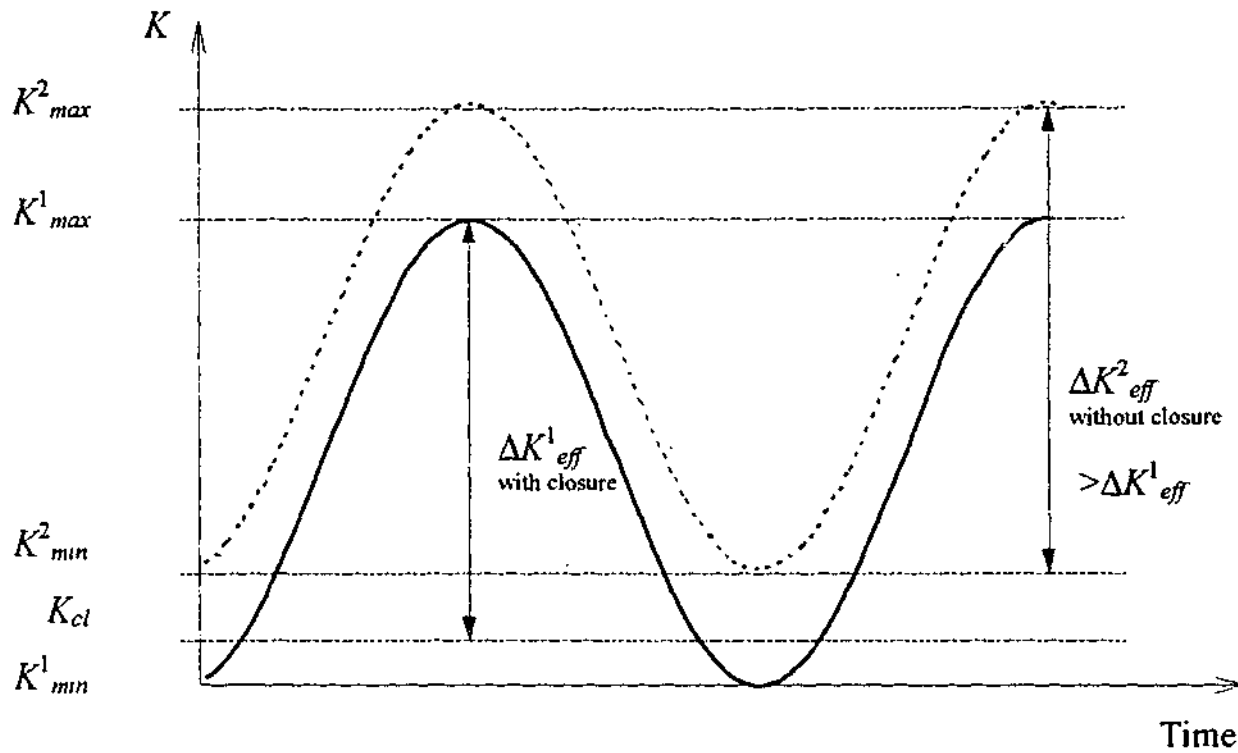


Figure 2.3: Effect of crack closure and  $R$ -ratio on effective stress intensity factor  $K_{eff}$ .

As the previous discussion in section 2.4.5 points out, crack initiation lifetime can be thought of as the time required for a small crack to grow to visibility. If this is the case, then the fact that crack initiation lifetimes show little or no reliance on mean loads can be attributed to crack closure. In the paper by Suresh and Ritchie (1984), results show crack closure effects on small cracks to be much less than those for long cracks, with the effect essentially decreasing with crack size.

Empirical attempts to include provision for  $R$ -ratio and crack closure effects into the Paris Law are numerous. Most simple of these approaches is the direct substitution of  $\Delta K_{eff}$  for  $\Delta K$ . This is known as the Walker Law where:

$$\Delta K_{eff} = \frac{\Delta K}{(1 - R)^m} \quad [2.12]$$

and  $m$  is a material constant.

Torronen and Cullen (1982) use a similar adjustment with some success to model the effects of high  $R$ -ratios on crack growth in reactor pressure vessel steels in a light water environment. The modified Paris Law takes the form given below:

$$\frac{da}{dN} = C(\Delta K)^m \left( \frac{\sqrt{1-R^2}}{1-R} \right)^m \quad [2.13]$$

Statistical methods have also been applied, notably the work by Soboyejo et al (1998). In this work, the parameters  $\Delta K$ ,  $K_{cl}$  and  $R$  were combined in a "simple" multi-parameter, linear-regression-based equation for the prediction of crack growth. Predictions for the crack growth rates in pressure vessel steel using this method were suitably accurate in the moderate  $\Delta K$  regime. However, crack arrest was predicted in a non-conservative manner, indicating that crack growth at low  $\Delta K$  values was underestimated. The complexity of this approach also reduces the probability of its widespread use.

#### 2.5.1.2 Effect of mean loads on thermal fatigue

##### *a) Crack initiation*

As thermal fatigue is a strain-controlled mechanism, the effects of mean loads on crack initiation may be considered the same as in mechanical testing of the same nature. As it is explained in section 2.5.1.1 (b) and (c), mean stresses are felt to have little effect when they are significantly below the yield stress, particularly when the stress amplitude itself is greater than yield.

##### *b) Crack growth*

In 1973, by which time linear elastic fracture mechanics was being used to model crack growth, Rau et al (1973) analysed the effects of mean stress and strain on crack growth in nickel and cobalt-base superalloys. Their results showed that for small crack growth rates ( $<10^{-4}$  in/cycle), the crack growth rate was independent of

mean stress or strain. However, for larger crack growth rates, this independence was removed and in some cases, the presence of a mean strain markedly accelerated the crack growth rate and led to secondary cracking.

It is generally accepted now that increases in mean stress results in an increase in crack growth rate in both air and water environments. This is reflected in the crack growth curves provided by codes such as the ASME Boiler and Pressure Vessel Code Section XI (1998), BS 7910 (1999), API 579 (1999).

### *c) Ratchetting*

Ratchetting refers to the phenomenon of incremental gross plastic deformation of a specimen subjected to a certain combination of steady state tensile stress and superimposed fatigue loading. This effect can lead to rapid failure of a component. A method for determining the likelihood of ratchetting occurring during RTS combined with primary loading (a case of strain controlled cyclic loading with a mean stress) has been completed by Skelton (1983). The effect of ratchetting on crack growth is reported to be small, particularly when the ratchetting growth itself is small, ie  $\approx 0.1\mu\text{m}/\text{cycle}$  (Bree, 1967, Beer, 1971 and Goodman 1981). The effect of high levels of ratchetting on crack growth is less clear but not relevant to the current thesis.

## **2.5.2 Environment**

The effect of environment on crack initiation and growth is a particularly complicated subject. Since 1960, a great deal of research on the topic has been conducted. Wei and Gangloff (1989) completed a notable review of this work through to 1989. This work identifies that a successful analysis of environmentally assisted crack growth requires an understanding of the complex interplay between chemical, mechanical and metallurgical factors occurring at the crack tip. Despite this complexity, some general findings of the effect of aggressive environments on crack growth have been made. For example, Bolotin (1999) states that as a rule, moist air, natural water and other active media intensify the process of fatigue crack growth.

Identifying the exact mechanism of this crack growth intensification is extremely difficult as it may vary for each different material-environment combination. Indeed, current design and analysis codes include only generalised descriptions of how to deal with environmentally assisted cracking. BS 7910 (1999) and API 579 (1998) provide only brief clauses based upon superposition models with no numeric guidelines. A number of these superposition models, allowing for the effect of corrosion on fatigue crack growth, have been formulated (Wei and Landes, 1969, Austen and Walker, 1977 and Gabetta et al, 1990). In essence, these models involve combining the effect of frequency dependent corrosion factors with frequency independent inert environment fatigue relationships. Research on the effects of environment on initiation and growth will now be looked at in turn. To reduce complexity, only work related to the material/environment combinations directly related to the work of this thesis will be analysed (ie fossil fuel power plant boiler equipment operating below 400°C). In effect this is a carbon steel and water/steam combination.

#### **2.5.2.1 Crack initiation**

Marshall (1983), in his review on environmental effects in fatigue, reports on the wide range of results researchers have produced when trying to evaluate the effect of environment on crack initiation lifetime. For every study that had shown a dependence of crack initiation lifetime on environment (in particular air and vacuum environments) another would show little or no dependence. The rupture of oxide films, particularly at grain boundaries in the air tests, were attributed the cause for any observed differences. Marshall also reports that corrosion due to environmental interaction can also lead to a reduced fatigue life, particularly if pitting occurs. This is supported by the observations of Tomkins (1979) who observes that corrosive environments provide pits and cracks along grain boundaries that become preferential sites for crack initiation.

In the more particular case of a water environment, as would be encountered in a thermal power station, the effect of environment is indicated to be potentially significant. An investigation by Chopra and Shack (1999) into the effects of Light Water Reactor (LWR)

environments on crack initiation of carbon steel reports reductions in life of up to 70 times when compared to similar testing in air. The level of dissolved oxygen (D.O.) in the water is found to decrease fatigue life logarithmically above 0.05ppm with the effect levelling off at 0.5ppm.

Models for the effects of environment on fatigue life are not commonly available. Fitness for service codes such as the American Petroleum Industries API 579 (1998) suggest that, if possible, fatigue life for a component should be determined from test data obtained in an environment as close as possible to that of operation.

#### 2.5.2.2 Crack growth - superposition and competition models

As mentioned in the introduction to this section, the effect of environment on crack growth rates have been analysed and modelled by many researchers. For the material/environment combination of carbon steel and water, the effects of corrosion become the focal point for this research. The superposition models used to do this are based on a form of the following equation (Wei and Landes, 1969, Austen and Walker, 1977, Shoji 1978):

$$\frac{da}{dN_E} = \frac{da}{dN_V} + \frac{da}{dN_{CF}} \quad [2.14]$$

Where:

$\frac{da}{dN_E}$  = Total crack growth rate.

$\frac{da}{dN_V}$  = Crack growth rate due to mechanical fatigue in a vacuum

$\frac{da}{dN_{CF}}$  = Additional crack growth rate due to corrosion.

The success of this simplified model is dependent on the last term in the equation and how it is defined.

In the Austen and Walker (1977) "process competition" model, the corrosion effects are divided into the categories of true corrosion fatigue (TCF) and stress corrosion fatigue (SCF). In TCF, the effect of an aggressive environment on crack growth is to increase the growth rate uniformly for all values of stress intensity factor range. For SCF, the effect of environment is negligible for stress intensity factor ranges below a certain "threshold" value. Above this value, the crack growth rate is increased substantially to a rate that is independent of the stress intensity factor, resulting in a "knee" in the curve. The value of the crack growth rate at this knee is thought to be related to the time dependent process of stress corrosion cracking (SCC), making its value dependent on the loading frequency and not on  $\Delta K$ . Above the knee, the crack growth rate returns to the regular crack growth curve, which at this level of  $\Delta K$ , is quite rapid.

Austen and Walker (1977) also propose that it is possible for particular material-environment combinations to exhibit SCF "superimposed" on TCF. This results in a crack growth rate that is accelerated for all values of stress intensity factor ranges and also exhibits the stress intensity factor independent "knee".

Figure 2.4 shows the three examples of corrosion fatigue as defined above as compared to a baseline curve for pure mechanical fatigue based on the Paris Law.

Stress corrosion cracking (SCC) is a common damage mechanism in a number of material/environment combinations. Normally however, it is not associated with carbon and low alloy steels in a boiler water environment (Jones, 1996). It is usually seen as the slow growth of a crack in a component due to the combined effects of a steady load and the environment. There is no requirement for cyclic loading for the crack growth to occur. A stress intensity factor limit, below which SCC cracking will not occur, can be defined for each material/environment combination. This limit is often referred to as  $K_{ISCC}$ . This means that in case of cyclic loading, SCC becomes a possibility as  $K_{max} > K_{ISCC}$ .

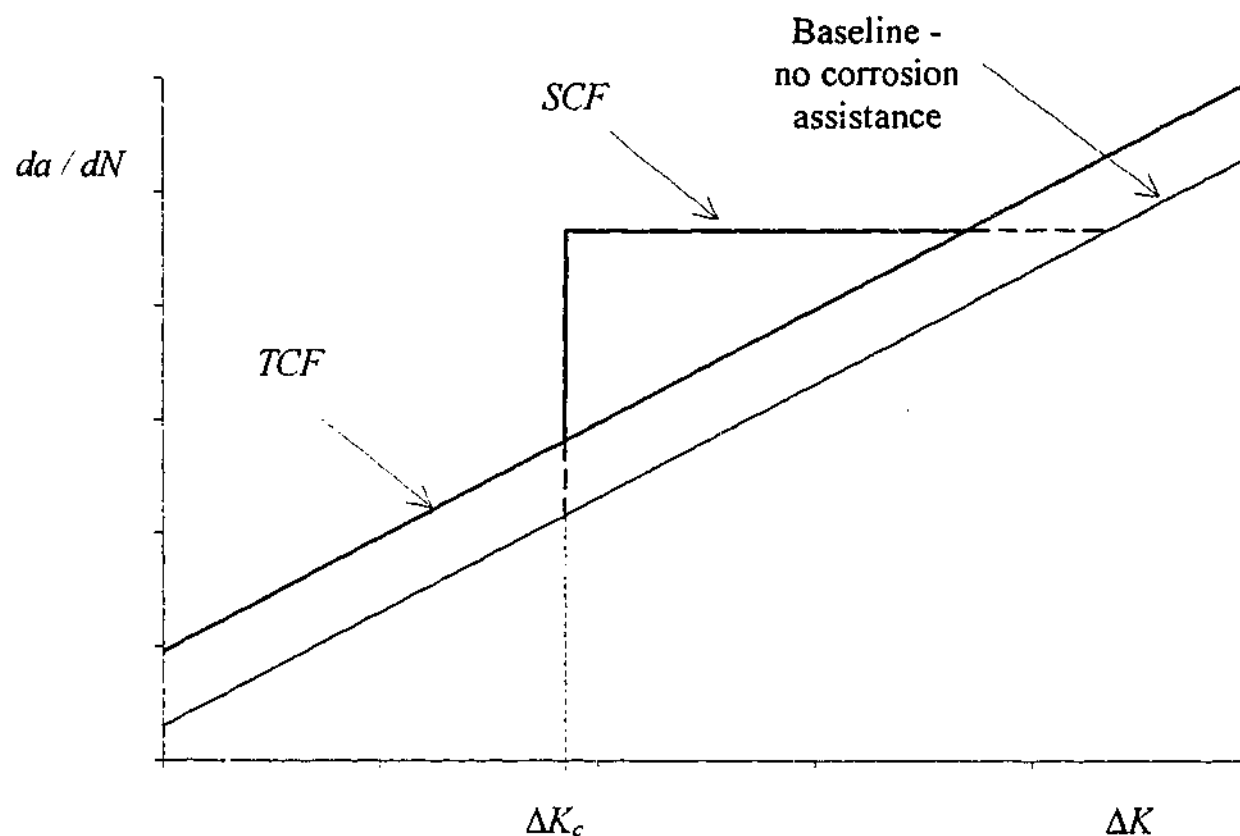


Figure 2.4: Crack growth rate as a function of  $\Delta K$  for various forms of corrosion fatigue (Austen and Walker, 1977).

Using the same methodology, it can be assumed that the onset of SCF as shown in figure 2.4 occurs when the maximum stress intensity factor developed during a cycle is larger than some SCF threshold value  $K_{ISCF}$ . This means the threshold  $\Delta K_c$  is actually a function of  $K_{ISCF}$  and the  $R$ -ratio:

$$\Delta K_c = K_{ISCF} (1 - R) \quad [2.15]$$

Mixed success has been reported in trying to relate  $K_{ISCF}$  to  $K_{SCC}$  indicating that the two mechanisms (SCC and SCF) are not necessarily equivalent.



### 2.5.2.3 Crack propagation mechanisms

Corrosion fatigue involves an interaction between reversed plastic deformation and local chemical reactions. While growth mechanisms may be specific to individual material-environment combinations, Gangloff (1990) identifies two possible mechanisms that research from the previous 25 years may suggest as being responsible for the chemical damage portion. These are hydrogen environment embrittlement and film rupture coupled with anodic dissolution. Opinion is split as to which of these mechanisms is more correct as both provide explanations for separate observed effects of variables on corrosion fatigue. Both mechanisms are outlined below.

#### *a) Hydrogen embrittlement*

Hydrogen embrittlement may be used to explain environmental assisted crack growth in alloy-gaseous or aqueous environment systems. Here in essence, atomic hydrogen is absorbed into new crack surfaces and diffuses through the crack-tip plastic zone. The effects of this free hydrogen are not fully known. Marshall (1983) outlines four principal mechanisms that may be responsible for the ensuing embrittlement.

1. An increase in internal pressure in the plastic zone produced at internal voids or defects such as grain boundaries where the atomic hydrogen recombines to form molecular hydrogen
2. A reduction of the surface energy by the absorbed atomic hydrogen
3. As reduction in cohesion energy between atoms in the presence of hydrogen concentrations (such as at the crack tip)
4. Crack closure

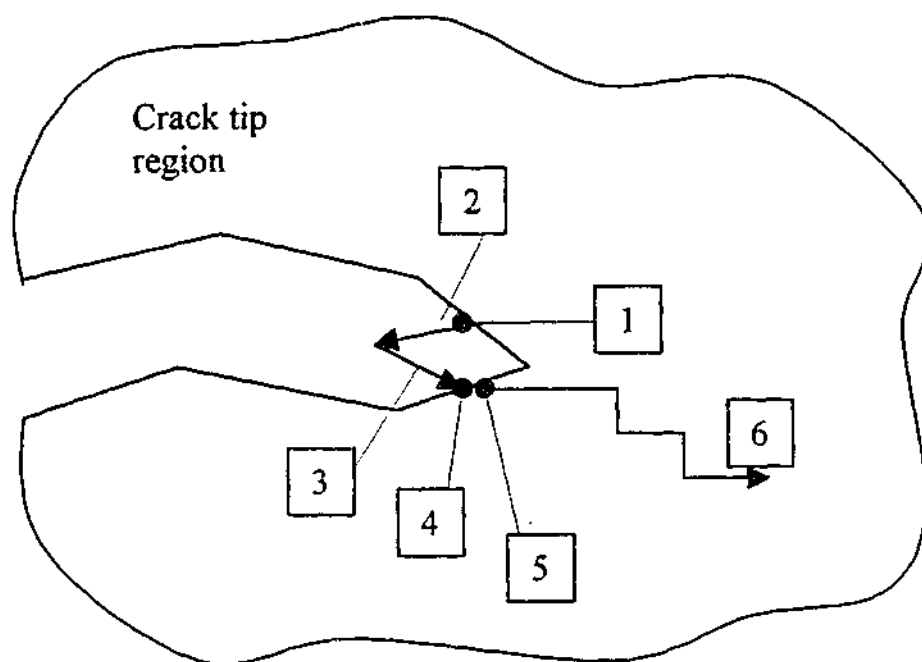
Regardless of which, if any, of the above mechanisms are correct, hydrogen embrittlement does allow for an explanation of the frequency dependence of corrosion fatigue crack growth, as growth is limited by the slowest step in the hydrogen absorption process. Austin and Walker (1977) use the hydrogen

embrittlement model to assist in explaining the enhanced crack growth during both true and stress corrosion fatigue.

Torronen and Cullen (1982) also favor the hydrogen embrittlement mechanism in their explanation of the effect of light water reactor environments on the fatigue crack growth in pressure vessel steels. This opinion is based primarily on fractographic analysis of the crack path. The process of hydrogen absorption into the crack tip is described by an electrochemical reaction at the crack tip. Assuming that the pH level at the crack tip is in the acidic regime, an anodic reaction "involving metal-surface dissolution" occurs. This is accompanied by a cathodic reaction that either occurs at the crack tip or the external surface. The level of dissolved oxygen in the water determines the form of the cathodic reaction, be it either the reduction of hydrogen ions to atomic hydrogen or the reduction of dissolved oxygen to hydroxyl ions. Torronen and Cullen assume that the environment near the crack tip is nearly or totally deoxygenated, allowing the model presented in figure 2.5 to be adopted.

Typically, as defined by Jones (1996), cracks growing by the hydrogen embrittlement mechanism are either transgranular or intergranular in appearance. The cracks are usually unbranched (or exhibit a small amount of branching), with sharp tips. Hydrogen induced cracking is also accelerated by cathodic polarisation and becomes less common at temperatures above room temperature.

Research into the mechanisms responsible for hydrogen embrittlement is on going. A recent issue of the journal "Engineering Fracture Mechanics" has been solely devoted to articles examining hydrogen embrittlement in metals, ranging in issues from micromechanics studies of hydrogen transport (Taha and Sofronis, 2001) to hydrogen induced plasticity (Delafosse and Magnin, 2001). This continuing interest indicates that as yet, no satisfactory model for the complete process has been developed.



1. Local anodic reaction:  $Fe \rightarrow Fe^{2+} + 2e$
2. Hydrolysis and generation of  $H^+$ :  $Fe^{2+} + H_2O \rightarrow FeOH^+ + H^+$
3. Liquid phase transport
4. Local cathodic reaction:  $H^+ + e \rightarrow H$
5. Hydrogen adsorption
6. Hydrogen transport in lattice

Fig. 2.6: Model for absorption of Hydrogen into crack tip (taken from Torronen and Cullen, 1982)

*b) Film rupture and anodic dissolution.*

The film rupture and anodic dissolution mechanism was originally developed to assist in explaining stress corrosion cracking (SCC). It is now felt to be particularly important during the corrosion fatigue of carbon and stainless steels exposed to high-temperature water environments. As outlined by Gangloff (1990), the high plastic strain rate due to fatigue at the crack tip ruptures any protective films, allowing crack advance to occur during transient anodic dissolution of the metal at the breached film. Repassivation of the surface controls the growth rate. In a model

for explaining environmentally assisted crack growth for reactor pressure vessel steel in a water environment developed by Gabetta et al (1990), the relative values of the active surface creation and passivation rates are used to explain the frequency dependence of the onset of stress corrosion fatigue. The process of anodic dissolution requires an oxidising source of which dissolved oxygen is an example.

In addition to using anodic dissolution as an explanation for stress corrosion cracking, Woodtli and Kieselback (2000) introduce so-called "strain-induced stress corrosion cracking". Here the mechanical load plays a more important role leading to the initial crack growth. This type of cracking is said to be important during alternating operating conditions. In addition, thermal strains are felt to be sufficient to act as the mechanical load. Further descriptions of how strain-induced corrosion cracking differs from classic anodic dissolution controlled corrosion cracking are vague. According to Jones (1996), cracking due to anodic dissolution is unbranched and transgranular in nature. The crack tip is usually blunt and, if externally introduced, cathodic polarisation suppresses the growth.

#### **2.5.2.4 Transient nature of environmentally assisted crack growth**

In the presence of an aggressive environment like high temperature water, the fatigue crack growth per cycle in carbon steel has repeatedly been observed to be a function of cycle frequency. This is unlike testing in a relatively benign environment (ie laboratory air, vacuum), where crack growth per cycle is independent of frequency. This frequency dependence has been linked to the time required for corrosion reactions to occur at the crack tip.

There are numerous examples (e.g. Austen and Walker, 1977, Bamford, 1977, Torronen and Cullen, 1982 and Gabetta, 1987) in which the frequency dependence of fatigue crack growth is shown to be related to the rise time of the loading cycle. It is during this portion of the cycle that deformation is occurring at the crack tip and fresh metal is being exposed to the environment. This means that crack growth rate is also a function of load cycle shape

(ie sinusoidal, square wave, triangular), as well as frequency. Conversely this means that hold times in the cycle have little or no effect on crack growth.

In a report by Gabetta et al (1990) describing corrosion assisted fatigue in reactor pressure vessels, the Austen and Walker model (see section 2.5.2.2) for environmental assisted crack growth is modified to allow for frequency effects. It is argued that while the true corrosion fatigue (TCF) component of environmental crack growth enhancement does not exhibit frequency dependence, the stress corrosion fatigue (SCF) component does. Writing SCF as a time dependent crack growth ( $da/dt_{SCF}$ ), equation [2.14] can be re-written:

$$\frac{da}{dN_E} = \frac{da}{dN_V} + \frac{da}{dN_{TCF}} + \tau \frac{da}{dt_{SCF}} \quad [2.16]$$

Where  $\tau$  is the rise time of the loading cycle.

The value  $da/dt_{SCF}$  can be estimated from isolation of effects during testing. For a low alloy steel in reactor grade water, the time dependent crack growth rate is reported by Gabetta et al to be approximately  $10^{-4}$  mm/s and is independent of the dissolved oxygen level in the water environment.

As reported in section 2.5.2.2, it has been observed that the SCF effect is only observed in fatigue above a certain threshold value of  $\Delta K_c$ . Gabetta et al believe this threshold limit occurs when a suitable rate of fresh metal is being created at the crack tip during each load cycle by a process of anodic dissolution (see section 2.5.2.3(b)). This fresh metal is active in a chemical sense, giving the term Active Surface Creation Rate ( $ASCR$ ). For a specimen under strain controlled loading, the  $ASCR$  can be related to the rate of change of crack mouth opening distance in a cycle, which in the LEFM region can be equated to  $\Delta K$  as below in equation [2.17] (taken from Gabetta et al, 1990).

$$ASCR = \alpha_{ASCR} \cdot \frac{1}{\tau \sigma_y E} \cdot \Delta K^2 \cdot \frac{1+R}{1-R} \quad [2.17]$$

Where  $\sigma_y$  and  $E$  are the yield stress and Young's modulus of the material respectively and  $\alpha_{ASCR}$  is a constant that relates the  $ASCR$  to the rate of change of crack mouth opening distance during a cycle.

It is assumed that the onset of SCF occurs when the  $ASCR$  is comparable to the stress corrosion crack growth rate. Then, substituting  $da/dt_{SCF}$  for  $ASCR$  in [2.17] and  $\Delta K_c$  for  $\Delta K$ , an equation that predicts the onset of SCF is generated.

$$\Delta K_c^2 = \frac{1}{\alpha_{ASCR}} \cdot \sigma_y E \tau \cdot \frac{1-R}{1+R} \frac{da}{dt_{SCF}} \quad [2.18]$$

An interesting implication of equation [2.18] is that for a particular material-environment combination, the onset of the "knee" in the SCF crack growth curve is dependent on both the frequency of loading as well as the  $R$ -ratio. Gabetta et al (1990) provide experimental evidence that this is the case for low alloy pressure vessel steel in a reactor water environment.

#### 2.5.2.5 Other environmentally assisted crack growth models

Even though the exact mechanism for environmentally affected fatigue growth is unclear, models for prediction of crack growth rates are abundant. With particular reference to crack growth in steel in a water/steam environment and apart from those already mentioned in this review, a search found models developed by Tomkins (1979), Torronen and Cullen (1982) and Gilman (1987). The large number of models available in the literature is due, in part, to the need for accurate modelling of this crack growth in the nuclear power industry.

In all cases, the crack growth models are based on some form of a modified Paris Law with an inclusion for the time dependence of the environmental contribution. And although each model is promising for a certain combination of experimental variables (loading cycle shape and size, temperature, specimen size and shape), none provide a universal concept for even a single material-environment combination. Time dependent models have also been

developed (Shoji et al, 1981) where the time-based crack growth rate  $da/dt$  is related to the crack tip strain rate. This shows that the environmental interaction during fatigue is particularly complicated and may not be able to be modelled by a single mechanism.

### **2.5.3 Temperature**

Although primary loads and environmental effects are the primary factors affecting RTS crack growth in thermal power station equipment, operating temperature may also influence crack growth. The temperatures of interest in this investigation are, by definition, those encountered in the operation of thermal power plant below the creep range for low carbon steels. This equates to a temperature range between 25°C (cold feedwater in a thermal power station) and around 400°C. Effects in this temperature range are limited to those mentioned below.

#### **2.5.3.1 Effect of temperature on fatigue crack growth**

In general, it has been observed that an increase in mean temperature during thermal cycling leads to a decrease in fatigue life (Coffin and Wesley, 1954, White, 1971). However, in most reported cases, the effects of temperatures above 400°C were used, with data on the effects of mean temperatures below this too scarce to allow any conclusions to be drawn.

#### **2.5.3.2 Low temperature creep**

A form of low-temperature creep cracking that has been observed in both carbon-manganese and low-carbon steels is possible in the temperature range of 300-420°C (Dooley and McNaughton, 1996). This form of time-dependent cracking forms at high primary stress regions (including residual stresses) and may be superficially mistaken for stress corrosion or fatigue cracking. Microscopically, cracks are typically intergranular in nature.

## **2.6 Summary**

This chapter has outlined the current state of knowledge in the field of predicting crack initiation and crack growth due to the repeated thermal shock (RTS) loading of a carbon steel component in a water environment. Interest has also been paid on analysing the effects of external factors including the effects of steady state mean loads and environment. This review shows that the individual fields of thermal shock stress analysis, thermal fatigue crack growth, mean load ratio effects and environmental modeling have all been investigated quite thoroughly at an individual level. However, they have not yet been brought together in an attempt to correctly model the cracking phenomenon that is currently observed in thermal power station pressure equipment exposed to RTS at temperatures below the creep range. It is the intention of this investigation to apply the individual kernels of knowledge of each of the above fields to give a full picture and allow accurate modeling of the RTS phenomenon.



## **Chapter 3:**

### **Test Method-**

### **Experimental Analysis of RTS Crack Growth**

#### ***3.1 Introduction***

In this chapter, the test method for the experimental analysis section of this thesis is detailed. The chapter is divided into three sections. The first section is a literature review outlining previous experimental techniques used for thermal fatigue investigations. The second describes, in some detail, the test-rig used for this investigation in some detail, including specimen development. The third section discusses the techniques used in the analysis of the results. Results and discussion are presented separately in Chapter 4.

#### ***3.2 Review of Experimental Design***

A review of past experimental designs for the analysis of thermal fatigue shows a trend towards two main types of construction. The most frequently mentioned is the thermal-mechanical fatigue type, introduced by Coffin and Wesley (1954) (eg. Rau et al, 1973; Gemma et al, 1976; Lawson, 1987; Alvarez-Armas et al, 1994; Pistorious and Marais, 1995). In this design, cyclic thermal loading is applied to a fully constrained specimen that may or may not undergo a separate cyclic mechanical loading. The advantage of this arrangement is that a single specimen (typically a thin cylinder) can be subjected to a selection of mechanically applied strain ranges for a single temperature range. This simplifies the generation of low cycle fatigue  $\epsilon$ - $N$  curves at different temperatures.

These designs do not take into account any environmental effects nor do they correctly model the thermal gradients that are developed during shock loading. As discussed in Chapter 2, the effect of the environment (including temperature and atmospheric composition) on fatigue crack initiation and growth is significant and difficult to account for analytically. In a review of past work in the area, Marshall (1983) indicated that modification of the environment could decrease the fatigue life of a specimen by up to two orders of magnitude when compared to the same test performed at room temperature and in a vacuum. Marshall concludes that the best way to allow for the effects of environment is to carry out the fatigue tests in an environment that closely simulates that which will be present during service. To take into account environmental effects, the thermal-mechanical fatigue type of test-rig can have the specimen housed in an autoclave in which the environment is controlled (e.g. Kawakubo et al, 1980; Prater et al, 1980).

The second type of experiment is the thermal stress fatigue type (eg. Howes, 1973; Mowbray et al, 1973; Beck & Santhanam, 1976). In these experiments, the specimen (typically disk shaped) is subjected to a sudden change in temperature, usually by submersion in a heated/cooled medium. The advantages of this method are that the stress profile is faithfully reproduced and that very severe shocks are possible in a very short period. For example, Howes (1973) reports a surface temperature rise of up to 600°C in 4 seconds using steel specimens. Although this may be useful for analysing high temperature components such as turbine blades, for steels operating below the creep range there is no need for testing over such a range of temperatures. The other problem with these methods of testing is a lack of an accurate reproduction of the environment, external loading and geometry of industrial applications.

Another form of experimental procedure not covered by either of the above methods involves the testing of a heated hollow cylinder. Thermal shocks are then applied by the running of cool water through the center of the heated cylinder. Skelton and Miles (1984) and Skelton and Nix (1987) use examples of this type of rig. The advantage with this method is that it is possible to accurately reproduce the operating condition of pressure vessel constructions exposed to repeated thermal shock, including environmental effects,

with the cylindrical specimen working as its own autoclave. Unfortunately, this construction does not allow for crack initiation or growth observations to be made during testing.

In order to analyse the crack depths when using the hollow cylinder test method, the specimens must be sectioned and crack growth assessed by counting striations on the crack surface or taking measurements of oxide thickness. Because striations are thought to be related to crack growth per cycle and oxide thickness is a representation of how long a freshly created crack surface has been exposed to an environment (Pinder, 1981), the crack growth rate can be inferred. However, the relating of either of these values to crack growth rates is a difficult and time-consuming procedure and includes a large margin for error. In essence, this type of test is only suitable for ranking the relative resistance of different materials to crack growth due to repeated thermal shock.

In addition to the experimental work completed by researchers into thermal fatigue, a great deal of analysis has also been placed on the effects of one off thermal shock transients on notched (or pre-fatigued) components. This work is encouraged by the nuclear power industry where severe cooling of operating equipment can occur, such as during a Large Break Loss of Coolant Accident (LBLOCA), producing what is referred to as a Pressurised Thermal Shock (PTS). Vitale and Beghini (1991) provide a good example of this work, in which pre-cracked large plate specimens of A533-B steel were heated to 100°C and then flooded with liquid nitrogen. In these types of tests, a single extended transient produces an unstable crack growth, sometimes resulting in complete fracture of the specimen. Good correlation of these fracture events with current fracture mechanics techniques has been produced.

As will be seen in the following sections, the design chosen for use in this investigation may be considered as a compromise between the thermal-mechanical and thermal stress fatigue techniques. It is in some ways similar to the SPLASH facility used by Fissolo et al (1995) to investigate crack initiation in 316L stainless steel and the test rig used by Marsh (1981) to analyse thermal shock fatigue in 304 and 316 stainless steels. In these rigs,

resistance-heated, flat plate specimens were quenched with room temperature water to produce the thermal shock loads. In both of these investigations, this type of experimental set-up proved reliable and generated suitable results.

### **3.3 Test Rig Description**

A thermal fatigue test rig has been purpose built for the investigation of crack initiation and growth due to repeated thermal shock loading. Consisting of a convection furnace, static loading structure and quenching system, it allows for the monitored growth of cracks for a wide variety of component geometries. Unlike prior investigations, a loading cycle typical of many thermal power station components is reproduced. In addition, the use of a novel specimen design allows many different tests to be completed at one time with a variety of notches.

The key advantages of this test rig over previous those used in previous studies are:

1. The component is heated by convection, resulting in no unwanted heat effects at the crack tip as may be the case for induction or resistance heating.
2. The component is quenched by room temperature pH and O<sub>2</sub> controlled water.
3. The specimen size is representative of typical industrial components.
4. Large specimen size permits multiple simultaneous experiments.
5. An unloaded "control" specimen can be tested simultaneously
6. Approximately one-dimensional conditions exist at any one crack because of use of thermal masses as described below

The principal disadvantage of the rig is the lengthy testing period required, which can be up to several months in duration for each set of test specimens.

The testing rig is detailed in figures 3.1, 3.2 and 3.3 and can be divided into four main physical components

1. The load frame,
2. the furnace and controller,
3. the quenching rig and PC and
4. the specimen.

The design of each component will be examined in turn.

### **3.3.1 Furnace**

The furnace is rectangular in shape, with a removable front face allowing specimen insertion. Slotted recesses in the top and bottom of the furnace allow the specimen to pass through for application of the primary load. Heating is performed by two 1kW-resistance type heating elements located on either side of the central heating area that measures around 100x150x400mm. This central area contains a thin-walled, stainless steel "quenching chamber" which houses the specimen and prevents the heating elements from being damaged by the quenching water. This chamber also has a large vent that protrudes from the bottom of the furnace, allowing the escape of steam and water after each quenching cycle.

The furnace can be operated at temperatures of up to 500°C (930°F). Although convection heating does not provide the most economical method in terms of time taken to heat a sample, it was a conscious design selection made after careful deliberation of other alternatives. Direct resistance heating by passing a current through the specimen (Coffin and Wesley, 1954; Sheffler & Doble, 1973; Ginsztler, 1987) provides a more rapid heating option but also produces a localised heating effect around the tip (Pernot and Mall, 1989). Radiant heating, as with induction heating (Marsh et al, 1986; Okazaki & Koizumi, 1987), was discounted due to the damage that could occur during quenching. Alternatively contact heaters (Lawson, 1987) reduce the flexibility of the system, having to be modified for each specimen shape and size.

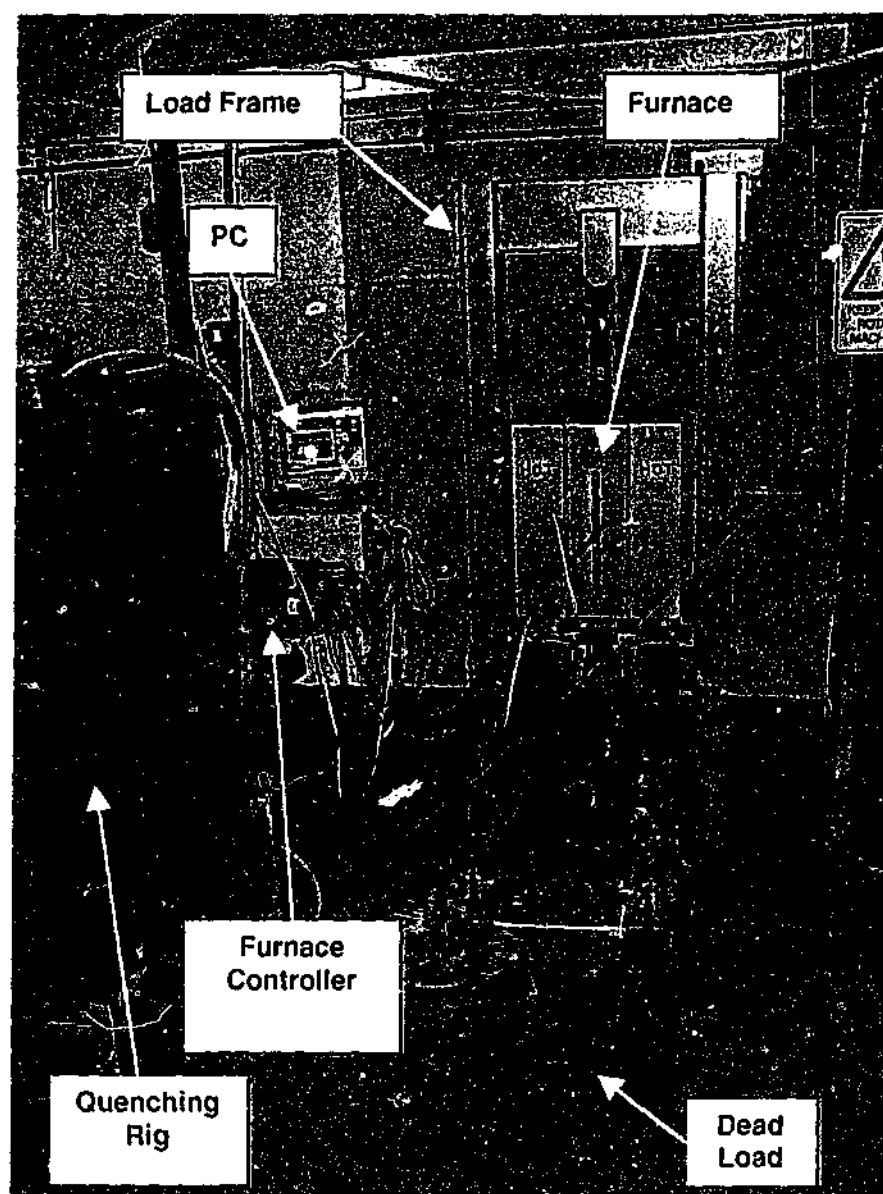


Figure 3.1: Photo of testing rig layout.

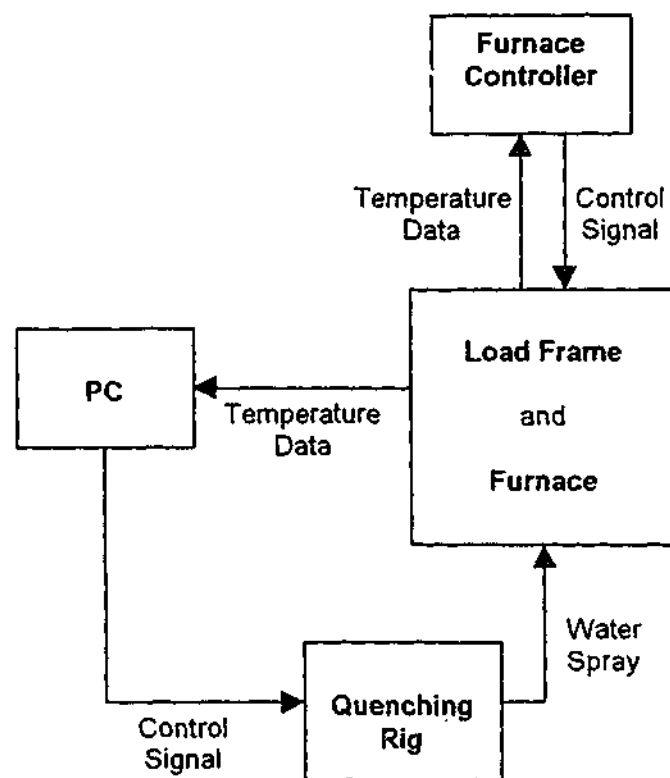


Figure 3.2: Schematic of testing rig layout.

### 3.3.2 Quenching Rig

The quenching rig was designed to operate automatically, relying on feedback of the specimen temperature. A manifold installed with 6 x ¼" full cone spray nozzles is permanently installed in the front wall of the furnace (see figure 3.1) and passes into the quenching chamber. When the temperature of the specimen uniformly reaches the set point, the quenching cycle is triggered. Up to 9L/min of water supplied via a 240V centrifugal pump can be applied to the specimen through the spray heads. A PC running LabView software, controls spray execution and duration. This PC also doubles as a data logger, recording the temperature of the specimen. The water used for quenching is stored in a 500L tank (to the left in figure 3.1), allowing its chemistry to be controlled to that representative of water used in thermal power stations (eg. pH level, controlled using ammonia and dissolved oxygen, controlled by boiling). By exposing the specimen directly to the water during cooling (and the steam remaining in the chamber during heating), the actual conditions of a component exposed to the steam cycle are well represented.

### **3.3.3 Steady State Load Application**

The steady state load frame utilises a 50:1 ratio lever design to apply dead loads of up to 80 kN to the specimen. A pinned-pinned connection system was chosen for attachment of the specimen to prevent the generation of unwanted constraint stresses during the thermal shock loading (ie creating a thermal-mechanical type loading). Engineering sketches of the frame design are included in Appendix A (BBK9806 to BBK9810).

### **3.3.4 Specimen**

The material chosen for examination in these experiments was low carbon steel, grade AS 1548-7-430R (AS, 1995). The 300mm long specimens have a cross-section of 10 x 65mm as shown in figure 3.3. These dimensions were chosen to give a central section suitable for one-dimensional cooling similar to that achieved with the large plates used for thermal shock analysis by Vitale and Beghini (1991). To achieve the uniform one-dimensional transient temperature field during quenching, steel masses were attached to both sides of the specimen. Thermocouples were fitted to the masses in direct contact with the specimen allowing the temperature profiles existing during the quenching to be monitored to within  $\pm 1^{\circ}\text{C}$ . Not having the thermocouples physically attached to the specimen allows for the uninhibited growth of the cracks.

Quenching occurs on the narrow front face. A preliminary analysis showed that the likely elastic stress amplitudes generated by a thermal shock from temperatures below the creep range were too low to produce crack initiation within a reasonable number of cycles (ie around 10,000). For this reason, small starter notches were machined into the narrow face. The length of the specimen allowed the placement of a variety of notches spaced by 50mm. Typical notch radii ( $r$ ) were 0.25mm and 0.1mm. All notch depths were 3.5mm.



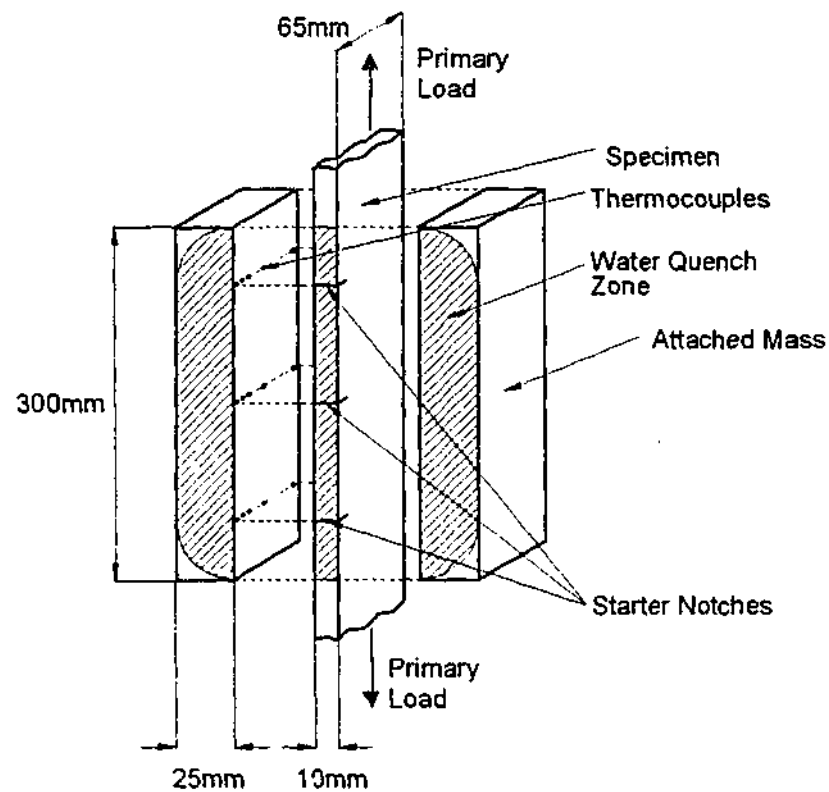


Figure 3.3: Specimen design (not to scale).

Multiple notches on one specimen allow for the simultaneous testing of a number of cracks. The disadvantage of having more than one crack on a specimen however is that neighbouring cracks may influence each other during growth. To estimate the possible effect of having more than one crack, the stress intensity factor produced at the tip of a single crack had to be compared with that produced at the tip of multiple cracks spaced 50 mm apart. To enable such a comparison, the stress intensity factor solutions reported in Murakami (1990) for multiple edge cracked, semi-infinite plates subjected to uniform tension were utilised.

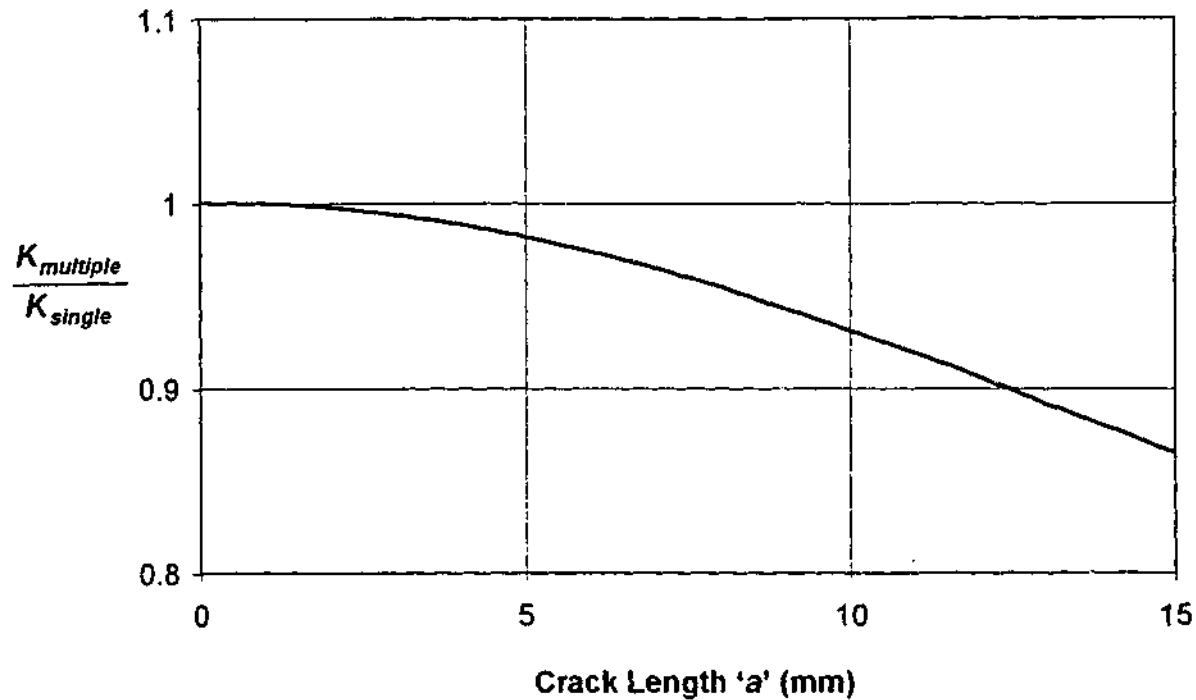


Figure 3.4: Stress intensity factor ratio for multiple cracks separated by 50mm and a single crack.

The results of the comparison using a crack spacing of 150mm are shown in figure 3.4. From this plot, it follows that two adjacent cracks could be permitted to grow to a depth of 10mm before a stress intensity factor error of approximately 6% is produced by assuming only one crack is present. Assuming that the tests will be discontinued before the cracks reach 10mm in length, this level of accuracy was determined to be appropriate for this investigation.

Engineering sketches of the specimens and attached masses are given in Appendix A (BBK9811, BBK9903, BBK9905 and BBK9906).

### **3.4 Experimental Analysis Techniques**

A major objective of this work is to present results directly applicable to practical calculations for both the numbers of cycles to small crack initiation and the crack growth rate. As mentioned in the previous chapter, the length (or size) of a crack when it is deemed to have initiated depends on the terms of reference. In this work, the engineering definition of crack initiation will be used. That is, when a crack can be seen either with the naked eye or under low level magnification ( $\sim 10\times$ ). This agrees with the definition used in standard codes of practice against which the experimental results of this investigation will be compared (see Chapters 4 and 6). In order to analyse initiation, descriptions of the stress-state at the location of initiation must be derived. This is also the case for analysis of longer crack growth.

As described in Chapter 2, Linear Elastic Fracture Mechanics (LEFM) is currently the most widely accepted tool for use in analysing "long" crack growth. Similarly,  $S-N$  (or fatigue life) diagrams are the most common method used for prediction of crack initiation. Consequently, for analysis purposes, it is required to determine the stress amplitude generated at the specimen surface for crack initiation and the stress intensity factor generated at the tip of any cracks that may form for crack growth. The following sections of this chapter outline how this was achieved.

#### **3.4.1 Notch Root Stresses**

Transient effects, localised plastic strains, cyclic loading, high stress non-linearity and notch sensitivity of the material combine to make the process of determining the stress amplitude at a notch in a plate subjected to repeated thermal shock very difficult. Although no single method can be used to solve for the stress, a number of theoretical and empirical solutions have been developed that can be adapted for use. A brief description of those methods' potential for use in this analysis will be presented here, with an analysis of the advantages and disadvantages of each. For a more thorough analysis of the background and theory relating to these methods, resources such as Juvinal (1967) and Bannantine (1990) are suggested.

Note that in all cases, plain stress is assumed to exist at the notch due to the relative small thickness (10mm) of the specimens used. This assumption requires justification through examination of the specimen crack characteristics after testing is completed (see Chapter 4).

### 3.4.1.1 Stress profile linearisation

The first method for estimating the stress at the notch is the most classical in terms of mechanical design and involves linearising the thermal stress distribution across the specimen and substituting uniform (or membrane) and bending components,  $\Delta\sigma_m$  and  $\Delta\sigma_b$  respectively. The stress profile analysed is the nominal stress profile of the reduced specimen cross-section (ie ignoring the notch). This is directly obtained from the temperature profile of the reduced section. An example of this linearisation is shown in figure 3.5.

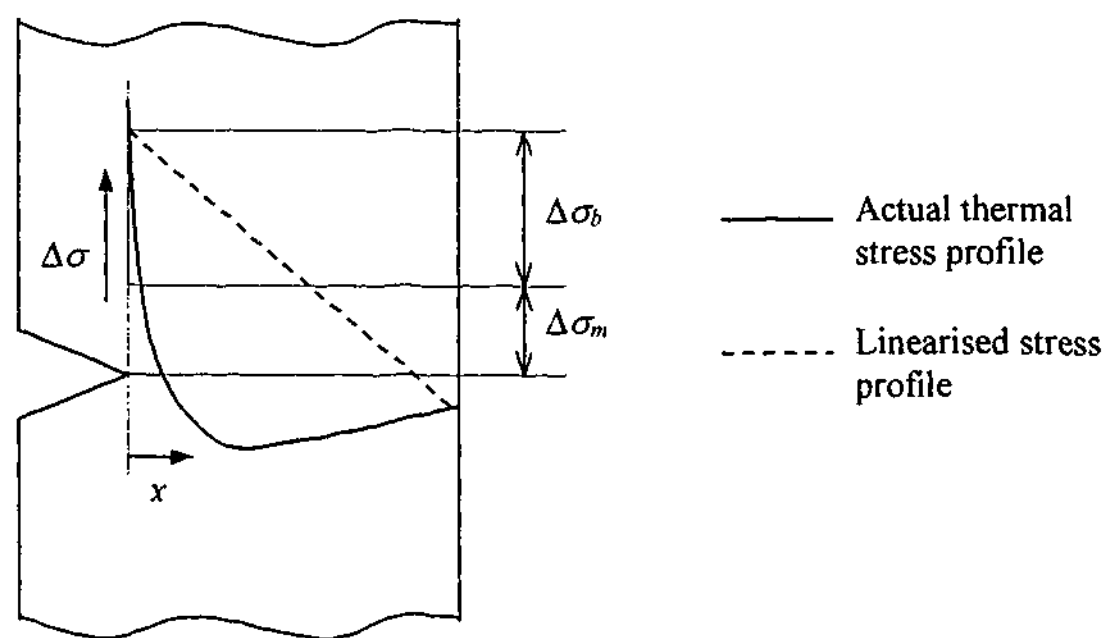


Figure 3.5: Example of linearisation of a thermal shock stress in a flat plate with notch.

Once the membrane and bending components of the linearised stress profile have been obtained, the stress amplitude ( $S_a$ ) is determined from:

$$S_a = \frac{k_{tb} \cdot \Delta\sigma_b + k_{tm} \cdot \Delta\sigma_m}{2} \quad [3.1]$$

Where  $k_{tb}$  and  $k_{tm}$  are the theoretical bending and uniform load stress concentration factors for a notched plate, obtained from printed sources (eg, Pilkey, 1997).

Advantages:

1. Method is simple,
2. Theoretical stress concentration factors can be obtained from published sources.

Disadvantages:

1. Thermal stresses are highly non-linear and the choice of a linear approximation may be excessively conservative,
2. Ignores many complicating factors including notch sensitivity and plastic effects.

#### 3.4.1.2 Sharp notch approximation

The second method simply applies the elastic stress intensity factor calculations by assuming that the notch is "sharp". Thus,

$$S_a = \Delta K_{max} / \sqrt{\pi r} \quad [3.2]$$

where  $S_a$  is the alternating elastic stress at the notch tip,  $\Delta K_{max}$  is the maximum stress intensity factor range during the cycle assuming the notch acts as a sharp crack, and  $r$  is the notch radius. The stress intensity factors are calculated using the method described in section 3.4.2.

As has been shown through investigation (Wilson, 1974), equation [3.2] is correct to within 5% for notches of radii less than 1mm, with the error reducing further with smaller radii. As all notches in this investigation have radii less than 1mm, they are considered adequately small for its application.

Advantages:

1. Method is simple,
2. Stress intensity factor solutions will already be obtained, as they are necessary for use in crack growth analysis (see section 3.4.3).

Disadvantages:

1. Ignores many complicating factors including notch sensitivity and plastic effects.

#### 3.4.1.3 Notch sensitivity analysis

In the case of cyclic loading, the effect of notches has been found to be less than the theoretical solutions given by methods 3.4.1.1 and 3.4.1.2 would indicate. This may be due to individual material response, which is ignored by the above methods. Thus, in a notch sensitivity analysis, allowance is made for a particular material behaviour by a reduction in the *theoretical* stress concentration factor.

In this analysis, equation [3.2] is used to determine the theoretical sharp notch stress amplitude, which in turn is used to estimate the overall theoretical stress concentration factor ( $k_t$ ) from the following equation:

$$k_t = \frac{S_a}{S_n} \quad [3.3]$$

Where  $S_n$  is the *nominal* alternating stress at the notch tip (ie assuming no stress concentration due to notch). In the case of thermal shock loading of a notched specimen,  $S_n$  is difficult to determine. In this work, it will be assumed that the reduced cross section in the notch plane has the same temperature distribution as it does remote from the notch plane, allowing the nominal stress to be determined.

This stress concentration value ( $k_t$ ) is not directly used in a crack initiation life analysis but rather converted into the fatigue notch factor by a notch sensitivity analysis, whereby:

$$k_f = 1 + \frac{k_t - 1}{1 + \sqrt{\rho_n/r}} \quad [3.4]$$

where  $k_f$  is the fatigue notch factor, and  $\rho_n$  is a material constant.

Equation [3.4] is an empirical fit taken from tests by Neuber (1946) (many other equivalent empirical equations exist, see Juvinall, 1967). The material constant  $\sqrt{\rho_n}$  is known as the Neuber constant and is claimed to be dependent on grain size, representing the materials' sensitivity to notches. Multiplying the nominal stress by this factor provides the stress amplitude necessary for a fatigue life analysis.

$$S_a = k_f S_n \quad [3.5]$$

Advantages:

1. Accounts for reduction in notch sensitivity for cyclic loading.

Disadvantages:

1. Ignores plastic effects.

#### 3.4.1.4 Neuber notch pseudostress analysis

When strains at the notch are largely plastic, an elastic material behaviour assumption as used in 3.4.1.2 and 3.4.1.3 is no longer applicable. It becomes necessary to define the "pseudostress" amplitude ( $S'_a$ ) as the strain at the notch multiplied by Young's Modulus, ie

$$S'_a = \varepsilon_a E \quad [3.6]$$

Where  $\varepsilon_a$  is the total local strain amplitude at the notch.

After yielding occurs, stress and strain concentrations are no longer defined by the single term, ie  $k_t$ . Instead, the stress concentration decreases and the strain concentration increases in accordance with the Neuber relationship such that:

$$k_t = \sqrt{k_\sigma k_\epsilon} = \sqrt{\frac{\sigma_a \epsilon_a}{S_n e_n}} \quad [3.7]$$

Where  $k_\sigma$  is the stress concentration factor and  $k_\epsilon$  is the strain concentration factor,  $\sigma_a$  is the local stress amplitude at the notch and  $e_n$  is the nominal strain amplitude at the notch.

When material behaviour remote from the notch is predominantly elastic, the nominal strain ( $e_n$ ) can be written in terms of stress divided by Young's Modulus ( $S_n/E$ ) so:

$$k_t S_n = \sqrt{\sigma_a \epsilon_a E} \quad [3.8]$$

Now, substituting [3.6] into [3.8] and [3.2], the notch pseudostress ( $S'_a$ ) can be obtained in terms of the stress intensity factor and the local stress (Prater and Coffin, 1987):

$$S'_a = \frac{\Delta K^2}{\pi \sigma_a} = \frac{(k_t S_n)^2}{\sigma_a} \quad [3.9]$$

Now, with knowledge of the cyclic stress strain relationship of the material, [3.9] can be solved for any value of stress intensity factor.

Substitution of  $k_f$  for  $k_t$  in [3.9] has been suggested by Topper et al (1969) to take into account notch sensitivity during cyclic loading.

$$S'_a = \frac{(k_f S_n)^2}{\sigma_a} \quad [3.10]$$



**Advantages:**

1. Describes notch stress-state when plastic strains are large

**Disadvantages:**

1. Complicated
2. Requires relations between cyclic stress and strain for the material to be known.

**3.4.1.5 Selection of preferred method**

Of the methods outlined in the preceding sections, the notch sensitivity analysis (section 3.4.1.3) was considered to provide the most accurate estimation of the elastic stress at the notch tip for fatigue analysis. For cases when plastic strains at the notch tip are large however, this method will not adequately model the stresses in the region. In this case, and when plastic stresses are restricted to the area surrounding the notch tip, a Neuber notch pseudostress analysis as outlined in section 3.4.1.4 needs to be applied. In cases when plastic strains dominate a large portion of the specimen, other methods should be adopted (eg. Seeger's analysis, see Bannantine, 1990). Such an analysis is not required during RTS however as plastic strains are typically restricted to a small region near the shocked surface.

Note that a limit to the value of  $k_f$  used in fatigue analysis is sometimes suggested in the literature. For example the ASME Pressure Vessel and Boiler Code, Section VIII, Division 2 (1998), suggests in article 5-111 that any stress concentration factors used in a fatigue analysis as outlined in the code can be limited to 5.0 or less. This is a simple way of dealing with many complicating factors surrounding fatigue analysis, including localised plasticity at the notch root and the so-called "worst-case notch effect". This limit on  $k_f$  will be considered during the analysis of notch root stresses in Chapter 4.

**3.4.2 Determining Time (Cycles) to Crack Initiation**

Having adopted the engineering definition of crack initiation, it is necessary to outline how, in practice, a test specimen was determined to have "initiated" a crack. Two methods for achieving this were developed, namely using long crack extrapolation and by defining a crack size at which initiation was said to have been complete. Both methods are

approximations as they over-simplify the crack growth dynamics. However, the technical accuracy of the method is relatively unimportant, as long as it allows for the comparison and analysis of test data points and provides a means for comparison with published data.

### **3.4.3 Crack Tip Stress Intensity Factors ( $K_I$ )**

As mentioned in Chapter 2, the most generally accepted method for determining stress intensity factors in a cracked structure exposed to thermal shock loading is that of the weight function technique (Skelton, 1983). Basically, the weight function technique operates on the superposition principle and allows the stress intensity factor solution for a certain set of boundary conditions in a structure to be applied to any other arbitrary boundary conditions in the same geometry. Equation 3.11 gives the generalised form:

$$K_I = \int_0^a \sigma(x) m(x, a) dx \quad [3.11]$$

Where  $a$  is the crack length,  $\sigma(x)$  describes the stress distribution across the geometry and  $m(x, a)$  are the weight functions developed for that geometry.

The simplified weight function technique as outlined in Appendix A, article A-3000 of the ASME Boiler and Pressure Vessel Code, Section XI (1998) has been selected for use in this analysis. This method, developed for surface flaws, requires a third order polynomial to be fit to the elastic stress distribution of the uncracked specimen.

The elastic stress distribution in a plate subjected to an arbitrary 1-d temperature distribution can be calculated for the case of plain stress from the following integral (taken from Timoshenko and Goodier, 1982):

$$\sigma(x) = -\alpha T(x)E + \frac{1}{2c} \int_{-\frac{W}{2}}^{\frac{W}{2}} \alpha T(x)E \cdot dx + \frac{3x}{2c^3} \int_{-\frac{W}{2}}^{\frac{W}{2}} \alpha T(x)E \cdot dx \quad [3.12]$$

Where the origin is defined in the middle of the plate,  $\alpha$  and  $E$  are the coefficient of thermal expansion and Young's Modulus of the material respectively and  $W/2$  is the half-thickness of the plate.

A third order polynomial is then fitted to the stress distribution using:

$$\sigma(x) = A_0 + A_1\left(\frac{x}{a}\right) + A_2\left(\frac{x}{a}\right)^2 + A_3\left(\frac{x}{a}\right)^3 \quad [3.13]$$

Where  $x$  is the distance through the specimen, now measured from the flawed surface,  $a$  is the crack depth and  $A_0$ ,  $A_1$  and  $A_3$  are constants determined by best fit techniques.

The stress intensity factor is determined by the following equation:

$$K_I = \left( (A_0 + A_p)G_0 + A_1G_1 + A_2G_2 + A_3G_3 \right) \sqrt{\pi \frac{a}{Q}} \quad [3.14]$$

Here  $K_I$  is the stress intensity factor of the first mode,  $G_i$  and  $Q$  are the free surface correction factors and the flaw shape parameter respectively (and  $i = 0, 1, 2, 3$ ).

The flaw shape parameter  $Q$  contains a plastic zone correction factor that is dependent on the material yield strength and is determined from the equation below.

$$Q = 1 + 4.593(a/l)^{1.65} - q_y \quad [3.15]$$

where  $l$  is the width of the flaw and  $q_y$  is the plastic zone correction factor calculated from:

$$q_y = \left[ (A_0G_0 + A_1G_1 + A_2G_2 + A_3G_3) / \sigma_{ys} \right]^2 / 6 \quad [3.16]$$

where  $\sigma_{ys}$  is the yield stress of the specimen. All yield stresses in this investigation were taken from the elevated temperature data contained in Appendix B. Equation [3.16] is based on monotonic loading and plane strain assumptions. For plane stress cyclic loading, the plastic zone size is reduced, replacing the dividing factor of 6 with 8. In the case of plain strain cyclic loading, the zone is further reduced and the 6 is replaced by 24 (Bannantine, 1990).

Note that whenever yielding occurs,  $Q$  decreases in value and an associated increase in the stress intensity factor is produced.

#### **3.4.4 Limitations of LEFM Analysis**

The application of the stress intensity factor to describe the stress condition at the tip of the cracked, notched specimen is limited by a couple of factors. Firstly, the crack must be of sufficient length such that the presence of a notch does not interfere with the stress distribution at the crack tip. Secondly, the plastic zone size must be small in comparison to both the specimen thickness and the crack length.

##### **3.4.4.1 Notch effect**

In 1977, Smith and Miller completed a study on the effect of notches on crack growth rates. Their analysis concluded that the notch influence was limited to a depth of  $0.13\sqrt{Dr}$  where  $D$  is the depth of the notch and  $r$  is the notch radius. When the crack is smaller than this length, the notch modifies the crack tip conditions, as observed during crack growth. Beyond this depth, the notch can be ignored and the effective crack length is simply a sum of the notch depth and any crack growth that has occurred from its base. Smith and Miller do not describe limitations of this approach in their original work, and the range of stress intensity factors for which it is applicable is indeterminate.

#### 3.4.4.2 Plastic zone size

The size of the plastic zone developed at a crack tip during cyclic loading can be estimated from the following (Bannantine, 1990):

$$r_y = \frac{1}{8\pi} \left( \frac{K_I}{\sigma_{ys}} \right)^2 \quad \text{for plane stress conditions} \quad [3.17]$$

$$r_y = \frac{1}{24\pi} \left( \frac{K_I}{\sigma_{ys}} \right)^2 \quad \text{for plane strain conditions} \quad [3.18]$$

In the case of the flat plate specimens used in this analysis, plane stress conditions are assumed to dominate. Substituting a conservative material yield stress of 250MPa and a maximum acceptable cyclic plastic zone radius of 1mm (much less than specimen width of 10mm), the maximum allowable stress intensity factor for use in LEFM analysis is determined to be approximately 40MPa $\sqrt{\text{m}}$ . This will be used as a limit throughout the experimental analysis.

#### 3.4.5 Temperature Dependence of Test Material

It is assumed throughout the experimental work in this thesis that material properties are independent of temperature. In reality this is not the case. Both the coefficient of expansion ( $\alpha$ ) and the Young's Modulus ( $E$ ) of carbon steel change with temperature. However, over the range of interest (100-400°C), the changes are small (~10%) and the product of these two properties remains close to constant. For this reason, steady values of these two properties will be assumed throughout the remainder of this analysis.

Unlike  $\alpha$  and  $E$ , the yield stress ( $\sigma_{ys}$ ) of carbon steel can be heavily affected in the temperature range of 100 to 400°C. Holding steady for lower temperature, the yield stress begins to drop rapidly at temperatures above 250°C. Details on high temperature testing of the material used in the experimental section of this thesis are given in Appendix B. In all analysis using this material, yield stress has been substituted as a function of temperature, calculated by fitting a curve through the data presented in Appendix B.

#### **3.4.6 Temperature Analysis**

From the proceeding analysis outline, it becomes evident that the accurate measurement of the temperature condition of the specimen during thermal shock cycling is extremely important. As detailed in the test rig description, thermocouples embedded in the attached mass on one side of the specimen allowed this to be completed at discrete time intervals. Numerical techniques were adapted in an attempt to model the transient temperature profiles and allow extrapolation and interpolation of the data. Unfortunately, the relative complexity of the heat transfer conditions developed during quenching prevented the development of a suitable model. Instead, curve fitting of the recorded temperature data was solely relied upon. The attempts for numerical modelling are summarised below.

The numerical analysis consisted of using finite element techniques to model the quenching as a one-dimensional heat transfer problem. Selection of the appropriate boundary conditions at the quenched face presented the largest difficulty for this analysis. It is assumed that most of the heat transfer will occur when the quenching water boils at the face of the heated specimen. This means the cooling medium can be estimated to be at around 100°C. The heat transfer coefficient developed between the boiling water and a heated vertical plate however is very difficult to estimate. Mills (1999) reports that this coefficient may be anywhere between 3,000 and 100,000 W/m<sup>2</sup>K.

Because of this difficulty in obtaining a direct theoretical solution, a number of heat transfer coefficients were modelled using the finite element process and the results compared with the experimentally obtained data points. A degree of correlation was found across a wide range of coefficients, between 3,000W/m<sup>2</sup> and an infinite coefficient. As mentioned above, in all cases, the quenching environment was set to 100°C. Figures 3.6 – 3.8 show the results of the transient analyses for heat transfer coefficients of 3,000W/m<sup>2</sup>K, 10,400W.m<sup>2</sup>K and an infinite coefficient respectively. These values were chosen to encompass the values indicated by Mills(1999). The value of 10,400W/m<sup>2</sup>K was obtained from an illustrative heat transfer coefficient in the literature from Vitale and Beghini (1991) in their analysis of large plates of A533 steel exposed to thermal shocks.

Also shown on figures 3-6 –3.8 are the experimental data points corresponding to a 10s shock from 370°C. These points have been recorded for 4s, 5s, 7s and 10s after the start of the down-shock. The comparison with the numerical results shows that the transient profile developed during the experiment cannot be modelled by one value of the heat transfer coefficient. While a value of 3,000W/m<sup>2</sup>K may seem acceptable at around 4s into the shock, this changes to 10,400W/m<sup>2</sup>K for 5s and closer to infinity for 10s. The changing heat transfer coefficient is a function, amongst other things, of:

1. The changing surface temperature of the shocked specimen and,
2. Transients in the quenching system (filling of the manifold, operation of the pump).

Because generalisation of the thermal profiles using numerical techniques proved to be difficult and prone to error, it was accepted that further analysis would best be served by simply curve-fitting the experimentally obtained temperature data. This was completed using the analytical solution for a plate exposed to one-sided thermal shock provided by Zhi-He and Yui-Wing (1995). The analytical solution was modified (by changing the size and length of the shock) until the data produced a best fit for the experimental results. The results for 10s quench from 370°C is shown in figure 3.9.

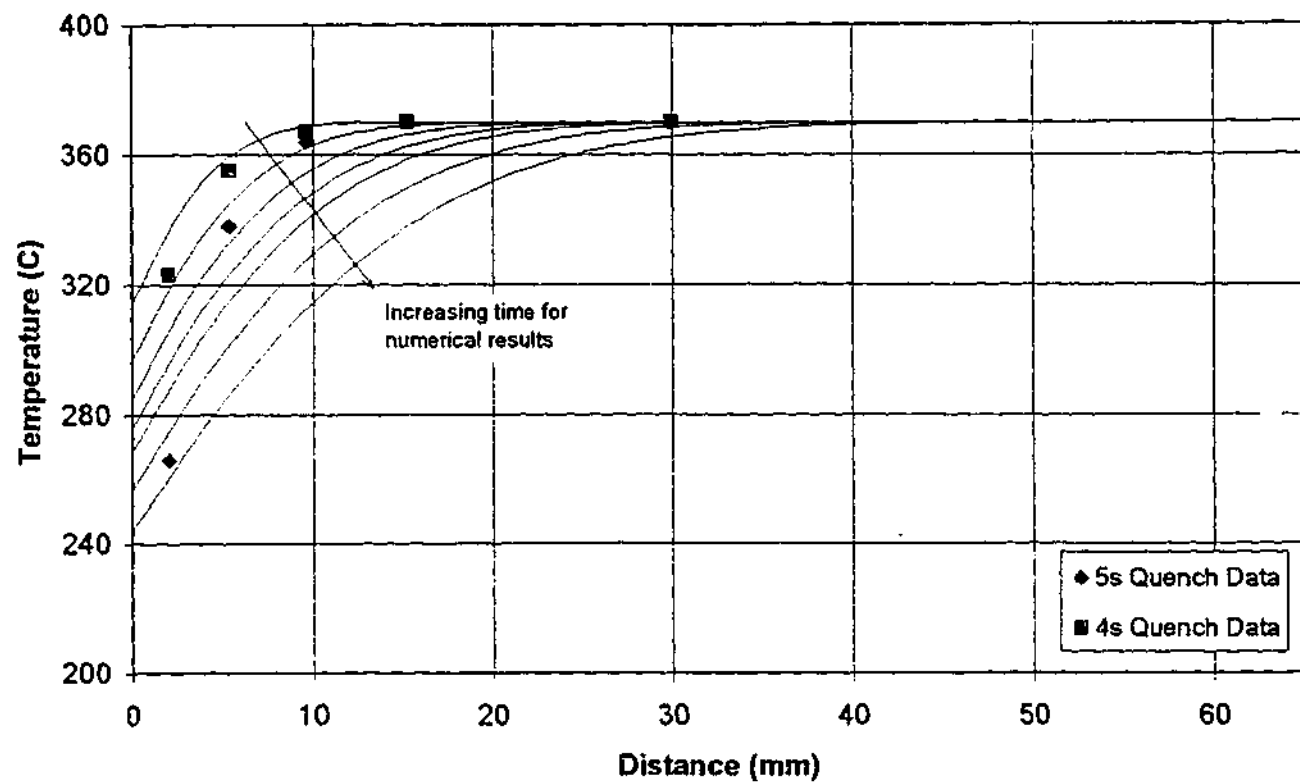


Figure 3.6: Temperature profiles developed during one-dimensional thermal shock of flat plate specimen from 370°C. Heavy points show experimental data. Light lines represent numerical results using a surface heat transfer coefficient of 3,000W/m<sup>2</sup> at time of 1-10s.

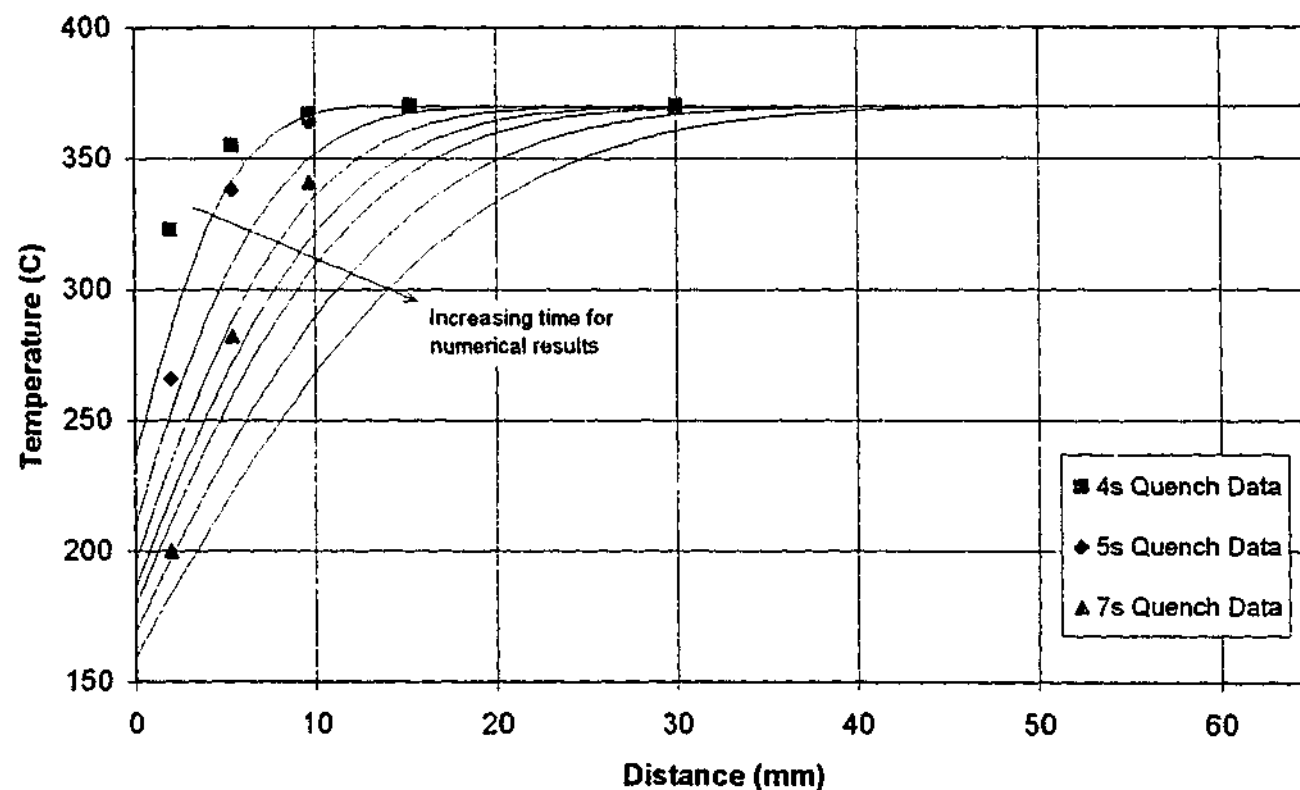


Figure 3.7: Temperature profiles developed during one-dimensional thermal shock of flat plate specimen from 370°C. Heavy points show experimental data. Light lines represent numerical results using a surface heat transfer coefficient of 10,400W/m<sup>2</sup> at time of 1-10s.



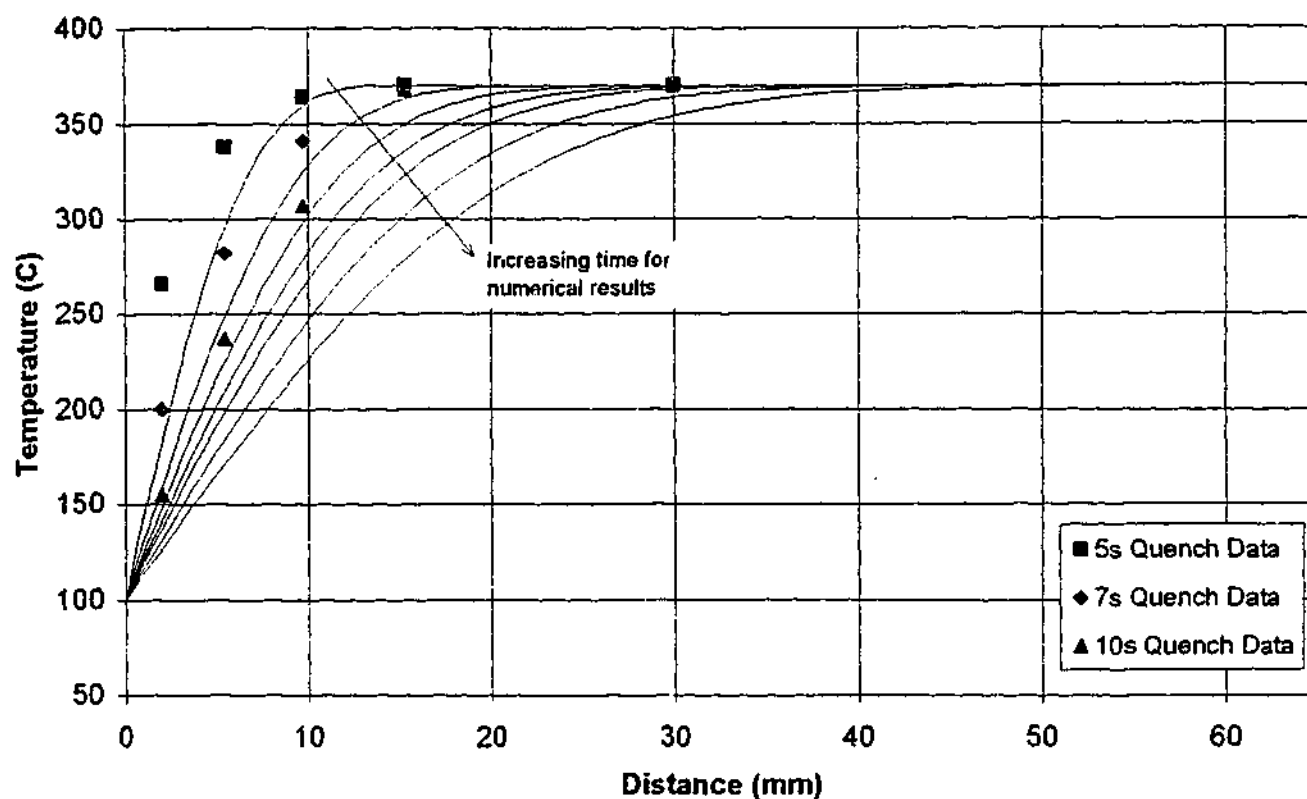


Figure 3.8: Temperature profiles developed during one-dimensional thermal shock of flat plate specimen from 370°C. Heavy points show experimental data. Light lines represent numerical results using an infinite surface heat transfer coefficient at times of 1-10s.

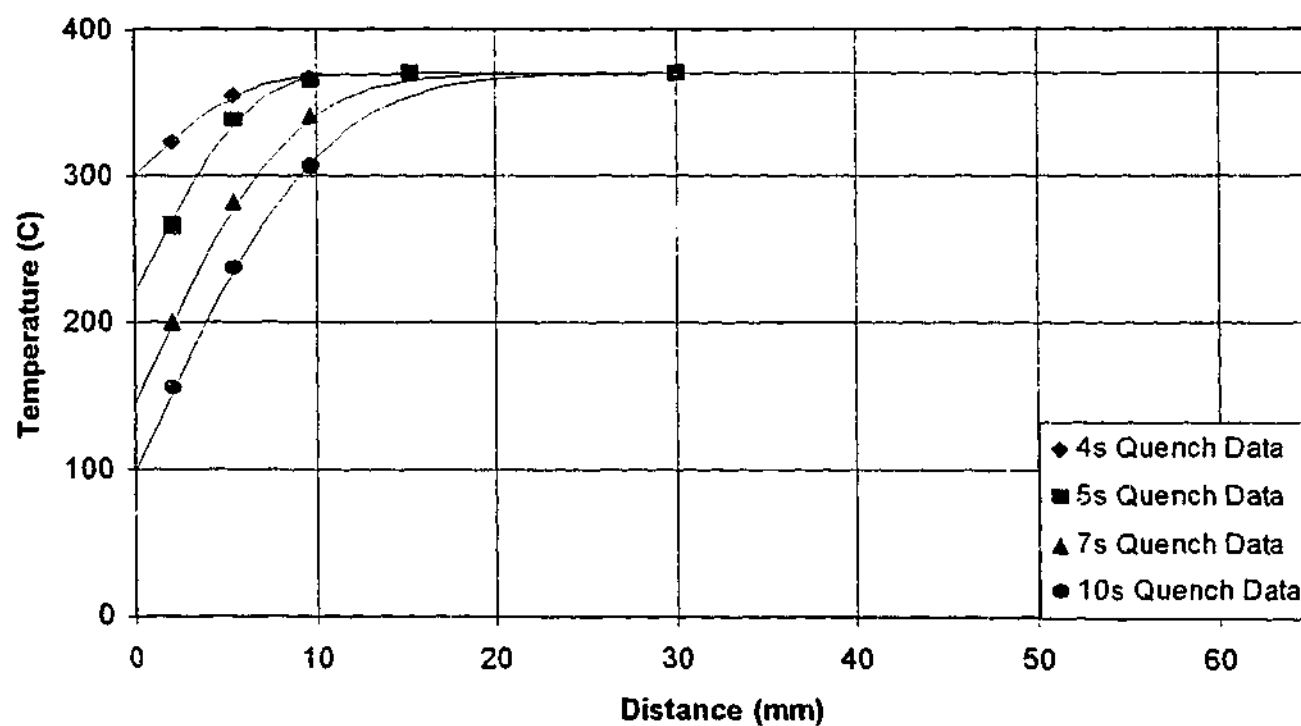


Figure 3.9: Curve fits of experimental quench data for times of up to 10s. Specimen temperature prior to down-shock is 370°C. Heat transfer coefficient varies with time.

A note should be made here regarding the possible sources for error in this technique for generating temperature profiles. Of high concern is the limited number of data points taken across the specimen depth. Because of this, the curve fitting process was quite difficult, allowing much room for incorrect interpretation. Unfortunately the reasons for the lack of data points stem from the specimen design and the physical limitations of the recording equipment used. Generally however, it should be noted that most of the recorded data has been satisfactorily covered by the techniques described here.

Similar charts to that of figure 3.9 have been produced for other test conditions used during the experimental work. These are reproduced in Appendix C along with other experimental data including stress and stress intensity factor profiles.

## **Chapter 4:**

### **Experimental Results and Analysis – Crack Growth in a Flat Plate Specimen**

#### ***4.1 Introduction***

This chapter outlines the results obtained from the experimental stream of the investigation. It also provides an analysis and discussion of the results achieved with particular respect to primary load and environmental interactions during repeated thermal shock. Raw result data can be found in Appendix C, tables C.1 to C.8.

#### ***4.2 Description of Test Conditions***

Tests were set up to allow the analysis of the following factors on small crack initiation and crack growth rates using the test equipment and procedures outlined in Chapter 3.

1. Effect of primary loads
2. Effect of water chemistry
3. Effect of stress concentrators – notches & welds

In total, four sets of test data were obtained during operation of the test rig. The first set was used simply for verification that the rig was capable of initiating and growing thermal shock cracks and to allow for refinement of the specimen design. No data from this specimen was intended for use in later analysis. The remaining three of the test sets were designed so the overall data could be used for analysis of the above effects. The testing matrix given in table 4.1 identifies the key factors of each test set including the original verification tests.

Table 4.1: Experimental testing matrix.

Test #	Date conducted	Specimen #	Set temperature (°C)	Shock duration	Mechanical loads	Dissolved oxygen level
1	Jan-99 – Mar-99	1	300	Set	No	High
2	Jun-99 – Dec-99	2 & 3	330	Set	Yes	High
3	May-00 – Dec-00	4 & 5	330	Set	Yes	Low
4	Jan-01 – Apr-01	6 & 7	330	Variable	Yes	Low

The test material in all cases was pressure vessel standard steel, grade AS 1548-7-430R. The typical chemical composition for this steel is listed on table 4.2.

Table 4.2: Chemical composition specification (%), steel grade AS 1548-7-430R.

C	Mn	Mn	Si	P	S	Nb	Al	Ti
Max.	Min.	Max.	Max.	Max.	Max.	Max.	Max.	Max.
0.22	0.50	1.60	0.50	0.040	0.030	0.010	0.100	0.040

#### **4.2.1 Verification Test (Test #1)**

The verification test was conducted to determine whether the test rig was suitable for initiating and growing thermal shock cracks. In this test, one specimen prepared as per drawing BBK-9811 (see Appendix A) was exposed to repeated 10s thermal quenches from a set temperature of 300°C. A variety of end loads were enforced on the specimen during the 2000 cycles. In addition to proving the abilities of the test equipment it was also required to generate data on how, if necessary, the test specimen could be modified to allow the generation of more efficient and accurate results.

The results of this test were satisfactory, showing crack initiation and growth from a base of a number of hand cut notches in the specimens. Most importantly the verification test showed that the crack growth was heavily influenced by surface roughness. The

verification specimen was left in the as-machined condition, with milling cutter marks still visible on the surface. During testing and after initiation, crack growth was found to follow these machine marks, whose orientation was at an angle to the direction of primary stress. Figure 4.1 shows a surface replication along the length of one of the cracks with the influence of the machining marks clearly visible. Steps were consequently taken to improve the surface finish of specimens. However, the test does indicate the importance of surface roughness on growth direction, an effect found also in ex-plant specimens, as shown in Chapter 5, figure 5.21.

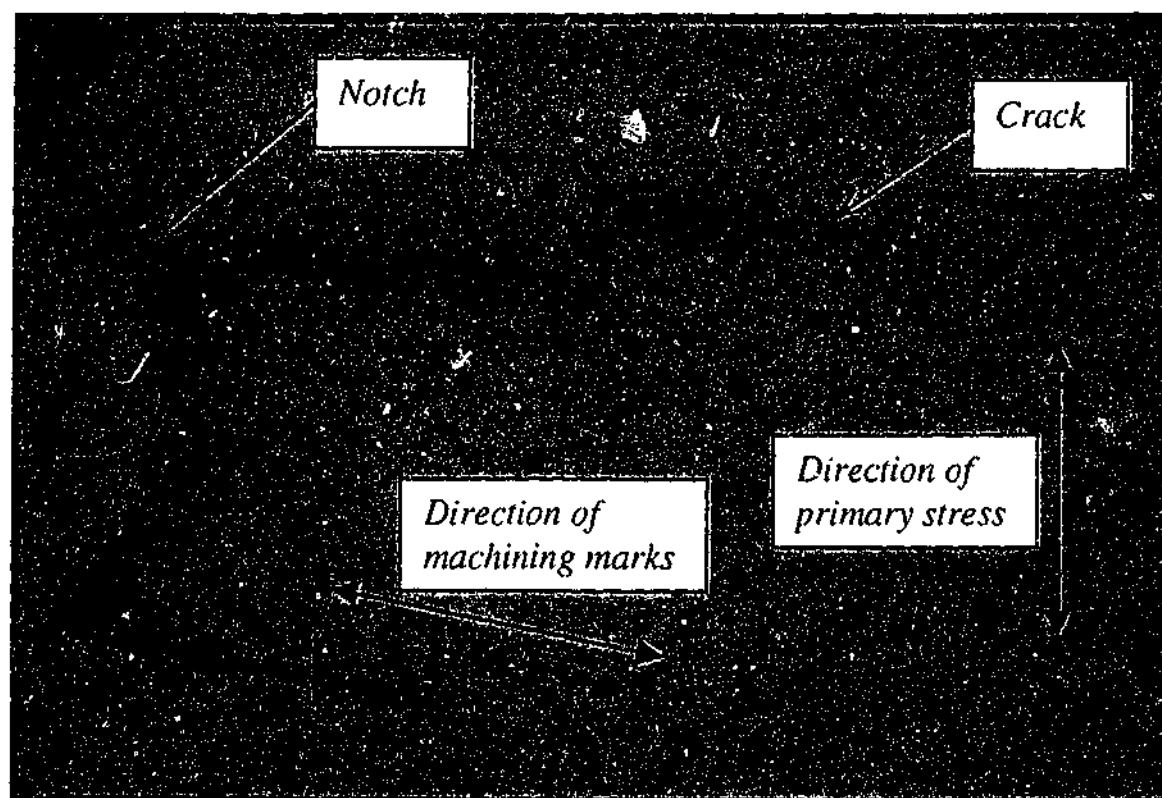


Fig. 4.1: Replication of verification specimen surface. Effect of machining marks on crack growth direction is clearly visible.

#### 4.2.2 Controlled Testing (Tests #2 - #4)

The first two sets of controlled tests (Tests #2 & 3) were designed to concentrate on identifying the effects of primary loads and water chemistry on crack initiation and growth during repeated thermal shock. The third and final set (Test #4) was designed to extend the applicability of the test results obtained in tests #2 and #3 by observing crack growth at a

number of different thermal shock severities and noting whether it could be described by the models developed for the previous tests.

Each test consisted of simultaneously trialing two mild steel specimens placed side by side, one subjected to a 90MPa uniform mechanical tensile stress and the other left unloaded. Each specimen was prepared with a combination of geometric crack starters (notches and welds) machined into the front (quenched) face. Test #2 used specimens of design shown in drawing BBK-9903 while the remaining tests used specimens as shown in drawing BBK-9905 (see Appendix A for drawing details).

The upper specimen temperature in all tests was limited to less than 400°C. This was enforced to remove the likelihood of the onset of creep. Water chemistry was monitored in the constant level supply tank. PH levels were held steady at around 8.0 while dissolved oxygen (D.O.) was varied between tests. Test #2 used fully oxygenated tap water with D.O. of around 8ppm. This water was vigorously pre-boiled in Tests #3 and #4, driving off excess oxygen and reducing the D.O. to around 2ppm.

Each thermal shock cycle consisted of a slow heat to the central specimen set temperature followed by a several second water quench. Cycle time was dependent on the severity of the shock. Due to the fact that the specimens were positioned vertically in the furnace, the thermal gradient present prevented a uniform temperature from being achieved along the whole specimen length. Rather the temperature from top to bottom of the specimen varied linearly by about 80°C.

After each period of 500 thermal shock cycles, the specimens were removed from the furnace and investigated for cracking at a low magnification (10 to 60x). A rough estimate of crack initiation lifetime was defined as when a full-width hairline crack was visible at the base of the notch. Extrapolations of the long crack growth data were used to confirm when initiation occurred (see Appendix C, figures C.1 to C.8). Any subsequent crack growth after initiation was measured on each side of the specimen, the average of these two values taken as the through depth. Using edge depths for crack growth analysis was justified by an

analysis of the fracture surface after testing was completed, see section 4.6.4 for further information.

It should be noted that interrupted testing for the purpose of crack measurement may be thought of as a possible source for error during environmentally assisted crack growth. In an example given by Torronen and Cullen (1982), three specimens of the same material were cycled simultaneously in an aggressive environment and subjected to interrupted testing. It was found that specimen to specimen differences introduce more reversals and accelerations in cyclic crack growth than external factors like test interruptions.

### **4.3 Test Results Summary**

In this section, a summary of raw result data from the controlled tests #2 - #4 is presented.

#### **4.3.1 Test #2; Specimens #2 & #3**

In this test, thermal shocks were conducted from a central specimen temperature of 330°C. The thermal shock duration was constant at 7s, giving a cycle time of around 15min (0.001 Hz). Dissolved oxygen levels in the quenching water were left at 8ppm. In total, 10,000 thermal shocks were applied to the specimens. A summary of the test results is given in table 4.3.

#### **4.3.2 Test #3; Specimens #4 & #5**

In this test, thermal shocks were conducted from a central specimen temperature of 330°C. The thermal shock duration was constant at 7s, giving a cycle time of around 15min (0.001 Hz). The dissolved oxygen level in the quenching water was controlled at 2ppm. In total, 10,500 thermal shocks were applied to the specimens. A summary of the test results is given in table 4.4.

Table 4.3: Summary of experimental results for test #2, specimens #2 & #3.

Specimen	Crack / Notch position	$\Delta T$ (°C) <sup>1</sup>	Geometric starter <sup>2</sup>	Mechanical load (MPa)	Cycles to crack initiation	Total cycles	Growth length <sup>3</sup> (mm)
#2	1	230	A	90	1,500	10,000	5.80
#2	2	220	C	90	*	10,000	0.0
#2	3	210	B	90	2,900	10,000	2.55
#2	4	195	D	90	3,000	10,000	0.40
#2	5	185	A	90	4,000	10,000	0.70
#3	1	230	A	0	1,600	10,000	1.90
#3	2	220	C	0	*	10,000	0.0
#3	3	210	B	0	3,000	10,000	0.65
#3	4	195	D	0	3,000	10,000	0.35
#3	5	185	A	0	4,500	10,000	0.35

- 1  $\Delta T$  = Approximate temperature difference between surface of specimen at completion of shock and surface temperature prior to shock.
- 2 Geometric starters as follows (see specimen drawings, Appendix A for further details):  
A = 3.5mm deep, 0.25mm radius notch, opening angle 45°  
B = 3.5mm deep, 0.1mm radius notch, opening angle 90°  
C = 6mm deep fillet weld with crown ground flush to specimen face  
D = 6mm deep fillet weld complete with crown
- 3 Measured from the base of the notch.
- \* No crack initiation observed.



Table 4.4: Summary of experimental results for test #3, specimens #4 & #5.

Specimen	Crack / Notch Position	$\Delta T$ (°C) <sup>1</sup>	Geometric starter <sup>2</sup>	Mechanical Load (MPa)	Cycles to crack initiation	Total cycles	Growth length <sup>3</sup> (mm)
#4	1	230	A	90	1,000	10,500	5.10
#4	2	220	A	90	1,700	10,500	2.9
#4	3	210	A	90	3,000	10,500	1.45
#4	4	195	A	90	-	10,500	0.0
#4	5	185	A	90	-	10,500	0.0
#5	1	230	A	0	1,200	10,500	3.20
#5	2	220	A	0	2,000	10,500	1.50
#5	3	210	A	0	-	10,500	0.65
#5	4	195	A	0	-	10,500	0.0
#5	5	185	A	0	-	10,500	0.0

1  $\Delta T$  = Approximate temperature difference between surface of specimen at completion of shock and surface temperature prior to shock.

2 Geometric starters as follows (see specimen drawings, Appendix A for further details):  
A = 3.5mm deep, 0.25mm radius notch, opening angle 45°

3 Measured from the base of the notch.

\* No crack initiation observed.

#### **4.3.3 Test #4: Specimens #6 & #7**

In this test, with the aim of observing the consequence of changing thermal shock length, thermal shocks were conducted from a central specimen temperature of 330°C in three stages. The first stage consisted of 3276 cycles with a shock length of 4s. With no crack initiation observed after this, the second stage was completed with 3039 cycles of 7s length. This resulted in the initiation of several cracks and was followed by stage 3 consisting of 2363 cycles of 5s length. Loading frequency was constant throughout all tests at around 0.001 Hz. Dissolved oxygen levels in the quenching water was controlled at 2ppm. A summary of the test results is given in table 4.5.

Table 4.5: Summary of experimental results for test #4, specimens #6 & #7.

Specimen	Crack / Notch Position	Geometric starter <sup>1</sup>	Mechanical Load (MPa)	Stage I <sup>2</sup>	Stage II <sup>3</sup>		Stage III <sup>4</sup>	
				Initiation	Initiation	Final Length (mm)	Initiation	Final Length (mm)
#6	1	A	90	No	Yes	1.35	-	1.90
#6	2	A	90	No	Yes	5	-	1.25
#6	3	A	90	No	Yes	5	-	0.95
#6	4	A	90	No	No	-	Yes	0.40
#6	5	A	90	No	No	-	No	-
#7	1	A	0	No	Yes	5	-	0.80
#7	2	A	0	No	Yes	5	-	5
#7	3	A	0	No	No	-	Yes	5
#7	4	A	0	No	No	-	No	-
#7	5	A	0	No	No	-	No	-

1 Geometric starters are as follows (see specimen drawings for further details):

A = 3.5mm deep, 0.25mm radius notch, opening angle 45°.

2 Stage I: 3276 cycles, 4s shocks.

3 Stage II: 3039 cycles, 7s shocks.

4 Stage III: 2363 cycles, 5s shocks.

5 No depth measurement possible.

#### 4.4 Test Data

In this section, data relating to the condition of the specimens during testing is presented. In particular, the temperature, elastic stress and stress intensity factor profiles generated during the thermal shock transients are presented for each notch position in accordance with the methods given in Chapter 3, section 3.4.

##### 4.4.1 Temperature Data

As reported in Chapter 3, thermocouples were used to determine temperature profiles across the specimen depth during the thermal shock transients. The cross section temperature profiles for a number of different time length shocks carried out from the same set conditions as for tests #2 - #4 for each individual notch position are reproduced in Appendix C as figures C.9 - C.13. A typical profile obtained during a thermal shock at crack position 1 is reproduced below as figure 4.2.

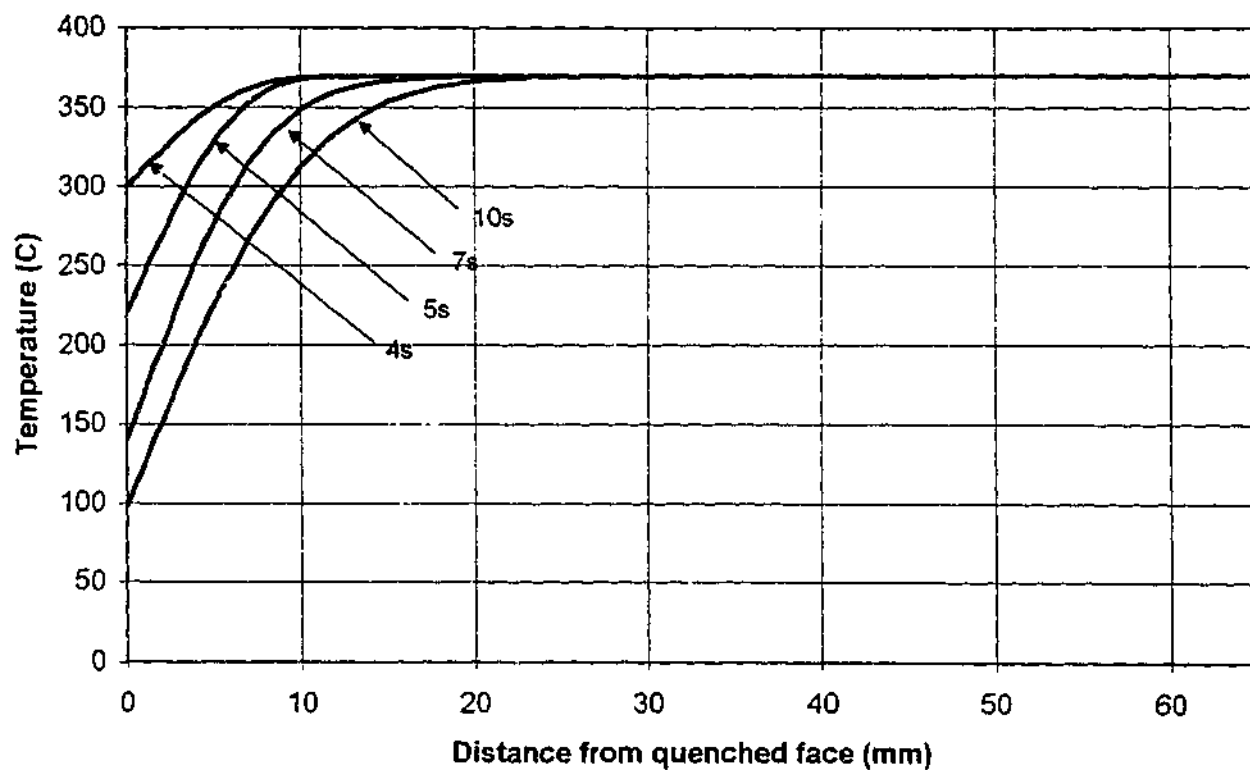


Figure 4.2: Typical temperature profiles for thermal shocks of 4s, 5s, 7s and 10s at crack position 1 from central specimen set temperature of 330°C.

#### 4.4.2 Stress Analysis

The temperature profiles shown in Appendix C were used in combination with equation [3.12] to determine the elastic stress profiles developed across the specimens at each notch position. Results for these profiles for a number of shock lengths are reproduced in Appendix C as figures C.14 - C.18. A typical profile obtained during a thermal shock at crack position 1 is reproduced below as figure 4.3

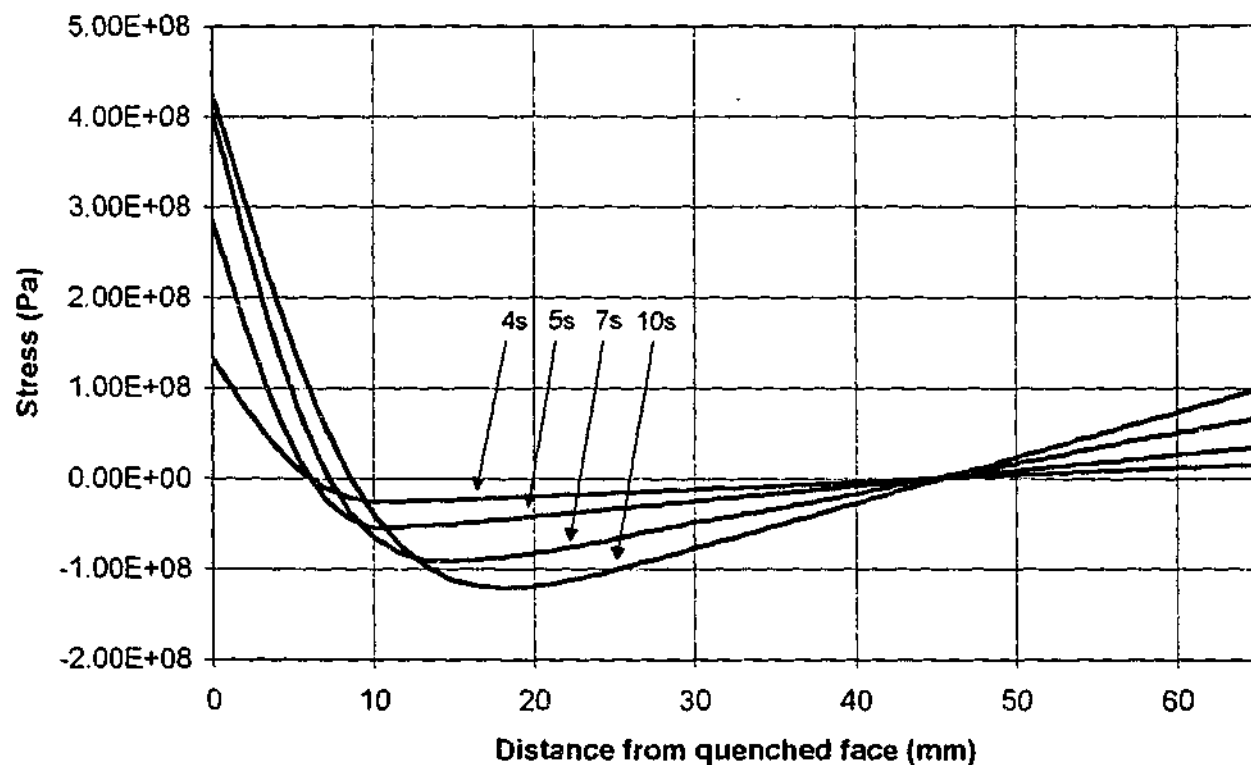


Figure 4.3: Typical elastic stress profiles for thermal shocks of 4s, 5s, 7s and 10s at crack position 1 from central specimen set temperature of 330°C.

#### 4.4.3 Stress Intensity Factor Analysis

Using the methods outlined in section 3.4.3, the elastic stress distributions shown in Appendix C were used to generate stress intensity factor profiles for the growth of a crack from each notch position. These profiles are also shown in Appendix C as figures C.19 - C.28. Typical profiles obtained during a thermal shock at crack position 1 are reproduced on the next page as figures 4.4 and 4.5.

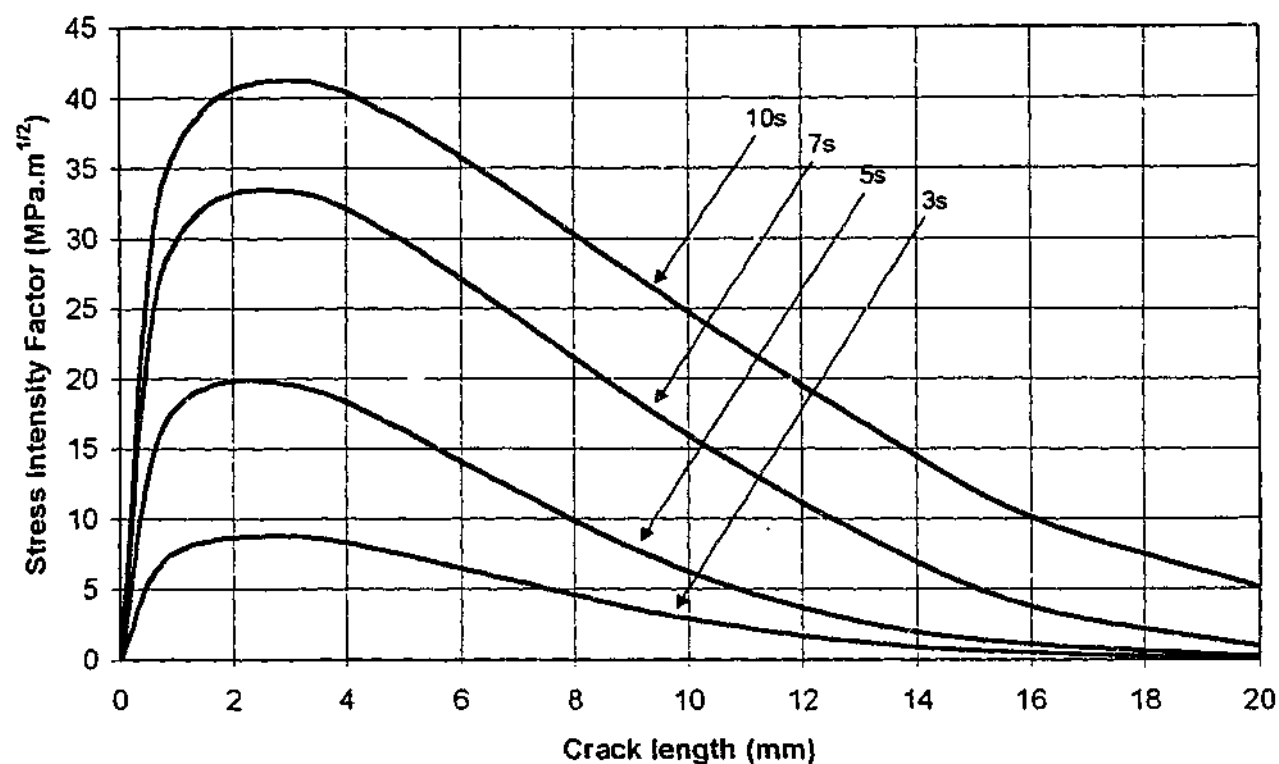


Figure 4.4: Cyclic change in stress intensity factor ( $\Delta K_I$ ) as a function of crack depth for thermal shocks of 4s, 5s, 7s and 10s at crack position 1 from central specimen set temperature of 330°C. No primary mechanical load.

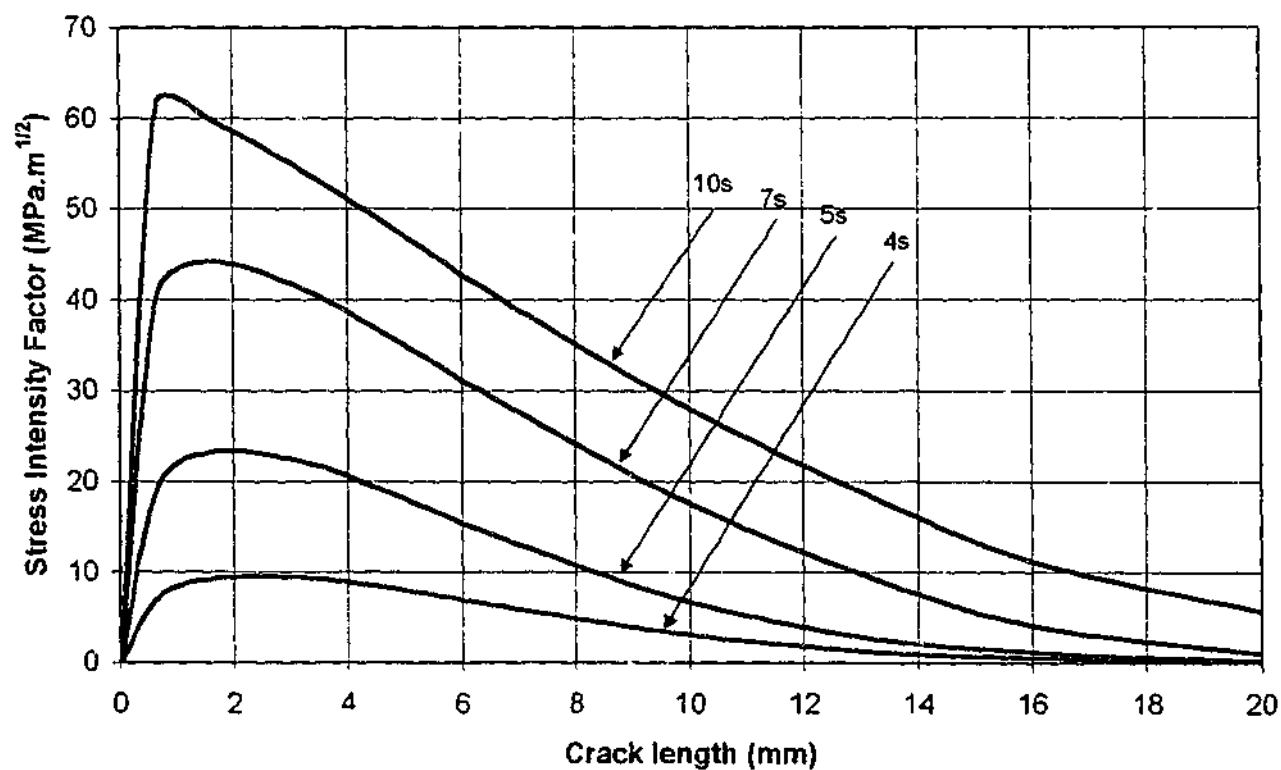


Figure 4.5: Cyclic change in stress intensity factor ( $\Delta K_I$ ) as a function of crack depth for thermal shocks of 4s, 5s, 7s and 10s at crack position 1 from central specimen set temperature of 330°C. 90MPa primary mechanical load included.

#### 4.4.4 Notch Root Stress Amplitude

For use in calculating crack initiation times and generation of  $S-N$  diagrams it is necessary to define the amplitude of stresses generated at the notch root for each notch position. The methods used for determining these root stresses was outlined in Chapter 3, section 3.4.1. The variables required for solving the cyclic stress amplitude are summarised in table 4.6 along with stress amplitude results for a number of assumptions defined in the table notes. Data from cyclic stress strain curves generated for pressure vessel steel of similar standard to that used in testing have been taken from Prater and Coffin (1983). Neubers constant  $\sqrt{\rho}$  for steel of ultimate strength of around 430MPa is taken from Bannantine et al (1990) as 0.5 $\sqrt{\text{mm}}$ .

For use in table 4.6:

$P$  = Primary steady state mechanical loading.

$\Delta K_{max}$  = Maximum change in stress intensity factor developed at notch root assuming sharp notch approximation.

$S_a^1$  = Elastic stress amplitude at notch root using theoretical sharp notch approximation [3.2].

$S_n$  = Nominal stress amplitude with no notch present.

$k_t$  = Theoretical stress concentration factor.

$k_f$  = Fatigue notch factor.

$S_a^2$  = Elastic stress amplitude using sharp notch approximation and notch sensitivity analysis, equation [3.5].

$S_a^3$  = Elastic stress amplitude using sharp notch approximation and notch sensitivity analysis (equation [3.5]), with  $k_f < 5.0$ .

$S_a'^1$  = Pseudostress amplitude using sharp notch approximation, notch sensitivity analysis and Neuber notch pseudostress analysis, equation [3.10].

$S_a'^2$  = Pseudostress amplitude using sharp notch approximation, notch sensitivity analysis and Neuber notch pseudostress analysis (equation [3.10]), with  $k_f < 5.0$ .

Table 4.6: Notch root stresses developed during 7s thermal shock from a central specimen temperature of 330°C.

Notch Position	Notch Radius (mm)	$P$ (MPa)	$\Delta K_{max}$ (MPa $\sqrt{m}$ )	$S_a^1$ (MPa)	$S_n$ (MPa)	$k_t$	$k_f$	$S_a^2$ (MPa)	$S_a^3$ (MPa)	$S_a'^1$ (MPa)	$S_a'^2$ (MPa)
1	0.25	0	32.7	1167	122.7	9.5	5.2	644	613	1005	941
1	0.25	90	40.2	1434	122.7	12	6.3	779	613	1378	941
2	0.25	0	30.1	1074	119.4	9.0	5.0	597	597	887	887
2	0.25	90	36.4	1299	119.4	11	5.9	704	597	1163	887
3	0.1	0	29.1	1642	116.5	14	6.1	711	582	1183	850
3	0.1	90	35.0	1975	116.5	17	7.2	839	582	1554	850
3	0.25	0	29.1	1038	116.5	8.9	4.9	577	577	838	838
3	0.25	90	35.0	1248	116.5	11	5.8	682	582	1104	850
4	0.25	0	26.2	935	108.3	8.6	4.8	520	520	706	706
4	0.25	90	29.6	1056	108.3	9.8	5.4	585	541	857	754
5	0.25	0	24.3	867	102.3	8.5	4.7	481	481	621	621
5	0.25	90	27.4	978	102.3	9.6	5.3	542	511	756	686

## **4.5 Analysis of Raw Test Data**

Analysis and discussion of each set of raw test data given in section 4.4 is now made in turn.

### **4.5.1 Temperature Data**

Points of interest to be taken from the temperature data summarised in Appendix C, figures C.9 to C.13, are described individually below.

1. Each notch position has an individual series of profiles. This is because of the vertical arrangement of the specimen and the manifold. For example, short duration quenches are less severe at the top of the specimen because delays in the time taken for water to reach the specimen. As outlined in Chapter 3, this (and other complicating factors) makes it impossible to model the specimen with one temperature function. Rather each notch must be analysed individually at discrete time intervals using the developed temperature profiles.
2. Typical maximum temperatures for each notch position prior to quenching for a central temperature of 330°C are as follows:
  - Notch position #1 ~ 370°C,
  - Notch position #2 ~ 350°C,
  - Notch position #3 ~ 330°C (centre of specimen),
  - Notch position #4 ~ 310°C and,
  - Notch position #5 ~ 285°C.

This is also due to the vertical positioning of the specimen in the furnace.

3. Specimen surface temperatures vary as functions of time during each quench. This makes it difficult to determine a single  $\Delta T$  value that is representative of the quench condition for each notch position. As mentioned in the notes for tables 4.3 and 4.4, the best alternative for change in temperature ( $\Delta T$ ) characterisation is the difference in surface temperature before and after quenching.



#### **4.5.2 Stress Data**

Points of interest to be taken from the elastic stress profile data summarised in Appendix C, figures C.14 to C.18, are described individually below.

1. As the elastic stress profiles are calculated directly from the temperature data, it follows that each notch position has an individual stress profile series. This is particularly noticeable for notch position 1 where maximum surface stresses take much longer to develop than for other positions.
2. In all cases, stress profiles are highly non-linear, peaking at the shocked surface and reducing in magnitude as a function of distance from the surface.
3. Stresses above yield ( $\sim 300\text{MPa}$ ) are observed only for long shocks ( $>5\text{s}$ ) at notch positions 1 and 2. Even in these cases, profiles drop quickly away and beyond the region of notch influence (i.e.  $>4\text{mm}$ ), elastic stresses dominate. This suggests that for longer cracks (ie  $>4\text{mm}$ ), the stress intensity factor should be sufficient to characterise the stress profile at the crack tip.

#### **4.5.3 Stress Intensity Factor Data**

##### **4.5.3.1 General observations**

The stress intensity factor ( $\Delta K_I$ ) profiles (Appendix C, figures C.19 to C.28) developed from the elastic stress data are typical of thermal shock conditions. They show a rapid increase for a crack of short length followed by a plateau and a steady decline as crack length increases. Application of the  $\Delta K_I$  data for the description of small cracks in the region of plastic strain influence is questionable. Therefore the more interesting part of the profile is the plateau and the steady decrease. Assuming a Paris law type crack growth relationship, this type of profile predicts a general decrease in the crack growth rate as the crack becomes longer, leading to possible crack arrest.

In general, the stress intensity factor profiles exhibit a decrease in overall magnitude moving from notch position 1 to 5. This again is due to the vertical temperature gradient in the furnace. The effect of adding a primary mechanical load of 90MPa is also seen to increase the profiles, particularly for short cracks at notches 1 and 2 exposed to a long duration quenches. This is due to the plastic zone correction allowed for in the stress intensity factor correlations as discussed in Chapter 3, section 3.4.3.

#### 4.5.3.2 *R*-ratio

Figures C.19 to C.28 of Appendix C represent the change in stress intensity factor ( $\Delta K_I$ ) that the specimen is subject to during a thermal shock. In the case of the presence of a steady state mechanical load, they do not represent the maximum stress intensity factor generated ( $K_{max}$ ). To calculate this, it is necessary to add the stress intensity factor generated by the mechanical load alone. Figure 4.2 shows the stress intensity factor profile for a mechanical load of 90MPa. Superimposed on the figure are typical thermal shock stress intensity factor profiles (in this case, a 7s quench at notch position 1, taken from figures 4.4 and 4.5) for the case when the mechanical load is present and when it is not. This allows the calculation of  $K_{max}$ ,  $K_{min}$  and  $\Delta K$  values for both the cases when mechanical load is added and it is not.

Figure 4.6 shows that when a primary load is present in combination with a cycling thermal shock load, the *R*-ratio ( $K_{min}/K_{max}$ ) becomes a function of the crack length. Calculating the *R*-ratio from the above figure gives the result shown as figure 4.7. In the case of no mechanical loading, the *R*-ratio is always 0.

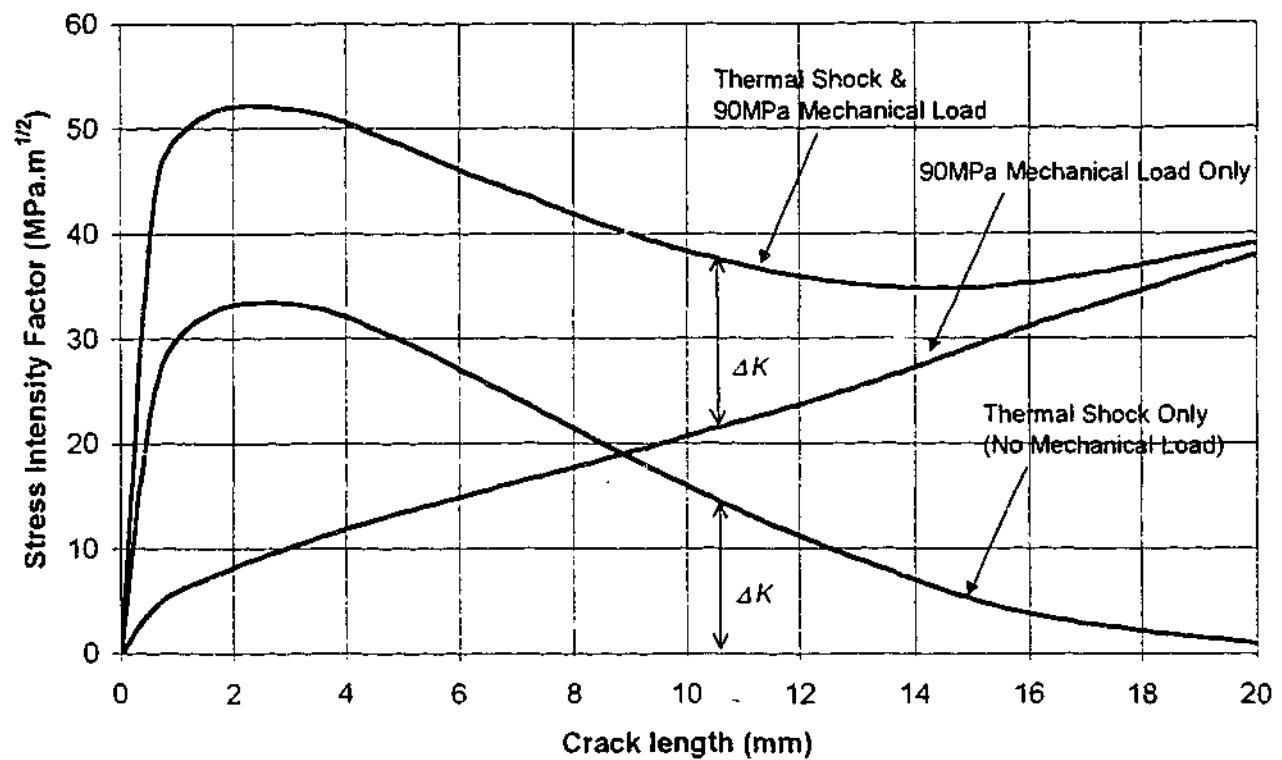


Figure 4.6: Stress intensity factor profiles for 7s thermal shock at notch position 1 from central specimen temperature of 330°C showing effects of adding 90MPa mechanical load.

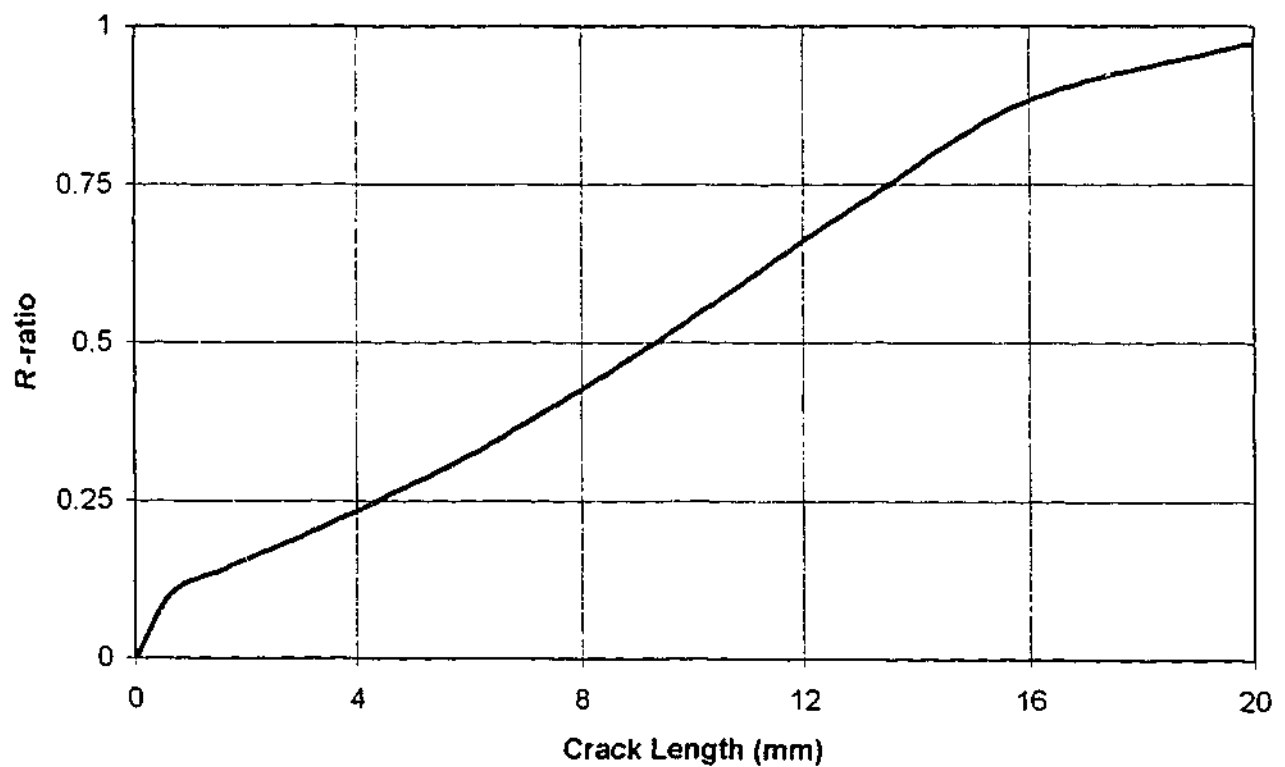


Figure 4.7: R-ratio as a function of crack length for a 7s quench with 90MPa mechanical load, at notch position 1 from a central specimen temperature of 330°C.

Assuming that an increase in the  $R$ -ratio results in an increase in crack growth (see Chapter 2, section 2.5.1), then a relative increase in crack growth rate with an increase in crack depth may be expected for the specimens with primary loading. How this affects the predicted slow down in crack growth as expected from the  $\Delta K_I$  profiles is discussed during the crack growth results analysis of section 4.6.2.

#### 4.5.3.3 History effects

As discussed in Chapter 2, section 2.4.4, the applicability of a Paris type growth law to predict crack growth is dependent on crack growth history. In all the testing conducted in this thesis, long crack growth is occurring in a decreasing  $\Delta K$  field (see figures C.19 – C.28, Appendix C). If the rate of decrease is large enough, plastic zone interference occurs and premature crack arrest can occur. As reported in Chapter 2, equation [2.8], a limit below which this effect is found to occur has been suggested (ASTM E 647-95a, 1995):

$$C = \frac{1}{\Delta K} \frac{d\Delta K}{da} > -0.08\text{mm}^{-1} \quad [2.8]$$

This figure is not an absolute limit. An absence history effects at values of  $C$  less than this have been reported during the testing of several steel alloys in laboratory air over a range of  $R$  values (ASTM E 647-95a, 1995).

Figure 4.8 shows  $C$  calculated as a function of crack length using a number of the  $\Delta K_I$  profiles for 7 second quenches (as used in tests #2 and #3). For clarity, the results for notch positions #2 and #4 have been left of the chart. In all cases,  $C$  decreases with increases in crack length. Thus as cracks increase in length, the chance of history effects becoming more important increases. This will have to be taken into consideration when analysis of the crack growth is made.

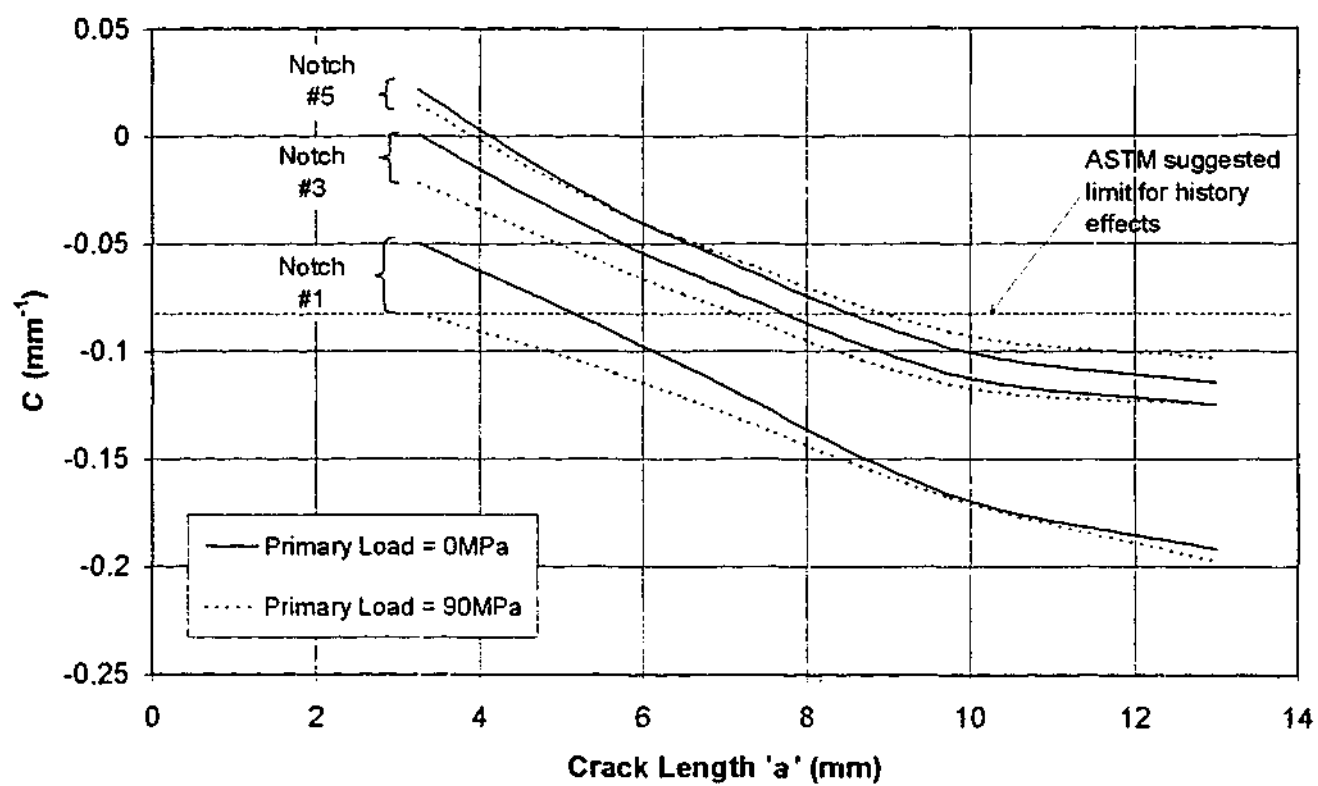


Figure 4.8: Rate of change of stress intensity factor ( $C$ ) for the range of test cases.

## 4.6 Interpretation of Test Results

### 4.6.1 Crack Initiation

#### 4.6.1.1 General observations – notched specimens

A portion of table 4.6 is reproduced below, along with crack initiation times observed during tests #2 and #3. This provides the raw data required for the crack initiation analysis.

Table 4.7: Notch root stresses developed during repeated thermal shocks and number of cycles to crack initiation.

Notch Position	Notch Radius (mm)	P (MPa)	$S_a^2$ (MPa)	$S_a^3$ (MPa)	$S_a'^1$ (MPa)	$S_a'^2$ (MPa)	$N_i$ (D.O. = 8ppm)	$N_i$ (D.O. = 2ppm)
1	0.25	0	644	613	1005	941	1600	1200
	0.25	90	779	613	1378	941	1500	1000
2	0.25	0	597	597	887	887	*	2000
	0.25	90	704	597	1163	887	*	1700
3	0.1	0	711	582	1183	850	3000	*
	0.1	90	839	582	1554	850	2900	*
3	0.25	0	577	577	838	838	*	3500 <sup>#</sup>
	0.25	90	682	582	1104	850	*	3000
4	0.25	0	520	520	706	706	*	5000 <sup>#</sup>
	0.25	90	585	541	857	754	*	4000 <sup>#</sup>
5	0.25	0	481	481	621	621	4500 <sup>#</sup>	6500 <sup>#</sup>
	0.25	90	542	511	756	686	4000 <sup>#</sup>	4500 <sup>#</sup>

\* No crack initiation observed.

# Crack initiation readings from visual inspections only, not confirmed by analysis of long crack growth data (due to lack of data thereof). See Appendix C, figures C.1 to C.8 for long crack growth analysis of other cracks.

Several observations can be made directly from table 4.7.

1. Changing of dissolved oxygen levels from 8ppm to 2ppm has little or no effect on crack initiation times. This indicates that environmental interactions that are dependent on dissolved oxygen are of reduced importance to the initiation process.
2. Application of a 90MPa primary load has little or no effect on crack initiation times. This confirms the observations outlined in Chapter 2, which indicate that at stress amplitudes greater than yield, primary loads have little effect on crack initiation times.

#### 4.6.1.2 The use of $S-N$ curves for predicting crack initiation

Figures 4.9 to 4.12 represent the data that is presented in table 4.7 as separate  $S-N$  curves with ASME Boiler and Pressure Vessel Code, Section VIII, Division 2 (1998) fatigue crack initiation data included. Note that this is the actual ASME *fatigue* data as opposed to *design* data which is published in the code and has a built in conservatism of 2 times on stress and 20 times on lifetime, whichever is more conservative. Note also that the ASME curve, suitable for carbon and low alloy steels, is only applicable at temperatures below 370°C and does not take into account the effects of "unusually corrosive" environments.

As can be seen from the comparisons shown in figures 4.9 to 4.12, the accuracy of the ASME fatigue data curves to predict crack initiation during thermal shock depends heavily on the method chosen to calculate the stress amplitude at the notch during the transient. The use of an elastic sharp notch approximation (figures 4.9 and 4.10) with and without a limit on the notch fatigue factor ( $k_f$ ) shows non-conservative results. On the other hand, a Neuber notch pseudostress approximation gives a conservative comparison when no limit on  $k_f$  is made (figure 4.11). However, a high level of correlation is obtained when a limit of 5.0 for  $k_f$  is enforced (figure 4.12).

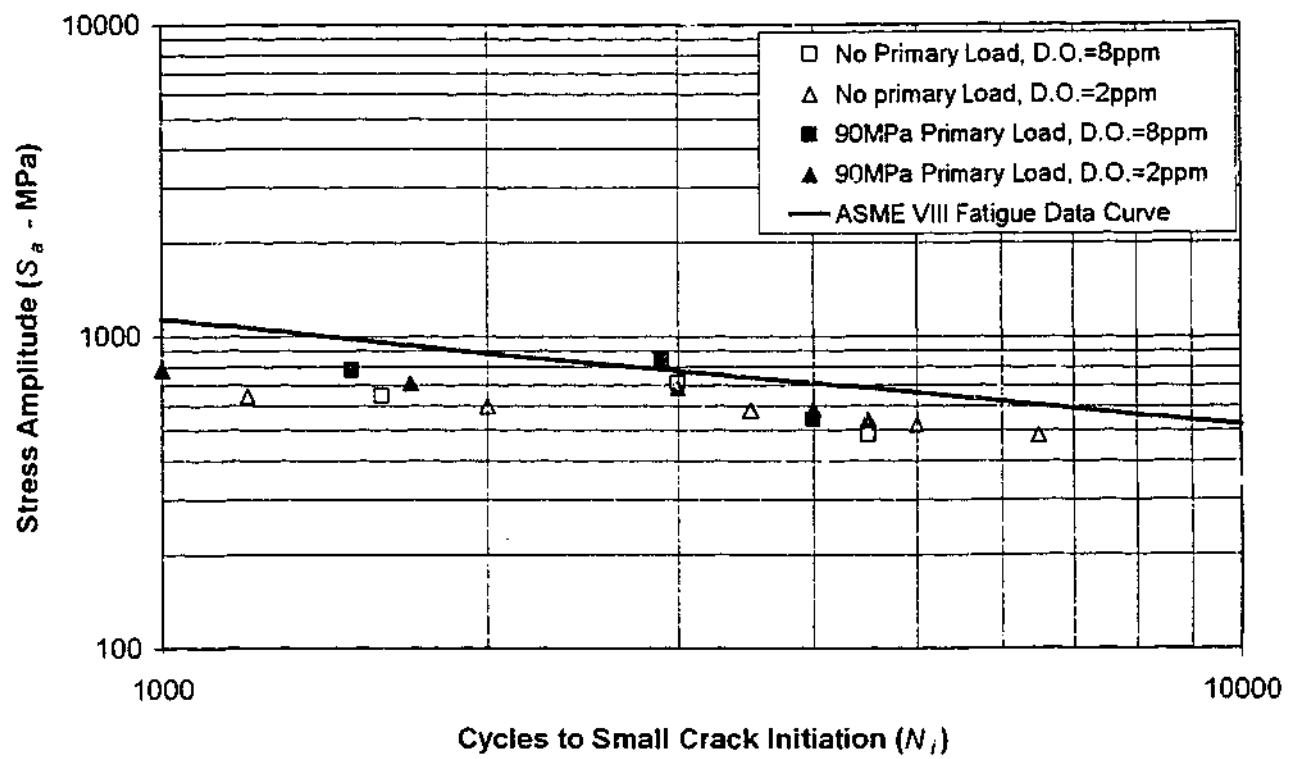


Figure 4.9: Number of cycles to crack initiation versus elastic notch stress amplitude ( $S_a^2$ ) for a sharp notch approximation with notch sensitivity analysis (Chapter 3, section 3.4.1.3).

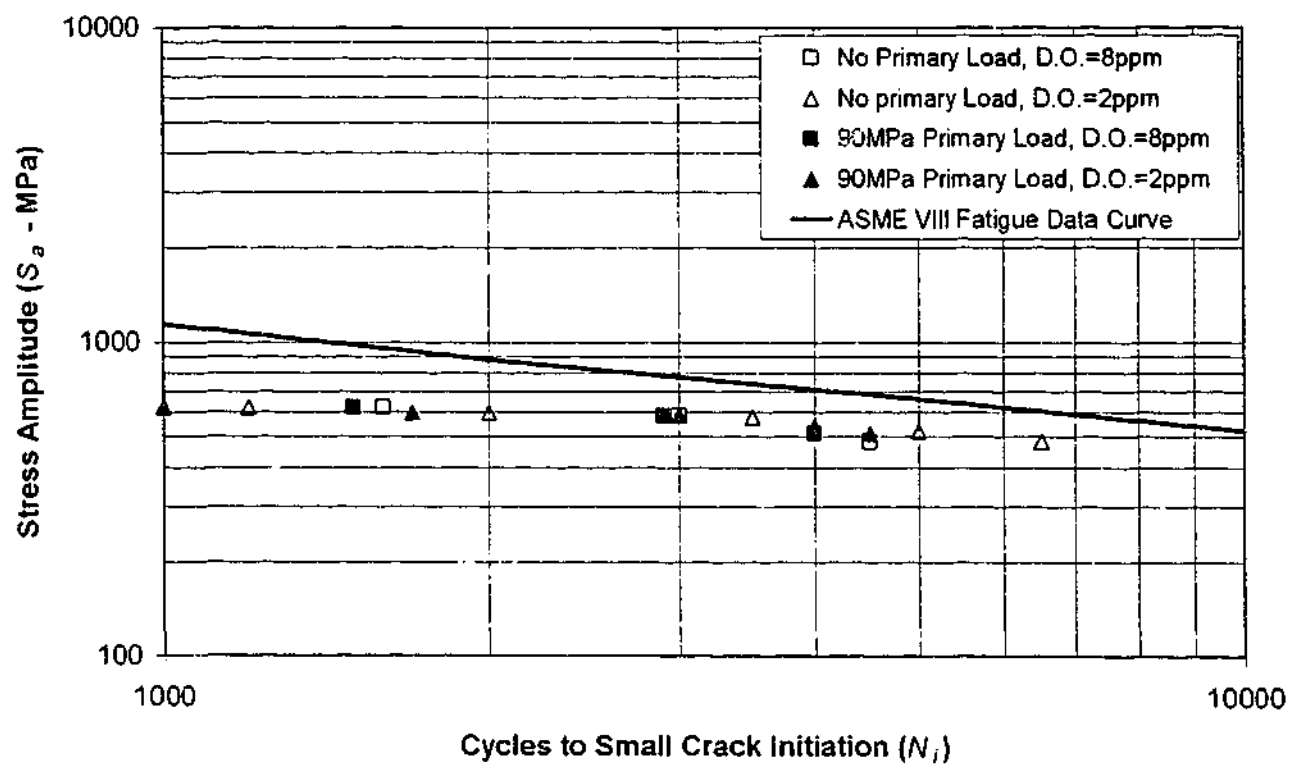


Figure 4.10: Number of cycles to crack initiation versus elastic notch stress amplitude ( $S_a^3$ ) for a sharp notch approximation with notch sensitivity analysis,  $k_f$  limited to 5.0 (Chapter 3, section 3.4.1.3).



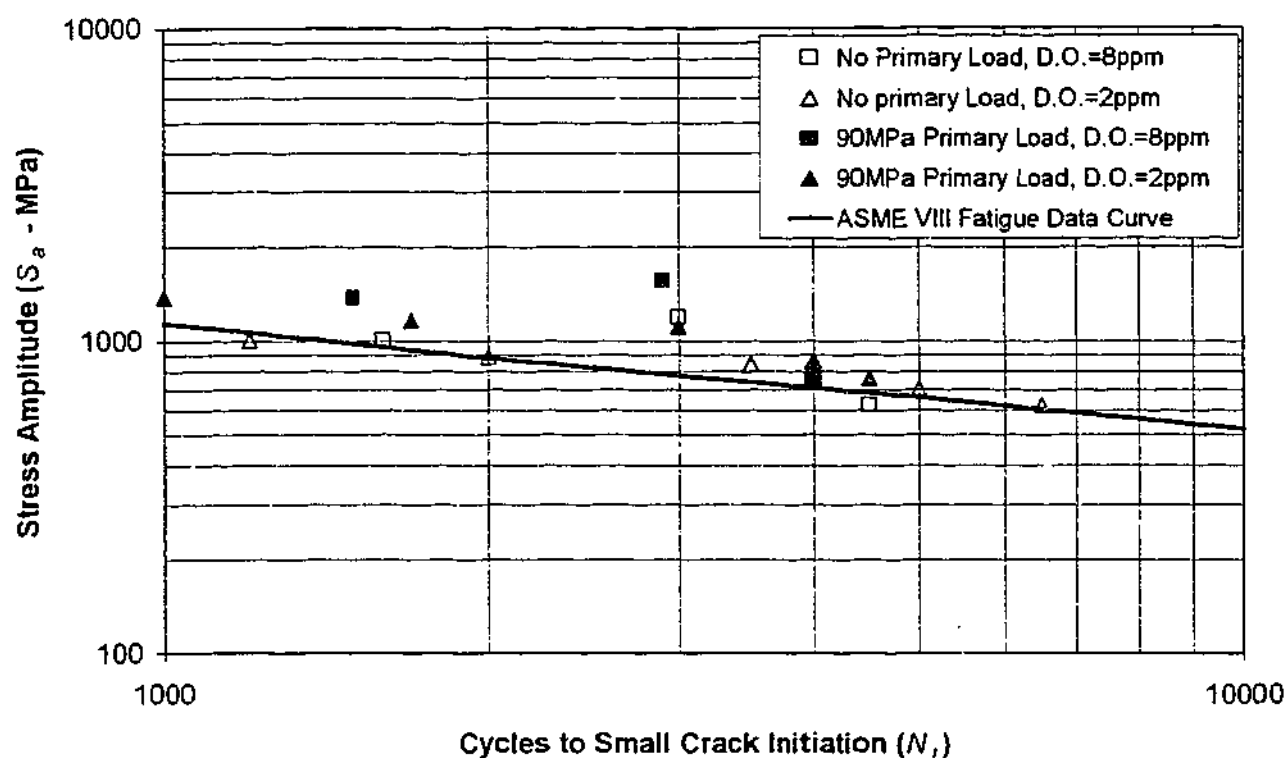


Figure 4.11: Number of cycles to crack initiation versus Neuber notch pseudostress amplitude ( $S'_a{}^1$ ) for a sharp notch approximation with notch sensitivity analysis (Chapter 3, section 3.4.1.4).

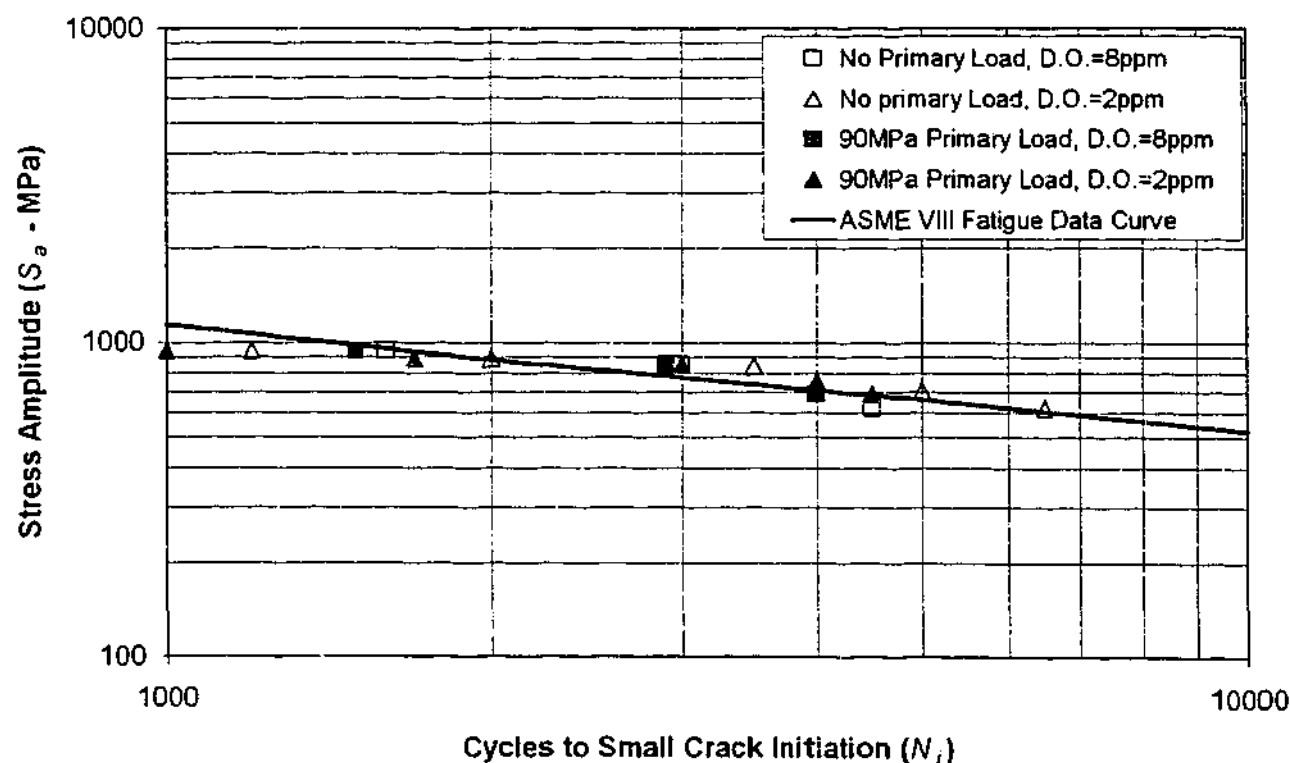


Figure 4.12: Number of cycles to crack initiation versus Neuber notch pseudostress amplitude ( $S'_a{}^2$ ) for a sharp notch approximation with notch sensitivity analysis,  $k_f$  limited to 5.0 (Chapter 3, section 3.4.1.4).

From these observations it appears that, contrary to the instructions of the ASME code, an elastic stress analysis should not be used in conjunction with the ASME Section VIII fatigue data to determine crack initiation lifetimes in notched specimens exposed to RTS. To do so could lead to non-conservative estimates. Instead, a Neuber notch pseudostress analysis with a limit on the notch fatigue factor  $k_f$  should be performed. If however, a pure elastic analysis is necessary (for example, due to lack of material data), a different approach to lifetime estimation may be required. As the narrow spread of experimental data on figure 4.10 seems to indicate, a form of limit analysis may be more appropriate than the linear  $S-N$  curve. For example, elastic stress amplitudes larger 500MPa could be seen to result in rapid crack initiation (<10,000 cycles) while smaller amplitudes will require a much longer time.

Regardless of the method used to estimate stress amplitudes, any attempt to use the ASME Section VIII curves to predict crack initiation should be approached with care. This is because the ASME fatigue curves are based on uniaxial strain controlled testing of small cylindrical specimens. Failure in one of these specimens is defined as when complete fracture occurs. It is then assumed that the failure of these small specimens is equivalent to the initiation of a small crack in a larger structure.

Referring to ASTM E 8M – 96 (1996), the standard small cylindrical specimen size for tensile tests is 12.5mm in diameter. Depending on the stress amplitude during fatigue testing and the presence of mean stresses, a small amount of crack growth will occur before specimen failure, probably in the order of a few millimetres. This means however that no exact “initiation” size can be known to allow comparison with experimental data from large specimens. In the experimental work of this thesis, crack initiation is defined as when a full thickness edge crack is developed. Crack depth at this stage is also not clear. Therefore, any correlation between the two methods must remain qualitative. Namely, the Neuber notch pseudostress developed at a notched carbon steel specimen exposed to RTS can be related to number of cycles to initiation in a linear manner similar to the ASME fatigue data curve. Reciprocally this means the ASME fatigue data curve can be used as a guideline for

determining approximate times to develop small ( $<1\text{mm}$ ) deep cracks in carbon steel exposed to RTS.

#### 4.6.1.3 Placing limits on $k_f$ and the "worst case notch" approach

The placement of a constraint on the maximum value of  $k_f$  implies that there is a limit to the influence a stress raiser may have on time to crack initiation. That is, after increasing the severity of a stress concentration beyond a certain point, no further acceleration in crack initiation is observed. Prater and Coffin (1987) approached this observation by suggesting that there is such a thing as a "worst case notch", the presence of which has the greatest effect on crack initiation times. Increasing the severity of a notch beyond this value (say by decreasing the notch radius) has no further effect on crack initiation time. In their study of carbon steel in a high temperature water environment, Prater and Coffin calculated this worst case notch to have a radius of  $0.165\text{mm}$ .

Theoretically even machining marks, if deep enough, can also behave as a worst case notch. For this reason, the work by Prater and Coffin proposes a conservative approach that assumes all notches behave as the worst case. This approach is justified by assuming that machining marks are likely to be present in any notch.

The solution proposed by Prater and Coffin has some relevance to the results of this thesis. In fact, looking at the calculated values for  $k_f$  in table 4.6, the act of assuming a limit of 5.0 has affected all but three of the notches. If it is assumed that these three notches also have a  $k_f$  value of 5.0, and a Neuber notch pseudostress analysis is applied, the  $S-N$  curve as shown in figure 4.13 is developed.

The difference between figures 4.12 and 4.13 is minimal, yet the simplification of assuming a uniform  $k_f$  value of 5.0 is far reaching. Assuming that all notches behave the same, it is no longer required to determine the stress intensity factor as per the sharp notch approximation. It is similarly unnecessary to perform a notch sensitivity analysis. Further tests on less severe notches are required however to determine just how widely applicable this simplification may be.

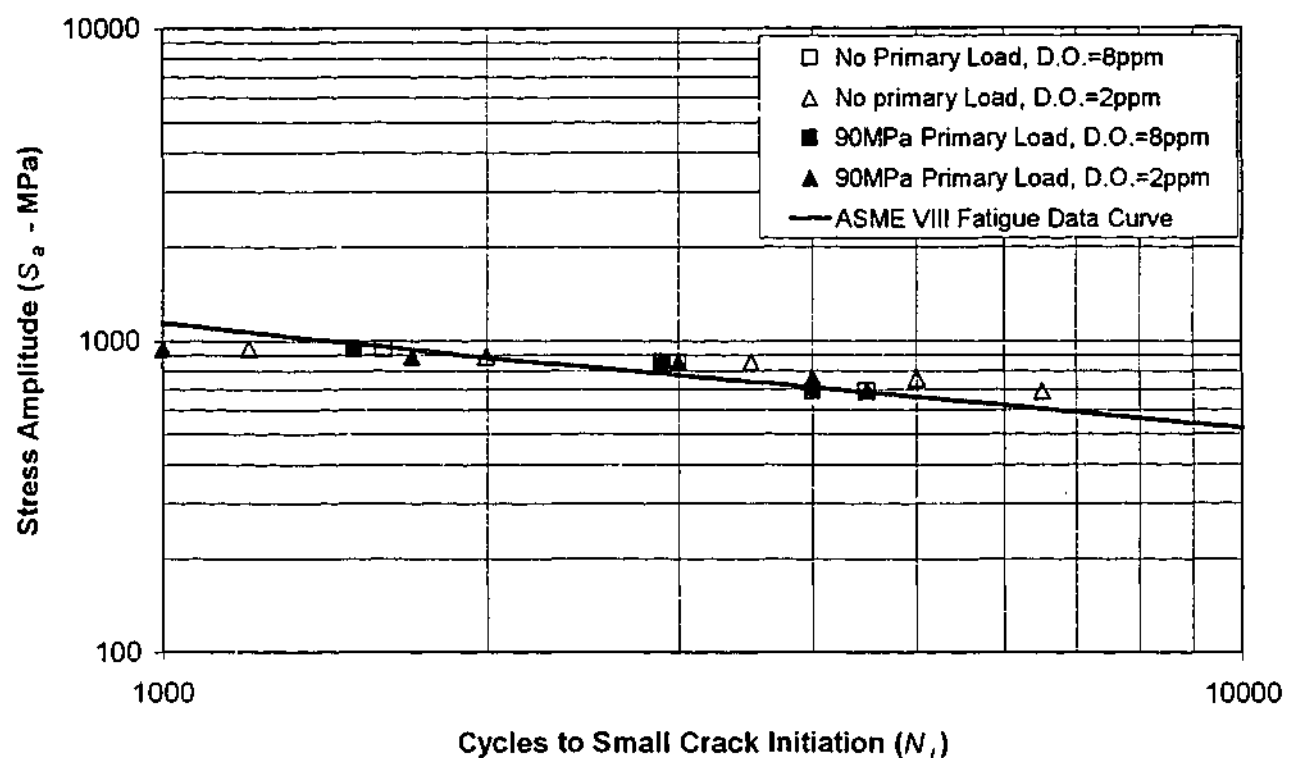


Figure 4.13: Crack initiation data using a Neuber notch pseudostress approach and assuming a uniform notch fatigue factor ( $k_f$ ) of 5.0 for all cases.

#### 4.6.1.4 Effect of welds on crack initiation

A common site for crack initiation in operating equipment exposed to cyclic loading is at welds. Numerous reasons can be cited for this, many of which are attributed to incorrect welding procedures. Assuming that correct procedures are followed however, and the weld itself is of good quality, it can still act as a stress raiser due to its geometry. To analyse the effects of weld geometry during RTS a number of welds were placed on specimens #2 and #3 in test #1. The specimen drawing in Appendix A (BBK-9903) shows how the welds were fashioned for the analysis. In total, four 10mm deep V welds were placed on the specimens at notch positions 2 and 4. The welds at position 2 had their crowns removed and were machined flat with the specimen face. The welds at position 4 were left in the as-welded condition.

As described in table 4.3, the welds with crowns removed displayed no crack initiation after 10,000 thermal shock cycles of around 220°C. On the other hand, the welds with crowns remaining quickly developed surface cracks after 3,000 cycles of 195°C. Figure 4.14

shows the typical cracking observed at the weld crown/base metal interface, which seems to confirm that the weld geometry acts as a stress raiser.

In accordance with the analysis of section 4.6.1.3, the weld crown could quite likely be thought of as a "worst case notch" and a fatigue notch factor of 5.0 applied. Assuming the surface stresses shown in Appendix C, figure C.17 apply, an elastic stress amplitude of around 750MPa can be calculated. Performing a Neuber elastic-plastic analysis gives a pseudostress of 1290MPa, which according to the  $S-N$  curve of figure 4.13 equates to a crack initiation time in the order of 1,000 cycles. This is a slightly conservative analysis, with actual estimates for crack initiation, as mentioned above, at 3,000 cycles.

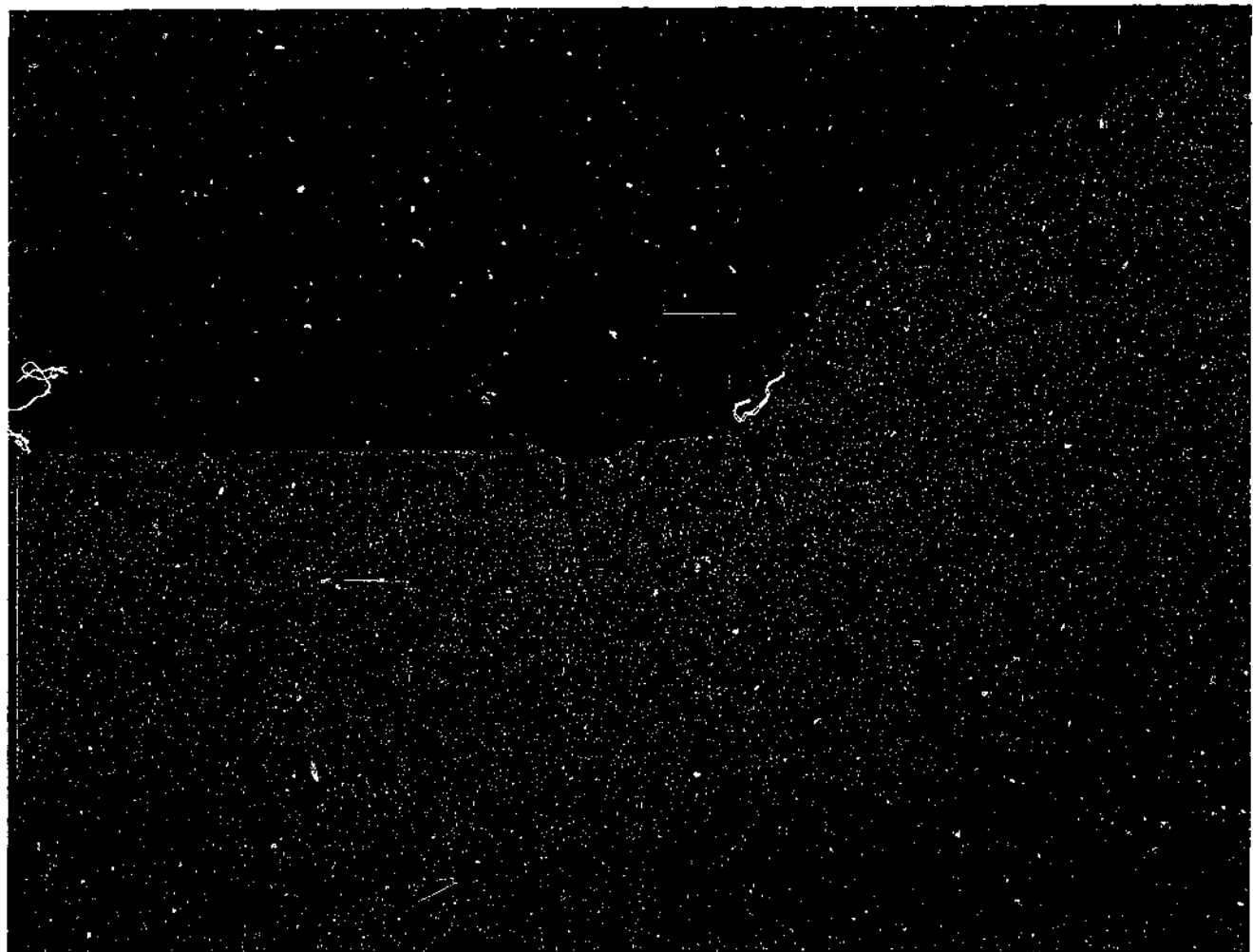


Figure 4.14: Crack initiation at the weld crown/base metal interface for specimen #2.

Working backward from the observed crack initiation times, an estimated notch fatigue factor can be developed. Assuming a pseudostress amplitude of 700MPa (to get an initiation time of 3000 cycles) and a nominal surface stress amplitude of 150MPa equates to a notch fatigue factor ( $k_f$ ) of 3.5. This observation signifies that the universal assumption of a worst case notch for all notch-like defects may in fact to be too conservative. Irrespective it is clear that the presence of the weld crown has significantly accelerated crack initiation.

#### 4.6.2 Crack Growth

Crack growth data from tests #2 and #3, plotted as crack length versus number of cycles is presented as figure 4.15. The data is as recorded during the tests and has not been adjusted in any way. Crack lengths include notch depths. Raw test data is contained in Appendix C. Note that the general trend of this data is towards crack growth deceleration, regardless of testing conditions.

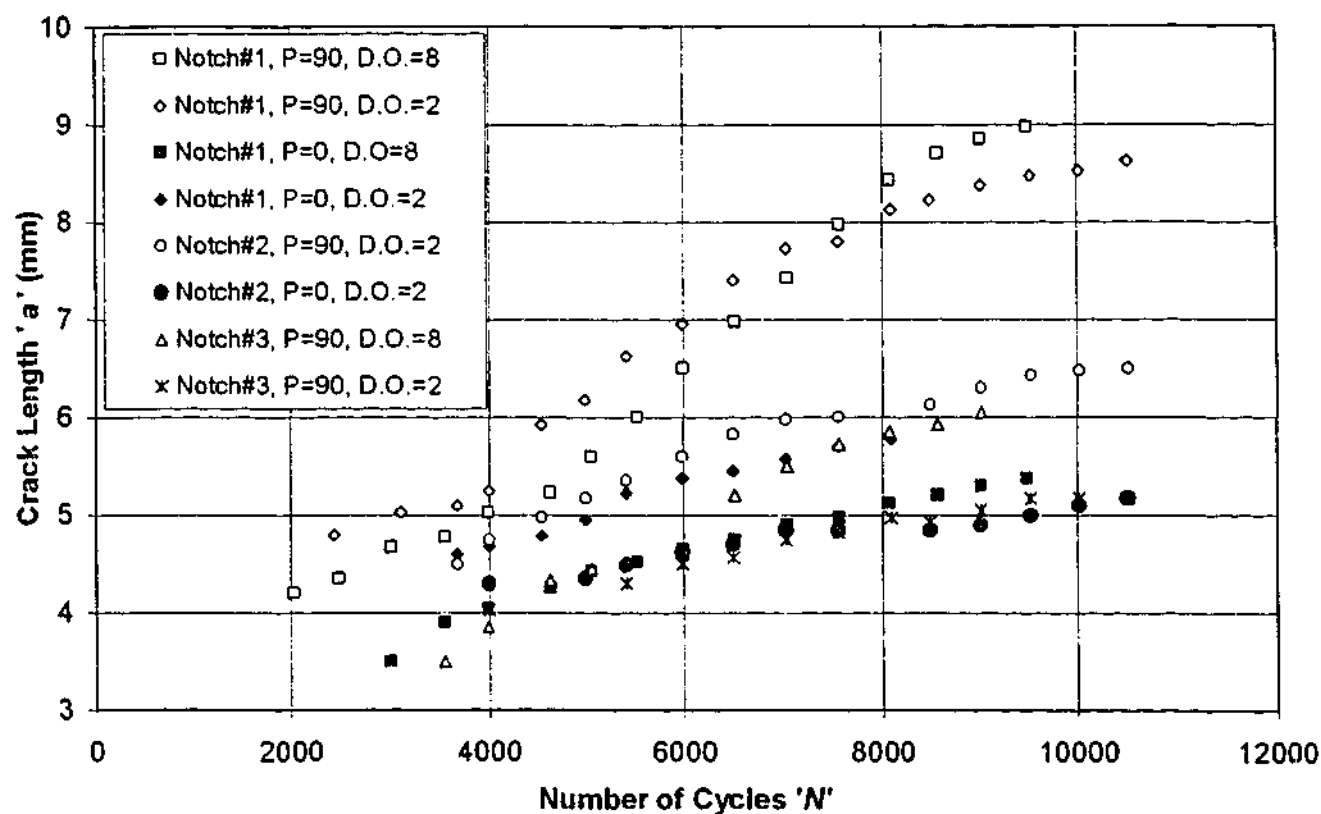


Figure 4.15: Raw crack length data, P = primary mechanical load (MPa), D.O. = dissolved oxygen level (ppm)

The crack growth data as presented in Fig. 4.15 is not very useful for developing an inclusive analysis of crack growth trends during RTS. The large number of variables included in the testing makes it difficult to complete any useful generalisation. As discussed in Chapters 2 and 3 however, LEFM may be successfully applied to RTS crack growth analysis as long as the plastic zone surrounding the crack tip is small in comparison with other specimen dimensions. In the case when this plastic zone is too large however, other methods must be used.

As shown in Appendix C, figures C.14 to C.18, thermal shock stresses larger than yield are confined to a region quite close to the surface. For this reason, crack growth analysis has been divided into two regions. The first is when the crack is short and plastic stresses/strains are dominant. The second is when the crack is longer, the bulk of the material is behaving elastically and LEFM can be applied.

#### **4.6.2.1 Short crack growth**

Figure 4.16 shows crack growth rate versus crack length for a number of individual cracks growing under a number of test combinations. This data shows a general trend of the cracks going through a period of acceleration followed by a period of deceleration. All data is taken from tests #2 and #3.

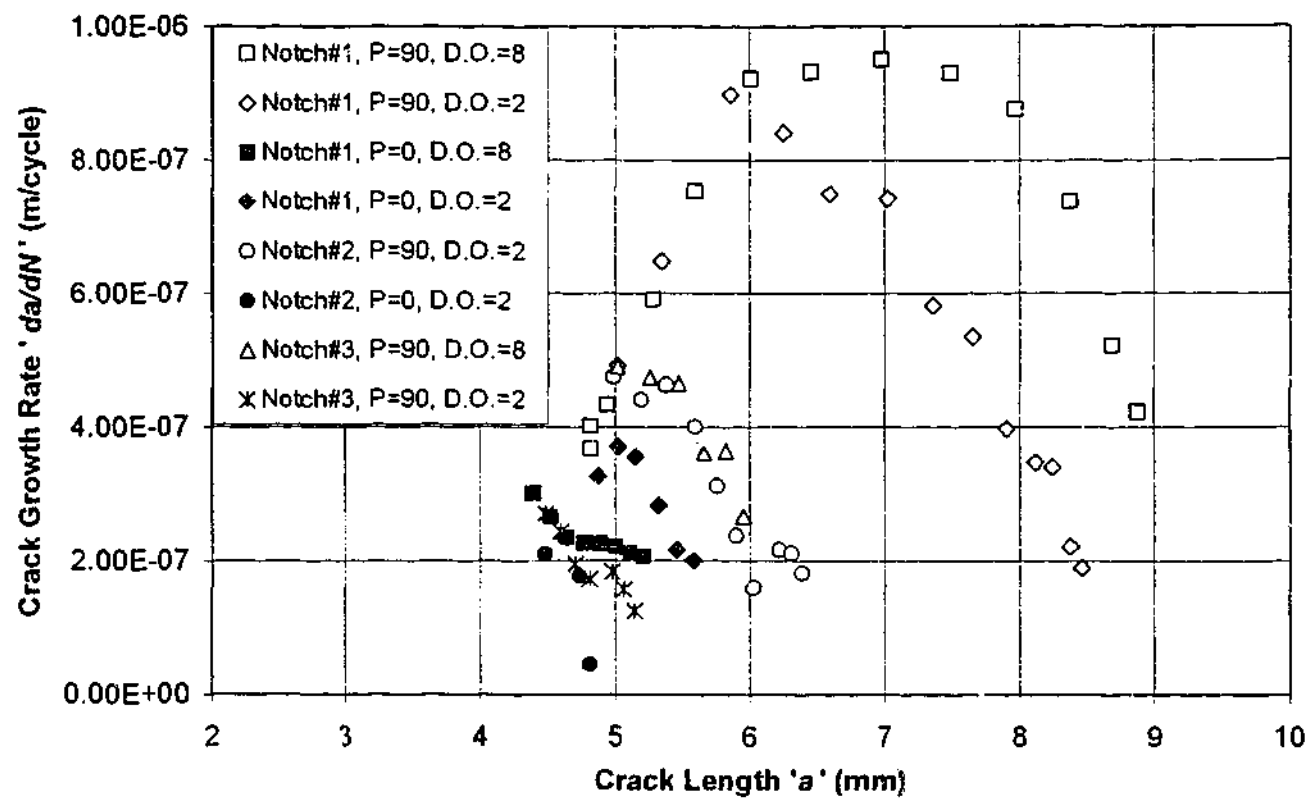


Figure 4.16: Crack growth rate versus crack length (includes notch depth) for a number of cracks grown by RTS. P = primary mechanical load (MPa), D.O. = dissolved oxygen level (ppm). Each symbol represents the growth of an individual crack.

As shown in figure 4.16, some cracks accelerate over a greater depth than others do. This depth of acceleration has a rough correlation with the size of the plastic zone generated during the thermal shock. The more severe the surface stress during a thermal shock, the greater the depth at which plastic strains develop and the deeper the region of crack acceleration.

When plastic strains dominate the region surrounding the crack tip, cyclic loading is sometimes referred to as high strain fatigue (HSF). As reported in Chapter 2, equation [2.5], crack growth rate in a HSF region can be linearly related to crack length (Skelton, 1983).

$$\frac{da}{dN} = B.a \quad [2.5]$$

Where  $a$  is the crack length and  $B$  is a constant.



Fitting a linear curve based on [2.5] over the region of crack acceleration in figure 4.12 yields the curve as shown in 4.17. As expected, the linear curve correlates well with the data during the period of acceleration. This reinforces the assumption that plastic stresses dominate in this region. Note that a constant value 'C' has been added to [2.5] to allow for the presence of a notch.

$$\frac{da}{dN} = B.a - C \quad [4.1]$$

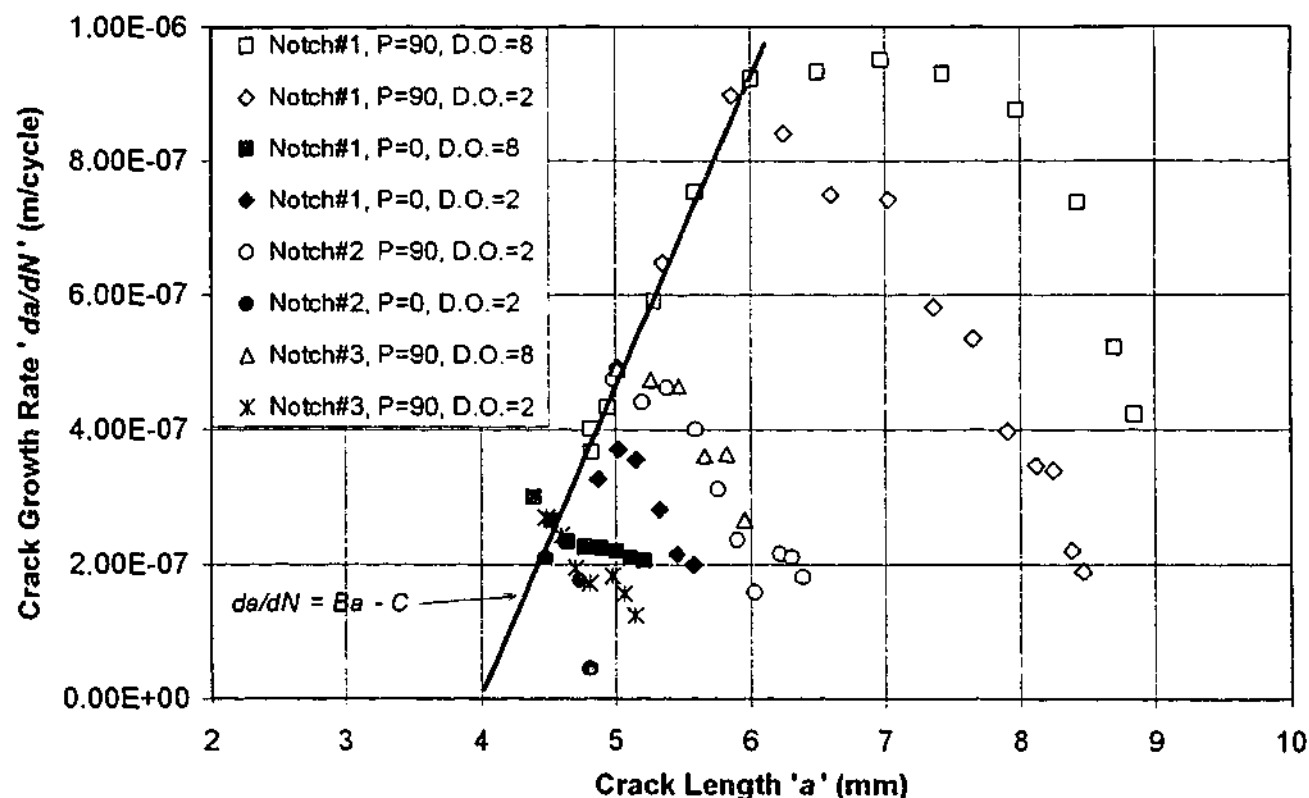


Figure 4.17: Crack growth as a function of crack length showing linear prediction curve for high strain fatigue (HSF) region. P = primary mechanical load (MPa), D.O. = dissolved oxygen level (ppm).

Substituting the values for  $B$  and  $C$  obtained from a best-fit analysis, the following relationship is obtained to describe the crack growth in the HSF region of a notched specimen exposed to RTS.

$$\frac{da}{dN} = 4.50 \times 10^{-4} a - 1.77 \times 10^{-6} \text{ m/cycle} \quad [4.2]$$

Where  $a$  is the crack length in metres.

In Chapter 2, section 2.4.3, it was reported that Marsh (1981) had developed an experimental correlation for the constant  $B$ , dependent on material properties and the cyclic plastic strain range [2.6]. The results here show however, that cracks grown in a range of cyclic plastic strains can be approximated by the one curve and hence a single value of  $B$ . In the work by Marsh, typical values for  $B$  for the plastic strain range of  $0.4-1.0 \times 10^{-3}$  were found to be  $2.0-3.3 \times 10^{-4}$ . The upper values of this work seem to compare favourably with the value for  $B$  of  $4.5 \times 10^{-4}$  obtained in this thesis. This value of  $B$  also compares favourably to that obtained by Skelton (1982) for a number of stainless steels exposed to a cyclic plastic strain range of around  $1.0 \times 10^{-3}$  in a high temperature air environment.

#### 4.6.2.2 Long Crack Growth

Once the crack has grown out of the HSF region and growth begins to decelerate, crack length alone is not sufficient as a parameter for describing the growth relationship. Providing the limitations outlined in Chapter 3, section 3.4.4 are satisfied (notch influence and plastic zone size) and elastic stresses are dominant, the elastic stress intensity factor may become a valid parameter for describing the stress field at the crack tip. As previous work in this area has suggested, the stress intensity factor can be related to crack growth via Paris law type equations.

For this work, the size of notch influence is quite small. As defined in section 3.4.4.1, for a notch of depth  $D$  and radius  $r$ , the size of notch influence is  $0.13\sqrt{Dr}$ . Taking the largest values for  $D$  and  $r$  used in this work, the maximum notch influence is around 0.13mm. This is well encompassed in the HSF region described in the previous section and hence satisfied in all cases. Additionally, the plastic zone size is considered adequately small if  $\Delta K_I$  is below  $40\text{MPa}\sqrt{\text{m}}$  (see section 3.4.4.2). This will be considered on a case by case basis.

Plotting of the cyclic change in stress intensity factor versus the crack growth rate for the raw crack growth data taken from tests #2 #3 is shown in figure 4.18. Included on the figure is an arrow that indicates the direction of growth of the cracks, reinforcing the fact that crack deceleration is occurring.

Stress intensity factors used in figure 4.18 have been determined from the curves reproduced in Appendix C as figures C.19-C.28. Crack growth rates have been calculated as per ASTM E 647-95a (1995). This code requires that each growth rate point shown in Figure 4.18 be calculated from the gradient of a 2<sup>nd</sup> order polynomial fit to a minimum of 5 successive raw growth data measurements.

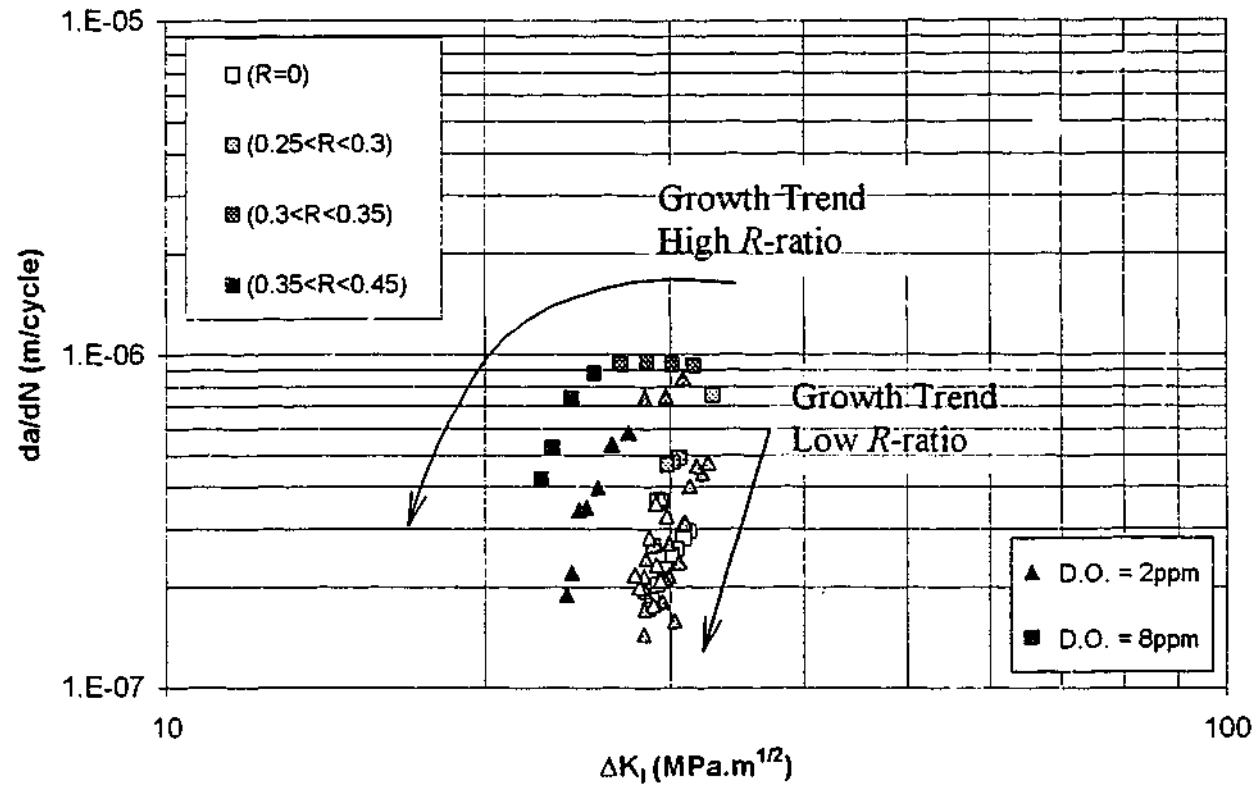


Figure 4.18: Change in stress intensity factor versus crack growth rate for RTS.

On first analysis, the data from figure 4.18 seems fairly scattered. However after grouping, several trends can be observed.

- 1) When primary loads are low ( $R < 0.3$ ), crack growth rate can be roughly related to stress intensity factor by means of a single power law. Changes in dissolved oxygen level have minimal effect on the overall growth rate.
- 2) When primary loads are high ( $R > 0.3$ ), crack growth rates are accelerated and cannot be modelled by a single power law fit. An increase in dissolved oxygen results in an increase in crack growth rate. It is assumed that this accelerated growth is evidence of an environmental interaction.
- 3) Increased levels of crack growth observed at high  $R$ -ratios and D.O. levels seems to plateau at around  $1 \times 10^{-6}$  m/cycle. This suggests the mechanism of environmental assistance may be stress corrosion fatigue (see Chapter 2, section 2.5.2.2).

- 4) A crack arrest trend for all cracks seems to be occurring as growth is in a reducing  $\Delta K_I$  field. The large arrow on the figure indicates this trend.

All of these trends become clearer when the raw data is smoothed. Smoothing was achieved by fitting a polynomial to the complete growth curve (figure 4.15) for each crack and then integrating to determine the growth rate as a function of number of cycles. Figure 4.19 shows the results, with data categorised by the  $R$ -ratio and the D.O. content of the cooling water.

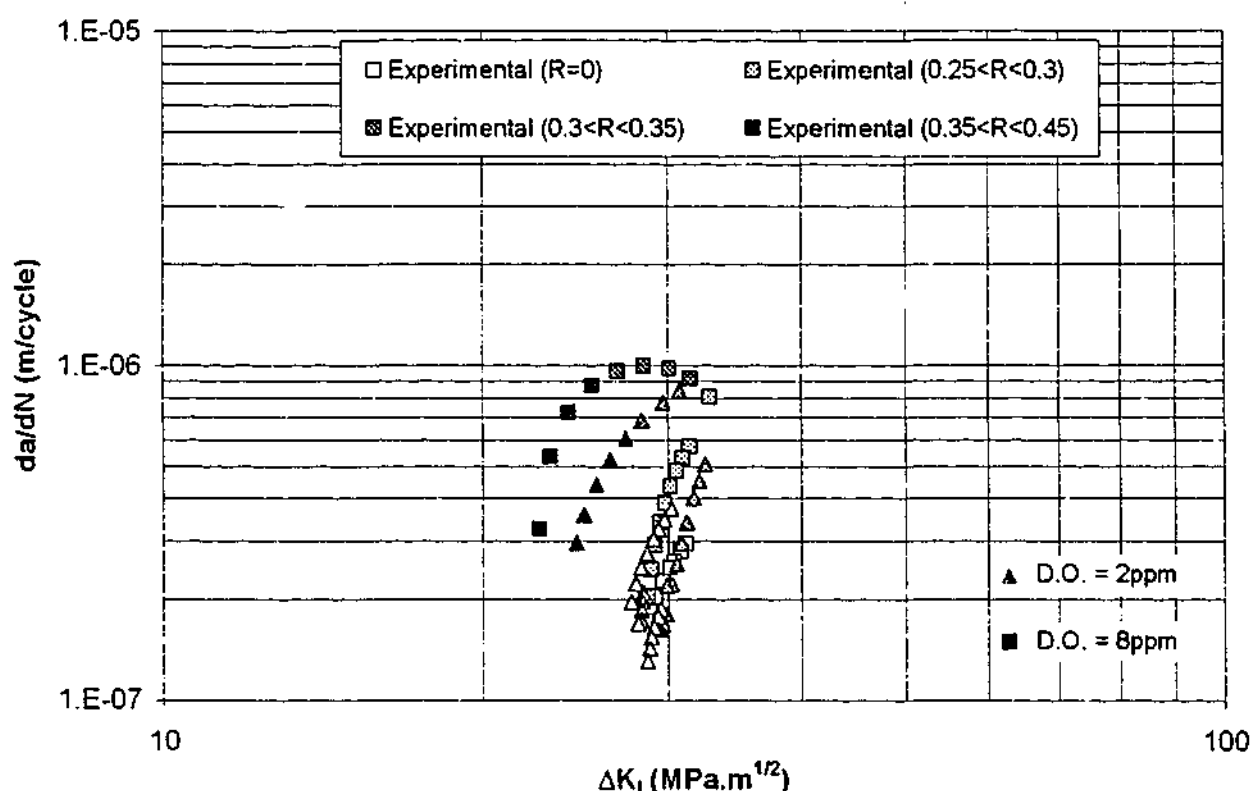


Figure 4.19: Crack growth as a function of stress intensity factor  $\Delta K$ , smoothed data.

One aspect that is unclear from these results is the relation for crack growth rates at mid-level  $R$ -ratios. Depending on the crack growth situation,  $R$ -ratios of around 0.3 produce values on both the upper environmentally accelerated growth curves and the lower power law curve. This may be a consequence of conducting crack growth in a decreasing  $\Delta K$  field. As described in section 4.5.3.3, the rate of  $\Delta K$  reduction in some of the cracks may be large enough to allow history effects to become important. In summary, from the few

results obtained, it seems that once crack growth has begun deceleration, a relative increase in  $R$ -ratio has less effect then when crack growth is accelerating or at a steady rate.

#### 4.6.2.3 Predicting crack growth rates at different shock severities

In test #4, the effect of changing the length of thermal shock on crack growth was investigated. In doing so, the test specimens were exposed to a different stress intensity factor profile during the shock. The results from using a curve fit from the test #3 data to predict crack growths observed in test #4 are summarised in table 4.8 below.

Table 4.8: Comparison of predicted and actual crack growth rates for specimen exposed to 5s thermal shocks from set temperature of 330°C.

$\Delta K$ (MPa $\sqrt{m}$ )	$R$	$da/dN$ – predicted (m/cycle)	$da/dN$ -actual (m/cycle)	~ Error (%)
24.3	0.36	$2.57 \times 10^{-7}$	$3.2 \times 10^{-7}$	-20%
24.1	0.37	$2.40 \times 10^{-7}$	$2.9 \times 10^{-7}$	-17%
23.8	0.38	$2.17 \times 10^{-7}$	$2.4 \times 10^{-7}$	-10%
27.8	0.33	$1.69 \times 10^{-7}$	$2.55 \times 10^{-7}$	-34%
22.9	0	$5.40 \times 10^{-8}$	$< 4.0 \times 10^{-8}$	35%
25.9	0	$1.11 \times 10^{-7}$	$< 4.0 \times 10^{-8}$	178%

With the exception of the last set of figures on the table, the use of data from test #3 to predict crack growth in test #4 is generally acceptable. This suggests that the effects on long crack growth from changing the thermal shock length may be characterised by the change in the stress intensity factor profile alone. Whether this is the case in regions that have a higher environmental influence (as observed in the 8ppm D.O. data of test #2) cannot be answered from this data.

### 4.6.3 Modelling Crack Growth in Elastic Region

In the HSF region, a single curve has been proposed for the prediction of crack growth (see figure 4.17). In the elastic region however, multiple curves are required to describe the growth. Elastic models for the growth of cracks under the influence of environment were presented in Chapter 2 and are compared against the test data here.

#### **4.6.3.1 Torronen and Cullen (1982)**

As introduced in Chapter 2, section 2.5.1.1, the work of Torronen and Cullen (1982) provides a model for the effects of high  $R$ -ratios during environmentally assisted fatigue. The equations used in the work are reproduced below:

$$\frac{da}{dN} = C(\Delta K)^m \quad \text{for } K_{max} < K_{lim} \quad [2.4]$$

$$\frac{da}{dN} = C(\Delta K)^m \left( \frac{\sqrt{1-R^2}}{1-R} \right)^m \quad \text{for } K_{max} > K_{lim} \quad [2.13]$$

Equation [2.4] is simply the Paris Law equation, while [2.13] has an allowance for an additional mean stress effect when the maximum stress intensity factor in a cycle exceeds the limit for environmental assistance. Fitting this to the data presented in figure 4.19 requires the solution for three unknowns ( $C$ ,  $m$  and  $K_{lim}$ ). This is completed by firstly using the data for  $R = 0$ . Fitting a power law curve to this data allows  $C$  and  $m$  to be determined. Then, assuming the rapid change in crack growth rate observed at  $\Delta K = 22 \text{ MPa}\sqrt{\text{m}}$  for  $R = 0.45$  corresponds to the onset of environmental assistance, the limit for environmental assistance ( $K_{lim}$ ) is found to be approximately  $40 \text{ MPa}\sqrt{\text{m}}$ . This gives the following set of equations:

$$\frac{da}{dN} = 5.28 \times 10^{-16} (\Delta K)^{5.89} \quad \text{for } K_{max} < 40 \text{ MPa}\sqrt{\text{m}} \quad [4.3]$$

$$\frac{da}{dN} = 5.28 \times 10^{-16} (\Delta K)^{5.89} \left( \frac{\sqrt{1-R^2}}{1-R} \right)^{5.89} \quad \text{for } K_{max} > 40 \text{ MPa}\sqrt{\text{m}} \quad [4.4]$$

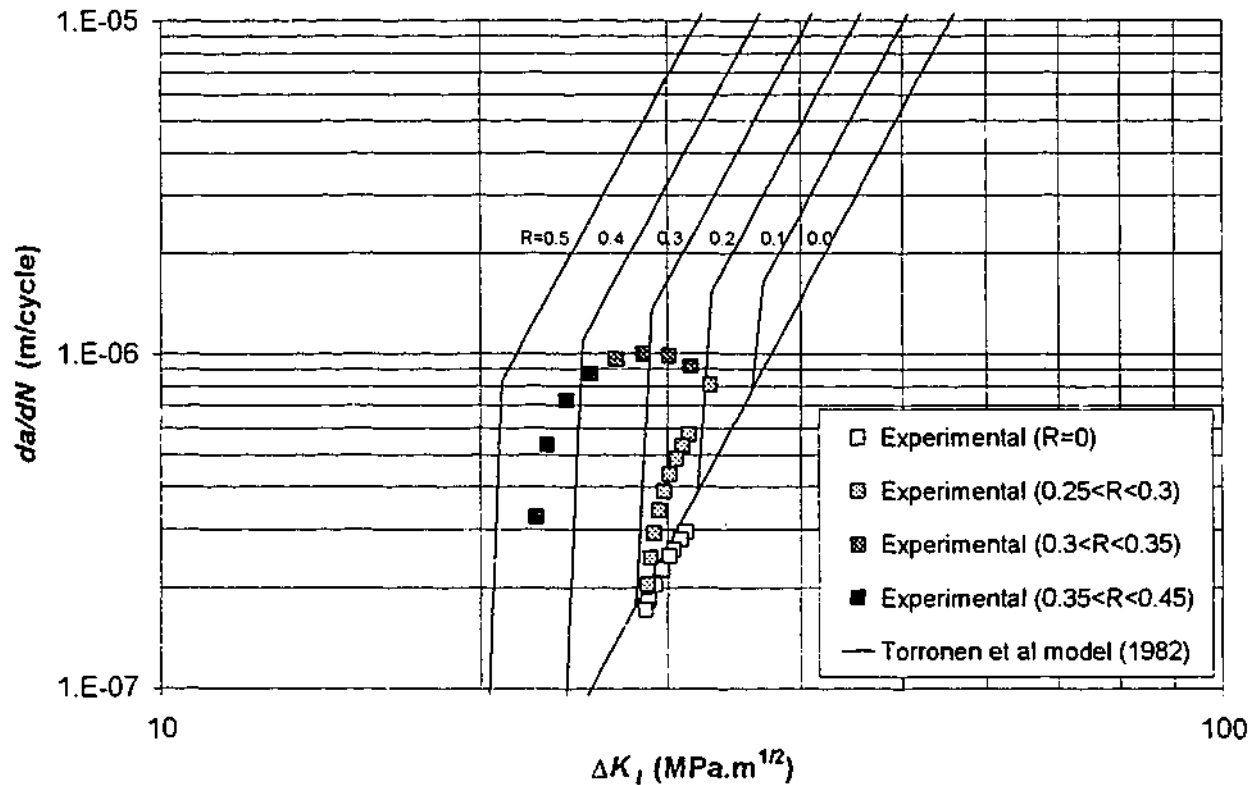


Figure 4.20: Smoothed experimental crack growth data plotted against a Torronen and Cullen (1982) model prediction, allowing for the effects of environment and primary load. Experimental data for DO=8ppm plotted.

Figure 4.20 shows this model applied to the data obtained during test #2 with the D.O. level for the quenching water set at 8ppm. Likewise, figure 4.21 shows the model applied to the data from test #3 with the D.O. level set to 2ppm. As would be expected from the method used to develop the model, crack growth rates for  $R=0$  are well described. Also well described are the  $\Delta K$  values at which environmental assistance occurs for different  $R$ -ratios. This is more so the case for the 8ppm D.O. data as opposed to the 2ppm D.O., possibly because environmental effects are more pronounced in the prior and are restricted to the higher  $R$ -ratios in the latter. In both cases however, the growth rates for larger  $\Delta K$  values seem to be largely overestimated, failing to model the plateau which appears to exist at  $da/dN = 1 \times 10^{-6}$  m/cycle.



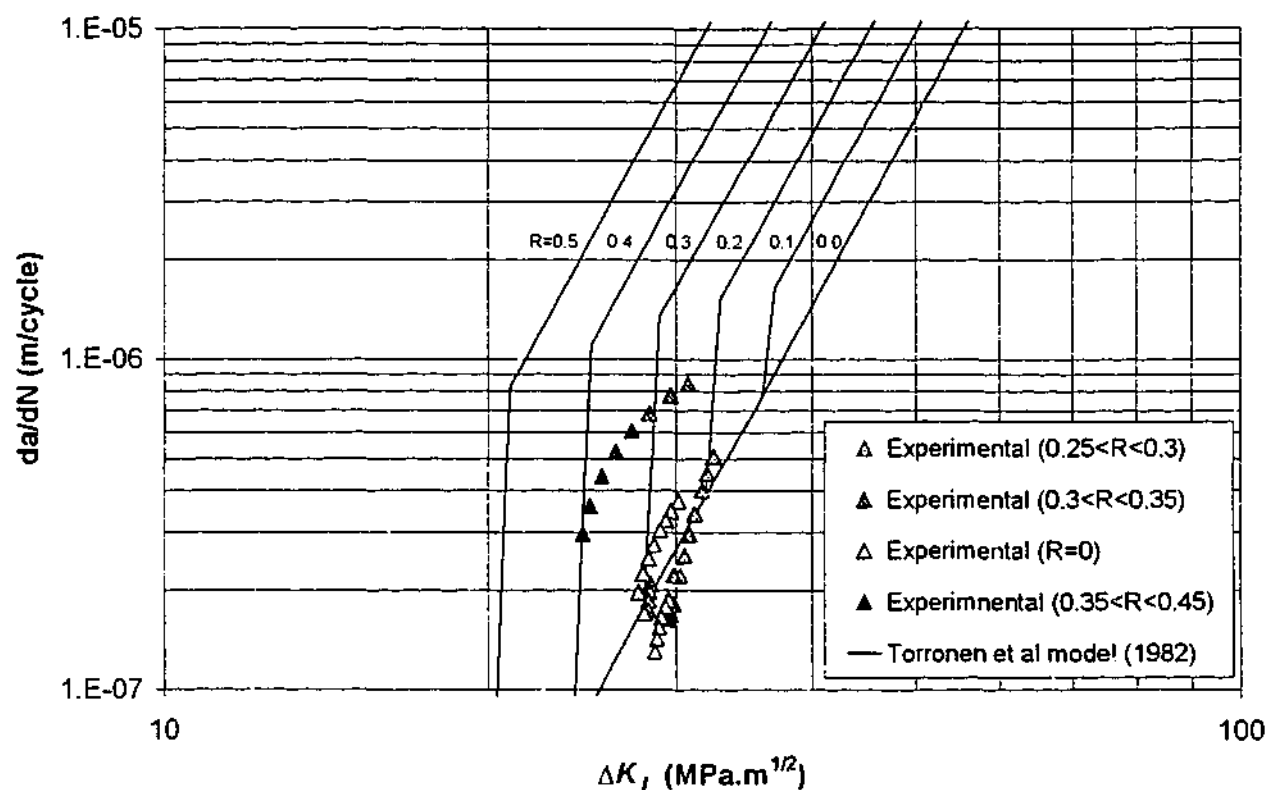


Figure 4.21: Smoothed crack growth data plotted against a Torronen and Cullen (1982) model prediction, allowing for the effects of environment and primary load. Experimental data for DO=2ppm plotted.

Attempts to address the shortcomings of the Torronen and Cullen model to predict the test data are contained in the next model.

#### 4.6.3.2 Gabetta et al (1990)

Described in detail in section 2.5.2.4, the model developed by Gabetta et al (1990) allows for environmental assistance by using a model based on the true corrosion fatigue (TCF) and stress corrosion fatigue (SCF) concepts developed by Austen and Walker (1977). The SCF component is thought to be the result of an anodic dissolution reaction, dependent on the loading rise time  $\tau$ .

$$\frac{da}{dN_E} = \frac{da}{dN_V} + \frac{da}{dN_{TCF}} + \tau \frac{da}{dt_{SCF}} \quad [2.16]$$

Substituting a Paris law type equation for the crack growth rates in a vacuum and additional growth due to true corrosion fatigue ( $da/dN_V + da/dN_{TCF}$ ), the following equation is obtained:

$$\frac{da}{dN} = C(\Delta K)^m + \tau \frac{da}{dt}_{SCF} \quad [4.5]$$

Where  $da/dt_{SCF} = 0$  for  $\Delta K < \Delta K_c$ .

This equation requires the solution for four unknowns ( $C$ ,  $m$ ,  $da/dt_{SCF}$  and  $\Delta K_c$ ). As outlined in section 2.5.2.4,  $\Delta K_c$  can be calculated by assuming that the onset of SCF occurs when the ASCR (active surface creation rate) is comparable to the SCF crack growth rate, ie:

$$\Delta K_c^2 = \frac{1}{\alpha} \cdot \sigma_y E \tau \cdot \frac{1-R}{1+R} \frac{da}{dt}_{SCF} \quad [2.18]$$

The rapid crack deceleration observed in the 8ppm D.O. data at  $\Delta K=22\text{MPa}\sqrt{\text{m}}$  and  $R=0.45$  (figure 4.14) is assumed to be evidence of the effects of SCF. Then, assuming a  $da/dt_{SCF}$  value of  $10^{-7}\text{m/s}$  (from Gabetta et al, 1990, for low alloy steel in a  $288^\circ\text{C}$  water environment), a value for the constant  $\alpha$  can be determined. Finally, using  $\sigma_y=300\text{MPa}$  and  $E=200\text{GPa}$ , for a 7s long thermal shock an equation to determine the effect of  $R$  on  $\Delta K_c$  is resolved:

$$\Delta K_c^2 = 1.45 \times 10^3 \frac{1-R}{1+R} \quad [4.6]$$

Curve fitting the data for  $\Delta K < \Delta K_c$  to determine  $C$  and  $m$  (as for the Torronen and Cullen model in the previous section), the following solution for crack growth due to repeated 7s long thermal shocks is obtained:

$$\frac{da}{dN} = 5.28 \times 10^{-16} (\Delta K)^{5.89} \quad \text{for } \Delta K < \Delta K_c \quad [4.7]$$

$$\frac{da}{dN} = 5.28 \times 10^{-16} (\Delta K)^{5.89} + 7 \times 10^{-7} \quad \text{for } \Delta K > \Delta K_c \quad [4.8]$$

Figures 4.22 and 4.23 show equations [4.7] and [4.8] plotted against the smoothed test data from tests #2 and #3 respectively.

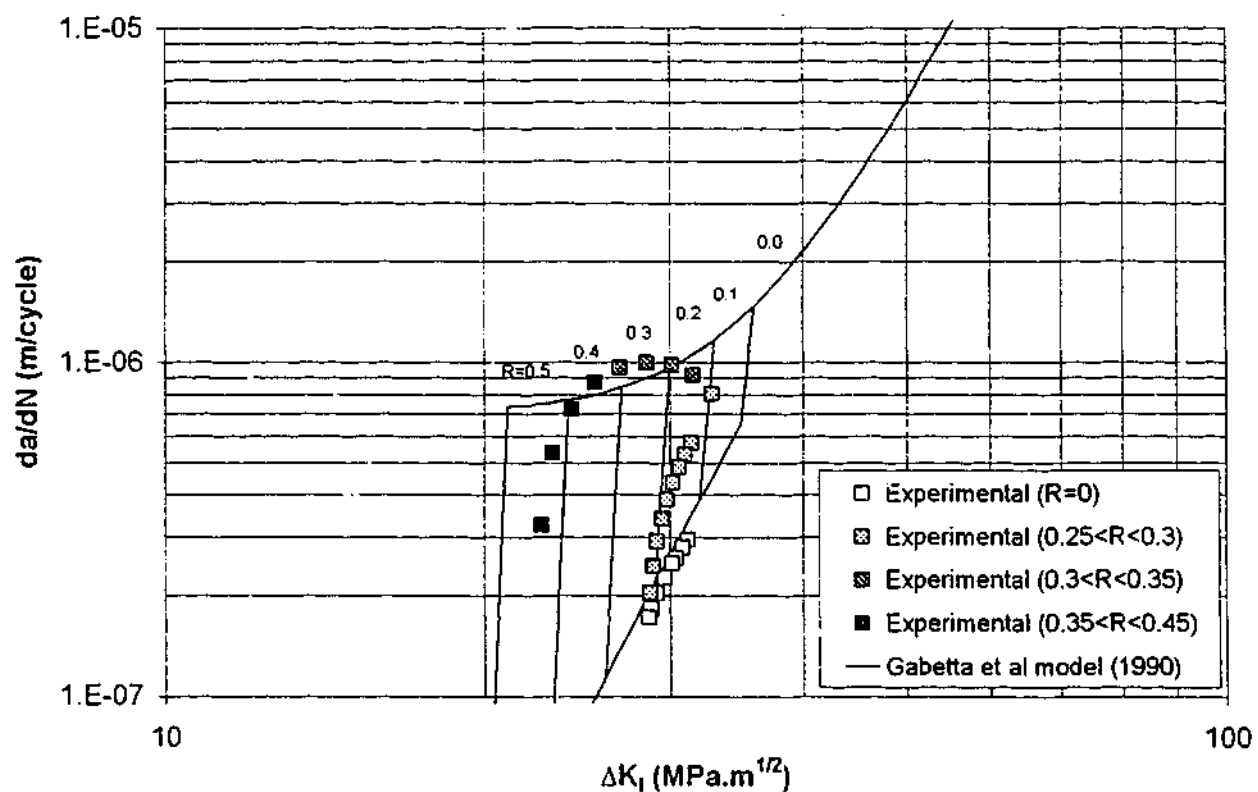


Figure 4.22: Smoothed experimental crack growth data plotted against a Gabetta et al (1990) model prediction, allowing for the effects of environment and primary load. Experimental data for DO=8ppm plotted.

Considering the number of simplifications made in this analysis, (including the values for  $da/dt_{SCF}$  and  $\alpha$ ), the Gabetta et al model provides a fairly good representation of the observed environmental assisted crack growth. As with the Torronen and Cullen model, crack growth outside of the assisted region (in this case the SCF region) is well defined. Similarly, the  $\Delta K$  value at which the enhanced crack growth begins is also anticipated.

Unlike the Torronen and Cullen model however, the plateau for the crack growth at around  $1 \times 10^{-6}$  m/cycle is fairly accurately predicted. This is because the SCF component (which is dependent on the  $R$ -ratio) becomes small in comparison with the TCF component for large  $\Delta K$  values. Note however that the continued validity of the Gabetta et al model at values of  $\Delta K$  above  $35 \text{ MPa}\sqrt{\text{m}}$  is yet to be verified. Limits on the applicability of LEFM (ie  $\Delta K$  must be below  $40 \text{ MPa}\sqrt{\text{m}}$ , see section 4.6.2.2) mean that verification of the model at higher  $\Delta K$  levels cannot be achieved using the current test method.

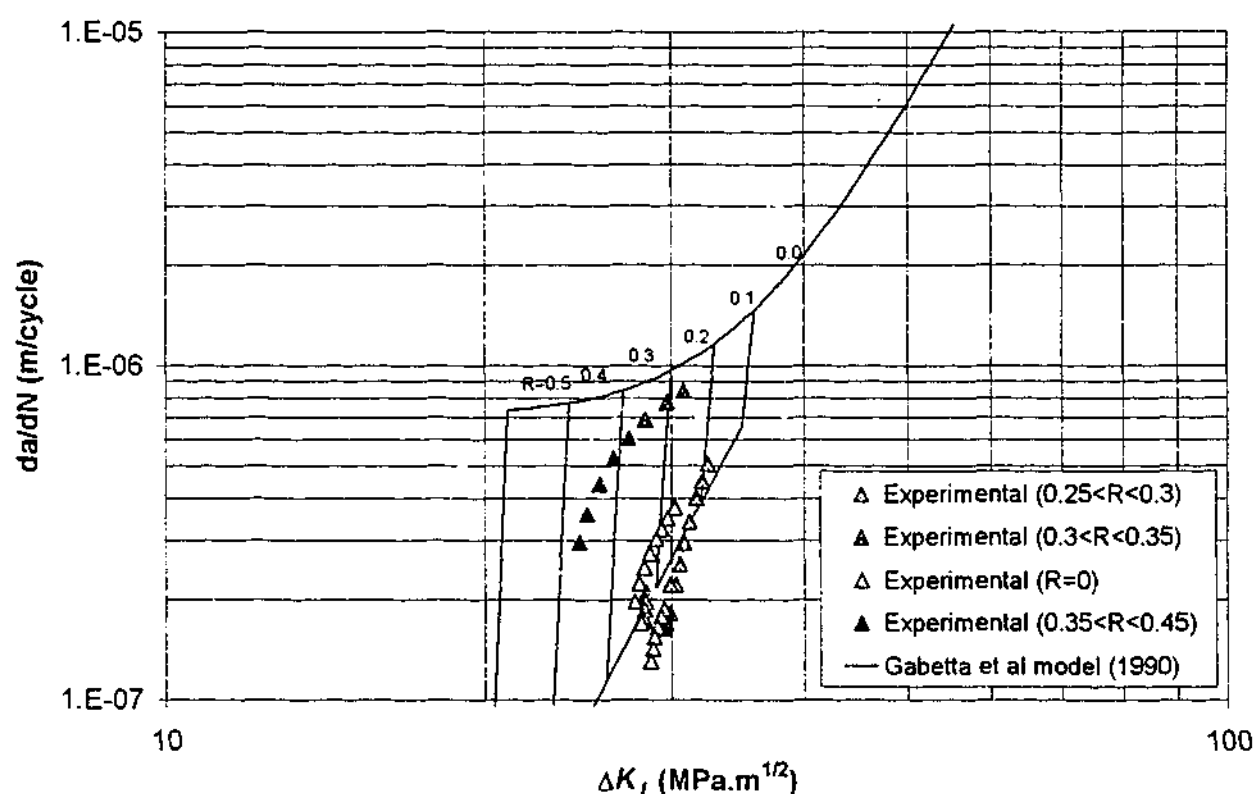


Figure 4.23: Smoothed experimental crack growth data plotted against a Gabetta et al (1990) model prediction, allowing for the effects of environment and primary load. Experimental data for DO=2ppm plotted.

#### 4.6.3.3 Discussion

Of the methods described in the previous two sections, the Torronen and Cullen (1982) model is the more simple to apply. Unfortunately, it fails to predict the apparent plateau of the crack growth observed at  $da/dN \approx 1 \times 10^{-6}$  m/cycle (figures 4.20 and 4.21). This means that the method may produce overly conservative results for cracks with non-zero  $R$ -ratios at high values of  $\Delta K$ . This was shown to particularly be the case when D.O. levels were reduced (figure 4.21).

As shown in figure 4.22 and 4.23, the Gabetta et al (1990) model better serves the experimental data. However, the method of development is much more complicated. Solution of equation [2.18] requires specific knowledge of the SCF crack growth rate ( $da/dt_{SCF}$ ), a value that is specific for each material-environment combination. In addition, [2.18] is also dependent on the load time of the cycle  $\tau$ , that in many applied cases is an unknown variable.

Therefore, selection of which crack growth model to use for analysis of RTS in the LEFM region is complicated. Depending on the amount of information about the situation that is available, a trade off between accuracy and complexity will need to be made. Lack of specific material data may lead to the use of the Torronen and Cullen model with the knowledge that crack growth rates at high  $\Delta K$  levels may be overestimated. When enough data is available, it would appear that more accurate results could be achieved by applying the Gabetta et al model.

#### **4.6.4 Fractography**

Investigations of the visual appearance of the cracks developed during the testing can help in forming conclusions on the mechanisms of their development and growth. This work will be approached in two stages. First a brief look at the crack mouth as it formed during initiation will be completed. This will be followed by more thorough investigation of the crack path and fracture surface developed as further crack growth occurred.

##### **4.6.4.1 Crack mouth**

The crack mouth appearance that was observed during the initiation phase is typical of that encountered in mechanical fatigue. Beginning with numerous sharp thumbnail cracks at the base of the notches, linking up to form a major full-width crack. Application of primary loads and changes in dissolved oxygen levels had no effect on this crack morphology. Figure 4.24 shows the crack surface for one of the unloaded specimens typical of the initiation of all cracks observed during testing.

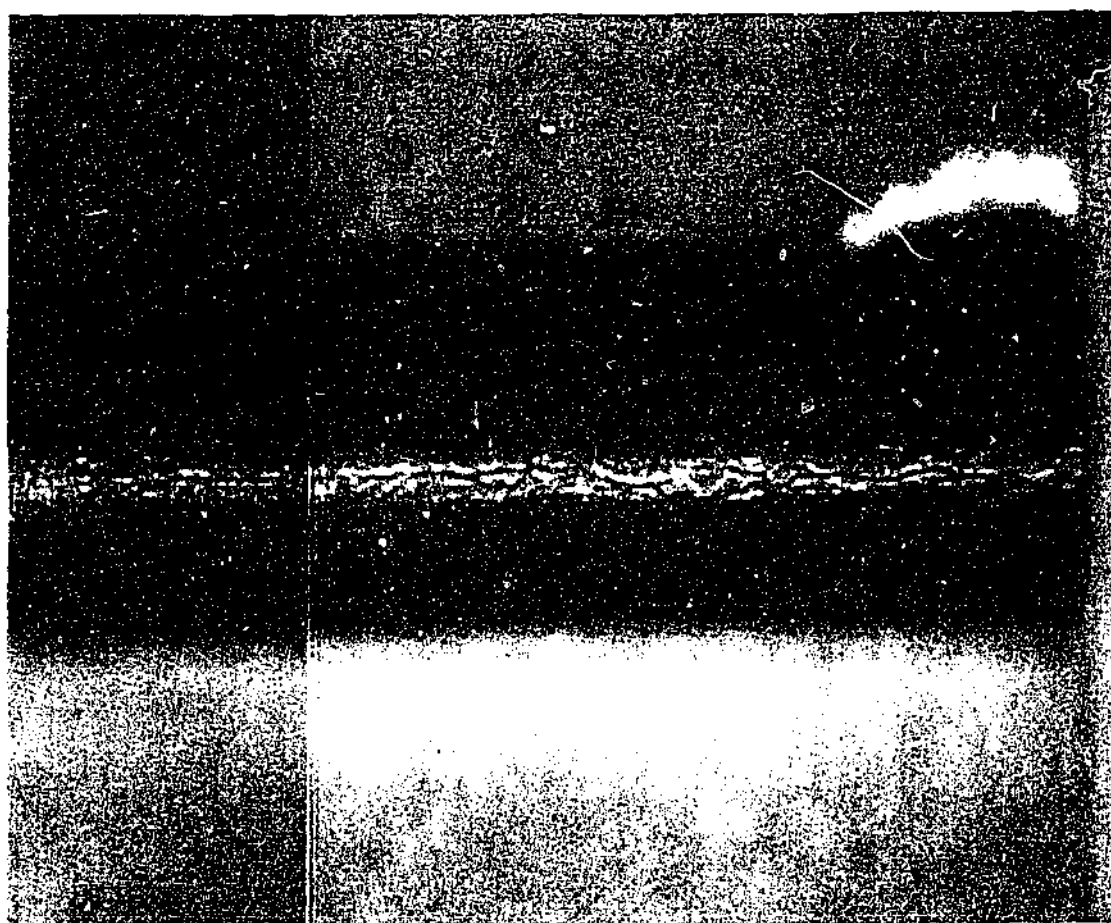


Figure 4.24: Crack mouth appearance after full-width initiation.

As cycling continued, the sharp crack mouth would progressively become more blunt, probably due to corrosion effects. This was more evident on the specimens with primary load, in which environmental influences on crack growth were found to be more prevalent.

#### 4.6.4.2 Crack length

Figures 4.25 through 4.31 show pictures taken along the crack lengths at completion of testing for specimens #2 through #5. Figures 4.32 and 4.33 show the crack growth surface obtained by breaking open two of the specimens. These figures may help provide some insight into the mechanisms of crack growth occurring during the testing which can be compared to the growth data outlined in sections 4.6.2 and 4.6.3. In summary, up to four regions of crack growth can be seen in the specimens with primary load and generally two regions are visible in the specimens without.

The first millimeter of growth in all specimens shows a slightly raised shiny fracture surface (figures 4.32 and 4.33). This may be due to the two fracture surfaces rubbing together during cycling. Plastic deformation during the crack initiation could explain this observation. This could also mean that the crack faces in both specimens are closed during a portion of the unloading cycle. The second region of growth, visible only on the specimens with high primary load is macroscopically smooth and exhibits a large amount of dark oxide build-up (figure 4.32). This area also corresponds to the HSF region where crack growth acceleration occurs. Looking along the crack length of all specimens in the HSF region (figures 4.25 to 4.31) shows a pattern with large amounts of corrosion product visible on either side of the crack.

The third region of growth, visible only on specimens with high primary load, represents the plateau and initial deceleration of long cracks in the loaded specimens (where  $R > 0.35$ ) as shown on figure 4.18. Some evidence of beach marks is visible in this area on a crack surface that has a moderate build-up of dark red oxide products (figure 4.32). Figures 4.25 and 4.27 show that the crack paths in this region are fairly narrow and have less evidence of corrosion products. Using the Austen and Walker (1977) model, the environmental assistance mechanism for growth in this region could be stress corrosion fatigue (SCF).

The final region of around 1mm visible on all specimens corresponds to the area of crack deceleration where only the "True Corrosion Fatigue" effects are seen. There is less oxide build-up on the crack surface in this region, with the beach marks due to the interrupted testing clearly visible (figures 4.32 and 4.33). Looking at the view along the crack length as shown in figures 4.25 to 4.31, the fracture path in this region is quite tortuous with evidence of some branching. Despite this, for all cases, the crack tip is sharp and transgranular crack growth dominates (see figure 4.34). This combination might indicate that both stress and environmental effects are still influential in driving the crack growth.

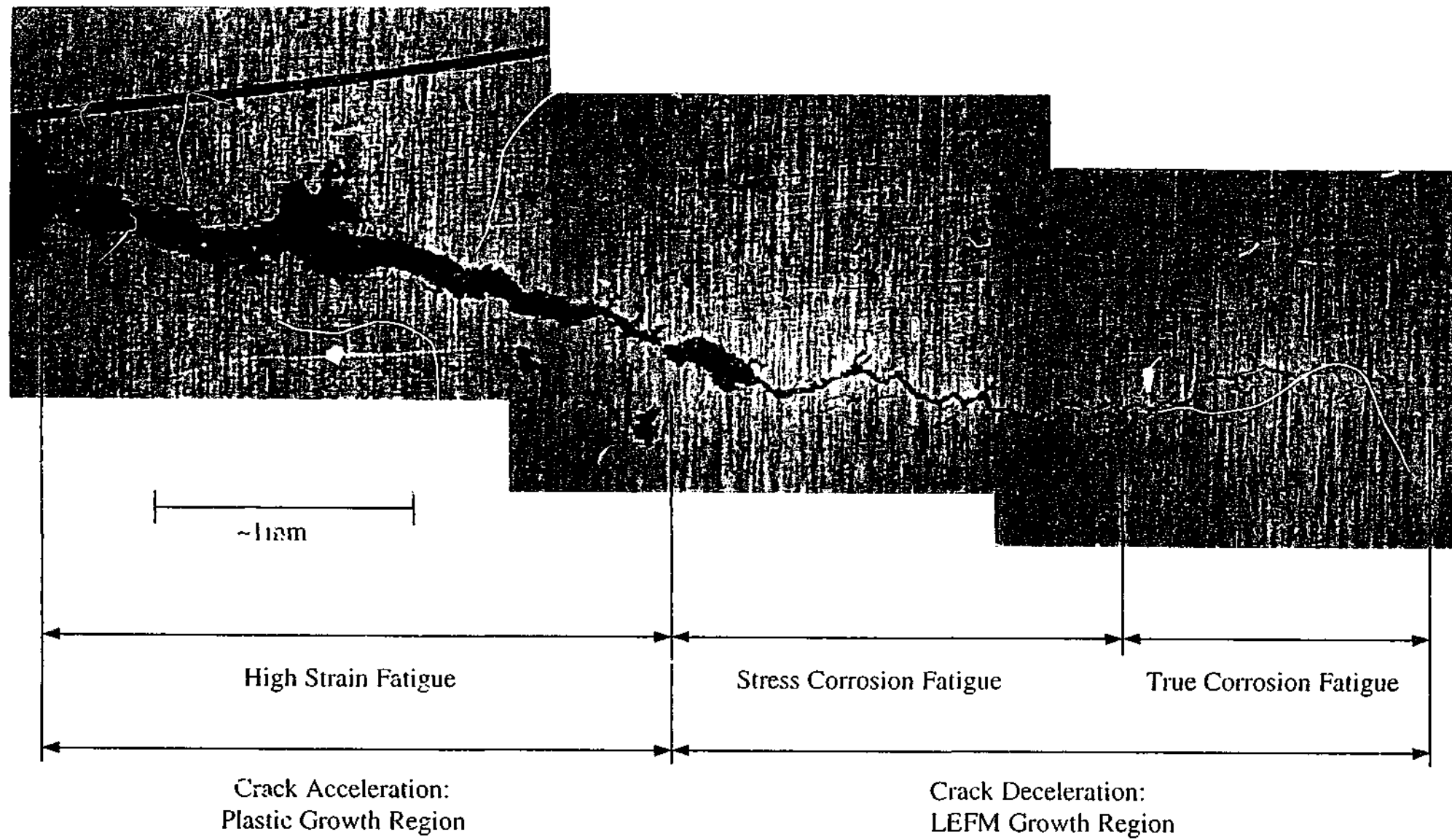


Figure 4.25: Final crack growth, specimen #2, notch position 1. Surface preparation by grinding only.



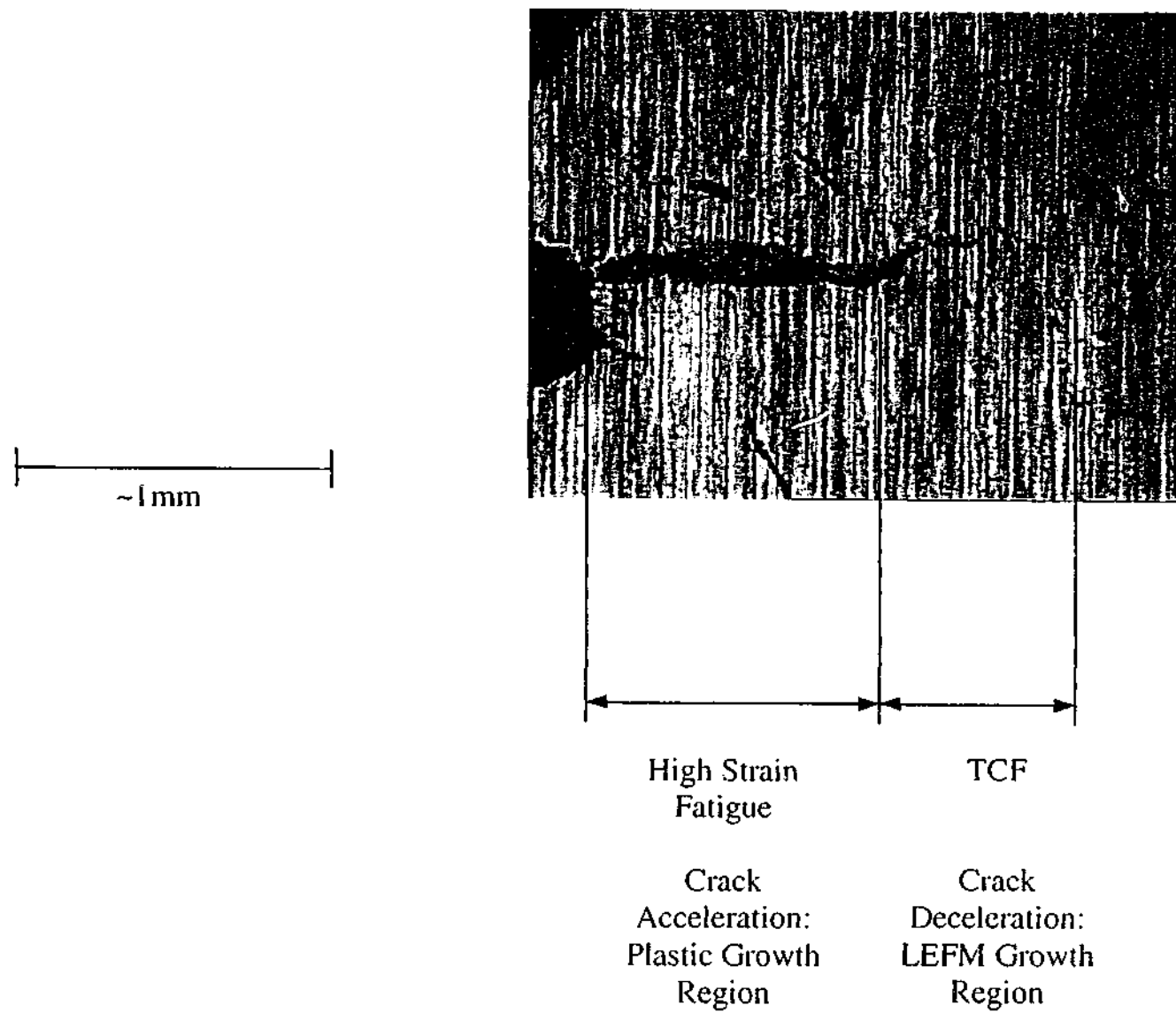


Figure 4.26: Final crack growth, specimen #3, notch position 1. Surface preparation by grinding only.

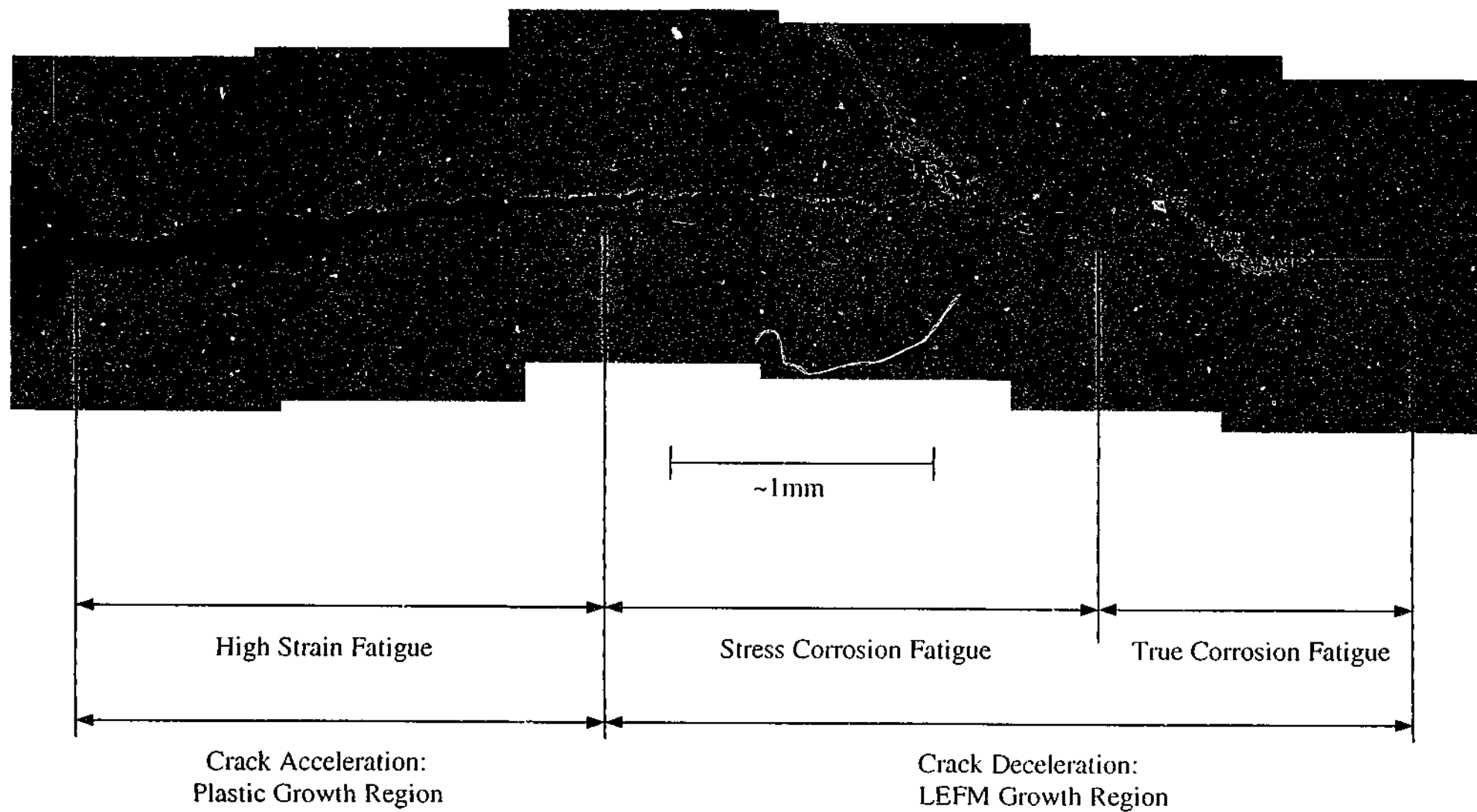


Figure 4.27: Final crack growth, specimen #4, notch position 1. Surface preparation by grinding and polishing.

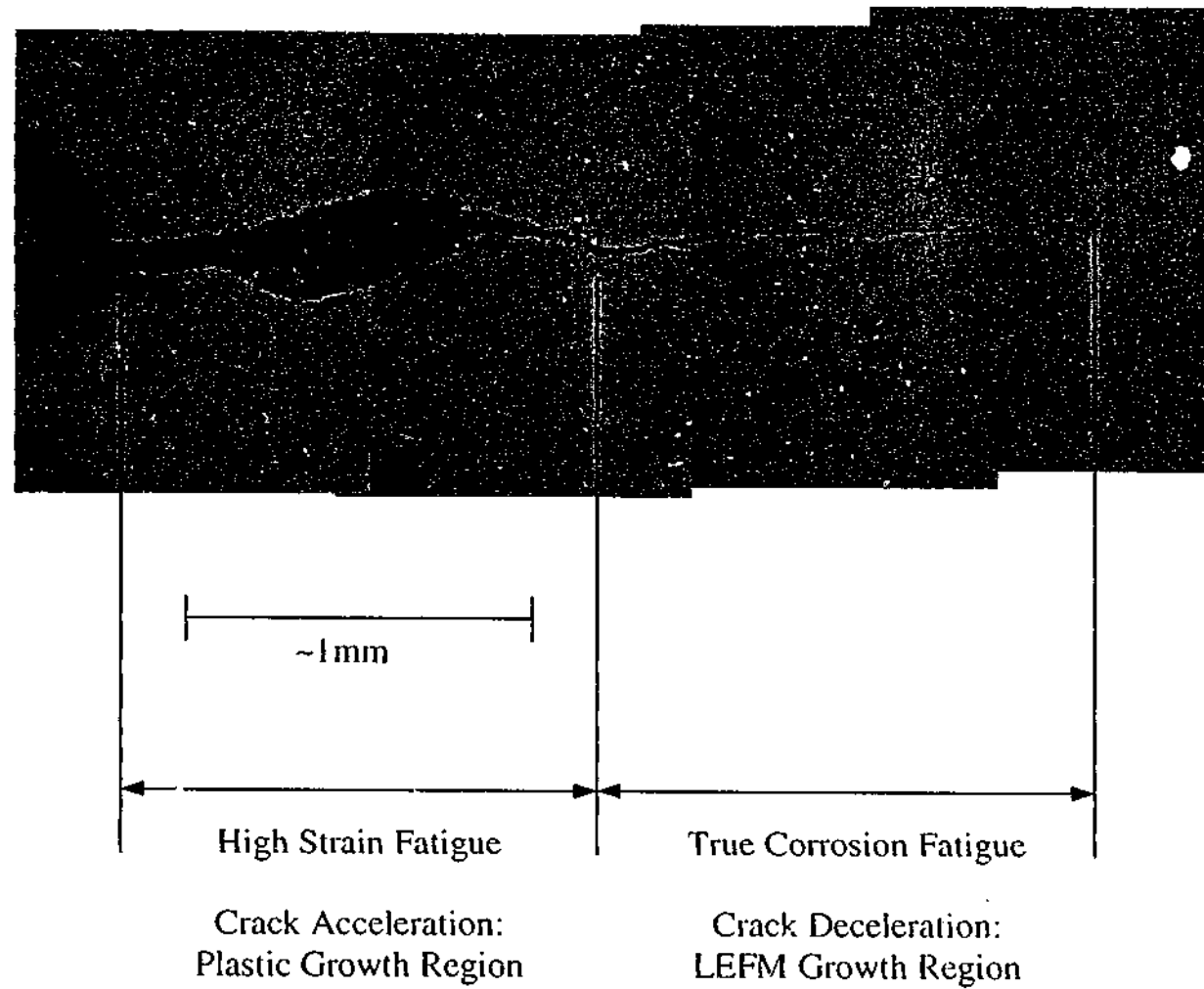
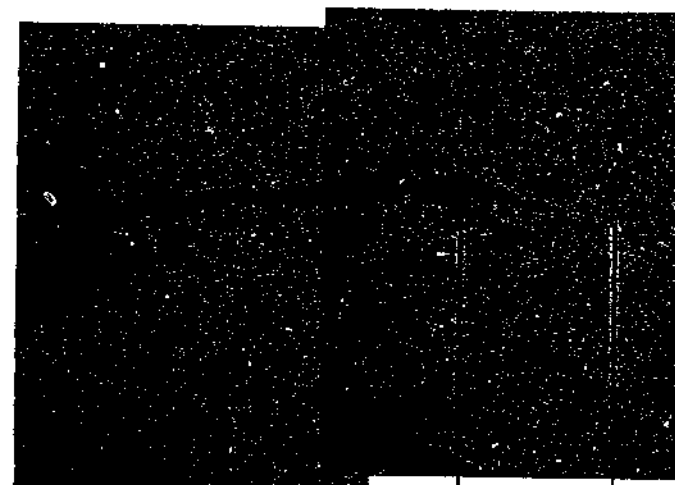


Figure 4.28: Final crack growth, specimen #4, notch position 2. Surface preparation by grinding and polishing.



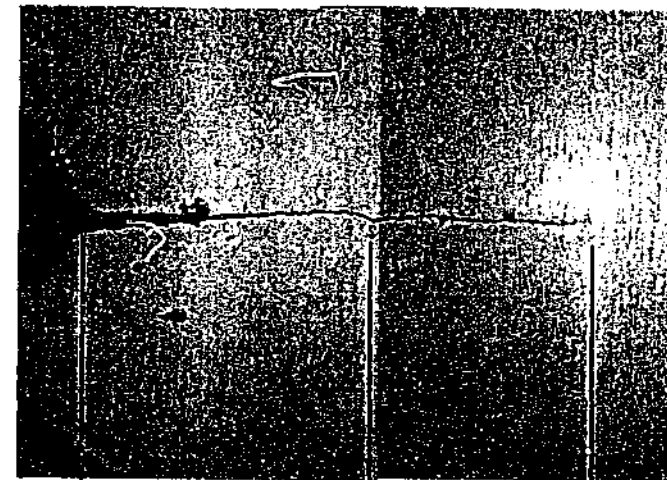
High Strain Fatigue

TCF

Crack  
Acceleration:  
Plastic Growth  
Region

Crack  
Deceleration:  
LEFM Growth  
Region

~1mm



High Strain  
Fatigue

TCF

Crack  
Acceleration:  
Plastic Growth  
Region

Crack  
Deceleration:  
LEFM Growth  
Region

Figure 4.29: Final crack growth, specimen #4, notch position 3. Surface preparation by grinding and polishing.

Figure 4.30: Final crack growth, specimen #5, notch position 2. Surface preparation by grinding and polishing.

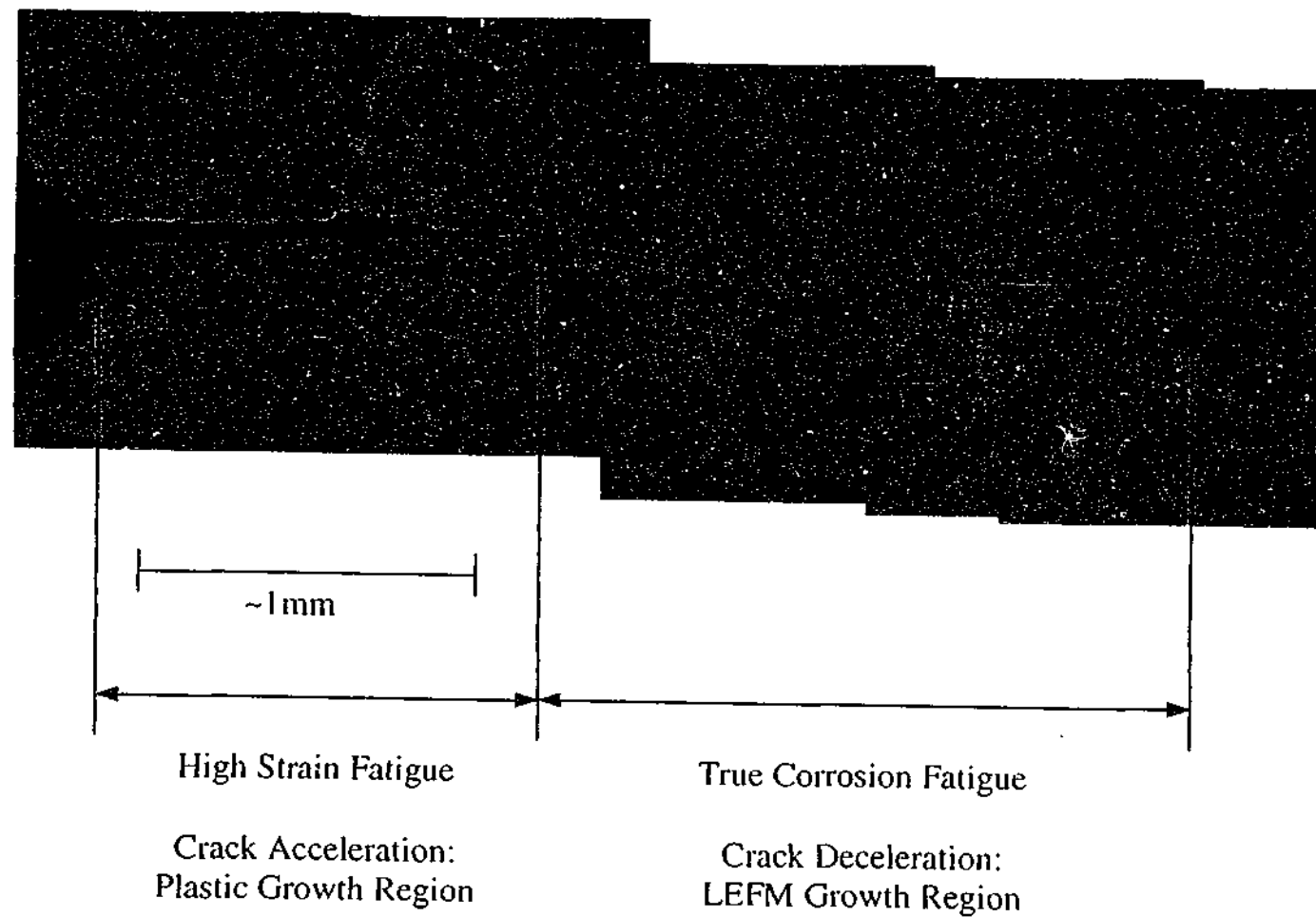


Figure 4.31: Final crack growth, specimen #5, notch position 1. Surface preparation by grinding and polishing.

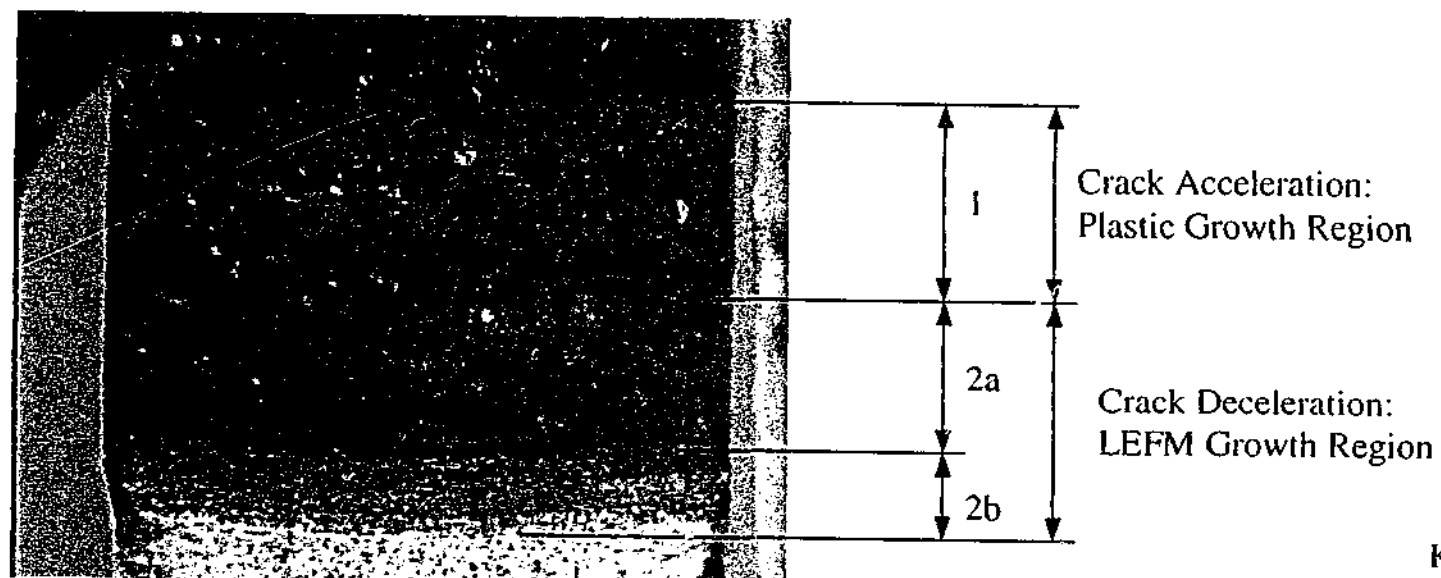


Figure 4.32 Fracture surface, specimen #2, notch position 1.

Key:

1: High Strain Fatigue

2a: Stress Corrosion Fatigue

2b: True Corrosion Fatigue

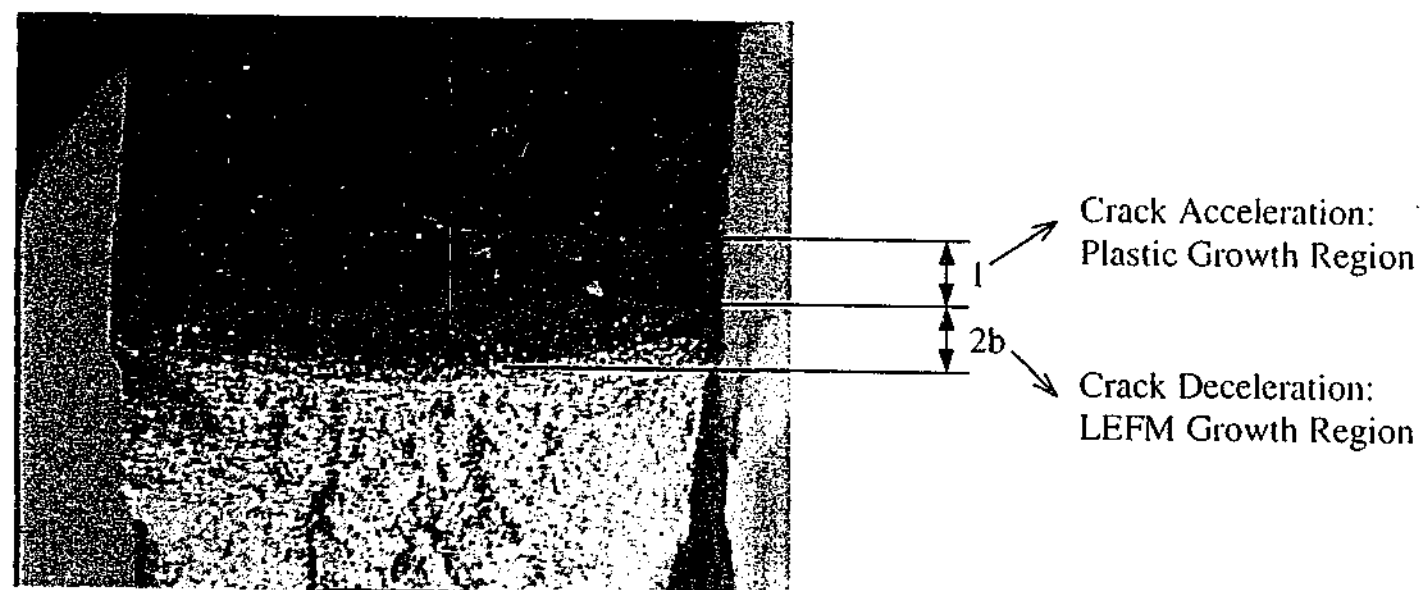


Figure 4.33: Fracture surface, specimen #3, notch position 1.

Hydrogen embrittlement is a possible mechanism for this final region of crack growth, with the crack appearance matching physical descriptions given by Jones (1996). Torronen and Cullen (1982) have previously proposed hydrogen embrittlement as a possible explanation for the effects of a light water reactor environment on fatigue crack growth in pressure vessel steel.

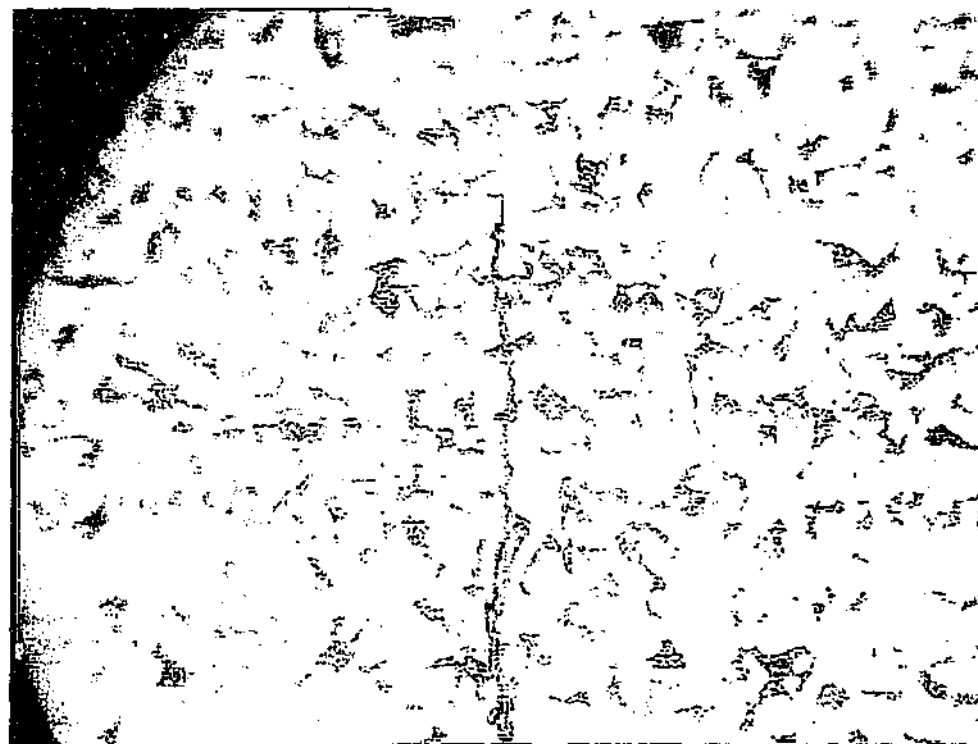


Figure 4.34: Transgranular growth of sharp tipped crack (400x magnification, specimen etched in 1% Nital).

#### 4.6.4.3 Justification of assumptions

A final note on the crack surface appearance is necessary with reference to the original assumption of the specimen being under a condition of plane stress made during the theory development of Chapter 3. The generally flat crack front seen in figures 4.32 and 4.33 is good evidence of this. In addition, the crack growth rates at both the free surfaces and the middle of the specimen are approximately the same, observed by the constant thickness beach marks across the specimen width. This means estimations of crack growth in the centre of the specimen by using observed crack sizes at the edges are justified.

## **4.7 Conclusions**

In this chapter, crack growth in carbon steel, flat plate specimens heated to temperatures below the creep range and exposed to repeat one-dimensional thermal shocks (RTS) with cold water has been experimentally examined. Qualifying the effects of stress concentrators, dissolved oxygen levels and primary loads on the initiation and growth of cracks has featured heavily. The following conclusions can be made from the work.

### **4.7.1 Crack Initiation**

The stress amplitude developed at the surface of the flat plate specimen during RTS has been successfully related to the number of cycles to small crack initiation. The method for calculating the stress amplitude has been refined, using the ASME Boiler and Pressure Vessel Code, Section VIII, Division 2 (1998) *fatigue data* curves as a guideline. Use of an elastic stress analysis alone provided results that showed the ASME data to be conservative. Removal of this conservatism was achieved by applying an elastic-plastic Neuber notch pseudostress analysis. The effects of dissolved oxygen levels, primary loads and stress concentrators on the time taken for crack initiation are summarised below:

1. Effect of D.O. levels: Variations in dissolved oxygen levels between 8ppm and 2ppm in the cooling water have little or no effect on the times taken for crack initiation in a notched specimen.
2. Effect of primary loads: A steady state mechanical load of 90MPa has little or no effect on time to crack initiation in a notched specimen.
3. Effect of stress concentrators: Various notches cut into the face of the specimen lead to rapid crack initiation. There seems to be a limit to the effect of the notches, and increasing the severity of a notch beyond a certain level results in no additional reduction in time to initiation. The limit of this effect occurs for the so-called "worst case notch" and corresponds to a fatigue notch factor of around 5.0. Other geometric discontinuities such as machining marks and welds also accelerate initiation, however assumption that these act as worst case notches can be conservative.



#### **4.7.2 Crack Growth**

Crack growth in a flat plate due to repeated thermal shock from temperatures below the creep range occurs in two main stages. The first is restricted to the region near the shocked surface where plastic strains are dominant. This area behaves as though it is subjected to high strain fatigue (HSF). Crack growth accelerates rapidly in this region. The second stage of growth occurs when the crack leaves the HSF region and enters an area that behaves in a predominantly elastic manner. Linear elastic fracture mechanics (LEFM) can be used to describe growth in this region. A reducing stress intensity factor field due to the thermal shock means that all cracks in this area tend eventually towards crack arrest. Conclusions relative to each region are summarised below.

##### **4.7.2.1 High strain fatigue region**

In this region, the thermal shock crack growth rate accelerates. This crack growth acceleration can be explained by a linear relationship relating the crack growth rate ( $da/dN$ ) to crack depth ( $a$ ):

$$\frac{da}{dN} = B.a - C \quad [4.1]$$

Where  $a$  is the crack length,  $B$  is a constant characteristic of the thermal shock loading and  $C$  is an allowance for the presence of a notch. A value for  $B$  of approximately  $4.5 \times 10^{-4}$  cycles<sup>-1</sup> was found through analysis of the experimental results. This value compares favourably with published data obtained from Marsh (1981) and Skelton (1982) for stainless steels exposed to elevated temperature HSF with a plastic strain range of  $1.0 \times 10^{-3}$ .

The depth of this crack acceleration region is related to the size of the plastic zone developed at the surface during the thermal shock. Consequently, the more severe the shock, the deeper the HSF region extends. Dissolved oxygen levels in the cooling water and primary mechanical loads having the following effects:

1. Effect of D.O. levels: Variations in dissolved oxygen levels between 8ppm and 2ppm in the cooling water have little or no effect on crack growth rates in the HSF region.
2. Effect of primary loads: Variations in the primary load have little or no effect on the crack growth equation [4.1]. They do however extend the plastic zone, increasing the size of the HSF region and hence the depth to which cracks accelerate.

#### 4.7.2.2 Elastic crack growth region

In this region, the specimen behaves elastically and the crack growth rate is generally found to decelerate. Unfortunately, modelling the crack growth in this region seems to be much more complex than in the HSF zone. The elastic stress intensity factor is a suitable parameter to correlate the crack growth, however environmental interactions and the effects of steady state mechanical loads mean that a single law cannot be developed to describe growth in the region. A number of models have been developed to explain data trends. The most encompassing of these models seems to be that of Gabetta et al (1990), can explain trends in the data:

$$\frac{da}{dN} = C(\Delta K)^m + \tau \frac{da}{dt}_{SCF} \quad [4.5]$$

Where  $C$  and  $m$  are constants dependent on the true corrosion fatigue (TCF) crack growth rate,  $\tau$  is the rise time of loading (ie the duration of the thermal shock) and  $da/dt_{SCF}$  is the stress corrosion fatigue crack growth rate, which is different for each material-environment condition. A stress intensity factor limit also exists ( $\Delta K_c$ ), below which, the SCF crack growth rate is zero.

$$\Delta K_c^2 = \frac{1}{\alpha_{ASCR}} \cdot \sigma_y E \tau \cdot \frac{1-R}{1+R} \frac{da}{dt}_{SCF} \quad [2.18]$$

Where  $\alpha_{ASCR}$  is a constant dependent on the active surface creation rate (ASCR) of the material-environment combination and  $R$  is the minimal to maximum cyclic stress intensity factor ratio.

Because stress intensity factor levels in a flat plate due to thermal shock decrease with crack depth, the tendency for all cracks is towards arrest. However, as [4.5] and [2.18] describe, the rate at which this deceleration occurs is highly dependent on environmental and primary load considerations. Effects of dissolved oxygen levels in the cooling water and primary mechanical loads are summarised below.

1. Effect of D.O. levels: An increase in dissolved oxygen levels in the cooling water from 2ppm to 8ppm results in an increase in crack growth rate for cracks with large  $R$ -ratios ( $R > 0.3$ ).
2. Effect of primary loads: The addition of a steady state primary load to a specimen exposed to thermal shock results in a stress intensity factor profile that produces an increase in the  $R$ -ratio with an increase in crack depth. The increase in  $R$ -ratio seems to create an increase in the crack growth rate, however only if the increase is encountered while the crack is accelerating or growing at a steady rate. This is thought to be an effect of loading history produced during RTS.

#### 4.7.2.3 Combined growth law

A combined law for explaining RTS crack growth through both the HSF and LEFM regions can be proposed from this work. The model is divided into two sections, the first when crack growth is inside the plastic zone close to the specimen surface and the second is the elastic region that is encountered at further depths. For crack growth in the plastic zone, a linear acceleration of crack growth rate with crack depth is suggested (equation [4.1]). For crack growth outside the plastic zone, the crack growth rate (typically of a decelerating nature) is predicted using a LEFM growth law such as that proposed by Gabetta et al (1990) (equation [4.5]).

The crack depth at which the crossover between the HSF and LEFM growth laws occurs is a critical parameter. Because crack growth will accelerate until this depth is reached, a crack of "crossover depth" can be assumed to rapidly appear during RTS loading. The smaller this depth is, the less chance that appreciable crack growth can occur in the ensuing LEFM region. This is verified by the experimental crack growth rate data, summarised in figure 4.16. At this stage, the crossover depth is seen to be roughly equal to the cyclic plastic stress depth, developed by the thermal shock and steady state stresses. Unfortunately, an estimation of the cyclic plastic depth can be quite complicated, particularly if local stress concentrators are present. Subsequent development of the combined growth law as described here would be well served by developing simple methods to estimate this depth.

#### **4.7.2.4 Crack growth mechanisms**

Observations of the crack growth geometry and fracture surface after test completion have led to a few conclusions about the mechanisms present during crack growth. In the HSF region, the presence of a large amount of oxide product visible along the crack sides indicate that environmental interaction is heavy in this area. Determining the mechanism of growth in this area is complicated by the corrosion damage to the crack surface.

Crack growth appearance in the elastic region depends on the presence of primary loads. Where these loads are high, producing a large  $R$ -ratio, a fair amount of corrosion product is still visible. This is consistent with the assumption that stress corrosion fatigue (SCF) is occurring by the mechanism of anodic dissolution. For cracks with smaller  $R$ -ratios or when cyclic stress intensity factors are below the SCF threshold  $\Delta K_c$ , true corrosion fatigue (TCF) is occurring and crack growth seems to be predominantly transgranular, with a sharp, twisted crack path. Hydrogen embrittlement could be accepted as a possible mechanism for the accelerated TCF growth in this region.

## **Chapter 5:**

### **Transient and Geometry Effects**

#### ***5.1 Introduction***

The aim of this chapter is to provide theoretical techniques for estimating the effect of altering shock duration and component geometry during a thermal shock transient. Data obtained from closed form analytical solutions, finite element techniques and experimental testing are used to assist the investigation. Where applicable, guidelines for crack initiation and growth are included. Development of these guidelines will assist in providing better techniques for predicting and extending lifetimes of complex components exposed to repeated thermal shock.

#### ***5.2 Effect of Quench Duration on Crack Growth***

As discussed in Chapter 2, thermal shock stresses are transient in nature. This implies that a full stress analysis of a component requires representation of the stress as a function of both position and time. It can be the case that the maximum stresses developed in separate parts of a component exposed to a thermal shock are developed at separate times. For this reason, a crack growth analysis performed on a component exposed to a thermal shock based on the stress profile for only one point in time may be very inaccurate. This section will attempt to provide a better understanding of how transient stresses affect the crack growth in a number of simple geometries.

##### **5.2.1 Flat Plate Exposed to a One-Dimensional Thermal Shock**

To best analyse the effects of altering thermal shock duration on crack growth, one of the less complicated geometry scenarios is analysed first. Namely a flat plate with an edge crack exposed to a one-dimensional thermal shock. The geometry is shown in figure 5.1.

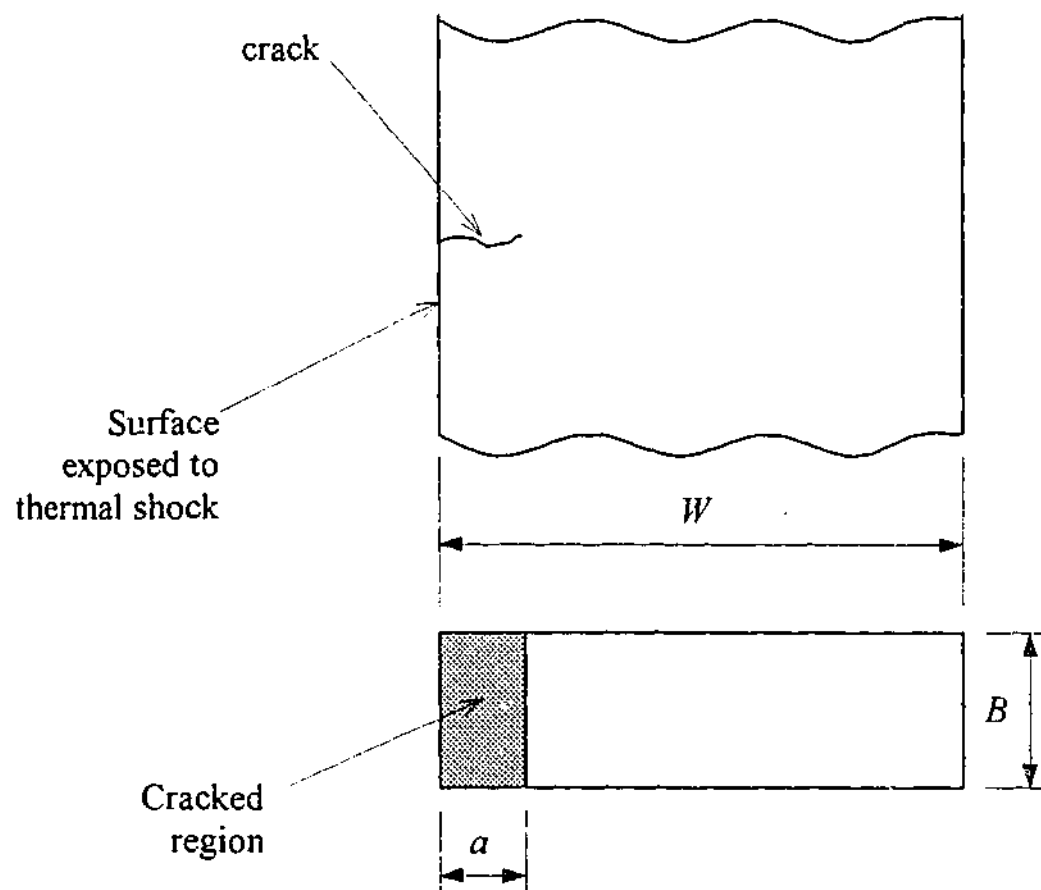


Figure 5.1: Flat plate geometry with edge crack exposed to 1-d thermal shock.

The following basic assumptions are made for the analysis:

1. Plate is exposed to a 1-d down-shock (ie sudden reduction in temperature along one surface)
2. Material properties ( $E$ ,  $\alpha$ ,  $k$ ,  $\rho$ ,  $c$ ) are independent of temperature.
3. Maximum temperature is below the creep range.
4. Stress levels and crack/specimen dimensions are such that the stress intensity factor adequately describes the stress field surrounding the crack tip.
5. No steady state primary loads.

These assumptions have been made to simplify the analysis somewhat and to keep it consistent with the experimental work completed in Chapter 4.

### 5.2.1.1 Stress intensity factor solutions

As shown in Chapter 4, the stress intensity factor can be used to model long crack growth rate data through modified Paris law equations such as equation [4.5]. Therefore, observations of how changes in thermal shock duration affect the stress intensity factor profiles will be directly applicable to crack growth rate predictions.

Based on finite element and analytical simulations, non-dimensional charts of expected stress intensity factor distributions for different quench lengths and heat transfer coefficients have been produced for the one-dimensional shock of flat plates.

The finite element package LUSAS (r13) was used for the transient thermal analysis. All models were 2-dimensional and used 4 sided, 8-node elements. The temperature profiles thus developed were converted to stresses and stress intensity factors using the techniques outlined in section 3.4.3. The resulting plots for the finite element approaches are shown in figures 5.2-4 for surface heat transfer coefficients of infinity, 10,400 W/m<sup>2</sup>K and 3,000 W/m<sup>2</sup>K respectively (the latter being values thought to be typical of those developed during thermal shock in industry, see Chapter 3, section 3.4.6). Analytical results using the solution by Zhi-He and Yiu-Wing (1995) were found to be within 1% of the infinite heat transfer case and are not reproduced here. The following definitions are to be used in conjunction with the charts.

$\Delta K_I / \Delta K_o =$  Non-dimensional change in thermal shock stress intensity factor;  
 $\Delta K_o = E\alpha\Delta T \cdot \sqrt{W}/q$  ( $E$  = Youngs Modulus,  $\alpha$  = coefficient of thermal expansion,  $\Delta T$  = thermal down-shock size,  $W$  = specimen depth,  $q = 1$  for plane stress,  $1-\nu$  for plane strain).

$\kappa t / W^2 =$  Non-dimensional thermal shock time;  $\kappa = k/\rho c$  ( $t$  = time or length of shock,  $c$  = specific heat,  $\rho$  = density,  $k$  = thermal conductivity).

$a/W =$  Non dimensional crack length ( $a$  = crack length).

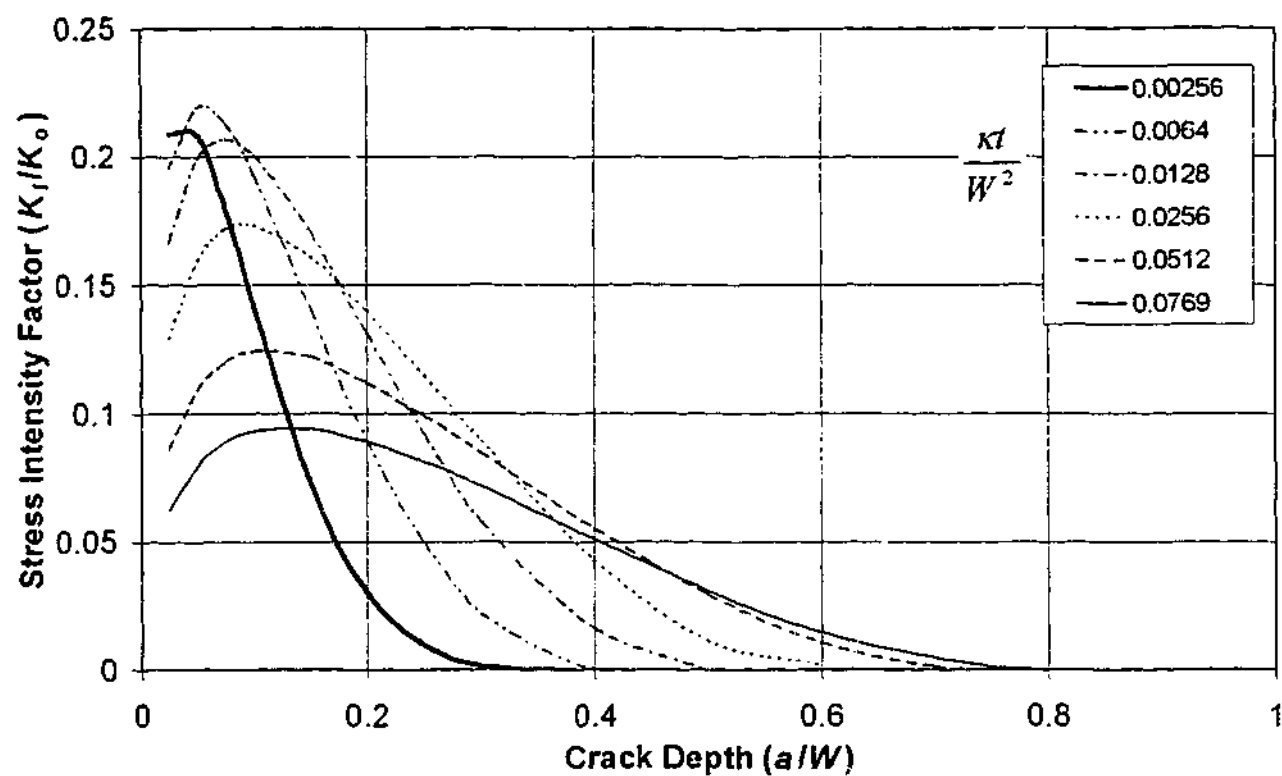


Figure 5.2: Effect of shock duration on theoretical stress intensity factor distributions for a flat plate of depth " $W$ " with a crack of depth " $a$ " exposed to one-sided thermal shock with infinite heat transfer coefficient.

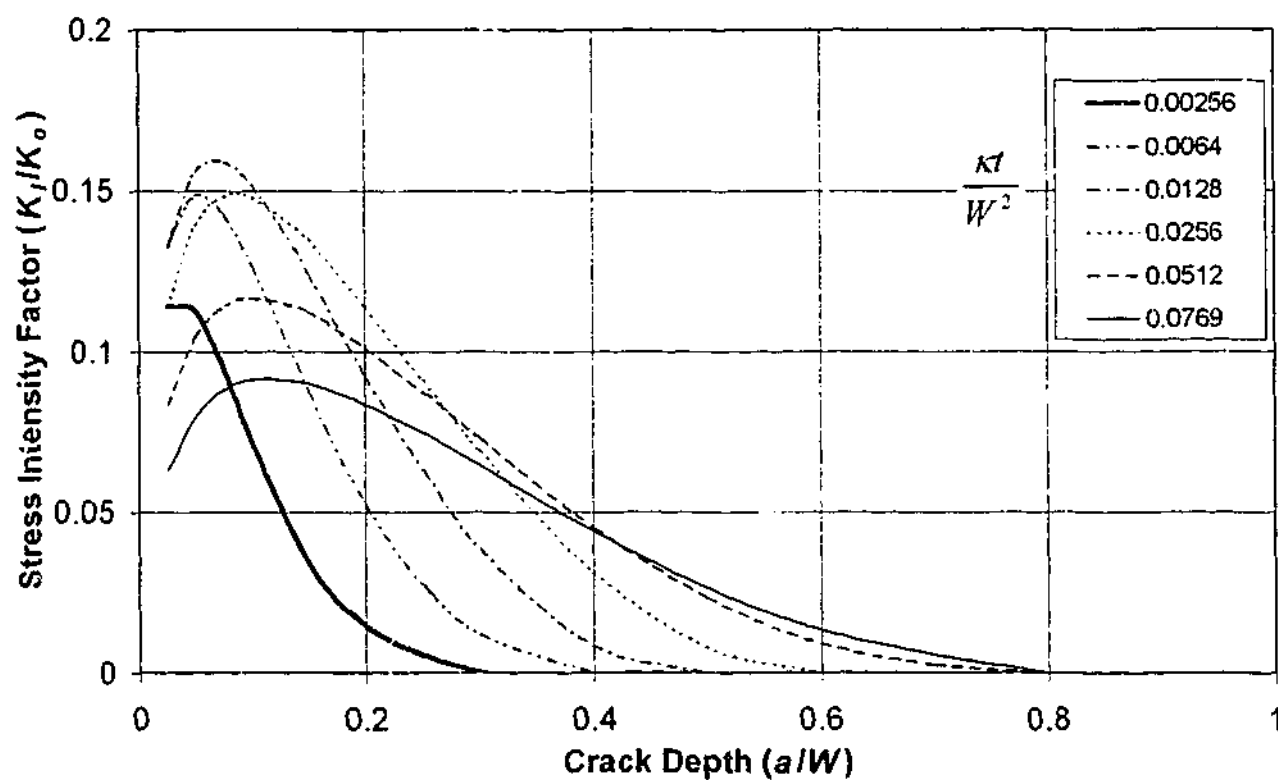


Figure 5.3: Effect of shock duration on theoretical stress intensity factor distributions for a flat plate depth " $W$ " with a crack of depth " $a$ " exposed to one-sided thermal shock with heat transfer coefficient  $10,400 \text{ W/m}^2$ .



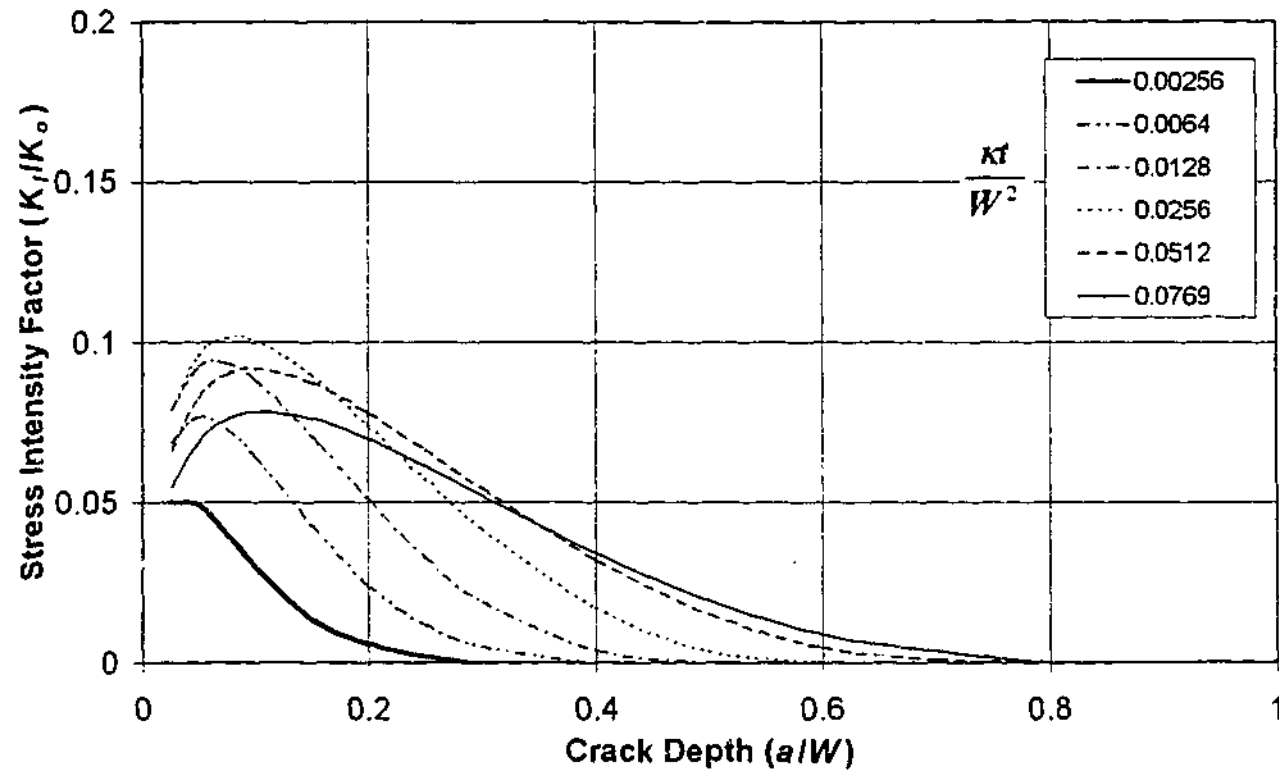


Figure 5.4: Effect of shock duration on theoretical stress intensity factor distributions for a flat plate depth " $W$ " with a crack of depth " $a$ " exposed to one-sided thermal shock with heat transfer coefficient  $3,000 \text{ W/m}^2$ .

#### 5.2.1.2 Discussion of stress intensity factor profile charts

Figures 5.2 to 5.4 show a complex interaction between crack length, quench duration and the developed stress intensity factor. In general however, the longer the crack, the longer the shock duration required to develop the maximum stress intensity factor.

A comparison of figures 5.2-5.4 shows that a reduction in heat transfer coefficient at the shocked surface from infinity to  $10,400 \text{ W/m}^2\text{K}$  and then to  $3,000 \text{ W/m}^2\text{K}$  has a large effect on the stress intensity factor developed for shorter cracks. For longer cracks and longer shock times, this difference is reduced, becoming almost negligible for crack lengths in excess of  $a/W = 0.5$ . For a conservative analysis, it would be advised that the infinite heat transfer chart be used (Fig. 5.1) for any case when the heat transfer coefficient is unknown.

In his analysis of transient thermal shock, Skelton (1983) suggests that only the maximum tensile stress be required to analyse crack growth. He labels the time at which this

maximum stress occurs as the "transition time" and equates it roughly to when the temperature of the back (non-shocked) face of the component of thickness  $W$  begins to fall. Experimental evidence presented by Skelton suggests that the transition time can be estimated for a variety of steels by the following empirical equation based on work by Biot (1961):

$$t = 0.088 \frac{W^2 \rho c}{k} \quad [5.1]$$

It is worth noting that this equation is independent of the surface heat transfer coefficient. The validity of this equation for roughly predicting the time of the onset of back surface cooling has been verified by finite element analysis for each of the heat transfer coefficients used in figures 5.2 to 5.4.

Re-arranging [5.1] and substituting  $\kappa$  for  $k/\rho c$  gives us a non-dimensional time ( $t'$ ) at which Skelton's estimate for maximum crack growth occurs for all cases:

$$t' = \frac{\kappa t}{W^2} = 0.088 \quad [5.2]$$

Looking at figures 5.2 to 5.4 and continuing the trends that are visible from increasing  $\kappa t/W^2$ , it would seem that an analysis at only  $\kappa t/W^2=0.088$  would underestimate the maximum stress intensity factors developed at crack depths of  $a/W < 0.4$ . This underestimation increases with increases in heat transfer coefficient. Consequently, a crack growth rate based on the "maximum stress" transit time could be seriously underestimated, particularly for short cracks.

Figure 5.5 shows the non-dimensional time  $t'$  at which a maximum stress intensity factor is developed as a function of crack length based on the data from figures 5.2-5.4.

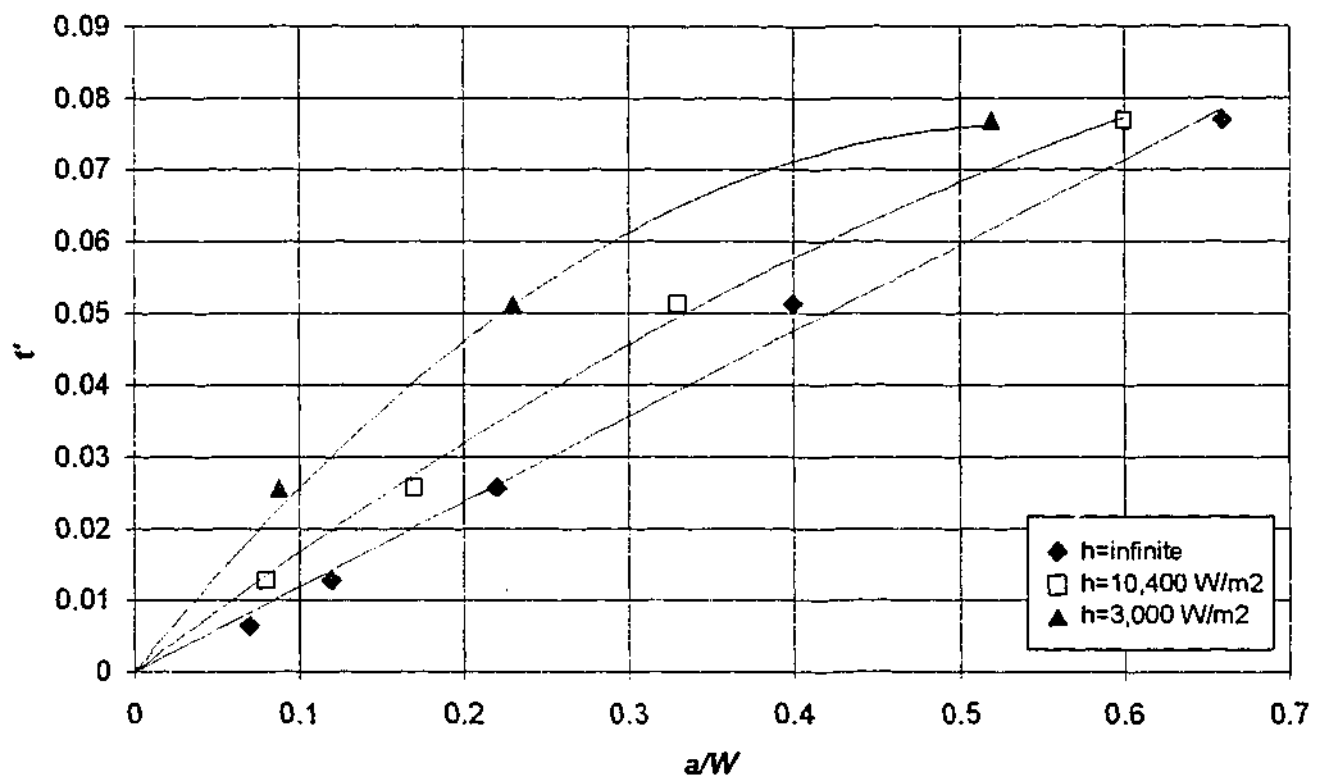


Figure 5.5: Non-dimensional time ( $t'$ ) for development of maximum stress intensity factors during 1-d thermal shock of an edge cracked plate. Results shown for individual heat transfer coefficients ( $h$ ), along with curves of best fit.

Unlike Skelton's suggestion that maximum crack growth estimates can be based on data from a single point in time, figure 5.5 shows that the time at which the maximum stress intensity factor (and hence growth) is developed at the tip of a crack is a function of the crack length. In addition, it is clear that it is also a function of the heat transfer coefficient, A decrease in the coefficient increases the time required to develop the maximum stress intensity factor. For the case of an infinite heat transfer coefficient, this time can be estimated by a linear relationship:

$$t' = 0.12 \left( \frac{a}{W} \right) \quad [5.3]$$

Substitution shows that equation [5.3] gives a smaller value of  $t'$  than suggested by [5.2] for all cracks with  $a/W < 0.7$ .

### 5.2.1.3 The use of transient stress intensity factor charts to predict crack arrest

The use of charts such as figures 5.2 to 5.4 stretches beyond prediction of stress intensity factors for certain crack lengths and shock times. It can also (and probably more usefully) be used to predict crack "arrest". To do so, first a critical stress intensity factor range ( $\Delta K_{Ia}$ ) must be found below which crack growth is at an acceptably small rate. Growth relations such as equation [4.5] can be used to complete this. This critical stress intensity factor is then substituted in figures 5.2-5.4 as  $\Delta K_I$ .  $\Delta K_o$  is calculated to coincide with the case under investigation, as is the non-dimensional time. A horizontal line is then drawn from the appropriate value of  $\Delta K_{Ia}/\Delta K_o$  until it crosses the appropriate non-dimensional time plot, the position at which this cross-over occurs gives the predicted crack arrest depth.

Figure 5.6 shows an example of using the charts to predict crack arrest in the manner given above. A thermal shock of non-dimensional time 0.0256, having a non-dimensional arrest stress intensity factor ( $\Delta K_{Ia}/\Delta K_o$ ) of 0.1 is plotted, showing a predicted crack arrest depth ( $a/W$ ) of ~0.23. Note that increasing the shock duration any longer would have no affect on the crack growth, as the stress intensity factor only decreases at this depth as the shock continues.

Using these charts to predict crack arrest is highly dependent on the value of crack growth rate at which arrest is said to have occurred. This is, in turn, dependent on what an acceptable amount of crack growth is. For example, assuming cracks less than 1mm are not critical for a component exposed to 10,000 thermal shocks in its lifetime, any concern over crack growth rates below  $10^{-7}$ m per cycle would seem to be conservative. Therefore, before use of these charts is made, a thorough analysis of the loads on a component needs to be completed so an estimate of allowable crack size can be determined ( $a_{allow}$ ). Then with an estimate of the number of thermal shock cycles a component will be subjected to ( $N_{lifetime}$ ), the crack growth limit  $da/dN$  can be determined from the following:

$$\frac{da}{dN} = \frac{a_{allow}}{N_{lifetime}} \quad [5.4]$$

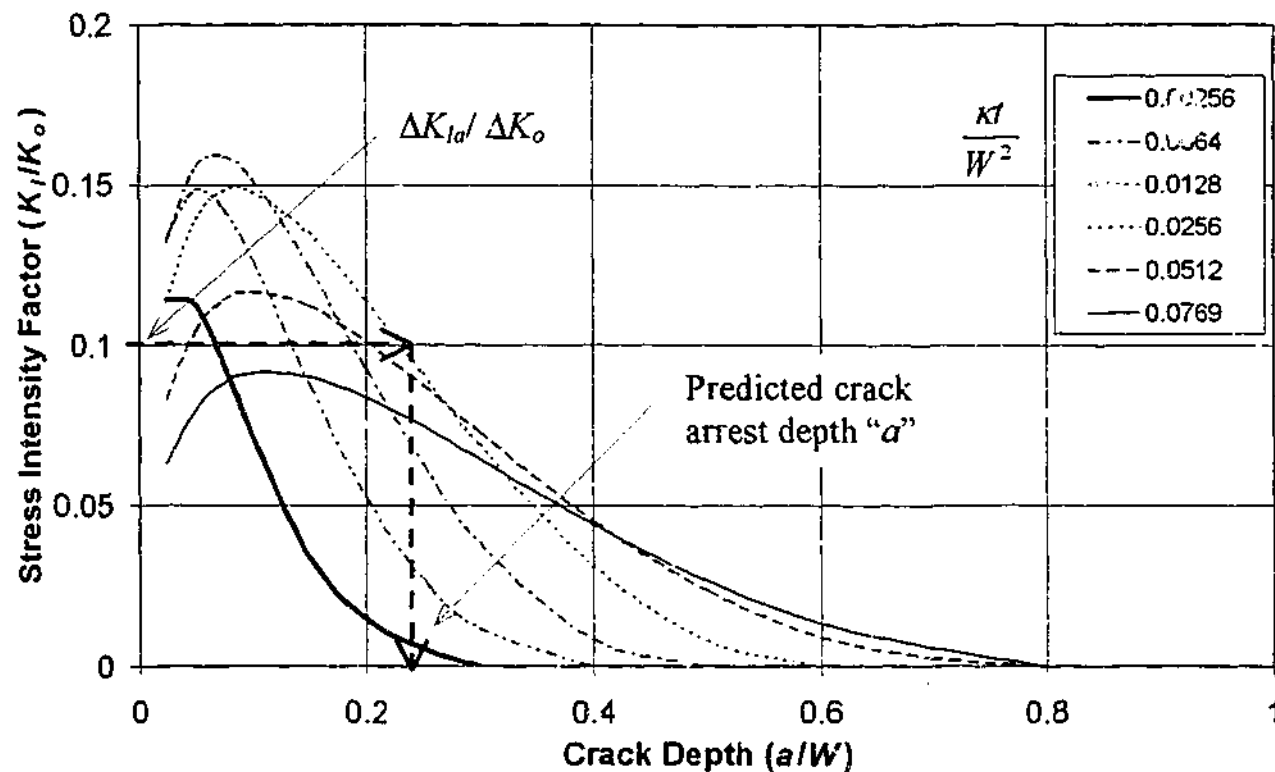


Figure 5.6: Example of using non-dimensional transient thermal shock stress charts to predict crack arrest depth for a shock of non-dimensional time  $(\kappa t/W^2) = 0.0256$ .

With this crack growth rate limit in mind, a suitable stress intensity factor limit ( $K_{Ia}$ ) can be selected. This limit will need to take into account primary loads and environmental interactions as outlined in the experimental work of Chapter 4.

#### 5.2.1.4 Limitations

The analysis outlined in the previous section has been completed for a flat plate geometry with a straight edge crack (ie constant crack depth across the specimen thickness). Application of these results to other crack and specimen geometries is not recommended, as stress profiles will not necessarily be equivalent. Although, in the case of a semi-elliptical (or thumbnail) crack in a flat plate (see figure 5.7), use of the charts presented in this chapter should be conservative, as stress intensity factors will be reduced for the same stress profile. In section 5.2.2 the consequences of changing the geometry to that of a hollow cylinder will be discussed.

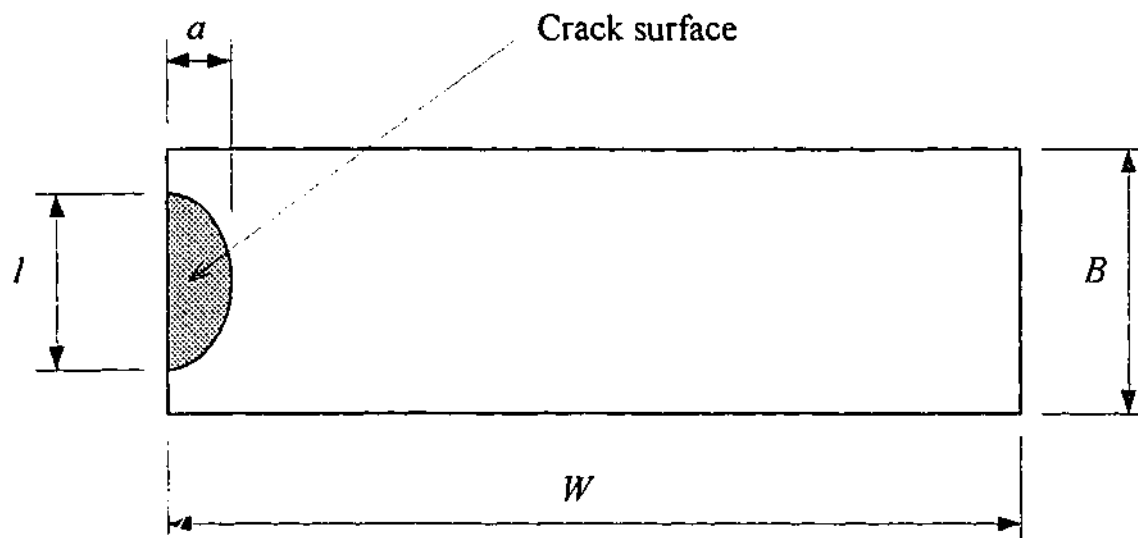


Figure 5.7: Semi-elliptical (thumbnail) crack in a flat plate.

#### 5.2.1.5 Application to experimental results

In this section, the analytical transient analysis conducted in the previous sections will be used to analyse the "arrest" of cracks observed in the experimental work (see Chapters 3 and 4). In this sense, arrest will be defined as the crack length obtained when crack growth rates were reduced to below  $1 \times 10^{-7}$  m/cycle. Using equations [4.7] and [4.8], which are based on the experimental results of figure 4.14, the following equations for the cyclic "arrest" stress intensity factor ( $\Delta K_{la}$ ) are obtained:

$$1 \times 10^{-7} = 5.28 \times 10^{-16} (\Delta K_{la})^{5.89} \quad \text{for } \Delta K < \Delta K_c \quad [5.5]$$

$$1 \times 10^{-7} = 5.28 \times 10^{-16} (\Delta K_{la})^{5.89} + 7 \times 10^{-7} \quad \text{for } \Delta K > \Delta K_c \quad [5.6]$$

Where  $\Delta K_c$  is defined by [4.6], reproduced below:

$$\Delta K_c^2 = 1.45 \times 10^3 \frac{1-R}{1+R} \quad [4.6]$$

It so happens that equation [5.6] is insoluble, meaning that for  $\Delta K > \Delta K_c$ ,  $\Delta K_{la} = \Delta K_c$ . This gives us:

$$\Delta K_{Ia} = 25 \text{ MPa}\sqrt{\text{m}} \quad \text{for } R < 0.38 \quad [5.7]$$

$$\Delta K_{Ia} = \sqrt{1.45 \times 10^3 \frac{1-R}{1+R}} \quad \text{for } R > 0.38 \quad [5.8]$$

Following the procedure given in the previous section, test results using the test data from Chapter 4 were placed into table 5.1. Most of the data in the table is self-explanatory. Clarification on the selection of  $\Delta T$  should be made though. Selecting this value from the test results is particularly hard, as the surface temperature changes during quenching (as discussed in Chapter 3, section 3.4.6). For simplicity, the temperature change has been selected as the set temperature prior to shock commencement, less  $100^\circ\text{C}$  (corresponding to the boiling point of water at which most of the heat transfer is expected to occur).

Connecting the locus of all maximum values of the transient curves (see figures 5.2 – 5.4) with non-dimensional times less than or equal to that used in the experiments simplifies the comparison and gives an “analytical arrest solution” curve. Anything to the left of this curve indicates conservatism, as “arrest” depth is over-predicted.

Fig. 5.8 gives an idea of the conservatism delivered by assuming an infinite heat transfer coefficient in this approach and how the variables affect it. The presence of primary load is a clear source for reducing the conservatism, particularly as the analytical solution was developed for no primary load. It is probably recommended that the effect of primary load be covered by the generation of separate arrest curves. Note that the prediction curve based on heat transfer data of  $10,400 \text{ W/m}^2\text{K}$  is much closer to the experimentally observed results.

Table 5.1: Experimental data for use in crack "arrest" prediction.

$\Delta T$ (°C)	$P$ (MPa)	$R$	$\Delta K_o$ (MPa√m)	$\Delta K_{Ia}$ (MPa√m)	$\Delta K_{Ia}/\Delta K_o$	$A$ (mm)	$a/W$
270	90	0.47	165.2	22.8	0.14	9.3	0.14
270	90	0.45	165.2	23.5	0.14	8.5	0.13
270	0	0	165.2	25	0.15	5.4	0.08
270	0	0	165.2	25	0.15	6.7	0.10
250	90	0.34	156.2	25	0.16	6.5	0.10
250	0	0	156.2	25	0.16	5.2	0.08
230	90	0.33	147.3	25	0.17	6.1	0.94
230	90	0.31	147.3	25	0.17	5.3	0.82

Notes: -  $\Delta T$  is taken as the maximum temperature less 100°C.

-  $a$  is the depth of crack measured at observed "arrest".

-  $R$  is measured at the crack arrest depth " $a$ ".

The following additional test data have been used in the construction of the table:

Specimen depth;	$W = 65\text{mm}$
Duration of shock;	$t = 7\text{s}$
Material specification;	AS 1548-7-430R
Material properties;	$E = 200\text{GPa}$ , $\alpha = 1.2\text{e-}5$ and $\rho = 7800\text{kg/m}^3$ , $k = 500\text{W/m}$ , $C_p = 500\text{KJ/kg.K}$ , (giving $\kappa t/W^2 = 0.021$ ).
Crack "arrest" growth rate;	$1 \times 10^{-7} \text{ m/cycle}$



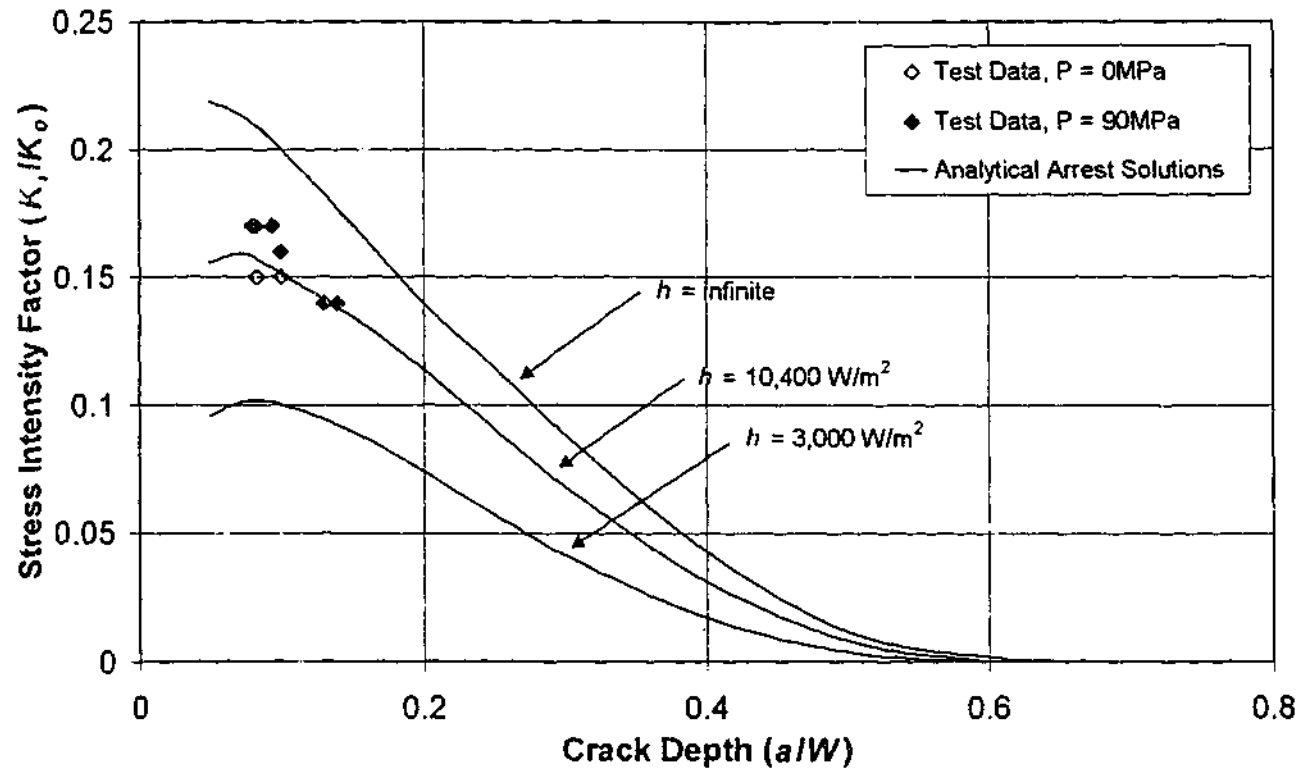


Figure 5.8: Comparison of analytical solutions for crack "arrest" depth with experimental results for non-dimensional time of 0.021.

### 5.2.2 Application to Hollow Cylindrical Geometry

The stress intensity factor profiles produced by a thermal transient are heavily dependent on the geometry of the component under investigation. Consequently, care needs to be taken when applying the results from the previous section to another geometry. In thermal power station plant, large proportions of the components exposed to thermal shock are cylindrical in shape. This section takes a brief look at how a cylindrical geometry behaves during thermal shock transients.

Stress intensity factor analysis of a cracked cylinder is much more complex than that of a through thickness cracked flat plate. First to consider is the crack shape and direction. Generally, cracks in cylinders are found to run around the circumference or along the longitudinal axis of the pipe (corresponding to the directions of principal stress in a cylinder under pressure). In addition, the crack itself may not run the full circumference or length of the cylinder. In fact, it is more common for the flaw to be semi-elliptical (or thumbnail) in shape. Secondly, the geometry of the cylinder itself requires greater definition than that of a flat plate, with both diameter and wall thickness being variable. Summarising, the large

number of possible crack and cylinder geometry combinations makes general analysis of a cracked cylinder very difficult, as each case generates a unique stress intensity factor profile.

Figures 5.10 and 5.11 show the "worst-case" transient stress intensity factor plots for internal annular circumferential and full-length axial cracks respectively in a long hollow cylinder exposed to an internal down-shock. These figures were constructed using temperature profile data obtained from a finite element model assuming an infinite heat transfer on the internal surface of the cylinder. Temperature profiles were then converted to circumferential and axial stress profiles using the following equations (taken from Timoshenko and Goodier, 1982):

$$\sigma_{\theta} = \frac{\alpha E}{1-\nu} \frac{1}{r^2} \left( \frac{r^2 + R_i^2}{R_o^2 - R_i^2} \int_{R_i}^{R_o} T(r) r dr + \int_{R_i}^r T(r) r dr - T(r) r^2 \right) \quad [5.9]$$

$$\sigma_z = \frac{\alpha E}{1-\nu} \left( \frac{2}{R_o^2 - R_i^2} \int_{R_i}^{R_o} T(r) r dr - T(r) \right) \quad [5.10]$$

where  $\sigma_{\theta}$  and  $\sigma_z$  are the circumferential and axial thermal stresses produced in the wall of the cylinder and  $T(r)$  is the temperature profile in the wall as a function of radius. Other nomenclature is defined in figure 5.9.

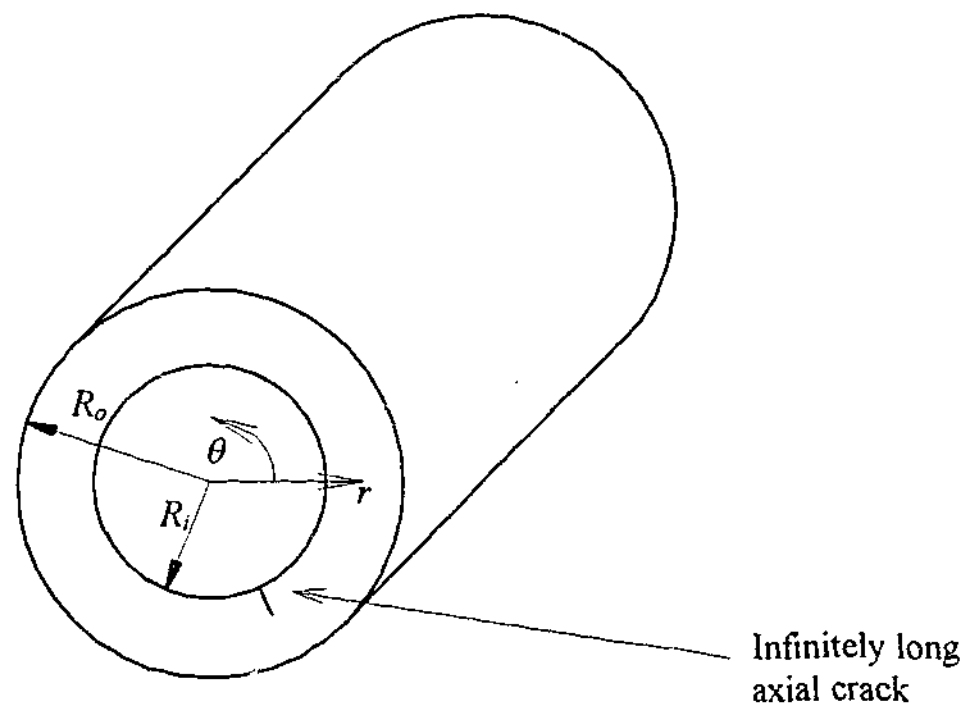


Figure 5.9: Geometry definitions for hollow cylinder.

The main reason for these differences in stress intensity factor profiles for different geometries seems to emanate from the stress profiles generated during a thermal transient. A comparison of the two profiles for a hollow cylinder and a flat plate is given in figure 5.8. This figure shows the stresses for a flat plate and cylinder of wall thickness 0.1m exposed to a 20s thermal shock. The ratio of inside to outside radius for the cylinder is 0.8.

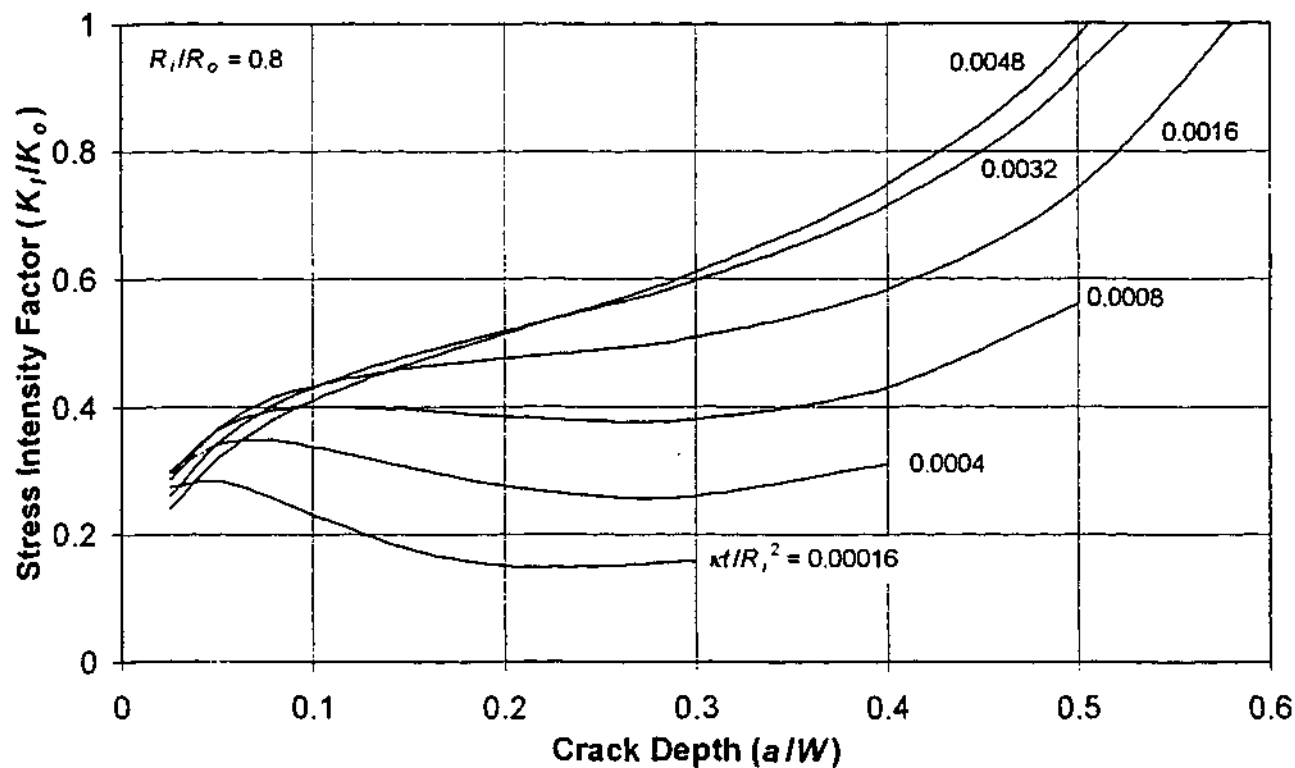


Figure 5.10: Stress intensity factors for an internal axial crack in a hollow cylinder exposed to internal thermal down-shock for different non-dimensional times.

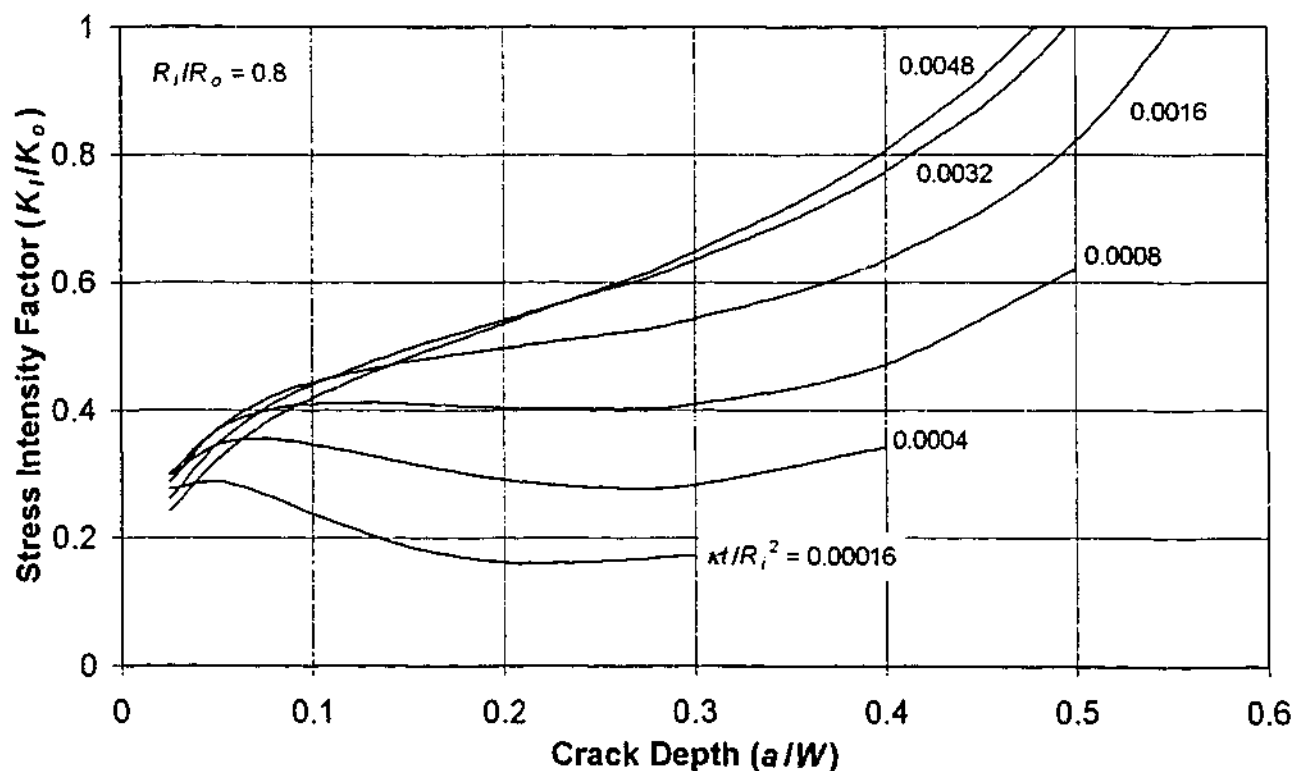


Figure 5.11: Stress intensity factors for an internal circumferential crack in a hollow cylinder exposed to internal thermal down-shock for different non-dimensional times.

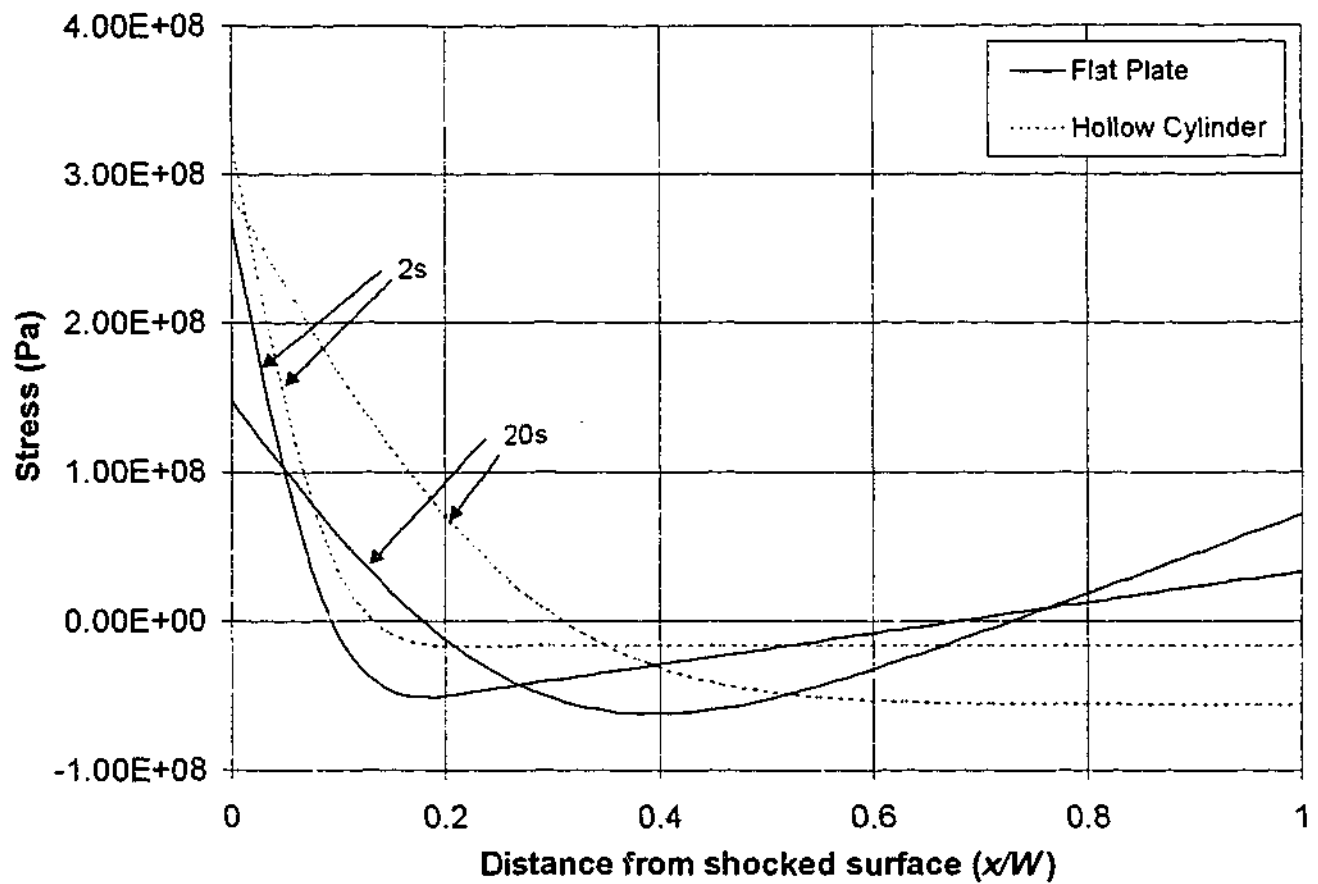


Figure 5.12: Effect of geometry on transient stresses developed during thermal shock. Hollow cylinder and flat plate geometries, for thermal shocks of 2s and 20s.

The difference in profiles is due to the additional restraint to bending provided by the cylindrical geometry that is not present in the flat plate. This restraint is because of the axisymmetric nature of the geometry and allows the development of a bending moment that is not present in the flat plate. As is shown in figure 5.12, this bending moment increases with shock duration.

The stress intensity factor profiles represented in figures 5.10 and 5.11 are, as mentioned previously, the worst case scenario (i.e. infinitely long cracks and large inside to outside radius ratio -  $R_i/R_o$ ) for a cracked cylinder. Most other combinations of flaw shape and radius ratio provide more conservative stress intensity factor profiles tending towards those developed for the flat plate scenario.

Methods for developing stress intensity factor profiles during thermal shock in a cylinder that take into account the effect of cylinder and crack geometry are provided by Olivera and Wu (1987) and Kotousov and Price (1998). A general observation that can be taken from a combination of these works and that presented here relates to the effect of the cylinder thickness on crack growth. For the case of identical thermal shock loading and non-dimensional crack depth ( $a/W$ ), a thin cylinder (ie a large ratio of inside to outside radius -  $R_i/R_o$ ) will produce a larger stress intensity factor than for a thick cylinder. This may help explain observed examples of thin tubes exposed to thermal shock growing through thickness wall cracks while thicker walled specimens tend towards crack arrest. This observation should be approached with care however as it only applies to infinitely long axial or full circumference cracks, both of which are uncommon in industry.

### 5.3 Cracking at Corners Exposed to Thermal Shocks

Cracking at corners in industrial components exposed to thermal shock loads is quite common. In thermal power plant, examples of cracking at corners can be found in equipment such as economiser inlet headers, feedwater heater boxes and waterwall tubing. Typically, cracking occurs at both internal and external corners as depicted in figures 5.13 and 5.14.

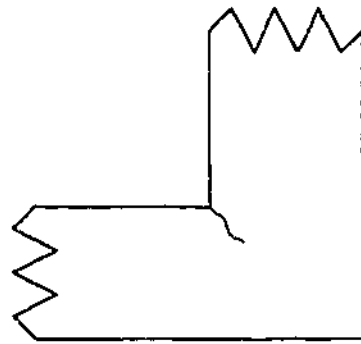


Figure 5.13: Corner cracking at an internal corner, eg. feed-water heater box.

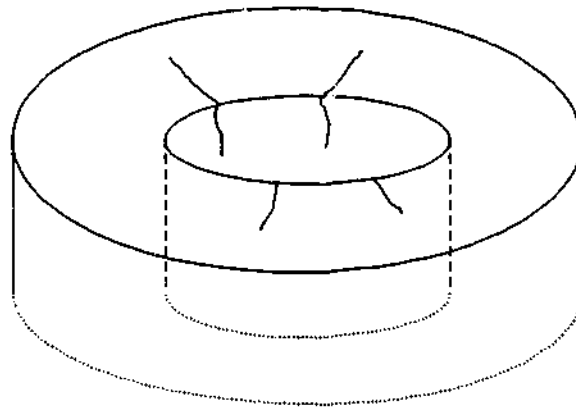


Figure 5.14: Corner cracking at an external corner, eg. tube penetration into a thick walled header.

The distribution of stresses at these corners is a complex phenomenon that has been actively investigated for various loading and boundary conditions for more than 40 years. Examples of relevant work include Williams (1952), Gross and Mendelson (1971), Portela and Allabadi (1991) and Seweryn and Molski (1996) all of which are primarily analytical

analyses concerned with steady state mechanical loading. In the research presented in this section, work on geometry effects has similarly been limited to analytical solutions and finite element analyses. The aim being, to determine the effect a corner has on the stress distribution generated during thermal shock. A proper understanding of the important factors in describing the stress distributions will allow conclusions relating to modifications of operating conditions and design of equipment to reduce the likelihood of failure due to thermal shock. The remaining analysis of corner geometry has been divided into two parts. The first concentrates on dealing with corners of included angle greater than  $180^\circ$  (i.e. internal corners) and the second looks at angles less than  $180^\circ$  (i.e. external corners).

### **5.3.1 Vertex Angles Greater than $180^\circ$ (Internal Corners)**

#### **5.3.1.1 Introduction**

As described in the initial work by Williams (1952), a corner with free edges and a vertex angle greater than  $180^\circ$  (see figure 5.15) produces a singular stress field in the vicinity of the apex. The presence of this singularity increases the likelihood of failure occurring in this position when the geometry is subjected to external loads (static or cyclic). An Airy stress function approach to describing the stresses in the vicinity of the corner was originally proposed in Williams' work. Here, the minimum real eigenvalues ( $\lambda$ ) of the eigen equation [5.11] are proposed as a measure of the strength of the singularity at the corner. Note that this equation is dependent only on the vertex angle  $2\gamma$ .

$$\sin(\lambda 2\gamma) = \pm \sin(2\gamma)\lambda \quad [5.11]$$

Numerical approaches to geometries producing a stress singularity are usually based on finite element analyses, where special elements fill the core region of the corner. The asymptotic behavior of the stress field at the corner must agree with the eigenvalues of the exponent  $\lambda$  from [5.11]. Coefficients of the singular components of the stress field are often called "generalised stress intensity factors" and given the same meaning as the stress intensity factor in linear elastic fracture mechanics. Some examples of this type of analysis



can be found in the literature (Lin and Tong, 1980, Groth 1988). The application of the boundary element method is also described in Portela and Aliabadi (1991).

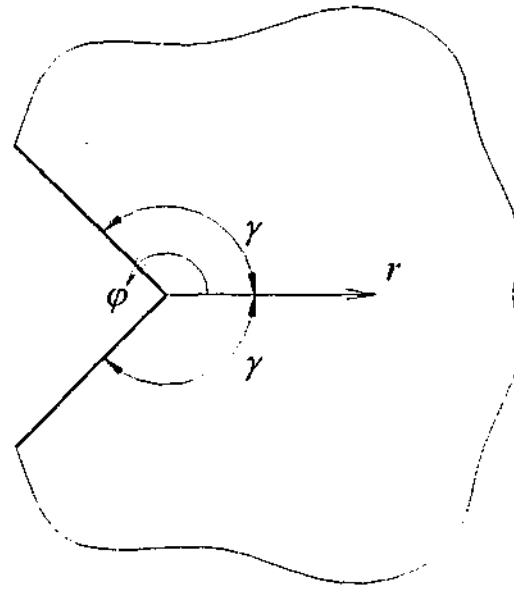


Figure 5.15: Corner with vertex angle ( $2\gamma$ ) greater than  $180^\circ$  and coordinate system.

Transient thermal shock or thermo-mechanical loading of a corner has, as yet, not received as much attention in literature as pure static mechanical loading. Experimental investigations on the thermal shock of pre-notched specimens, such as that completed by Marsh (1981) and Vitale and Beghini (1991) (and the work in Chapters 3 and 4 of this thesis to some extent), usually ignore any temperature disturbance caused by the notch and apply a crack approximation for the stress field. From a theoretical point of view such approximation is valid only if the opening angle is zero (a vertex angle of  $360^\circ$ ). However, as mentioned by Lazzarin and Tovo (1996), in practical use such an expression is acceptable, as long the value for  $\lambda$  determined from [5.11] is similar to that determined for a crack, namely  $\frac{1}{2}$ .

The stress fields generated by a thermal shock in a corner of vertex angle greater than  $180^\circ$  are rather complex. Only for an angle of  $180^\circ$  (half-space or flat plate) and  $360^\circ$  (semi-infinite cut or crack) can analytical or semi-analytical solutions be obtained. In all other cases the temperature and stress fields can normally only be investigated numerically.

However, as was mentioned previously in this section the stress field has a singularity component. This, combined with a rather complex type of loading (such as thermal shock) can generate significant numerical errors.

In the remainder of this section, the singular stress field developed in a corner subject to thermal shock is analysed using analytical solutions and FE techniques. Based on the approach of Lazzarin and Tovo (1996), the effect of adding a radius to the corner is also discussed at the end of the section.

### 5.3.1.2 Asymptotic stress field

In the current work, a corner with the vertex angle  $2\gamma$  as shown in figure 5.15 was considered. The corner is initially held at a constant temperature  $T_0$  and at time  $t=0$ , is suddenly changed to temperature  $T_1$  along the free surfaces. Following the work outlined by Kotousov, Price and Kerezsi (2000), and using the asymptotic Williams' solution, the singular elastic stress field in the corner can be written in the polar coordinates  $(r, \varphi)$  with an origin in the apex of the corner as:

$$\sigma_r = \frac{-E\alpha\Delta T}{q} \left(\sqrt{\kappa t}/r\right)^{1-\lambda} H_r(\varphi, \lambda) \quad [5.12]$$

$$\sigma_\varphi = \frac{-E\alpha\Delta T}{q} \left(\sqrt{\kappa t}/r\right)^{1-\lambda} H_\varphi(\varphi, \lambda) \quad [5.13]$$

$$\tau_{r\varphi} = \frac{-E\alpha\Delta T}{q} \left(\sqrt{\kappa t}/r\right)^{1-\lambda} H_{r\varphi}(\varphi, \lambda) \quad [5.14]$$

and in the case of the plane strain ( $\varepsilon_z=0$ ),

$$\sigma_z = -E\alpha\Delta T + \nu(\sigma_r + \sigma_\varphi) \quad [5.15]$$

$\Delta T = T_1 - T_0$  is the severity of the thermal shock,  $\alpha$  is the linear coefficient of the thermal expansion,  $\kappa$  is the coefficient of diffusivity ( $k/\rho c$ ),  $E$  is the Youngs modulus,  $q=1$  for plane stress,  $q=1-\nu$  for plain strain ( $\nu$  is Poisson's ratio), and  $\lambda$  is the minimal real eigenvalues obtained from the corresponding characteristic equation [5.11]. These eigenvalues are plotted in figure 5.16 for vertex angles between  $180^\circ$  and  $360^\circ$ .

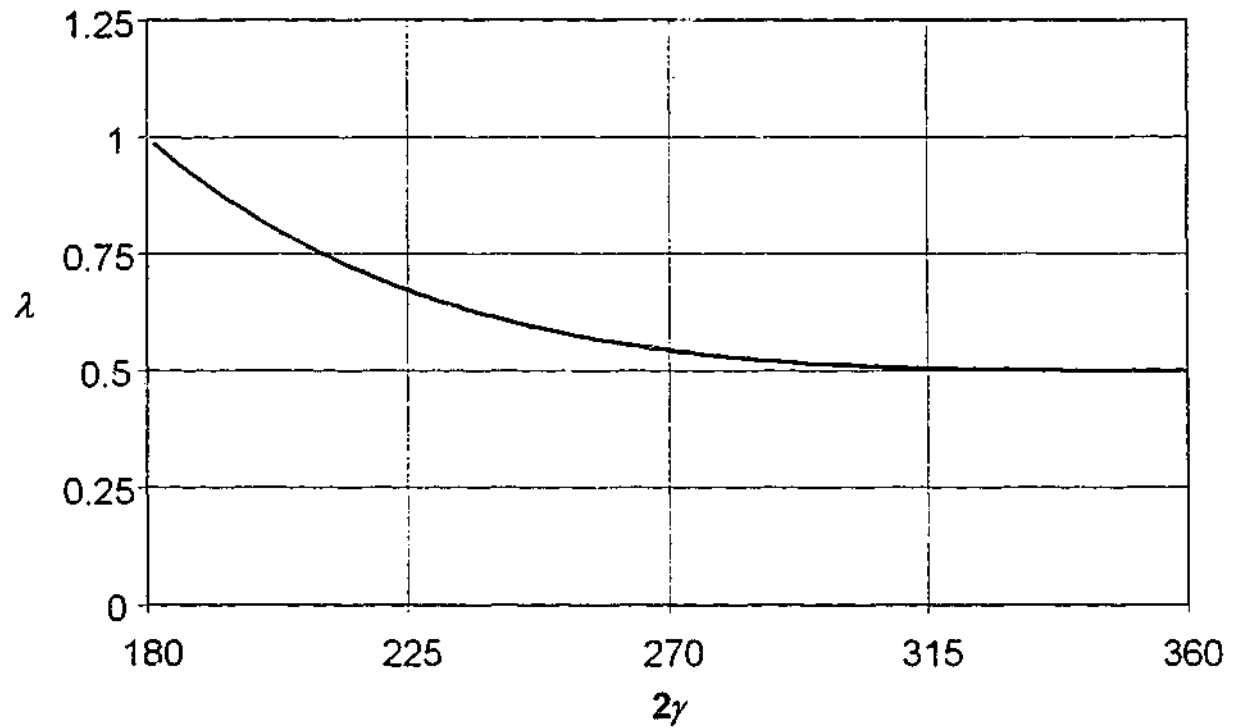


Figure 5.16: Relationship between the real part of the minimum eigenvalue  $\lambda$  and vertex angle  $2\gamma$  from equation [5.11].

$H_r(\varphi, \lambda)$ ,  $H_\varphi(\varphi, \lambda)$  and  $H_{,\varphi}(\varphi, \lambda)$  are non-dimensional functions of the angle  $\varphi$  and  $\lambda$  (which in turn makes them a function of  $\alpha$ ). Examples of these functions, as given in the work of Seweryn and Molski (1996), are reproduced below:

$$H_r(\varphi, \lambda) = \frac{1}{C_1} \left\{ \frac{3-\lambda}{1+\lambda} \cdot \cos[(1+\lambda)\gamma] \cdot \cos[(1-\lambda)\varphi] + \cos[(1-\lambda)\gamma] \cdot \cos[(1+\lambda)\varphi] \right\} \quad [5.16]$$

$$H_r(\varphi, \lambda) = \frac{1}{C_1} \{ \cos[(1+\lambda)\gamma] \cdot \cos[(1-\lambda)\varphi] - \cos[(1-\lambda)\gamma] \cdot \cos[(1+\lambda)\varphi] \} \quad [5.17]$$

$$H_r(\varphi, \lambda) = \frac{1}{C_1} \left\{ \frac{1-\lambda}{1+\lambda} \cdot \cos[(1+\lambda)\gamma] \cdot \sin[(1-\lambda)\varphi] - \cos[(1-\lambda)\gamma] \cdot \sin[(1+\lambda)\varphi] \right\} \quad [5.18]$$

where  $C_1 = \cos[(1+\lambda)\gamma] - \cos[(1-\lambda)\gamma]$

Using definitions given by Gross and Mendelson (1972), the mode one generalised stress intensity factor ( $K_I$ ) for the corner can be written as:

$$K_I = \sqrt{2\pi} \lim_{\varphi=0, r \rightarrow 0} r^{1-\lambda} \sigma(t, r, \varphi) = -\sqrt{2\pi} \frac{E\alpha\Delta T}{q} (\sqrt{\kappa t})^{1-\lambda} H_\varphi(0, \lambda) \quad [5.19]$$

Because functions  $H_r(\varphi, \lambda)$ ,  $H_\sigma(\varphi, \lambda)$  and  $H_\varphi(\varphi, \lambda)$  are independent of the type and intensity of the loading, only two parameters are required to characterise the asymptotic stress at the corner, ie  $\lambda$  and  $K_I$ . While  $\lambda$  is a unique function of the vertex angle (see Fig.5.16), the generalised stress intensity factor ( $K_I$ ) needs to be defined for each set of loading conditions and is dependent on both the size and length of thermal shock.

### 5.3.1.3 Analytical solutions for generalised stress intensity factor $K_I$

As it has been noted above, the determination of the generalised stress intensity factor is a rather complex problem. Thus any analytical solutions that can be obtained are very valuable. As shown in the work by Kotousov, Price and Kerezsi (2000), the values for the two limiting cases:  $2\gamma = \pi$  (half-space) and  $2\gamma = 2\pi$  (semi-infinite cut) can be determined in this manner.

At  $2\gamma = \pi$  (half-space),  $\lambda=1$  (see Fig. 5.16) and in effect, the singularity vanishes. Using the definition of the generalised stress intensity factor [5.19] and substituting  $\lambda=1$ ,  $H_\lambda(0,\lambda)$  reduces to 1 giving:

$$K_I(\pi) = -\sqrt{2\pi} \frac{E\alpha\Delta T}{q} \quad [5.20]$$

For a vertex angle of  $360^\circ$  ( $\gamma=\pi$ ), the work by Kotousov and Price (1998) suggests:

$$K_I(2\pi) = 0 \quad [5.21]$$

From physical considerations it follows that the generalised stress intensity factor should be a continuous function of the vertex angle. So, a linear approximation of this function can be directly obtained as a line passing these two reference points. This can be visualised in figure 5.17 for the non-dimensional generalised stress intensity factor  $\bar{K}_I$  based on the solutions [5.23] and [5.24].

$$\bar{K}_I = \frac{K_I (\sqrt{\kappa})^{\lambda-1}}{-(E\alpha\Delta T)/q} \quad [5.22]$$

Giving:

$$\bar{K}_I(\pi) = \sqrt{2\pi} \quad [5.23]$$

$$\bar{K}_I(2\pi) = 0 \quad [5.24]$$

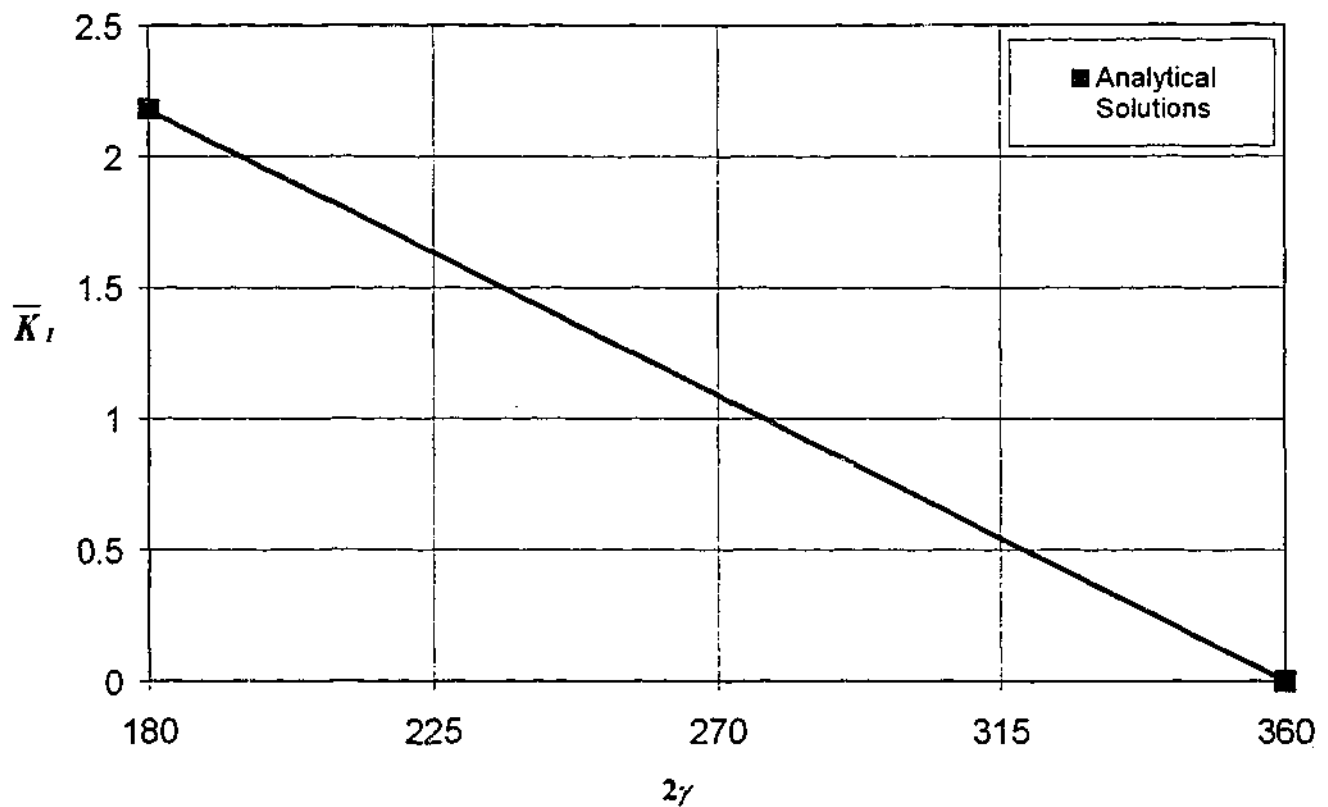


Figure 5.17: Non-dimensional generalised stress intensity factor ( $\bar{K}_I$ ) as a function of vertex angle ( $2\gamma$ ).

#### 5.3.1.4 Corner tip radius effect

In reality, equipment designed to operate under thermal shock condition (or any loading conditions for that matter) does not contain sharp corners. Instead, corners are machined with radii, (although sometimes these radii are quite small as machining permits). The singularity present at a sharp corner will produce extremely high stresses resulting in plastic deformation and perhaps leading to premature failure. A radius in the corner reduces the stresses and thus extends equipment life. The exact effect of adding a radius in terms of stress distributions is not self-evident and solutions developed for sharp corners can no longer be applied.

Over the years, great effort has been made to produce analytical expressions of stress fields when a radius is introduced into a sharp corner. With the aim to evaluate theoretical concentration factors, Neuber (1946) obtained an expression of the principal stress component along the axis of transverse symmetry for an open notch with a radius. More recently, Lazzarin and Tovo (1996) have reported a unified approach for the asymptotic

stress field similar to that of Linear Elastic Fracture Mechanics. According to this work, the stress field in close proximity to the notch can still be expressed in terms of the generalised stress intensity factor with a translation of the reference system on the focus of the ellipse that forms the notch.

When a corner tip radius greater than zero is considered, approximate solutions similar to those of linear elastic mechanics have been derived in a number of papers. On the basis of the modification of Williams' solution the maximum stress at the apex of the corner can be linked to the radius  $r$  as follows (Lazzarin and Tovo, 1996):

$$\sigma_{\max} = \frac{4K_I \delta^{\lambda-1}}{\sqrt{2\pi} [(1+\lambda) + \chi(1-\lambda)]} \quad [5.25]$$

where

$$\chi = -\frac{\sin(1-\lambda)\gamma}{\sin(1+\lambda)\gamma} \quad \text{and} \quad \delta = \frac{r \left( \gamma - \frac{\pi}{2} \right)}{\gamma}$$

For the limiting case of  $\gamma \rightarrow \pi$  the last equation produces the well-known Neuber formulae for the maximum stress in a crack-like notch:

$$\sigma_{\max} = \frac{2K_I}{\sqrt{\pi r}} \quad [5.26]$$

While these formulas have been obtained for infinite geometries, the work by Lazzarin and Tovo (1996) suggests their accuracy remains acceptable for finite configurations. However, for finite bodies, a size correction factor, involving the notch depth and the length of a ligament ahead of the notch tip can be introduced to increase the range of validity of the solution. An example of one such technique is given in the work completed by Xu et al (1995) for plates with various notches and holes exposed to uniform tensile stresses.

### 5.3.1.5 Numerical simulations

In the current work, the finite element simulation package ABAQUS (version 5.8-14) was used to simulate a thermal shock in an infinite corner with a radius. Transient results for the maximum stress produced at the root of the notch were obtained for a number of fixed angles over a range of notch radii and a fixed thermal shock size. In all models, 2 dimensional, 4-sided quadratic elements were used and stress analysis was limited to elastic.

In an attempt to model an infinite geometry, the basic dimensions of the finite element model were chosen to exclude the effect of boundary conditions on the temperature and stress fields. This can normally be achieved when the basic dimensions of the model are much larger than the diffusive length of the thermal shock ( $\sqrt{\kappa t}$ ). This becomes difficult when models with small notch radii are being analysed. This is due to the requirement that elements near the radius be small enough to produce valid temperature and stress solutions. Moreover, special conditions on the minimum allowed time increment must be imposed to ensure the convergence of the numerical procedure. According to Comini et al (1994), the following equation must be followed in order to ensure convergence of the transient solution for a 2-d finite element model with quadratic elements:

$$\Delta t \leq \sigma \frac{\rho c}{k} (\Delta L)^2 \quad [5.27]$$

$\Delta t$  is the time step,  $\Delta L$  is a dimension that is characteristic of the smallest element adjacent to the shocked surface, and  $\sigma$  is a constant dependent on the finite element model characteristics (in this analysis,  $\sigma=1/6$ ).

In accordance with the above discussion, the size of the smallest element in the finite element model is limited to approximately the size of the notch radius ( $r$ ). Substituting this into [5.27] and re-arranging allows for the generation of an equation relating the minimum



number of steps ( $N$ ) required in a solution in terms of the non-dimensional parameter  $\sqrt{\kappa t}/r$ .

$$N \geq \frac{1}{\sigma} \left( \frac{\sqrt{\kappa t}}{r} \right)^2 \quad [5.28]$$

These conditions and the size of the model required to simulate infinite boundary condition, lead to physical limitations on the maximum feasible non-dimensional time ( $\sqrt{\kappa t}/r$ ) which can be achieved during a numerical analysis. In the analyses presented here, this time was limited to around 6 (requiring around 200 time steps).

The finite element mesh developed for the analysis of a vertex angle ( $2\gamma$ ) of  $270^\circ$  is shown in figure 5.18. Figures 5.19 and 5.20 show, in turn, typical temperature distributions and associated stress distributions developed during the thermal shock. In this model, a  $100^\circ\text{C}$  thermal shock was applied to a specimen with material properties based on those of mild steel. In figure 5.20, stresses in the  $y$  direction are plotted, clearly showing a maximum that is several orders larger than the maximum stress that can be developed in a flat plate (ie.  $E\alpha\Delta T/q$ ). Figure 5.21 shows a magnified view of the stresses developed in the corner.

The plot of the non-dimensional maximum stresses ( $\bar{\sigma}_{\max}$ ) for the vertex angle  $2\alpha = 270^\circ$  obtained from a number of numerical analyses similar to those shown in figures 5.18-5.21 is presented in figure 5.22.

$$\bar{\sigma}_{\max} = \frac{\sigma_{\max}}{E\alpha\Delta T/q} \quad [5.29]$$

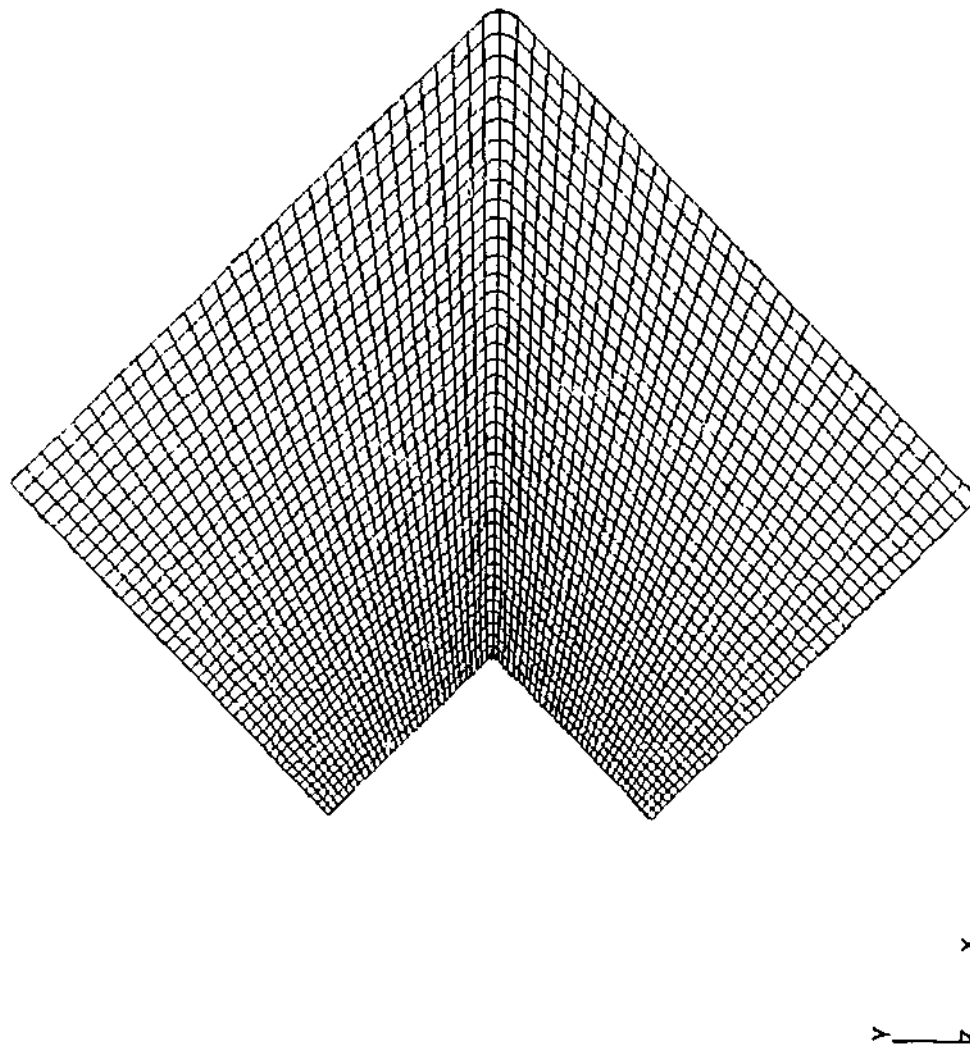


Figure 5.18: Finite element mesh for analysis of  $270^\circ$  corner with radius exposed to a symmetrical thermal shock.

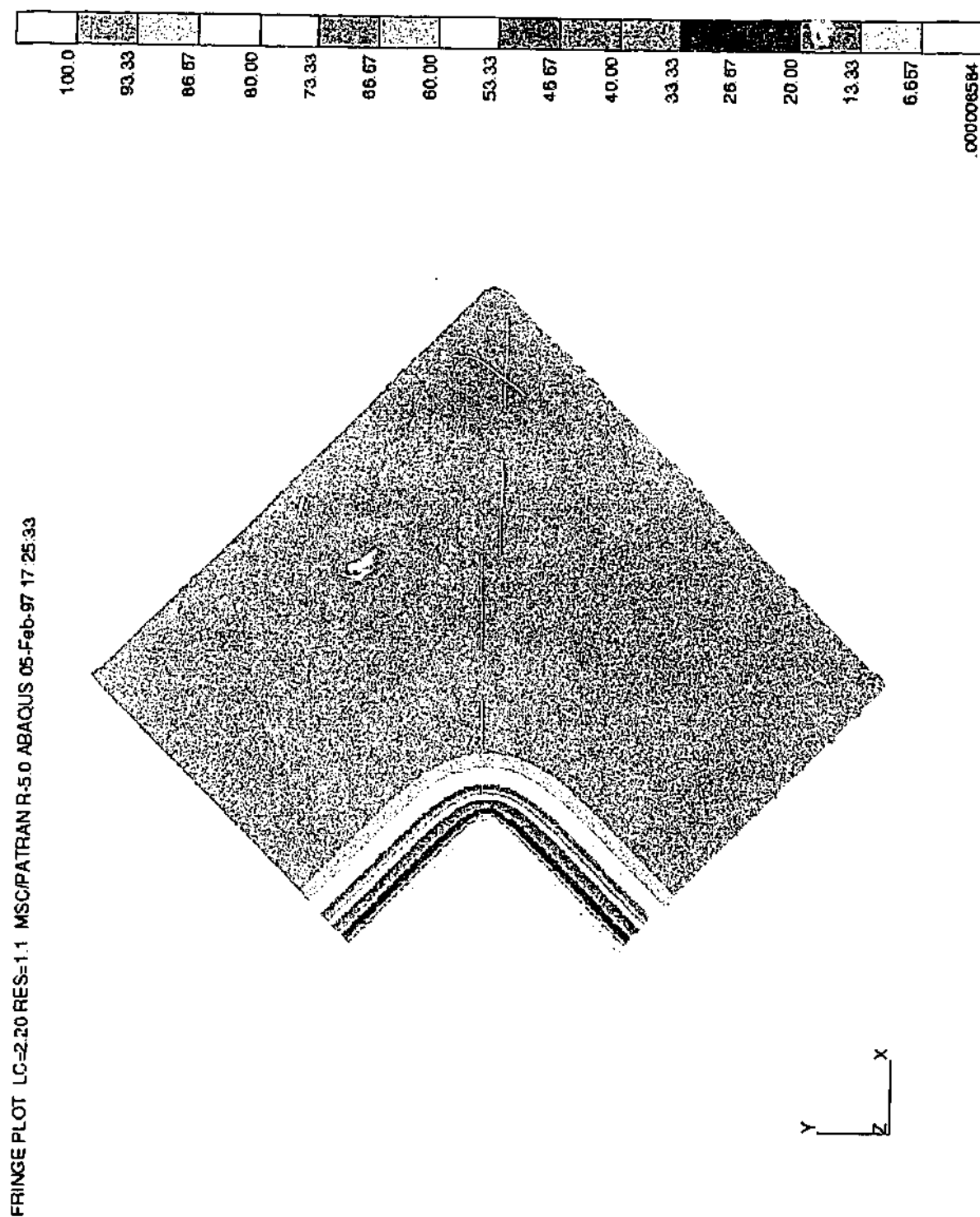
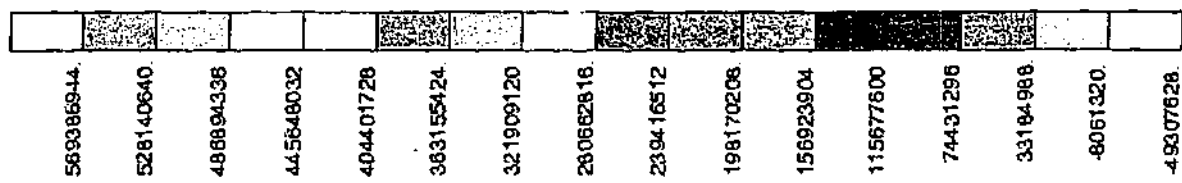


Figure 5.19: Typical temperature contours for a 270° corner with radius exposed to symmetrical 100°C thermal down-shock.



FRINGE PLOT LC=2.33 RES=1.1 (YY COMP) MSC/PATRAN R.5.0 ABAQUS 05-Feb-97 17:28.49

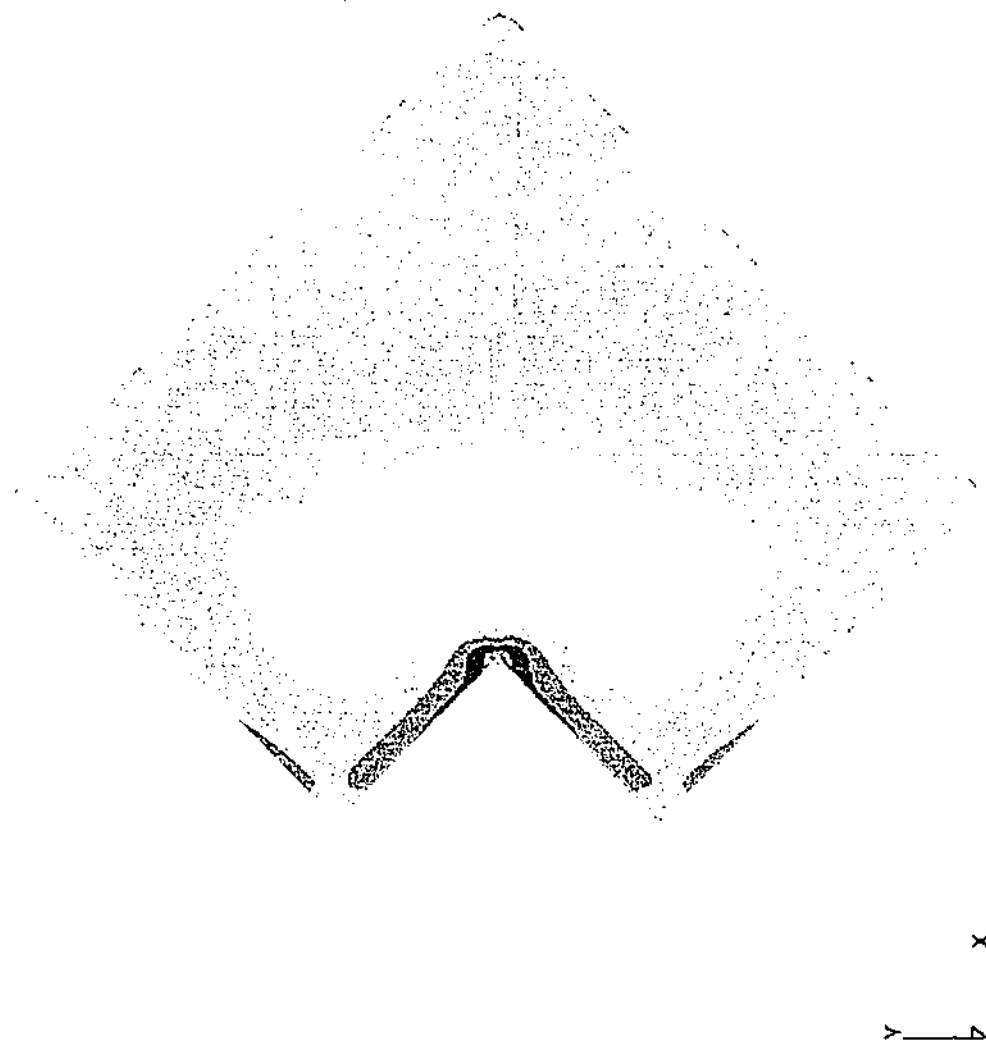


Figure 5.20: Stress contours for a 270° corner with radius exposed to a symmetrical 100°C thermal down-shock. Stresses are in the y-direction and are reported in Pa.

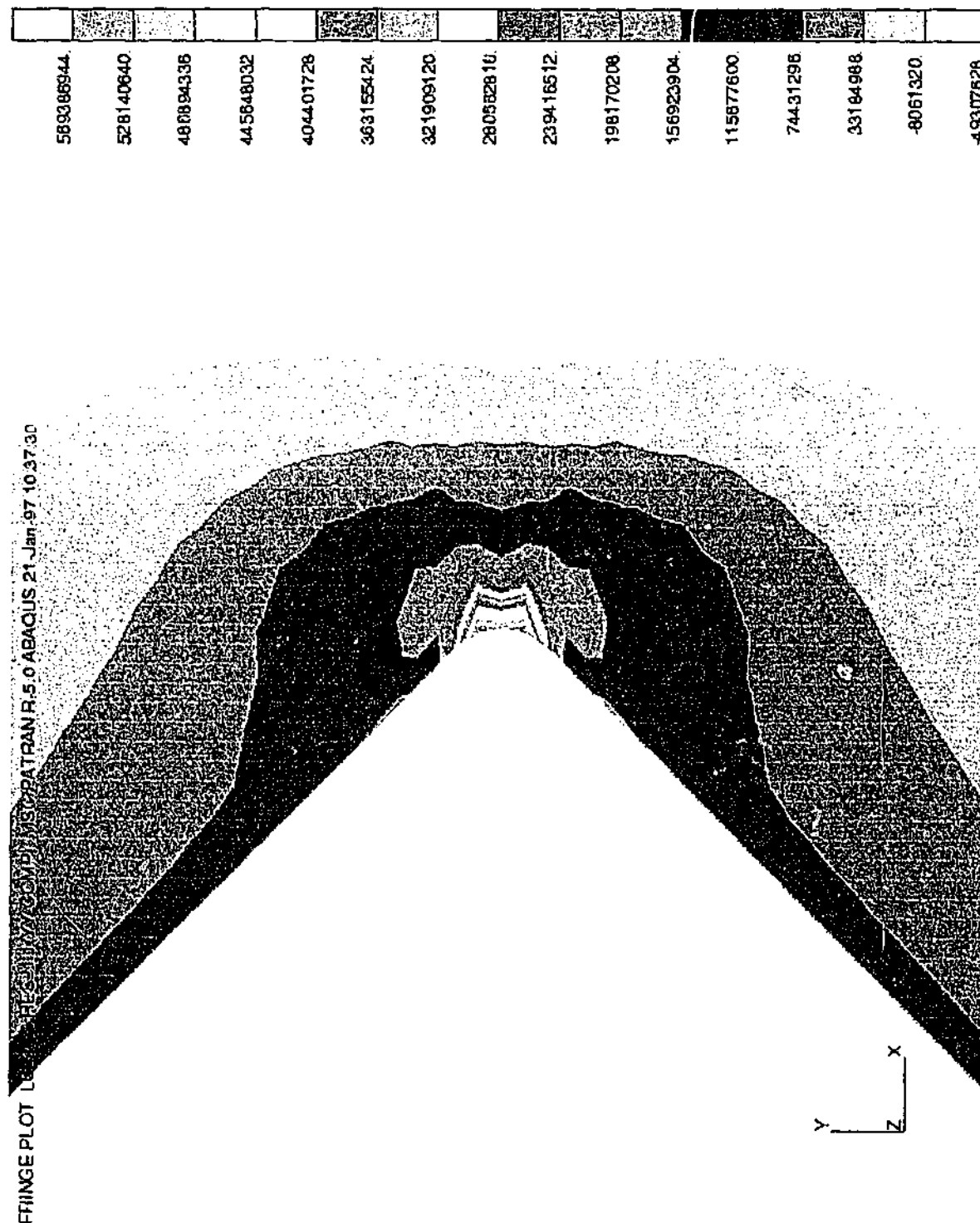


Figure 5.21: Close-up view of stress contours at the corner radius for a 270° corner exposed to a symmetrical 100°C thermal down-shock. Stresses are in the Y direction and reported in Pa.

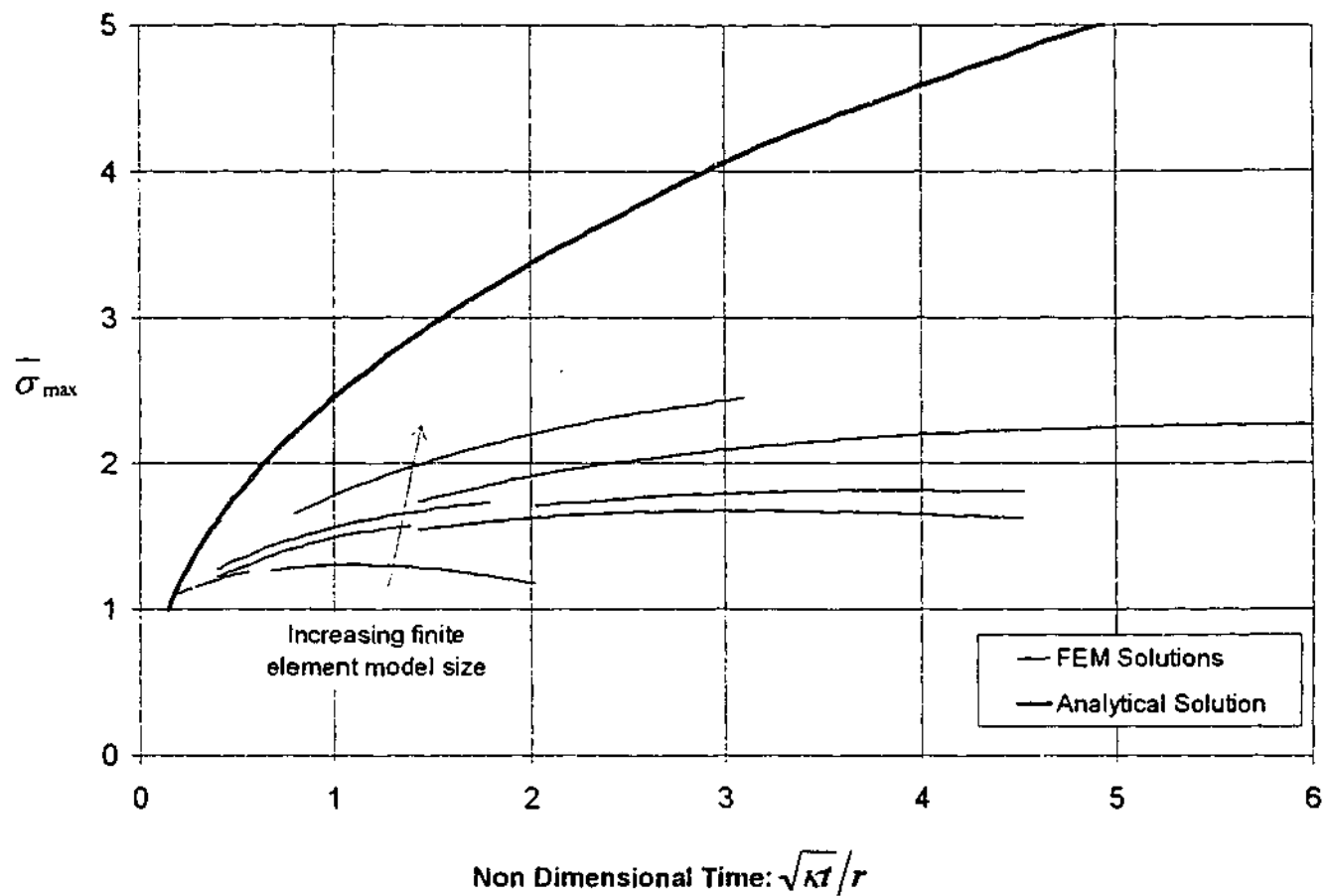


Figure 5.22: Maximum non-dimensional stress ( $\bar{\sigma}_{\max}$ ) produced at a corner with vertex angle  $2\gamma = 270^\circ$  and corner radius  $r$ , exposed to thermal shock of time  $t$ . Both analytical solution and solutions from several finite element models are plotted.

Also included on the figure is a theoretical solution for the notch root stress. The theoretical solution is obtained using [5.25] and the value for the generalised stress intensity factor from a linear interpolation as shown on Fig.5.17. As expected, the results show that for small values of  $\sqrt{\kappa t}/r$ , the maximum stresses are similar to those on the exposed surface far from the notch (ie. plane surface thermal shock stress). With increasing length of the thermal shock, the corner geometry contributes additional stresses, resulting in an overall increase in the maximum stress. The decreases in maximum corner stress, observed in some of the smaller finite element results for large values of  $\sqrt{\kappa t}/r$ , are due to the effect of boundary interference, which for finite structures is a real effect.

Comparing the analytical to numerical solutions, it seems that in all cases, the analytical solution provides an upper-bound solution for the corner stress. Increases in both the non-

dimensional time  $\sqrt{kt}/r$  and decreases in the size of the numerical model increase the difference between the analytical and numerical solutions. Production of any numerical results closer to the analytical solution were hampered by time and computing power constraints. These numerical results however give an idea of the effect of finite boundaries on the maximum stress developed in the corner. From these observations, some argument could be made for placing a maximum value of around 3.0 on  $\bar{\sigma}_{\max}$  in equation [5.29] when estimating finite boundary solutions.

### 5.3.1.6 Discussion

The analysis of a sharp corner alone, resulting in the generation of the generalised stress intensity factor shown in figure 5.17 is by itself rather meaningless. This is because the generalised stress intensity factor cannot be used as a characteristic for comparing the intensity of a thermal shock for corners of two differing angles. This is due to the varying level of stress singularity at each corner, which in turn is due to the relation of  $\lambda$  and  $\gamma$ . The generalised stress intensity factor can however be used to compare the strength of two shocks on a corner of the same vertex angle.

The most useful work from this analysis comes from the introduction of a radius to the corner. Not only does it more correctly model corners observed in industry but it also removes the effect of the singularity dependence on the vertex angle. Two major points of discussion can then be taken from the work completed on the stresses developed at a notch under symmetrical thermal shock. These are the effects of thermal shock length and vertex angle.

Analysing shock duration, it is clear from figure 5.22 that increasing the time a thermal shock lasts results in an increase in the stresses developed at the corner. This is unlike the case of a semi-infinite flat plate, where thermal shock stresses at the edge of the plate are constant over time. Reducing the notch radius in a corner has a similar effect to increasing time.

The analytical solution [5.25] developed in this section provides a method for determining the effect changing various features of a corner has on the maximum stress developed during a thermal shock transient. It also provides a bounding estimate of the value of stresses developed at the notch tip during a symmetric thermal shock. This is limited by the restriction that the dimensions of the corner under examination be suitably larger than the "diffusive length"  $\sqrt{\kappa t}$  to prevent any boundary effects. However even in the case of geometries with dimensions similar to the diffusive length, the analytical solution should still be able to be applied as a conservative bounding estimate by applying a maximum non-dimensional limit of around 3.0 to equation [5.29].



### 5.3.2 Vertex Angles of Less than 180° (External Corners)

The most common vertex angle of less than 180° that exist in component geometry are that of 90° corners. Figure 5.23 shows this geometry. Failure at a 90° corner is observed in one of the widespread examples of thermal fatigue failure in the steam power plant. This is the failure observed between tube connections on the inside surface of a header (Dooley, 1997 and Viswanathan, 2000). Figure 5.24 shows an example of this type of failure.

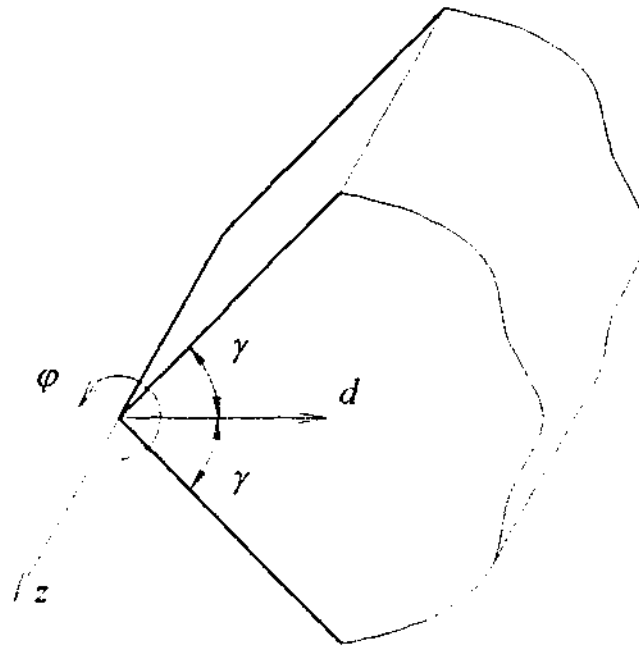


Figure 5.23: Corner with vertex angle ( $2\gamma$ ) less than 180° and coordinate system.

#### **5.3.2.1 Stress theory**

Why thermal shock cracks form at external corners is unclear. A number of analyses, both numerical and experimental have been conducted with the aim of determining possible crack growth from a 90° corner with a flaw subjected to thermal shock (Krolop et al, 1986, Yagawa and Ishihara, 1989 and Ng and Lee, 1997). In each of these cases however, a pre-existing flaw is assumed at the corner. How such a flaw would initially be developed and if thermal shock alone could be responsible is not discussed in these texts.

The application of Williams stress solutions [5.12 – 5.15], suggest that in the case of plane strain, it is possible to develop stresses in the z-direction that are larger than the radial and tangential directions by the influence of Poisson's strain.

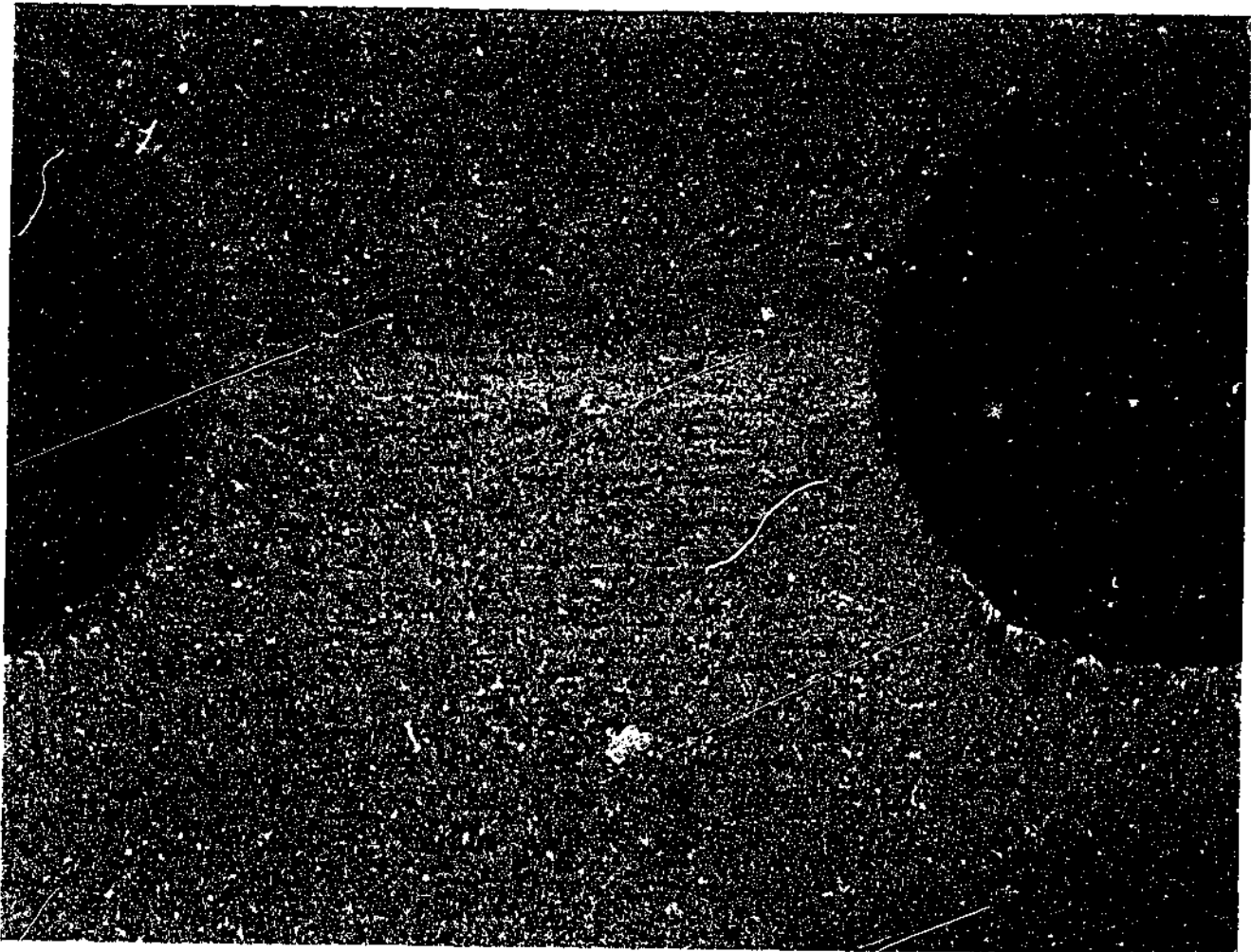


Figure 5.24: Cracking around the inside surface of an economiser inlet header at a tube connection.

For external corners, the real eigenvalues ( $\lambda$ ) are larger than 1 (as indicated by the trend in Fig. 5.16 and calculated by Seweryn and Molski, 1996). This means that the radial and tangential stresses calculated by equations [5.12 & 5.13] would be reduced to a value of zero at the notch tip. Essentially this produces a region of uniaxial stress in the z direction at the corner where the stresses are described in terms of the simple one-dimensional thermal stress equation described in Chapter 2.

$$\sigma_z = -E\alpha\Delta T \quad [5.30]$$

Further from the corner, but along either of the free edges there is only one free surface which allows an increase in the  $z$  direction stresses due to the restraint of Poisson's strain. The resulting maximum free surface stress along these edges now becomes:

$$\sigma_z = \frac{-E\alpha\Delta T}{1-\nu} \quad [5.31]$$

This means that the material at the tip of the corner is actually under less stress than that produced along the free surfaces away from the corner. For a Poisson's ratio of 0.3, this corresponds to an increase of around 43%. This, in turn, makes the formation of cracking such as that depicted in figure 5.25 difficult to explain in terms of thermal shock stresses alone and accepted theories of failure such as Tresca and the maximum distortion energy theorem.

#### 5.3.2.2 Finite element analysis

To help generate a better understanding of the stress distributions developed in a corner of vertex angle less than  $180^\circ$  exposed to thermal shock, a number of finite element models were developed. Using the finite element package ABAQUS (version 5.8-14), models of a  $90^\circ$  corner, exposed to symmetric thermal shock were developed for both cases of axisymmetric and 3-dimensional geometry. Axisymmetric models used 4 sided 8-noded elements and 3-d models used 6 faced 20-noded elements.

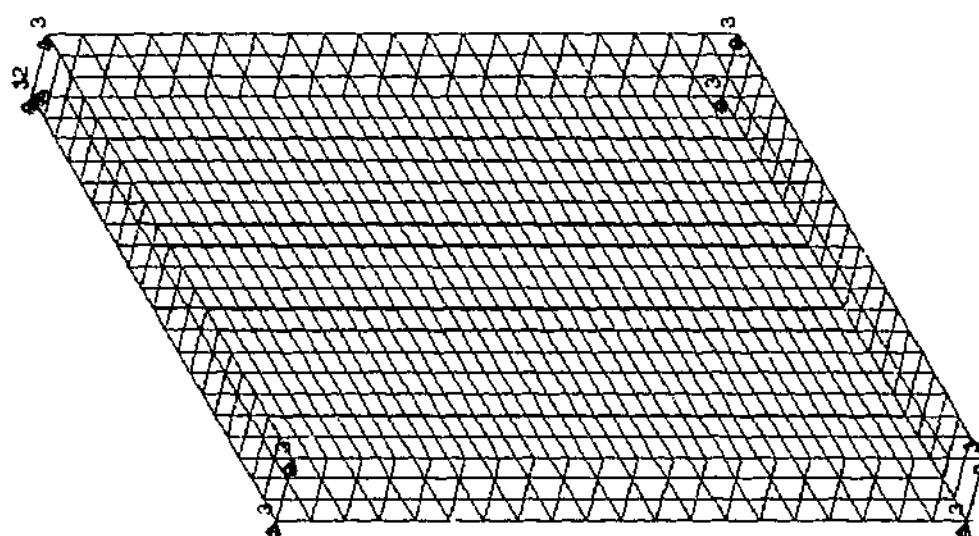


Figure 5.25: A 3-d finite element model for 90° corner exposed to symmetrical thermal shock.

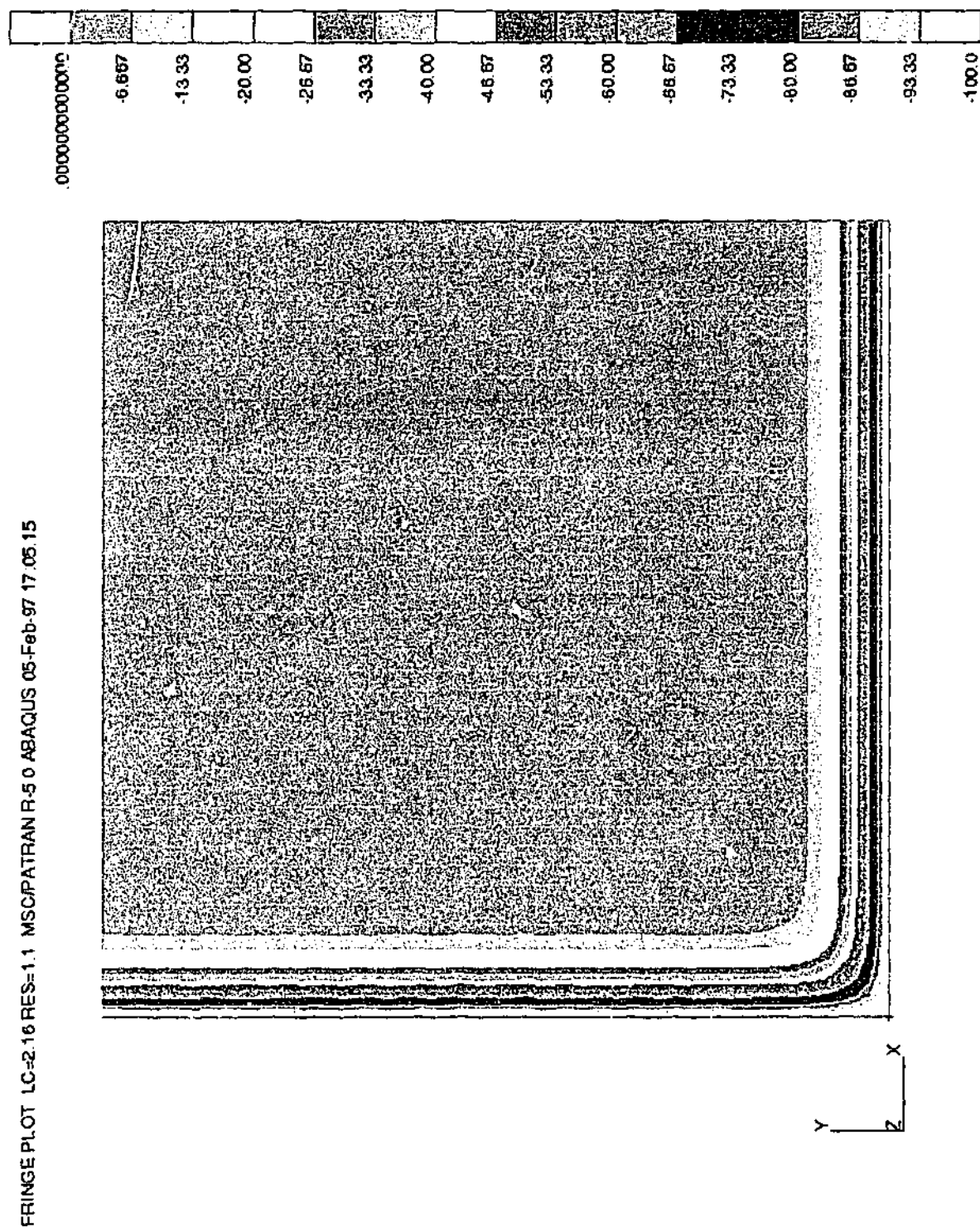


Figure 5.26: Temperature contours for 90° corner exposed to symmetrical 100°C down-shock.

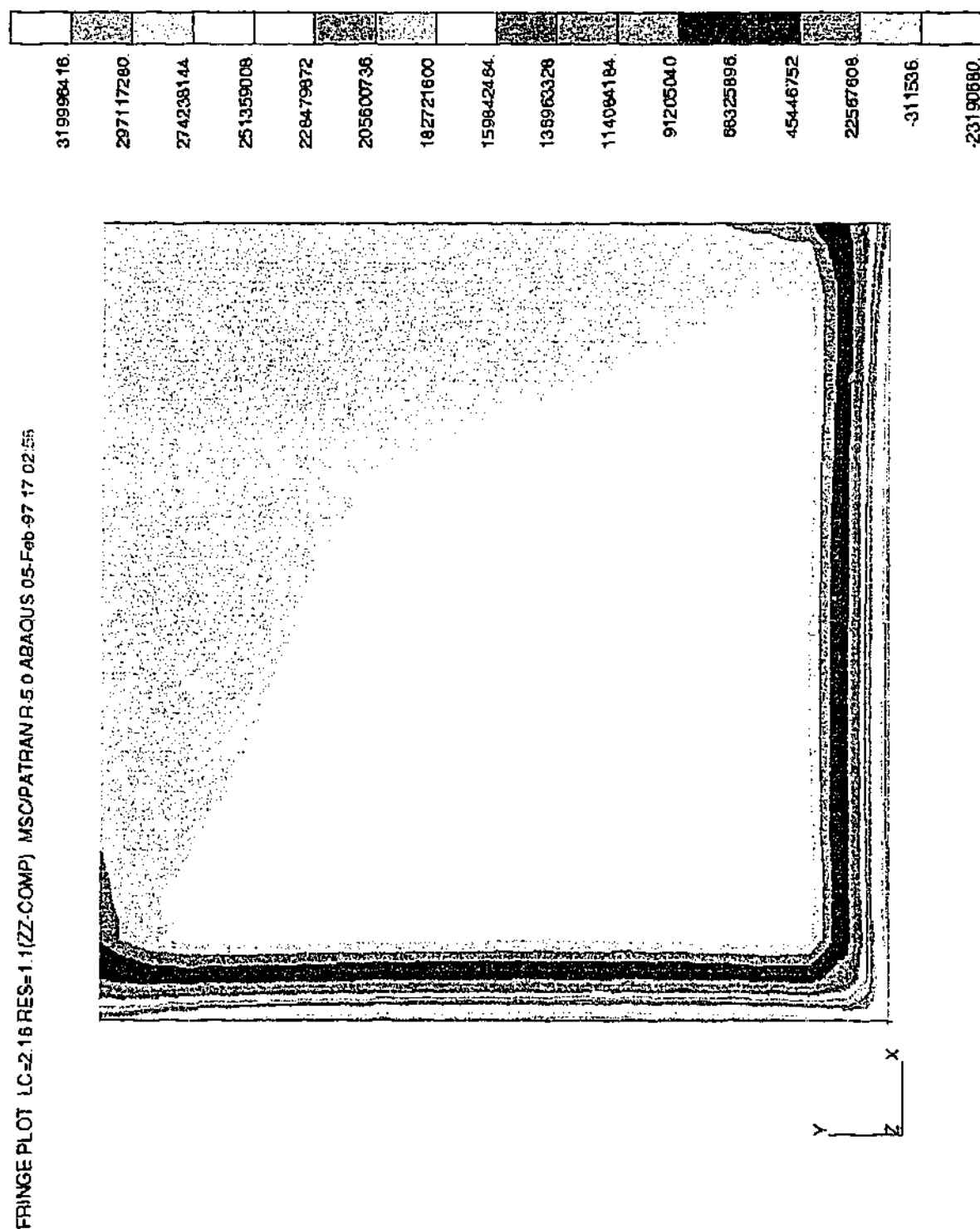


Figure 5.27: z-direction stress contours for 90° corner exposed to symmetrical 100°C down-shock.

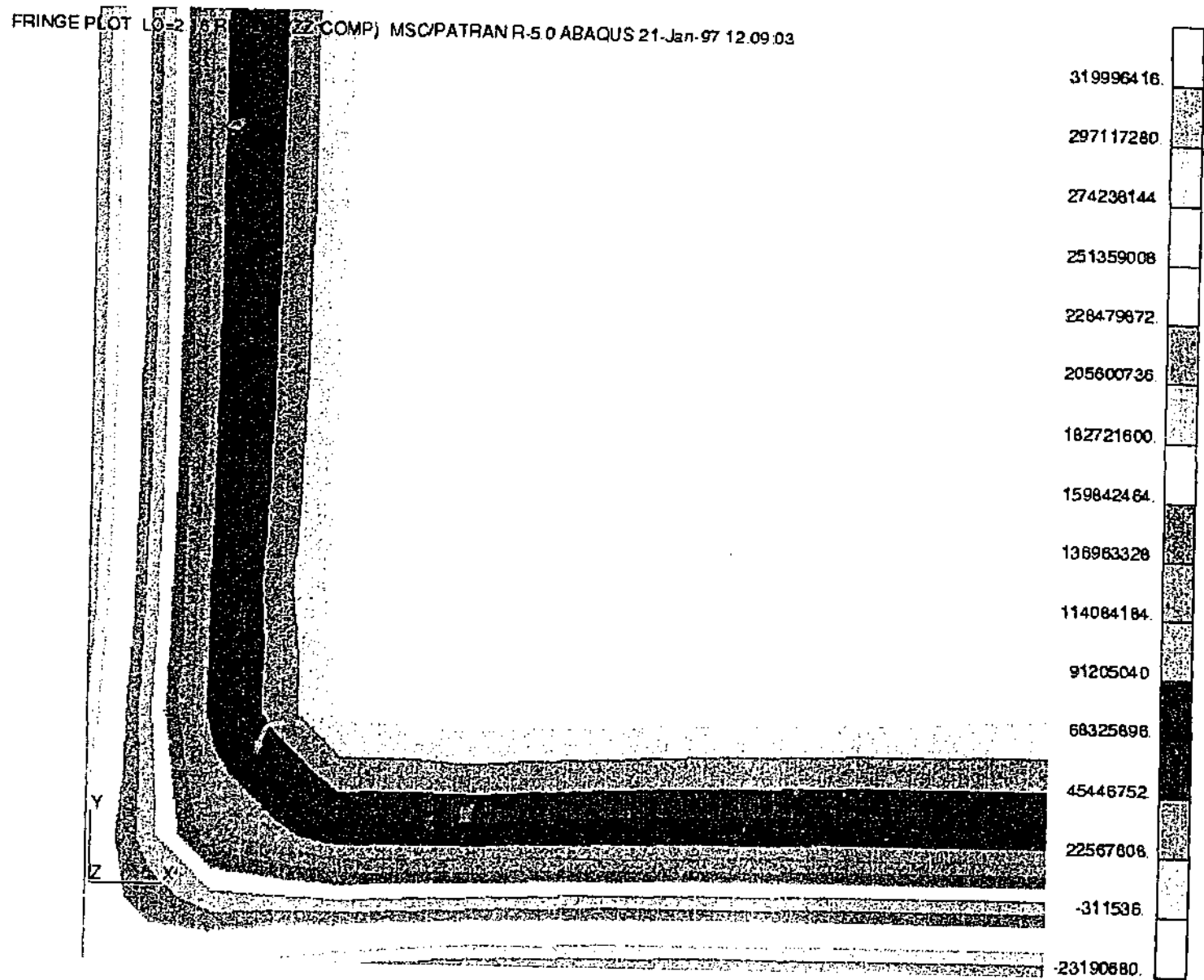


Figure 5.28: Close-up view of z-direction stress contours at the 90° corner for a symmetrical 100°C down-shock.

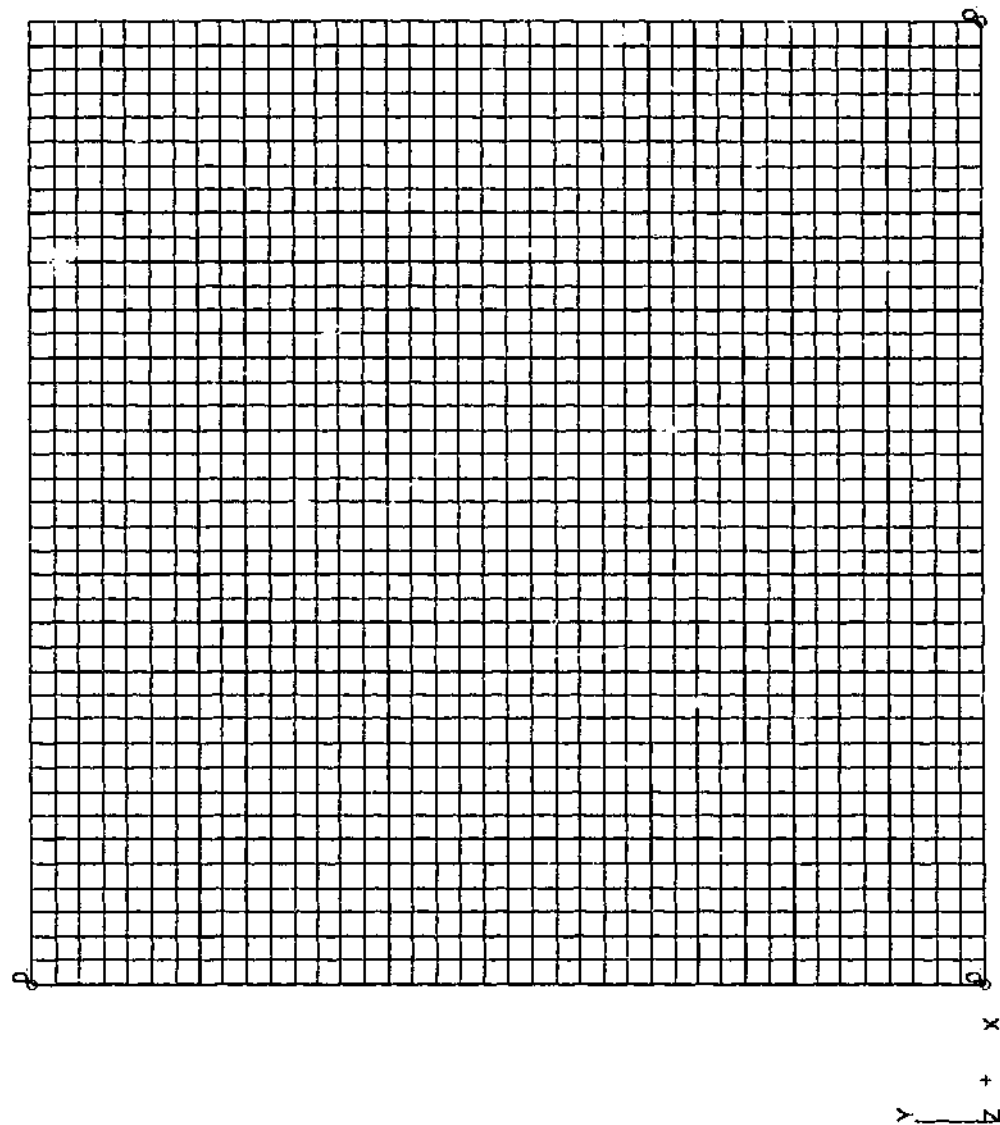


Figure 5.29: Axisymmetric model for 90° corner symmetric thermal shock. Edges exposed to thermal shock indicated by "0.". Axis of symmetry is the y-axis.



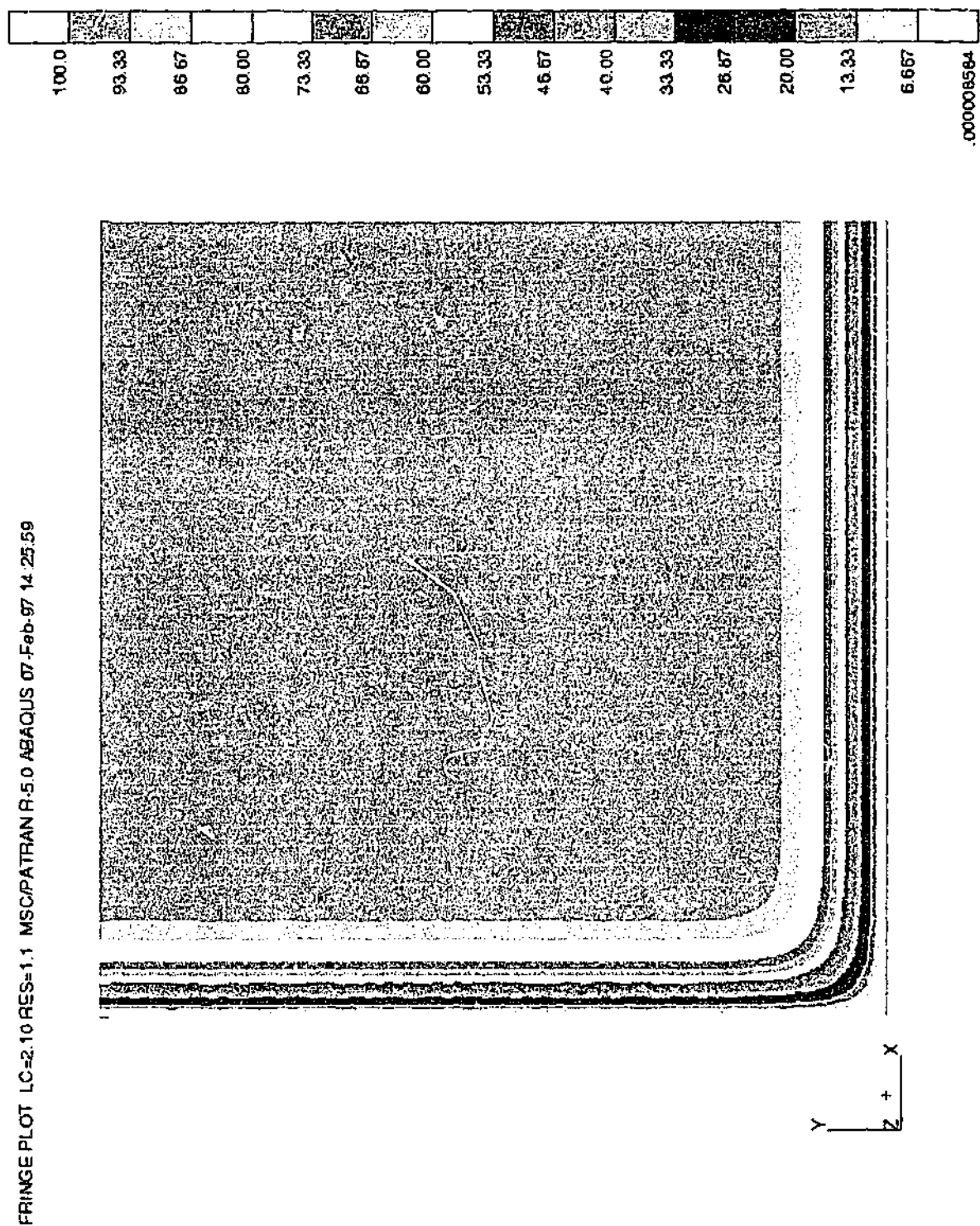


Figure 5.30: Temperature contours for axisymmetric corner model exposed to symmetric thermal down-shock of 100°C.

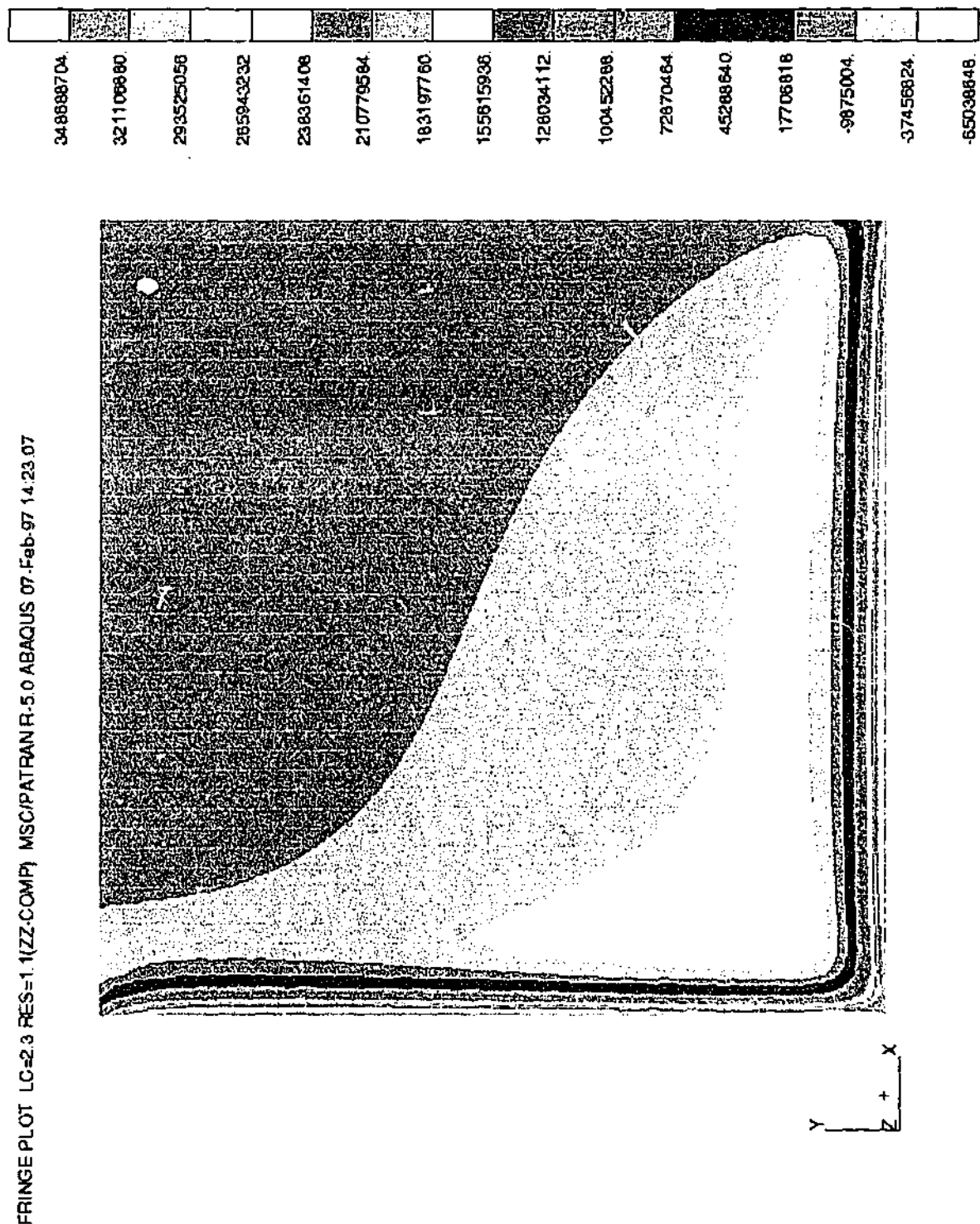


Figure 5.31: z-direction stress contours for axisymmetric 90° corner exposed to symmetric thermal down-shock of 100°C.

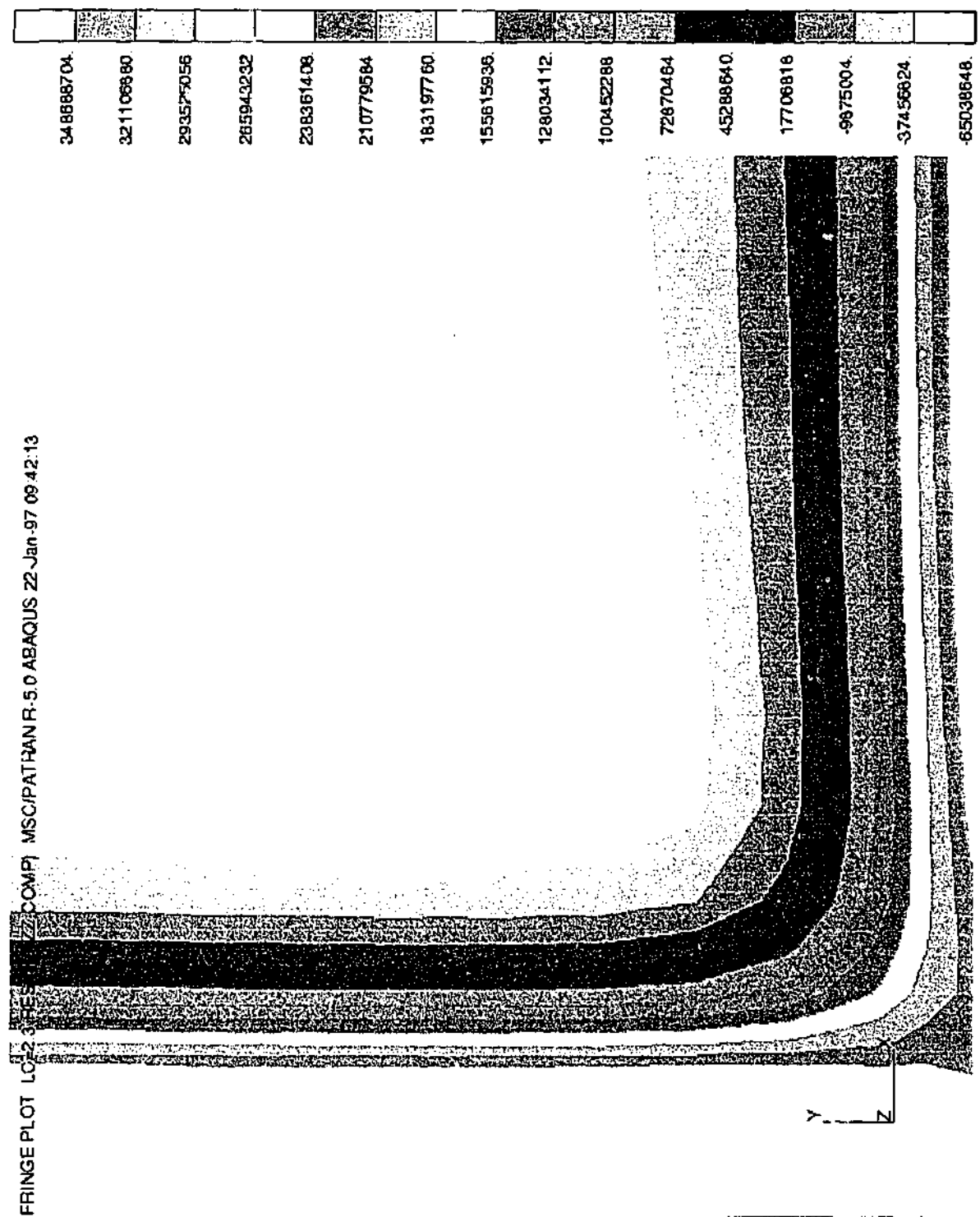


Figure 5.32: Close-up view of z-direction stress contours at the 90° axisymmetric corner for a symmetrical 100°C down-shock.

Figures 5.26 – 5.32 show the models developed during the finite element analysis and the resulting temperature and stress contour plots for discrete time periods.

The temperature distributions depicted in figures 5.26 and 5.30 show that the corner is cooled faster than the surrounding material due to the two-dimensional shock. Basic considerations suggest that if the contraction due to this cooling is fully restrained, then a region of high stress should form at the corner. However this does not take into account the effect of geometry on the stresses. As is expected from the theoretical considerations (section 5.3.2.1), figures 5.27, 5.28, 5.31 and 5.32 show that the stresses produced at the tip of the corner are somewhat less than those generated along the free surfaces away from the corner.

The stresses developed at the free surfaces have subsequently been recorded and plotted as functions of distance from the corner ( $d$ ). These charts are reproduced below as figures 5.33 and 5.34. They clearly show the stress at the corner to be equal to the one-dimensional thermal stress solution [5.30]. The stress then increases away from the corner towards a maximum that is dictated by the plane-strain thermal stress equation [5.31].

An interesting note to be taken from figure 5.34 is the effect that the axisymmetric geometry has on the surface stresses. In this case, the two surfaces forming the corner produce slightly different stress profiles. The face corresponding to the curved surface (parallel to the  $y$ -axis) behaves very similarly to that of the plain 3-d face. The face corresponding to the flat surface however produces slightly lower stresses, including a region near the corner where the stress drops below the one-dimensional thermal stress value. This is a phenomenon that may be related to restraint and may also help explain why certain forms of crack growth are observed.

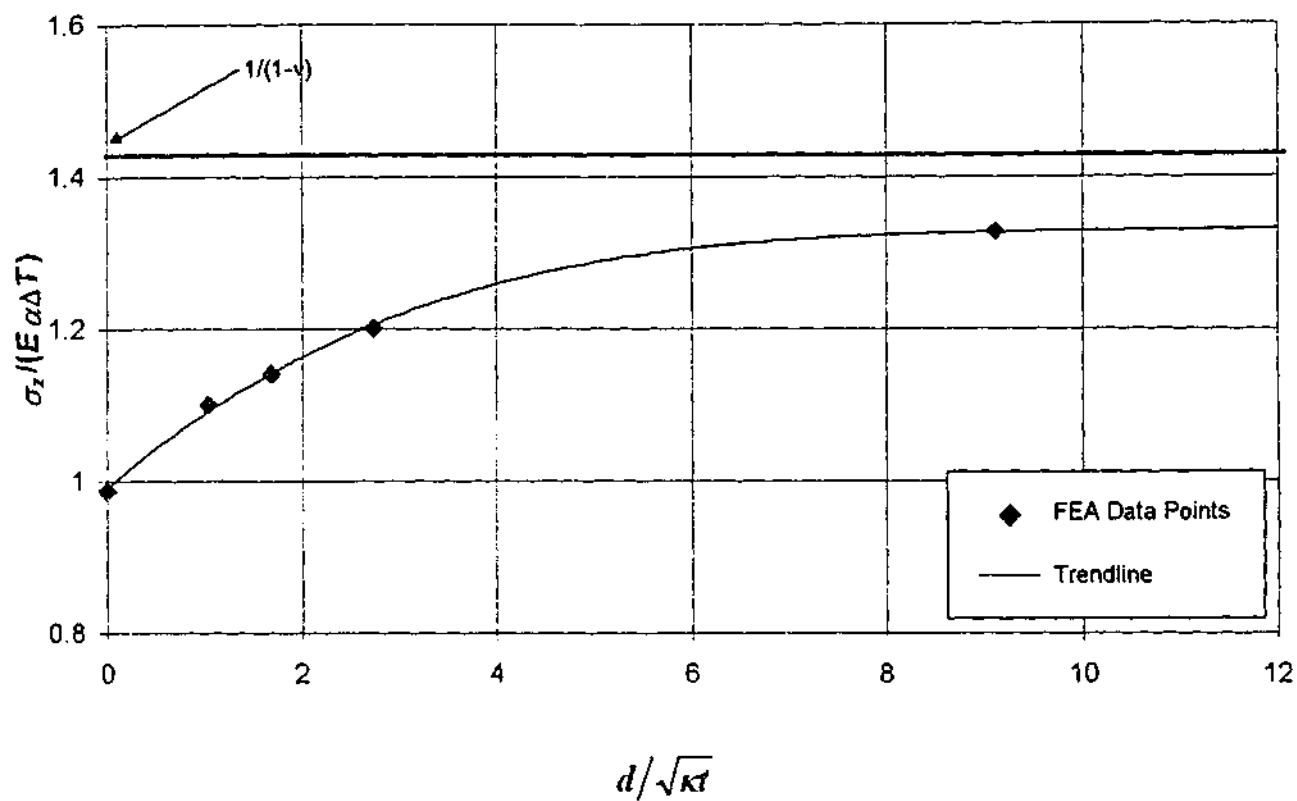


Fig. 5.33: z-direction stresses developed along the free surface of a 3-d corner as a function of distance ( $d$ ) from the corner for fixed time  $t$ .

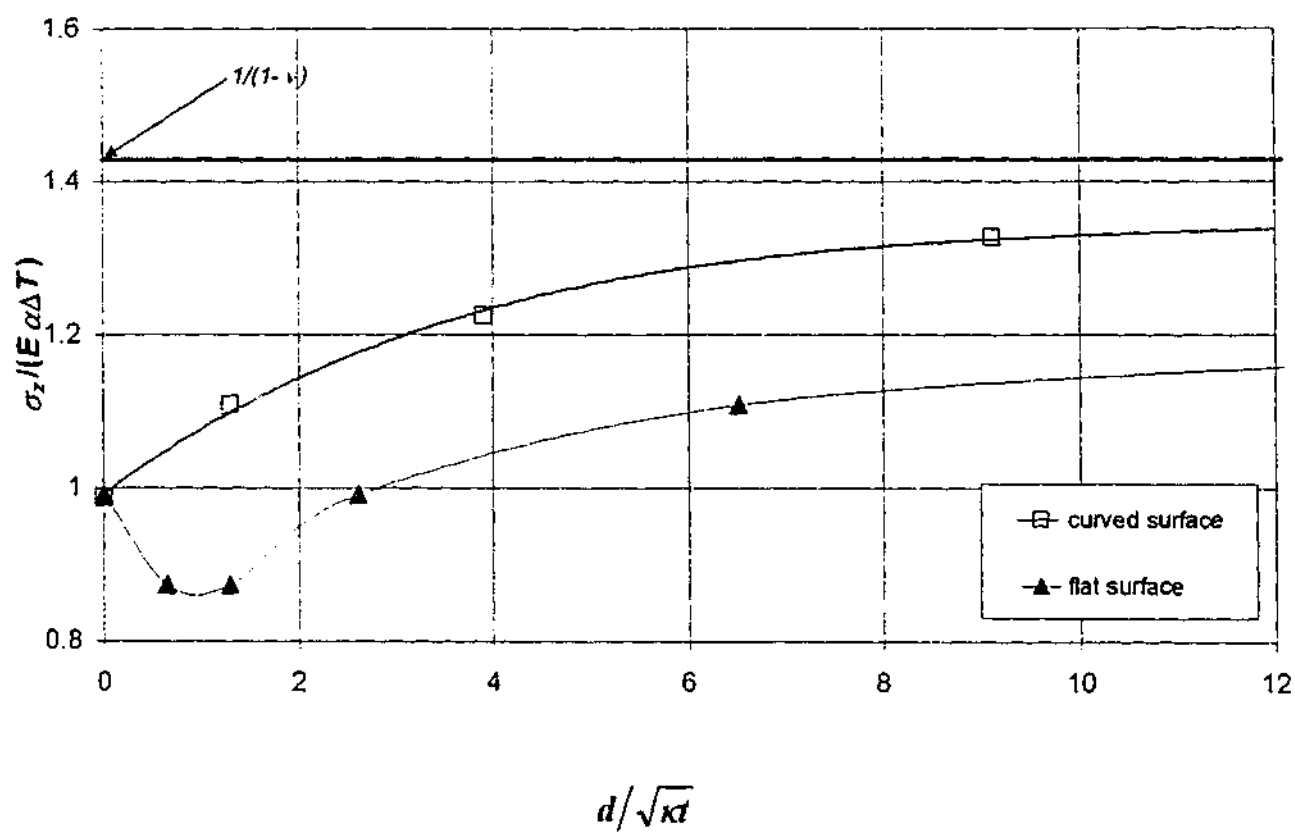


Fig. 5.34: Stresses developed along the free surfaces of an axisymmetric corner as a function of distance ( $d$ ) from the corner for fixed time  $t$ .

### 5.3.2.3 Discussion

From the observations presented in the last section, the corner geometry with vertex angle less than  $180^\circ$  should be safer (less likely to fail) than that of a flat plate, plane strain geometry when exposed to a thermal shock. However, as can be seen from figure 5.24, this is sometimes not the case. In this example, the theory suggests that failure should have occurred at a suitable distance from the tube entry.

The effect of altering the heat transfer conditions around the corner (due to fluid flow) will no doubt alter the stress distributions that are generated during a thermal shock. However, they will not change the fact that stresses at the corner are uniaxial and consequently smaller than those generated a small distance away.

Effects other than those due to thermal shock may be responsible for the observed failures. This geometry does produce a stress concentration around the hole that in turn will increase the primary loading. Manufacturing and operating conditions that extend beyond the influence of the corner geometry may also be part of the explanation.

It is interesting to also briefly consider here what the effect of adding a radius to the corner would do. In practice, when failures such as that shown in figure 5.24 are seen, a typical engineering reaction would be to introduce a radius to the corner to reduce any stress concentration. In fact however, this would have the effect of removing the region of uniaxial stress at the corner, making the stress field more uniform, possibly resulting in more rapid failure. Such a result cannot be confirmed or denied due to lack of field experience. There is also the issue of increased primary stresses which clearly affect crack growth as seen in Chapter 4.

## 5.4 Conclusions

In this chapter, two main issues have been investigated with the aid of analytical and numerical techniques. First was an analysis of the effect of changing thermal shock duration on the stress intensity factors and hence crack growth in flat plate and hollow cylinder geometries. Second was the analysis of the stress fields developed in the vicinity of the apex of a corner exposed to a thermal shock load have been investigated. Both investigations have developed analytical tools that can assist in the analysis of real life situations of thermal shock. The following conclusions can be made from the work.

1. A form of chart has been developed that can assist in identifying the severity of thermal shocks on an edge cracked, flat plate geometry. With knowledge of the thermal shock conditions a plate is exposed to (namely duration and size of shock, environment and likely number of shocks in the component lifetime), a user can predict crack arrest depth, or in the case of pre-existing cracks determine the likely stress intensity factor developed.
2. A hollow cylinder exposed to an internal thermal shock can, depending on the ratio of inside to outside diameter and the flaw aspect ratio, produce stress intensity factors for long, deep cracks that are much larger than for a flat plate. This makes the crack arrest issue in hollow cylindrical equipment more complicated than in a flat plate as observed in the experimental analysis of Chapter 4.
3. Analytical solutions have been obtained for the maximum stress developed in a corner in an infinite space with a vertex angle greater than  $180^\circ$  exposed to a symmetric thermal shock. These solutions (figure 5.22 in particular) can be reasonably applied to finite corner configurations in the case of short duration thermal shocks when component size is sufficient to prevent the any boundaries effects. A maximum non-dimensional stress ( $\bar{\sigma}_{\max}$ ) limit of 3.0 is suggested for use with the analytical solution in a finite geometry situation.

4. Theory and finite element solutions suggest that for corners with vertex angles less than  $180^\circ$ , thermal stresses in the vicinity of the corner should be less than those observed in a flat plate under conditions of plane strain. The analytical results are in apparent conflict with observed industrial failures such as figure 5.24. Determining the reasons for this apparent discrepancy is an area of proposed further study.



## Chapter 6:

### RTS Crack Growth Prediction Using Design & Analysis Codes

#### 6.1 Introduction

The aim of this chapter is to compare current methods for predicting repeated thermal shock crack growth with data obtained during the experimental portion of this thesis. Any areas of large conservatism in the methods currently used in industry need to be identified and possible alternative, less conservative solutions suggested.

Currently, thermal shock crack growth with environmental assistance cannot be fully analysed with the tools available in the codes and standards commonly used in industry for the analysis of in-service flaws. In Australian power generation industry, the typical crack growth analysis will follow one of the following standards:

1. ASME Boiler and Pressure Vessel Code (in particular, Section XI Appendix A) (1998),
2. BS 7910 – Guide on methods for assessing the acceptability of flaws in fusion welded structures (in particular Section 8 and Annex M) (1999),
3. API Recommended Practice 579 – Fitness-For-Service (in particular Section 9 and associated appendices) (1999).

In general, the codes listed above allow for analysis of crack growth at low temperatures in select environments (eg, air, Light Water Reactor) or at high temperatures where creep conditions exist. The intermediate area (in the case of carbon and low alloy steels of 200-370°C) is not covered, nor are the particularly complicated environmental interactions that can occur. Looking for example at BS 7910, it is suggested that data for crack growth rates that is not provided by the code should be collated through testing, with replication of:

1. material,
2. environment,
3. loading frequency and waveform,
4. temperature,
5. geometry (including machining marks),
6. dynamic effects.

Such testing is very time consuming and expensive to conduct. Therefore, any generalisations that can be made will be well received.

The remainder of this chapter is devoted to the analysis of the ASME and British Standard codes in turn. Results from the code analyses will be compared to the data obtained during the experimental portion of this thesis. Advantages and disadvantages of each code will be discussed, and suggestions made on how they could be updated for wider application.

## **6.2 ASME Boiler and Pressure Vessel Code, Section XI (1998)**

### **6.2.1 Introduction**

The ASME Boiler and Pressure Vessel Code (1998) is currently one of the most widely accepted standards for the analysis of cracks in pressure equipment. In particular, it is Appendix A of Section XI that deals with the analysis of flaws. Developed for use in the nuclear power industry, it provides the tools required for prediction of crack propagation rates. Figures A-4300-1&2 of Section XI provide the crack growth reference curves for translating the stress intensity factors produced at the tip of a crack into crack growth rates for carbon and low alloy ferritic steels exposed to air and water reactor environments respectively. These reference curves also provide for the effect of load ratio ' $R$ ' (defined as the ratio of the minimum to maximum stress intensity factors over a cycle -  $K_{min}/K_{max}$ ). Water reactor environments are basically A.V.T. (All Volatiles water Treatment) thus oxygen and pH are controlled at less than 10ppb and about 7.0-9.0, respectively.

The ASME XI crack growth curves are produced on tensile test machines. In the case of the water reactor environment, the specimen is immersed in a treated but stagnant fluid supposedly simulating the water reactor environment. The thermal shock case is not like the oscillating primary load of the tensile test machine since the thermal stress component quickly diminishes from the surface. The environment in thermal shock also changes, either from hot to cold water, from steam to cold water or from air to cold water. In addition, the fluid is also in violent motion. Consequently, the choice of which of the ASME XI crack growth reference curves to use in a thermal shock analysis is unclear.

As mentioned above, ASME data also requires a quantification of the  $R$  ratio. A problem is posed when deciding what the  $R$ -ratio is at the crack tip during thermal shock. Thermal shock stresses are highly non-linear (see Chapters 2 & 4 for further descriptions) and decrease rapidly away from the shocked surface resulting in a reduction in  $K_{max}$  with crack growth (see Appendix C, figures C.19 to C.28). This means that for cases of non-zero primary stress and hence non-zero  $K_{min}$ , the  $R$  ratio is increasing as the crack grows. This makes selection of a crack growth reference curve representative of the thermal shock condition very difficult.

The ASME Boiler and Pressure Vessel Code is based on Linear Elastic Fracture Mechanics (LEFM) and relies on the stress intensity factor being suitable to describe the stress condition surrounding the crack tip. As discussed in Chapter 2, this is only the case when the bulk of the material is behaving predominantly in an elastic manner. Results from Chapter 4 show that in the case of RTS, LEFM is a suitable method when the crack has outgrown the high strain fatigue region. The ASME method for determining stress intensity factors in a component under arbitrary stress conditions has been summarised in Chapter 3, section 3.4.3.

### **6.2.2 Crack Growth Analysis**

Figure 6.1 shows the experimental data from Chapter 4 plotted as cyclic crack growth versus  $\Delta K$ . Only crack growth data outside of the high strain fatigue region has been included. Superimposed on the figure are the Paris Law reference growth laws suggested in

the ASME Boiler and Pressure Vessel Code for air and water environments. It is immediately visible that the water environment curves of the ASME code provide very conservative estimates of crack growth when compared to the experimental results, regardless of  $R$ -ratio or environment. In fact in some cases, a factor of 10 conservatism on growth rate is observed. Alternatively, the ASME air curves seem to lie much closer to the bulk of the test data, particularly that generated at low  $R$ -ratios. The conservatism shown by the ASME code can be partially attributed to the fact that the crack growth reference curves are based on the upper bounds of their own testing data.

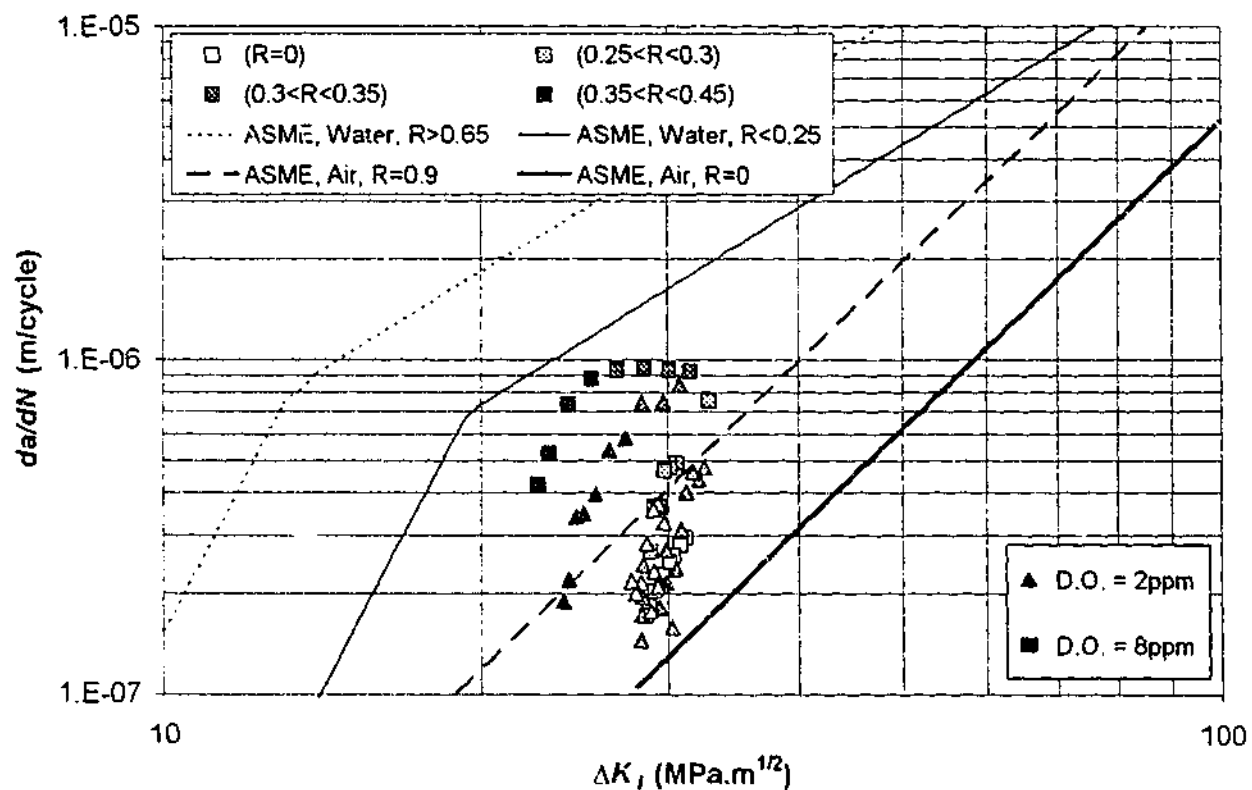


Figure 6.1: Comparison of experimental crack growth data with prediction curves of ASME Boiler and Pressure Vessel Code, Section XI (1998), Appendix A.

Comparing actual experimental crack growth to that predicted by using the ASME Paris Law reference curves is a simple procedure as the appropriate stress intensity factor profiles for the experimental cases have already been determined (Appendix C, figures C.19 to C.28). Converting these curves to crack growth is a simple case of integrating the appropriate reference curves along the desired crack length.

$$N = \frac{1}{C} \int_{a_i}^{a_f} (\Delta K)^{-m} da \quad [6.1]$$

Where  $N$  is the number of cycles to grow a crack from length  $a_i$  to  $a_f$ , and  $C$  and  $m$  are the Paris Law coefficients obtained from the ASME code itself.

Figures 6.2 and 6.3 show crack length against number of thermal shock cycles for growing an established crack that is 5mm deep. Experimental test data are shown as points and predicted data shown as solid curves.

From these curves, it seems that the ASME code is successfully predicting the trends of the experimental crack growth. As expected, predictions using the water reference curves are fairly conservative. Even with an assumption of  $R=0$ , predictions based on the water curves still over-estimate actual experimental crack growth rates.

In Chapter 4 it was observed that during RTS crack growth, any environmental assistance was highest when  $R$ -ratios were above 0.3. This is reflected in the results shown here. Growth curves based on the ASME water reference curve seem to predict the enhanced growth of the test data with  $R < 0.5$  (figure 6.2), while the growth curves based on the air reference curves provide better predictions for all data where  $R < 0.3$  (figures 6.2 and 6.3).

Ultimately, this means that careful selection of the appropriate ASME crack growth reference curve must be made before an analysis is conducted. Unfortunately, the number of curves provided by the code and the complex manner in which  $R$ -ratios are handled makes this selection quite difficult.

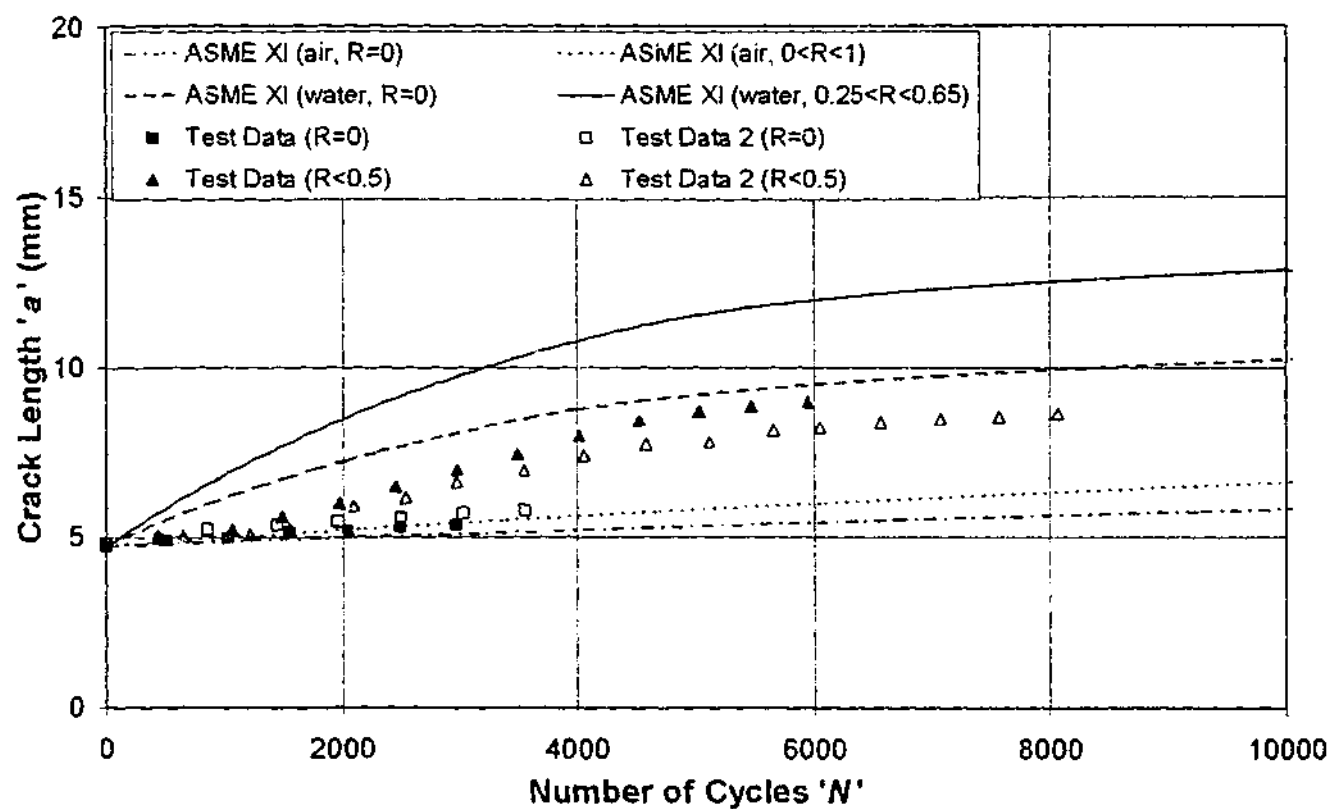


Figure 6.2: Crack length vs. number of cycles. Comparison of actual data with ASME XI (1998) predictions for a 7s thermal shock from 370°C. Solid points refer to test data taken with D.O. 8ppm, hollow points for data with D.O. of 2ppm.

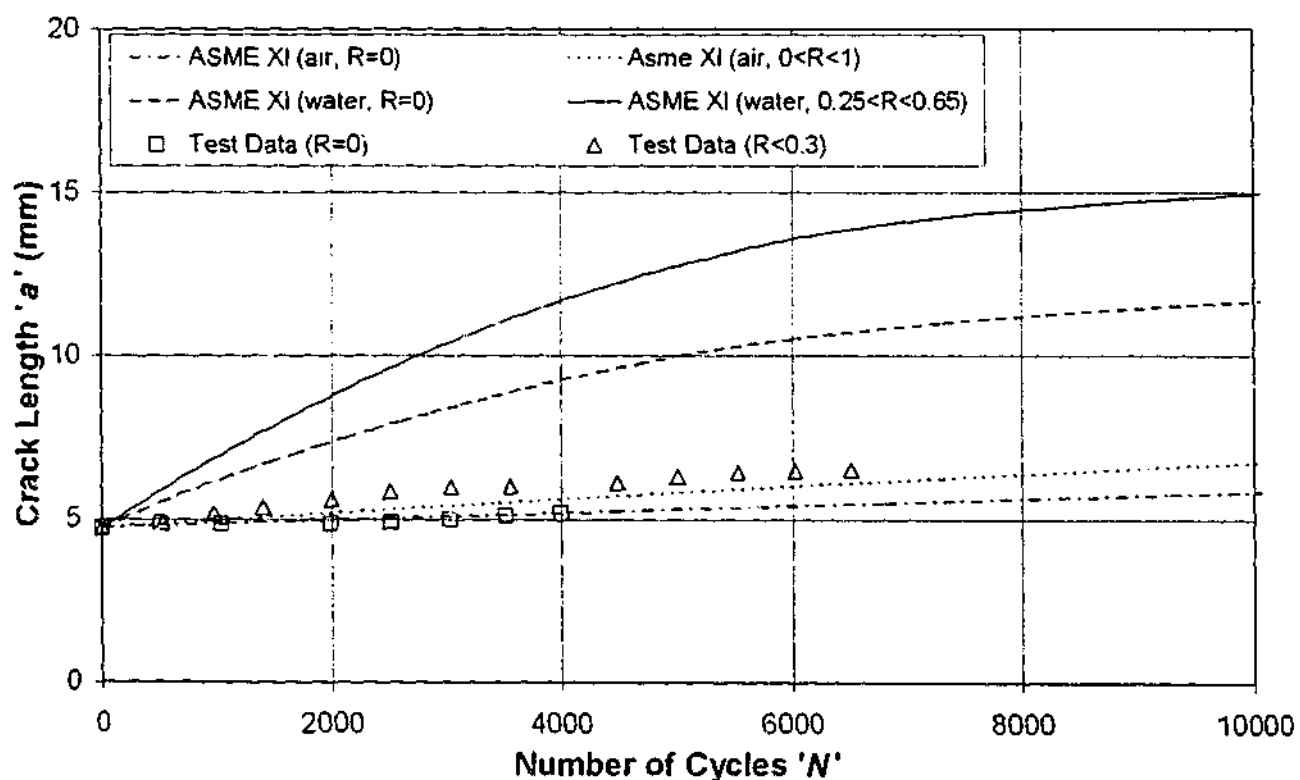


Figure 6.3: Crack length vs. number of cycles. Comparison of actual data with ASME XI (1998) predictions for a 7s thermal shock from 350°C. D.O level for test data is 2ppm.

## **6.3 BS 7910 (1999)**

### **6.3.1 Introduction**

The British Standard BS 7910 (1999), although entitled "Guide on Methods for Accessing the Acceptability of Flaws in Fusion Welded Structures", has applications extending to the analysis of flaws in non-metallic and non-welded structures. As with the ASME Boiler and Pressure Vessel Code (1998) it is widely used in Australian industry and also forms the basis for a number of crack analysis computer programs (eg CRACKWISE). The code uses Failure Assessment Diagrams (FADs) to determine the acceptability of flawed structures. The diagrams are based on determining the flaw size-loading combination required for fracture and plastic collapse of the component. Projected flaw sizes are calculated using a method for predicting crack growth similar to that in the ASME Boiler and Pressure Vessel Code (1998) Section XI. The focus of the analysis in this section will be on the crack growth analysis used in BS 7910 (1999) section 8, however some use of the FADs will also be made.

### **6.3.2 Crack Growth Analysis**

#### **6.3.2.1 Generation of stress intensity factor profiles**

The first step in the BS 7910 (1999) crack growth analysis requires the simplification of the stress profile in the material into two components, namely the membrane and bending stresses. In the case of a highly non-linear stress profile, as is the case with thermal shock, correctly following the code procedure can result in a very conservative result. Figure 6.4 shows a typical stress profile generated during the thermal shock of the specimens used in the experimental analysis section of this work. Also included is the suggested BS 7910 "linearisation" profile.

This rather conservative approach (over-estimation of stress through the component thickness) is required due to the fact that fluctuating thermal stresses are treated as primary (as opposed to secondary) loads in a fatigue assessment (BS 7910, 1999, section 6.4.3).

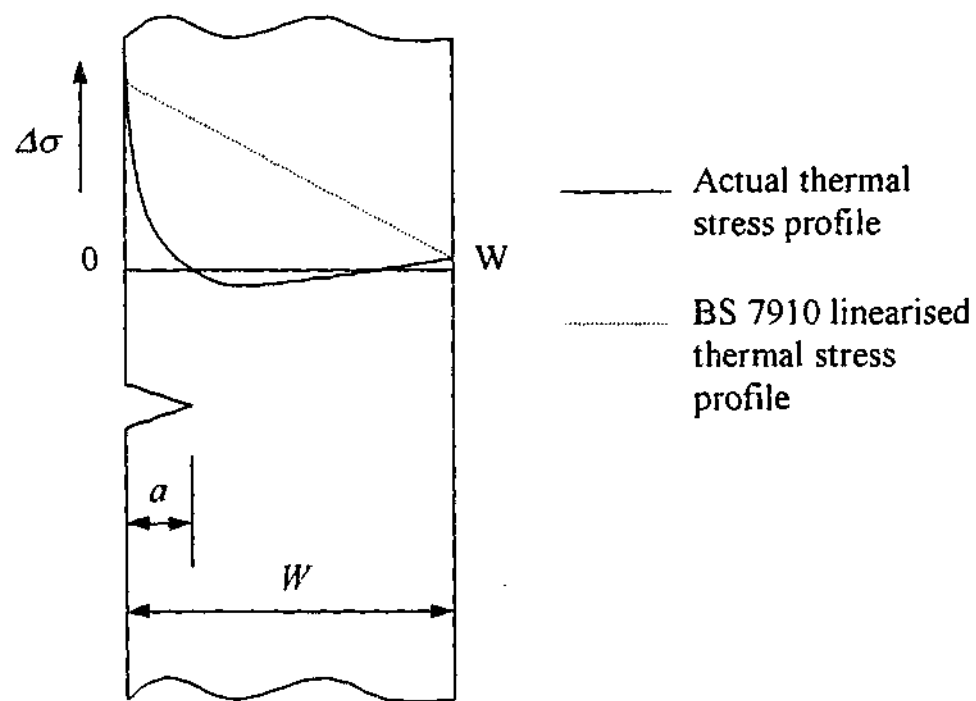


Figure 6.4: Stress linearisation for fatigue analysis in BS 7910 (1999) for crack length ' $a$ ' in plate of width ' $W$ '.

The results of this stress linearisation are combined with the equations provided in BS 7910, Annex M to calculate  $\Delta K$  for a number of complex flaw geometries including provisions for finite component size. Crack growth rates are then predicted using Paris Law type equations. Derivatives of the Paris Law equations are provided to take into account environment (air and marine environments) and load ratio  $R$ . Unfortunately, the data is provided with a number of restrictions on its use. Included in these restrictions are that the air data be used only for non-aggressive environments at temperatures less than 100°C and that the marine data only be used for environments of less than 20°C. No suggestion is given for where data can be sourced for components operating outside of these limits.

#### 6.3.2.2 Crack growth reference curves

Figures 6.5 and 6.6 show the experimental data plotted as cyclic crack growth versus  $\Delta K$ . Superimposed on these figures are the crack growth reference curves that are presented in BS 7910 for dry and marine environments respectively. Each set of curves from BS 7910 consists of three individual curves. The first is based on mean test data, the second on mean test data plus two standard deviation (+2D) data and the third "simple" curve is based



on a conservative analysis. Initial observations of figures 6.5 and 6.6 show that the dry curves do a good job of bounding the experimental data obtained at low  $R$ -ratios when environmental influence is small. Similarly, the marine curves do a good job of bounding the experimental data obtained at high  $R$ -ratios when environmental influence is large.

The following is a list of suggested guidelines for using the BS 7910 growth curves in predicting RTS crack growth in a water environment. They are based on comparisons with the experimental data shown in figures 6.5 and 6.6 only.

1. For a slightly conservative analysis at all points, the "simple" BS 7910 data curves can be used for crack growth prediction. The marine curves would be used for high  $R$ -ratio data and dry curves for low  $R$ -ratio data. Trends indicate however that these curves could well under-estimate crack growth rates at  $\Delta K$  values smaller than those used in the experimental work.
2. For slightly more accurate predictions, the mean +2D data from the marine and dry curve sets could be used. Use of the curves outside of the experimental data region is not suggested until more data can be collected.
3. The use of the mean curves for crack growth prediction is not recommended, as they sometimes under-estimate observed crack growth rates.

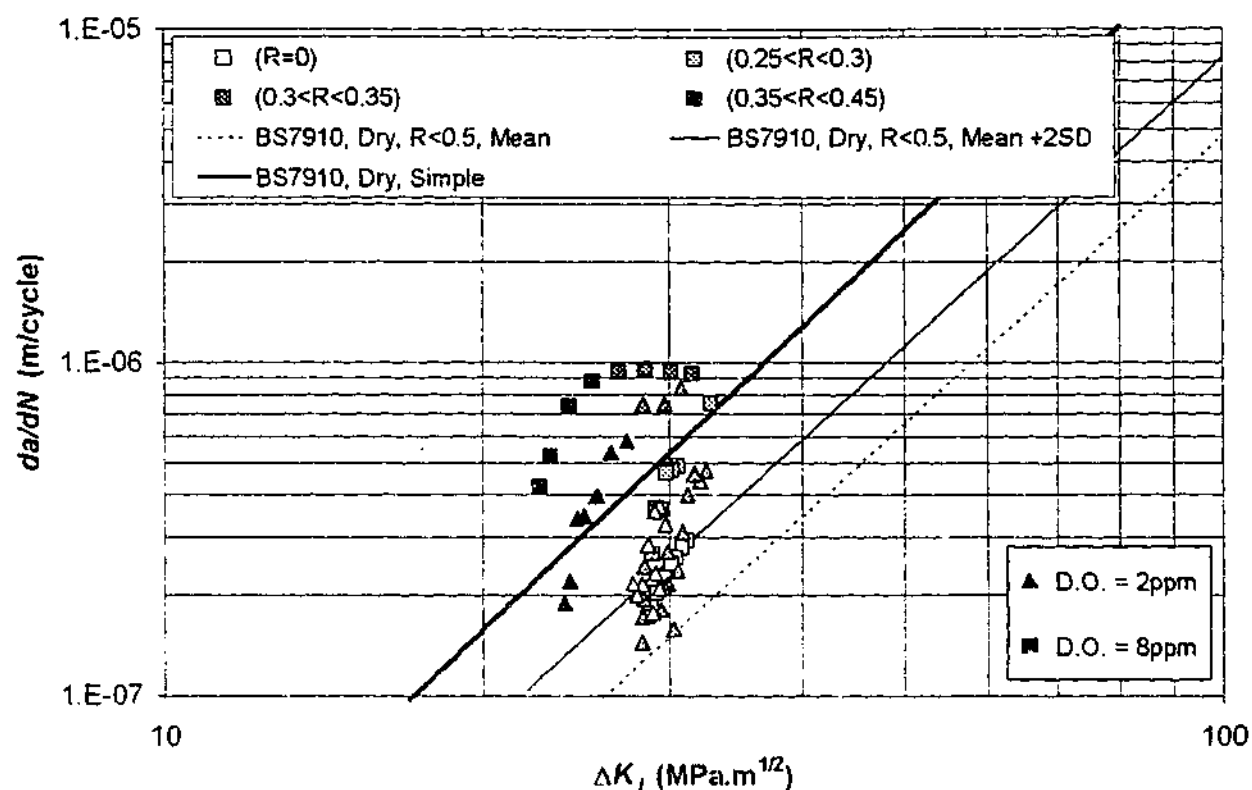


Figure 6.5: Comparison of experimental crack growth data with dry environment prediction curves of BS 7910 (1999). BS 7910 curves for  $R < 0.5$  are shown for: mean data, mean data plus two standard deviations (2SD), and simplified growth data.

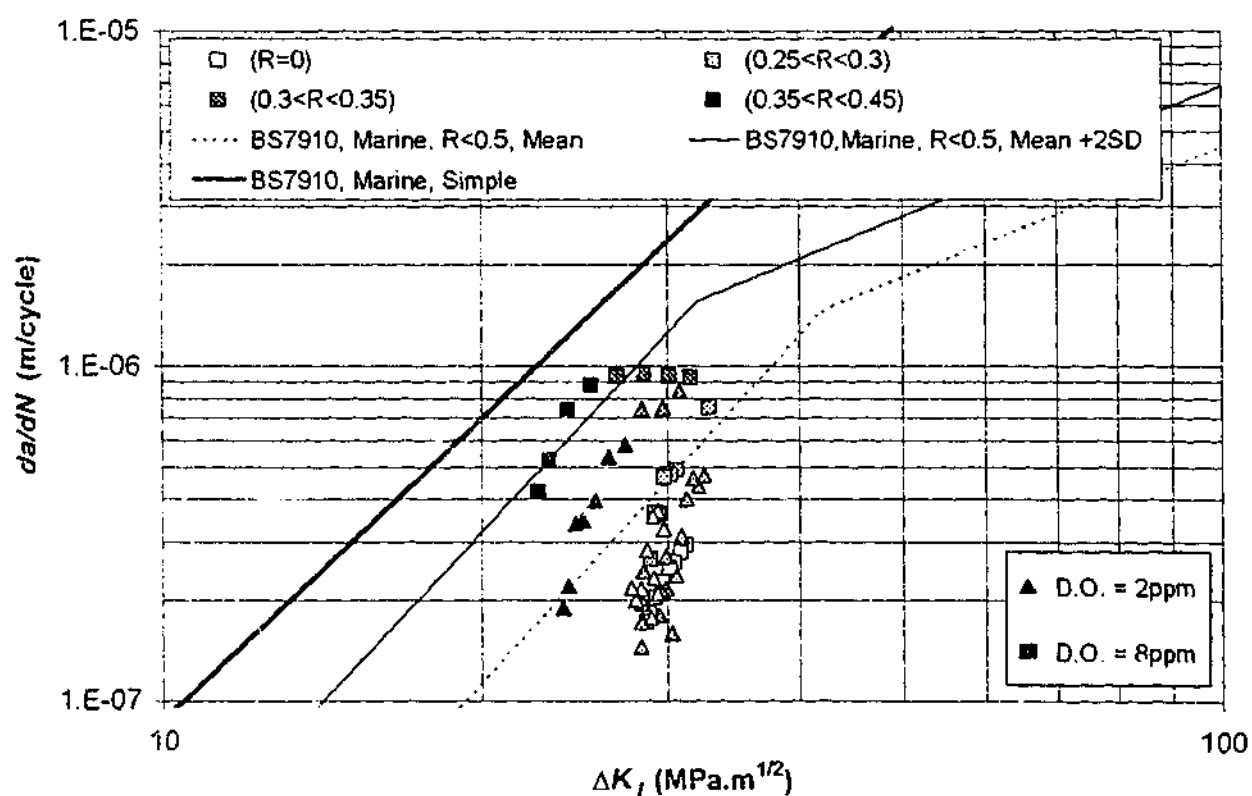


Figure 6.6: Comparison of experimental crack growth data with marine environment prediction curves of BS 7910 (no cathodic protection). BS 7910 curves for  $R < 0.5$  are shown for: mean data, mean data plus two standard deviations (2SD), and simplified growth data.

### 6.3.2.3 Comparison with experimental data

Figures 6.7 and 6.8 show crack length versus number of cycles for a starting crack length of 5mm. Experimental crack growth data is compared with that generated using the BS 7910 technique of stress linearisation and the mean data Paris Law reference curves. The conservatism generated by the BS 7910 analyses is very large. According to the analysis, crack growth due to the repeated thermal shocks will accelerate into the test specimen until failure (by fracture or plastic collapse) occurs. As observed experimentally however, this is far from the case with slow crack growth tending towards deceleration and possible crack arrest observed in all experimental cases.

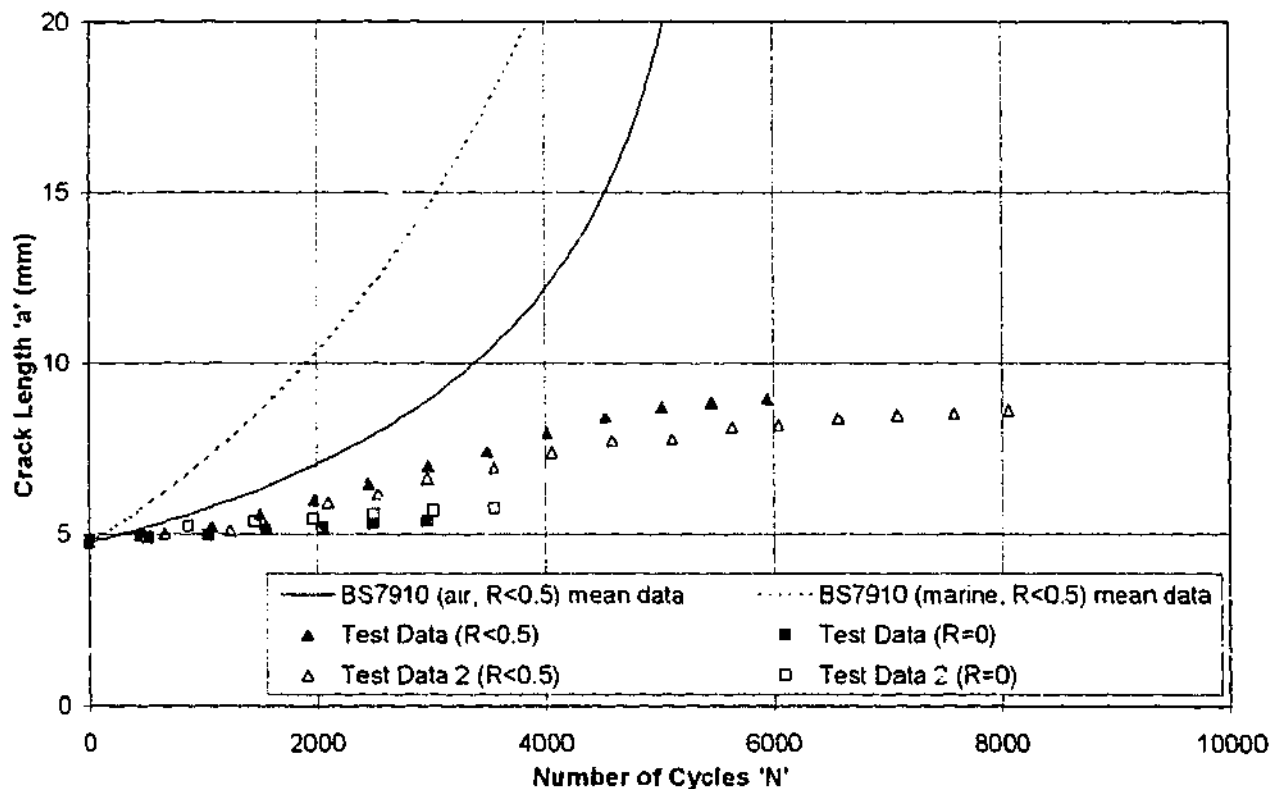


Figure 6.7: Crack length vs. number of cycles. Comparison of actual data with BS 7910 (1999) predictions for a 7s thermal shock from 370°C. Solid points refer to data taken with D.O. 8ppm, hollow points for data with D.O. of 2ppm.

The large amount of conservatism shown by figures 6.7 and 6.8 is not due to variations in the Paris Law reference equations. Instead, it is due to inaccuracies developed by applying the linear approximation to the thermal shock stress profile as shown in figure 6.4.

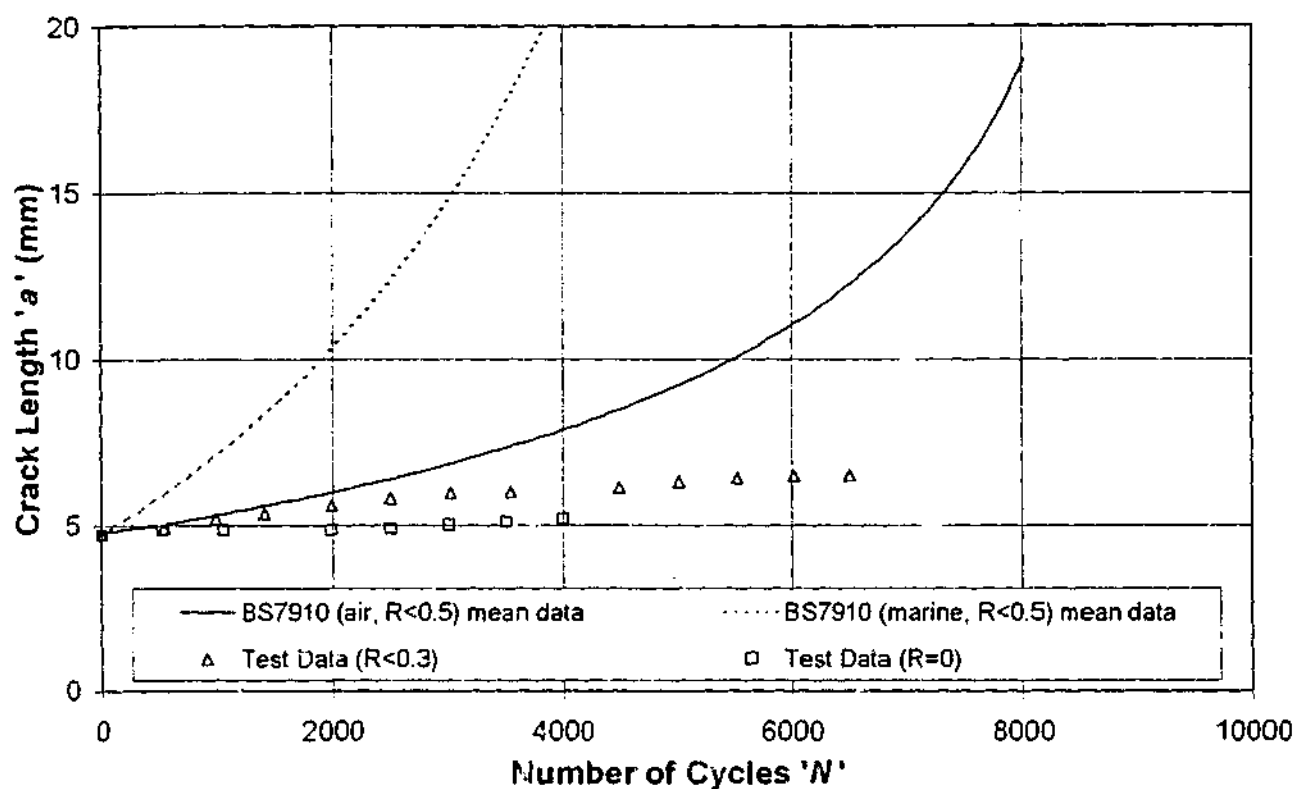


Figure 6.8: Crack length vs. number of cycles. Comparison of actual data with BS 7910 (1999) predictions for a 7s thermal shock from 350°C. D.O. level for test data is 2ppm.

#### 6.3.2.4 A modified approach

In addition to providing stress linearisation profiles for fatigue analysis, BS 7910 (1999) also provides similar, yet less conservative, methods for use in fracture analysis. An example of applying these methods to the case of thermal shock stress is given in figure 6.9. Note that using this method, the stress profile along the crack length is modelled much more accurately. The process of modelling stresses only along the crack length is also used in the ASME Boiler and Pressure Vessel Code (1998).

The use of this form of stress profile linearisation results in the following comparison of observed and predicted crack growth shown in figures 6.10 and 6.11. It is clear that the models now more closely fit the observed data. However, crack deceleration is still not adequately predicted. Rather, predicted crack growth appears to continue at a constant rate until failure. The disadvantage with this method is that the stress profile must be recalculated for each increment of crack growth. Fortunately, automation of such a procedure is fairly simple using modern computational software.

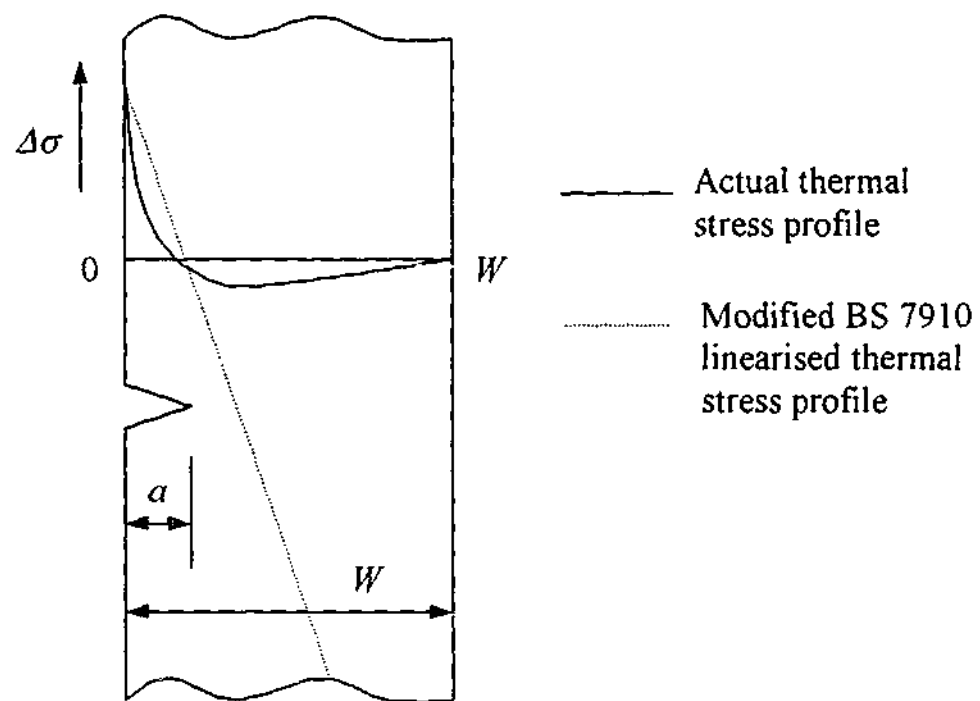


Figure 6.9: Modified stress linearisation for fatigue analysis in BS 7910 (1999) for crack length ' $a$ ' in plate of width ' $W$ '.

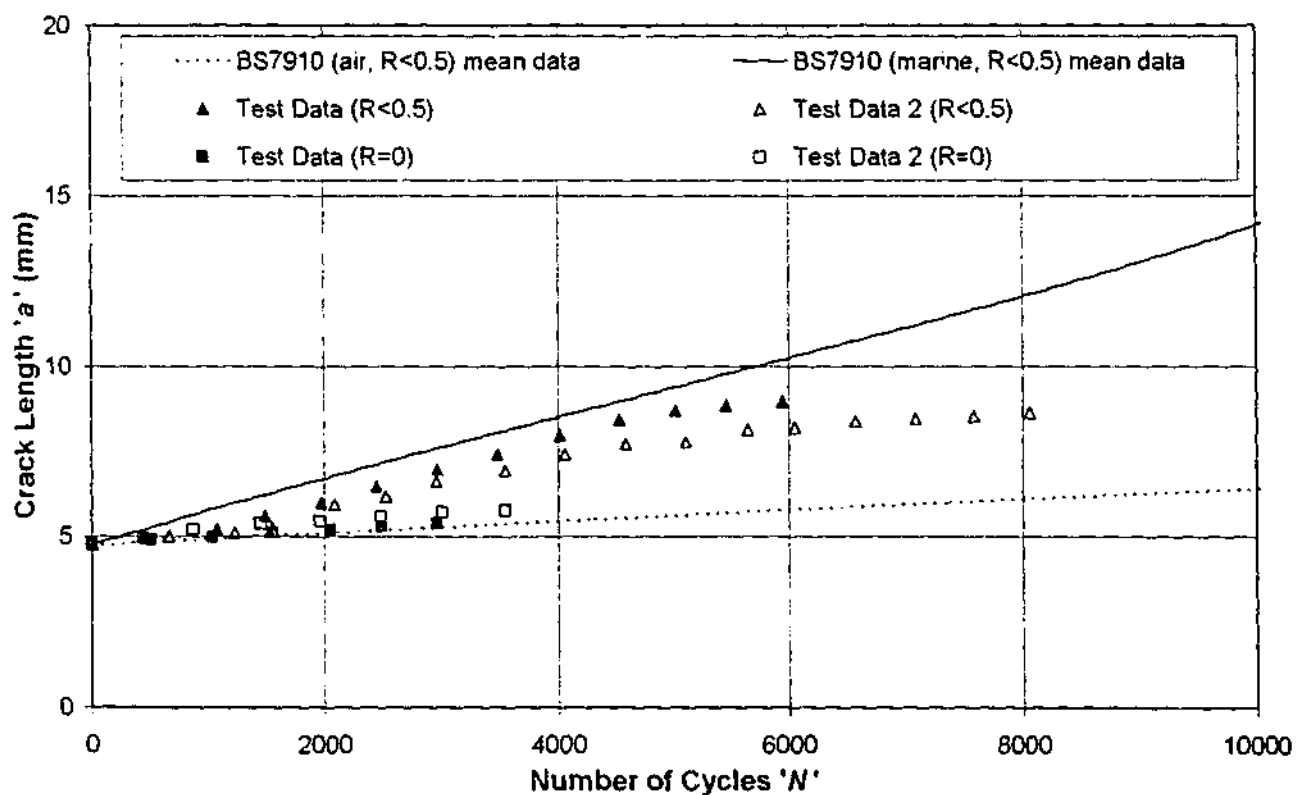


Figure 6.10: Crack length vs. number of cycles. Comparison of actual data with modified BS 7910 (1999) predictions for a 7s thermal shock from 370°C. Solid points refer to data taken with D.O. 8ppm, hollow points for data with D.O. of 2ppm.

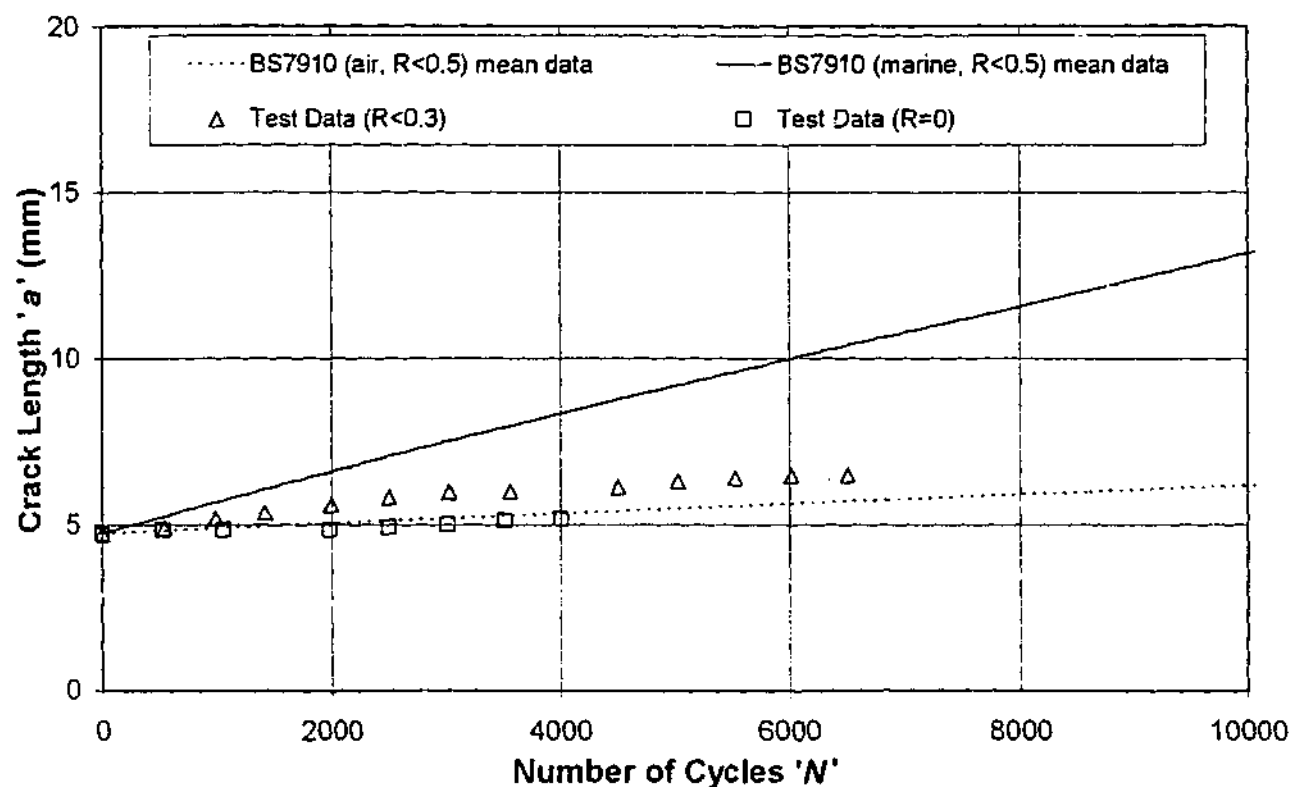


Figure 6.11: Crack length vs. number of cycles. Comparison of actual data with modified BS 7910 (1999) predictions for a 7s thermal shock from 350°C. D.O. level for test data is 2ppm.

#### 6.4 Combining ASME and BS 7910 Approaches

While the stress intensity factor profile for RTS is accurately modelled by the ASME code (as described in section 6.2), the generation of accurate crack growth data from this can be difficult and confusing. Alternatively, the British Standard method (described in section 6.3) provides inaccurate solutions for generating RTS stress intensity factor profiles, although it does recommend a series of Paris Law reference curves that are relatively accurate and easy to apply. Consequently, a combination of the two methods may provide a better alternative than the application of either alone.

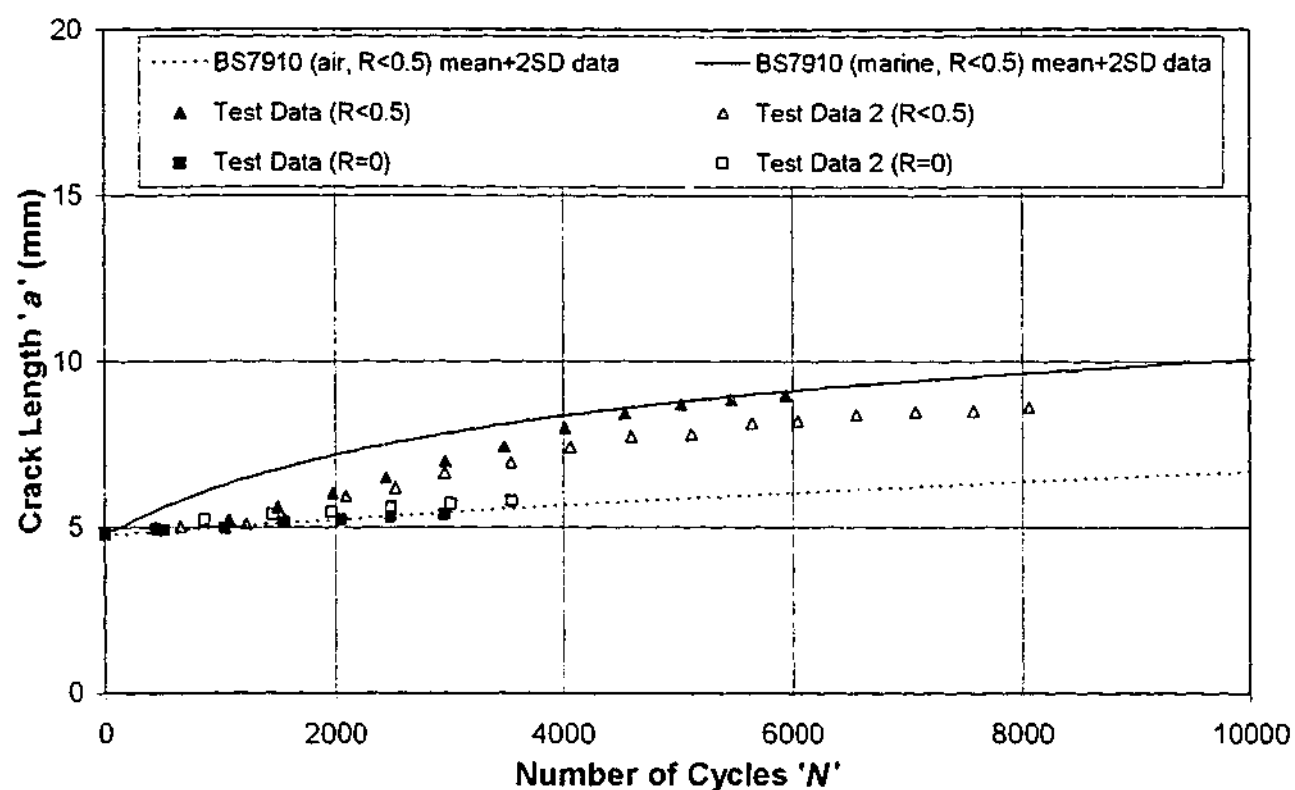


Figure 6.12: Crack length vs. number of cycles. Comparison of actual data with combined ASME XI (1998) and BS 7910 (1999) approach for a 7s thermal shock from 370°C. Solid points refer to data taken with D.O. 8ppm, hollow points for data with D.O. of 2ppm.

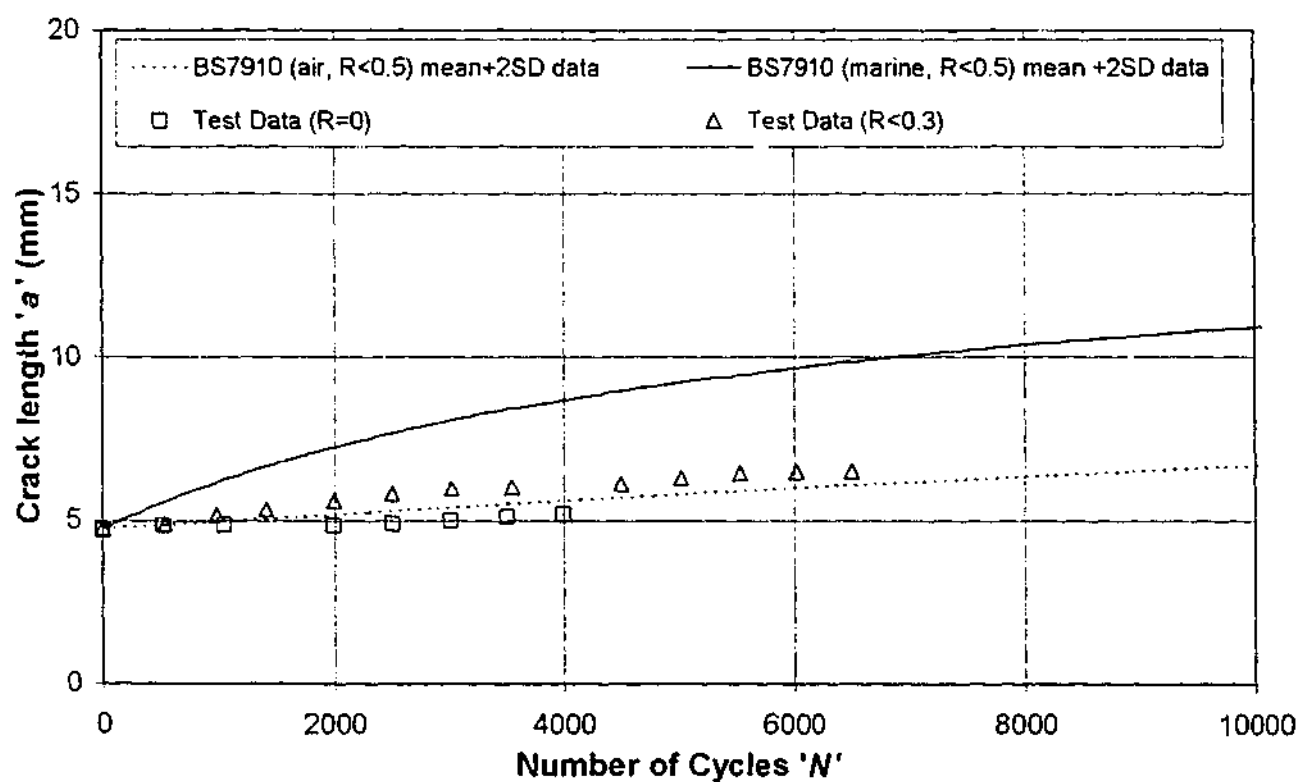


Fig. 6.13: Crack length vs. number of cycles. Comparison of actual data with combined ASME XI (1998) and BS 7910 (1999) approach for a 7s thermal shock from 350°C. D.O. level for test data is 2ppm.

Figures 6.12 and 6.13 show the results of a combined analysis. Crack length versus number of cycles is plotted again, this time using the ASME weight function technique combined with BS 7910 crack growth reference curves (mean +2SD data). For the case of high  $R$ -ratios (and hence high environmental interaction) the marine reference curves provide good crack growth estimations. Similarly, while  $R$ -ratios are low (as is the environmental influence), the dry reference curves provide a good growth estimation.

### **6.5 Comparisons of Alternate Analysis Techniques**

In service, when a cracked component is discovered, a fracture mechanics analysis can be performed to see whether the component should be immediately replaced or if it is safe to return to service. Typically, the component is replaced if the crack is of a size that threatens the industrial integrity of the component. If the component is not in danger of failure, but the crack is predicted to continue growing, a schedule for inspection of the component is required if the component is returned to service. Monitoring of the crack growth needs to be made to ensure removal before failure. The schedule is based on the predicted crack growth rate, which in the case of a component exposed to RTS would be one of the methods outlined in sections 6.2 to 6.4. Identification of which method provides the best balance between accuracy and conservatism is important, as costly shutdowns and component replacements can be safely avoided.

To place the various levels of conservatism generated by the techniques outlined in the previous three sections into perspective, the predicted number of cycles required for a crack to grow to a predetermined length will be compared. This will give an idea of how each of the methods would perform in a typical industrial analysis on which decisions on inspection intervals and component replacement would be based.

The crack length at which failure in a component will occur can be conservatively estimated using a level one FAD from BS 7910. For this analysis the test specimen used in the experimental work will be used (see Chapters 3 and 4). The crack length at which failure is expected when the test specimen is exposed to repeat 7s thermal shocks from



370°C, combined with a primary load of 90MPa, has been calculated as approximately 23 mm. The number of cycles taken for a crack to grow to a length of 23mm from an initial flaw size (crack depth) of 4.8mm are shown in Table 6.1 for each of the methods outlined in sections 6.2 to 6.4.

Table 6.1: Predicted number of cycles required for a crack to grow from 4.8mm to 23mm in the experimental specimen when exposed to repeated 7s thermal shocks from 370°C combined with a 90MPa steady state primary load.

Method	Description	Stress Approximation	Crack growth prediction curve used	Number of cycles
1	BS 7910 analysis	Linear across component	BS 7910, Simple, Marine curve	350
2	BS 7910 analysis	Linear across component	BS 7910, Mean + 2SD, Marine curve	2,770
3	Modified BS 7910 analysis	Linear along crack face	BS 7910, Simple, Marine curve	5,930
4	Modified BS 7910 analysis	Linear along crack face	BS 7910, Mean + 2SD, Marine curve	9,710
5	ASME XI analysis	Polynomial along crack face	ASME, Water curves	$6.955 \times 10^8$
6	Combined ASME and BS 7910 analysis	Polynomial along crack face	BS 7910, Simple, Marine curve	$3.317 \times 10^8$
7	Combined ASME and BS 7910 analysis	Polynomial along crack face	BS 7910, Mean + 2SD, Marine curve	$3.317 \times 10^9$

As shown in table 6.1, methods 1-4, based on conservative linear approximations of the thermal shock stress profiles, all predict crack growth to a length suitable for specimen failure in a relatively small number of cycles. Depending on the number of thermal shock cycles a component was expected to face in service, using this analysis could easily (and most probably) lead to a recommendation of component replacement.

Alternatively, methods 5-7 are based on more accurate polynomial stress profile approximations and weight function techniques. The results of these solutions indicate that the specimen should have essentially an infinite life. This means the specimen is flaw tolerant and should be suited to continued operation. Inspection of in-service crack growth in the specimen could be carried out at the time of the next planned shutdown, with no additional down-time expenses.

Based on a balance of simplicity of application and accuracy, method 6 could be deemed the most successful. This is because it has shown sufficient accuracy to avoid the incorrect conclusion that the component should be replaced and is still based on data taken from a single Paris Law reference curve, irrespective of  $R$ -ratio and  $\Delta K$  values.

## **6.6 Conclusions**

This chapter has provided a comparison of existing design and analysis code techniques that are commonly applied for crack growth prediction with actual experimental test data for a flat plate specimen exposed to RTS. The following code specific conclusions can be made:

### **ASME Boiler and Pressure Vessel Code**

1. The polynomial stress profile approximation and weight function technique produce an accurate model of the crack length versus number of cycles growth curve for a flat plate specimen exposed to RTS.
2. The selection of the provided crack growth reference curves appropriate for converting stress intensity factors to crack growth rates is not immediately obvious when environmental interaction occurs.

### **BS 7910**

1. The stress linearisation techniques used for determining stress intensity factor profiles are too conservative for use with the highly non-linear stresses generated during a thermal shock.

2. The crack growth reference curves for a marine environment provide a good approximation of observed experimental crack growths when environmental assistance is present (ie when  $R > 0.3$ ).
3. The crack growth reference curves for a dry environment provide a good approximation of observed experimental crack growth rates when environmental assistance is small or not present (ie with  $R < 0.3$ ).

It is observed that a combined technique using the ASME approach for calculating the stress intensity factor profile and the simple crack growth reference curves from BS 7910 provide a good balance between accuracy and simplicity when estimating crack growth due to RTS.

## **Chapter 7:**

### **Conclusions**

#### ***7.1 Introduction***

The aim of this thesis is to investigate the major factors contributing to crack growth in carbon steel exposed to repeated thermal shock (RTS) at temperatures below the creep range. Experimental, numerical and theoretical techniques have all been applied to analyse the effects of mechanical loading, environment, transients and geometry on crack initiation and growth. The following conclusions have been extracted from the work.

#### ***7.2 Review of Literature***

The current state of knowledge in the field of predicting crack initiation and crack growth due to the repeated thermal shock loading of a carbon steel component in an aqueous environment has been reviewed. The review has shown that, though the individual fields of thermal shock stress analysis have all been investigated thoroughly at an individual level, they have not been brought together in an attempt to correctly model the cracking that is currently observed in thermal power station pressure equipment exposed to RTS.

#### ***7.3 Test Method***

A unique test rig has been developed for use in this thesis. The test rig is capable of applying large thermal shocks to multiple heated specimens using a chemically controlled medium. The rig is also capable of applying large steady state mechanical loads. In

addition, the specimen design itself is unique, giving many advantages over previous work in the field. In particular, the following key advantages over previously recorded testing techniques are obtained through the use of the test rig:

1. The component is heated by convection, resulting in no unwanted heat effects at the crack tip as may be the case for induction or resistance heating.
2. The component is quenched by room temperature pH and O<sub>2</sub> controlled water.
3. The specimen size is representative of typical large industrial components.
4. Large specimen size permits multiple simultaneous experiments.
5. A mechanically unloaded "control" specimen can be tested simultaneously.
6. Approximately one-dimensional thermal shock conditions are produced at any one crack.

The principal disadvantage of the rig is the lengthy testing period required of many months that is a consequence of the convection heating technique.

#### **7.4 Test Results**

Temperature, stress and stress intensity factor profiles obtained during the experimental testing are contained in Appendix C. Typical profiles for each are reproduced on the next two pages (Figures 4.2, 4.3, 4.4 and 4.5).

Qualification of the effects of stress concentrators, dissolved oxygen levels and primary loads on the initiation and growth of cracks feature heavily in the experimental work. Conclusions on lifetimes to crack initiation and crack growth behaviour are summarised in the next two sections.

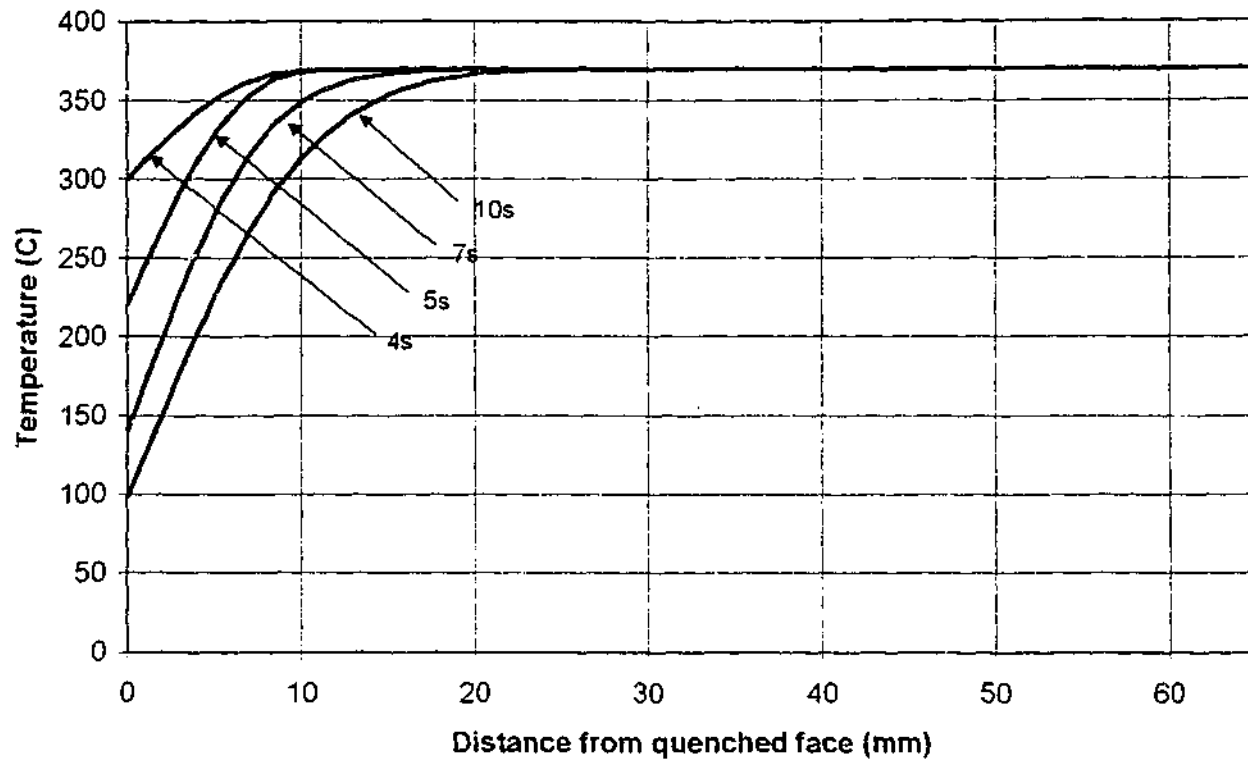


Figure 4.2: Typical temperature profiles for thermal shocks of 4s, 5s, 7s and 10s at crack position 1 from central specimen set temperature of 330°C.

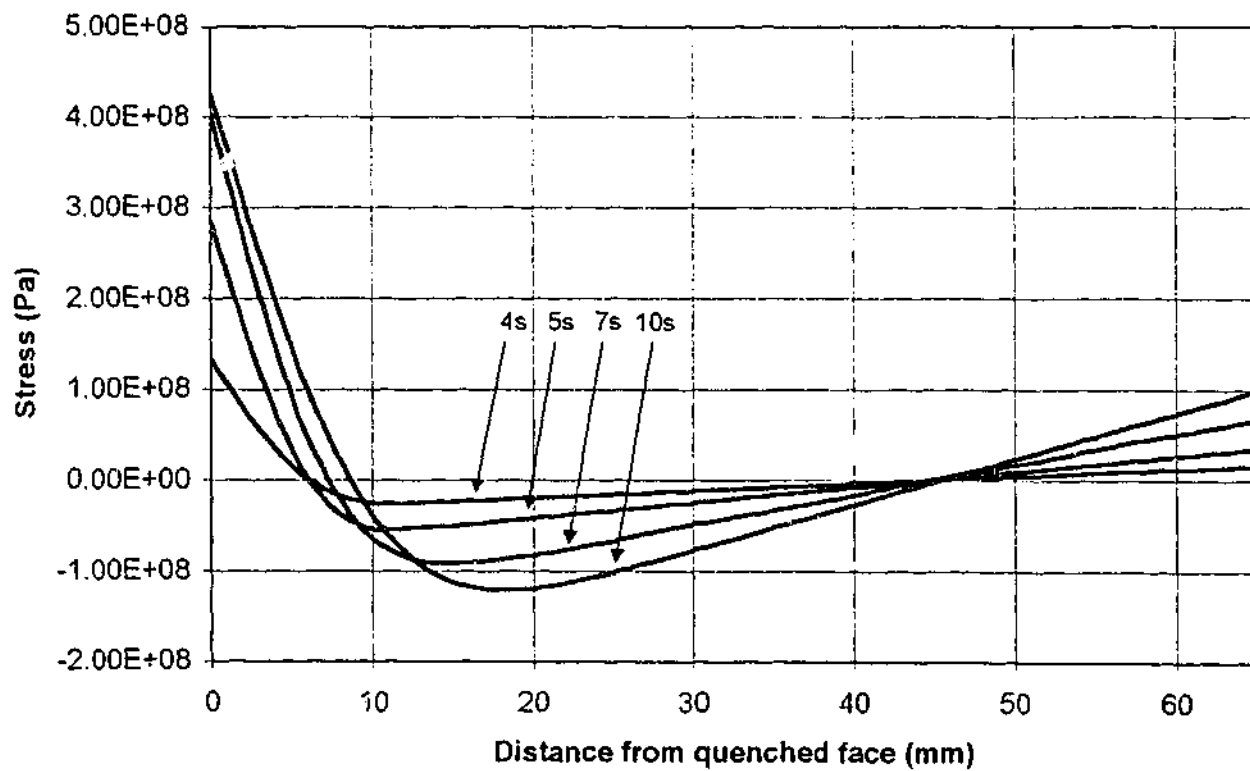


Figure 4.3: Typical elastic stress profiles for thermal shocks of 4s, 5s, 7s and 10s at crack position 1 from central specimen set temperature of 330°C.

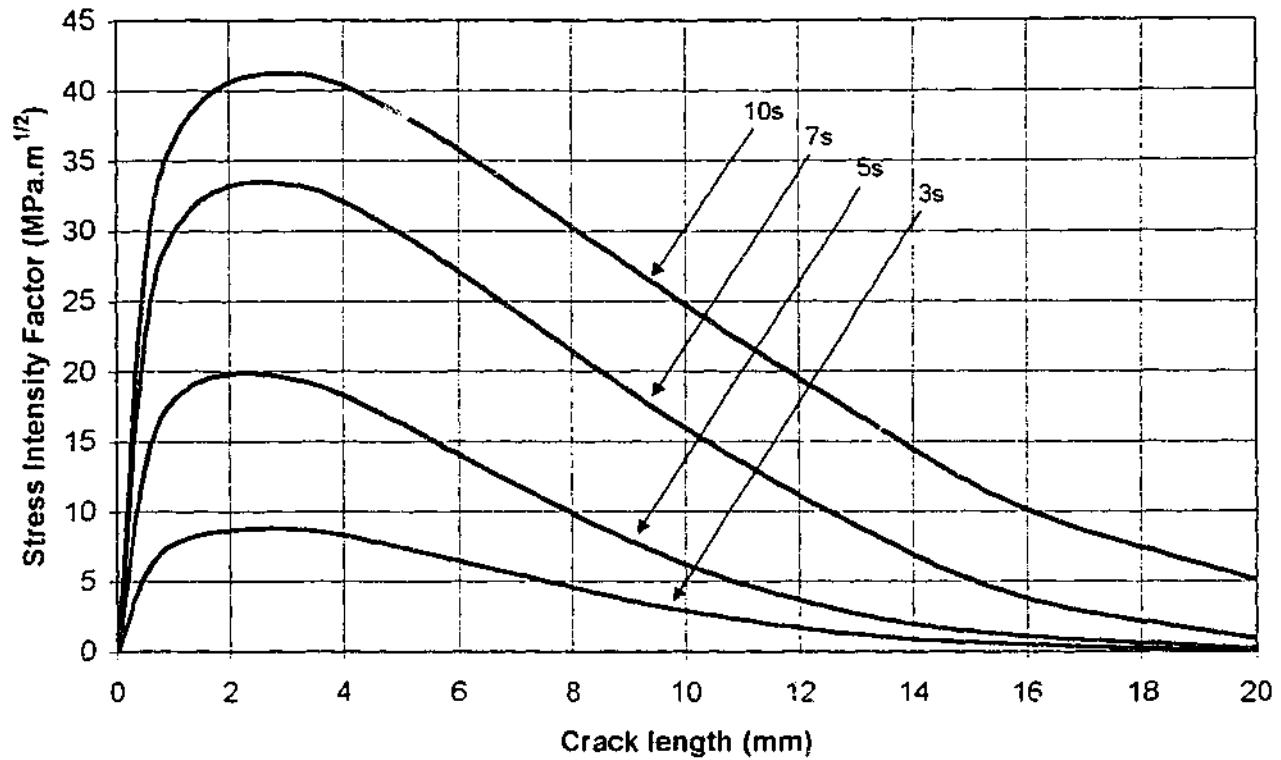


Fig 4.4: Cyclic change in stress intensity factor ( $\Delta K_I$ ) as a function of crack depth for thermal shocks of 4s, 5s, 7s and 10s at crack position 1 from central specimen a set temperature of 330°C. No primary mechanical load.

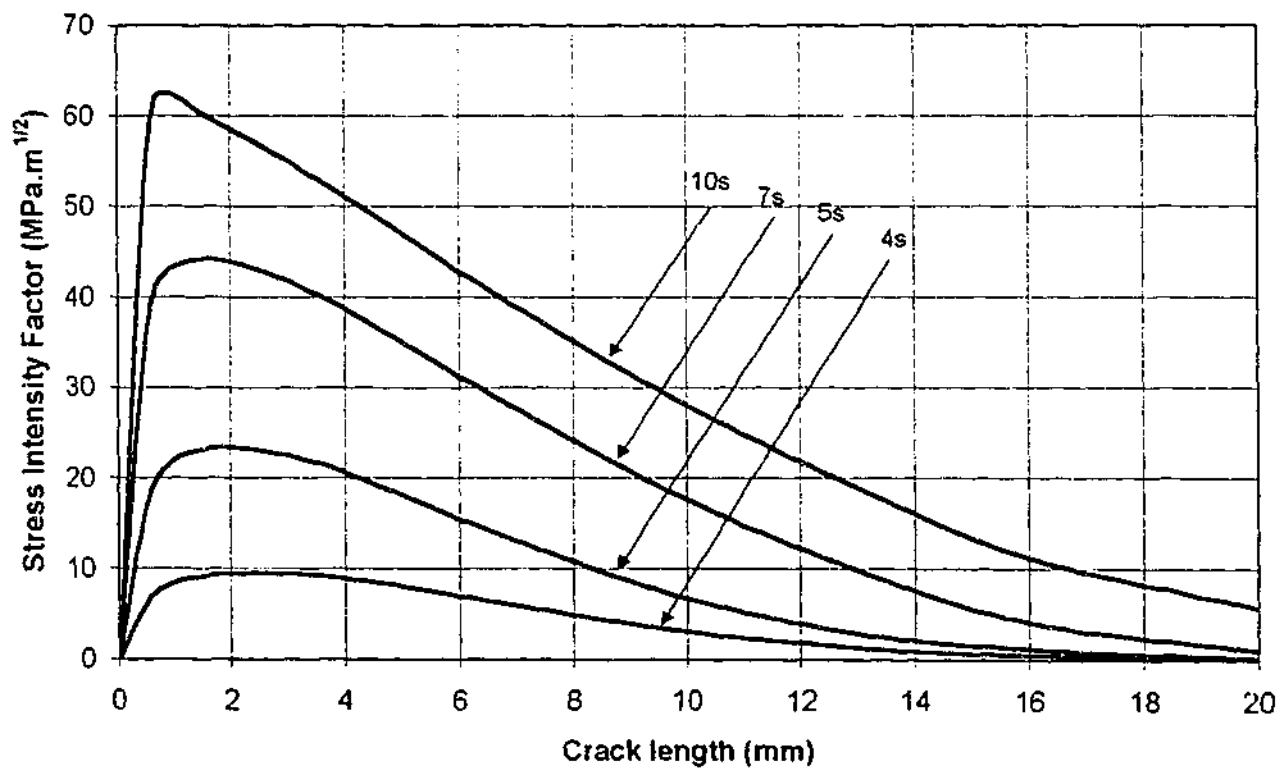


Fig 4.5: Cyclic change in stress intensity factor ( $\Delta K_I$ ) as a function of crack depth for thermal shocks of 4s, 5s, 7s and 10s at crack position 1 from central specimen a set temperature of 330°C. 90MPa primary mechanical load included.

#### 7.4.1 Crack Initiation

The stress amplitude developed at the surface of a flat plate specimen during RTS has been successfully related to the number of cycles to small crack initiation. The method for calculating the stress amplitude has been refined, using the ASME Boiler and Pressure Vessel Code, Section VIII, Division 2 (1998) *fatigue* data curves as a guideline. When compared with test data obtained using a purely elastic analysis, the ASME fatigue data was shown to be non-conservative (see figure 4.10, reproduced on the next page). Removal of this non-conservatism was achieved by applying a Neuber notch pseudostress analysis to the test data (see figure 4.12, also reproduced on the next page).

Note that in the ASME *fatigue* data curves printed on figures 4.10 and 4.12, the conservatism of two times on stress (or twenty times on lifetime, whichever is larger) that is built into the ASME *design* data curves (as printed in the code) is removed.

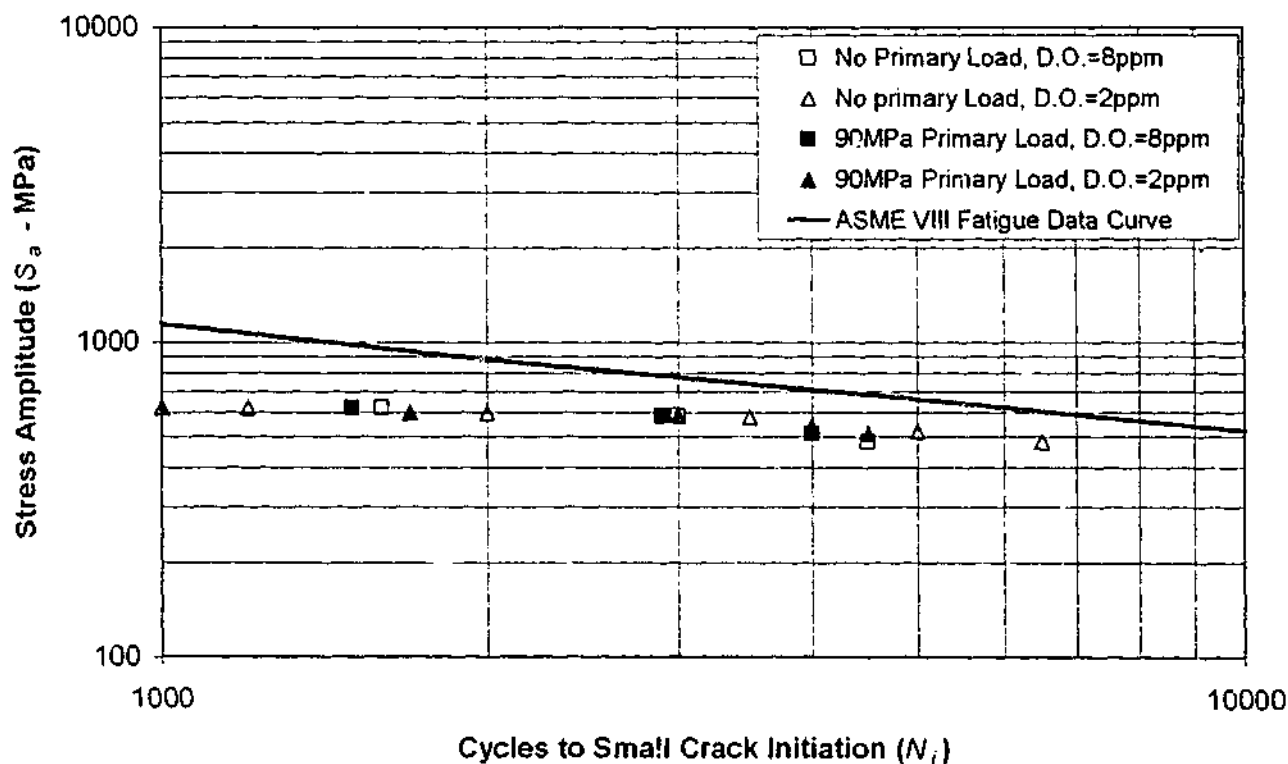


Figure 4.10: Number of cycles to crack initiation versus elastic notch stress amplitude ( $S_a^3$ ) for a sharp notch approximation with notch sensitivity analysis,  $k_f$  limited to 5.0 (Chapter 3, section 3.4.1.3).



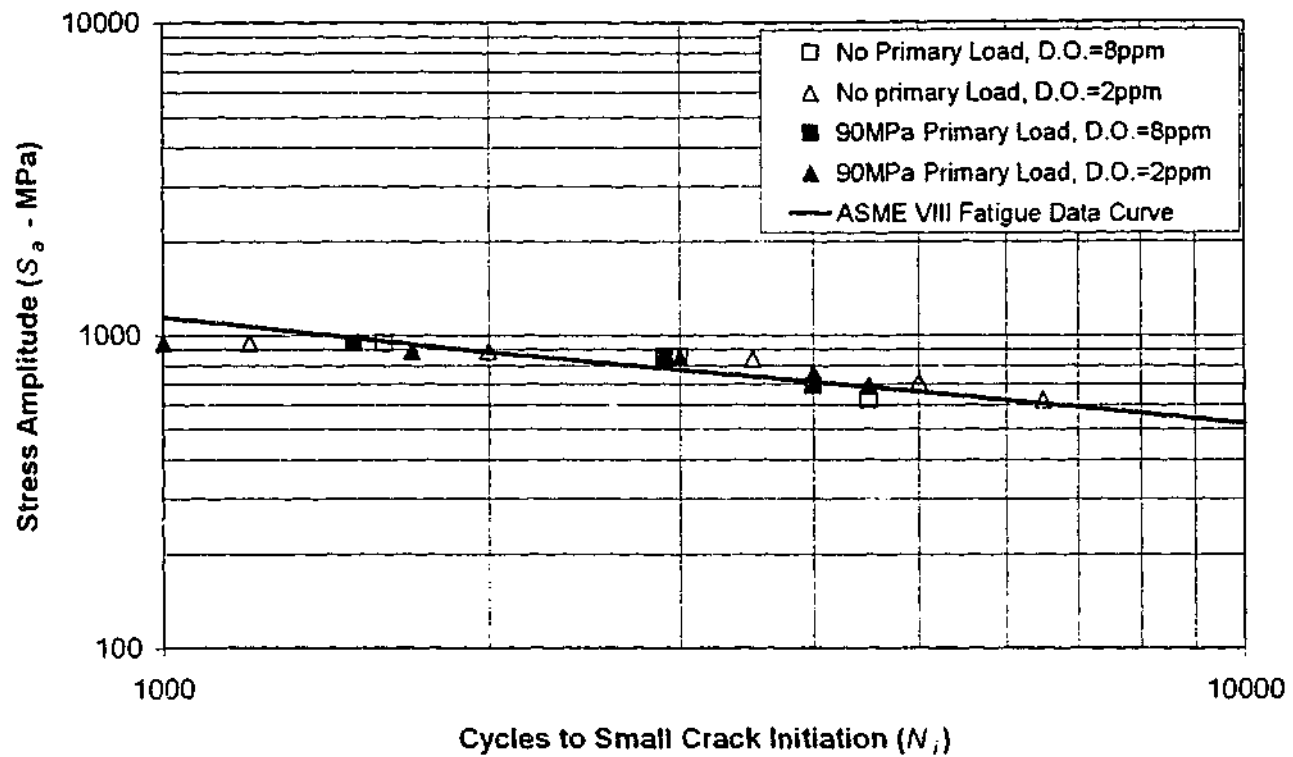


Figure 4.12: Number of cycles to crack initiation versus Neuber notch pseudostress amplitude ( $S'_a$ ) for an elastic sharp notch approximation with notch sensitivity analysis,  $k_f$  limited to 5.0 (Chapter 3, section 3.4.1.4).

These results suggest that, in order to avoid any non-conservatism in results when use is made of the ASME code fatigue data to predict crack initiation in a notched specimen, a Neuber notch pseudostress analysis should be applied in preference to a straight elastic stress analysis.

The effects of dissolved oxygen (D.O.) levels, primary loads and stress concentrators on the time taken for crack initiation are summarised below:

1. Effect of D.O. levels: Variations in dissolved oxygen levels between 8ppm and 2ppm in the cooling water have little or no effect on the times taken for crack initiation in a notched specimen.
2. Effect of primary loads: A steady state mechanical load of 90MPa has little or no effect on time to crack initiation in a notched specimen.

3. Effect of stress concentrators: Various notches cut into the face of the test specimens lead to rapid crack initiation. There seems to be a limit to the effect of the notches, and increasing the severity of a notch beyond a certain level results in no additional reduction in time to crack initiation. The limit of this effect occurs for the so-called "worst case notch" that corresponds to a fatigue notch factor of around 5.0. Other geometric discontinuities such as machining marks and weld crowns were also found to accelerate initiation. However, the assumption that these discontinuities also act as worst case notches can occasionally be conservative.

#### **7.4.2 Crack Growth**

Crack growth in a flat plate due to repeated thermal shock from temperatures below the creep range occurs in two main stages. These two stages are clearly visible on the crack growth rate versus crack length chart, figure 4.16, (reproduced on the next page). The first stage is located near the shocked surface where the material stresses are above yield. This region of material is subjected to high strain fatigue (HSF) and the crack growth accelerates in a roughly linear manner with an increase in crack length. The second stage of growth occurs when the crack leaves the HSF region and enters an area that behaves in a predominantly elastic manner. Linear elastic fracture mechanics (LEFM) can be used to describe growth trends in this region. At this crack depth, the reducing stress intensity factor field due to the thermal shock (see figures 4.4 and 4.5) means that all cracks in this area generally decelerate towards crack arrest. Conclusions relative to each region are summarised in the next two sections.

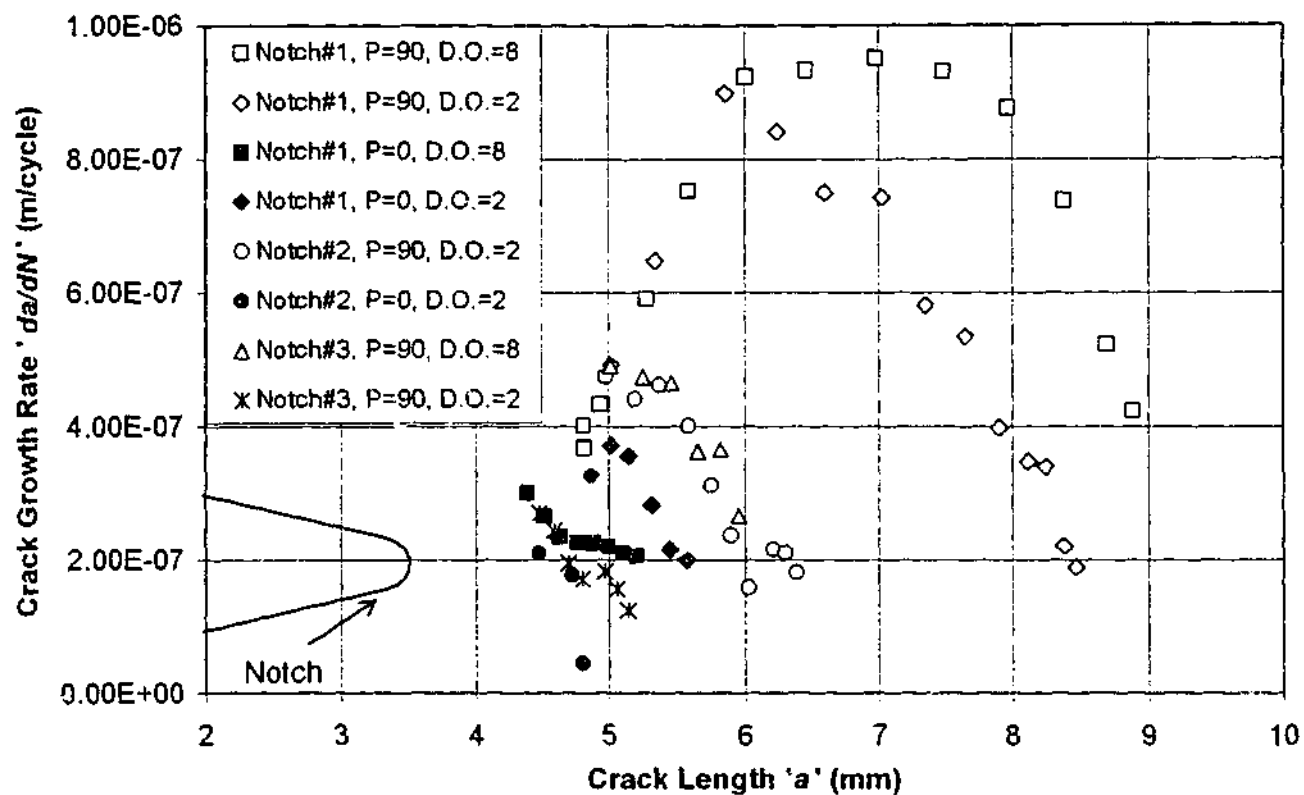


Figure 4.16: Crack growth rate versus crack length (includes notch depth) for a number of cracks grown by RTS. P = primary mechanical load (MPa), D.O. = dissolved oxygen level (ppm). Each symbol represents the growth of a different crack.

#### 7.4.2.1 High strain fatigue region

In this region, the thermal shock crack growth rate accelerates. This crack growth acceleration can be explained by a linear relationship relating the crack growth ( $da/dN$ ) rate to crack depth ( $a$ ):

$$\frac{da}{dN} = B.a - C \quad [4.1]$$

Where  $a$  is the crack length,  $B$  is a constant characteristic of the thermal shock loading and  $C$  is an allowance for the presence of a notch. A value for  $B$  of approximately  $4.5 \times 10^{-4}$  cycles<sup>-1</sup> was found through analysis of the experimental results. This value is similar to published data obtained from Marsh (1981) and Skelton (1982) for stainless steels exposed to elevated temperature HSF with a plastic strain range of around  $1.0 \times 10^{-3}$ . The fit of equation [4.1] to the first stage of crack growth is shown in figure 4.17 (reproduced on the next page).

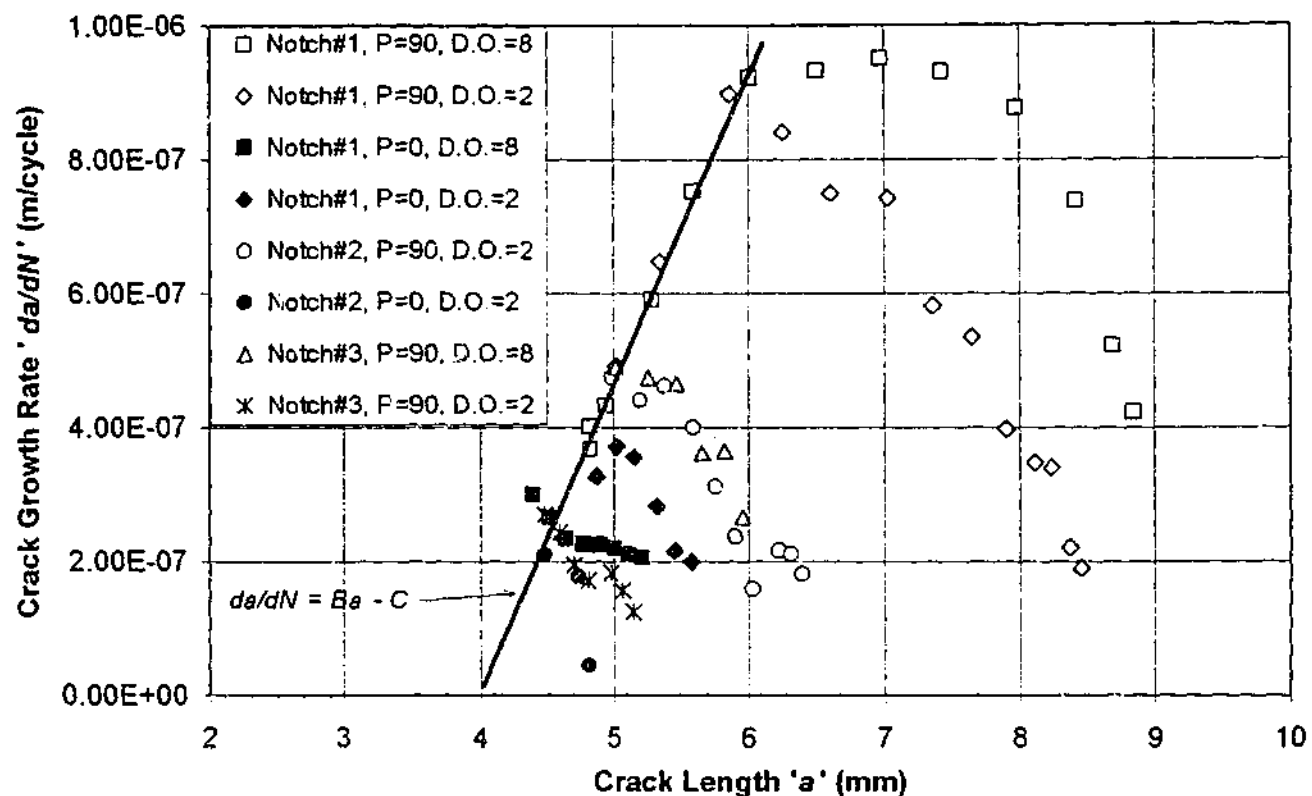


Figure 4.17: Crack growth as a function of crack length showing linear prediction curve for High Strain Fatigue (HSF) region. P = primary mechanical load (MPa), D.O. = dissolved oxygen level (ppm)

The depth of this crack acceleration region is related to the size of the plastic zone developed at the surface during the thermal shock. Consequently, the more severe the shock, the deeper the HSF region extends.

Dissolved oxygen levels in the cooling water and primary mechanical loads have the following effects:

1. Effect of D.O. levels: Variations in dissolved oxygen levels between 8ppm and 2ppm in the cooling water have little or no effect on crack growth rates in the HSF region.
2. Effect of primary loads: Variations in the primary load have little or no effect on the crack growth equation [4.1]. They do however affect the depth of the plastic zone. An increase in primary load increases the size of the HSF region and hence the depth to which cracks will accelerate.

#### 7.4.2.2 Elastic crack growth region

In this region, the specimen behaviour is primarily elastic and the crack growth rate is generally found to decelerate. Modelling of the crack growth in this region is much more complex than in the HSF zone. The elastic stress intensity factor is a suitable parameter to correlate crack growth, nevertheless environmental interactions and the effects of steady state mechanical loads imply that a simple law cannot be developed to describe growth in the region.

Models that allow for the influence of environment and mean loads have been applied to the crack growth rate in this region with some success. This thesis has followed the work by Gabetta et al (1990), which proposes the following equation for predicting crack growth:

$$\frac{da}{dN} = C(\Delta K)^m + \tau \frac{da}{dt}_{SCF} \quad [4.5]$$

Where  $C$  and  $m$  are constants dependent on the true corrosion fatigue (TCF) crack growth rate (unique for the particular material-environment combination),  $\tau$  is the rise time of loading (ie the duration of the thermal shock) and  $da/dt_{SCF}$  is the stress corrosion fatigue crack growth rate, (also unique for each material-environment combination).

A stress intensity factor limit also exists ( $\Delta K_c$ ), below which, the stress corrosion fatigue (SCF) crack growth rate ( $da/dt_{SCF}$ ) is found to be zero. A theoretical equation for determining this limit, which assumes anodic dissolution is responsible for the enhanced crack growth, has also been devised by Gabetta et al:

$$\Delta K_c^2 = \frac{1}{\alpha_{ASCR}} \cdot \sigma_y E \tau \cdot \frac{1-R}{1+R} \frac{da}{dt}_{SCF} \quad [2.18]$$

Where  $\alpha_{ASCR}$  is a constant that is dependent on the active surface creation rate (ASCR) of the material-environment combination and  $R$  is the minimum to maximum cyclic stress intensity factor ratio. Smoothed experimental crack growth data in the LEFM region is

plotted in addition to prediction curves based on equations [4.5] and [2.18] in figures 4.22 and 4.23 (reproduced on the next page).

Because stress intensity factor levels in a flat plate due to thermal shock generally decrease with crack depth outside the HSF zone (see figures 4.4 and 4.5), the tendency for all cracks in the LEFM region is towards arrest. However, as equations [4.5] and [2.18] describe, the rate at which this deceleration occurs is highly dependent on environmental and primary load considerations. Effects of dissolved oxygen levels in the cooling water and primary mechanical loads are summarised below.

1. Effect of D.O. levels: An increase in dissolved oxygen levels in the cooling water from 2ppm to 8ppm results in an increase in crack growth rate for cracks with large  $R$ -ratios ( $R > 0.3$ ).
2. Effect of primary loads: The addition of a steady state primary load to a specimen exposed to thermal shock results in a stress intensity factor profile that yields an increasing  $R$ -ratio ( $K_{min}/K_{max}$ ) with crack depth (see figures 4.6 and 4.7, reproduced on page 202). Increases in  $R$ -ratio seem to result in an associated rise in the crack growth rate. However, this seems only to be the case if the  $R$ -ratio increase is encountered while the crack growth rate is rising or steady. This is thought to be an effect of the loading history produced during RTS.

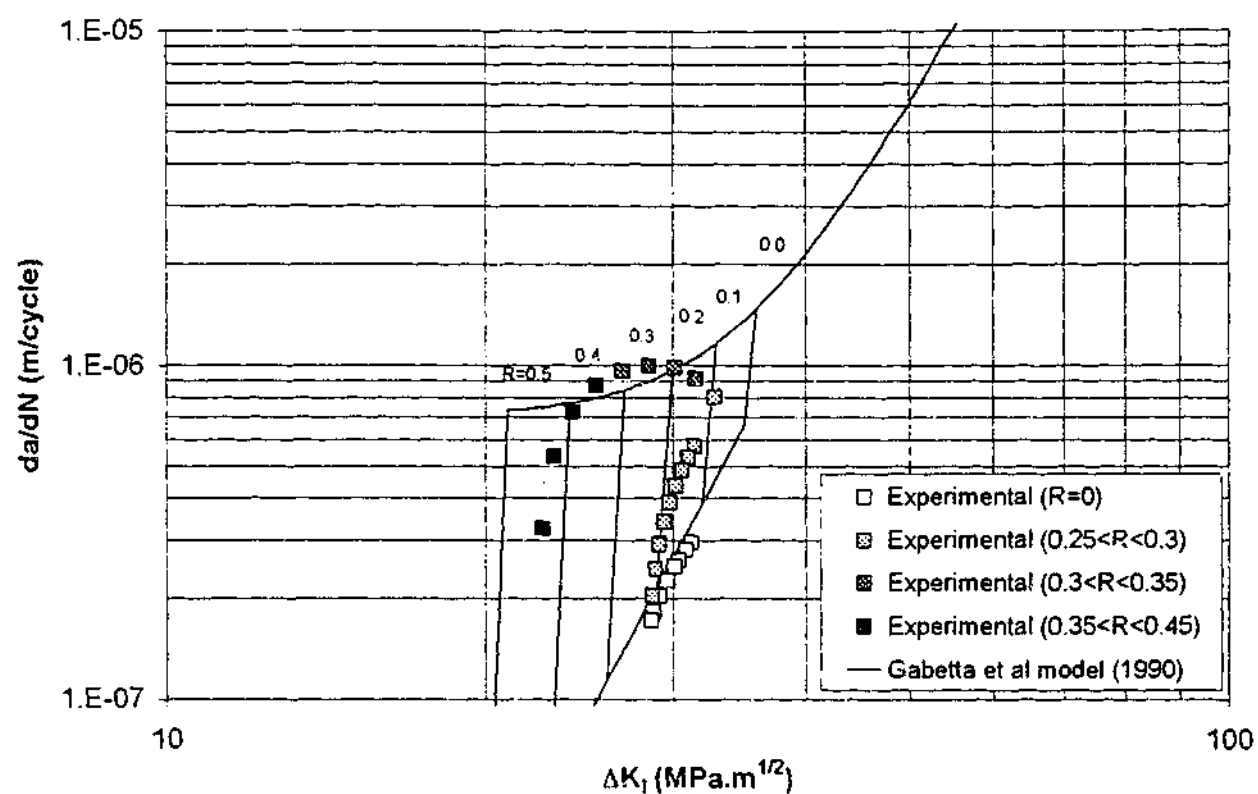


Figure 4.22: Smoothed experimental crack growth data plotted against a Gabetta et al (1990) model prediction, allowing for the effects of environment and primary load. Experimental data for D.O.=8ppm plotted.

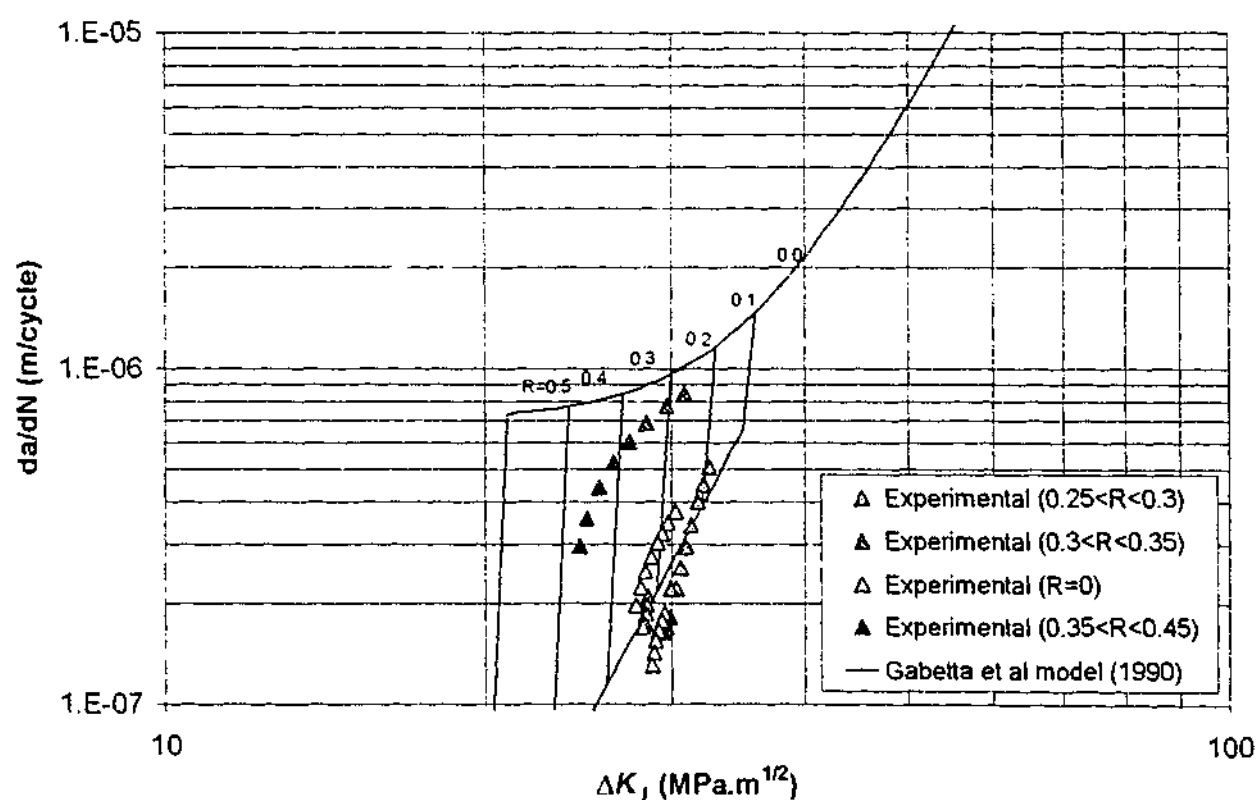


Figure 4.23: Smoothed experimental crack growth data plotted against a Gabetta et al (1990) model prediction, allowing for the effects of environment and primary load. Experimental data for D.O.=2ppm plotted

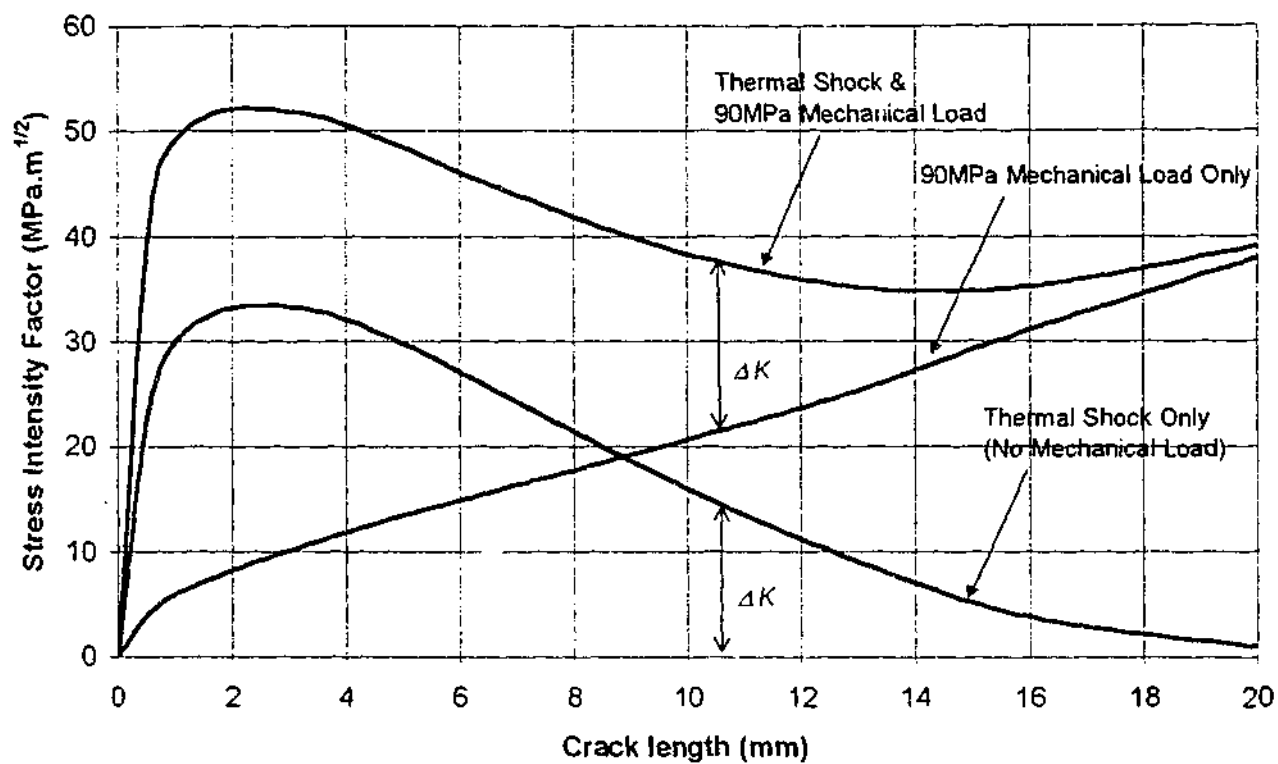


Figure 4.6: Stress intensity factor profiles for 7s thermal shock at notch position 1 from central specimen temperature of 330°C showing effects of adding 90MPa mechanical load.

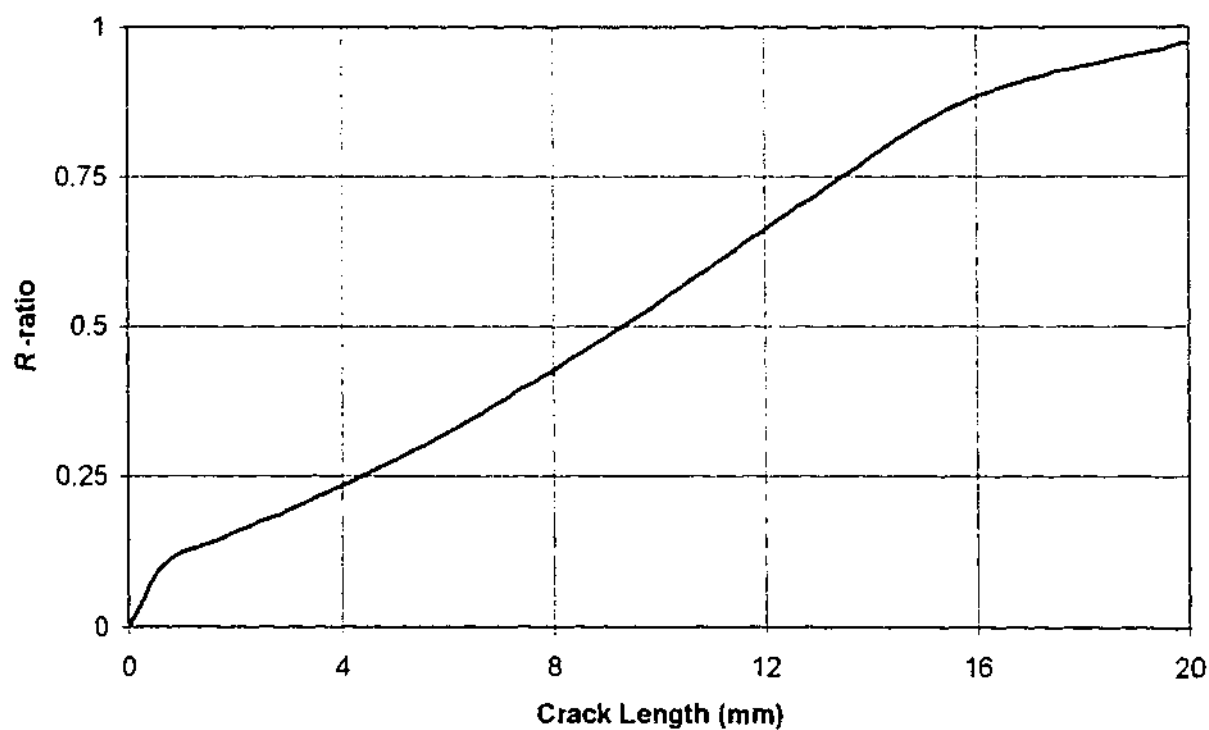


Figure 4.7: R-ratio as a function of crack length for a 7s quench with 90MPa mechanical load, at notch position 1 from a central specimen temperature of 330°C.



#### **7.4.2.3 A combined growth law**

A combined growth law developed to explain RTS crack growth through both the HSF and LEFM regions can be proposed from this work. The model is divided into two sections, the first occurs when crack growth is inside the plastic zone close to the specimen surface and the second is the elastic region that is encountered at greater crack depths. For crack growth in the plastic zone, a linear acceleration of crack growth rate with crack depth is suggested (equation [4.1]). For crack growth outside the plastic zone, the crack growth rate (typically of a decelerating nature) is predicted using a LEFM growth law shown in equation [4.5].

The crack depth at which the crossover between the HSF and LEFM growth laws occurs is a critical parameter. Because crack growth will accelerate until this depth is reached, a crack of "crossover depth" can be assumed to rapidly appear during RTS. The smaller this depth is, the less chance that appreciable crack growth can occur in the ensuing LEFM region. This is verified by the experimental crack growth rate data, summarised in figure 4.16. The crossover depth is seen to be roughly equal to the cyclic plastic zone size, developed during a thermal shock and assisted by steady state stresses. Unfortunately, estimation of this cyclic plastic zone size can be quite complicated, particularly if local stress concentrators are present. Development of the combined growth law as described here would be well served by researching simple methods to estimate the crossover depth. This is a proposed area of further work.

#### **7.4.2.4 Crack growth mechanisms**

Observations of the crack growth geometry and fracture surface after test completion have led to a few conclusions about the mechanisms present during crack growth. In the HSF region, the presence of a large amount of oxide product, visible along the crack sides, indicates that environmental interaction is concentrated in this area. Determining the mechanism of growth in this area is hindered by the large amount of corrosion damage to the crack surface.

Crack growth appearance in the LEFM region depends on the presence of primary loads. Where these loads are high, producing a large  $R$ -ratio, a fair amount of corrosion product is still visible. This is consistent with the assumption that stress corrosion fatigue (SCF) is occurring in this region by the mechanism of anodic dissolution. For cracks with smaller  $R$ -ratios or when cyclic stress intensity factors are below the SCF threshold  $\Delta K_{sc}$ , crack growth is thought to be occurring by the mechanism of true corrosion fatigue (TCF). In this region, the crack growth appears to be predominantly transgranular in nature, with a sharp, twisted crack path. Hydrogen embrittlement could be accepted as a possible mechanism for the accelerated TCF growth in this region.

### ***7.5 Transient and Geometry Effects***

Two of the major factors which affect RTS crack growth, neither of which were addressed in the experimental analysis, were investigated with the aid of analytical and numerical techniques. First to be analysed was the effect of altering the thermal shock duration on the stress intensity factors and hence long crack growth (outside HSF region) in flat plate and hollow cylinder geometries. Second was the analysis of the stress fields developed in the vicinity of the apex of a corner exposed to a thermal shock. Both investigations have developed analytical tools that can be used to assist in the analysis of real life situations of thermal shock. The following conclusions can be made from the work.

1. A form of chart has been developed that can assist in identifying the severity of thermal shocks on an edge cracked, flat plate geometry. With knowledge of the thermal shock conditions a plate is exposed to (namely duration and size of shock, environment and likely number of shocks in the component lifetime), a user can predict crack arrest depth, or in the case of pre-existing cracks, determine the likely stress intensity factor developed. An example of this chart (figure 5.2) developed for an infinite surface heat transfer coefficient is reproduced on the next page.

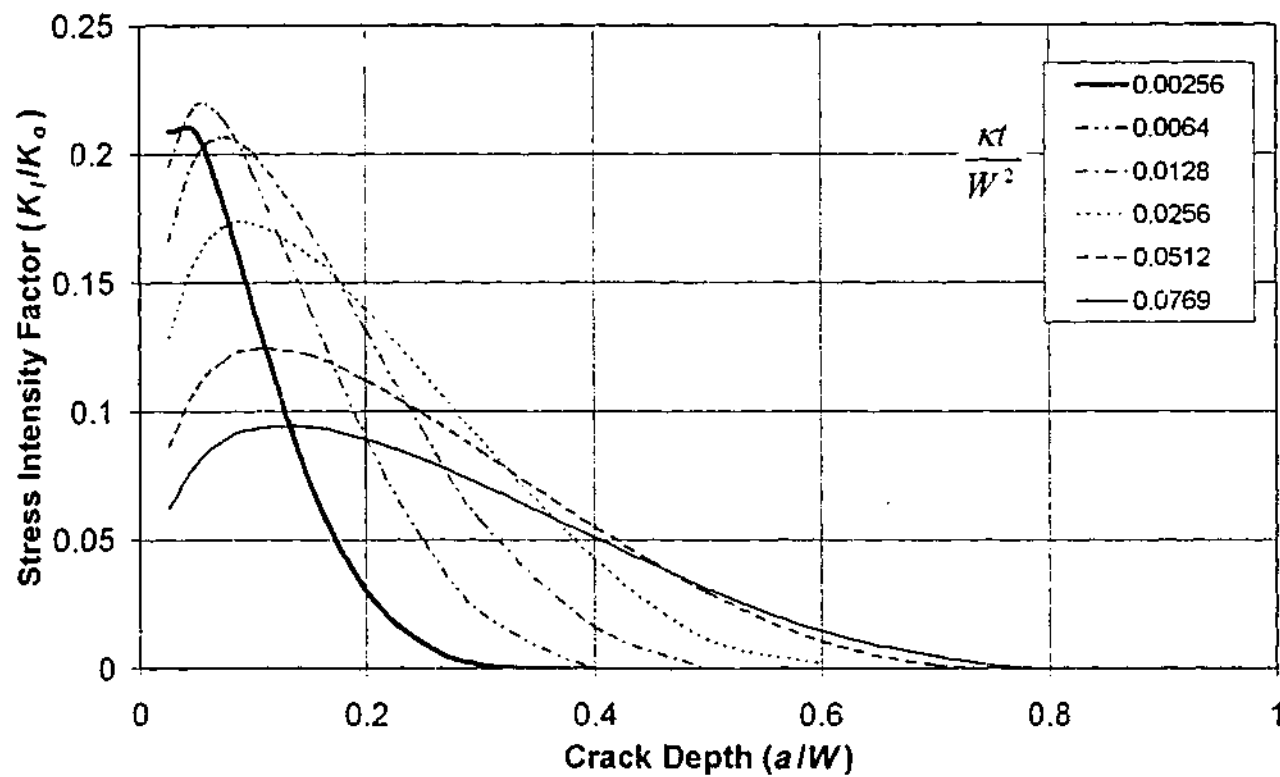


Figure 5.2: Effect of shock duration on theoretical stress intensity factor distributions for a flat plate of depth  $W$  with thermal diffusivity  $\kappa$  and a crack of depth  $a$ , exposed to one-sided thermal shock of time  $t$  with infinite surface heat transfer.

2. A hollow cylinder exposed to an internal thermal shock can, depending on the ratio of inside to outside diameter and the flaw aspect ratio, produce stress intensity factors for long, deep cracks that are much larger than for an edge crack, flat plate. This makes the crack arrest issue in hollow cylindrical equipment (such as pressure vessels and piping) more complicated than in a flat plate as observed in the experimental analysis.
3. An analytical solution has been obtained for the maximum stress developed in a corner of radius  $r$  in an infinite space with a vertex angle greater than  $180^\circ$  (see figure 5.15, reproduced on the next page) exposed to a symmetric thermal shock.

$$\sigma_{\max} = \frac{4K_t \delta^{\lambda-1}}{\sqrt{2\pi} [(1+\lambda) + \chi(1-\lambda)]} \quad [5.25]$$

Where  $K_I$  is the generalised stress intensity factor for a corner exposed to a thermal shock,  $\lambda$  is a measure of the strength of singularity developed at the corner and:

$$\chi = -\frac{\sin(1-\lambda)\gamma}{\sin(1+\lambda)\gamma} \quad \text{and} \quad \delta = \frac{r\left(\gamma - \frac{\pi}{2}\right)}{\gamma}$$

The form of this solution is summarised in figure 5.22 along with finite element model results. The figure shows that equation [5.25] can be reasonably applied to finite corner configurations in the case of short duration thermal shocks when component size is sufficient to prevent the any boundaries effects. A maximum non-dimensional stress ( $\bar{\sigma}_{\max}$ ) limit of 3.0 is suggested for use with the analytical solution in a finite geometry situation.

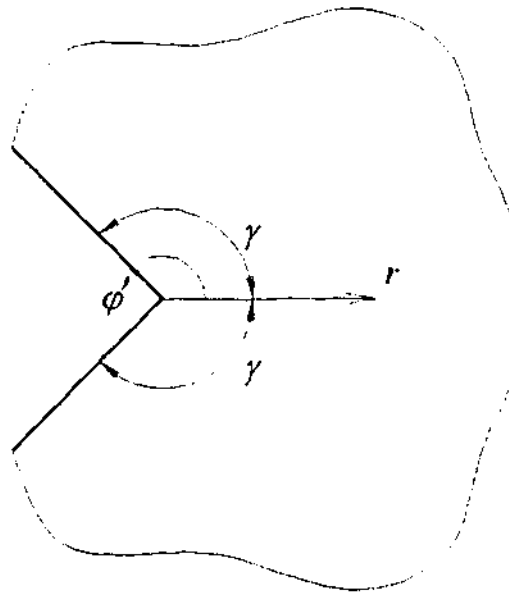


Figure 5.15: Corner with vertex angle ( $2\gamma$ ) greater than  $180^\circ$  and coordinate system.

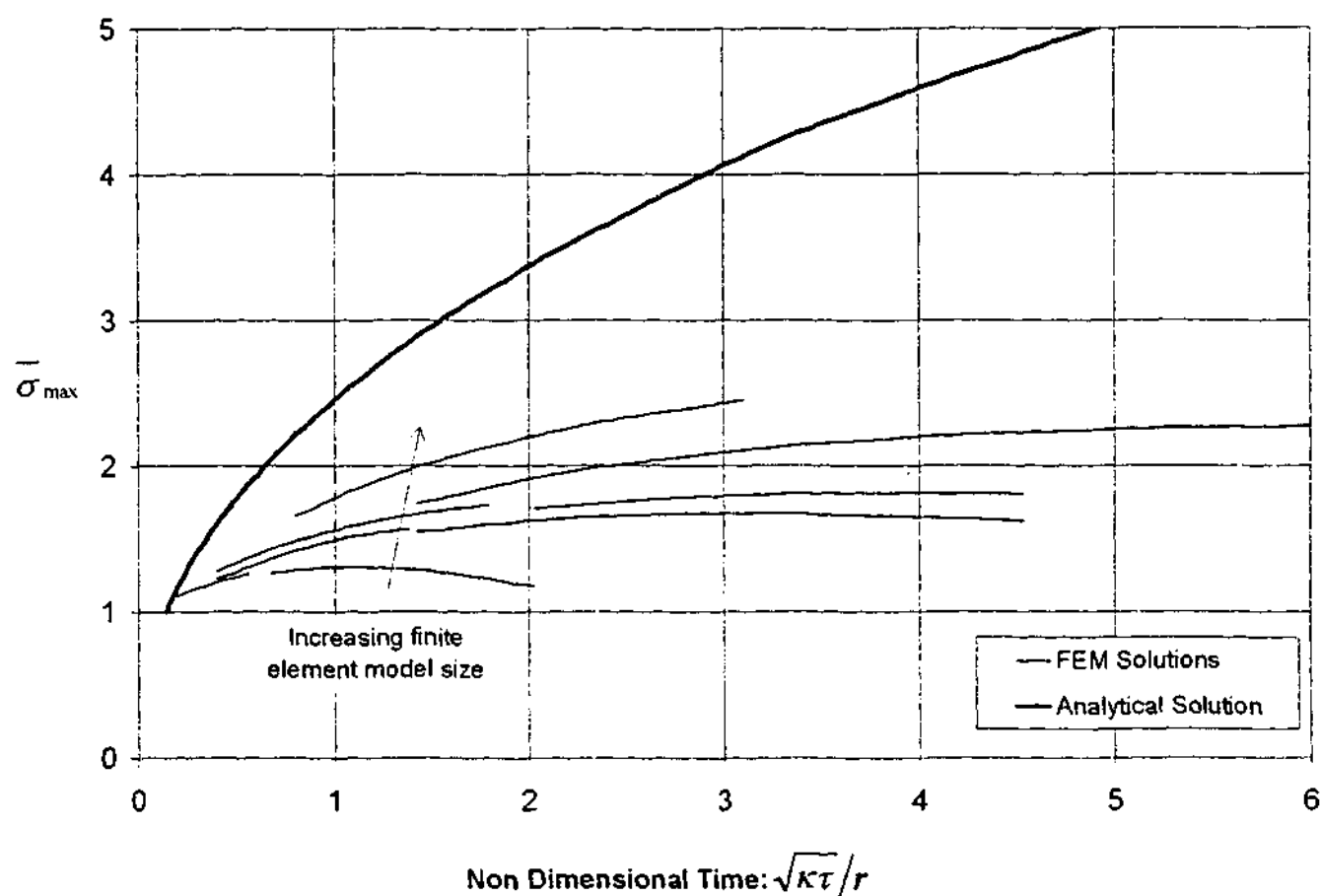


Figure 5.22: Maximum non-dimensionalised stress ( $\bar{\sigma}_{\max}$ ) produced at a corner with vertex angle  $2\gamma = 270^\circ$  and corner radius  $r$ , exposed to thermal shock of time  $\tau$ . Both analytical solution and solutions from several finite element models are plotted.

4. Theory and finite element solutions suggest that for corners with vertex angles less than  $180^\circ$  (see figure 5.24, reproduced on the next page), thermal stresses in the vicinity of the corner should be less than those observed in a flat plate under conditions of plane strain. The analytical results are in apparent conflict with observed industrial failures such as cracking at tube penetrations in a thick-walled header. The explanation of such failures is an area of proposed further study.

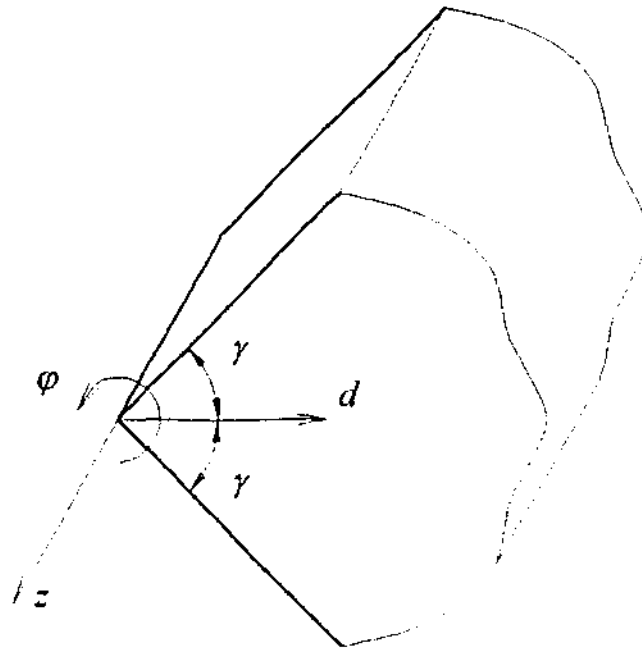


Figure 5.24: Corner with vertex angle ( $2\gamma$ ) less than  $180^\circ$  and coordinate system.

## 7.6 Code Analysis

A comparison of existing design and analysis code techniques that are commonly applied for crack growth prediction against actual experimental test data for a flat plate specimen exposed to RTS was conducted. The work focussed on the ASME Boiler and Pressure Vessel Code, Section XI (1998), "Rules for inspection and testing of components of light water cooled plants" and British Standard BS 7910 (1999), "Guide on methods for assessing the acceptability of flaws in fusion welded structures". The following code specific conclusions can be made:

### 7.6.1 ASME Boiler and Pressure Vessel Code, Section XI (1998)

1. The polynomial stress profile approximation and weight function technique produce an accurate model of the crack length versus number of cycles growth curve for a flat plate specimen exposed to RTS.

2. The selection of the provided reference LEFM crack growth curves appropriate for converting stress intensity factors to crack growth rates is not clear when environmental interaction occurs.

#### **7.6.2 BS 7910 (1999)**

1. The stress linearisation techniques used for determining stress intensity factor profiles are too conservative for use with the highly non-linear stresses generated during a thermal shock.
2. The reference LEFM crack growth curves for a marine environment provide a good approximation of observed experimental crack growths when environmental assistance is present (ie when  $R > 0.3$ ).
3. The reference LEFM crack growth curves for a dry environment provide a good approximation of observed experimental crack growth rates when environmental assistance is small or not present (ie with  $R < 0.3$ ).

#### **7.6.3 Combined Technique**

It is observed that a combined technique using the ASME approach for calculating the stress intensity factor profile and the simple reference crack growth curves from BS 7910 provide a good balance between accuracy and simplicity when estimating LEFM crack growth due to RTS.

## **7.7 Recommendations for Further Work**

The following recommendations for further work rise out of the conclusions of this thesis.

1. Experimental and theoretical analysis of thermal shock crack growth in the HSF region. The aim of this work should be to develop simple relations for the determination of the effects that thermal shock size, primary mechanical loads and specimen geometry (including the presence of stress concentrators) have on the size of this region. Quantification of the size of this region will allow easier application of the two-stage RTS crack growth model that was introduced in this thesis.
2. Further analysis of thermal shock cracking at corners of vertex angles less than  $180^\circ$ . This investigation would be primarily experimental with the aim to determine the conditions under which this form of cracking preferentially occurs. Particularly, what combinations of thermal shock and primary load (if any) can initiate this type of cracking. The ability to reduce the frequency of this type of cracking by introducing changes in the geometry such as including a corner radius should also be investigated. A better understanding of the conditions that lead to this form of cracking and how to reduce the occurrence can assist in preventing failures as observed at the tube penetrations in thick-walled headers.



## References

Alvarez-Armas I., Armas A.F. and Petersen C., (1994). Thermal fatigue of a 12% chromium martensitic stainless steel, *Fatigue and Fracture of Engineering Materials and Structures*, Vol. 1, No. 6, pp. 671-681.

Anderson T.L., (1995). *Fracture Mechanics: Fundamentals and Applications*, Second Edition, CRC Press, Boca Ranton.

API, (1999). API 579: *Recommended Practice for Fitness for Service*, American Petroleum Institute Publishing Services, Washington.

AS, (1995). AS 1548-995, *Australian Standard: Steel Plates for Pressure Equipment*, Standards Australia, Homebush.

ASME, (1998). ASME Boiler and Pressure Vessel Code, Section VIII, *Pressure Vessels, Division 2: Alternative Rules*, American Society of Mechanical Engineers, New York.

ASME, (1998). ASME Boiler and Pressure Vessel Code, Section XI, *Rules for Inservice Inspection of Nuclear Power Plant Components*, American Society of Mechanical Engineers, New York.

ASTM, (1995). ASTM E 647-95a, *Standard Method for Measurement of Fatigue Crack Growth Rates*, American Society for Testing and Materials, Philadelphia.

ASTM, (1996). ASTM E 8M-96, *Standard Test Method for Tension Testing of Metallic Materials [metric]*, American Society for Testing and Materials, Philadelphia.

Austen I.M. and Walker E.F., (1977). Quantitative understanding of the effects of mechanical and environmental variables on corrosion fatigue crack growth behaviour, *The Influence of Environment on Fatigue*, Institute of Mechanical Engineers Conference Publications, London, pp. 1-10.

Bamford W.H. (1977). The effect of pressurized water reactor environment on fatigue crack propagation of pressure vessel steels, *The Influence of Environment on Fatigue*, Institute of Mechanical Engineers Conference Publications, London, pp. 51-56.

Bannantine J.A., Comer J.J. and Handrock J.L., (1990). *Fundamentals of Metal Component Fatigue Analysis*, Prentice Hall, New Jersey.

Beck C.G. and Santhanam A.T., (1976). Effect of microstructure on the thermal fatigue resistance of a cast cobalt-base alloy, Mar-M509, *Thermal Fatigue of Materials and Components*, ASTM STP 612, American Society for Testing and Materials, Philadelphia, pp. 123-140

Beer F.J., (1971). Plastic growth of a pressurised shell through interaction of steady pressure with cyclic thermal stresses, *Thermal stresses and thermal fatigue*, Proceedings of the International Conference, Berkeley, UK. 22nd-26th Sept. 1969, pp. 3-26.

Biot M.A., (1961). New methods in heat flow analysis with application to flight structures, *Journal of Aeronautical Science*, Vol. 24, pp. 857-873.

Blackburn W.S and Jackson A.D., (1977). An integral associated with the state of a crack tip in a non-elastic material, *International Journal of Fracture*, Vol. 13, No. 2, April, pp. 183-199.

Bolotin V.V., (1999). *Mechanics of Fatigue*, CRC press, New York.

Bree J., (1967). Elasto-plastic behaviour of thin tubes subjected to internal pressure and intermittent high heat fluxes with application to fast-nuclear reactor fuel elements, *Journal of Strain Analysis*, Vol. 2, pp. 226-238.

BSI, (1993). BS7608: 1993 - *Fatigue and Design Assessment of Steel Structures*, BSI, London.

BSI, (1999). BS 7910: 1999 - *Guide on Methods for Assessing the Acceptability of Flaws in Fusion Welded Structures*, BSI, London.

Bueckner H.F., (1970). A novel principle for the computation of stress intensity factors, *Zeitschrift für Angewandte Mathematik und Mechanik*, Vol. 50, pp. 529-545.

Chopra O.K. and Shack W.J., (1999). Overview of fatigue crack initiation in carbon and low-alloy steels in light water reactor environments, *Journal of Pressure Vessel Technology*, Vol. 121, pp. 49-60.

Coffin L.F., (1954). A study of the effects of cyclic thermal stresses on ductile metal, *Transactions ASME*, Vol. 76, pp.931-950.

Coffin L.F. and Wesley R.P., (1954). Apparatus for study of effects of cyclic thermal stresses on ductile metals, *Transactions ASME*, Vol. 76, pp. 923-930.

Comini G., Giudice S.D. and Carlo N., (1994). *Finite Element Analysis in Heat Transfer*, Taylor and Francis, Washington.

Czuck G., Mattheck C., Munz D. and Stamm H., (1985). Crack growth under cyclic thermal shock loading, *Nuclear Engineering and Design*, Vol. 84, pp. 189-199.

Delafosse D. and Magnin T. (2001). Hydrogen induced plasticity in stress corrosion cracking of engineering systems, *Engineering Fracture Mechanics*, Vol. 68, Issue 6, pp. 693-729.

Dooley B., (1997). Don't let those boiler tubes fail again: Part 2, *Power Engineering*, August, pp. 31-40.

Dooley R.B. and McNaughton W.P., (1996). *Boiler Tube Failures: Theory and Practice, Volume 2: Water-Touched Tubes*, Electric Power Research Institute, California.

Elber W., (1970). Fatigue crack closure under cyclic tension, *Engineering Fracture Mechanics*, Vol. 2, pp. 37-45.

Eshelby J.D., (1951). The force on an elastic singularity, *Philosophical Transactions of the Royal Society*, Pergamon Press, London, pp. 2563-2570.

Fissolo A., Marini B., Berrada A., Nais G. and Wident P., (1995). Initiation and growth of cracks under thermal fatigue loading for a 316L type steel, *Fatigue Under Thermal and Mechanical Loading: Mechanisms, Mechanics and Modelling*, Proceedings held at Petten, The Netherlands 22-24 May, pp. 67-77.

Gabetta G., (1987). The effect of frequency in environmental fatigue tests, *Fatigue and Fracture of Engineering Materials and Structures*, Vol. 10, No. 5, pp. 373-383.

Gabetta G., Rinaldi C. and Pozzi D., (1990). A model for environmentally assisted crack growth rate, *Environmentally Assisted Cracking: Science and Engineering*, ASTM STP 1049, American Society for Testing and Materials, Philadelphia, pp. 266-282.

Gamble R.M. and Paris P.C., (1976). Cyclic crack growth analysis for notched structures at elevated temperatures, *Mechanics of Crack Growth*, ASTM STP 590, American Society for Testing and Materials, Philadelphia, pp. 345-367.

Gangloff R.P., (1990). Corrosion fatigue crack propagation in metals, *Proceedings, Environment-Induced Cracking of Metals*, eds., R.P. Gangloff and M.B. Ives, National Association of Corrosion Engineers, NACE-10, Houston, pp. 55-109.

Gemma A.E., Langer B.S. and Leverant G.R., (1976). Thermomechanical fatigue crack propagation in an anisotropic (directionally solidified) nickel-base superalloy, *Thermal Fatigue of Materials and Components*, ASTM STP 612, American Society for Testing and Materials, Philadelphia, pp. 199-213.

Gilman J.D., (1987). Further development of a model for predicting corrosion fatigue crack growth in reactor pressure vessel steels, *Transactions of the ASME, Journal of Pressure Vessel Technology*, Vol. 109, August 1987, pp. 340-346.

Ginsztler J., (1987). Retarding the crack initiation process during low cycle thermal shock fatigue, *Low Cycle Fatigue and Elasto-Plastic Behaviour of Materials*, 2nd International Conference on Low Cycle Fatigue and Elasto-Plastic Behaviour of Materials, pp. 643-648.

Goodman A.M., (1981). The influence of rapid thermal transients on elastic-plastic ratchetting, *Journal of Engineering Structures*, Vol. 3, pp. 17-26.

Gross A. and Mendelson A., (1972). Plane elastostatic analysis of V-notched plates, *International Journal of Fracture Mechanics*, Vol. 8, pp. 267-276.

Groth H.L., (1988). Stress singularities and fracture at interface corners in bonded joints, *International Journal of Adhesion and Adhesives*, Vol. 8, No 2, pp. 107-113.

Hellen T.K., Cesari F. and Maitan A., (1981). *The Application of Fracture Mechanics in Thermally Stressed Structures*, Central Electricity Generating Board, Research Division, Berkeley Nuclear Laboratories, RD/B/5039N81.

Howes M.A.H., (1973). Evaluation of thermal fatigue resistance of metals using the fluidized bed technique, *Fatigue at Elevated Temperatures*, ASTM STP 520, American Society for Testing and Materials, Philadelphia, pp. 242-254.

Jones D.A., (1996). *Principles and Prevention of Corrosion*, Prentice-Hall, New Jersey.

Juvinall R.C., (1967). *Stress, Strain and Strength*, McGraw-Hill, New York.

Kardomateas G.A. and Carlson R.L., (1998). Predicting the effects of load ratio on the fatigue crack growth rate and fatigue threshold, *Fatigue and Fracture of Engineering Materials and Structures*, Vol. 21, pp. 411-423.

Kawakubo T., Hishida M., Amano K. and Katsuta M., (1980). Crack growth behaviour of type 304 stainless steel in oxygenated 290°C pure water under low frequency loading, *Corrosion-NACE*, Vol. 36, No. 11, pp. 638-647.

Kim K.S. and Van Stone R.H., (1997). Crack growth under thermo-mechanical and temperature gradient loads, *Engineering Fracture Mechanics*, Vol. 58 No.1/2 pp.133-147

Kotousov A. and Price J.W.H., (1998). Elastic analysis of semi-elliptical cracks in cylinders under thermal shock using the BS7910 framework, *International Journal of Pressure Vessels and Piping*, Vol. 76, pp. 831-837.

Kotousov A. and Price J.W.H., (1998). Stress Intensity Factor for Semi-Infinite Crack Formed by Moving Thermal Source, *International Journal of Fracture: Letters in Fracture and Micromechanics*, Vol. 90, pp. L39 – L42.

Kotousov A., Price J.W.H. and Kerezsi B., (2000). Thermal shock at corners, *Design and Analysis of Pressure Vessels and Piping*, 2000 ASME Pressure Vessels and Piping Conference, PVP-Vol. 399, American Society of Mechanical Engineers, New York, pp. 17-23.

Krolop S., Pfeffer P. and Stegmeyer R., (1986). Fracture mechanical assessment of cracks under cyclic thermal shock and operational conditions, *Nuclear Engineering and Design*, Vol. 96, pp. 363-379.

Lawson L.R., (1987). Thermal cycling apparatus for thermomechanical fatigue testing, *Review of Scientific Instrumentation*, Vol. 58, No. 10, pp. 1942-1944.

Lazzarin P. and Tovo R., (1996). A unified approach to the evaluation of linear elastic stress fields in the neighborhood of cracks and notches, *International Journal of Fracture*, Vol. 78, pp. 3-19

Lin K.Y. and Tong P., (1990). Singular finite elements for the fracture analysis of V-notched plate, *International Journal of Numerical Methods in Engineering*, Vol. 15, pp. 1343-1354.

Lindholm U.S. and Davidson D.L., (1973). Low-cycle fatigue with combined thermal and strain cycling, *Fatigue at Elevated Temperatures*, ASTM STP 520, American Society for Testing and Materials, Philadelphia, pp. 473-481.

Manson, S.S., (1953). *Behaviour of Materials under Conditions of Thermal Stress*, NACA TN-2933.

Manson S.S., (1966), *Thermal Stress and Low Cycle Fatigue*, McGraw Hill, New York.

Marsh D.J., (1981). A thermal shock fatigue study of type 304 and 316 stainless steels, *Fatigue of Engineering Materials and Structures*, Vol. 4, No. 2, pp. 179-195.

Marsh D., Green D. and Parker R., (1986). Comparison of theoretical estimates and experimental measurements of fatigue crack growth under severe thermal shock conditions - part 1: Experimental Observations, *Journal of Pressure Vessel Technology*, Vol. 108, pp. 501-506.

Marshall P., (1983). The influence of environment on fatigue, *Fatigue at High Temperatures*, Skelton H.P. ed, Elsevier Science Publishing, pp. 259-303.

Mc Evily A.J. and Ritchie R.O., (1998). Crack closure and the fatigue-crack propagation threshold as a function of load ratio, *Fatigue and Fracture of Engineering Materials and Structures*, Vol. 21, pp. 847-855.

Miller K.J., (2000). Fatigue limits: Fact or fiction and the initiation v propagation argument, *Structural Integrity and Fracture 2000*, Symposium Proceedings, Australian Fracture Group, University of Technology, Sydney, pp. 1-11.

Mills A.F., (1999). *Heat Transfer*, 2<sup>nd</sup> Edition, Prentice Hall, New Jersey.

Mowbray D.F., Woodford D.A. and Brandt D.E., (1973). Thermal fatigue characterization of cast cobalt and nickel-base superalloys, *Fatigue at Elevated Temperatures*, ASTM STP 520, American Society for Testing and Materials, Philadelphia, pp. 416-426.

Murakami, (1990). *Stress Intensity Factors Handbook* - Vol 1 (Russian Edition). Japan: The Society of Materials Science.

Neuber H., (1946). *Theory of Notch Stresses: Principals for Exact Stress Calculations*, J.W. Edwards, Ann Arbor.

Ng H.W. and Lee C.K., (1997). Remaining life of a vessel containing an internal corner crack under repeated thermal shock. *Proceedings of the Institution of Mechanical Engineers*, Vol. 211, Part E, pp. 215-219.

Okazaki M. and Koizumi T., (1987). Relationship between crack growth of thermal mechanical fatigue and that of isothermal low-cycle fatigue at elevated temperatures, *Low Cycle Fatigue and Elasto-Plastic Behaviour of Materials*, 2nd International Conference on Low Cycle Fatigue and Elasto-Plastic Behaviour of Materials, pp. 637-642.

Oliveira R. and Wu X.R., (1987). Stress intensity factors for axial cracks in hollow cylinders subjected to thermal shock, *Engineering Fracture Mechanics*, Vol. 27, No. 2, pp. 185-197.

Paris P.C. and Erdogan F., (1960). A critical analysis of crack propagation laws, *Journal of Basic Engineering*, Vol. 85, pp. 528-534.

Paris P.C., Gomez M.P. and Anderson W.E., (1961). A rational analytic theory of fatigue, *The Trend in Engineering at the University of Washington*, Vol. 13, No. 1, pp. 9-14.

Paris P.C. (1998). Fracture mechanics and fatigue: A historical perspective, *Fatigue and Fracture of Engineering Materials and Structures*, Vol 21, pp. 535-540.

Pernot P.P. and Mall S., (1989). A thermal-mechanical fatigue crack-growth testing system, *Experimental Techniques*, Feb., pp. 24-28.

Pilkey W.D., (1997). *Peterson's Stress Concentration Factors*, 2<sup>nd</sup> Edition, Wiley, New York.

Pinder L.W., (1981). Oxide characterization for service failure investigations, *Corrosion Science*, Vol. 21, pp. 749-763.

Pistorius P.G.H. and Marais J.J., (1995). Thermal fatigue of steel tires on urban railway systems, *International Journal of Fatigue*, Vol. 17, No. 7, pp. 471-475.

Portela A. and Aliabadi M.H., (1991). Efficient boundary element analysis of sharp notched plates, *International Journal of Numerical Methods in Engineering*, Vol. 32, pp. 445-458.

Prater, T.A. and Coffin, L.F., (1983). The use of notched compact-type specimens for crack initiation design rules in high-temperature water environments, *Corrosion Fatigue: Mechanics, Metallurgy, Electrochemistry, and Engineering*, ASTM STP 801, American Society for Testing and Materials, Philadelphia, pp. 423-444.

Prater, T.A. and Coffin, L.F., (1987). Notch fatigue crack initiation in high temperature water environments: Experiments and life prediction, *Journal of Pressure Vessel Technology*, Vol. 109, pp. 124-134.

Prater T.A., Ford F.P. and Coffin L.F., (1980). Crack growth behaviour of structural materials in high-temperature water environments, *Metal Science*, August-September, pp.424-432.

Rau C.A., Gemma A.E. and Leverant G.R., (1973). Thermal-mechanical fatigue crack propagation in nickel- and cobalt-base superalloys under various strain-temperature cycles, *Fatigue at Elevated Temperatures*, ASTM STP 520, American Society for Testing and Materials, Philadelphia, pp. 166-178.

Reimers P., (1993). Fracture mechanical analysis of a reactor pressure vessel under thermal shock loading, *Computers and Structures*, Vol 47, No4/5 pp815-827.

Rice J.R. (1968), The elastic-plastic mechanics of crack extension, *International Journal of Fracture Mechanics*, Vol. 4, pp. 41-47.

Rice J.R., (1972). Some remarks on elastic crack-tip stress fields, *International Journal of Solids and Structures*, Vol. 8, pp. 751-758.

Sanders J.L., (1961). On the Griffith-Irwin fracture theory, *ASME Journal of Applied Mechanics*, Vol. 27, No. 2, pp. 352-353.

Seweryn A. and Molski K., (1996). Elastic stress singularities and corresponding generalised stress intensity factors for angular corners under various boundary conditions, *Engineering Fracture Mechanics*, Vol. 55, pp. 529-556.

Sheffler K.D. and Doble G.S., (1973). Thermal fatigue behavior of T-111 and ASTAR 811C in ultrahigh vacuum, *Fatigue at Elevated Temperatures*, ASTM STP 520, American Society for Testing and Materials, Philadelphia, pp. 491-499.

Shoji T., Aiyama S., Takahashi H. and Suzuki M., (1978). Effects of stress intensity rate  $\dot{K}$  and stress ratio  $R$  on corrosion fatigue crack growth enhancement below  $K_{ISCC}$ , *Corrosion NACE*, Vol. 34, No. 8, pp. 276-282.

Shoji T., Takahashi H., Suzuki M. and Kondo T., (1981). A new parameter for characterizing corrosion fatigue crack growth, *Journal of Engineering Materials and Technology*, Vol. 103, pp. 299-304.

Skelton R.P. (1982). Growth of short cracks during high strain fatigue and thermal cycling, *Low-Cycle Fatigue and Life Prediction*, ASTM STP 770, American Society for Testing and Materials, Philadelphia, pp. 337-381.

Skelton R.P., (1983). Crack initiation and growth in simple metal components during thermal cycling, *Fatigue at high temperature*, Skelton R.P. ed, 1983, pp. 1-62.

Skelton R.P. and Miles L., (1984). Crack propagation in thick cylinders of 1/2CrMoV steel during thermal shock, *High Temperature Technology*, Vol. 2, No.1, pp. 23-34.

Skelton R.P. and Nix K.J., (1987). Crack growth behaviour in austenitic and ferritic steels during thermal quenching from 550°C, *High Temperature Technology*, Vol. 5, No. 1, pp. 3-12.

Smith R. and Miller K.J., (1977). Fatigue cracks at notches, *International Journal of Mechanical Science*, Vol. 19, pp. 11-22.

Soboyejo W.O., Ni Y., Li Y., Soboyejo A.B.O. and Knott J.F., (1998). New multiparameter approach to the prediction of fatigue crack growth, *Fatigue and Fracture of Engineering Materials and Structures*, Vol. 21, No. 5, pp. 541-555.

Spera D.A., (1976). What is thermal fatigue?, *Thermal Fatigue of Materials and Components*, ASTM STP 612, American Society for Testing and Materials, Philadelphia, pp. 3-9.

Suresh, S. and Ritchie R.O., (1984). Propagation of short fatigue cracks, *International Metals Reviews*, Vol. 29, pp.445-476.

Taha A. and Sofronis P., (2001). A micromechanics approach to the study of hydrogen transport and embrittlement, *Engineering Fracture Mechanics*, Vol. 68, Issue 6, pp. 803-837.

Timoshenko S.P. and Goodier J.N., (1982). *Theory of Elasticity*, 3<sup>rd</sup> Edition, McGraw Hill, London.

Tomkins B., (1979). Role of mechanics in corrosion fatigue, *Metal Science*, July, pp. 387-395



Topper T.H., Wetzel R.M. and Morrow J., (1969). Neuber's rule applied to fatigue of notched specimens, *Journal of Materials*, Vol. 4, No. 1, pp. 200-209.

Torronen K. and Cullen W.H. Jr., (1982). Effect of light-water reactor environments on fatigue crack growth rate in reactor pressure vessel steels, *Low-Cycle Fatigue and Life Prediction*, ASTM STP 770, American Society of Testing and Materials, Philadelphia, pp. 460-481.

Udoguchi T. and Wada T., (1971). Thermal effect on low cycle fatigue strength of steels, *Thermal Stresses and Thermal Fatigue*, Proceedings of the International Conference, Berkeley, UK. 22nd-26th Sept. 1969, pp. 109-123.

Viswanathan R., (2000). Life management of high temperature piping and tubing in fossil power plants, *Journal of Pressure Vessel Technology*, Vol. 122, pp. 305-317.

Vitale E. and Beghini M., (1991). Thermal shock fracture experiments on large size plates of A533-B steel, *International Journal of Pressure Vessels and Piping*, Vol. 46, pp. 289-338.

Wei R.P. and Landes J.D., (1969). Correlation between sustained-load and fatigue crack growth in high strength steels, *Materials Research and Standards*, July, pp. 25-46.

Wei R.P., and Gangloff R.P., (1989). Environmentally assisted crack growth in structural alloys: perspectives and new directions, *Fracture mechanics: Perspectives and Directions*, ASTM STP 1020, American Society for Testing and Materials, Philadelphia, pp. 233-264.

White D.J., (1971). "Some contributions to British work on thermal and high strain fatigue, *Thermal Stresses and Thermal Fatigue*, Proceedings of the International Conference, Berkeley, UK. 22nd-26th Sept. 1969, pp. 3-26.

Williams M.L., (1952). Stress singularities resulting from various boundary conditions in angular corners of plates in extension, *Journal of Applied Mechanics*, Vol. 19, pp. 526-528.

Wilson, (1974). Elastic-plastic analysis of blunt notched CT specimens and applications, *Journal of Pressure Vessel Technology*, November, pp. 293-298.

Woodtli J. and Kieselback R., (2000). Damage due to hydrogen embrittlement and stress corrosion cracking, *Engineering Failure Analysis*, Vol. 7, pp. 427-450.

Xu R.X., Thompson J.C. and Topper T.H., (1995). Practical stress expressions for stress concentration regions, *Fatigue and Fracture of Engineering Materials and Structures*, Vol. 18, pp. 885-895.

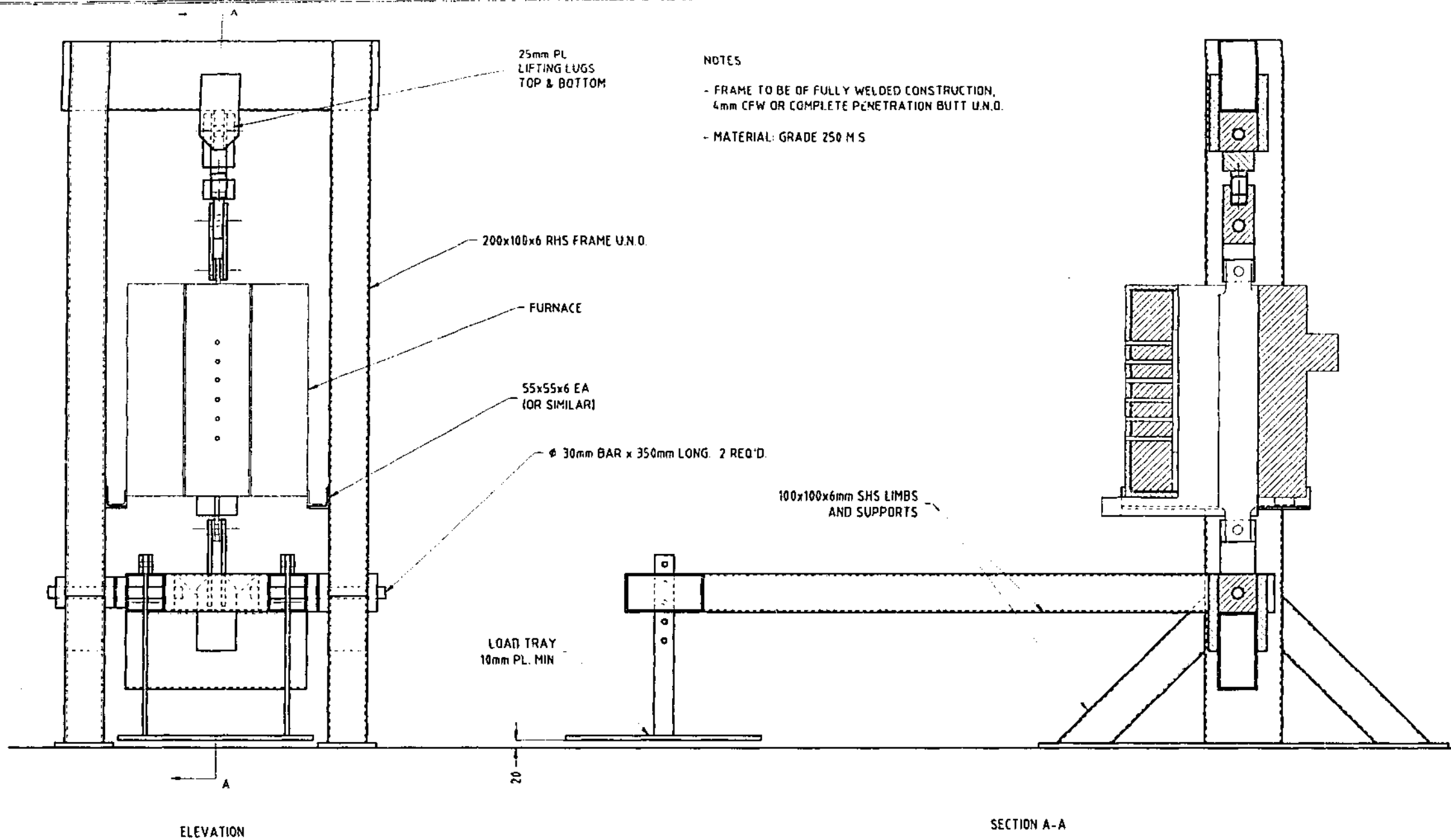
Yagawa G., Ando Y., Ishihara K, Iwadata T. and Tanaka Y., (1989). Stable and unstable crack growth of A508 class 3 plates subjected to combined force of thermal shock and tension, *Journal of Pressure Vessel Technology*, Vol. 111, p. 235-240.

Yagawa G. and Ishihara K., (1989). Cleavage and ductile thermal shock fractures of corner cracked nozzles, *Journal of Pressure Vessel Technology*, Vol. 111, pp. 241-247.

Zhi-He J. and Yiu-Wing M., (1995). Effects of damage on thermal shock strength behaviour of ceramics, *Journal of the American Ceramic Society*, Vol. 78, No. 7, pp.1873-1881.

## **Appendix A:**

### **Test Rig and Specimen Drawings**



REVISIONS

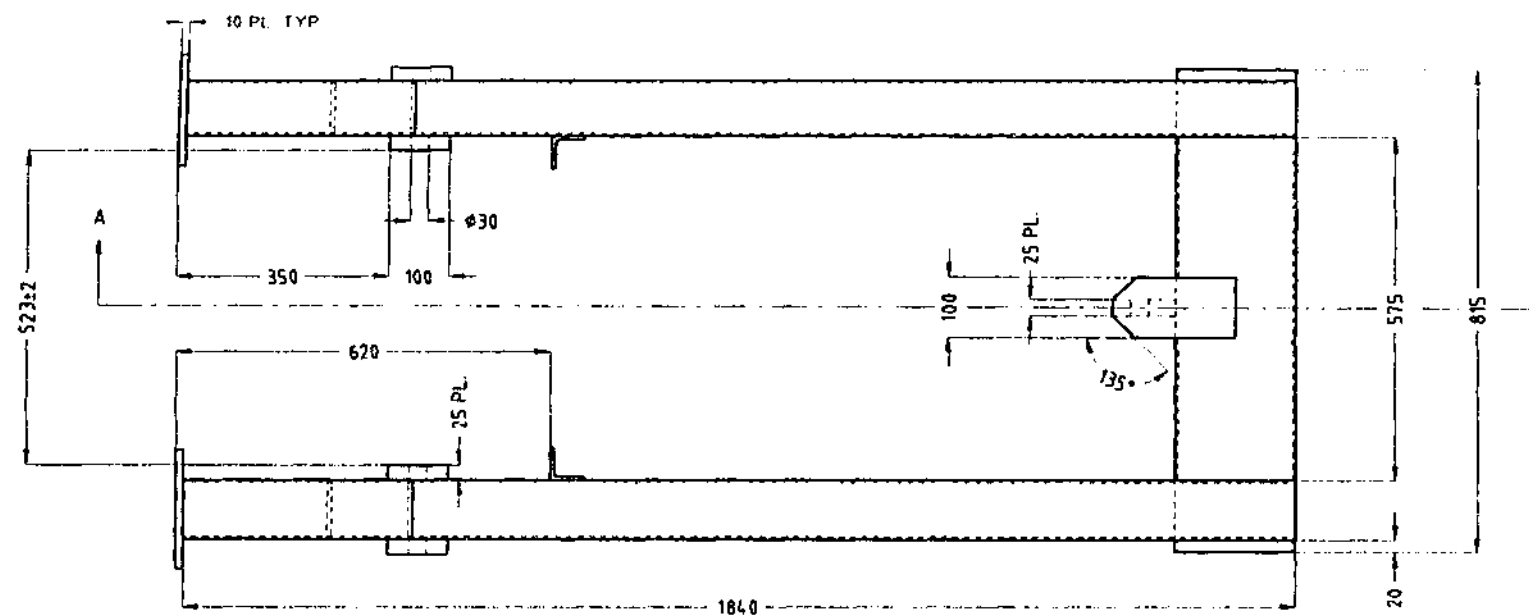
DRAFTING STANDARD: AS1500  
UNLESS OTHERWISE STATED ALL DIMENSIONS IN MILLIMETRES  
DO NOT SCALE  
THIRD ANGLE PROJECTION

DRAWN Brian Kerezsi	DATE 28/10/98
CKD	DATE

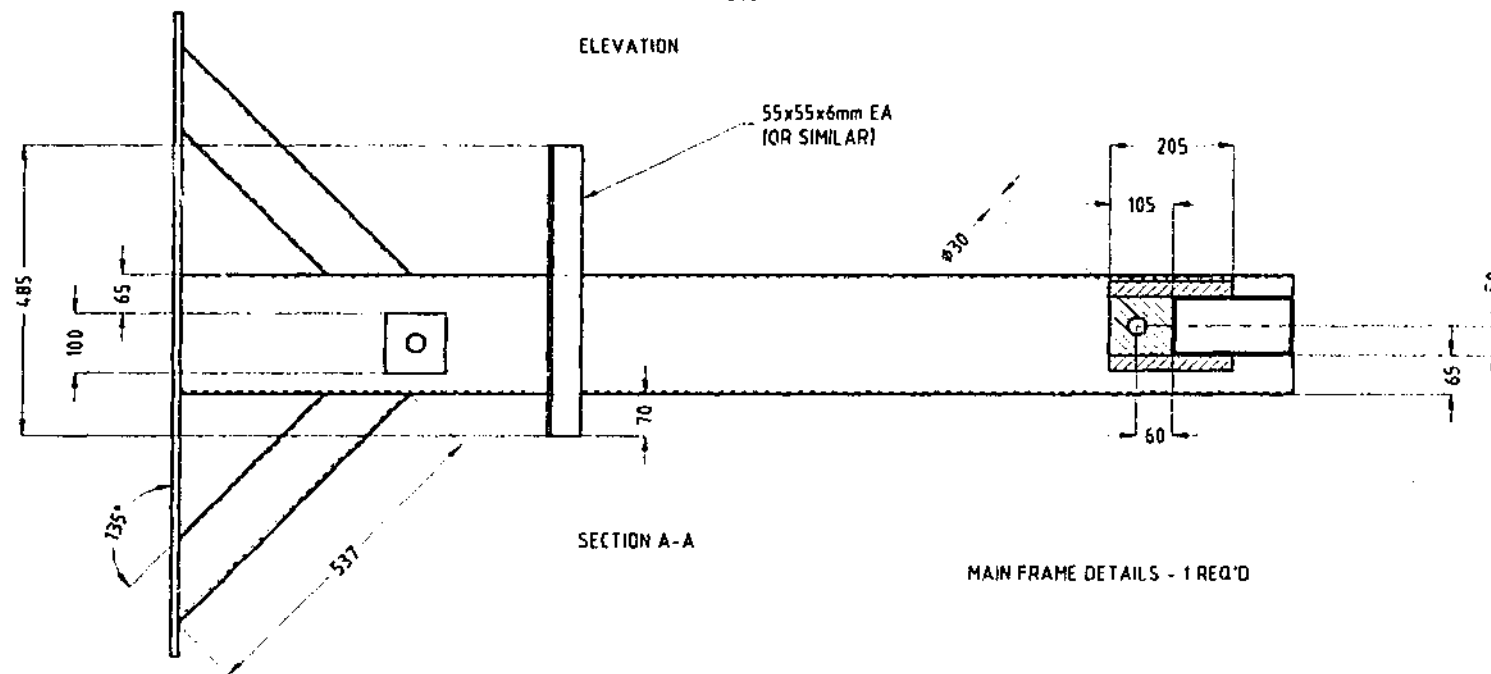
MONASH UNIVERSITY

TITLE  
**THERMAL SHOCK TEST RIG  
DEAD LOAD APPLICATION FRAME  
GENERAL LAYOUT**

SCALE 1:10	DRAWING NO BBK-9806	SHEET A3
---------------	------------------------	-------------

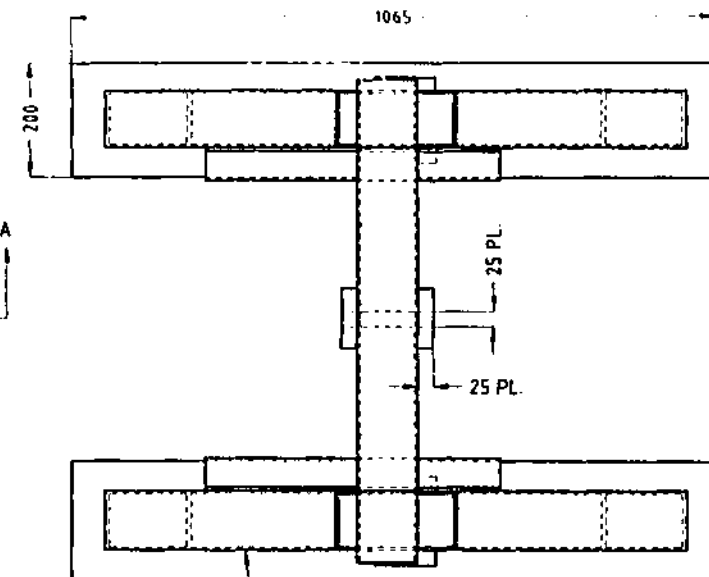


ELEVATION



SECTION A-A

MAIN FRAME DETAILS - 1 REQ'D



PLAN

NOTES:

- FRAME CONSTRUCTED FROM 200x100x6mm RHS U.N.O.
- FRAME TO BE OF FULLY WELDED CONSTRUCTION, 4mm CFW OR COMPLETE PENETRATION BUTT U.N.O
- MATERIAL: GRADE 250 M.S.

REVISIONS

DRAWING STANDARD: AS 1100  
UNLESS OTHERWISE STATED ALL DIMENSIONS IN MILLIMETRES  
DO NOT SCALE  
THIRD ANGLE PROJECTION

DRAWN  
Brian Kerezsi  
DATE  
4/11/98

CKD  
DATE

MONASH UNIVERSITY

TITLE  
THERMAL SHOCK TEST RIG  
DEAD LOAD APPLICATION FRAME  
MAIN FRAME DETAILS

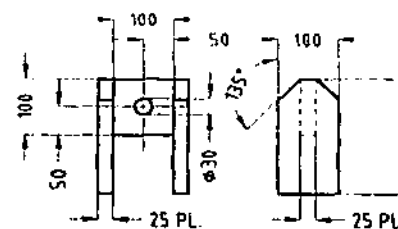
SCALE  
1:10

DRAWING NO  
BBK-9807

SHEET  
A3

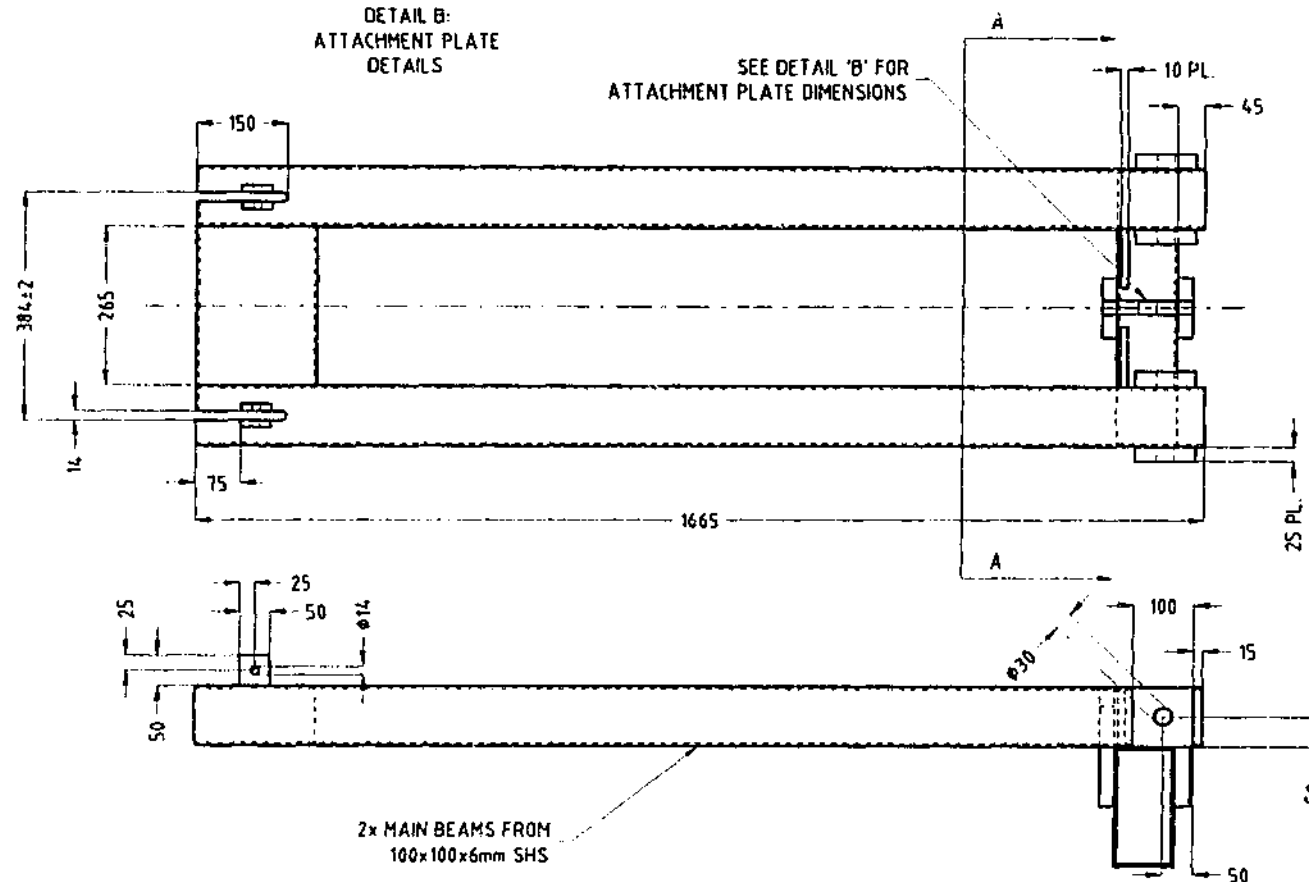
LOAD PLATFORM DETAILS - 1 REQ'D.

VIEW A-A



DETAIL B:  
ATTACHMENT PLATE  
DETAILS

SEE DETAIL 'B' FOR  
ATTACHMENT PLATE DIMENSIONS.



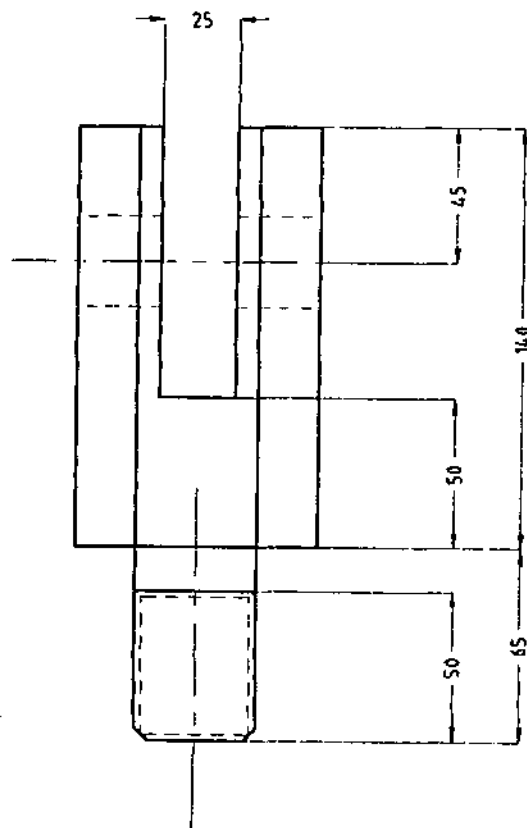
MAIN CANTILEVER DETAILS - 1 REQ'D

NOTES:

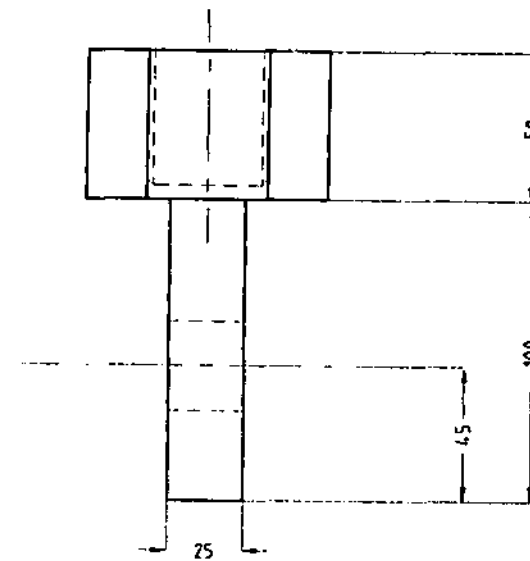
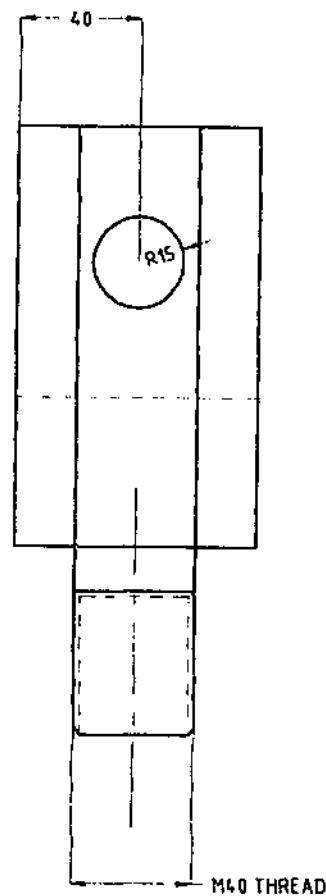
- FRAME CONSTRUCTED FROM 200x100x6mm RHS U.N.D
- FRAME TO BE OF FULLY WELDED CONSTRUCTION, 4mm CFW OR COMPLETE PENETRATION BUTT U.N.D.
- MATERIAL: GRADE 250 M.S.

REVISIONS	<p>DRAFTING STANDARD: ALL DIMENSIONS UNLESS OTHERWISE STATED ARE DIMENSIONS IN MILLIMETRES DO NOT SCALE THIRD ANGLE PROJECTION</p>	MONASH UNIVERSITY			
		TITLE <i>THERMAL SHOCK TEST RIG DEAD LOAD APPLICATION FRAME LOADING CANTILEVER DETAILS</i>			
		DRAWN Brian Kerezsi	DATE 5/11/98	SCALE	DRAWING NO
		CKD	DATE	1:10	BBK-9808
				SHEET	A3

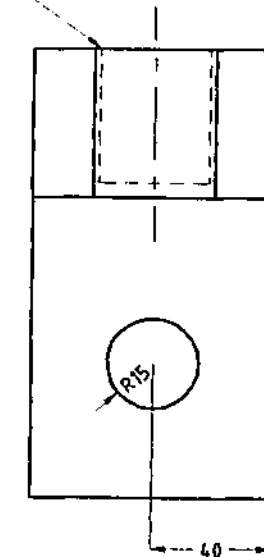
DRILL & TAP M40x45



TOP CLEVIS AND THREAD - 1 REQ'D



BOTTOM PLATE - 1 REQ'D



NOTES:

- MACHINE FROM 80mm HEX BAR
- MATERIAL: GRADE 250 M.S.

REVISIONS

DRAFTING STANDARD: AS1100  
UNLESS OTHERWISE STATED ALL DIMENSIONS ARE IN MILLIMETRES  
DO NOT SCALE  
THIRD ANGLE PROJECTION

DRAWN  
Brian Kerezsi  
CKD

DATE  
14/12/98  
DATE

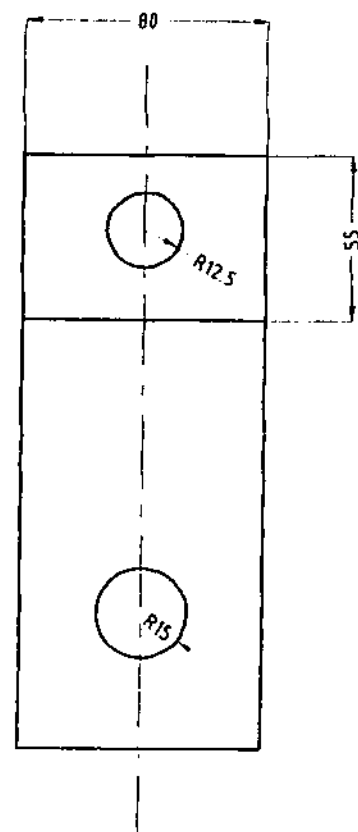
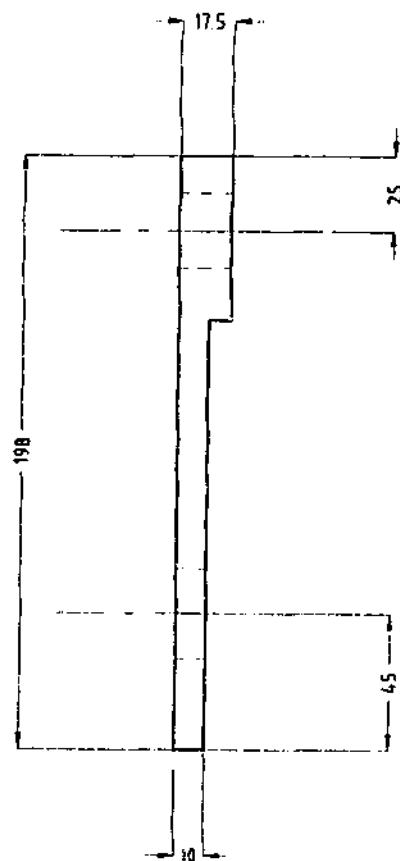
MONASH UNIVERSITY

TITLE  
**THERMAL SHOCK TEST RIG  
DEAD LOAD APPLICATION FRAME  
HEIGHT ADJUSTMENT**

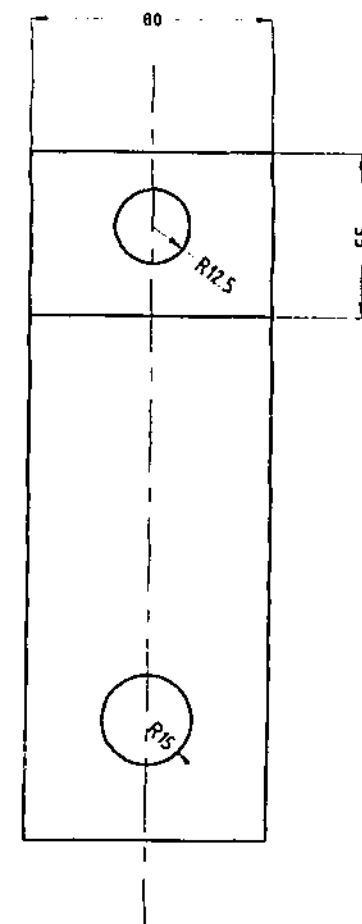
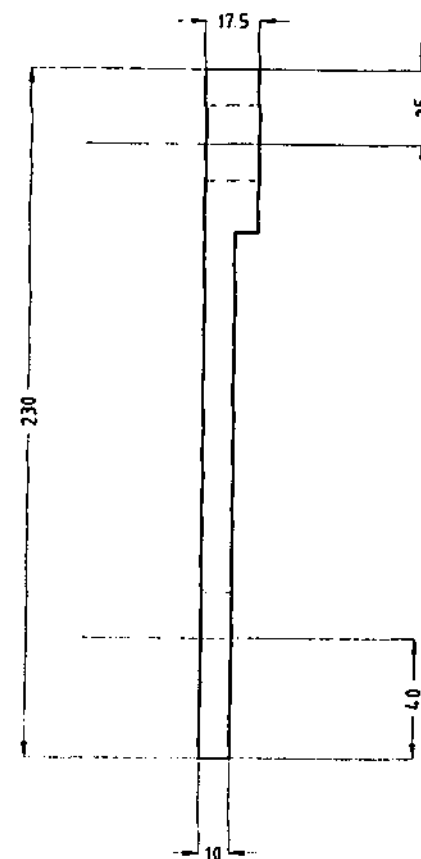
SCALE  
1:2

DRAWING NO  
BBK-9809

SHEET  
A3



TOP PLATE - 2 REQ'D  
MATERIAL - MILD STEEL



BOTTOM PLATE - 2 REQ'D  
MATERIAL - MILD STEEL

REVISIONS

DRAWING STANDARD: AS100  
UNLESS OTHERWISE STATED ALL DIMENSIONS IN MILLIMETRES  
DO NOT SCALE  
THIRD ANGLE PROJECTION

DRAWN  
Brian Kerezsi

DATE  
16/12/98

CKD

DATE

MONASH UNIVERSITY

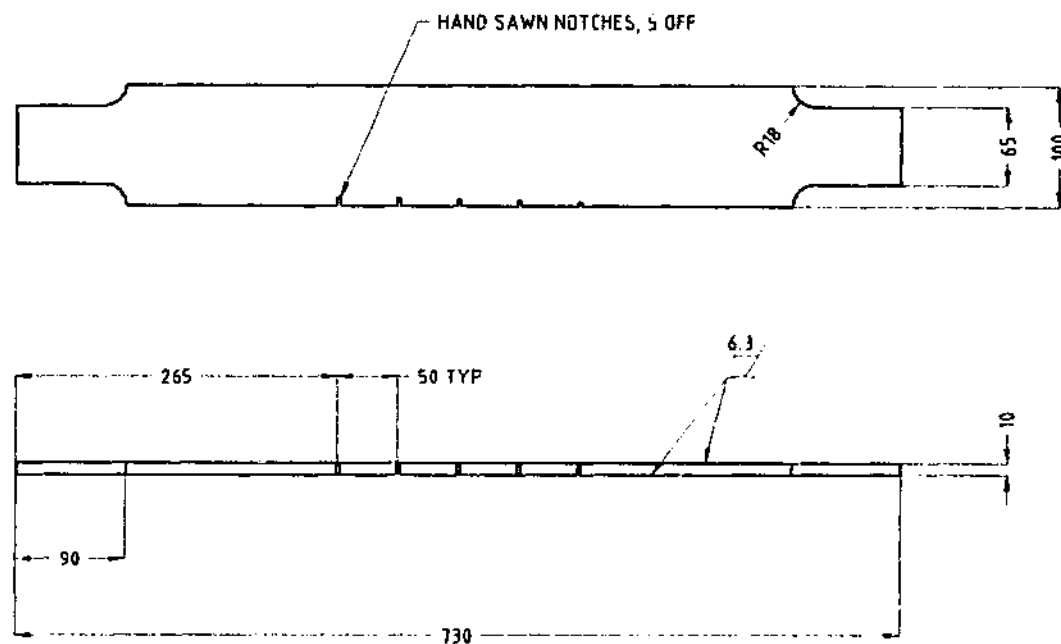
TITLE  
**THERMAL SHOCK TEST RIG  
DEAD LOAD APPLICATION FRAME  
FLAT SPECIMEN ADAPTER PLATES**

SCALE  
1:2

DRAWING NO  
BBK-9810

SHEET  
A3





## THERMAL SHOCK TEST SPECIMEN #1

NOTES:  
- MATERIAL SPECIFICATION:  
CARBON STEEL, GRADE AS 1548-430r

REVISIONS

DRAWING STANDARD: AS1500  
UNLESS OTHERWISE STATED ALL DIMENSIONS ARE IN MILLIMETRES  
DO NOT SCALE  
THIRD ANGLE PROJECTION

DRAWN  
**Brian Kerezsi**  
CKD

DATE  
**19/5/98**  
DATE

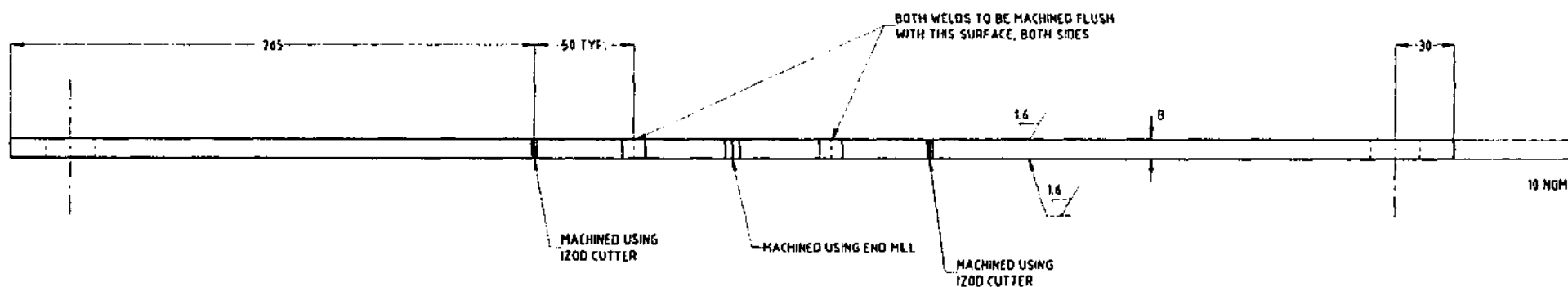
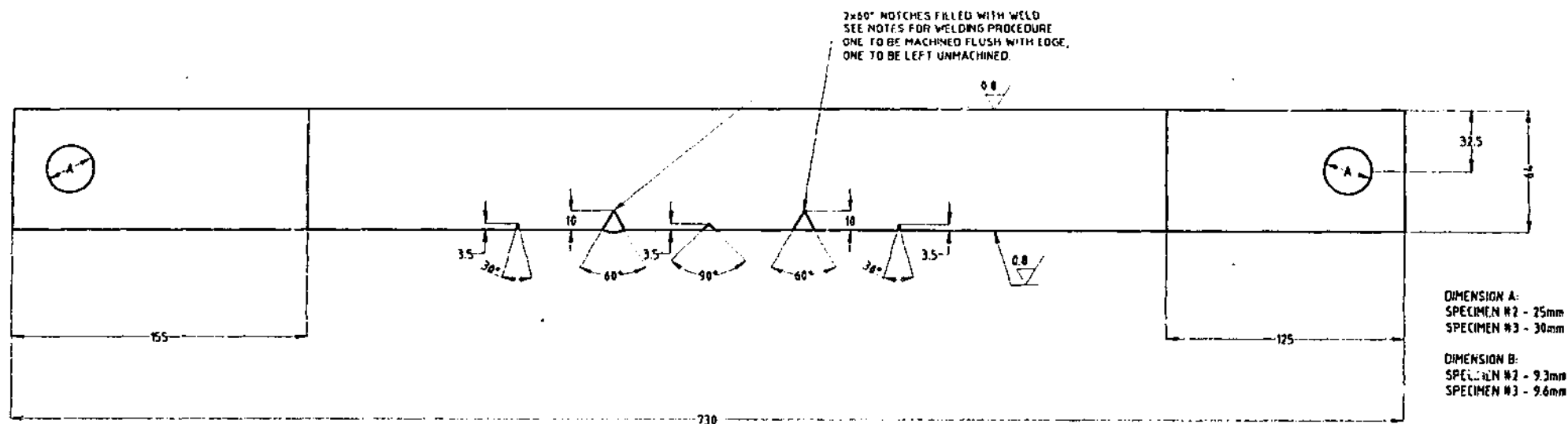
MONASH UNIVERSITY

TITLE  
**THERMAL SHOCK TEST RIG  
FLAT PLATE SPECIMEN #1  
SPECIMEN DETAILS**

SCALE  
**1:5**

DRAWING NO  
**BBK-9811**

SHEET  
**A3**



# THERMAL SHOCK TEST SPECIMEN MK.II 2 REQ'D. - SPECIMENS # 2 & 3

## NOTES:

- MATERIAL: CARBON STEEL, GRADE AS 1548-7-430E
- ALL DIMENSIONS IN mm.
- WELDING TO BE PERFORMED IN ACCORDANCE WITH AS4458:1997 SECTION 9 AND AS/NZS3992:1998 SECTION 2, TYPE: SINGLE-WELDED, SINGLE-VBUTT (TABLE 2.3, ITEM 1).
- NOTCH DEPTHS TO BE  $\pm 0.5$ mm, SLOW MILLED, NOTCH RADIUS 0.5mm
- ALL OTHER TOLERANCING TO BE  $\pm 1$ mm U.M.O.
- ONLY THOSE SURFACES INDICATED REQUIRE MACHINING. REMAINING SURFACES TO BE CLEANED UP.

## REVISIONS

13/5 As Built Modifications  
BK

DRAWING STANDARD: AS1100  
UNLESS OTHERWISE STATED ALL DIMENSIONS ARE IN MILLIMETRES  
DO NOT SCALE  
THIRD ANGLE PROJECTION

DRAWN  
Brian Kerezsi

DATE  
17/3/99

CKD

DATE

## MONASH UNIVERSITY

### TITLE

THERMAL SHOCK TEST RIG  
THERMAL SHOCK SPECIMEN MK.II  
SPECIMEN DETAILS - DOUBLE SPECIMEN

### SCALE

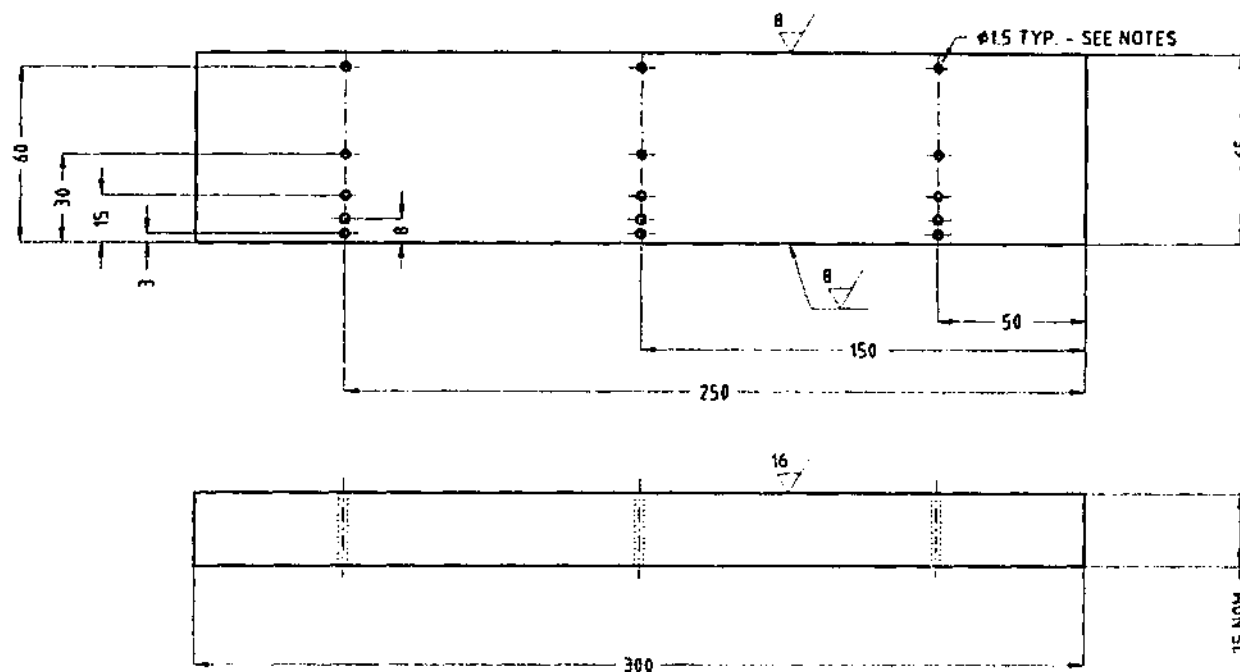
1:2.5

### DRAWING NO

BBK-9903

### SHEET

A3



**THERMAL SHOCK ATTACHED MASS MKII**  
**MATERIAL : MILD STEEL**

**NOTES:**

- TWO PLATES REQ'D, ONE WITH HOLES, ONE WITHOUT.
- TOLERANCING TO BE  $\pm 1\text{mm}$  U.N.O.
- MACHINING REQUIRED ONLY ON THOSE FACES INDICATED. REMAINING SURFACES TO BE CLEANED UP.

REVISIONS

DRAWING STANDARD - AS1500  
 UNLESS OTHERWISE STATED ALL DIMENSIONS IN MILLIMETRES  
 DO NOT SCALE  
 THIRD ANGLE PROJECTION

DRAWN  
 Brian Kerezsi

DATE  
 21/3/99

CHECKED  
 DATE

**MONASH UNIVERSITY**

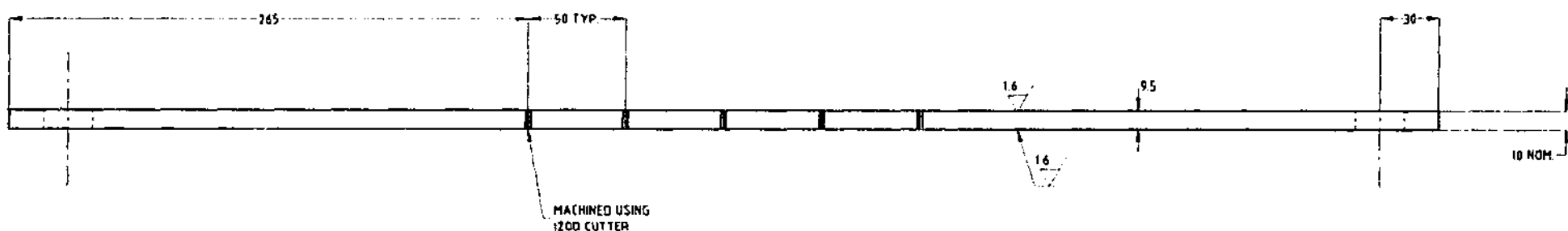
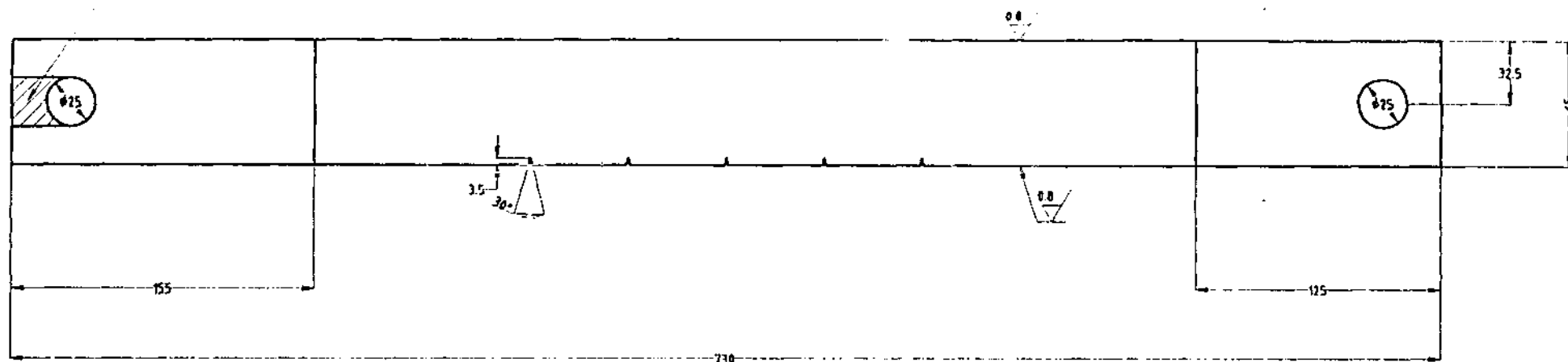
TITLE  
**THERMAL SHOCK TEST RIG  
 THERMAL SHOCK SPECIMEN  
 ATTACHED MASS DETAILS - MKII**

SCALE  
 1:2

DRAWING NO  
 BBK-9905

SHEET  
 A3

SPECIMENS #5 & #7 TO BE SLOTTED  
THIS REGION OF MATERIAL TO BE REMOVED



THERMAL SHOCK TEST SPECIMEN MK.III  
4 REQ'D. - SPECIMENS # 4 & 5, 6 & 7

NOTES.

- MATERIAL: CARBON STEEL, GRADE AS1548-7-430R
- ALL DIMENSIONS IN mm
- NOTCH DEPTHS TO BE  $\pm 0.5$ mm, SLOW MILLED, NOTCH RADIUS 0.5mm.
- ALL OTHER TOLERANCING TO BE  $\pm 1$ mm U.N.O.
- ONLY THOSE SURFACES INDICATED REQUIRE MACHINING REMAINING SURFACES TO BE CLEANED UP.

REVISIONS

QUOTING STANDARD: AS1548-7-430R  
UNLESS OTHERWISE STATED ALL DIMENSIONS IN MILLIMETRES  
DO NOT SCALE  
THIRD ANGLE PROJECTION

MONASH UNIVERSITY

TITLE  
**THERMAL SHOCK TEST RIG  
THERMAL SHOCK SPECIMEN MK.III  
SPECIMEN DETAILS - DOUBLE SPECIMEN**

DRAWN  
**Brian Kerezsi**

DATE  
**21/2/00**

CKD

DATE

SCALE  
**1:2.5**

DRAWING NO  
**BBK-9906**

SHEET  
**A3**

## **Appendix B**

### **Results of Elevated Temperature Mechanical Tests to Carbon Steel Specimens**

Report no. ME/98/154

Date. 30/10/98

HRL Technology Pty Ltd  
ACN 062 076 199

677 Springvale Road  
Mulgrave Victoria  
Australia 3170

Telephone (03) 9565 9888  
Facsimile (03) 9565 9777

## MECHANICAL TEST REPORT

CLIENT : BCIRP Project, Monash University

ORDER No:

DESCRIPTION : Elevated temperature tensile test of mild steel

SAMPLE IDENTIFICATION : Test pieces machined from mild steel flat bar

TEST CONDITIONS : 24°C, 50°C, 100°C, 200°C, 350°C

TEST PROCEDURE : Sample tested to AS1391-1991, Strain cat. S

TEST EQUIPMENT : Schenck Universal Testing Machine.  
Tensile pieces machined to Materials Technology  
Methods Manual HT100

TEST DATE : 28/10/98 ,

Sample I.D.	Test temperature (°C)	Diameter (mm)	Gauge Length (mm)
HAH03/05-1	24	11.22	56.35
HAH03/05-2	50	11.29	56.38
HAH03/05-3	100	11.19	56.23
HAH03/05-4	200	11.27	56.17
HAH03/05-5	350	11.26	56.44

Sample I.D.	Upper Yield Stress (MPa)	UTS (MPa)	% Elongation	% reduction in area	Comments
HAH03/05-1	324	456	39.24	67.56	
HAH03/05-2	295	446	36.87	66.44	
HAH03/05-3	289	460	16.24	59.88	FO, NO
HAH03/05-4	288	617	21.43	46.70	FO, NO
HAH03/05-5	183	498	34.78	62.91	FO

**Note:**

Samples commented FO failed outside mid third.

Samples commented NO had necking partially outside the gauge length

Plots of tensile load versus extension are shown in Figures 1 to 5

Signed:  .....

Ross Ulmer  
Technical Officer

No part of this report may be reproduced by any process, stored in a retrieval system, transmitted nor disclosed to others without prior written permission of HRL Limited, except that the client may reproduce the report for its own internal use. The report is issued free of alterations and subject to the foregoing, may only be reproduced in full.

HRL Technology Pty Ltd

QSIAM009  
Version 1

ME/98/154

Page 1 of 4

FIGURE 1 – Load versus extension plot at 24 °C

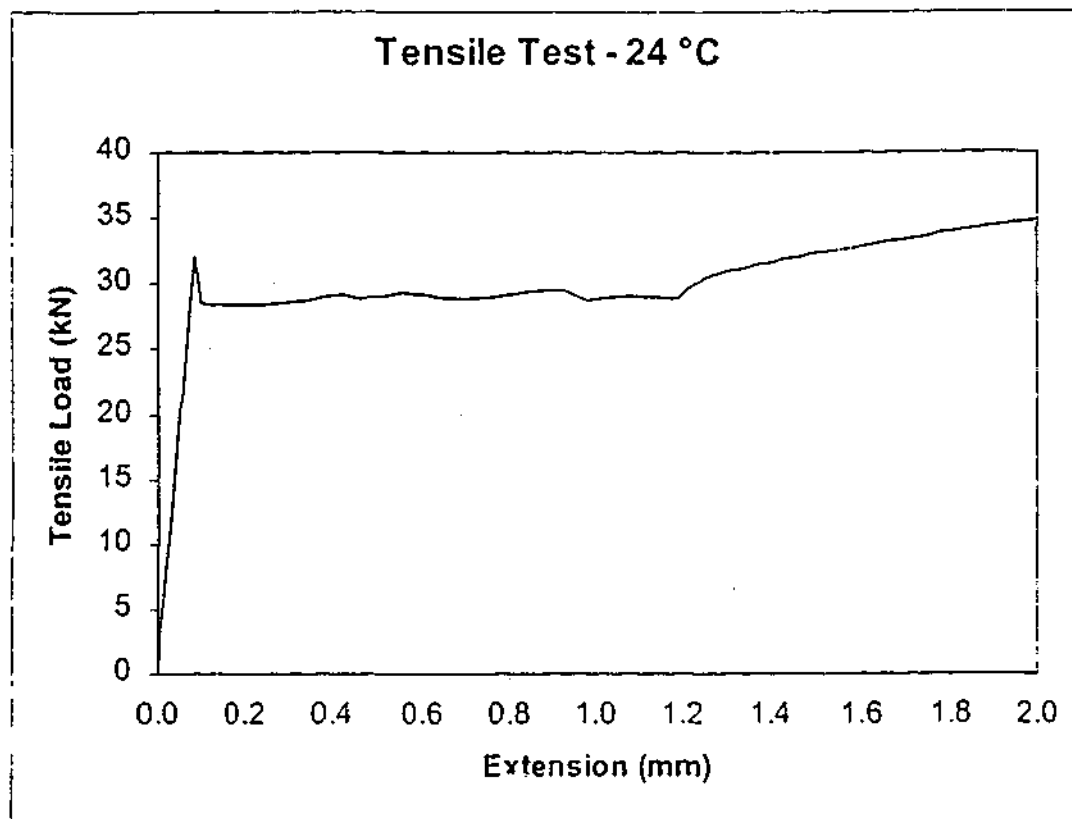


FIGURE 2 – Load versus extension plot at 50 °C

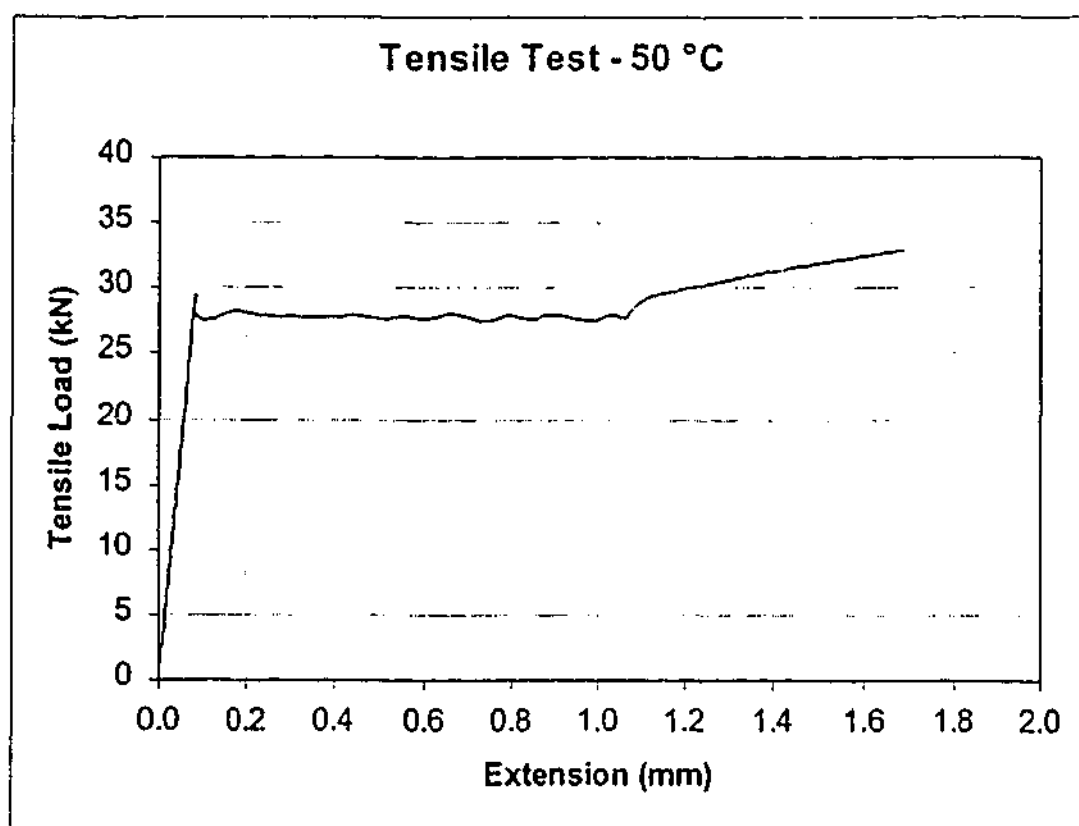


FIGURE 3 – Load versus extension plot at 100 °C

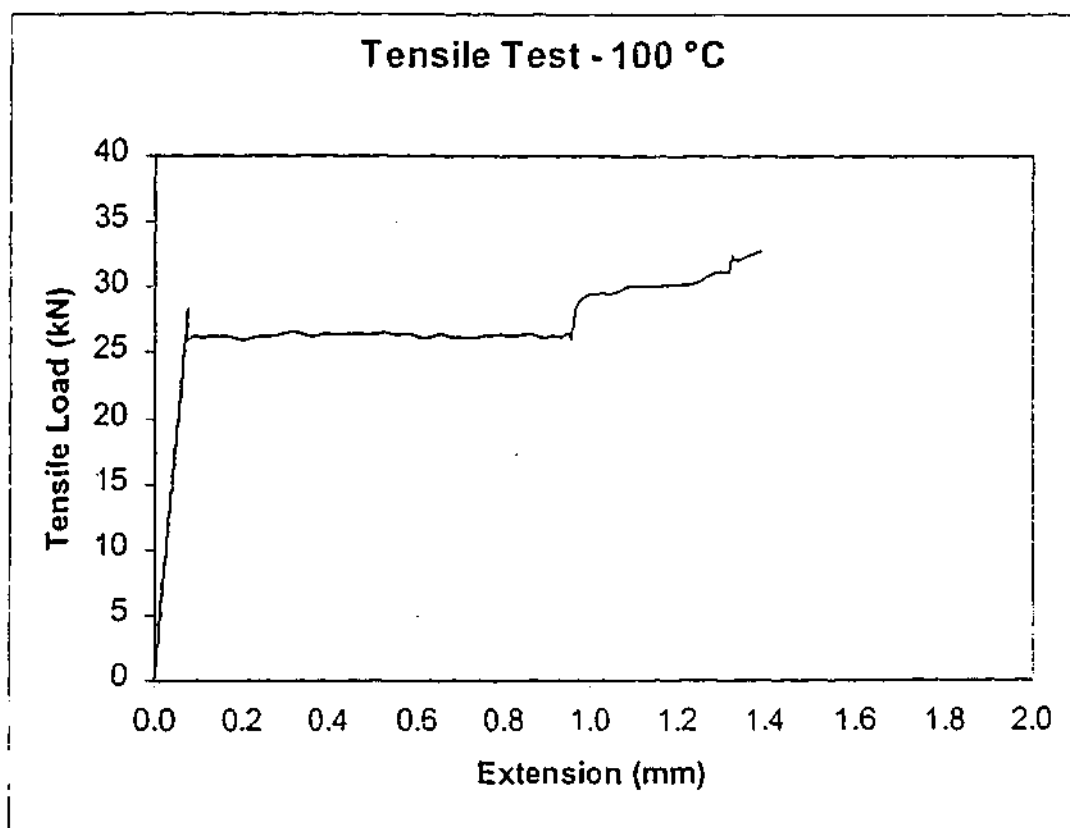


FIGURE 4 – Load versus extension plot at 200 °C

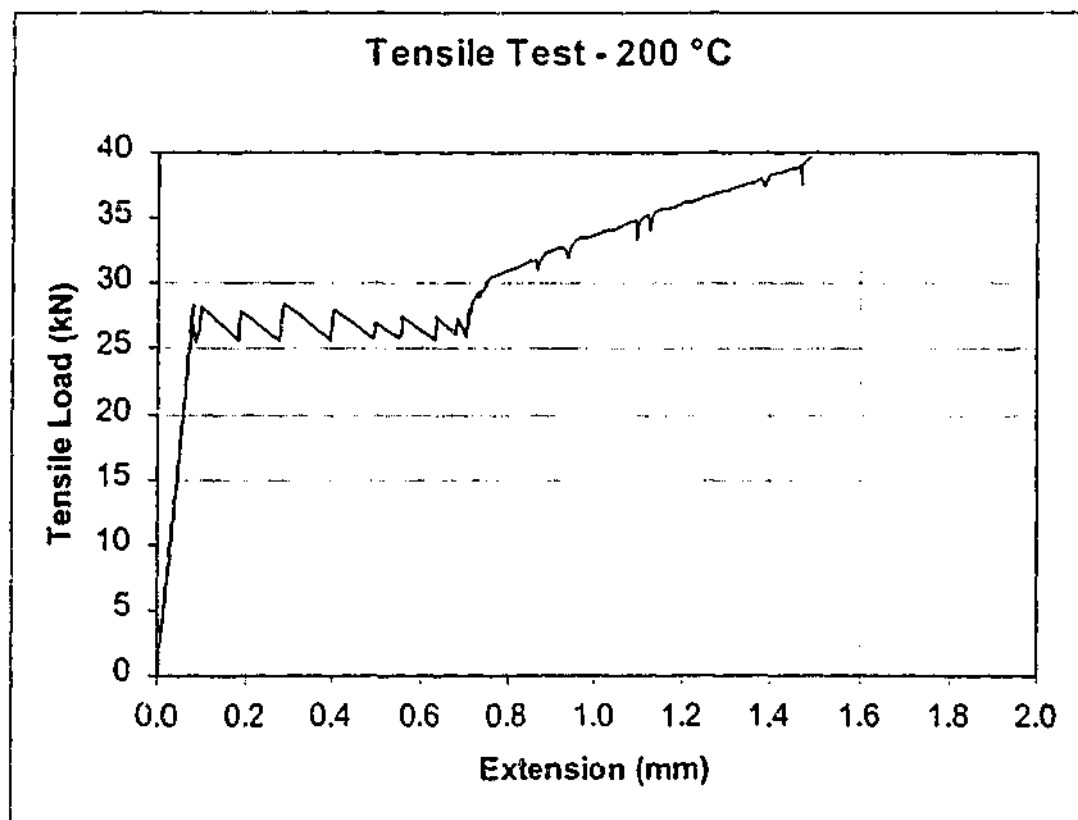
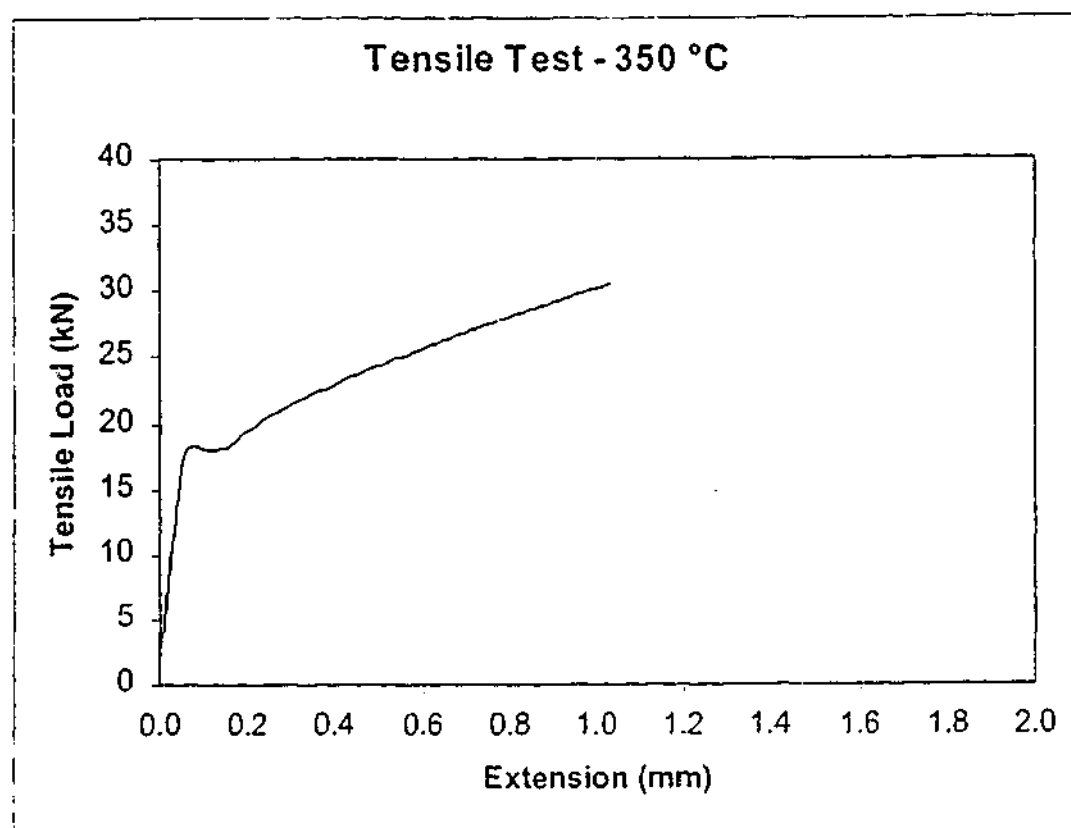




FIGURE 5 – Load versus extension plot at 350 °C



## **Appendix C**

### **Experimental Test Result Data**

Table C.1: Raw test data for specimen #2, crack position #1

Number of Cycles	Crack Length (mm)			Growth (mm)	Growth/Cycle (m/cycle)
	Inside	Outside	Average		
2485	4.3	4.4	4.35		
3003	4.6	4.75	4.675	0.325	6.3E-07
3546	4.7	4.85	4.775	0.1	1.8E-07
3990	4.9	5.15	5.025	0.25	5.6E-07
4624	5.1	5.35	5.225	0.2	3.2E-07
5042	5.55	5.65	5.6	0.3	7.2E-07
5522	5.95	6.05	6	0.4	8.3E-07
5996	6.2	6.8	6.5	0.5	1.1E-06
6519	6.8	7.15	6.975	0.475	9.1E-07
7036	7.35	7.5	7.425	0.45	8.7E-07
7565	7.85	8.1	7.975	0.55	1.0E-06
8076	8.3	8.55	8.425	0.45	8.8E-07
8570	8.65	8.75	8.7	0.275	5.6E-07
9009	8.8	8.9	8.85	0.15	3.4E-07
9488	8.9	9.05	8.975	0.125	2.6E-07

Table C.2: Raw test data for specimen #2, crack position #3

Number of Cycles	Crack Length (mm)			Growth (mm)	Growth/Cycle (m/cycle)
	Inside	Outside	Average		
3990	3.85	3.85	3.85	-	-
4624	4.35	4.3	4.325	0.475	7.5E-07
5042	4.4	4.5	4.45	0.125	3.0E-07
5522	-	-	-	-	-
5996	-	-	-	-	-
6519	5.5	4.9	5.2	0.75	5.07786E-07
7036	5.8	5.2	5.5	0.3	5.80271E-07
7565	6	5.45	5.725	0.225	4.25331E-07
8076	6.05	5.65	5.85	0.125	2.44618E-07
8570	6.05	5.8	5.925	0.075	1.51822E-07
9009	6.05	6.05	6.05	0.125	2.84738E-07

Table C.3: Raw test data for specimen #3, crack position #1

Number of Cycles	Crack Length (mm)			Growth (mm)	Growth/Cycle (m/cycle)
	Inside	Outside	Average		
3546	3.9	3.9	3.9	-	-
3990	3.95	4.15	4.05	0.15	3.4E-07
4624	4.1	4.4	4.25	0.2	3.2E-07
5042	4.25	4.6	4.425	0.175	4.2E-07
5522	4.35	4.7	4.525	0.1	2.1E-07
5996	4.5	4.8	4.65	0.125	2.6E-07
6519	4.6	4.9	4.75	0.1	1.9E-07
7036	4.8	5	4.9	0.15	2.9E-07
7565	4.8	5.15	4.975	0.075	1.4E-07
8076	5.1	5.15	5.125	0.15	2.9E-07
8570	5.2	5.2	5.2	0.075	1.5E-07
9009	5.2	5.4	5.3	0.1	2.3E-07
9488	5.25	5.5	5.375	0.075	1.6E-07

Table C.4: Raw test data for specimen #4, crack position #1

Number of Cycles	Crack Length (mm)			Growth (mm)	Growth/Cycle (m/cycle)
	Inside	Outside	Average		
2443	4.85	4.75	4.8	-	-
3106	5	5.05	5.025	0.225	3.4E-07
3675	5.1	5.1	5.1	0.075	1.3E-07
3998	5.25	5.25	5.25	0.15	4.6E-07
4537	5.95	5.9	5.925	0.675	1.3E-06
4976	6.15	6.2	6.175	0.25	5.7E-07
5409	6.75	6.5	6.625	0.45	1.0E-06
5993	7.1	6.8	6.95	0.325	5.6E-07
6504	7.45	7.35	7.4	0.45	8.8E-07
7029	7.8	7.65	7.725	0.325	6.2E-07
7557	7.9	7.7	7.8	0.075	1.4E-07
8091	8.2	8.05	8.125	0.325	6.1E-07
8492	8.25	8.2	8.225	0.1	2.5E-07
9014	8.3	8.45	8.375	0.15	2.9E-07
9524	8.4	8.55	8.475	0.1	2.0E-07
10020	8.5	8.55	8.525	0.05	1.0E-07
10505	8.65	8.6	8.625	0.1	2.1E-07

Table C.5: Raw test data for specimen #4, crack position #2

Number of Cycles	Crack Length (mm)			Growth (mm)	Growth/Cycle (m/cycle)
	Inside	Outside	Average		
3998	4.45	4.15	4.3	-	-
4986	4.45	4.25	4.35	0.05	5.1E-08
5409	4.5	4.475	4.4875	0.1375	3.3E-07
5993	4.55	4.7	4.625	0.1375	2.4E-07
6504	4.65	4.75	4.7	0.075	1.5E-07
7029	4.85	4.85	4.85	0.15	2.9E-07
7557	4.85	4.85	4.85	0	0.0E+00
8492	4.85	4.85	4.85	0	0.0E+00
9012	4.9	4.9	4.9	0.05	9.6E-08
9524	5.1	4.9	5	0.1	2.0E-07
10020	5.25	4.95	5.1	0.1	2.0E-07
10505	5.25	5.1	5.175	0.075	1.5E-07

Table C.6: Raw test data for specimen #4, crack position #3

Number of Cycles	Crack Length (mm)			Growth (mm)	Growth/Cycle (m/cycle)
	Inside	Outside	Average		
3998	3.85	4.2	4.025	-	-
5409	4.35	4.25	4.3	0.275	1.95E-07
5993	4.45	4.55	4.5	0.2	3.42E-07
6504	4.45	4.675	4.5625	0.0625	1.22E-07
7029	4.7	4.8	4.75	0.25	2.41E-07
7557	4.8	4.85	4.825	0.075	1.42E-07
8091	4.9	5.05	4.975	0.15	2.81E-07
8492	4.95	4.9	4.925	0.1	1.07E-07
9012	5.15	4.95	5.05	0.075	8.14E-08
9524	5.2	5.15	5.175	0.25	2.42E-07
10020	5.2	5.15	5.175	0.125	1.24E-07
10505	5.2	5.15	5.175	0	0.00E+00

Table C.7: Raw test data for specimen #5, crack position #1

Number of Cycles	Crack Length (mm)			Growth (mm)	Growth/Cycle (m/cycle)
	Inside	Outside	Average		
3675	4.55	4.65	4.6	-	-
3998	4.65	4.72	4.685	0.085	2.6E-07
4537	4.8	4.78	4.79	0.105	1.9E-07
4986	5.05	4.85	4.95	0.16	3.6E-07
5409	5.05	5.4	5.225	0.275	6.5E-07
5993	5.25	5.5	5.375	0.15	2.6E-07
6504	5.4	5.5	5.45	0.075	1.5E-07
7029	5.6	5.55	5.575	0.125	2.4E-07
7557	5.75	5.65	5.7	0.125	2.4E-07
8091	5.8	5.75	5.775	0.075	1.4E-07

Table C.8: Raw test data for specimen #5, crack position #2

Number of Cycles	Crack Length (mm)			Growth (mm)	Growth/Cycle (m/cycle)
	Inside	Outside	Average		
3998	4.45	4.15	4.3	-	-
4986	4.45	4.25	4.35	0.05	5.1E-08
5409	4.5	4.475	4.4875	0.1375	3.3E-07
5993	4.55	4.7	4.625	0.1375	2.4E-07
6504	4.65	4.75	4.7	0.075	1.5E-07
7029	4.85	4.85	4.85	0.15	2.9E-07
7557	4.85	4.85	4.85	0	0.0E+00
8492	4.85	4.85	4.85	0	0.0E+00

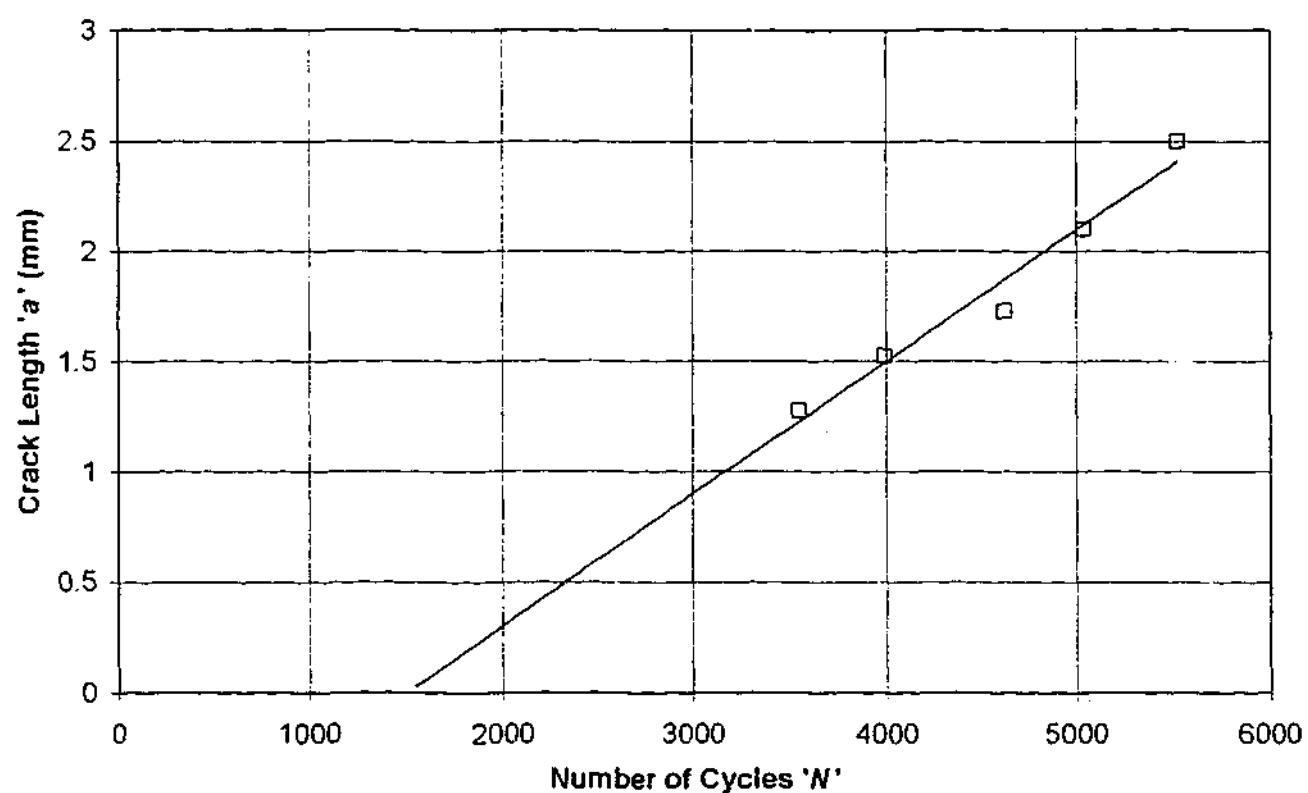


Figure C.1: Estimate for cycles to crack initiation from long crack growth data. For specimen #2, crack position #1.

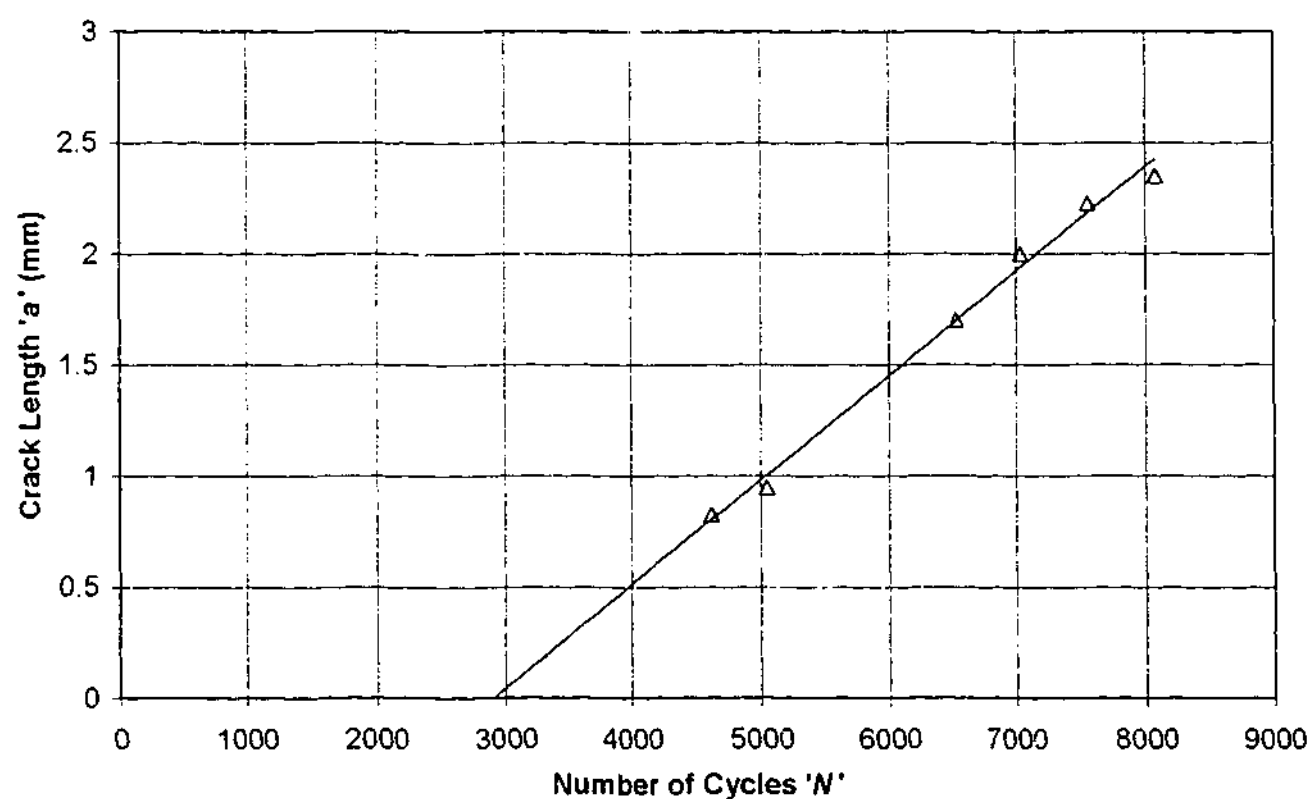


Figure C.2: Estimate for cycles to crack initiation from long crack growth data. For specimen #2, crack position #3.

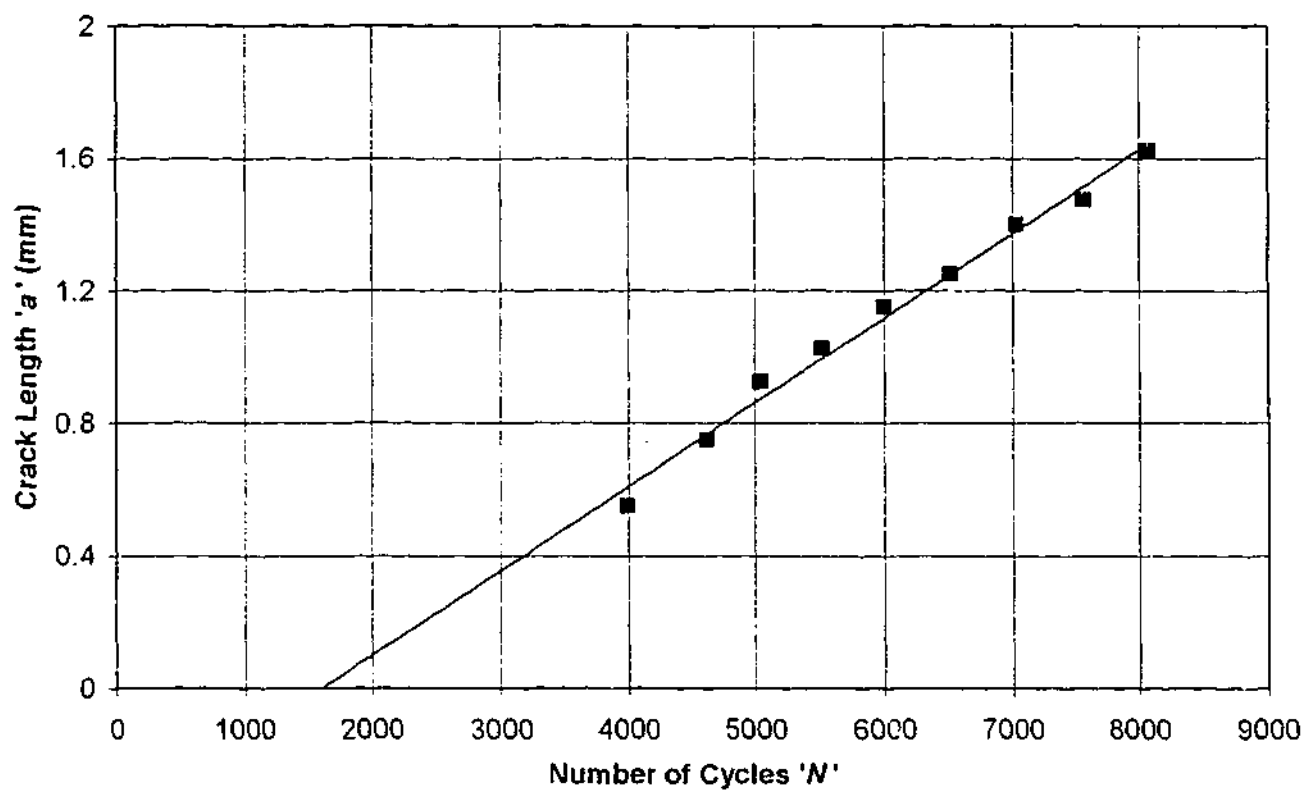


Figure C.3: Estimate for cycles to crack initiation from long crack growth data. For specimen #3, crack position #1.

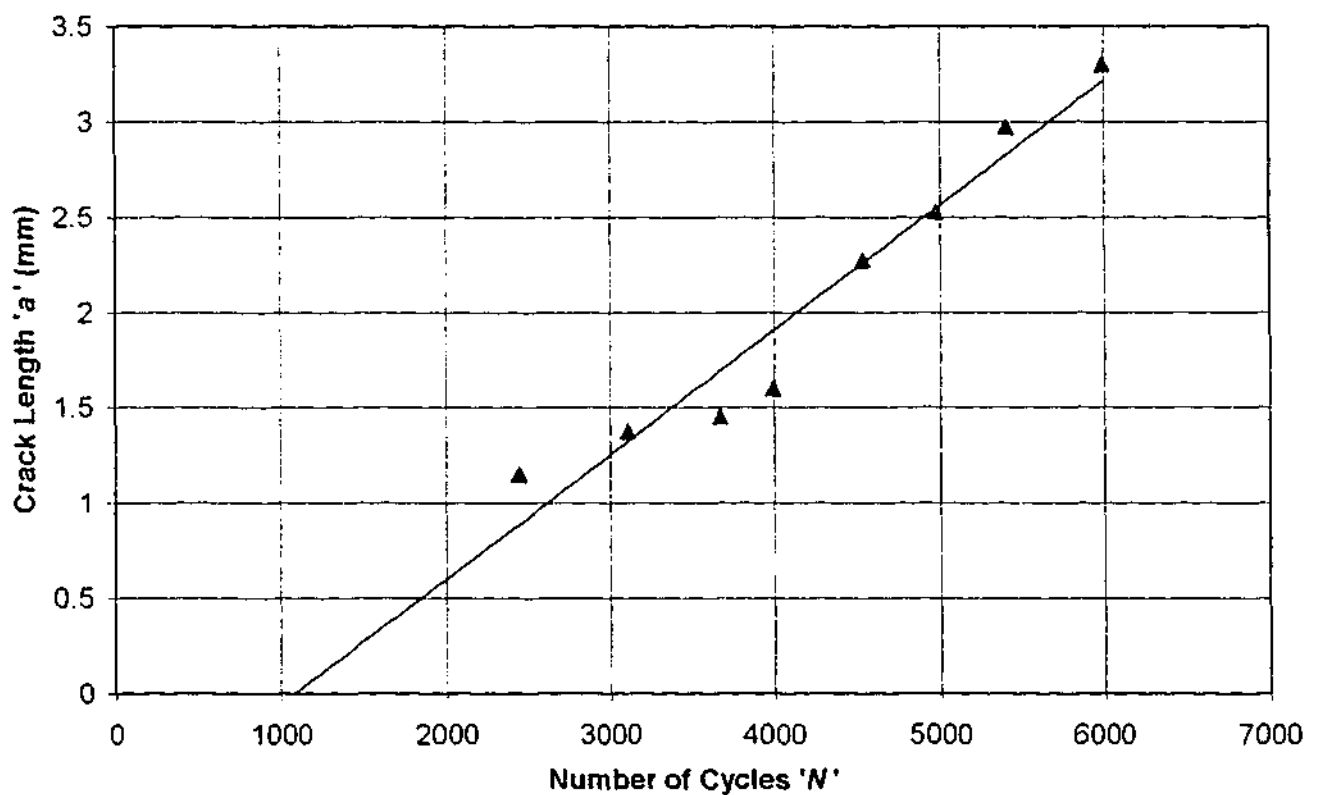


Figure C.4: Estimate for cycles to crack initiation from long crack growth data. For specimen #4, crack position #1.



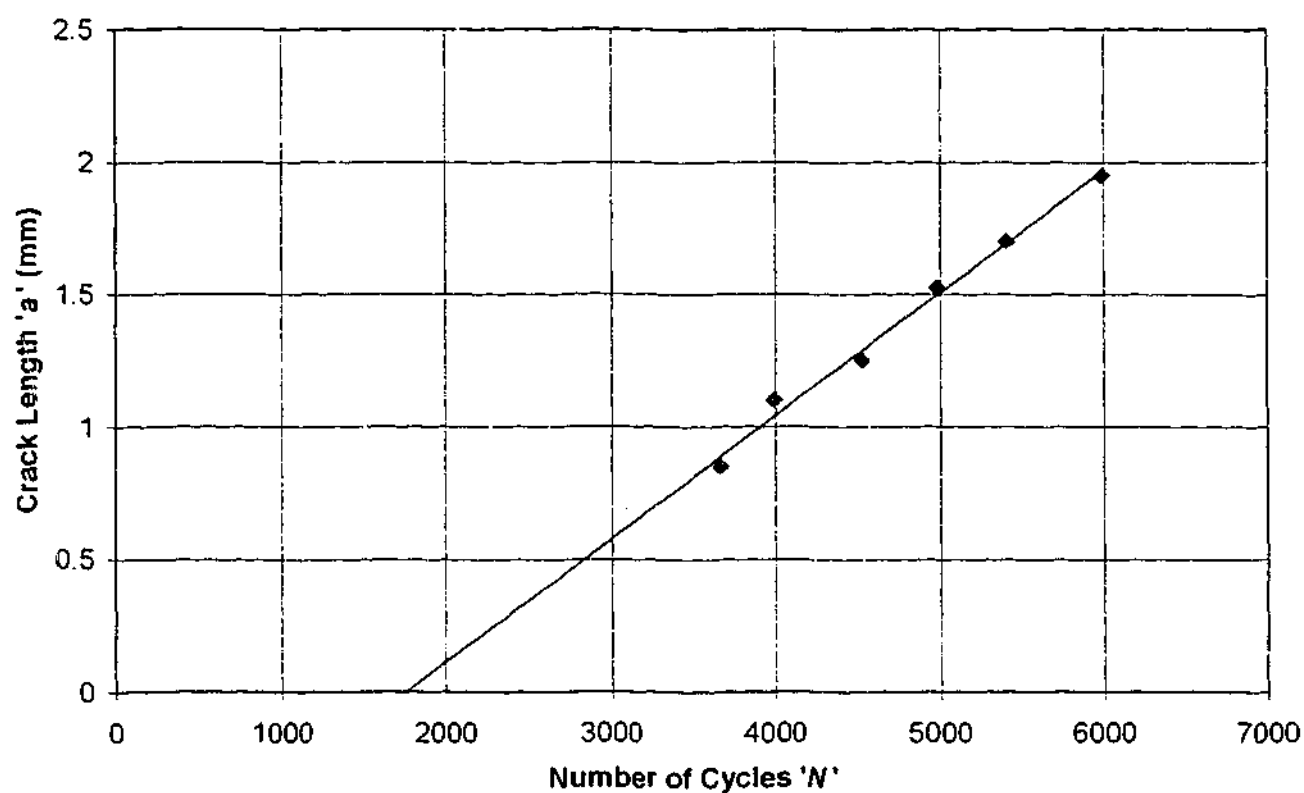


Figure C.5: Estimate for cycles to crack initiation from long crack growth data. For specimen #4, crack position #2.

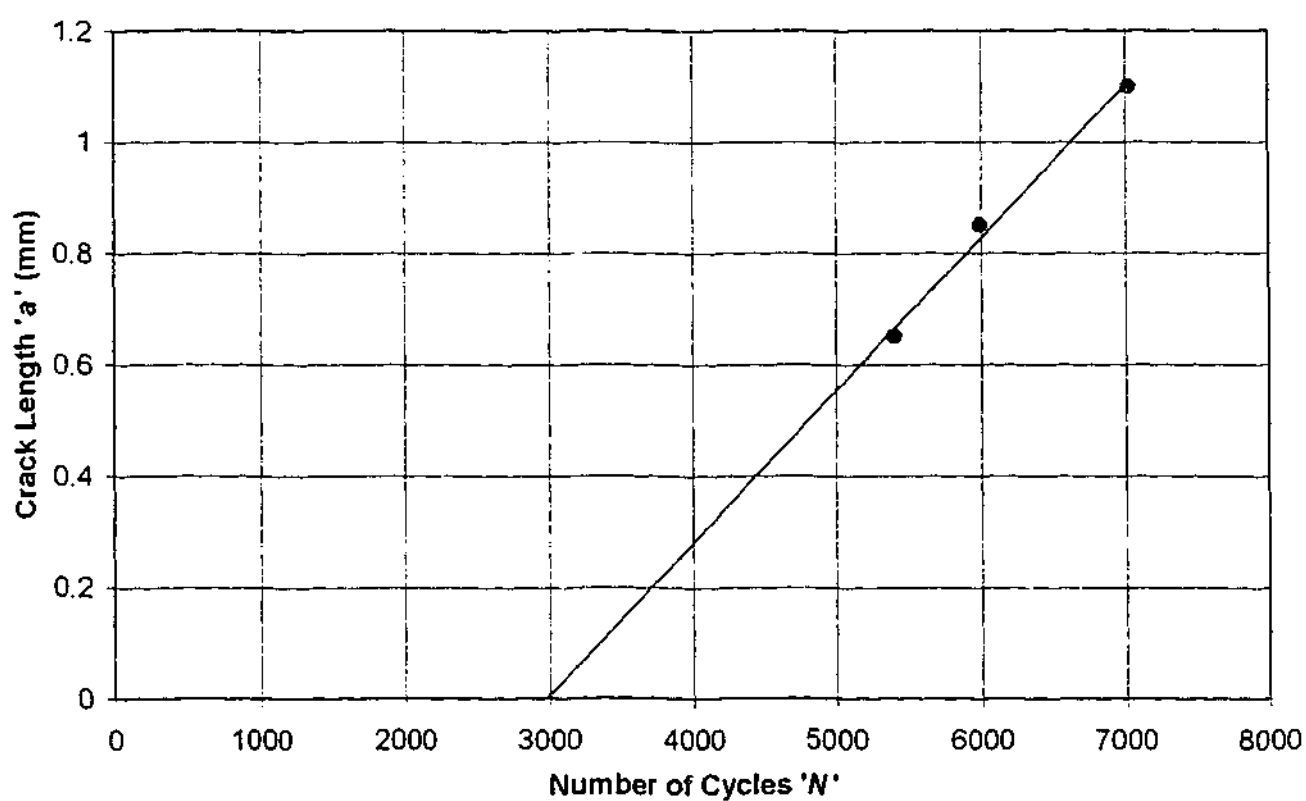


Figure C.6: Estimate for cycles to crack initiation from long crack growth data. For specimen #4, crack position #3.

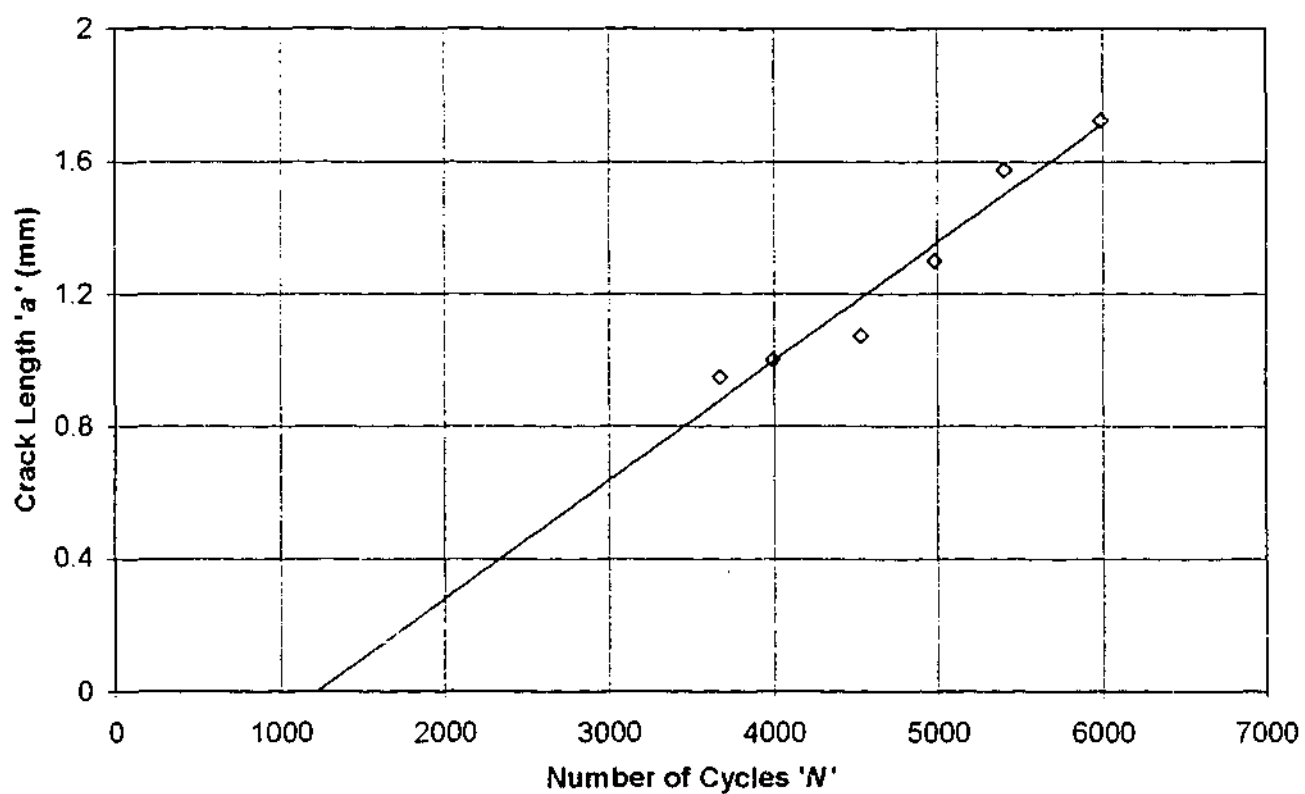


Figure C.7: Estimate for cycles to crack initiation from long crack growth data. For specimen #5, crack position #1.

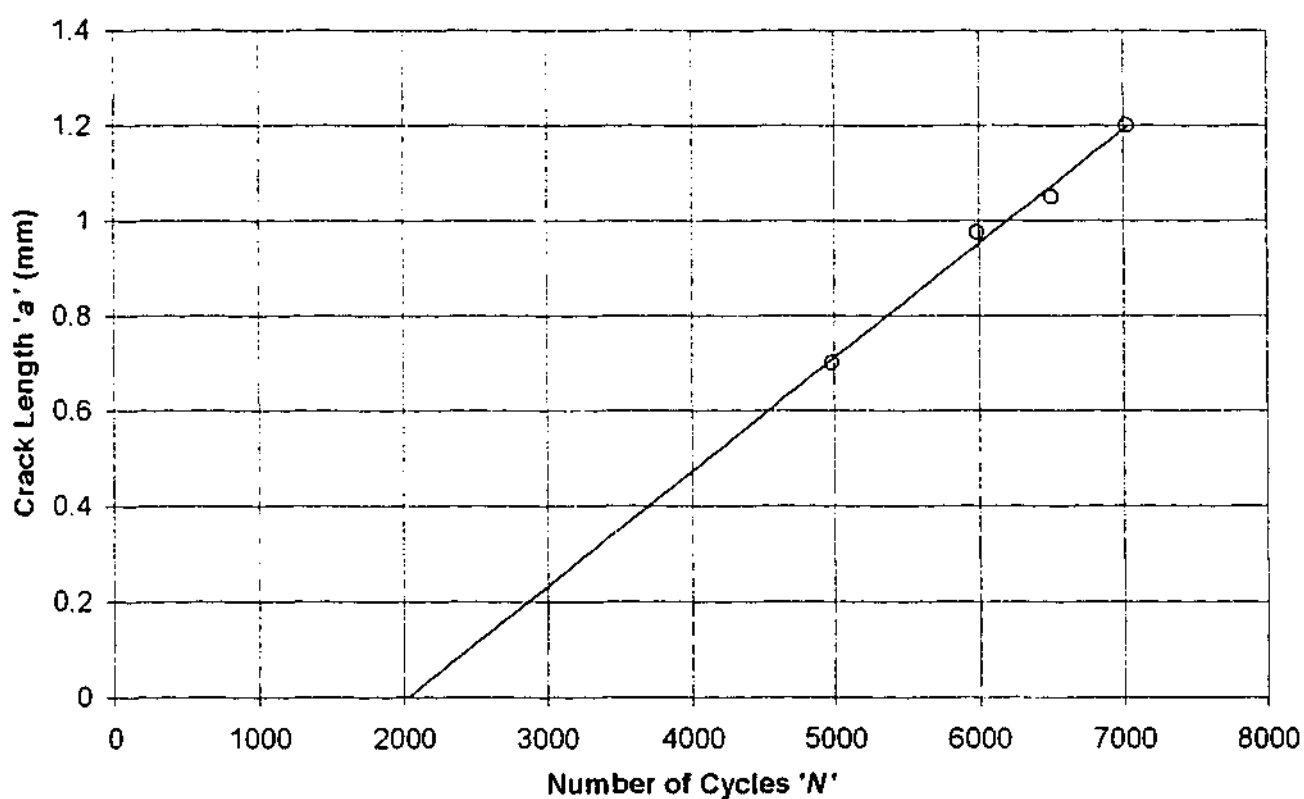


Figure C.8: Estimate for cycles to crack initiation from long crack growth data. For specimen #5, crack position #2.

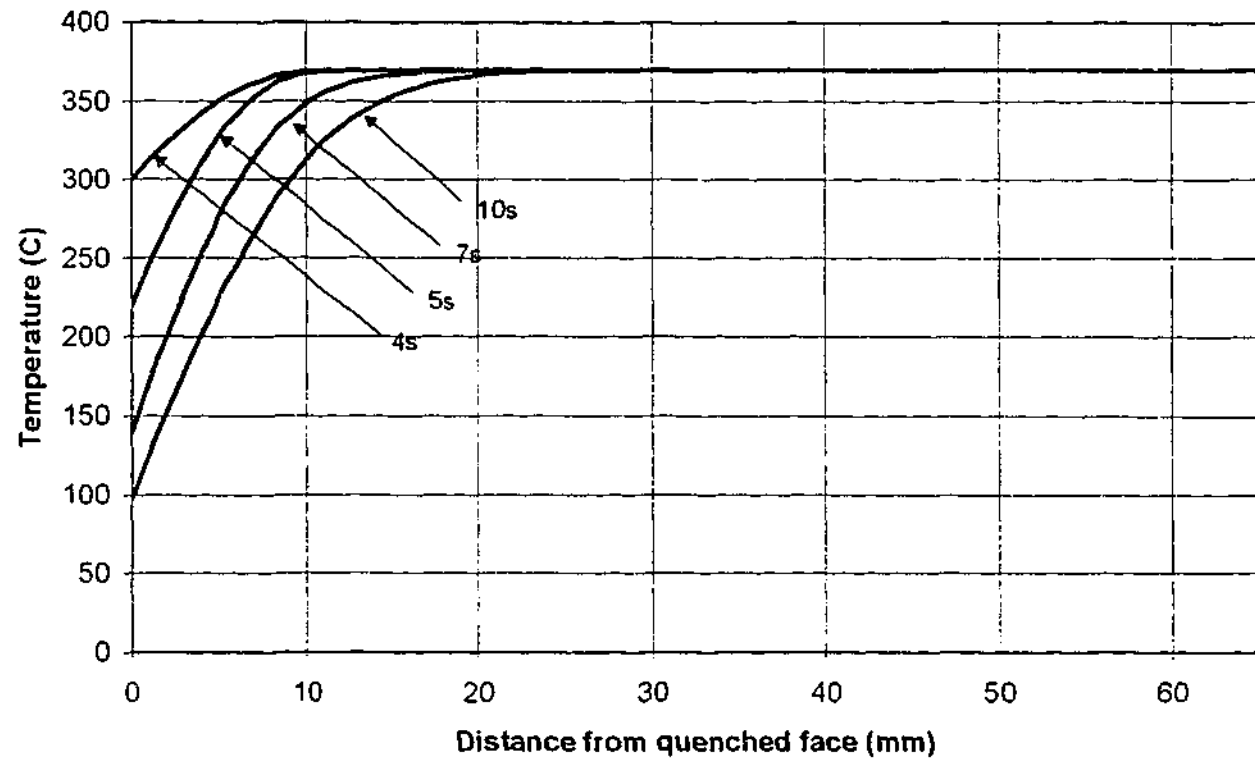


Figure C.9: Typical temperature profiles for thermal shocks of 4s, 5s, 7s and 10s at crack position 1 from central specimen set temperature of 330°C.

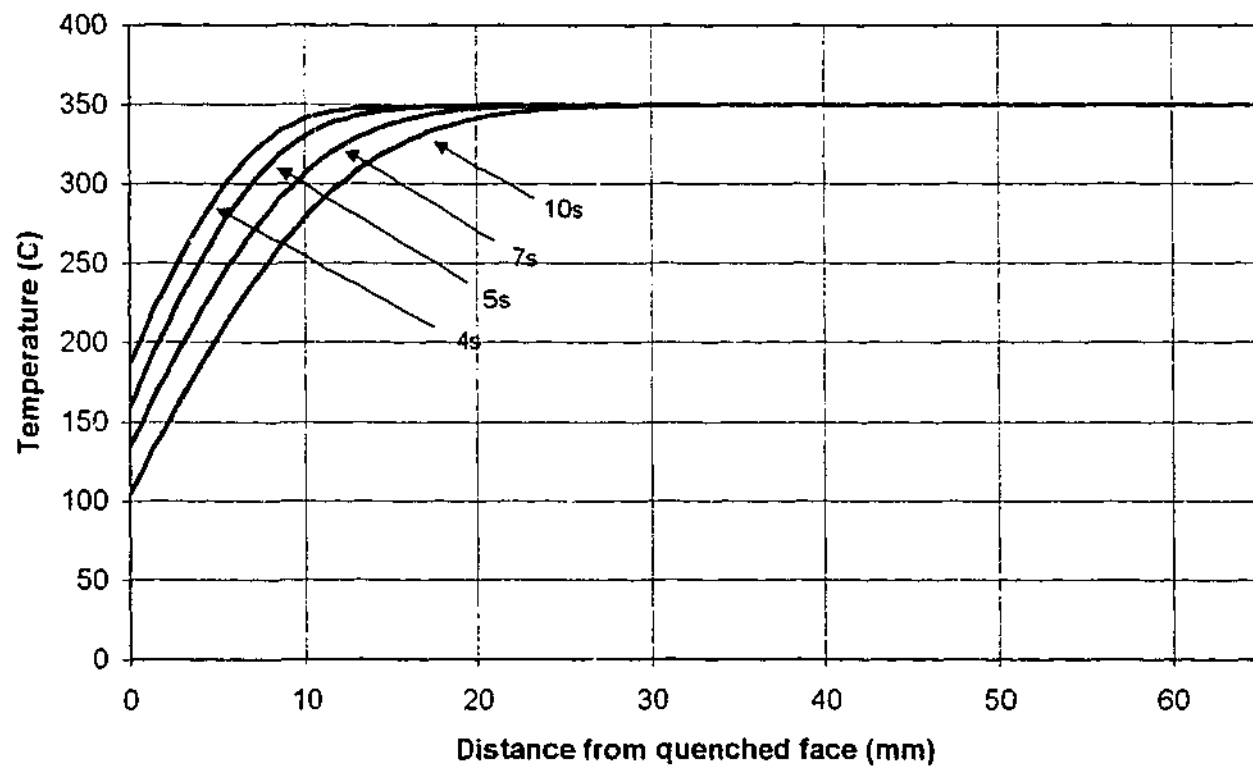


Figure C.10: Typical temperature profiles for thermal shocks of 4s, 5s, 7s and 10s at crack position 2 from central specimen set temperature of 330°C.

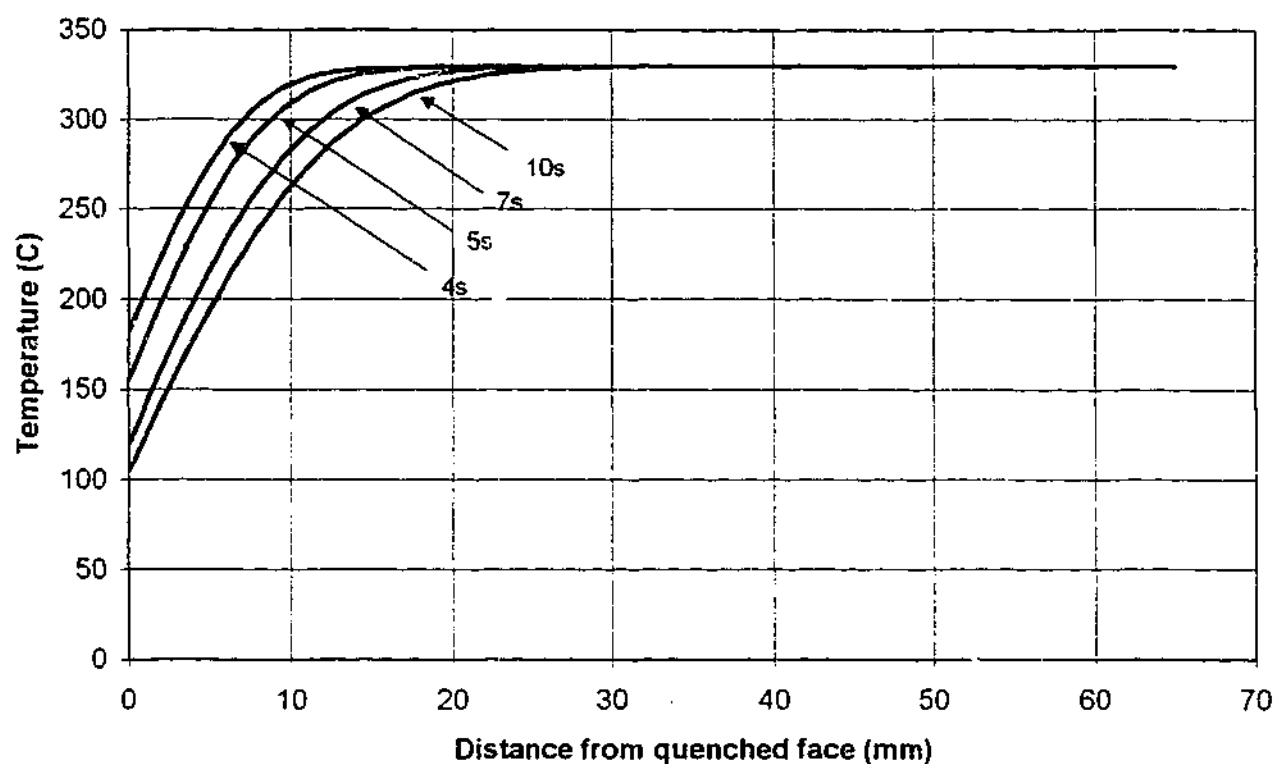


Figure C.11: Typical temperature profiles for thermal shocks of 4s, 5s, 7s and 10s at crack position 3 from central specimen set temperature of 330°C.

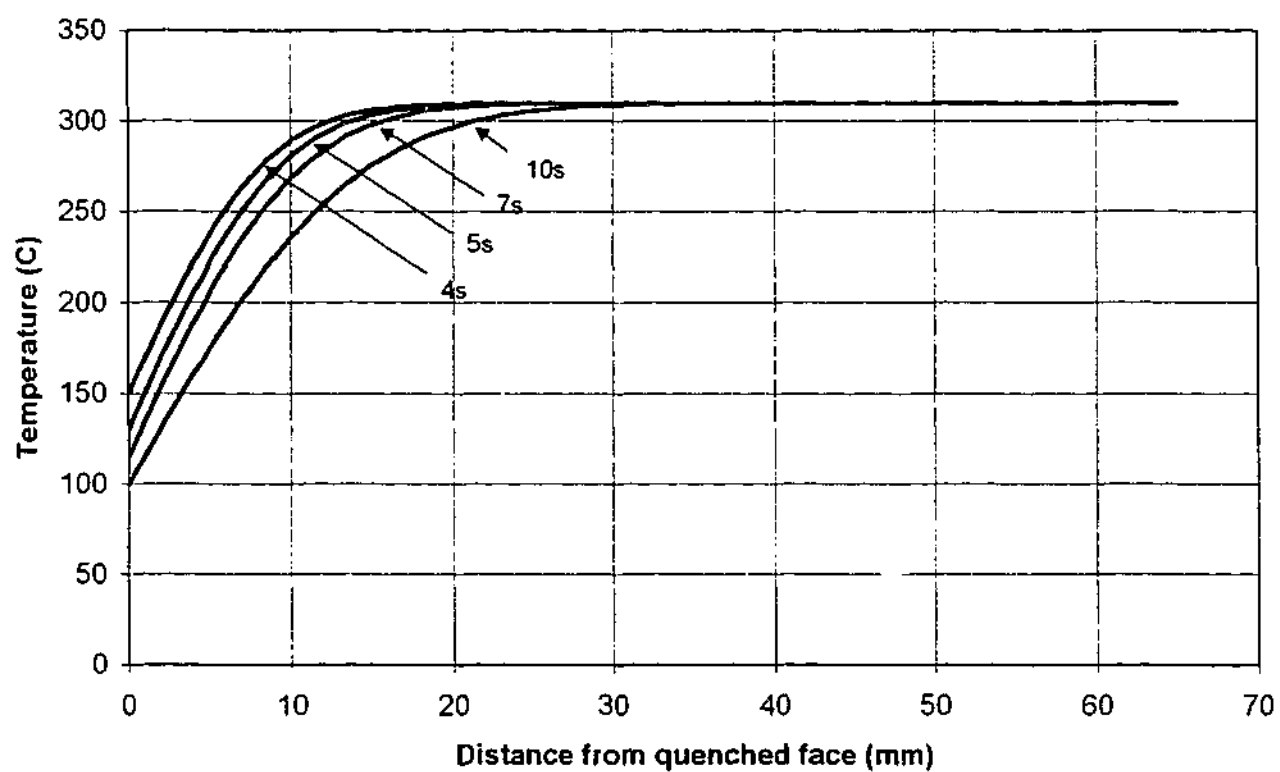


Figure C.12: Typical temperature profiles for thermal shocks of 4s, 5s, 7s and 10s at crack position 4 from central specimen set temperature of 330°C.

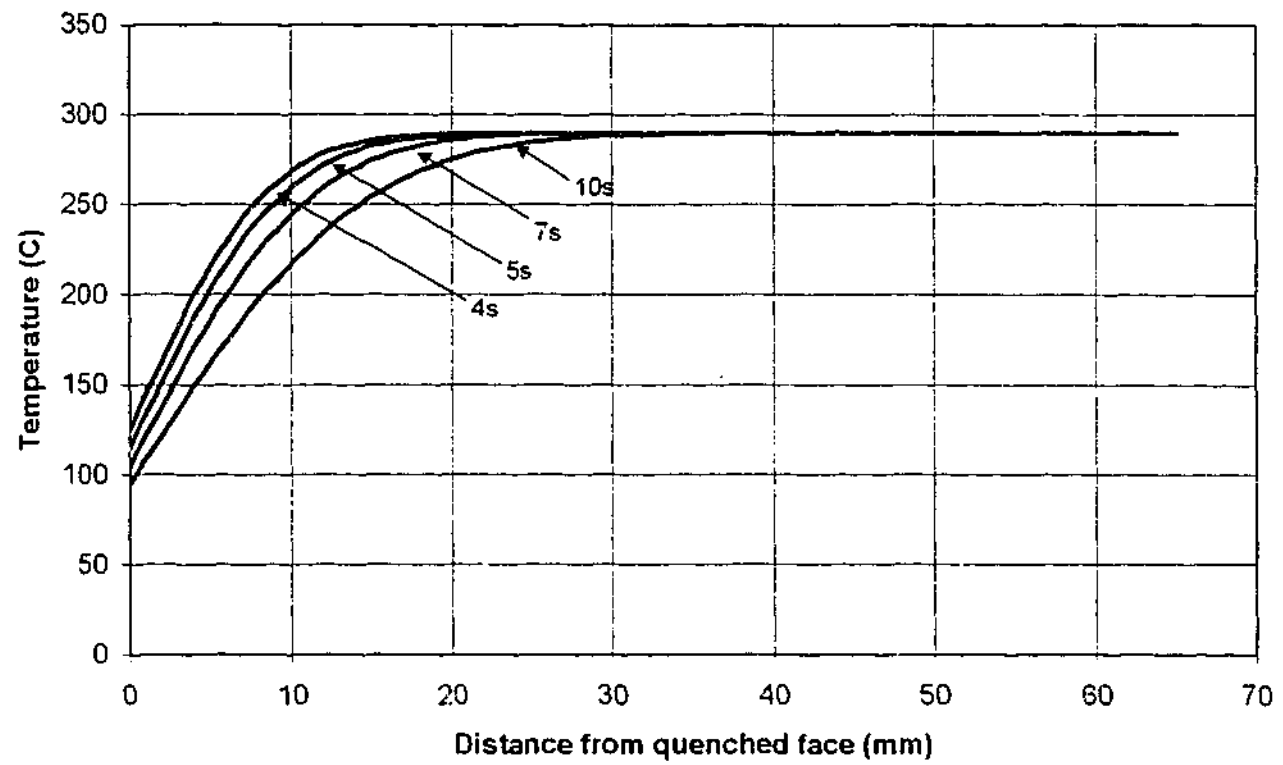


Figure C.13: Typical temperature profiles for thermal shocks of 4s, 5s, 7s and 10s at crack position 5 from central specimen set temperature of 330°C.

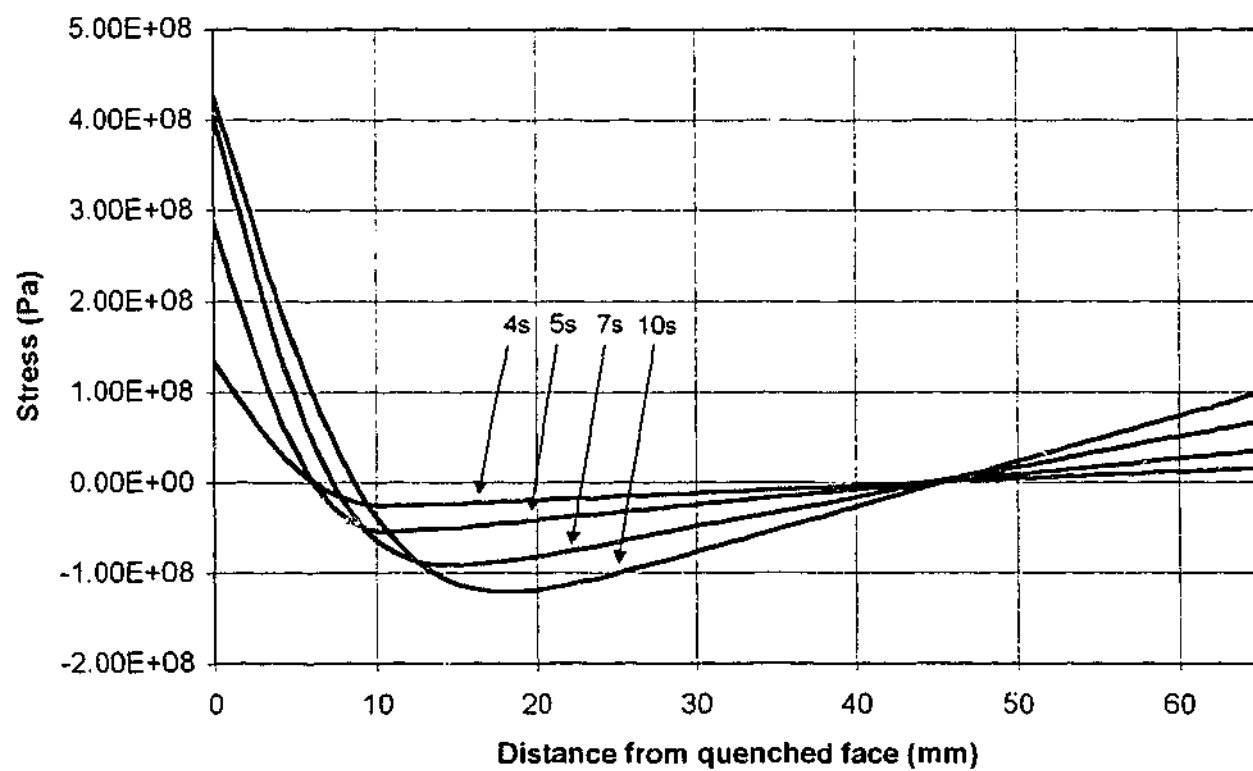


Figure C.14: Typical elastic stress profiles for thermal shocks of 4s, 5s, 7s and 10s at crack position 1 from central specimen set temperature of 330°C.

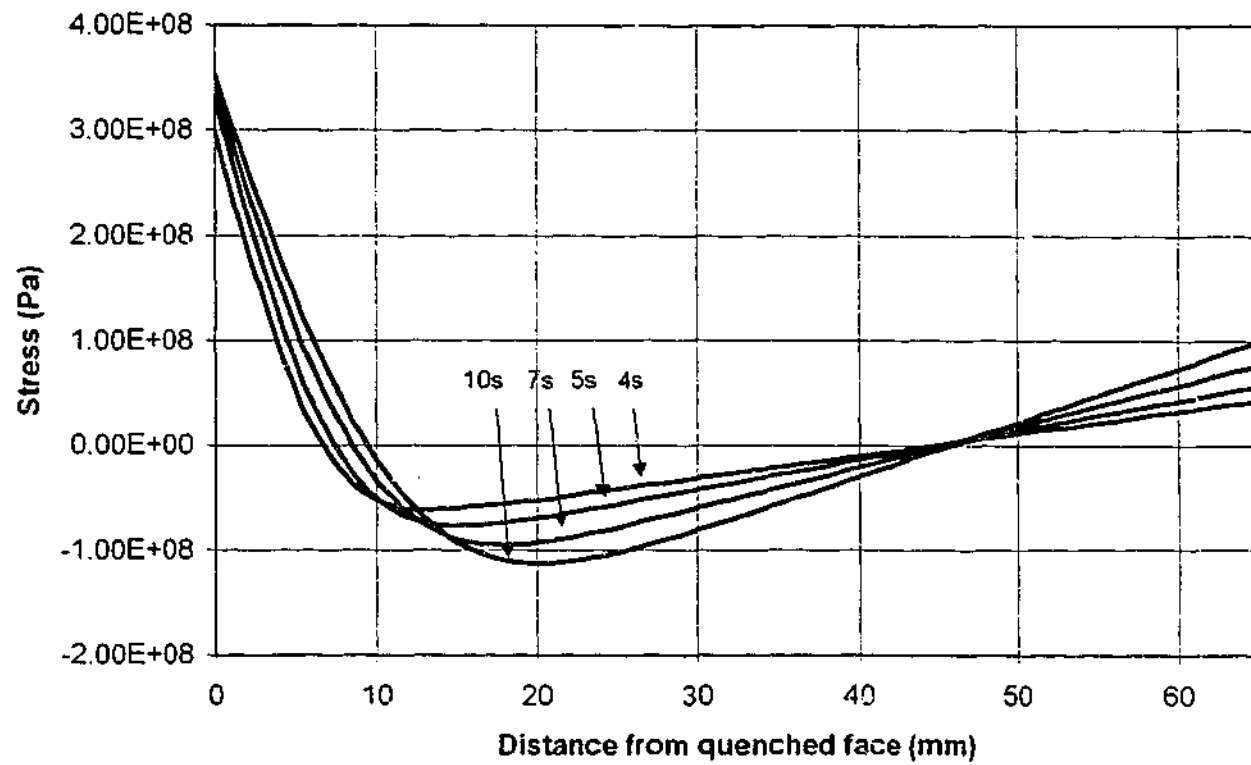


Figure C.15: Typical elastic stress profiles for thermal shocks of 4s, 5s, 7s and 10s at crack position 2 from central specimen set temperature of 330°C.

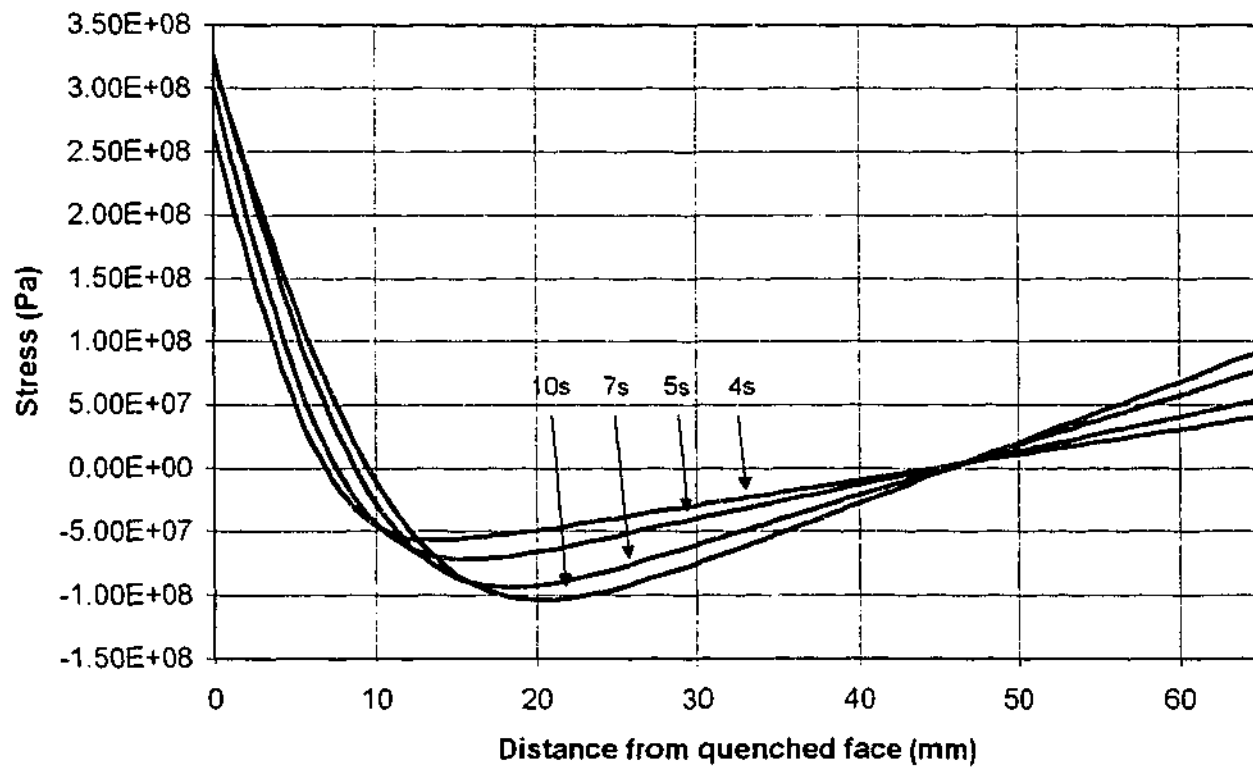


Figure C.16: Typical elastic stress profiles for thermal shocks of 4s, 5s, 7s and 10s at crack position 3 from central specimen set temperature of 330°C.

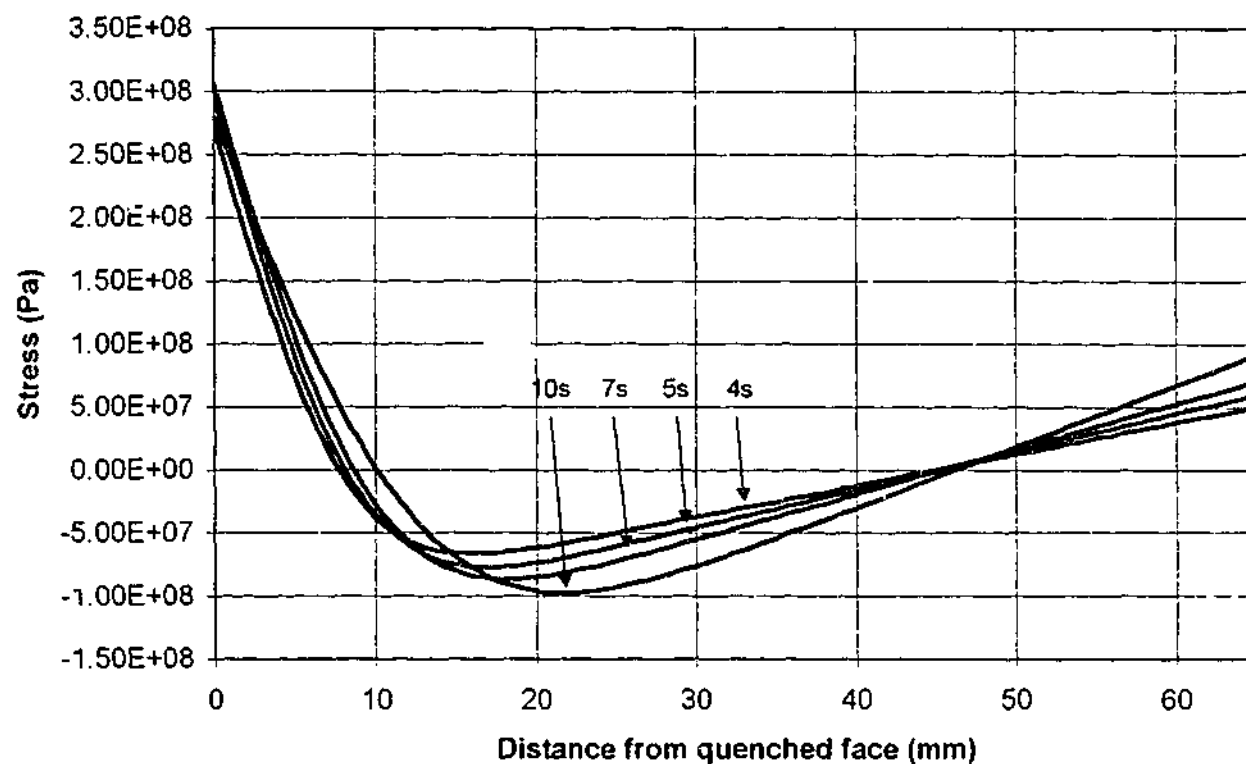


Figure C.17: Typical elastic stress profiles for thermal shocks of 4s, 5s, 7s and 10s at crack position 4 from central specimen set temperature of 330°C.

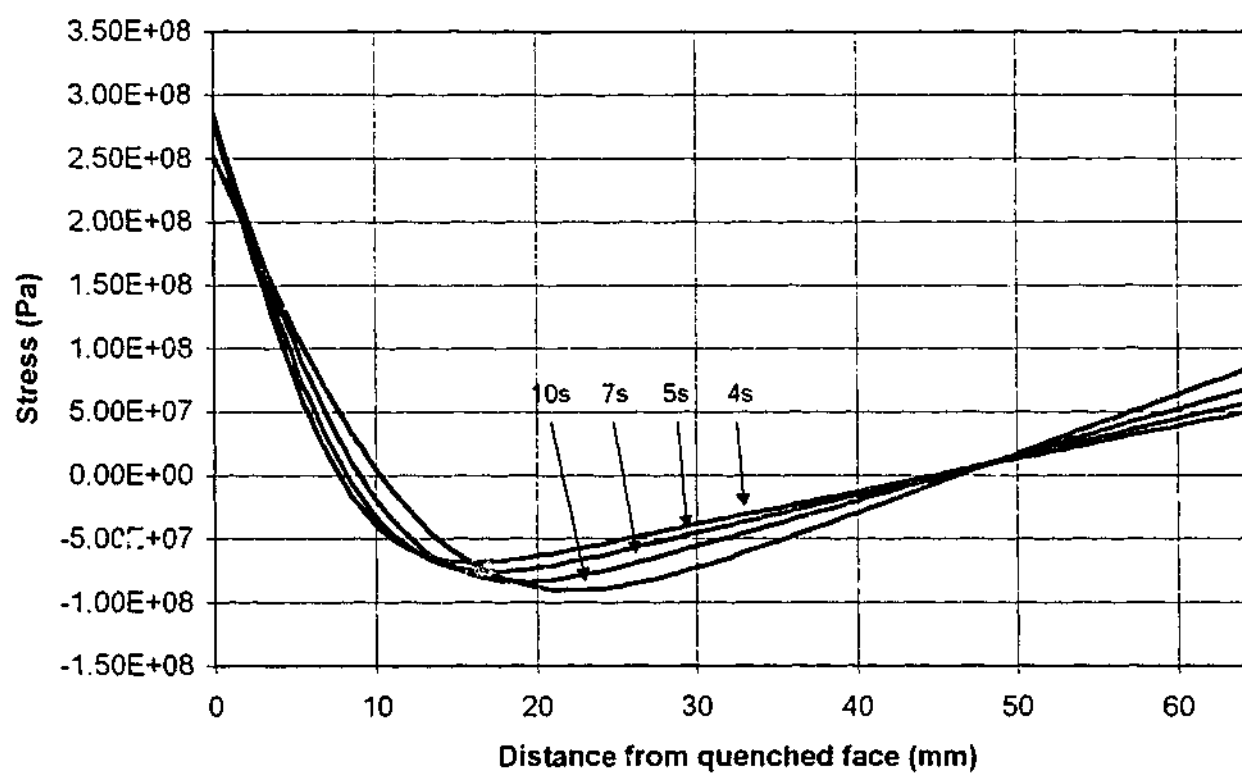


Figure C.18: Typical elastic stress profiles for thermal shocks of 4s, 5s, 7s and 10s at crack position 5 from central specimen set temperature of 330°C.

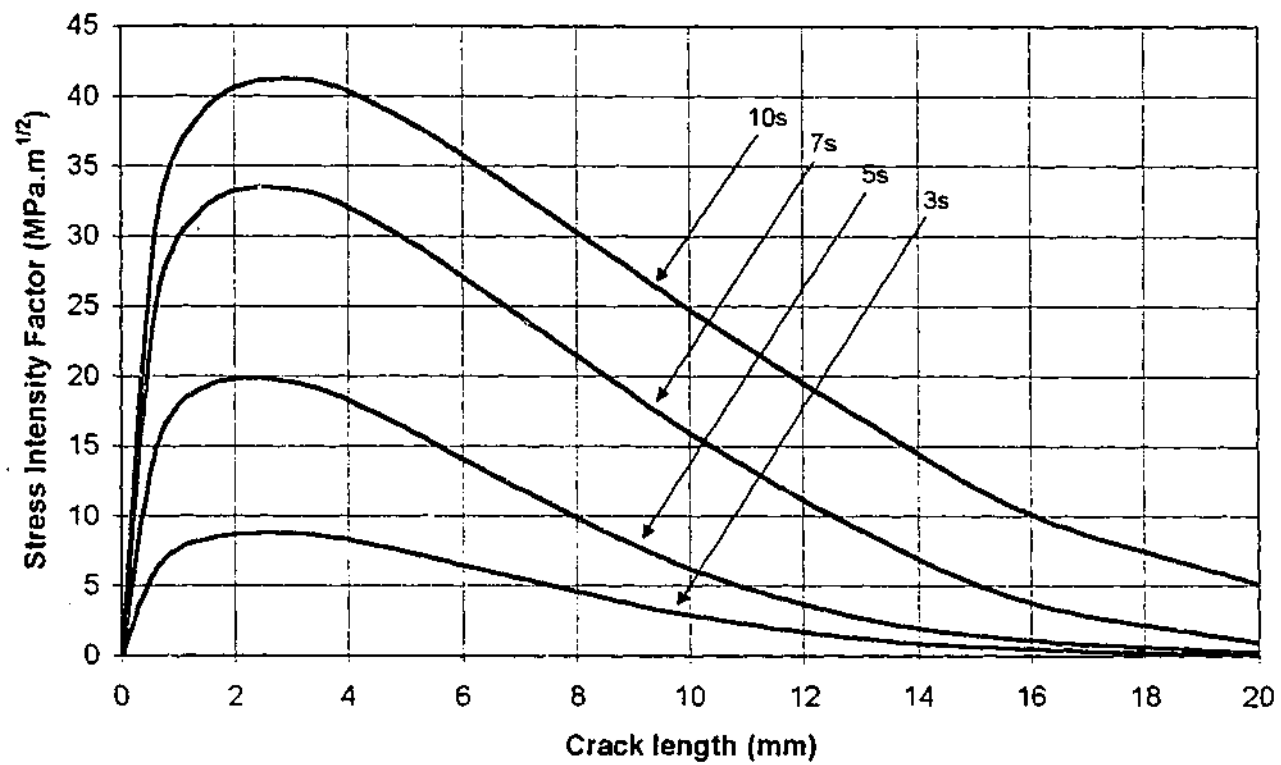


Fig C.19: Cyclic change in stress intensity factor ( $\Delta K_I$ ) as a function of crack depth for thermal shocks of 4s, 5s, 7s and 10s at crack position 1 from central specimen a set temperature of 330°C. No primary mechanical load.

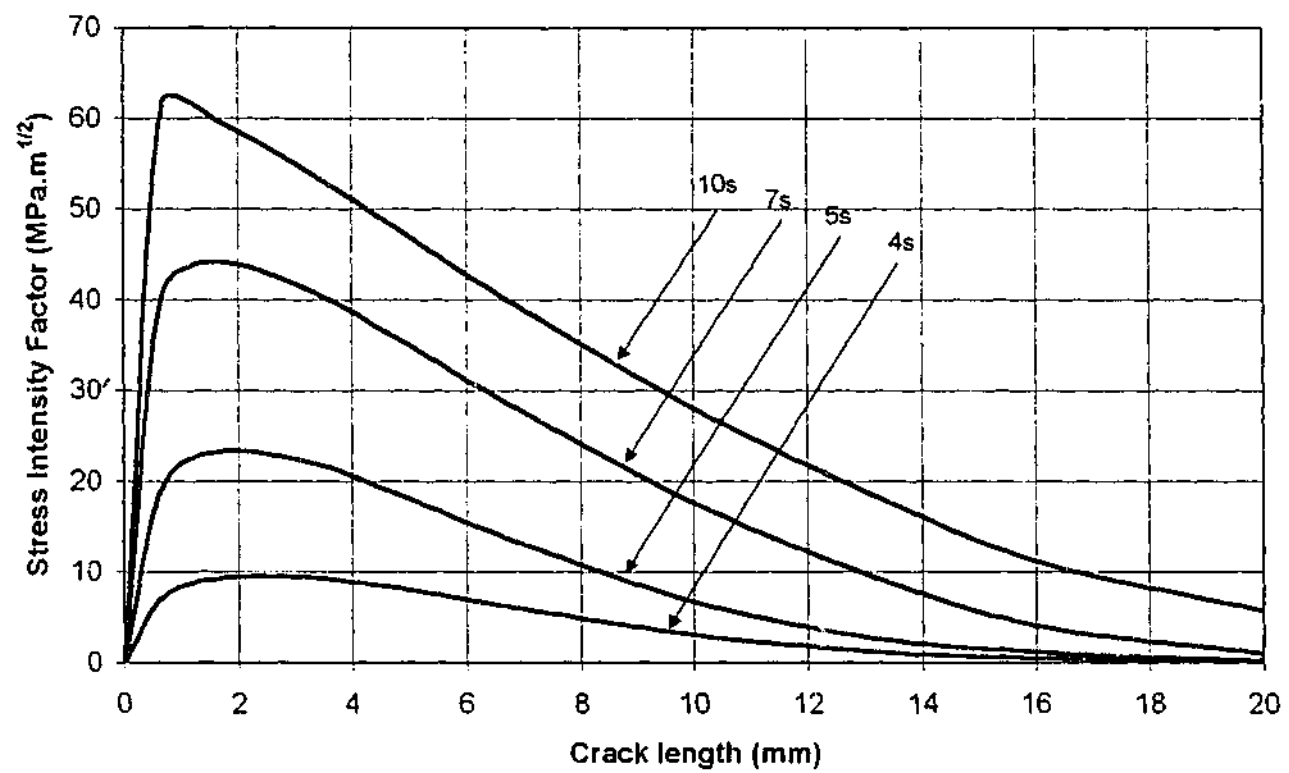


Fig C.20: Cyclic change in stress intensity factor ( $\Delta K_I$ ) as a function of crack depth for thermal shocks of 4s, 5s, 7s and 10s at crack position 1 from central specimen a set temperature of 330°C. 90MPa primary mechanical load included.



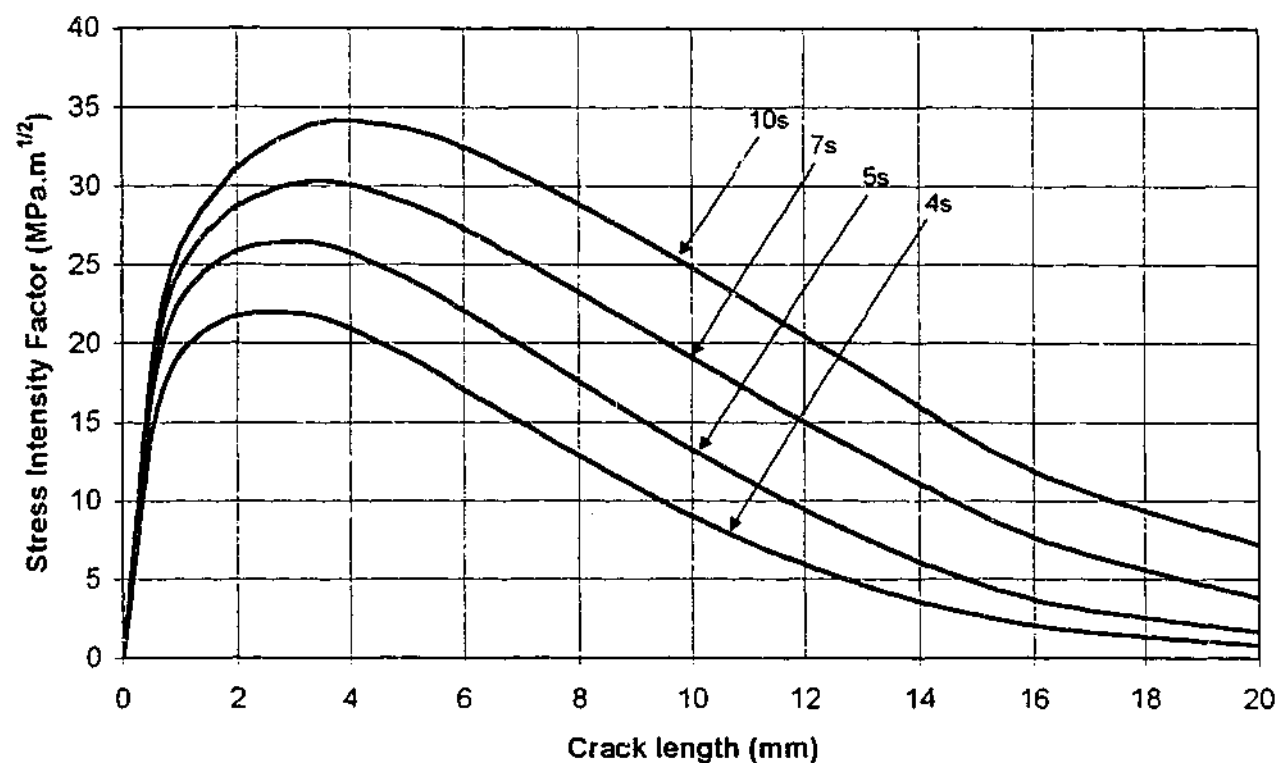


Fig C.21: Cyclic change in stress intensity factor ( $\Delta K_I$ ) as a function of crack depth for thermal shocks of 4s, 5s, 7s and 10s at crack position 2 from central specimen a set temperature of 330°C. No primary mechanical load included.

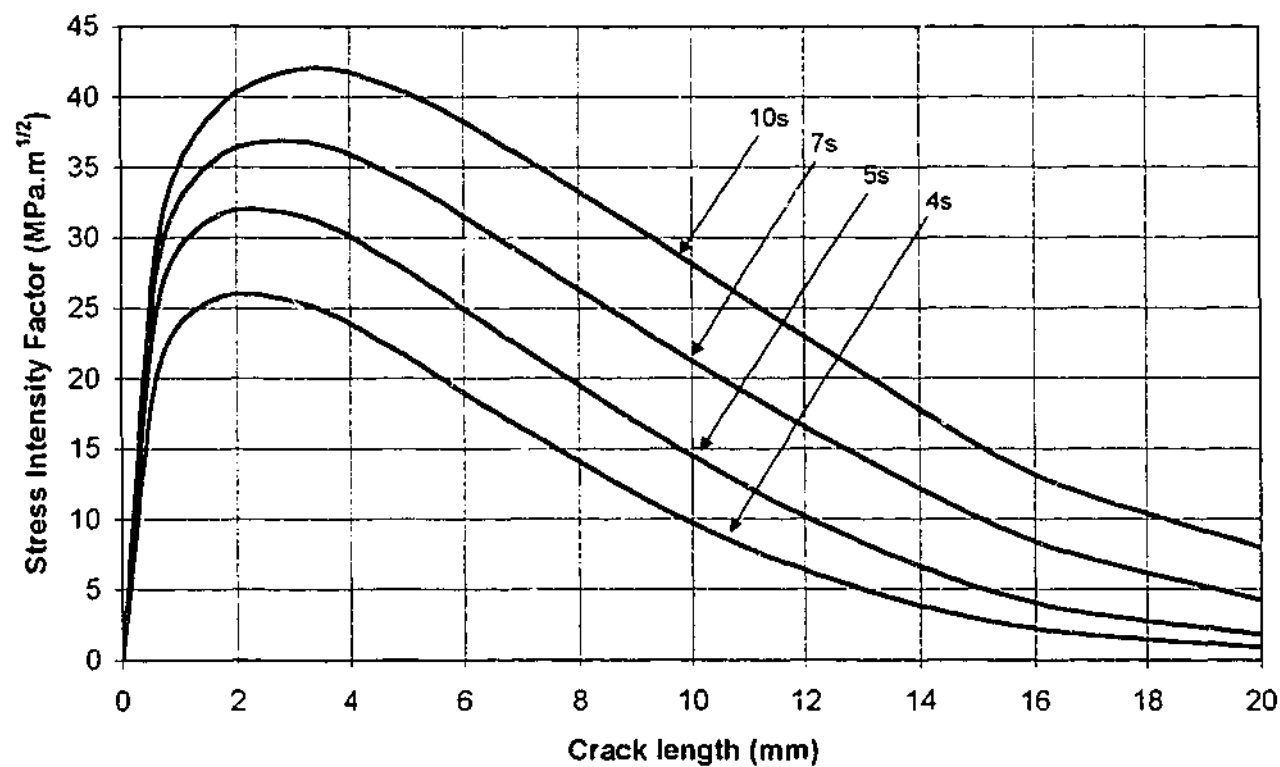


Fig C.22: Cyclic change in stress intensity factor ( $\Delta K_I$ ) as a function of crack depth for thermal shocks of 4s, 5s, 7s and 10s at crack position 2 from central specimen a set temperature of 330°C. 90MPa primary mechanical load included.

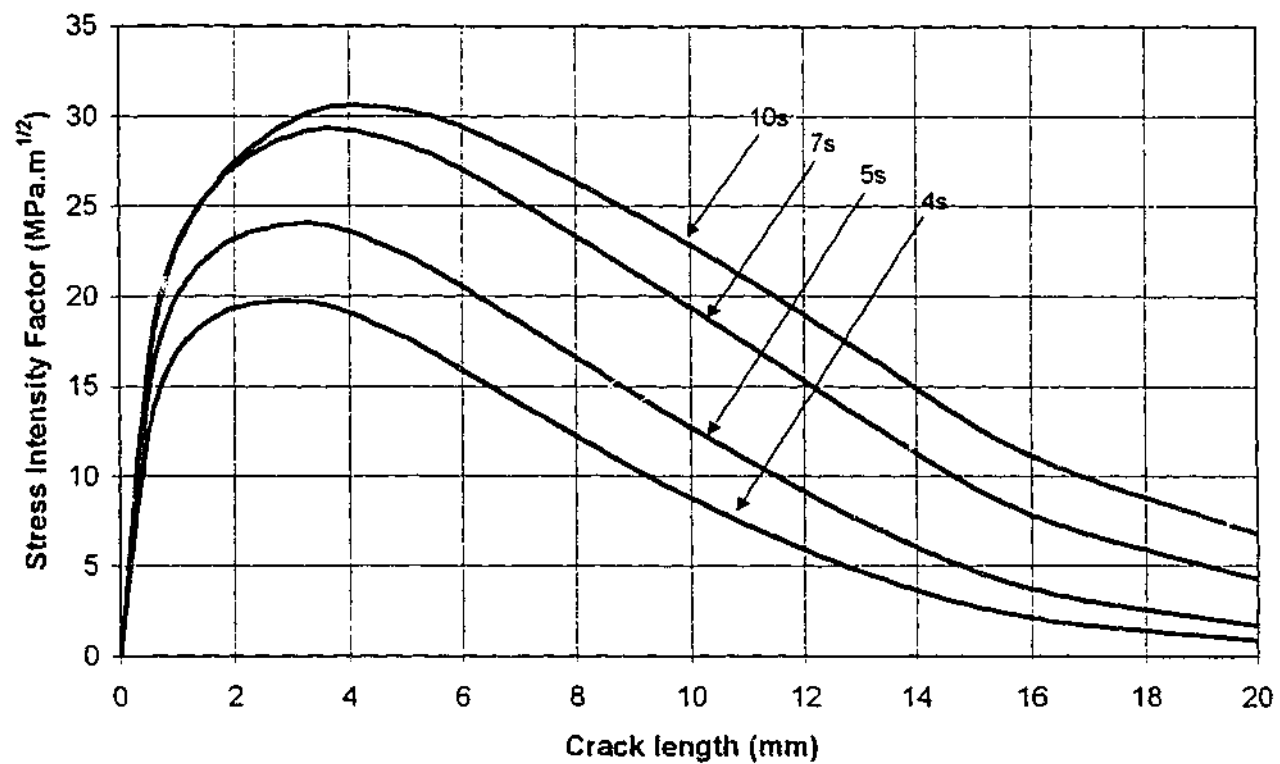


Fig C.23: Cyclic change in stress intensity factor ( $\Delta K_I$ ) as a function of crack depth for thermal shocks of 4s, 5s, 7s and 10s at crack position 3 from central specimen a set temperature of 330°C. No primary mechanical load included.

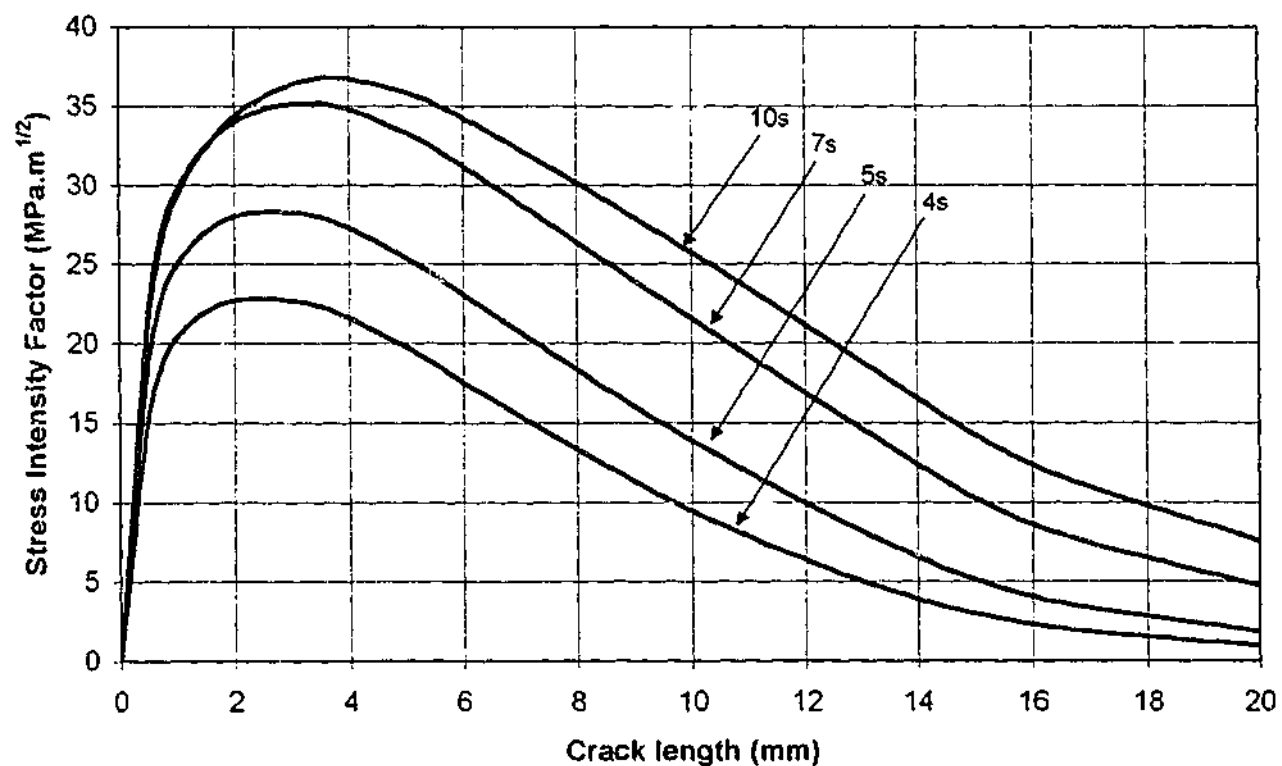


Fig C.24: Cyclic change in stress intensity factor ( $\Delta K_I$ ) as a function of crack depth for thermal shocks of 4s, 5s, 7s and 10s at crack position 3 from central specimen a set temperature of 330°C. 90MPa primary mechanical load included.

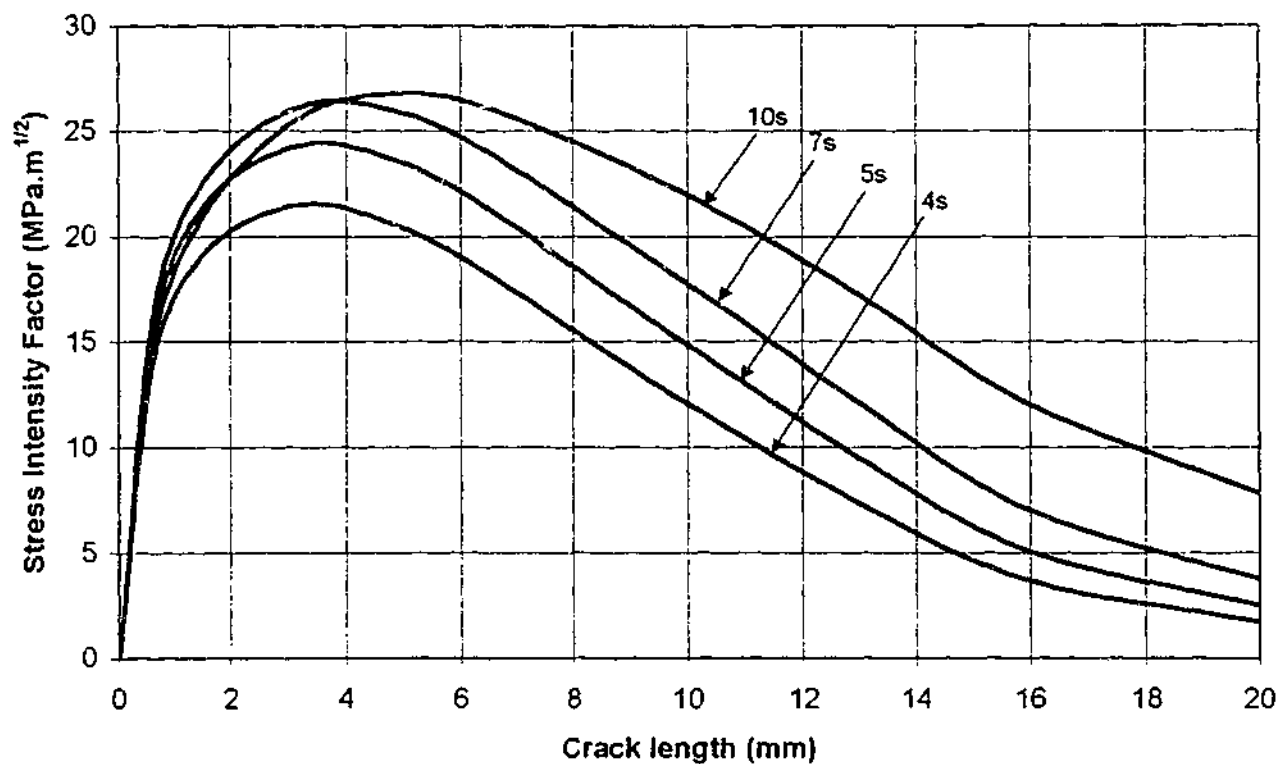


Fig C.25: Cyclic change in stress intensity factor ( $\Delta K_I$ ) as a function of crack depth for thermal shocks of 4s, 5s, 7s and 10s at crack position 4 from central specimen a set temperature of 330°C. No primary mechanical load included.

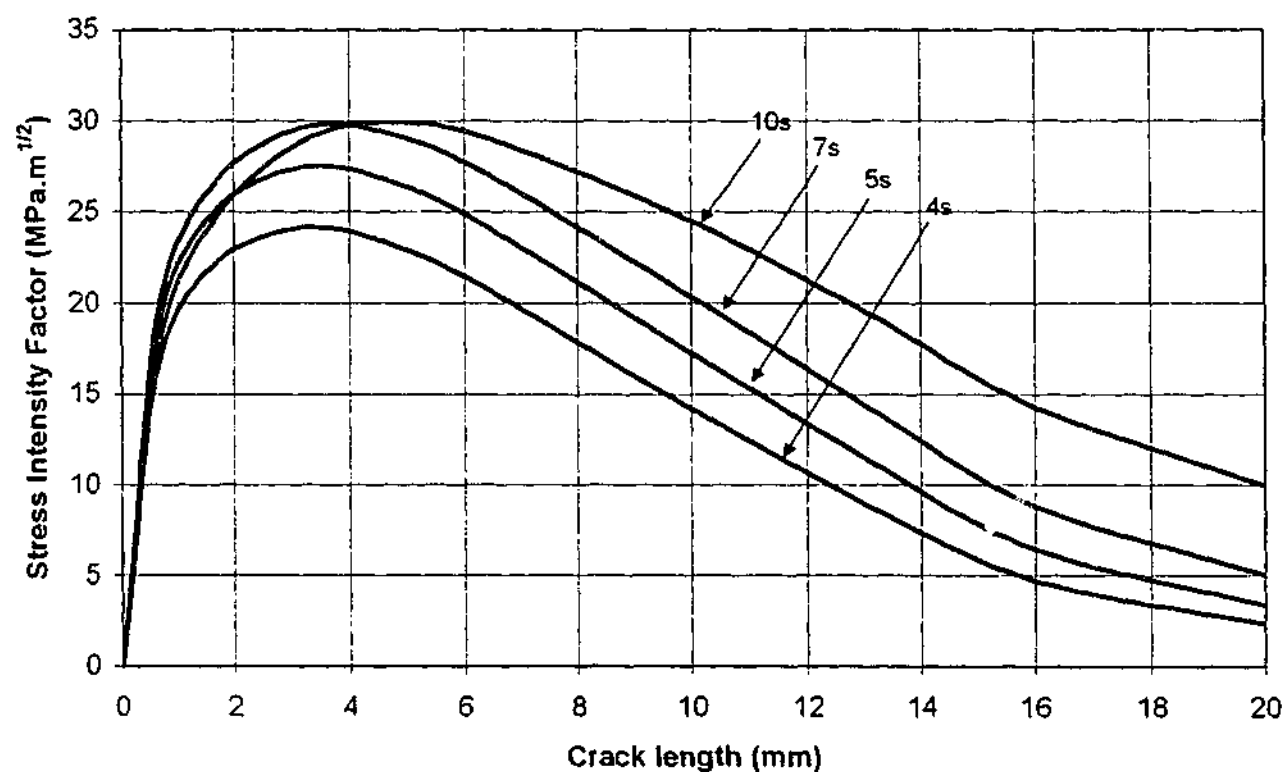


Fig C.26: Cyclic change in stress intensity factor ( $\Delta K_I$ ) as a function of crack depth for thermal shocks of 4s, 5s, 7s and 10s at crack position 4 from central specimen a set temperature of 330°C. 90MPa primary mechanical load included.

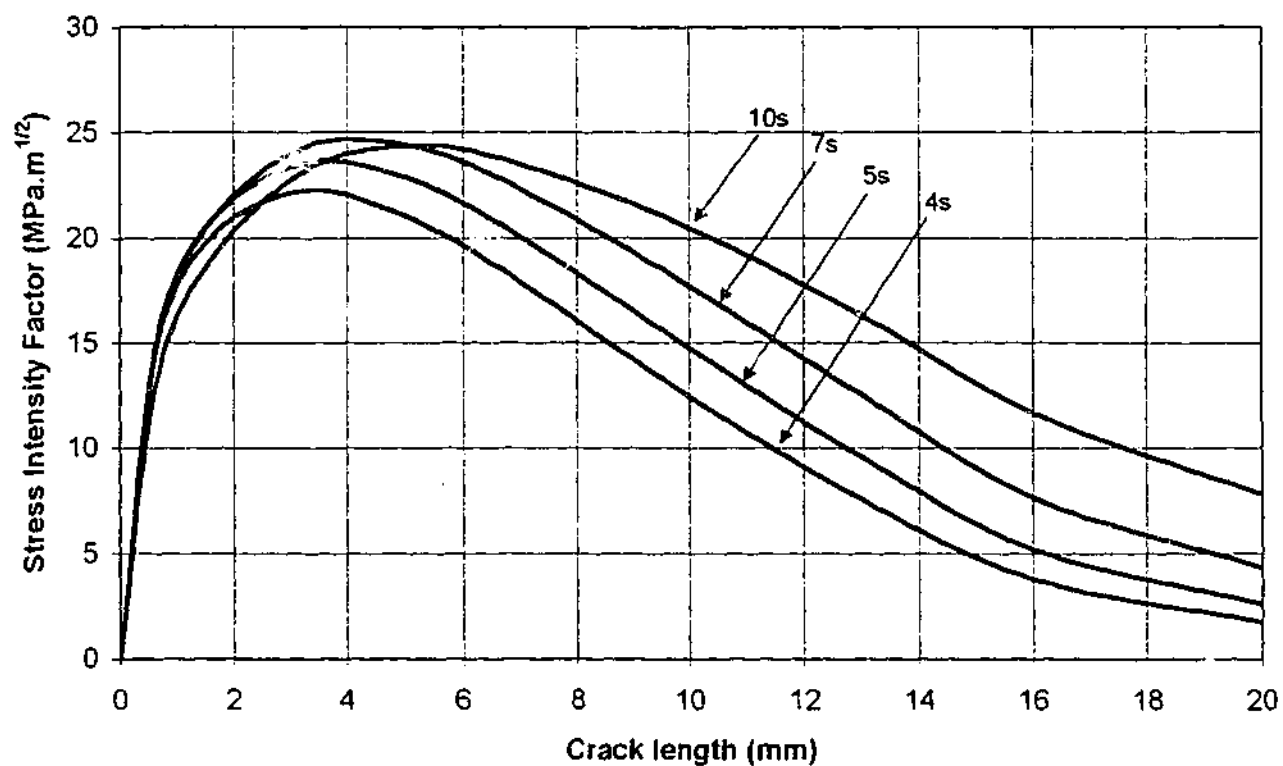


Figure C.27: Cyclic change in stress intensity factor ( $\Delta K_I$ ) as a function of crack depth for thermal shocks of 4s, 5s, 7s and 10s at crack position 5 from central specimen a set temperature of 330°C. No primary mechanical load included.

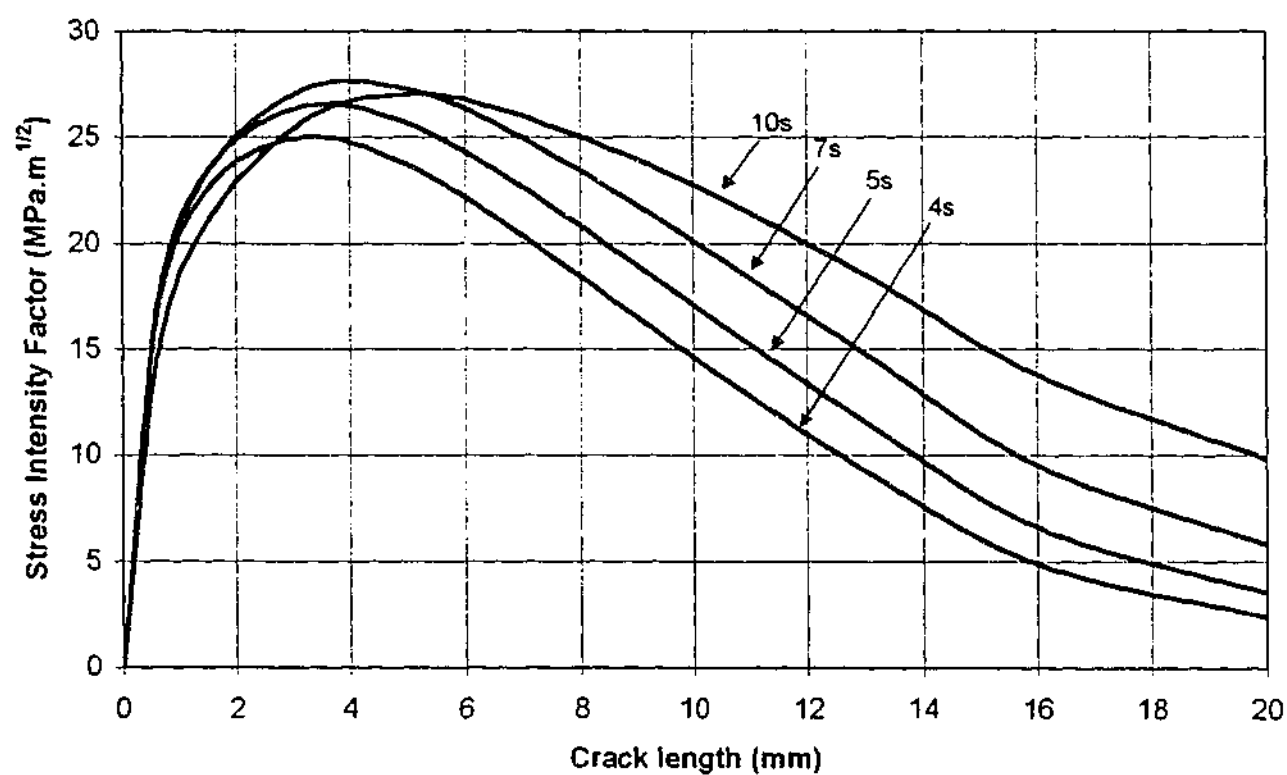


Figure C.28: Cyclic change in stress intensity factor ( $\Delta K_I$ ) as a function of crack depth for thermal shocks of 4s, 5s, 7s and 10s at crack position 5 from central specimen a set temperature of 330°C. 90MPa primary mechanical load included.

## **Appendix D**

### **Authors Relevant Publications**

## Experimental apparatus for thermal shock fatigue investigations

B.B. Kerezsi\*, A.G. Kotousov, J.W.H. Price

*Department of Mechanical Engineering, Monash University, P.O. Box 197, Caulfield East, Vic. 3145, Australia*

Received 21 January 2000; revised 1 April 2000; accepted 28 April 2000

### Abstract

An experimental rig developed for investigating crack growth in pressure vessels and piping equipment is described. The rig allows full scale modeling of cyclic thermal shock conditions that occur in operating thermal power station pressure equipment. It has the ability to apply a primary steady state mechanical load and to control the quenching environment allowing the study of the effect of welds and stress concentrators under conditions that simulate operational loadings. These results can be used for lifetime assessment.

Preliminary results from the test rig analysing the effect of primary load on crack initiation and growth are presented and discussed briefly. A comparison with prediction methods from the ASME Boiler and Pressure Vessel Code is made. It is concluded that the primary load has little or no effect on crack initiation times, however it significantly affects the crack growth rate. © 2000 Elsevier Science Ltd. All rights reserved.

**Keywords:** Thermal shock; Fatigue; Crack growth; Test rig; Pressure equipment; Primary load

### 1. Introduction

The growth and arrest of cracks due to repeated thermal shock loading is of interest in industrial applications where predictions will allow decisions to be made on the necessity of planned inspections and component replacements. It is of particular interest in the thermal power generation industry where process variations and transients often lead to the rapid thermal shock loading of pressure piping components such as headers and tubes. These components will provide the focus for these investigations.

Current methods for the analysis of thermal shock crack initiation and growth rely on standards such as the ASME Boiler and Pressure Vessel Code Section VIII, Division 2 and Section XI Appendix A (1998) [1,2] that use a conservative model based on isothermal mechanical fatigue tests and simplified stress profiles. In our work, we carry out tests that simulate closely the real life conditions of thermal shock, which are intended to develop a model that will allow the estimation of the conservatism of the current codes. The work is conducted at temperatures below the creep range in a conscious effort to reduce the complexity of the analysis.

Apart from the conservatism of existing codes, the

simplifications used in their development ignore the effect of many influential factors. Foremost amongst this are the effect of external primary loads, the environment in which the crack is growing and the severity of the shock. The external loads can be a direct result of the pressure or mechanical loading of the components, the effect of which is to open any cracks, exposing them to the environment. The environment is dependent on the process in which the component is being used, which in the case of thermal power station equipment is often aqueous in nature (including chemical treatment to control pH and oxygen levels) and will modify conditions at the crack tip. The time over which the shock is applied can be regarded as the "severity" of the thermal shock and this will also influence crack growth substantially.

A unique test rig specifically developed for this investigation provides the focus for this paper and is described in detail. A short history of the development of thermal fatigue analysis is also provided.

### 2. Background

A brief background of thermal fatigue research is now presented. Particular attention is paid to the general history of thermal fatigue research, the design of test rigs and the application of standards.

\* Corresponding author. Tel.: +61-3-9903-2739; fax: +61-3-9903-2766.  
E-mail address: brian.kerezsi@eng.monash.edu.au (B.B. Kerezsi).

## 2.1. General historical review

Although the theory and industrial implications of thermal stresses in metals is an old and well established subject in engineering, it was not recognized as a field in its own right until the 1950s. Manson [3] and Coffin [4] were the first to complete thorough investigations into thermal stress fatigue loading, producing what are now referred to as the seminal studies in the area. These investigations provided the theoretical and experimental platform upon which thermal fatigue research would rest until the middle of the 1970s. During this time, most work concentrated on determining the effect of temperature on low cycle (or high strain) fatigue strength of materials and production of the appropriate  $\epsilon$ - $N$  curves.

The majority of this work was completed using both high temperature isothermal and thermal-mechanical fatigue testing such as described in Ref. [4], (see also [5,6]) utilizing servo-hydraulic test machines. In addition, some work was completed using the fluidized bed technique, described more fully in a review [7]. Irrespective of the test method, the concentration was on identifying crack initiation for use in life prediction rather than monitoring the crack growth. White [8] provides a more comprehensive review of investigations at this time, concentrating on British contributions.

During the mid 1970s, the introduction of Linear Elastic Fracture Mechanics (LEFM) into the tool-kits of researchers lead to a fresh batch of testing in thermal fatigue, this time concentrating more on identifying crack growth relationships rather than lifetime correlation. The description of crack growth in turbine blade steels during thermal-mechanical testing was completed by Rau et al. [9]. The effect of minimum and maximum temperature, strain range, mean strain and cycle shape was included in the investigation with the conclusion that the stress intensity factor ( $\Delta K$ ) was an acceptable parameter for modelling of the crack growth for small plastic strain values. Mowbray et al. [10] completed a similar investigation using the fluidised bed technique and tapered disk specimens, also for turbine blade materials. Although these tests both provided encouraging results, they did no more than show that LEFM was a valid technique for crack growth under cyclic thermal stress conditions.

The most comprehensive work to date in the region of crack initiation and growth due to thermal fatigue has been completed by Skelton [11]. Although this text is over 15 years old, it still represents the most concerted effort in the field. The format is primarily as a review of the previous works in the area, with particular reference to his investigations. Emphasis is placed on modelling of crack growth using Paris Law type equations, and the prediction of crack arrest using LEFM generated  $\Delta K$  (stress intensity factor range) profiles. The temperature distribution is used to define the thermal stress distribution from which the  $\Delta K$  profile can be determined via the weight function method.

## 2.2. Experimental test rigs

A review of the past experimental designs for the analysis of thermal fatigue shows a trend towards two main types of design. The most frequently mentioned is the thermal-mechanical fatigue type (e.g. [9,12–15]). In this design, cyclic thermal loading is applied to a fully constrained specimen that may or may not undergo a separate cyclic mechanical loading. The advantage of this arrangement is that a single specimen (typically a thin cylinder) can be subjected to a selection of mechanically applied strain ranges for a single temperature range. This simplifies the generation of low cycle fatigue  $\epsilon$ - $N$  curves at different temperatures.

Unfortunately, these designs neither take into account any environmental effects nor do they correctly model the thermal gradients that are developed during shock loading. The effect of the environment (including temperature and atmospheric composition) on fatigue crack initiation and growth is significant and difficult to account for, analytically. In a review of past work in the area, Marshall [16] indicated that modification of the environment could decrease the fatigue life of a specimen by up to two orders of magnitude when compared to the same test performed at room temperature and in a vacuum. Marshall concludes that the best way to allow for the effects of environment is to carry out the fatigue tests in an environment that simulates closely that will be present during service.

The second type of experiment is the thermal stress fatigue type (e.g. [6,10,17,18]). In these experiments, the specimen (typically disk shaped) is subjected to a sudden change in temperature, usually by submersion in a heated/cooled medium. The advantages of this method are that the stress profile is reproduced faithfully and that very severe shocks are possible in a very short time period. For example, Howes [7] reports a surface temperature rise of up to 600°C in 4 s using steel specimens. Although this may be useful for analysing high temperature components such as turbine blades, for steels operating below the creep range there is no need for such a range of temperatures. The other problem with these methods of testing is the lack of an accurate reproduction of the environment, external loading and geometry of industrial applications.

As will be seen, the design chosen for use in this investigation may be called a compromise between the thermal-mechanical and thermal stress fatigue techniques. It is in some ways similar to the SPLASH facility used by Fissolo et al. [19] to investigate crack initiation in 316 L stainless steel. In their rig, a resistance-heated specimen was quenched with room temperature water to produce the thermal shock loads.

## 2.3. Issues in ASME XI [2]

As mentioned previously, in this document the ASME Boiler and Pressure Vessel Code is currently one of the

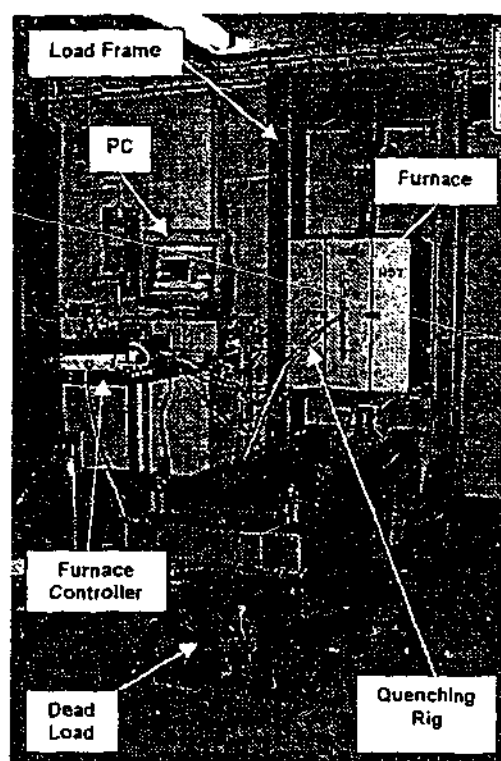


Fig. 1. Photo of testing rig layout.

most widely accepted standards for the analysis of cracks in pressure equipment. In particular, it is Appendix A of Section XI [2] that deals with the analysis of flaws. Developed for use in the nuclear power industry, it provides the tools required for the prediction of crack propagation rates. Figs. A-4300-1 and 2 provide the reference curves for translating the stress intensity factors produced at the tip of a crack into crack growth rates for carbon and low alloy ferritic steels exposed to air and water reactor environments, respectively. They also include the effect of  $R$ -ratio. Water reactor environments are basically AVT (All Volatiles water Treatment), thus oxygen and pH are controlled at less than 10 ppb and about 7.0–9.0, respectively.

The ASME XI [2] crack growth curves are produced on tensile test machines. In the case of the water reactor environment, the specimen is immersed in a treated but stagnant fluid supposedly simulating the water reactor environment, which, as is discussed below, results in a changing  $R$ -ratio. The thermal shock case is not like the oscillating primary load of the tensile test machine since the thermal stress component quickly diminishes from the surface. The environment in thermal shock also changes, either from hot to cold water, from steam to cold water or from air to cold water. In addition, the fluid is also in violent motion. Consequently, the choice of the ASME XI [2] curves to be used in a thermal shock analysis is unclear.

The importance of the variation of environment is shown in an investigation by Czuck et al. [20]: a semi-elliptical crack on a heated specimen (300°C) was exposed to a high pressure (38 bar) water blast. The crack growth was

then compared to estimates from the ASME B&PV Code. This comparison revealed that the crack growth along the free surface (exposed directly to the cooling spray) was bounded by the wet curve, while growth at the tip of the crack (obscured from the water by the unloaded crack geometry) was bounded by the dry growth curve. Unfortunately, the method of applying the water spray may have placed indirectly a compressive force at the crack tip that may have influenced the crack growth.

The ASME data also requires a quantification of the  $R$  ratio (defined as the ratio of the minimum to maximum stress intensity factors over a cycle— $K_{min}/K_{max}$ ). A problem is posed when deciding what the  $R$ -ratio is at the crack tip during thermal shock. As mentioned, the thermal shock stress is highly non-linear and decreases rapidly away from the shocked surface resulting in a reduction in  $K_{max}$  with crack growth. This means that for cases of non-zero primary stress and hence non-zero  $K_{min}$ , the  $R$ -ratio is increasing as the crack grows. According to the theory, this should result in a relative increase in crack growth rate. In addition, the  $R$ -ratio should have an effect on crack mouth opening distance and hence the environment at the crack tip. Hour and Stubbins [21] have completed a series of tests to monitor the effect of  $R$ -ratio changes for elevated temperature mechanical fatigue of alloy 800 H. Unfortunately these were carried out in the creep range with the result that as the  $R$ -ratio was increased, so did the creep component of the crack growth. The effect during thermal shock below the creep range is not reported.

In this paper, the ASME method has been used for determining  $K$ . Many investigations ([20,22,23]) have successfully applied the weight function technique to determine  $K$  values during thermal shock loading of various geometries. Section XI, Appendix A of the ASME Boiler and Pressure Vessel code has adopted a modified form of the weight function to calculate the stress intensity factors by fitting a third-order polynomial to the pseudo-elastic stress profile.

### 3. Description of the apparatus

A thermal fatigue test rig has been purpose built for the investigation of crack initiation and growth due to repeated thermal shock loading. Consisting of a convection furnace, static loading structure and quenching system it allows for the monitored growth of cracks for a wide variety of component geometries. Unlike prior investigations, a loading cycle typical of many thermal power station components is reproduced. In addition, the use of a novel specimen design allows many different tests to be completed at one time with different notches.

The key advantages of our rig over previous studies are:

- The component is heated by convection, which means that there are no unwanted heat effects at the crack tip as may be the case for induction or resistance heating.



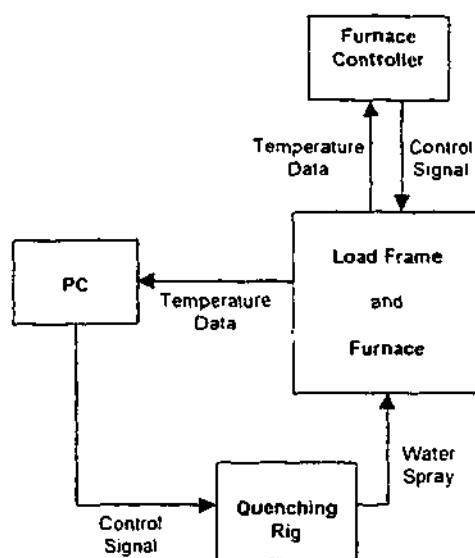


Fig. 2. Schematic of testing rig layout.

- The component is quenched by room temperature pH and  $O_2$  controlled water.
- The specimen size is representative of typical industrial components.
- Large specimen size permits multiple simultaneous experiments.
- An unloaded "control" specimen can be used.
- Approximately one-dimensional (1D) conditions exist at any one crack because of use of thermal masses as described below

The principal disadvantage of the rig is the lengthy testing period (many months) required.

The testing rig is pictured in Figs. 1–3 and can be divided into four main physical components:

- The load frame.
- The furnace and controller.
- The quenching rig and PC.
- The specimen.

The design of each component will be examined in turn.

### 3.1. Furnace

The furnace is rectangular in shape, with a removable front face allowing specimen insertion. Slotted recesses in the top and bottom of the furnace allow the specimen to pass through for the application of the primary load. Heating is performed by two 1 kW resistance type heating elements located on either side of the central heating area, which measures around  $100 \times 150 \times 400 \text{ mm}^2$ . This central area contains a thin walled stainless steel "quenching chamber", which houses the specimen and prevents the heating elements from being damaged by the quenching water. This chamber also has a large vent that protrudes from the

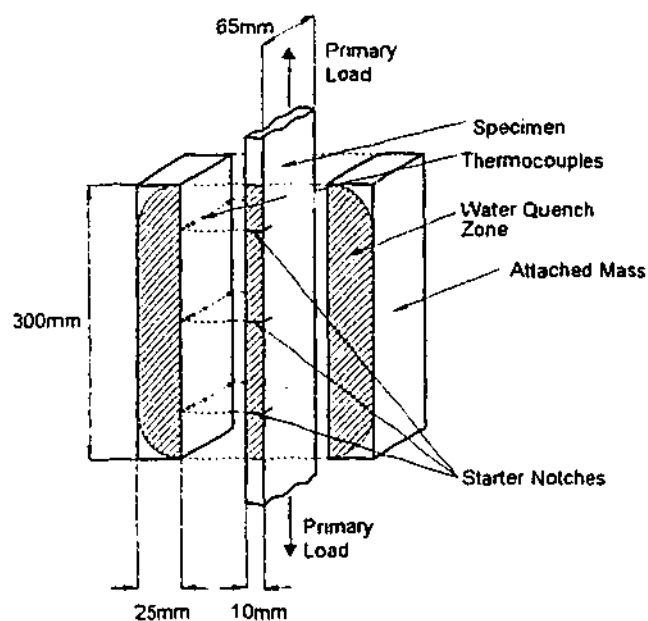


Fig. 3. Specimen design (not to scale).

bottom of the furnace, allowing the escape of steam and water after each quenching cycle.

The furnace is capable of extended use at temperatures of up to  $500^\circ\text{C}$  ( $930^\circ\text{F}$ ). Although convection heating does not provide the most economical method in terms of time taken to heat a sample, it was a conscience design selection made after careful deliberation of other alternatives. Direct resistance heating by passing a current through the specimen ([3,24,25]) provides a more rapid heating option but also produces a localised heating effect around the tip ([26]). Radiant heating as with induction heating ([27,28]) was discounted due to the damage that could occur during quenching. And contact heaters ([13]) reduce the flexibility of the system, having to be modified for each specimen shape and size.

### 3.2. Quenching rig

The quenching rig was designed to operate automatically, relying on the feedback of the specimen temperature. A manifold installed with  $6 \times 1/4 \text{ in.}$  full cone spray nozzles is permanently installed in the front wall of the furnace (see Fig. 1) and passes into the quenching chamber. When the temperature of the specimen uniformly reaches the set point, the quenching cycle is triggered. Up to  $9 \text{ L min}^{-1}$  of water supplied via a 240 V centrifugal pump can be applied to the specimen through the spray heads. A PC running LabView software, controls spray execution and duration. This PC also doubles as a data logger, recording the temperature of the specimen. The water used for quenching is stored in a 500 L tank (to the left in Fig. 1), allowing its chemistry (e.g. pH level controlled using ammonia and dissolved oxygen controlled by boiling) to be controlled to that representative of water used in thermal power stations. By exposing the

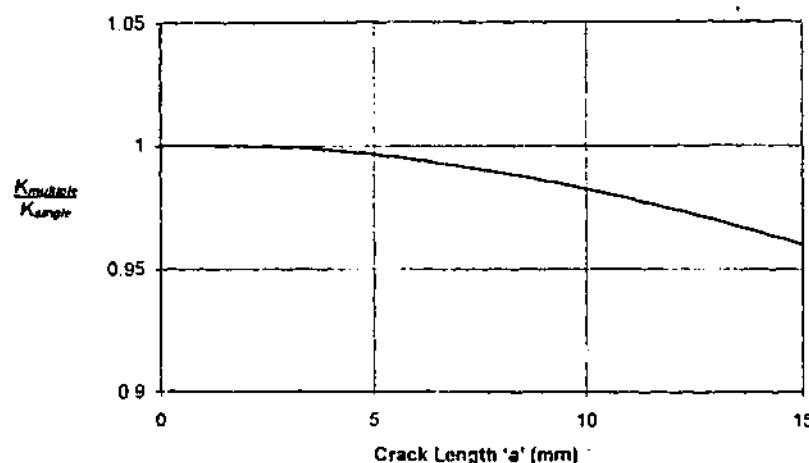


Fig. 4. SIF ratio for multiple cracks separated by 100 mm and a single crack.

specimen directly to the water during cooling (and the steam remaining in the chamber during heating), the actual conditions of a component exposed to the steam cycle are well represented.

### 3.3. Steady state load application

The steady state load frame utilises a 50:1 ratio lever design to apply dead loads of up to 80 kN to the specimen. A pinned–pinned connection system was chosen for attachment of the specimen to prevent the generation of any unwanted constraint stresses during the thermal shock loading (i.e. creating a thermal–mechanical type loading).

### 3.4. Specimen

The material chosen for examination in these experiments was low carbon steel, grade AS 1548-1995. The 300 mm long specimens have a cross-section of  $10 \times 65 \text{ mm}^2$  as shown in Fig. 3. These dimensions were chosen to give a central section suitable for ID cooling similar to that achieved with the large plates used for thermal shock analysis by Vitale and Beghini [18]. To achieve the uniform ID transient temperature field during quenching, masses were attached to both sides of the specimen. Thermocouples were fitted to the masses in direct contact with the specimen allowing the temperatures profiles existing during the quenching to be monitored within  $\pm 1^\circ\text{C}$ . Having the thermocouples not physically attached to the specimen allows for the uninhibited growth of the cracks.

Quenching occurs along one of the narrow faces. An initial analysis showed that the thermal stresses generated by a thermal shock from below the creep range were too low to produce crack initiation within a reasonable number of cycles. For this reason, small starter notches were machined into the narrow face. The length of the specimen allowed the placement of three notches spaced at 100 mm, further increasing the testing effectiveness. Two of the notches were given a notch radius ( $r$ ) of 0.25 mm and the other 0.1 mm. All notch depths are 3.5 mm.

The disadvantage in having more than one crack on a specimen is that the neighbouring cracks may influence each other during growth. To estimate the possible effect of having more than one crack, the stress intensity factor produced at the tip of a single crack had to be compared with that produced at the tip of multiple cracks spaced 100 mm apart. To enable such a comparison, the stress intensity factor solutions reported in Ref. [29] for multiple edge cracked semi-infinite plates subjected to uniform tension were utilised.

The results of the comparison using a crack spacing of 100 mm are shown in Fig. 4. From this plot, it follows that two adjacent cracks could be allowed to grow to a depth of 10 mm before a stress intensity factor error of around 2% is produced by assuming only one crack is present. Assuming that the tests will be discontinued before the cracks reach 10 mm in length, this level of accuracy was determined to be appropriate for this investigation.

## 4. Analysis of results

A major objective of this work is to present results directly applicable to practical calculations for both the numbers of cycles to crack initiation and the crack growth rate. Consequently, it was necessary to derive the stress amplitude, or in accordance with the ASME Boiler and Pressure Vessel Code, Section VIII, Division 2 (1998) [1] the pseudo-stress amplitude at the notch roots. The elastic stress was obtained from stress intensity factor calculations of the initial geometry. Thus,

$$S_a = k_t S_n = \Delta K / \sqrt{\pi r} \quad (1)$$

where  $k_t$  is the theoretical stress concentration factor,  $S_n$  is the nominal stress amplitude,  $\Delta K$  is the stress intensity factor range and  $r$  is the notch radius.

As has been shown in investigations ([30]), Eq. (1) is correct within 5% for notches of radii less than 1 mm, with the error reducing further with smaller radii.

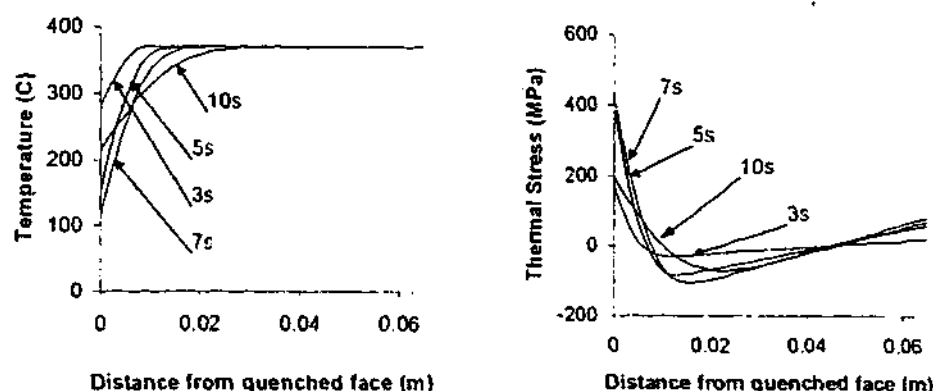


Fig. 5. (a) and (b) Temperature and pseudo-elastic stress profiles during 7 s quench from 365°C.

Consequently, the notches used in this investigation can be considered adequately small for its application.

Using Eq. (1), the theoretical stress concentration factor can be determined with the knowledge of the stress intensity factor and nominal stresses. This value cannot be used directly in a fatigue life analysis but can be converted into the fatigue notch factor by a notch sensitivity analysis, whereby:

$$k_f = 1 + \frac{k_t - 1}{1 + \sqrt{\rho/r}} \quad (2)$$

where  $k_f$  is the fatigue notch factor, and  $\rho$  a material constant.

Eq. (2) is an empirical fit taken from tests in Ref. [31]. The material constant  $\rho$  is known as the Neuber constant and is claimed to be related to grain size. Multiplying the nominal stress by this factor provides the stress amplitude necessary for a fatigue life analysis.

$$S_a = k_f S_n \quad (3)$$

The nominal stress at the notch root  $S_n$  is difficult to determine in the case of thermal shock loading. However, by assuming the reduced cross-section in the notch plane has the same temperature distribution as it has remote from the notch, a pseudo-elastic stress profile can be generated.

The ASME Boiler and Pressure Vessel Code, Section XI (1998) [2] method has been used to calculate the Stress Intensity Factors in this analysis. This method is a simplified weight function approach that requires a third-order polynomial best fit to the pseudo-elastic stress distribution. Then:

$$K_I = (A_0 G_0 + A_1 G_1 + A_2 G_2 + A_3 G_3) \sqrt{\pi \frac{a}{Q}} \quad (4)$$

Here  $K_I$  is the stress intensity factor of the first mode,  $a$  is the crack depth and  $A_n$ ,  $G_n$  and  $Q$  are the cubic stress distribution polynomial coefficients, the free surface correction factors and the flaw shape parameter, respectively, ( $n = 0, 1, 2, 3$ ). The flaw shape parameter contains a plastic zone correction factor that is dependent on the material yield strength. When

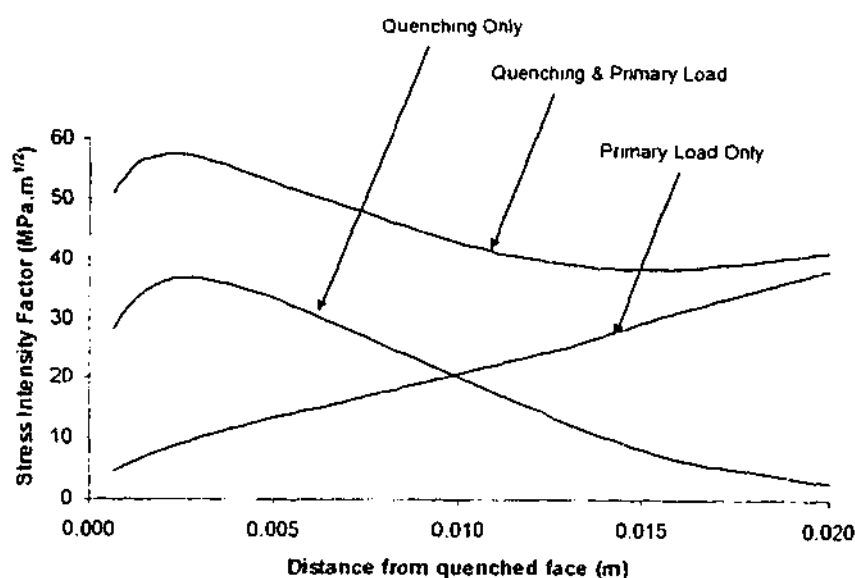


Fig. 6. Maximum stress intensity factor profiles during 7 s quench from 370°C.

Table 1  
Number of cycles to crack initiation and crack lengths after 10,000 cycles

Primary load (MPa)	Notch tip radius (mm)	Test temperature (°C)	Number of cycles to crack initiation (to nearest 100)	Crack length after 10,000 cycles (ignoring notch depth—mm)
90	0.25	365	1500	5.80
90	0.1	330	2900	2.55
90	0.25	290	4000	0.70
0	0.25	365	1600	1.90
0	0.1	330	3000	0.65
0	0.25	290	4500	0.35

yielding occurs,  $Q$  decreases in value and an associated increase in the stress intensity factor is produced.

### 5. Preliminary results

In this section, preliminary results taken from the test rig are presented and discussed briefly. These early tests have concentrated on identifying the effects of primary loads on crack initiation and growth during repeated thermal shock. This was completed by simultaneously testing two specimens placed side by side, one subjected to a 90 MPa (13 ksi) uniform tensile stress and the other left unloaded. The specimens were fitted vertically in the furnace with the upper temperature limited to 370°C to remove any creep effects. Water chemistry was monitored in the storage tank with a dissolved oxygen level of 5–8 ppm and a pH level of 7.

Each thermal cycle consisted of a slow heat to a central specimen temperature of 330°C followed by a 7 s water quench. Cycle time was around 15 min. Due to the fact that the specimens are vertical, there are thermal gradients in the furnace and because of this and the size of the specimen, a uniform temperature could not be achieved along its

whole length. Rather the temperature from top to bottom of the specimen varied linearly from 365°C to 290°C. A typical temperature profile for the top of the specimen is shown on Fig. 5a. This was used to calculate the stress cycle and determine the pseudo-elastic stress amplitude also shown in Fig. 5b. Fig. 6 shows the typical results of the stress intensity factor analysis using this data and Eq. (4). There is a slight difference in  $\Delta K$  for the specimens with and without primary load, this is due to the plastic zone correction. Note that the  $R$  ratio for the specimen with primary load is a function of the crack length.

After each period of 500 thermal cycles, the specimens were removed from the furnace and investigated for cracking at a low magnification (10–60×). A rough estimate of crack initiation lifetime was defined as when a full-face hairline crack was visible at the base of the notch. Extrapolations of the long crack growth data were used to further refine when initiation was to have occurred. Any subsequent crack growth after initiation was measured on each side of the specimen, the through depth taken as the average.

Times to crack initiation are detailed in Table 1. These details are shown graphically in Fig. 7, where number of cycles to initiation has been plotted against the stress

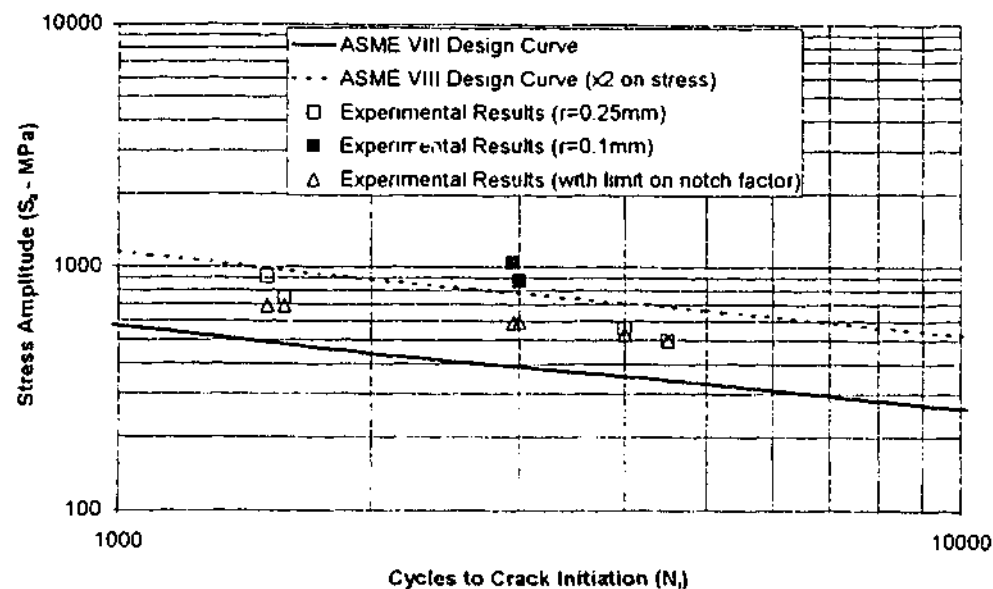


Fig. 7. Crack initiation lifetime.

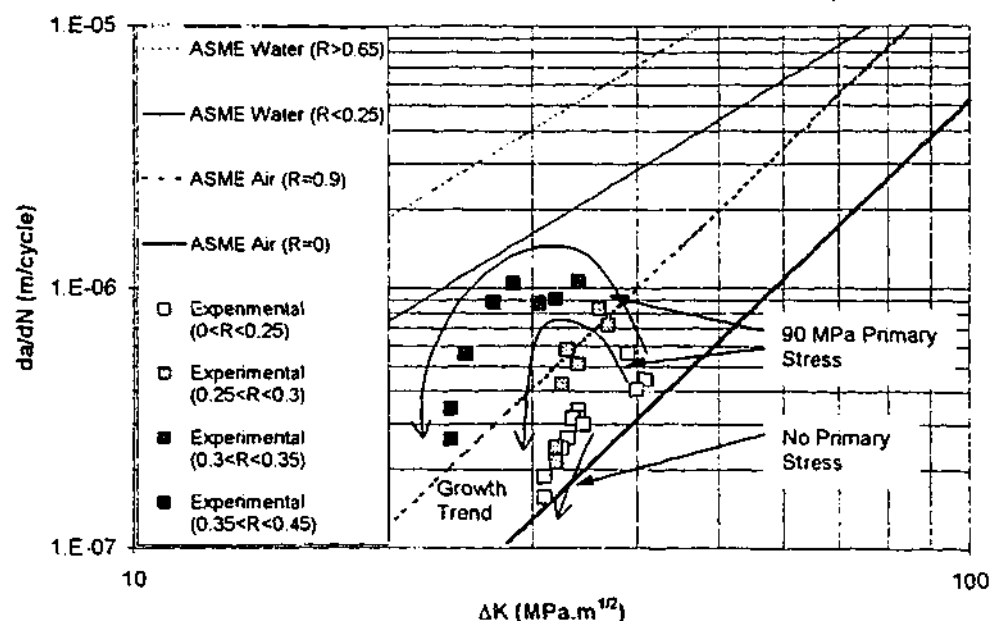


Fig. 8. Crack growth rates as a function of stress intensity factor. Squares correspond to measurements made during testing. The large arrows indicate only trends for individual crack growth—no curve fitting is implied.

amplitude as determined from the method outlined in Section 4. The fatigue design curve for low carbon steel taken from ASME Boiler and Pressure Vessel Code, Section VIII, Division 2 (1998) [1] has been included for comparison. This nominal fatigue design curve has a built in factor of safety of two on stress. A dashed line has been added to the figure to show the effect of removing this conservatism.

Crack growth results are shown in Fig. 8. Stress Intensity Factors determined using Eq. (4) have been plotted against crack growth rate. The stress intensity factor  $R$ -ratio value has been used to categorise the data. Both water and air environment crack growth curves from ASME Boiler and Pressure Vessel Code, Section XI, Appendix A, Figs. A-4300-1 and 2 (1998) [2] have been plotted for comparison.

Testing was discontinued after 10,000 cycles. The final crack depths at each notch are reported on Table 1.

## 6. Discussion

There are two major points of discussion that can be taken from the preliminary experimental results:

Firstly, as shown in Table 1, the application of a primary load displayed little or no effect on crack initiation lifetime. In all of the test cases, the ASME curve gives a conservative estimate of the number of cycles required to initiate fatigue cracks in low carbon steel under thermal shock below creep region temperatures. The ASME curve is even more conservative for the 0.1 mm radius notch than for the 0.25 mm (see Fig. 7). If, however, an upper limit of 5 is taken for  $k_t$ , as suggested in article 5-111 of ASME B&PV, Section VIII, Division 2 (1998) [1], the additional conservatism can be removed. This may be evidence of the so-called "worst case

notch effect" ([30]). The effect of doing so has been included in Fig. 7.

Secondly, the thermal shock fatigue crack propagation rate can be related to the elastic stress intensity factor, and correlated with the isothermal crack growth data of ASME B&PV, Section XI, Appendix A (1998) [2]. The result is conservative (see Fig. 8). However, for the specimen loaded with a primary stress, the crack growth rate moves from the dry environment ASME curves for  $R < 0.25$  towards the wet curves for  $R > 0.25$ . The crack with no primary loading ( $R = 0$ ) simply slows down, at all times only slightly above the  $R = 0$  air curve. This behaviour may indicate an environmental interaction that only takes place when the crack tip is open during cycling. Such behaviour is typical for lower strength steels and may be described as a corrosion fatigue mechanism. In this case high  $R$  ratios can lead to an order of magnitude effect on crack growth rate (Ref. [16]).

From the trend of the results in Figs. 6 and 8, it seems that crack arrest in the unloaded specimen, where  $R = 0$ , will occur. However, since the  $R$ -ratio increases with crack depth, the case of crack arrest for the specimen with the 90 MPa primary load is uncertain and complicated by the environmental interactions. However, even for this situation there is evidence of a downturn of crack growth rate as the crack depth increases.

## 7. Conclusions

1. A successful test method for analysing the initiation and growth of cracks in pressure vessels and piping equipment has been developed. The method simulates the

repeated thermal shock conditions produced in operating thermal power station equipment.

## 2. Initial results show:

- 2.1. The application of a primary stress has little or no effect on crack initiation lifetime during repeated thermal shock below the creep range.
- 2.2. Environmental interaction is highly influential in the growth of thermal shock cracks. Cracks with a low *R*-ratio (no primary stress) show signs of rapid arrest.

## 8. Further work

Tests analysing the effects of primary loading during thermal shock will continue with a new series of specimens and different load ratios. In addition, a second test rig is currently being developed. This rig is fundamentally the same as that described here, however, the specimen is loaded horizontally in the furnace, removing the vertical temperature gradient produced in the vertical specimen due to convection. This rig will be used to assist in the investigation of the effect of more complicated geometries such as bore holes.

## Acknowledgements

This work has been completed with the assistance of an Australian Research Council grant with contributions from HRL Technology Ltd, Optima Energy, Western Power, Pacific Power and the Electric Power Research Institute of USA.

## References

- [1] ASME (American Society of Mechanical Engineers). ASME Boiler and Pressure Vessel Code, Section VIII. New York: ASME, 1998.
- [2] ASME (American Society of Mechanical Engineers). ASME Boiler and Pressure Vessel Code, Section XI, Division 2. New York: ASME, 1998.
- [3] Manson SS. Behaviour of materials under conditions of thermal stress. NACA TN-2933, 1954.
- [4] Coffin L, Schenectady N, Wesley R. Apparatus for study of effects of cyclic thermal stresses on ductile metals. Transactions ASME 1954;76:923–30.
- [5] Udaguchi T, Wada T. Thermal effect on low cycle fatigue strength of steels. Thermal stresses and thermal fatigue. Proceedings of the International Conference held at Berkeley Castle, Gloucestershire, England, vols. 22–26, 1969. p. 109–23.
- [6] Lindholm US, Davidson DL. Low-cycle fatigue with combined thermal and strain cycling. Fatigue at elevated temperatures. ASTM STP 1973;520:473–81.
- [7] Howes MAH. Evaluation of thermal fatigue resistance of metals using the fluidized bed technique. Fatigue at elevated temperatures. ASTM STP 1973;520:242–54.
- [8] White DJ. Some contributions to British work on thermal and high strain fatigue. Thermal stresses and thermal fatigue. Proceedings of the International Conference held at Berkeley Castle, Gloucestershire, England, vols. 22–26, 1969. p. 3–26.
- [9] Rau CA, Gemma AE, Leverant GR. Thermal-mechanical fatigue crack propagation in nickel- and cobalt-base superalloys under various strain-temperature cycles. Fatigue at elevated temperatures. ASTM STP 1973;520:166–78.
- [10] Mowbray DF, Woodford DA, Brandt DE. Thermal fatigue characterization of cast cobalt and nickel-base superalloys. Fatigue at elevated temperatures. ASTM STP 1973;520:416–26.
- [11] Skelton RP. Crack initiation and growth during thermal cycling. In: Skelton RP, editor. Fatigue at high temperature, 1983. p. 1–62.
- [12] Gemma AE, Langer BS, Leverant GR. Thermomechanical fatigue crack propagation in an anisotropic (directionally solidified) nickel-base superalloy. Thermal fatigue of materials and components. ASTM STP 1976;612:199–213.
- [13] Lawson LR. Thermal cycling apparatus for thermomechanical fatigue testing. Review of Scientific Instrumentation 1987;58(10):1942–4.
- [14] Alvarez-Armas I, Armas AF, Petersen C. Thermal fatigue of a 12% chromium martensitic stainless steel. Fatigue and Fracture of Engineering Materials and Structures 1994;17(6):671–81.
- [15] Pistorius PGH, Marais JJ. Thermal fatigue of steel tires on urban railway systems. International Journal of Fatigue 1995;17(7):471–5.
- [16] Marshall P. The influence of environment on fatigue. In: Skelton RP, editor. Fatigue at high temperature. Amsterdam: Elsevier, 1983. p. 259–303.
- [17] Beck CG, Santhanam AT. Effect of microstructure on the thermal fatigue resistance of a cast cobalt-base alloy, Mar-M509. Thermal fatigue of materials and components. ASTM STP 1976;612:123–40.
- [18] Vitale E, Beghini M. Thermal shock fracture experiments on large size plates of A533-B steel. International Journal of Pressure Vessels and Piping 1991;46:289–338.
- [19] Fissolo A, Marini B, Berrada A, Nais G, Wident P. Initiation and growth of cracks under thermal fatigue loading for a 316L type steel. Fatigue under thermal and mechanical loading: Mechanisms, mechanics and modelling. Proceedings held at Petten, The Netherlands, vols. 22–24, 1995. p. 67–77.
- [20] Czuck G, Mattheck C, Munz D, Stamm H. Crack growth under cyclic thermal shock loading. Nuclear Engineering and Design 1985;84:189–99.
- [21] Hour K, Stubbins J. Effects of mean load on creep and fatigue crack growth at elevated temperature. Fracture Mechanics 24th volume. ASTM STP 1994;1207:498–509.
- [22] Oliveira R, Wu XR. Stress intensity factors for axial cracks in hollow cylinders subjected to thermal shock. Engineering Fracture Mechanics 1987;27(2):185–97.
- [23] Grebner H. Thermal shock of a pipe with a partly circumferential surface crack. Engineering Fracture Mechanics 1987;28(3):309–17.
- [24] Sheffler KD, Doble GS. Thermal fatigue behaviour of T-111 and ASTAR 811C in ultrahigh vacuum. Fatigue at elevated temperatures. ASTM STP 1973;520:491–9.
- [25] Ginsztler J. Retarding the crack initiation process during low cycle thermal shock fatigue. Low cycle fatigue and elasto-plastic behaviour of materials. In: Ric K T, editor. Second International Conference on Low Cycle Fatigue and Elasto-Plastic Behaviour of Materials, 1987. p. 643–8.
- [26] Pernot PP, Mall S. A thermal-mechanical fatigue crack-growth testing system. Experimental Techniques 1989;24–28 February.
- [27] Marsh D, Green D, Parker R. Comparison of theoretical estimates and experimental measurements of fatigue crack growth under severe thermal shock conditions—Part 1: Experimental observations. Journal of Pressure Vessel Technology 1986;108:501–6.
- [28] Okazaki M, Koizumi T. Relationship between crack growth of thermal mechanical fatigue and that of isothermal low-cycle fatigue at elevated temperatures. Low Cycle Fatigue and Elasto-Plastic Behaviour of Materials. In: Ric K-T, editor. Second International

- Conference on Low Cycle Fatigue and Elasto-Plastic Behaviour of Materials, 1987. p. 637–642.
- [29] Murakami. Stress intensity factors handbook, vol. 1. Japan: The Society of Materials Science, 1990 (Russian Edition).
- [30] Prater TA, Coffin LF. Notch fatigue crack initiation in high temperature water environments: experiments and life prediction. *Journal of Pressure Vessel Technology* 1987;109:124–34.
- [31] Neuber H. Theory of notch stresses: principals for exact stress calculations. Ann Arbor, MI: Edward Bros, 1946.

## AN APPLICATION OF CONTOUR INDEPENDENT INTEGRALS FOR CONSTRUCTIONS LOADED BY PRESSURE

Andrei G. Kotousov and Brian B. Kerezsi  
Department of Mechanical Engineering  
Monash University, Caulfield Campus  
P.O. Box 197, Caulfield East, Victoria 3145, Australia  
Tel.: +61 3 9903 2846, Fax: +61 3 9903 2766,  
E-mail: [REDACTED]

### ABSTRACT

Contour independent integrals may serve as an efficient tool in finding accurate solutions in fracture mechanics problems. A new form of contour independent integral is derived based on the original Sanders' work. This form is very suitable for finding analytical solutions for bodies containing singularities and loaded by a constant pressure. Two important examples of this type in pressure vessel design practice are the welded plug attachment and single filled lap weld, which have been adopted by the industry and various standards like the ASME Boiler and Pressure Vessel Code or BSI. Both contain significant built-in annular crack-like formations. These constructions are analyzed using the presented contour independent integrals, as is a pressurized cylinder containing a semi-infinite axial crack.

### NOMENCLATURE

$a_c$	constructed crack length
$C$	simple closed curve, contour
$dc$	element of curve $C$
$ds$	surface element
$ds_x$	projection of the surface element $ds$ on the plane perpendicular to $x$ -axis
$D$	flexural rigidity
$E$	Young's modulus
$f$	allowable design stress
$h$	plug thickness (welded plug construction)
$G$	specific surface energy, fracture toughness
$K_I$	stress intensity factor (first mode)
$K_{II}$	stress intensity factor (second mode)
$K_{eff}$	effective stress intensity factor
$K_{mat}$	material fracture toughness

$n_j$	components of the normal unit vector in the $j$ direction
$p_i$	boundary tractions
$P$	internal pressure
$r$	cylinder radius
$r_1$	tube inner radius
$r_2$	tube outer radius
$r_3$	outer tube outer radius (single lap weld construction)
$t$	tube/cylinder thickness
$S_n$	surface number $n$
$u_i$	displacement component in the $i$ direction
$W$	elastic energy density
$\delta$	virtual crack extension
$\sigma_\theta$	hoop stress
$\nu$	Poisson's ratio
$\eta$	welded joint efficiency
$v$	hoop displacement
$w$	radial displacement

### INTRODUCTION

Today there are thousands of literature references on contour independent integrals in applied mechanics. The basic property of these integrals is that their value is equal to zero for any contour capturing no singularities. Other names widely used everywhere for integrals possessing this property are path independent integrals and invariant integrals. In theory of elasticity, Eshelby was the first to introduce a contour independent integral while calculating the force acting on a singularity (Eshelby [1]). Soon after, Sanders gave a new mathematical formulation of the criterion of crack extension



according to the Griffith-Irwin theory in terms of a contour independent integral (Sanders [2]). Rice offered the  $J$ -integral as a characteristic of elasto-plastic fracture (Rice [3]).

Cherepanov noted another important characteristic of contour independent integrals. He showed that the invariant integrals are effective in finding accurate solutions of some boundary problems with singular points (Cherepanov [4]). The method, based on the contour independent integrals, is usually more simple than traditional analytical approaches however its application is limited to problems having an infinite geometry and particular boundary conditions (Cherepanov and Bykovtsev [5]).

In this paper a new form of the contour independent integrals is derived. Based on this form a new type of boundary problems with singularities can be considered, in particular, some cylindrical structures containing cracks and loaded by a constant pressure. This paper also shows the application of the new type of integrals firstly to two particular types of pressure vessel constructions containing built-in annular cracks and secondly to a cylinder with a semi-infinite axial crack.

#### COUNTOUR INDEPENDENT INTEGRALS

Suppose we have a plate with arbitrary boundaries on which we prescribe arbitrary boundary conditions (possibly time-dependent but all inertia effects are negligible). The plate is supposed to contain a crack. Following to Sanders [1], let  $C$  be some simple closed curve surrounding the crack. Then, the criterion for crack propagation based on the law of conservation of energy can be written as:

$$\frac{1}{2} \oint_C (p, \delta u_i / \delta - u_i, \delta p_i / \delta) dc = G \quad (1)$$

where  $p_i$  are the boundary tractions,  $u_i$  are the displacements,  $G$  is the fracture toughness and  $\delta$  is the virtual crack extension.

At fixed crack length

$$W = \frac{1}{2} A \quad (2)$$

where  $W$  is the elastic energy and  $A$  is the work of external forces.

Consequently

$$\frac{\delta W}{\delta} = \frac{\delta}{\delta} \frac{1}{2} \oint_C p_i u_i dc \quad (3)$$

or

$$\frac{\delta W}{\delta} = \frac{1}{2} \oint_C (p_i, \delta u_i / \delta + u_i, \delta p_i / \delta) dc \quad (4)$$

Adding (4) to (1) we can write the following equation

$$\oint_C p_i, \delta u_i / \delta dc - \frac{\delta W}{\delta} = G \quad (5)$$

The left side of equation (5) represents the well-known  $J$ -integral if one notices that  $\frac{\delta}{\delta} = -\frac{\partial}{\partial x_1}$ , where  $x_1$  is the direction of the crack propagation, and introduces  $W'$  under the integral sign using the Gauss theorem (5) becomes

$$\oint_C (W n_1 - p_i, \delta u_i / \delta) dc = G \quad (6)$$

Subtracting (4) from (1) one obtains another form of contour independent integral as

$$-\oint_C u_i, \delta p_i / \delta dc + \frac{\delta W}{\delta} = G \quad (7)$$

or

$$-\oint_C (u_i, \delta p_i / \delta + W n_1) dc = G \quad (8)$$

It was also assumed when deriving (6) and (8) that the edges of the crack are free from stress. If this assumption does not apply, then the equality is valid only when contour  $C$  also includes the crack faces. When the crack is straight and a constant pressure acts on the crack edges integral (8) produces zero value on the crack edges due to  $n_1 = 0$  and  $\delta p_i / \delta = 0$ . Thus the contour independent integral (8) is still valid for the original contour  $C$ . This makes it very valuable in application to constructions loaded by constant pressure. Below we consider two important examples.

#### APPLICATION TO PRESSURE VESSEL CONSTRUCTIONS WITH BUILT-IN ANNULAR CRACKS

In the construction of pressure vessels there are often situations where features which are essentially sharp cracks are built into the vessel. Particular cases of this are the welded plug attachment and the single circumferential lap welded geometry. The former is one of the permissible features of the group defined in the ASME Boiler and Pressure Vessel Code, Section VIII, Division 1 [6] as unstayed flat heads and covers, and is shown in Figure UG-34 (h) and with the weld detail on UW-13.2 (d). The latter is one of the acceptable welded joints outlined in Table UW-2 (2) and (6)(b) of the same code and is described in Figures UW-13.1 (a) and (k). The single circumferential lap-welded geometry is often referred to as a joggle joint and is also used for attaching a domed head. The geometries for these configurations are shown in Fig. 1a and 1b.

Assuming that the components are fabricated from one material (or of materials having the same coefficient of thermal expansion, Young's Modulus and Poisson's ratio), the annular crack-like formation that is created during construction will, in service, be opened by both pressure and thermal loads. Consequently, what is in effect a built-in flaw requires investigation for possible crack propagation and fracture.

Firstly, to analyze the single fillet lap weld, consider the infinite cylinder with semi-infinite annular crack as shown in Figure 2a. Let  $r_1$

be the inner radius of the cylinder,  $r_2$  the radius of the crack and  $r_3$  the outside radius of the cylinder, the surfaces of the crack and the inner surface of the cylinder are loaded by pressure  $P$ .

A circular segment of the cylinder is shown in Fig. 3.  $S_1$  and  $S_4$  are the axial planes,  $S_2$  and  $S_3$  are the inner and outer radial planes, while  $S_2$  and  $S_3$  complete the segment. The axis-symmetric modification of the  $J$ -integral for this segment may be written as:

$$G = -\oint_S u_i \partial p_i / \partial x_i ds + W ds, \quad (9)$$

Where  $ds$  is an element of the surface  $S$ , and  $ds_x$  is the projection of the surface element  $ds$  on to the plane perpendicular to  $x$ -axis.

Looking at (9) and fig. 3, it follows that only surfaces  $S_1$  and  $S_4$  produce non-zero values for the contour independent integral. This is due to zero values of either  $\partial p_i / \partial x_i$  on  $S_2$  or corresponding components of  $u_i$  for the remaining faces. If  $S_1$  and  $S_4$  are placed rather far from the tip of the crack, calculation of these values is simplified. The value of the integral on  $S_1$  and  $S_4$  is calculated by substitution into (1) of the stress distribution solutions for a solid under hydrostatic pressure and for a cylinder under internal pressure (Timoshenko and Goodier [7]). The result is given below:

$$G = \frac{P^2}{2Er_2} \left\{ \frac{r_3^4}{r_1^2 - r_2^2} \left[ \frac{3}{2}(1-2\nu) + (1+\nu) \frac{r_3^2}{r_2^2} \right] - \frac{r_1^4}{r_3^2 - r_2^2} \left[ \frac{3}{2}(1-2\nu) + (1+\nu) \frac{r_1^2}{r_2^2} \right] + \frac{3}{2}(1-2\nu)(r_3^2 - r_1^2) \right\} \quad (10)$$

For the effective stress intensity factor  $K_{eff}$ :

$$K_{eff}^2 = K_I^2 + K_{II}^2 = \frac{EG}{1-\nu^2} \quad (11)$$

Assuming  $t_1, t_2 \ll r$  equation (10) may be simplified:

$$K_{eff} \approx \frac{P \cdot r}{2\sqrt{(1-\nu^2)}} \sqrt{\left( \frac{t_1}{t_2} \cdot \frac{1}{(t_2 + t_1)} \right) \left( \frac{5}{2} - 2\nu \right)} \quad (12a)$$

Simplifying with  $t_1 = t_2 = t$  and  $\nu = 0.3$ :

$$K_{eff} = 0.51P \frac{r}{\sqrt{t}} = 0.51\sigma_s \sqrt{t} \quad (12b)$$

Employing the same theory for the welded plug geometry using the designations given in Fig. 1b and the associated semi-infinite model in Fig. 2b:

$$G = \frac{1}{2E} \frac{P^2 r_1^3}{r_1^2 - r_1^2} \left[ \frac{3}{2}(1-2\nu) + (1+\nu) \frac{r_2^2}{r_1^2} \right] + \frac{3}{4} r_1 \frac{P^2}{E} (1-2\nu) \quad (13a)$$

Assuming that  $t \ll r_1$  and substituting  $\nu = 0.3$  it follows:

$$K_{eff} \approx 0.72P \frac{r_1}{\sqrt{t}} = 0.72\sigma_s \sqrt{t} \quad (13b)$$

#### APPLICATION TO A SEMI-INFINITE AXIAL CRACK IN A PRESSURIZED CYLINDER

Let us consider a thin cylinder shell of radii  $r$  and constant thickness  $t$ , which is subjected to a uniform internal pressure  $P$  and contains a through-the-thickness semi-infinite crack. In this paper, we shall limit our considerations to elastic, isotropic and homogeneous cylinders that are subjected to small deformations.

Let us write the contour independent integral (9) for a circular segment of the cylinder as shown in Fig. 4. The integral is equal to zero on radial surfaces due to the constant pressure and  $n_i = 0$ . Thus the result can be calculated as the difference of corresponding values on the axial surfaces. When the radial surfaces are far from the crack tip analytical solutions can be used to calculate this difference.

So, for the uncracked surface we have

$$G(S_1) = \pi \frac{P^2}{E} \frac{r^3}{t^2} \quad (14)$$

To calculate the stress distribution in cracked section we can use Timoshenko's equations (Timoshenko and Woinowsky-Krieger [8]) for a thin cylindrical shell. The deformation here consists principally of bending. In such cases, the magnitude of deflection can be usually obtained with sufficient accuracy by neglecting entirely the strain in the middle surface of the cylinder. Omitting the above-mentioned terms, the following simplified system of equation can be written as a system of ordinary differential equations (Timoshenko and Woinowsky-Krieger [8]):

$$\begin{aligned} \frac{\partial^2 v}{\partial \varphi^2} - \frac{\partial w}{\partial \varphi} &= 0, \\ \frac{1}{r^4} \frac{\partial^4 w}{\partial \varphi^4} &= \frac{P}{D} \end{aligned} \quad (15)$$

where  $v$  and  $w$  are the hoop and radial displacements, the axial displacement is equal to zero and  $D = Et^3/12(1-\nu^2)$  is the flexural rigidity of the cylinder.

The boundary conditions are:

$$\frac{\partial^2 w}{\partial \varphi^2} = \frac{\partial^3 w}{\partial \varphi^3} = 0 \quad \text{at } \varphi = 0 \text{ and } 2\pi \quad (16)$$

which correspond to zero normal moment and zero equivalent vertical shear on the crack surfaces.

A solution of this problem  $w = w(\varphi)$  can be found as a forth order polynomial function with constant coefficients and the integral becomes:

$$G(S_2) = \frac{D}{2r^3} \int \left( \frac{\partial w}{\partial \varphi} + \frac{\partial^2 w}{\partial \varphi^2} \right)^2 d\varphi = \frac{\pi^3 P^2 r^3}{6 D t} \quad (17)$$

For thin cylinders  $G(S_1)$  is negligibly small in comparison with  $G(S_2)$  and assuming that bending and bulging effects are negligible for the stress intensity factor in the case of the plane stress one gets

$$K_I = \pi \sqrt{2(1-\nu^2)} P \frac{r^2}{t^2} \sqrt{\pi} \quad (18)$$

The solution obtained gives an upper limit for the stress intensity factor of the through thickness axial crack in a pressurized cylinder with respect to the crack length. It also produces a limit for the application of the Folias' solution (Folias [9]) and can be used in the analysis of large longitudinal ruptures of pipelines.

## CONCLUSIONS

Generally speaking the solutions obtained are applicable for only infinite geometries. However as it was shown by using FE methods (Price at all [10]) they are still applicable with a sufficient accuracy in the case of real constructions.

Equations (12), (13) and (18) show that an important feature of the considered constructions is the presence of a significant scale effect. This means that pressure constructions at the same stress level with a larger radius will be more apt to undergo crack growth and fracture. While some scale effects are considered in regulatory documents and pressure vessel standards, the fundamental design equations for this geometry take no account of this factor.

## ACKNOWLEDGEMENTS

The work was done with the assistance of an Australian Research Council grant with contributions from HRL Technology Ltd, Optima Energy, Western Power, Pacific Power and Electric Power Research Institute of USA

## REFERENCES

1. J.D. Eshelby, "The force on an elastic singularity", *Phil. Trans. Roy. Soc., London*, Pergamon Press, 2563 - 2570, 1951.
2. J.L. Sanders, "On the Griffith-Irwin fracture theory, *ASME J. of Applied Mech.*, Vol. 27, No 2, 352-353, 1961.
3. J.R. Rice, "The elastic-plastic mechanics of crack extension", *Int. J. of Fracture Mech.*, Vol. 4, 41 - 47, 1968.
4. G.P. Cherepanov, "Mechanics of Brittle Fracture", New York: McGraw Hill, 1979.
5. G.P. Cherepanov and A.S. Bykovtsev, "Some geophysical problems of fracture mechanics", *Advances in Fracture Research*, Proc. 6<sup>th</sup> Int. Conf. Fract. Oxford, 1984.
6. ASME, "Boiler and pressure vessel code, Division VIII, Section 1", ASME, New York, 1998.
7. S.P. Timoshenko and J.N. Goodier, "Theory of elasticity", McGraw-Hill Book Company, Second Edition, New York, 1970.
8. S. Timoshenko, and S. Woinowsky-Krieger, "Theory of plates and Shells", McGraw-Hill Book Company, Second Edition, New York, 1959.
9. Folias, E.S., "An axial crack in a pressurized cylindrical shell", *Int. J. of Fracture Mech.*, Vol. 1, 20-46, 1965.
10. J.W.H. Price, A.G. Kotousov and B. Kerezsi, "Annular Built-in Cracks in Pressure Vessels: Design and Fracture Mechanics Issues", Proc. of 5<sup>th</sup> Int. Conference & Exhibition "Operating Pressure Equipment", Melbourne, Australia, 19-21 April 1999.

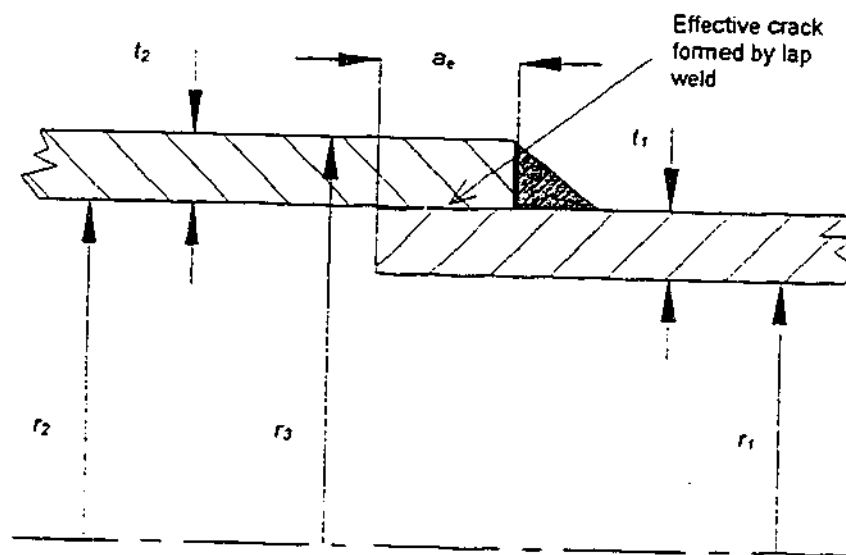


Fig. 1a Single Fillet Lap Weld

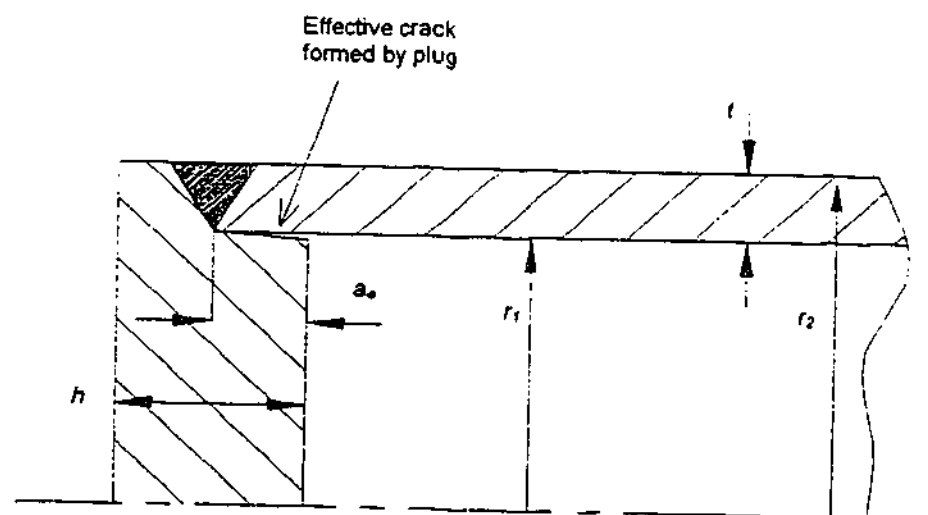


Fig. 1b Welded Plug Arrangement

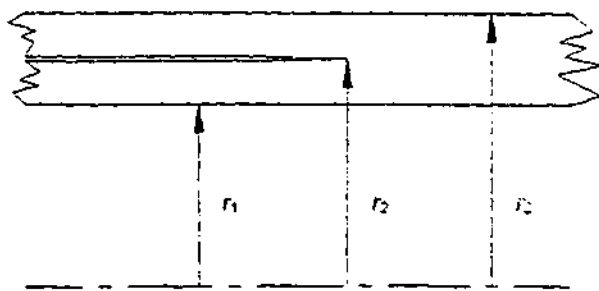


Fig.2a Infinite Geometry of the Single Lap Weld Attachment Suitable for Analytical Considerations

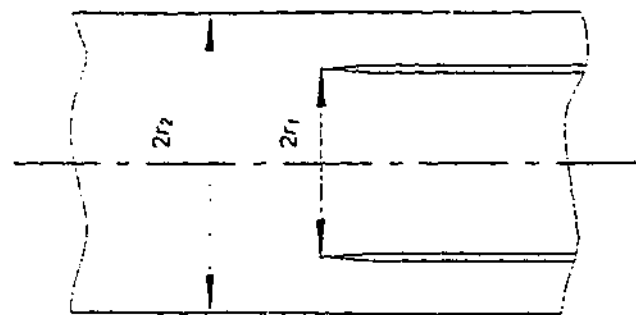


Fig.2b Infinite Geometry of the Welded Plug Attachment Suitable for Analytical Considerations

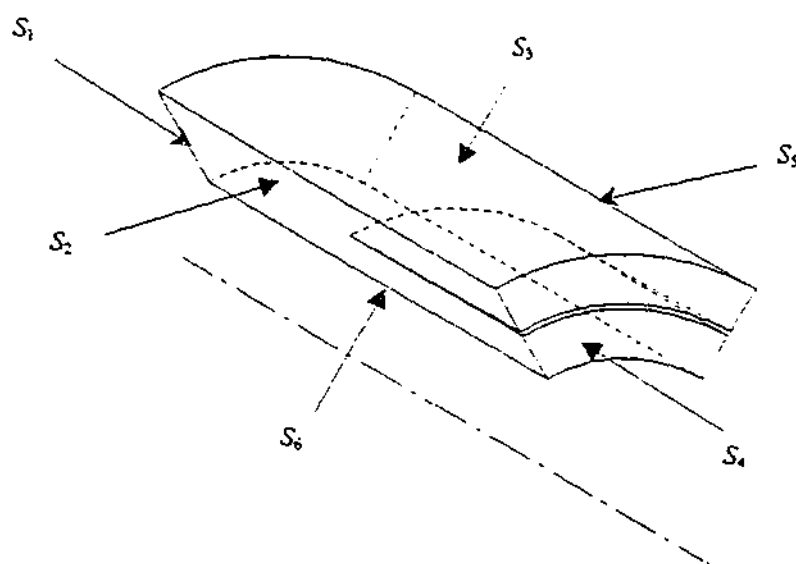


Fig.3 Circular Segment for Analytical Consideration of Single Fillet Lap Weld

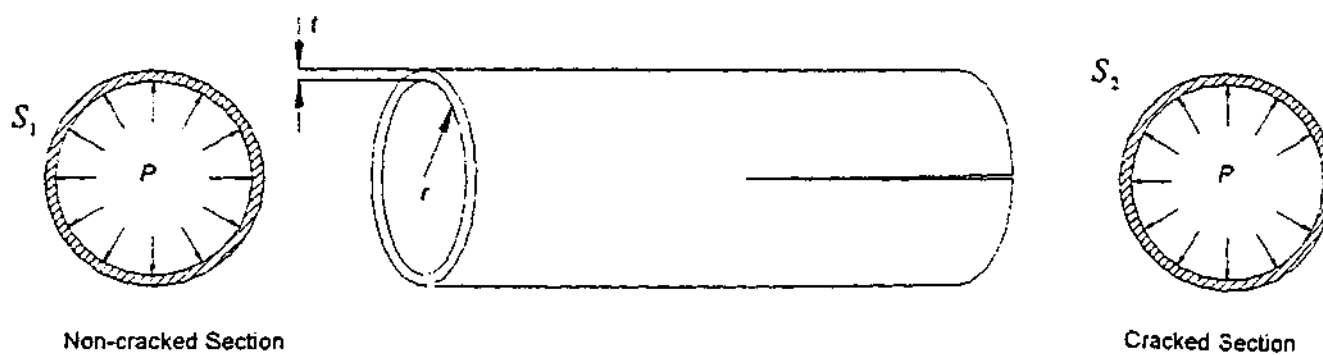


Fig.4 Pressurized Cylinder with Semi-infinite Axial Crack

## INVESTIGATION OF CRACK INITIATION AND GROWTH DUE TO REPEATED THERMAL SHOCK

Brian B. Kerezi, Andrei G. Kotousov and John W.H. Price  
Department of Mechanical Engineering,  
Monash University, Caulfield Campus  
P.O. Box 197, Caulfield East, Victoria 3145, Australia  
Phone: +61 3 9903 2288, Fax: +61 3 9903 2766  
E-mail: brian.kerezi@eng.monash.edu.au

### ABSTRACT

This paper describes an experimental test rig constructed for the investigation of the initiation and growth of cracks in steel specimens subjected to repeated thermal shock loading at temperatures below the creep range. Such loading is common in thermal power station equipment where process variations and transients can lead to thermal fatigue cracking of pressure equipment such as headers and tubes. Simulating operational conditions, the rig achieves large-scale thermal shocks by the repeated water quenching of heated flat plate specimens. The rig has significant advantages over known experimental techniques for the analysis of repeated thermal shock, including the ability for the simultaneous testing of multiple specimens under different primary end loads. The effect of stress raisers such as welds and notches on crack initiation and subsequent growth can also be investigated. Some preliminary results are analyzed and compared to empirical prediction methods from current fracture mechanics codes. An estimation of the level of conservatism of these codes is made.

### NOMENCLATURE

$a$	crack length
$A_n$	cubic stress distribution polynomial coefficients
$\Delta K$	stress intensity factor range
$K_{ISCC}$	threshold stress intensity factor for static stress corrosion cracking
$K_{min}$	minimum cyclic stress intensity factor
$k_f$	fatigue notch factor
$k_t$	theoretical stress concentration factor
$G_n$	free surface correction factors
$Q$	flaw shape parameter
$r$	notch radius
$R$	stress intensity factor ratio

$S_o$	notch-tip cyclic pseudo-stress amplitude
$S_n$	nominal cyclic pseudo-stress amplitude
$\sqrt{Y}$	Neuber constant

### INTRODUCTION

Thermal fluctuations are a recognized damage mechanism in thermal power station pressure vessels and piping equipment. Of particular interest is the crack initiation and growth due to thermal variations and transients in components operating below the creep range such as boiler tubes and economizer inlet header tubes (Dooley, [1]). Major portions of the fluctuations are connected with the process operation. Examples of this are start-up and shutdown procedures, temperature control through cold water injection, water jet cleaning and so on.

Prediction of crack initiation and growth in the case under investigation is a very complicated process due to the large number of factors associated with the working conditions for thermal power plant. A successful analysis would include allowances for component geometry, non-linear plastic effects, environmental factors, and temperature dependence of materials. The majority of crack initiation data available for the low carbon steel components under investigation has been obtained through isothermal uniaxial stress and strain cycling tests. The suitability of the application of this data needs to be addressed. In addition, it is also important to determine whether the subsequent crack growth can be described by a fracture mechanics approach in the same manner as the isothermal case.

This paper introduces a largely experimental investigation of crack initiation and growth in large flat-plate specimens exposed to repeated one-dimensional thermal shocks. A unique test rig specifically developed for this investigation is described and some preliminary results presented. Particular attention is paid to the effect

of stress raisers such as notches and welds on the formation and subsequent growth of cracks. The effect of having a primary steady state end load superimposed on the thermal shock is also analyzed. Comparison of actual crack initiation and growth data with empirical prediction methods from current design codes is made.

#### TEST RIG CONSTRUCTION

While designing the experimental program, the following requirements were identified as prerequisites:

- Range of temperatures, water chemistry and primary loads should correspond to typical working conditions for thermal power plant
- A relatively simple specimen geometry reflecting the actual size and characteristics of a pressure component is necessary to monitor crack initiation and growth during repeated thermal shock
- The ability to use a single specimen to obtain both crack initiation and crack growth testing data

The test cycle was chosen to be one of slow heating by convection followed by direct cooling by cold water quenching. A picture of the test rig is shown in Fig. 1 with a schematic shown as Fig. 2. In general terms, the system consists of the convection furnace, the static-loading structure and the quenching system.

#### Furnace

The furnace is rectangular in shape, with slotted recesses in the top and bottom, allowing the application of the primary load to the specimen. Heating is performed by two 1kW-resistance type heating elements located on either side of the central heating area. This central area contains a thin walled stainless steel "quenching chamber" which houses the specimen and prevents the heating elements from being damaged by the quenching water. This chamber also has a large vent that protrudes from the bottom of the furnace, allowing the escape of steam and water after each quenching cycle.

Although specimen heating by convection is not the most efficient method for high temperature testing, it provides distinct advantages over other techniques. Resistance heating (Coffin et al, [2]; Sheffler and Doble, [3]) provides for much smaller cycle times, however this method produces a localized heating effect at the tip of any cracks (Pernot and Mall, [4]). To avoid this in their analysis, Pernot and Mall used radiant heating by process of quartz lamps. As with induction heating (Marsh et al, [5]), this type of heating was discounted due to the likely damage that would occur to components during quenching. Contact heaters (Lawson, [6]) were also considered, however this was thought to reduce the flexibility of the system.

#### Primary Load Application

The steady state load frame utilizes a lever design to apply dead loads of up to 80kN to the specimen via 50kg dead weights. A pinned-pinned connection system was chosen for the specimen to prevent the generation of any unwanted external constraint during the thermal shock loading.

#### Quenching Rig

A manifold fitted with six 1/2" full cone spray nozzles is permanently installed in the front wall of the furnace and passes into the quenching chamber. When the temperature of the specimen reaches the set point, the quenching cycle is triggered. Up to 9L/min of water supplied via a 240V centrifugal pump can be applied to the specimen through the spray heads. A PC, running Lab View software controls spray execution and duration. This PC also doubles as a data logger, recording the temperature of the specimen. The water used for quenching is stored in a 500L tank (to the left in Fig. 1) allowing its chemistry to be controlled.

#### Specimen

The material chosen for examination in these experiments was low carbon steel, grade AS 1548-1995 [7]. The 300mm long specimens have a cross-section of 10 x 65mm as shown in Fig. 3. Quenching occurred along one of the narrow faces. An initial analysis showed that the thermal stresses generated by thermal shocks from temperatures below the creep range were too low to produce crack initiation within a reasonable number of cycles. For this reason, small notches of radii ( $r$ ) 0.1mm and 0.25mm were machined into the narrow face. The length of the specimen allowed the placement of several notches, further increasing the testing effectiveness.

To achieve a basically one-dimensional transient temperature field during quenching, steel masses were attached to both sides of the specimen. Thermocouples were fitted to the masses in direct contact with the specimen. This allowed the temperature profiles produced during the quenching to be monitored within  $\pm 1^\circ\text{C}$ . Not having the thermocouples physically attached to the specimen allows for the uninhibited growth of the cracks.

#### ANALYSIS OF TEST RESULTS

A major objective of this work is to present results directly applicable to practical calculations for both the numbers of cycles to crack initiation and the crack growth rate. Consequently it was necessary to derive the stress amplitude, or in accordance with the ASME Boiler and Pressure Vessel Code, Section VIII, Division 2 [8] the pseudo-stress amplitude at the notch roots. The elastic stress was obtained from stress intensity factor calculations of the initial geometry. Thus,

$$S_e = k_t S_n = \Delta K / \sqrt{\pi} \quad (1)$$

where  $k_t$  is the theoretical stress concentration factor,  $S_n$  is the nominal stress amplitude,  $\Delta K$  is the stress intensity factor range and  $r$  is the notch radius.

As has been shown in investigations (Prater and Coffin, [9]), equation (1) is correct within 5% for notches of radii less than 1mm, with the error reducing further with smaller radii. Consequently the notches used in this investigation can be considered adequately small for its application.

Using (1), the theoretical stress concentration factor can be determined with knowledge of the stress intensity factor and nominal

stresses. This value cannot be used directly in a fatigue life analysis but can be converted into the fatigue notch factor by a notch sensitivity analysis, whereby:

$$k_f = 1 + \frac{k_t - 1}{1 + \sqrt{\rho/r}} \quad (2)$$

where  $k_f$  is the fatigue notch factor and  $\rho$  is a material constant.

Equation (2) is an empirical fit taken from tests by Neuber [10]. The material constant  $\sqrt{\rho}$  is known as the Neuber constant and is related to grain size. For the material under consideration it can be taken as 0.25√mm (Juvinal, [11]). Multiplying the nominal stress by this factor provides the stress amplitude necessary for a fatigue life analysis.

$$S_n = k_f S_a \quad (3)$$

The nominal stress at the notch root  $S_n$  is difficult to determine in the case of thermal shock loading. However by assuming the reduced cross section in the notch plane has the same temperature distribution as it has remote from the notch, a pseudo-elastic stress profile can be generated.

The ASME Boiler and Pressure Vessel Code, Section XI [12] method has been used to calculate the Stress Intensity Factors in this analysis. This method is a simplified weight function approach that requires a third order polynomial be fit to the pseudo-elastic stress distribution. Then:

$$K_I = (A_0 G_0 + A_1 G_1 + A_2 G_2 + A_3 G_3) \sqrt{\pi \frac{a}{Q}} \quad (4)$$

Here,  $a$  is the crack depth and  $A_n$ ,  $G_n$  and  $Q$  are the cubic stress distribution polynomial coefficients, the free surface correction factors and the flaw shape parameter respectively. The flaw shape parameter contains a plastic zone correction factor that is dependent on the material yield strength. When yielding occurs,  $Q$  decreases in value and an associated increase in the stress intensity factor is produced.

## RESULTS

The first set of experiments to be completed using the test rig analyzed two of the flat specimens cycled simultaneously. The specimens were subjected to different end loading with one exposed to a 90MPa (13ksi) uniform tensile stress and the other left unloaded. The specimens were fitted vertically in the furnace with the upper temperature limited to 370°C to remove any creep effects. Water chemistry was monitored in the storage tank with a dissolved oxygen level of 5-8ppm and a pH level of 7.

Each thermal cycle consisted of a slow heat to a central specimen temperature of 330°C followed by a 7s water quench. Cycle time was around 15 minutes. Due to the thermal gradient in the furnace and the size of the specimen, a uniform temperature could not be achieved along its whole length. Rather the temperature from top to bottom of the specimen varied linearly from 365°C to 290°C. A typical temperature profile for the top of the specimen is shown on Fig. 4.

This was used to calculate the stress cycle and determine the pseudo-stress amplitude also shown on Fig. 4. Figure 5 shows the typical results of the stress intensity factor analysis using this data and (4). There is a slight difference in  $\Delta K$  for the specimens with and without primary load, this is due to the plastic zone correction. The  $R$ -ratio for the specimen with primary load is a function of the crack length.

After each period of 500 thermal cycles, the specimens were removed from the furnace and investigated for cracking at a low magnification (10 to 60x). Crack initiation was deemed to have occurred when a full-face hairline crack was visible at the base of the notch. Any subsequent crack growth was measured on each side of the specimen, the through depth taken as the average.

Results from the notch fatigue crack initiation are shown on Fig. 6. Time to crack initiation has been plotted against the stress amplitude as determined from the method developed in the previous section. The fatigue design curve for low carbon steel taken from ASME Boiler and Pressure Vessel Code, Section VIII, Division 2 [8] has been included for comparison. This nominal fatigue design curve has a built in factor of safety of two on stress. A dashed line has been added to the figure to show the effect of removing this conservatism.

Crack growth results are shown on Fig. 7. Stress Intensity Factors determined using (4) have been plotted against crack growth rate. The stress intensity factor  $R$ -ratio value has been used to categorise the data. Both water and air environment crack growth curves from ASME Boiler and Pressure Vessel Code, Section XI, Appendix A, figure A-4300-1 & 2 [12] have been plotted for comparison.

## DISCUSSION

There are several points of discussion that can be taken from the preliminary experimental results so far.

1. Primary load application has no effect on crack initiation lifetime. In all of the test cases, the ASME curve gives a conservative estimate of the number of cycles required to initiate fatigue cracks in low carbon steel under thermal shock below creep region temperatures.

2. The ASME curve is even more conservative for the 0.1mm radius notch than for the 0.25mm (see Fig. 6). If however, an upper limit of 5 is taken for  $k_f$  as suggested in article 5-111 of ASME B&PV, Section VII, Division 2 [8], the additional conservatism can be removed. This may be evidence of the so-called "worst case notch effect" (Prater and Coffin, [9]). The effect of doing so has been included on Fig. 6.

3. Thermal shock fatigue crack propagation rate can be related to the elastic stress intensity factor, and correlated with the isothermal water environment crack growth data of ASME B&PV, Section XI, Appendix A [12] with a conservative result. Further analysis shows that the crack growth rate moves from the dry environment ASME curves for  $R < 0.25$  towards the wet curves for  $R > 0.25$ . This indicates an environmental interaction that may only take place when the crack tip is open during cycling. Such behaviour is typical for lower strength steels and is determined by a corrosion fatigue mechanism, which for high  $R$  ratios can lead to an order of magnitude effect on crack growth rate (Marshall, [13]).

4. From the trend of the results in figures 5 and 7, it seems that crack arrest in the unloaded specimen, where  $R=0$ , will occur.



However, with the  $R$ -ratio increasing with crack depth, the case of crack arrest for the specimen with the 90 MPa primary load is uncertain and complicated by environmental interactions.

#### FURTHER WORK

At this stage in the investigations, only "short" crack growth up to a length of 10mm has been observed in the specimens. Further testing will include the observation of larger crack growth to see if environmental and primary load interaction will prevent crack arrest. Testing of other alloys and the effect of welds on crack initiation and growth will also be considered.

#### ACKNOWLEDGEMENTS

This work has been completed with the assistance of an Australian Research Council grant with contributions from HRL Technology Ltd, Optima Energy, Western Power, Pacific Power and the Electric Power Research Institute of USA

#### REFERENCES

1. Dooley, B., "Don't let those boiler tubes fail again: Part 2", *Power Engineering*, 31-39, August 1997.
2. Coffin L., Schenectady N. and Wesley R., "Apparatus for study of effects of cyclic thermal stresses on ductile metals", *Transactions ASME*, Vol. 76, 923-930, 1954.
3. Sheffer K.D. and Doble G.S., "Thermal fatigue behaviour of T-111 and ASTAR 811C in ultrahigh vacuum", *Fatigue at Elevated Temperatures*, ASTM STP 520, American Society for Testing and Materials, 491-499 1973.
4. Pernot P.P. and Mall S., "A thermal-mechanical fatigue crack-growth system", *Experimental Techniques*, 24-28, February 1989.
5. Marsh D., Green D. and Parker R., "Comparison of theoretical estimates and experimental measurements of fatigue crack growth under severe thermal shock conditions - Part 1: Experimental observations", *Journal of Pressure Vessel Technology*, Vol. 108, 501-506, 1986.
6. Lawson L.R., "Thermal cycling apparatus for thermomechanical fatigue testing", *Review of Scientific Instruments*, Vol. 58, No. 10, 1942-1944, 1987.
7. Australian Standards, "Steel plates for pressure equipment", AS 1548-1995, Standards Australia, Homebush, NSW, 1995.
8. ASME (American Society of Mechanical Engineers), "Boiler and pressure vessel code, Section VIII, Division 2", ASME, New York, 1998.
9. Prater, T.A. and Coffin, L.F., "Notch fatigue crack initiation in high temperature water environments: Experiments and life prediction", *Journal of Pressure Vessel Technology*, Vol. 109, 124-134, 1987.
10. Neuber, H., "Theory of notch stresses: Principles for exact stress calculations", Edwards, Ann Arbor, 1946.
11. Juvinall, R.C., "Engineering Considerations of stress, strain and strength", McGraw-Hill, New York, 1967.
12. ASME (American Society of Mechanical Engineers), "Boiler and pressure vessel code, Section XI", ASME, New York, 1998.
13. Marshall P., "The influence of environment on fatigue", in: Skelton, *Fatigue at High Temperatures*, Applied Science Publishers, Elsevier Science Publishing, 1983.

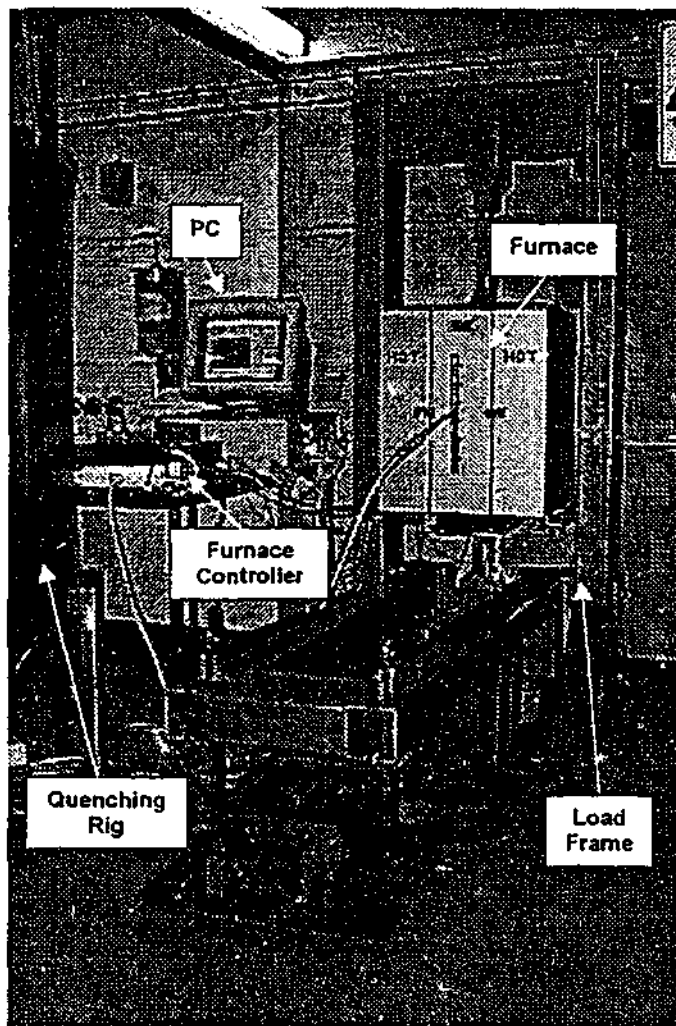


Fig. 1: Testing Rig

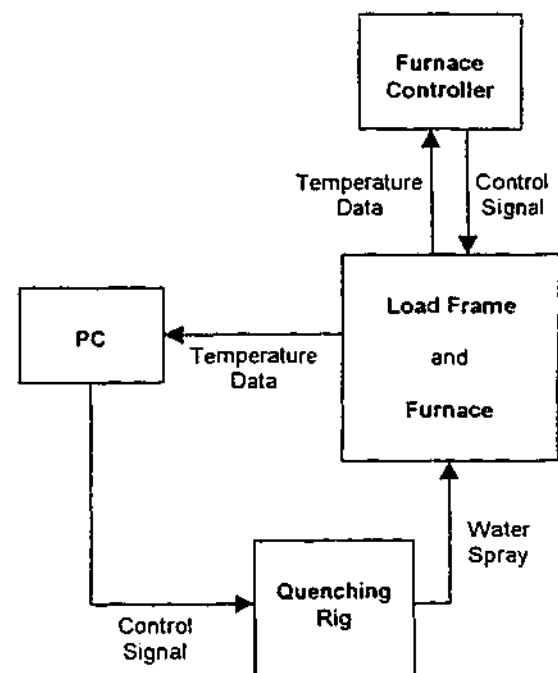


Fig. 2: Schematic of Testing Rig

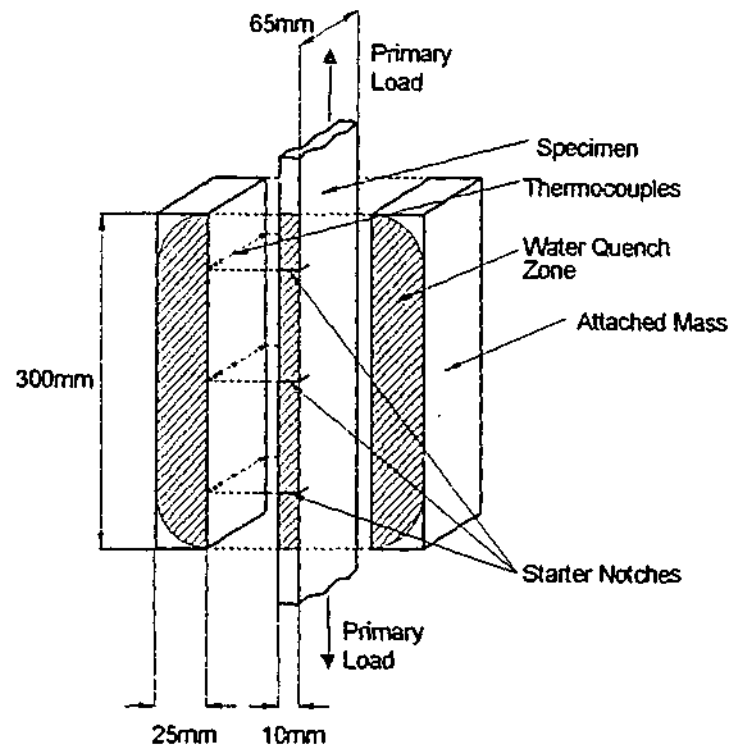


Fig. 3: Specimen Design (Not to scale)

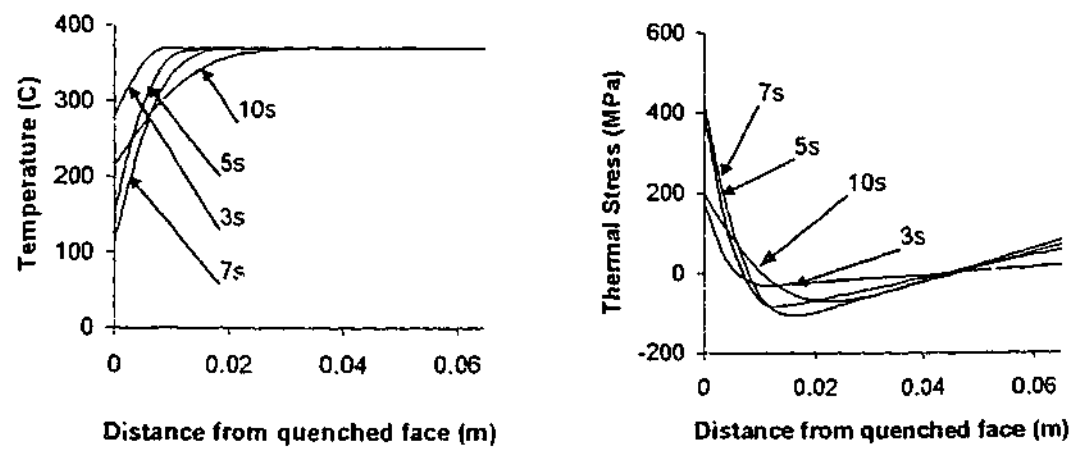


Fig. 4: Temperature and pseudo-stress profiles during 7s quench from 365°C

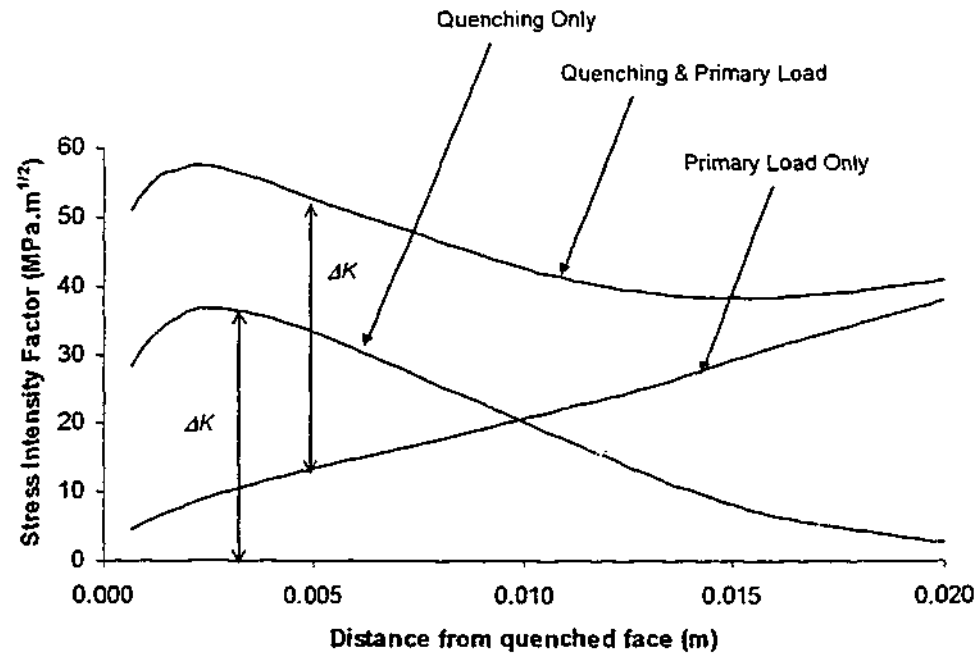


Fig. 5: Maximum stress intensity factor profiles during 7s quench from 370°C

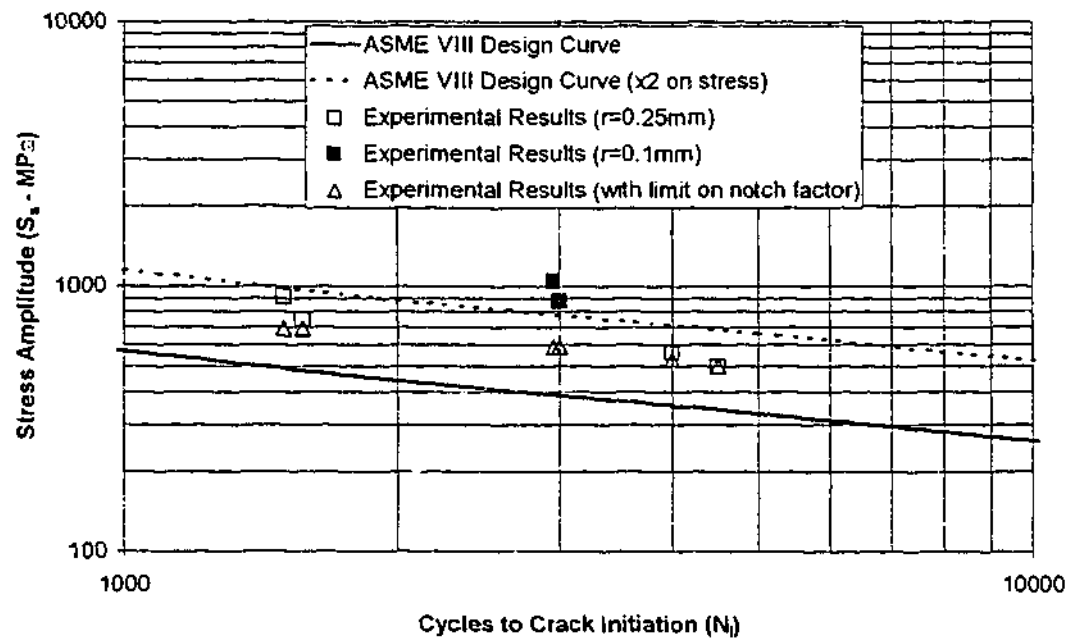


Fig. 6: Crack initiation lifetime

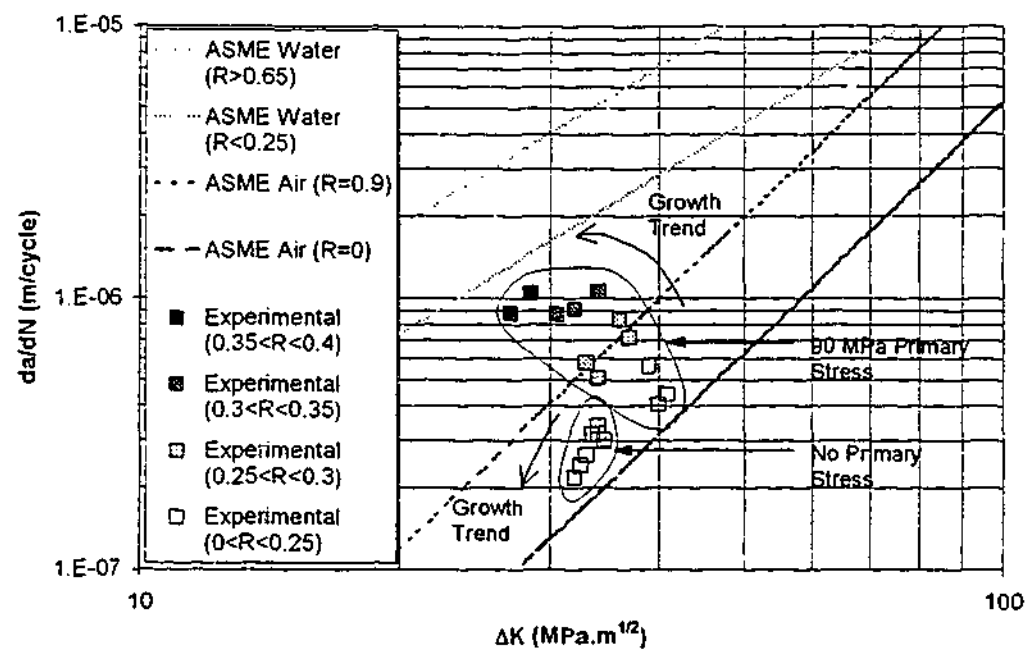


Fig. 7: Crack growth rates as a function of stress intensity factor

## STRESSES IN A CORNER UNDER THERMAL SHOCK

Andrei Kotousov, Brian Kerezsi and John Price

*Monash University, Department of Mechanical Engineering  
PO Box 197, Caulfield East, Victoria 3145, Australia*

**SUMMARY:** Thermal shock loading is common in many industrial situations including the operation of pressure equipment of power stations. Such loading may produce a very high level of thermal stress on the exposed surface that in the presence of a stress concentrator may lead to immediate crack nucleation or even to rapid fracture. One of the common and practically important structural concentrators is a corner or notch. This paper is concentrated on a theoretical analysis of the strength of an infinite corner with apex angle more than  $\pi$  being initially at a uniform temperature and suddenly cooled (heated) along the free surfaces. Based on dimensional considerations and FE analysis elastic solutions for a sharp corner and a corner with a tip radius are obtained. An application of solutions developed to a typical industrial situation connected with an operation of pressure equipment is considered.

**KEYWORDS:** thermal shock loading, strength of corner, dimensional analysis, singular point, FEA, elastic solution

### 1. INTRODUCTION

Thermal shock at corners has attracted more attention since thermal fluctuations were recognized as one of major damage mechanism sources in pressure vessels and piping equipment of power plants such as boiler tubes and economizer inlet header tubes. While some of the fluctuations are caused by uncontrolled factors, the major part of the fluctuations may be connected with normal operation. Fluctuations can occur during start up and shutdown procedures, temperature control (when water is injected into the system to decrease the operating temperature), cleaning, depressurization and so on. Cracks can begin to form at any location where the cyclic thermal stress is significantly high. Damage is initiated at stress concentrators such as corner and notch configurations associated for example with the bore hole or tube attachments. Typically, damage is developed in two stages, first by multiple cracks perpendicular to the principal direction of stress, after which one crack usually becomes dominant and leads to wall penetration. So it seems the damage has crack morphology characteristics similar to corrosion fatigue [1].

The stress field induced by a thermal shock in a corner is rather complex and normally can be investigated only numerically. However, the stress field of a sharp corner with vertex angles more than  $\pi$  may have a singularity component [2]. This, combined with a rather complex type

of loading (such as the transient loading under consideration) can generate significant numerical errors. Moreover there are special requirements on the size of finite elements and the time step to ensure the convergence of numerical procedures (such as FEM). This often makes obtaining a numerical solution for thermal shocks of longer duration very difficult.

Experimental investigations into the thermal shock of corners such as [3] and [4] usually ignore the temperature disturbance caused by the geometry and apply a crack approximation for the stress field. From a theoretical point of view such approximation is valid only if the opening angle is zero. In this paper we try to develop an analytical approach for a corner with vertex angle more than  $\pi$  subjected to the thermal shock loading when the principal dimensions of the corner geometry are much larger than the diffusive length of the thermal shock.

## 2. ANALYTICAL APPROACH

### 2.1 Asymptotic Stress Field

When the principal dimensions of a corner configuration are much bigger than the diffusive length of the thermal shock, an infinite geometry idealization can be applied. Consider an infinite corner with the vertex angle  $2\alpha$  as shown in Fig.1. The corner is initially at a constant temperature  $T_0$  and in a time moment, say  $t = 0$ , is suddenly cooled (heated) to a temperature  $T_1$  along the free surfaces. Within the assumption of temperature independent thermo-mechanical properties of the material and linear elasticity using the Goodier thermal potential [5] the problem can be reduced to a thermo-elasticity problem for infinite body and to a pure elastic problem for the actual geometry.

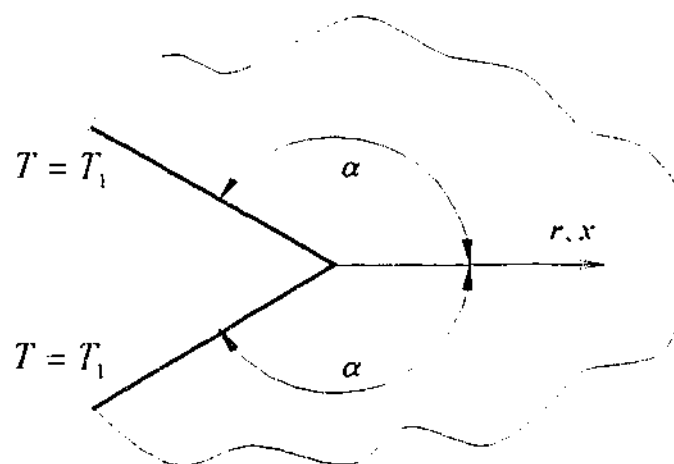


Fig.1 Formulation of the problem

The actual geometry of the problem (corner) produces a singular stress field [2]. This singular stress field in the case of the sharp corner will dominate in the vicinity close to the apex and presumably will be responsible for the initiation of fracture. Using dimensional considerations and asymptotic Williams' solution [2], the singular elastic stress field in the vicinity of the tip of the corner can be written in the polar coordinates  $(r, \varphi)$  with an origin in the apex of the corner as

$$\sigma_r = \mu \alpha_i \Delta T (\sqrt{\kappa t}/r)^{1-\lambda} H_r(\varphi, \lambda) \quad (1)$$

$$\sigma_\varphi = \mu \alpha_i \Delta T (\sqrt{\kappa t}/r)^{1-\lambda} H_\varphi(\varphi, \lambda) \quad (2)$$

$$\tau_{r\varphi} = \mu \alpha_i \Delta T (\sqrt{\kappa t}/r)^{1-\lambda} H_{r\varphi}(\varphi, \lambda) \quad (3)$$

and in the case of the plane strain

$$\sigma_z = \nu(\sigma_r + \sigma_\varphi) \quad (4)$$

$\Delta T = T_1 - T_0$  is the severity of the thermal shock,  $\alpha_i$  is the linear coefficient of the thermal expansion,  $\nu$  is Poisson's ratio,  $\kappa$  is the coefficient of diffusivity,  $\mu$  is the shear modulus and  $\lambda$  is the minimal real eigenvalues obtained from the corresponding characteristic equation. For free edges the dependence of  $\lambda$  from the vertex angle is given on Fig.2.  $H_r(\varphi, \lambda)$ ,  $H_\varphi(\varphi, \lambda)$  and  $H_{r\varphi}(\varphi, \lambda)$  are non-dimensional functions of the angle  $\varphi$  and  $\lambda$ . It is clear that the functions are also dependent of the vertex angle  $2\alpha$  due to the dependence of  $\lambda$  from the vertex angle. In the neighborhood of the apex these functions are defined, for example in [6] except for a constant value.

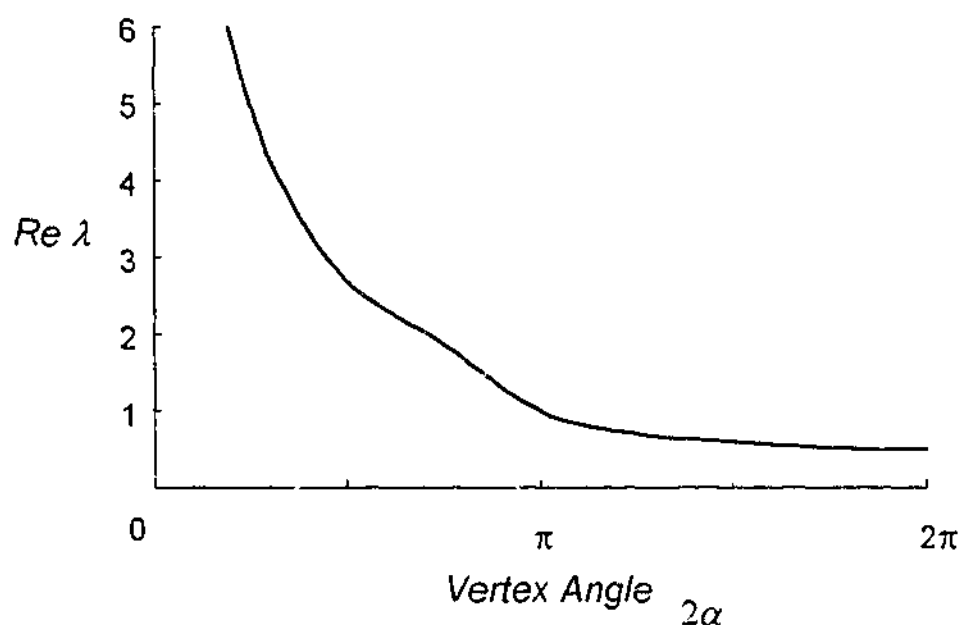


Fig.2 Variation of minimum real part of eigenvalue with vertex angle

Using definition from [6] the expression

$$K_I = \sqrt{2\pi} \lim_{\varphi \rightarrow 0, r \rightarrow 0} r^{1-\lambda} \sigma(t, r, \varphi) = \sqrt{2\pi} \mu \alpha_i \Delta T (\sqrt{\kappa t})^{1-\lambda} H_\varphi(0, \lambda) \quad (5)$$



constitutes the generalized stress intensity factor.

Because functions  $H_r(\varphi, \lambda)$ ,  $H_\varphi(\varphi, \lambda)$  and  $H_{r,\varphi}(\varphi, \lambda)$  are independent of the type and intensity of the loading only two parameters are required to characterize the asymptotic stress field in the case symmetric loading namely:  $\lambda$  and  $K_I$ . While  $\lambda$  is the unique function of the vertex angle (see Fig.2), the generalized stress intensity factor needs to be defined every time at every configuration and loading conditions. Now we consider an approximate analytical approach for the calculation of the generalized stress intensity factor.

## 2.2 Generalised Stress Intensity Factor

The determination of the generalized stress intensity factors is a rather complex problem. First we write down analytical solutions for two limiting cases:  $2\alpha = \pi$  (half-space) and  $2\alpha = 2\pi$  (semi-infinite cut)

At  $2\alpha = \pi$  (half-space)  $\lambda = 1$  (the singularity vanishes) and using the definition of the generalized stress intensity factor one can write

$$K_I(\pi) = -\sqrt{2\pi} 2\mu m \Delta T \quad (6)$$

where  $m = \frac{1+\nu}{1-\nu} \alpha_i$  for plane strain and  $m = (1+\nu) \alpha_i$  for plane stress problems.

At the vertex angle  $2\alpha = 2\pi$  (crack-like geometry), as might be expected [7-9]

$$K_I(2\pi) = 0 \quad (7)$$

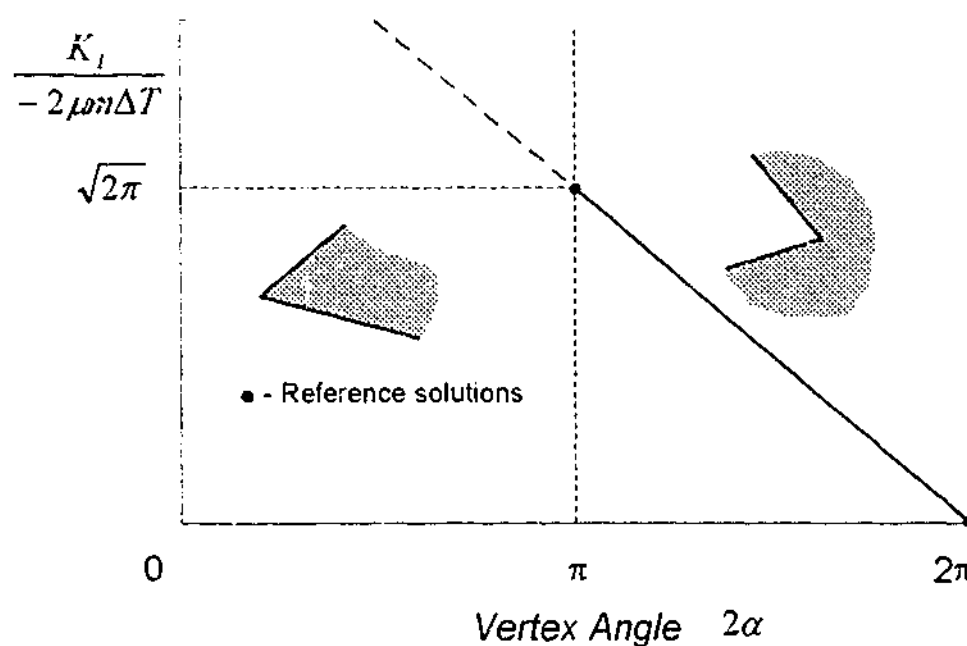


Fig.3 Generalized stress intensity factor as a function of the vertex angle

From physical considerations it follows that the generalized stress intensity factor should be a continuous function of the vertex angle  $2\alpha$ . So, a linear approximation of this function can be directly obtained as a line passing these two reference points. The plot of this function is shown on Fig.3.

Thus, the strength of the corner under thermal shock and mechanical loading will be determined by two values: the strength of singularity  $\lambda$  and the generalized stress intensity factor  $K_I$  in the case of symmetric loading. Consequently to estimate the strength of the corner we need two-parametric criterion connecting  $\lambda$  of the vertex angle with experimentally obtained value for the generalized stress intensity factor  $K_I^{mat}$ . It is clear that in the case when two sharp corners made from the same material have the same vertex angle the corner having smaller generalized stress intensity factor due to thermal and mechanical loading will be less apt to fracture. The generalized stress intensity factor in the case of the thermal shock loading under conditions considered above can be obtained from Fig.3. For mechanical loading various numerical methods are usually applied.

### 2.3 Corner Tip Radius Effect

When a corner tip radius greater than zero is considered the stresses in the corner will be finite and approximate solutions similar to those of linear elastic mechanics have been derived in a number of papers. On the basis of the modification of Williams' solution the maximum stress at the apex of the corner can be linked to the radius  $r$  as follows [10]

$$\sigma_{\max} = \frac{4K_I \rho^{\lambda-1}}{\sqrt{2\pi}[(1+\lambda) + \chi(1-\lambda)]} \quad (8)$$

where

$$\chi = -\frac{\sin(1-\lambda)\alpha}{\sin(1+\lambda)\alpha} \quad \text{and} \quad \rho = \frac{ar}{\alpha - \pi/2}$$

For the limiting case  $\alpha \rightarrow \pi$  the last equation produces the well-known Neuber formulae for the maximum stress in a crack-like notch:

$$\sigma_{\max} = \frac{2K_I}{\sqrt{\pi r}} \quad (9)$$

As it has been shown, these formulas have been obtained for infinite geometry however, their accuracy remains good also for a finite configuration [10]. In addition for finite bodies, a finite size correction factor, involving the notch depth and the length of a ligament ahead of the notch tip, should be introduced to increase the range of validity of the solution. This technique is well explained in [11].

Analysis of (8) shows that at the same severity of the thermal shock  $\Delta T$  and large values of the non-dimensional radii  $r/\sqrt{\kappa\tau} \rightarrow \infty$ , corners with larger vertex angles (consequently having smaller  $\lambda$  - see Fig.2) will have smaller level of stress. The opposite situation takes place for small values of the non-dimensional radius. Here lower stresses will take place for corners having smaller vertex angles.

It is clear that all of the solutions and considerations given above are applicable only when the area controlled by the singular solution is much larger than the notch radius. This is the case when the diffusive length of the thermal shock is much larger than the notch radius. Consequently, the approach developed will produce reasonable estimates for the generalised stress intensity factor for  $\sqrt{\kappa\tau}/r \gg 1$ . For small values of  $\sqrt{\kappa\tau}/r$ , numerical solutions are required.

### 3. NUMERICAL SOLUTION

The finite element simulation package ABAQUS (version 5.8-14) was used to simulate a thermal shock in an infinite corner with a radius. Non-dimensional parameters as shown on the Fig.4 below were used to make the findings applicable for a wide range of similar situations.

The basic dimensions of the finite element model have been chosen to exclude the effect of boundary conditions on the temperature and stress fields. It can be normally achieved when the basic dimensions of the model are much larger than the diffusive length of the thermal shock ( $\sqrt{\kappa\tau}$ , where  $\tau$  is the time length of the thermal shock). On the other hand the finite element size in the vicinity of the tip of the corner with radius has to be small enough to produce valid values for the temperature and stress fields. Moreover, special conditions on the minimum allowed time increment must be imposed to ensure the convergence of the numerical procedure. All of these conditions lead to physical limitations on the maximum feasible non-dimensional time ( $\sqrt{\kappa\tau}/r$ ) which can be achieved during a numerical analysis. In our analysis, the maximum non-dimensional time was around 3, which took half an hour of the processor time of a supercomputer.

The plot of the maximum stresses for the vertex angle  $\alpha = 3/4\pi$  obtained from numerical analysis and asymptotic analytical solution is presented on Fig.4. The theoretical solution is obtained using formulae (8) and the value for the generalized stress intensity factor from a linear interpolation as shown on Fig.3 and explained in section 2.2. As expected, in the beginning the maximum stresses are close to those on the exposed surface (surface thermal shock stress) far from the tip of the corner. With increasing length of the thermal shock the corner geometry contributes additional stresses and resulting in an overall increase. It may be suggested that for larger times of the thermal shock the maximum stress will have an asymptotic behaviour described by the analytical solution.

The analysis presented here assumes also that thermo-mechanical properties are constant during the thermal transient. This is an approximation, which will have to be considered and taken account of in every case.

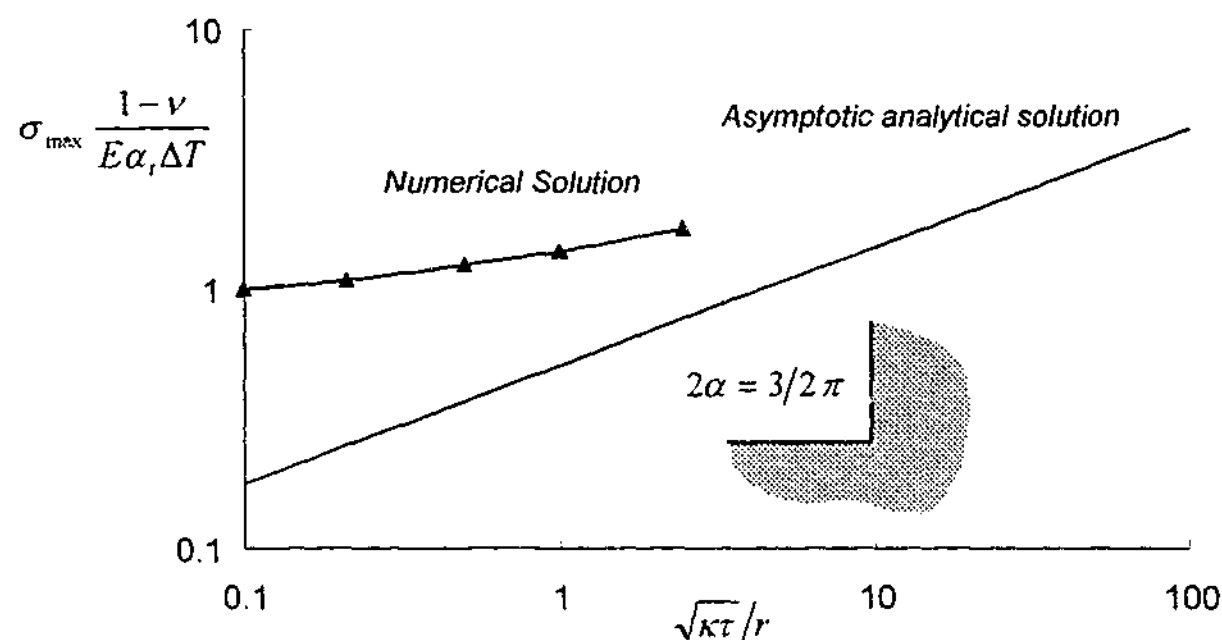


Fig.4 Analytical and numerical solutions for  $2\alpha = 3/2\pi$

#### 4. CASE STUDY

The suitability of the forgoing analysis for use in industry has been strengthened through the completion of a case study. In this study, the time for crack initiation in the internal corner of a feedwater heater water-box of a thermal power station was determined. Basic data on operating and start-up/shut-down conditions for the water-box were provided, allowing estimates of the size ( $\Delta T$ ) and duration ( $\tau$ ) of thermal shocks imposed on the system at around 200°C and 100s respectively. Maximum stress in the corner of the feedwater box was then determined using a corner radius of 30mm, standard material properties for low carbon steel, and the numerical solution data shown in figure 4. This analysis results in a maximum elastic thermal stress of around 1030 MPa. Repeated thermal shock crack initiation lifetime data taken from [12] was then used to estimate the number of cycles to crack initiation.

It was known at this stage through internal inspections that a number of cracks several millimetres deep were present in the corners of the water-box. These observations were consistent with our estimations, which put crack initiation times well before any of the inspections were carried out. It should be noted however that our analysis included a number of simplifying assumptions that were felt to have put a slight conservatism on the result. The exact level of this conservatism cannot be gauged, as accurate data on time to crack initiation in the feedwater box is unknown. Some of these assumptions could be removed in further analyses if more comprehensive operating data becomes available.

#### 5. CONCLUSION

In this paper, the stress field in the vicinity of a corner apex exposed to a thermal shock load has been investigated. Solutions obtained in this paper relate to infinite geometry that can be reasonably applied to finite corner configurations in the case of short duration of the thermal

shock when other than free corner boundaries have no significant effect on the temperature distribution.

The asymptotic stress field is controlled by the strength of singularity  $\lambda$  that is a known function of the vertex angle and by the generalized stress intensity factor. The last is a linear function of mechanical properties and the severity of the thermal shock  $\Delta T$  (5). An important finding is that the duration of the thermal shock and the coefficient of diffusivity increase the generalized stress intensity factor as a power function with an index from 0 for  $2\alpha = \pi$  to  $1/2$  for  $2\alpha = 2\pi$ . Thus, if a sharp corner is considered it is difficult to compare the strength of corners having different vertex angles due to the different strength of singularity produced by these vertex angles.

When a corner tip radius greater than zero is considered the strength of the corner can be estimated using maximum stress at the notch. Applying Neuber hypothesis the local plasticity effect can be added for cyclic loading. The stress amplitude obtained for corners can be directly used in the life assessment by plotting their values on the design curve. In the case of thermo-mechanical loading the corresponding mechanical component for the generalized stress intensity factor must be summed with the thermal component.

**ACKNOWLEDGEMENTS:** The work was done with the assistance of an Australian Research Council grant with contributions from HRL Technology Ltd, Optima Energy, Western Power, Pacific Power and Electric Power Research Institute of USA

## REFERENCES

1. Dooley, B., "Don't let those boiler tubes fail again: Part 2", Power Engineering, August 1997, 31-39.
2. Williams, M.L., "Stress singularities resulting from various boundary conditions in angular corners of plates in extension", Journal of Applied Mechanics, Vol.19, 1952, pp. 526-528.
3. Marsh, D.J., "A thermal shock fatigue study of type 304 and 316 stainless steels", Fatigue of Engineering Materials and Structures, 1981, Vol. 4, 179-195.
4. Vitale, E. and Beghini, M., "Thermal shock fracture experiments on large size plates of A533-B Steel", International Journal of Pressure Vessels and Piping, Vol. 46, 1991, 289-338.
5. Timoshenko, S.P. and Goodier, J.N., "Theory of Elasticity", McGraw-Hill Kogakusha, Ltd, Japan, 1951.
6. Seweryn, A. and Molski, K., "Elastic stress singularities and corresponding generalized stress intensity factors for angular corners under various boundary conditions", Engineering Fracture Mechanics, 1996, Vol. 55, pp. 529-556.
7. Kudriavzev, B.A. and Parton, V.Z., "A quasi-static thermal problem for plane with cut (in Russian)", Problems of Strength, 1970, No 2, pp. 46-51.
8. Kotousov, A. and Price, J.W.H., "Stress Intensity Factor for Semi-Infinite Crack Formed by Moving Thermal Source", International Journal of Fracture: Letters in Fracture and Micromechanics, Vol. 90, 1998, pp. L39 - L42.
9. Parton, V.Z. and Morozov, E.M., "Mechanics of Elasto-Plastic Fracture", Nauka Publisher, 1985.
10. Lazzarin, P. and Tovo, R., "A unified approach to the evaluation of linear elastic stress fields in the neighborhood of cracks and notches", International Journal of Fracture, Vol. 78, 1996, pp.3-19.

## FEATURES OF FATIGUE CRACK GROWTH DUE TO REPEATED THERMAL SHOCK

Brian B Kerezsi, Andrei G Kotousov and John WH Price

*Department of Mechanical Engineering, Monash University  
PO Box 197, Caulfield East, Victoria, 3145, Australia*

**SUMMARY:** Repeated thermal shock loading is common in many industrial situations including the operation of pressure equipment found in thermal power stations. Thermal shock can produce a very high stress level near the exposed surface that eventually may lead to crack nucleation. Further growth of the cracks under repeated thermal shock is a very complex phenomenon due to the transient nature of the highly non-linear thermal stresses and the strong influence of the environment. This paper describes an experimental analysis of the initiation and growth of cracks in low carbon steel specimens exposed to repeated thermal shock. A test-rig that achieves large-scale thermal shocks through the repeated water quenching of heated flat plate specimens is used. The effect of steady state loads on the growth is also analysed. Environmental effects due to the aqueous nature of the testing environment are found to be a major contributor to the crack growth kinetics.

**KEYWORDS:** thermal shock, fatigue, crack growth, test rig, pressure equipment, primary load, environmental assisted cracking.

### INTRODUCTION

The growth and arrest of cracks due to repeated thermal shock loading is of interest in industrial applications where predictions can allow decisions to be made on the necessity of planned inspections and component replacements. Current methods for the analysis of thermal shock crack initiation and growth rely on standards such as the ASME Boiler and Pressure Vessel Code Section VIII, Division 2 and Section XI Appendix A [1,2] that use a conservative model based on isothermal mechanical fatigue tests and simplified stress profiles. In this work, tests that closely simulate the real life conditions of thermal shock encountered in thermal power station pressure components are completed. These tests are intended to develop data that will provide for realistic determination of lifetime to crack initiation and crack growth rates for service components as well as allow for an estimation of the conservatism of the current codes.

Apart from the above-mentioned conservatism in existing codes, the simplifications used in their development ignore the effect of many influential factors. Foremost amongst this are the combined effect of external primary loads and the environment in which the crack is growing. The external loads can be a direct result of the pressure or mechanical loading of the components, the effect of which is to open any cracks, exposing them to the environment. The environment is dependent on the process in which the component is being used, which in

the case of thermal power station equipment is often aqueous in nature (including chemical treatment to control pH and oxygen levels) and will modify conditions at the crack tip.

The effect of environment on crack initiation and growth is a particularly complicated subject. Since 1960, a great deal of research on the topic has been completed, a notable review of this work through to 1989 was completed by Wei and Gangloff [3]. Further progress in the area since that time has been relatively slow. Indeed, current design and analysis codes include only generalised descriptions of how to deal with environmentally assisted cracking. BS 7910 [4] and API 579 [5] provide only brief clauses based upon superposition models with no numeric guidelines. A number of these superposition models for the effect of corrosion on fatigue crack growth have been formulated [6-8]. In essence, these models involve combining the effect of frequency dependent corrosion factors with frequency independent inert environment fatigue relationships.

In the Austen and Walker "process competition" model [7], the corrosion effects are divided into the categories of true corrosion fatigue (TCF) and stress corrosion fatigue (SCF). In TCF, the effect of an aggressive environment on crack growth is to increase the growth rate uniformly for all values of stress intensity factor range. For SCF, the effect of environment is negligible for stress intensity factor ranges below a certain "threshold" value. Above this value, the crack growth rate is increased substantially to a rate that is independent of the stress intensity factor, resulting in a "knee" in the curve. The value of the crack growth rate at this knee is thought to be related to the time dependent process of stress corrosion cracking, making its value dependent on loading frequency. The "threshold" value of the stress intensity factor is related to the maximum stress intensity factor range in the cycle and is hence dependent upon the R-ratio.

Austen and Walker also propose that it is possible for particular material-environment combinations to exhibit SCF "superimposed" on TCF. This results in a crack growth rate that is accelerated for all values of stress intensity factor ranges and also exhibits the stress intensity factor independent "knee".

In this paper, preliminary results from crack growth tests using a unique test-rig arrangement are presented. Comparisons of the actual results with empirical prediction methods from current design codes are made. A prefatory analysis of the primary load and environmental effects on the crack growth related to features of the actual crack surfaces is also made.

### **EXPERIMENTAL TECHNIQUE**

The testing completed in this investigation has been carried out on a thermal fatigue test rig that has been purpose built for the investigation of crack initiation and growth due to repeated thermal shock loading. Consisting of a convection furnace, static loading structure and quenching system it allows for the monitored growth of cracks for a wide variety of component geometries.

The key advantages of our rig over previous studies are:

- The component is heated by convection, which means that there are no unwanted heat effects at the crack tip as may be the case for induction or resistance heating.
- The component is quenched by room temperature pH and O<sub>2</sub> controlled water.
- The specimen size is representative of typical industrial components.
- Large specimen size permits multiple simultaneous experiments.

- An unloaded "control" specimen can be used.
- Approximately one-dimensional conditions exist at any one crack because of the unique specimen design.

A thorough analysis of the development of the test rig and specimen design, including a review of previous trends in the experimental investigations of thermal shock cracking can be found in [9].

The first set of tests has concentrated on identifying the effects of primary loads on crack initiation and growth during repeated thermal shock. This was completed by simultaneously testing two low carbon steel specimens (grade AS 1548-1995 [10]) placed side by side, one subjected to a 90MPa (13ksi) uniform tensile stress and the other left unloaded. The specimens both with 0.25mm and 0.1mm notches machined into the quenched faces were fitted vertically in the furnace. The upper specimen temperature was limited to 370°C to remove any creep effects. Water chemistry was monitored in the storage tank with a dissolved oxygen level of 5-8ppm and a pH level of 7.

Each thermal cycle consisted of a slow heat to a central specimen temperature of 330°C followed by a 7s water quench. Cycle time was around 15 minutes. Due to the fact that the specimens were positioned vertically, the thermal gradient in the furnace prevented a uniform temperature from being achieved along the whole specimen length. Rather the temperature from top to bottom of the specimen varied linearly from 365°C to 290°C.

After each period of 500 thermal cycles, the specimens were removed from the furnace and investigated for cracking at a low magnification (10 to 60x). A rough estimate of crack initiation lifetime was defined as when a full-face hairline crack was visible at the base of the notch. Extrapolations of the long crack growth data were used to further refine when initiation was to have occurred. Any subsequent crack growth after initiation was measured on each side of the specimen, the through depth taken as the average.

### **PRELIMINARY RESULTS**

A typical cross section temperature profile for the top of the specimen is shown on Fig. 1a. This was used to calculate the stress cycle and determine the pseudo-elastic stress amplitude shown on Fig. 1b. Figure 2 shows the typical results of the stress intensity factor analysis using this data and the fatigue notch factor ( $k_f$ ) method outlined in [9]. There is a slight difference in  $\Delta K$  for the specimens with and without primary load. This is due to the plastic zone correction. Note that the R ratio for the specimen with primary load is a function of the crack length.

Times to crack initiation are shown graphically in Fig. 3 where number of cycles to initiation has been plotted against the stress amplitude determined as detailed in [9]. The fatigue design curve for low carbon steel taken from the ASME Boiler and Pressure Vessel Code [1] has been included for comparison. This nominal fatigue design curve has a built in factor of safety of two on stress. A dashed line has been added to the figure to show the effect of removing this conservatism.



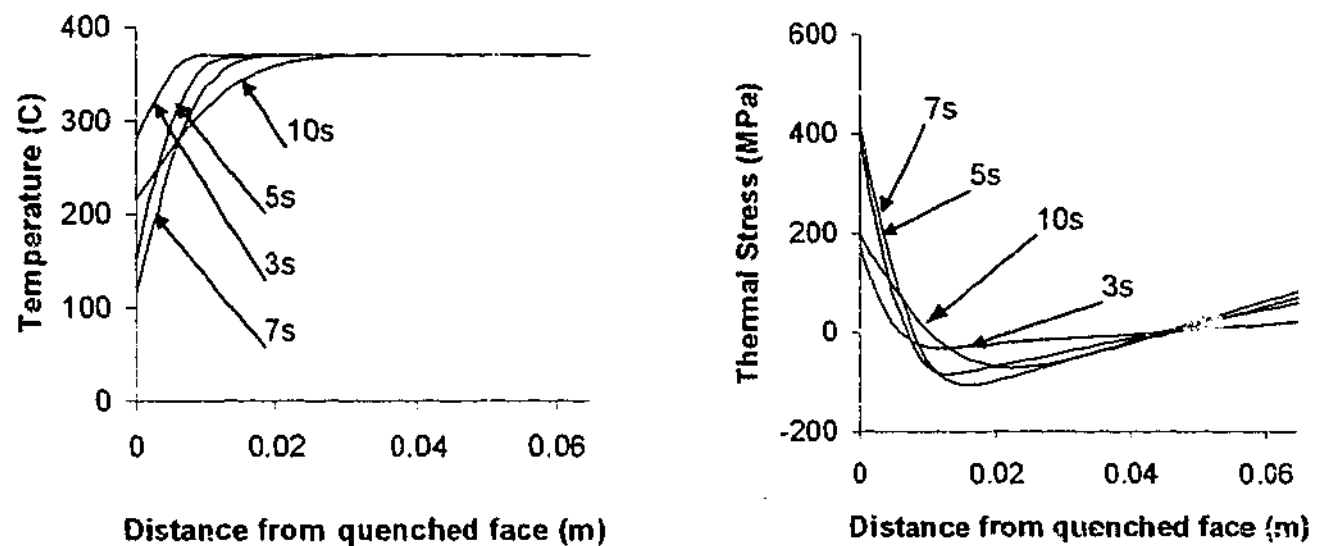


Fig. 1a & 1b: Temperature and pseudo-elastic stress profiles during 7s quench from 370 °C.

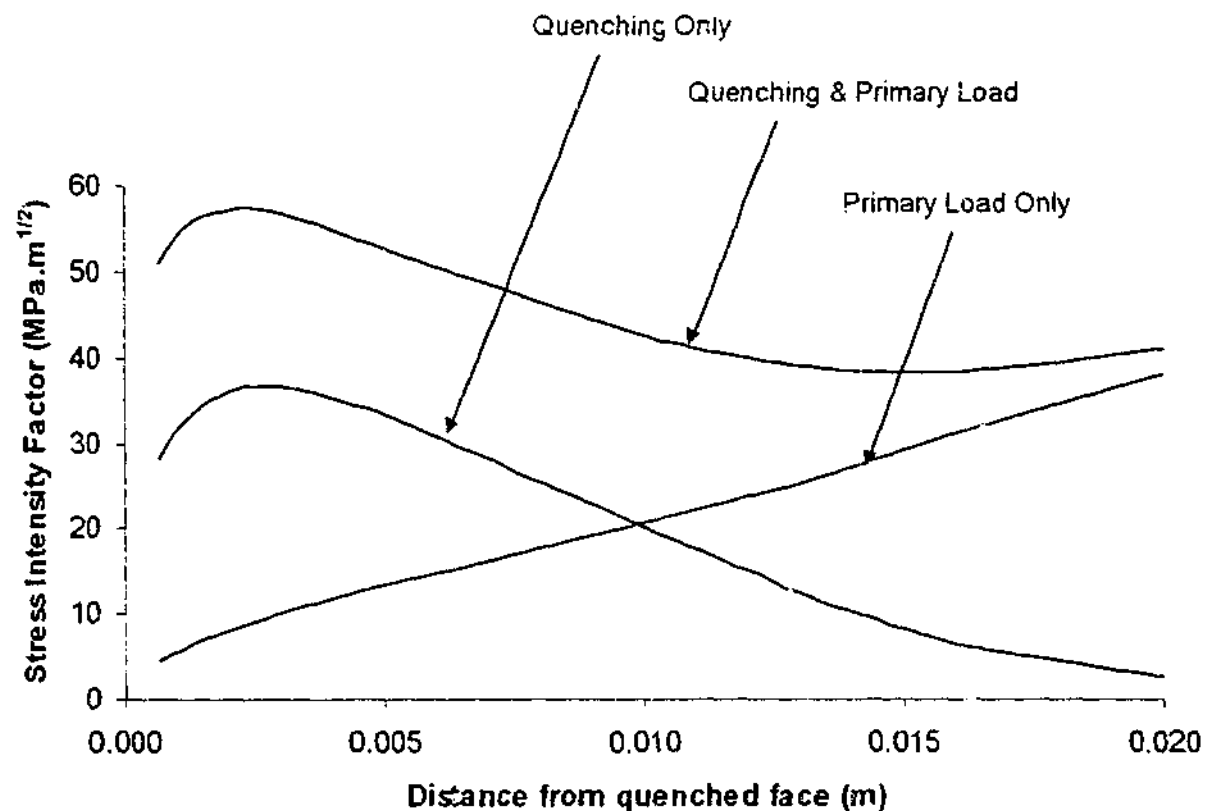


Fig. 2: Maximum stress intensity factor profiles during 7s quench from 370 °C.

Crack growth results are shown on Fig. 4. Stress intensity factors have been plotted against crack growth rate using the R ratio to categorise the data. Both water and air environment crack growth curves for carbon steel taken from the ASME Boiler and Pressure Vessel Code [2] are plotted for comparison.

Testing was discontinued after 10,000 cycles. Pictures of the typical cracks along their length after arrest and of their surface after breaking open the specimen are shown as Fig. 5 and 6.

11. Xu, R.X., Thompson, J.C. and Topper, T.H., Fatigue and Fracture of Engineering Materials and Structures, Vol. 18, 1995, pp.885-895.
12. Kerezsi, B.B., Kotousov, A.G. and Price, J.W.H., "Experimental apparatus for thermal shock investigations", International Journal of Pressure Vessels and Piping 2000; in print.

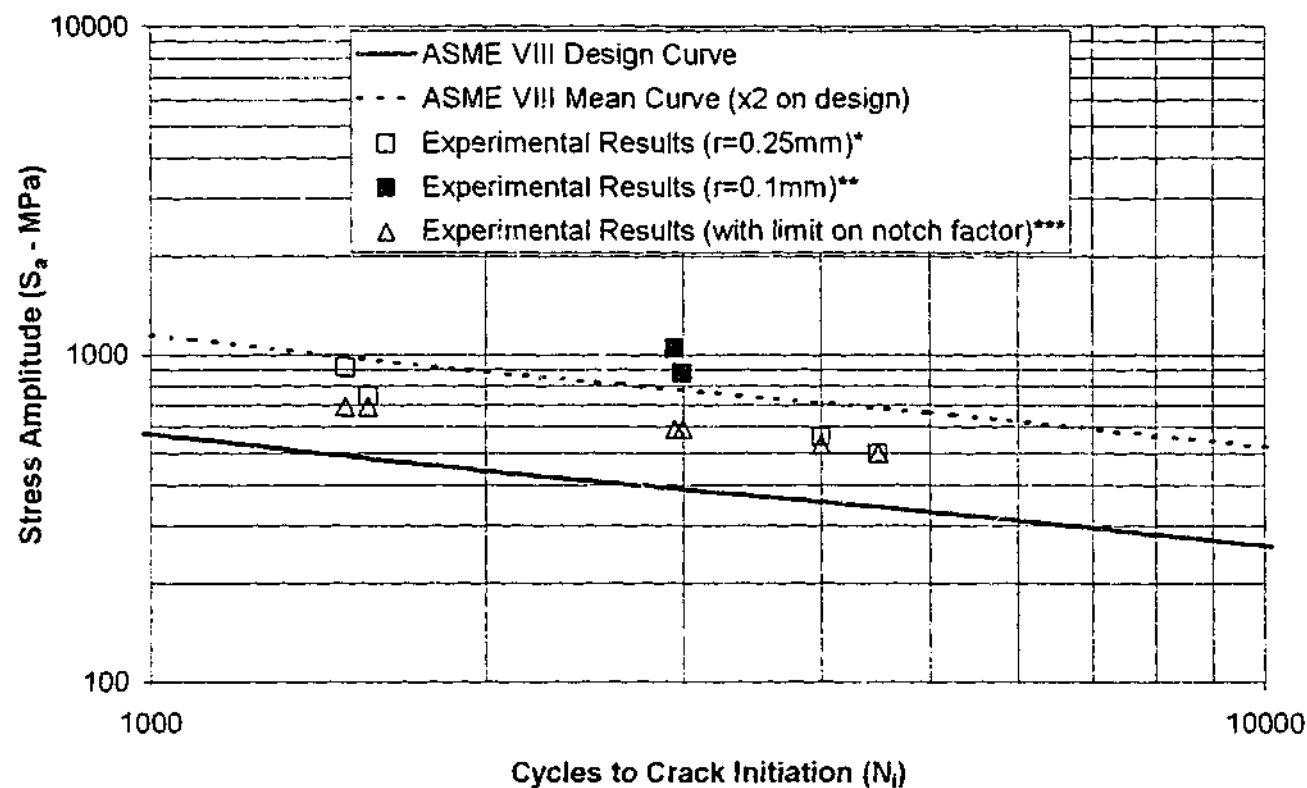


Fig. 3: Crack initiation lifetime

\* No limit on notch factor -  $k_f = 4.7 - 6.6$

\*\* No limit on notch factor -  $k_f = 7.4 - 8.8$

\*\*\* Limit on notch factor applied -  $k_f < 5.0$

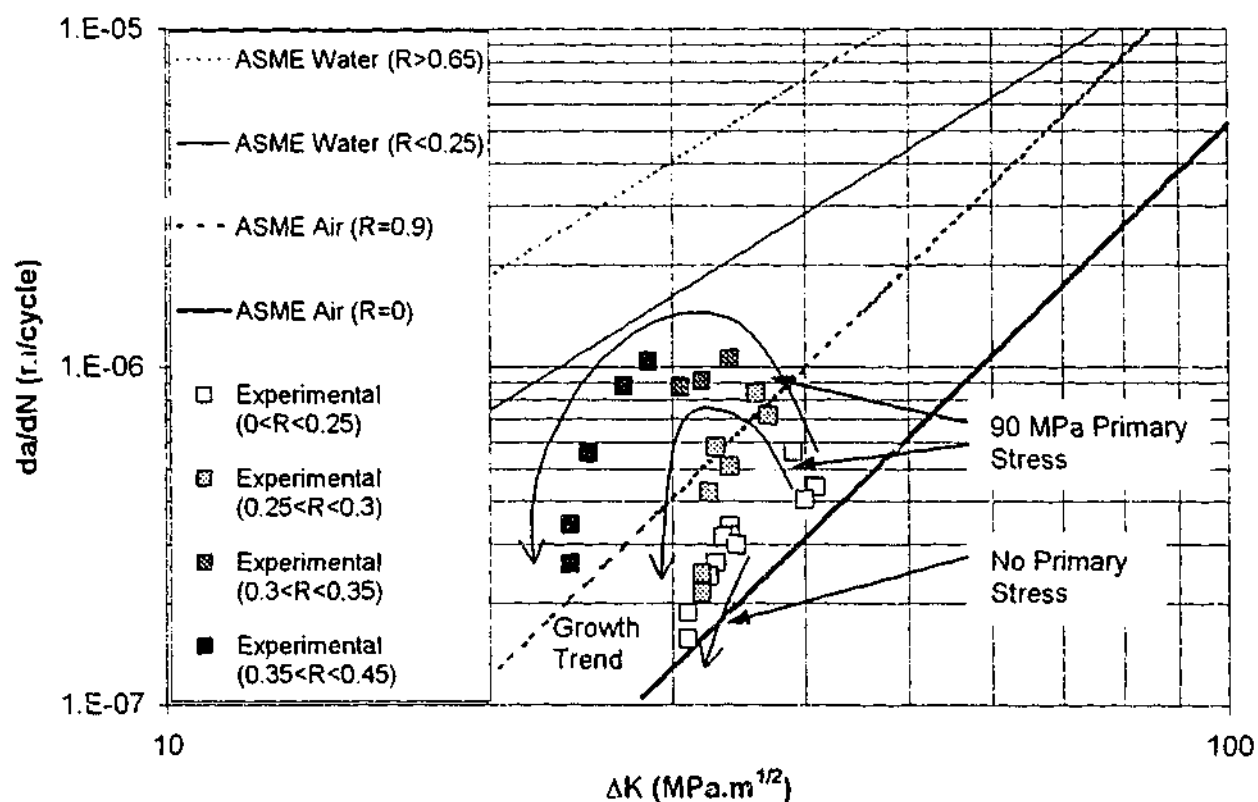


Fig. 4: Crack growth rates as a function of stress intensity factor. Squares correspond to measurements made during testing. The large arrows indicate only trends for individual crack growth - no curve fitting is implied.

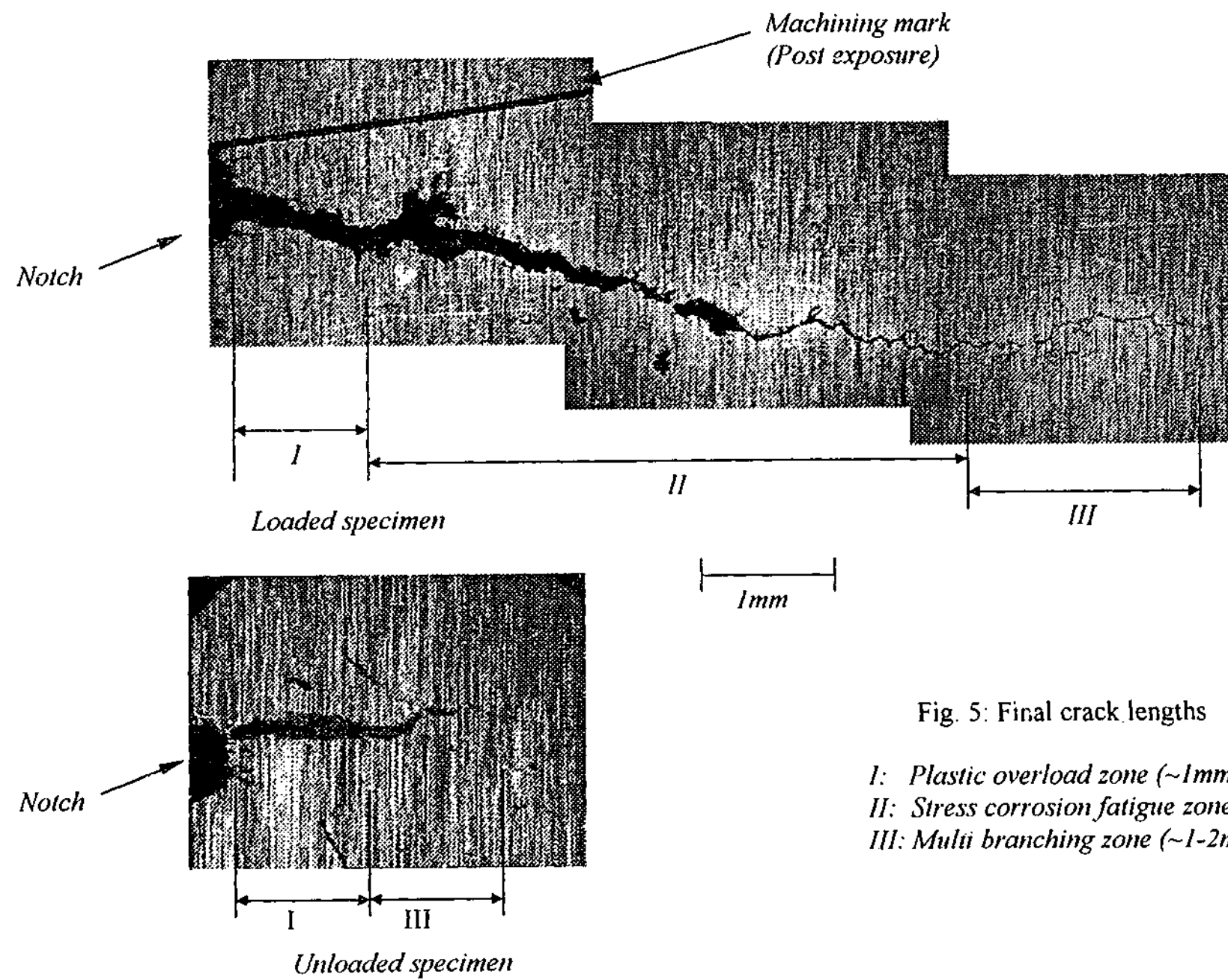
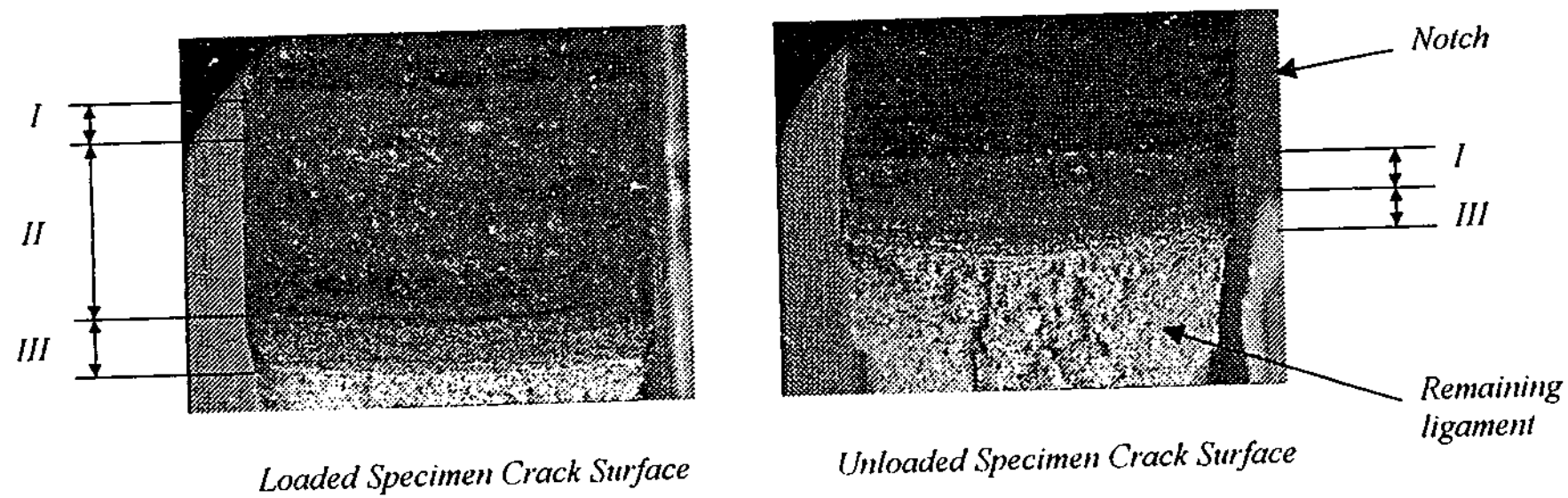


Fig. 5: Final crack lengths

- I: Plastic overload zone (~1mm)*
- II: Stress corrosion fatigue zone (~4mm)*
- III: Multi branching zone (~1-2mm)*



*Fig. 6: Fracture surfaces after opening.*

- I: Plastic overload zone (~1mm)*
- II: Stress corrosion fatigue zone (~4mm)*
- III: Multi branching zone (~1-2mm)*

## DISCUSSION

### Crack Initiation and Growth Relationships

As shown in Fig. 3, the application of a primary load displays little or no effect on crack initiation lifetime. In all of the test cases, the ASME curve gives a conservative estimate of the number of cycles required to initiate fatigue cracks in low carbon steel under thermal shock below creep region temperatures. The ASME curve is even more conservative for the 0.1mm radius notch than for the 0.25mm (see Fig. 3). If however, an upper limit of 5 is taken for the fatigue notch factor  $k_f$ , as suggested in article 5-111 of [1], the additional conservatism can be removed. This may be evidence of the so-called "worst case notch effect" [11]. The effect of applying this limit has been included on Fig. 3.

It should also be noted that the ASME design curve is created with a built-in conservatism of approximately two times on stress. Compared to the "mean curve" with the factor of two removed (represented by the dashed line on Fig. 3), the crack initiation data lies below the line when  $k_f$  is limited to 5. This means that the effect of repeated the thermal shocks in these experiments might be to reduce the fatigue life compared with the isothermal mechanical testing used in the ASME code.

For analysing the growth of cracks, the thermal shock fatigue crack propagation rate can be related to the elastic stress intensity factor, and correlated with the ASME isothermal crack growth data. For all of the plotted points, the ASME water curves provide a conservative result (see Fig. 4). For some points this conservatism is more than an order of magnitude.

From the trend of the results in Fig. 2 and 4, it seems that deceleration of all observed cracks is occurring. For the unloaded specimen, crack growth rates begin decreasing immediately after crack initiation. In contrast, after initiation, the cracks in the loaded specimen experience an increase in crack growth rate as the R-ratio increases. Then, after a period of rapid growth (at around 1mm/1000 cycles), the rate decreases rapidly. This high rate of crack growth, followed by the quick drop off may correspond to the knee in the growth curve as predicted for stress corrosion fatigue by Austen and Walker [7].

### Fractography

Information that can be obtained from the appearance of the crack surfaces shown in figure 6 can provide some insight into the mechanisms of crack growth occurring during the testing. Three regions of crack growth can be seen in the specimen with primary load and two regions are visible in the specimen without. The first millimetre of growth corresponding to initiation in both specimens shows a slightly raised shiny fracture surface. This may be due to the two fracture surfaces rubbing together during cycling. Plastic deformation during the crack initiation could explain this observation. This also means that the crack faces in both specimens would be closed during the unloading part of the cycle.

The second region of growth, visible only on the specimen with primary load is macroscopically smooth and exhibits a large amount of oxide build-up. This region corresponds to the maximum growth rates as shown on Fig. 4. Using the Austen and Walker model [7], the mechanism for growth in this region could be stress corrosion fatigue.

The final region of around 1mm in each specimen indicates the area of crack deceleration. There is less oxide build-up in this region, with the beach marks due to the interrupted testing being clearly visible. Looking at the side view along the crack length shown in Fig. 5, the fracture path in this region seems to be intergranular with multiple branching, indicating that environmental effects are still very important. One suggestion for this change of behaviour is

the longer diffusion paths for corrosion species and the narrowness of the crack. Marshall [12] has previously raised this hypothesis.

### **MAJOR CONCLUSIONS**

Initial results obtained from a test rig developed to simulate the repeated thermal shock conditions produced in operating thermal power station equipment show:

- a) The application of a primary stress has little or no effect on crack initiation lifetime during repeated thermal shock below the creep range. In addition, the thermal shock regime may lower crack initiation times when compared to isothermal air data.
- b) Environmental interaction is highly influential in the growth of thermal shock cracks. Cracks with a low R ratio (no primary stress) show signs of rapid deceleration and cracks with high R ratio show signs of deceleration after a period of environmentally enhanced growth.

### **FURTHER WORK**

Tests analysing the effects of primary loading during thermal shock will continue with a new series of specimens and different load ratios and environments. In addition, a second test rig is currently under development. This rig is fundamentally the same as that used in this work, however the specimen is loaded horizontally in the furnace, meaning all notches in the one test will experience the same temperature environment. This rig will be used to assist in the investigation of the effect of more complicated geometries such as boreholes and to increase the number of cracks studied.

### **ACKNOWLEDGEMENTS**

This work has been completed with the assistance of an Australian Research Council grant with contributions from HRL Technology Ltd, Optima Energy, Western Power, Pacific Power and the Electric Power Research Institute of USA

### **REFERENCES**

1. ASME (American Society of Mechanical Engineers), "ASME Boiler and Pressure Vessel Code, Section VIII, Division 2", ASME, New York, 1998.
2. ASME (American Society of Mechanical Engineers), "ASME Boiler and Pressure Vessel Code, Section XI", ASME, New York, 1998.
3. Wei R.P., and Gangloff R.P. "Environmentally assisted crack growth in structural alloys: perspectives and new directions", Fracture mechanics: Perspectives and directions ASTM STP 1020, American Society for Testing and Materials, Philadelphia, 1989, pp. 233-264.
4. BS (British Standards), "Guide on methods for assessing the acceptability of flaws in fusion welded structures, BS7910", BS, London, 1999.
5. API (American Petroleum Institute), "Fitness for service, API recommended practice 579", first edition, API, Washington DC, 1999.
6. Wei R.P. and Landes J.D., "Correlation between sustained-load and fatigue crack growth in high strength steels", Materials Research and Standards, July 1969, pp. 25-46.

7. Austen I.M. and Walker E.F., "Quantitative understanding of the effects of mechanical and environmental variables on corrosion fatigue crack growth behaviour", The influence of environment on fatigue, I Mech E Conference publications, London, 1977, pp. 1-10.
8. Gabetta G., Rinaldi C. and Pozzi D., "A model for environmentally assisted crack growth rate", Environmentally assisted cracking: Science and engineering ASTM STP 1049, American Society for Testing and Materials, Philadelphia, 1990, pp. 266-282.
9. Kerezsi B.B., Kotousov A.G. and Price J.W.H., "Experimental apparatus for thermal shock investigations", International Journal of Pressure Vessels and Piping, 2000, in print.
10. Australian Standards. "Steel plates for pressure equipment, AS 1548-1995", Standards Australia, Homebush, NSW, 1995.
11. Prater, T.A. and Coffin, L.F., "Notch fatigue crack initiation in high temperature water environments: Experiments and life prediction", Journal of Pressure Vessel Technology, Vol. 109, 1987, pp. 124-134.
12. Marshall, P., "The influence of environment on fatigue", in: Skelton, Fatigue at High Temperatures, Applied Science Publishers, Elsevier Science Publishing, 1983, pp. 259-303.